

City Research Online

City St George's, University of London

Citation: Ciofalo, M. (1992). Large-eddy simulation of turbulent flows with heat transfer in simple and complex geometries. (Unpublished Doctoral thesis, City, University of London)

This is the accepted version of the paper.

This version of the publication may differ from the final published version. To cite this item please consult the publisher's version.

Permanent repository link: https://openaccess.city.ac.uk/id/eprint/29072/

Copyright and Reuse: Copyright and Moral Rights remain with the author(s) and/or copyright holders. Copies of full items can be used for personal research or study, educational, or not-for-profit purposes without prior permission or charge, unless otherwise indicated, provided that the authors, title and full bibliographic details are credited, a hyperlink and/or URL is given for the original metadata page and the content is not changed in any way. For full details of reuse please refer to City Research Online policy.

City Research Online: http://openaccess.city.ac.uk/ publications@citystgeorges.ac.uk

LARGE-EDDY SIMULATION OF TURBULENT FLOWS WITH HEAT TRANSFER IN SIMPLE AND COMPLEX GEOMETRIES

by

Michele Ciofalo

A Thesis submitted to The City University of London
for the degree of Doctor of Philosophy in Mechanical Engineering

Department of Mechanical Engineering and Aeronautics
Thermo-Fluids Engineering Research Centre

1992

To my child Elena Aziza,
who is three, is turbulent,
and is thoroughly unpredictable



DECLARATION

No portion of the work referred to in this thesis has been submitted in support of an application for another degree or qualification of this or any other university or other institution of learning, either in the U.K. or abroad.

AKNOWLEDGEMENTS

A significant part of the work reported in this thesis was carried out while the author was spending two consecutive academical years at the City University, sponsored first by a NATO-CNR grant (Engineering and Architecture Sciences 1985) on 'Theoretical Study of Turbulent Flows by Large-Eddy Simulation and Application to Heat Transfer Problems', and then by a NATO advanced fellowship (IRT Award 0769/86) on 'Application of Large-Eddy Simulation to Heat Transfer Problems'.

Professor Michael Collins has consistently pursued for several years the idea that Large-Eddy Simulation should become a computational tool for engineering problems and not only a subject of theoretical interest; this work is largely an offspring of this idea. The author is indebted with him for his uninterrupted interest, encouragement, and suggestions.

The development team of the FLOW3D code at Harwell provided, since the beginning of the present research, not only the computational means required - well beyond the scope of existing collaborative agreements - but also interest, advice and friendly help; the author is especially grateful to Dr Ian Jones, Dr. Alan Burns, Dr. Nigel Wilkes and Mrs. Suzanne Simcox for several fruitful discussions which have resolved more than one impasse. He is also grateful to Dr. Andrew Splawsky for a discussion on wall boundary conditions in LES.

The simulations for the crossed corrugated air heaters were in the context of a research project funded by PowerGen, U.K.; the author wishes to thank Mr. Peter Chew for his clarifying comments on this rather excruciating geometry and Dr. Tadek Fodemski for his brave initial work on it.

Several other people have contributed, directly or indirectly, to this work. Among them, the author wishes to mention Dr. Tassos Karayiannis, Dr. Frank Henry and Prof. Jan Stasiek. He is also grateful to Professor Elio Oliveri, Dean of the Faculty of Engineering, and to the other colleagues at the University of Palermo who have shown interest in this project and often have contributed to support the (non negligible!) computational expenses required. Finally, the author wishes to thank Giuseppe Palazzolo and Gaetano Perrone for their help with the computations and the related graphics.

ABSTRACT

Turbulence is the last great unsolved problem of classical physics
[R. Feynman]

Some basic aspects of turbulence, transition to turbulence, and turbulence modelling, are summarized in **Chapter 1** (Introduction). Emphasis is put on the increasing understanding of turbulent phenomena made possible by recent advances in the theory of dynamical systems; on the concept of "coherent structure"; and on the parallel evolution of computing power and computational fluid dynamics.

Chapter 2 is a survey of the turbulence modelling technique known as Large Eddy Simulation (LES). The equations governing fluid flow and scalar transport are introduced; the direct simulation of turbulent flows and its limitations are briefly outlined; and the concept of LES, with the related topics of decomposition, filtering and subgrid modelling, is discussed. The state of the art in LES is reviewed in the last three sections, under the separate headings of proposed subgrid models; wall boundary conditions; and applications presented in the literature. An attempt is made to give the most complete and updated possible account of the subject; work carried out from the early 'Seventies up to now is considered. Emphasis is put more on physical models and corresponding performances than on numerical methods and computational details.

In **Chapter 3**, the finite-volume numerical techniques used in the present work are presented and discussed. Emphasis is put on those aspects and options which bear more relevance for the accuracy and quality of the results, such as the pressure-velocity coupling algorithm, the discretization of advective terms and the treatment of centred (co-located), body-fitted grids. The architecture and the basic features of the computer code Harwell-FLOW3D, Release 2, are outlined, while the modifications introduced in order to implement the Smagorinsky subgrid model and the appropriate boundary conditions for LES are described in detail.

In Chapters **4 - 6** results are presented and discussed for the basic geometries studied.

Chapter 4 deals with the flow between indefinite parallel plates (plane channel), one of which heated with a uniform heat flux. For this basic geometry, a detailed study is presented on the influence of numerical options (grid size, time step and time-stepping method, pressure-velocity coupling, discretization of the advective terms); model parameters (Smagorinsky constant, subgrid Prandtl number, near-wall damping); Reynolds number; and alternative wall boundary conditions. The issues of initial conditions, numerical transients and statistical processing of the results are also discussed with some depth.

In **Chapter 5**, computations are presented for a plane channel having one of the walls roughened by transverse square ribs. An extensive literature review of experimental and numerical studies on this geometry is included. The parametrical study is limited here to the influence of grid size and Reynolds number; LES results are presented in detail for a reference case, and are compared with experimental flow and heat transfer data.

Chapter 6 is dedicated to the geometry of cross-corrugated ducts, representative of storage-type air preheaters for fossil-fuelled power stations. Flow and heat transfer predictions from direct simulation and LES are presented; they are compared with experimental results and with numerical predictions obtained by a standard and a low-Reynolds number version of the k-ε turbulence model.

Finally, **Chapter 7** summarizes the main conclusions which can be drawn from the above studies. Emphasis is put on the basic issue of LES applicability to engineering problems of practical interest, and of its feasibility using a commercial, general-purpose (though highly sophisticated) computer code. A critical comparison with more conventional turbulence modelling approaches is outlined, and 'weak spots', or issues requiring further clarifications, are pointed out for future studies.

The work includes an extensive **bibliography** with almost 400 references, and an **appendix** on the tensorial formulation of the governing equations of fluid dynamics in general domains.

TABLE OF CONTENTS

TITLE ..... page 1
DEDICATION ..... page 2
DECLARATION ..... page 3
AKNOWLEDGEMENTS ..... page 4
ABSTRACT ..... page 5
TABLE OF CONTENTS ..... page 7
NOMENCLATURE ..... page 9

CHAPTER 1 - INTRODUCTION

1.1 Turbulence ..... page 13
1.2 Transition to turbulence ..... " 17
1.3 Coherent structures in turbulent flows ..... " 20
1.4 Turbulence modelling and direct or Large-Eddy Simulation" 23
Figures of Chapter 1 ..... " 27

CHAPTER 2 - LARGE-EDDY SIMULATION: THEORETICAL FRAMEWORK AND STATE-OF-THE-ART

2.1 Governing equations..... page 29
2.2 Direct Simulation ..... " 35
2.3 Large-Eddy Simulation and spatial filtering ..... " 42
2.4 Subgrid scale models for Large-Eddy Simulation ..... " 48
2.5 Wall boundary conditions for Large-Eddy Simulation ... " 64
2.6 Applications presented in the literature ..... " 70
Figures of Chapter 2 ..... " 86

CHAPTER 3 - THE HARWELL-FLOW3D CODE AND ITS APPLICATION TO LARGE-EDDY SIMULATION

3.1 Code overview ..... page 90
3.2 Numerical methods ..... " 100
3.3 Implementation of a subgrid model and of boundary conditions ..... " 123
Figures of Chapter 3 ..... " 133

CHAPTER 4 - APPLICATION TO TURBULENT FLOW WITH HEAT TRANSFER IN A PLANE CHANNEL

4.1 Introduction and literature review ..... page 137
4.2 Model and methods ..... " 138
4.3 General issues ..... " 143
4.4 Detailed results for a reference case ..... " 147
4.5 Influence of Re, model, grid and computational options " 152
4.6 Influence of wall boundary conditions ..... " 164
4.7 Conclusions ..... " 166
Figures of Chapter 4 ..... " 169

CHAPTER 5 - APPLICATION TO TURBULENT FLOW WITH HEAT TRANSFER IN A RIBBED CHANNEL

5.1 Introduction and literature review ..... page 215
5.2 Model and methods ..... " 223
5.3 Results and discussion ..... " 226
5.4 Conclusions ..... " 234
Figures of Chapter 5 ..... " 236

CHAPTER 6 - APPLICATION TO TURBULENT FLOW WITH HEAT TRANSFER IN A CROSSED CORRUGATED HEAT EXCHANGER GEOMETRY

6.1 Introduction and literature review ..... page 254
6.2 Model and methods ..... " 262
6.3 Results and discussion ..... " 270
6.4 Conclusions ..... " 278
Figures of Chapter 6 ..... " 281

CHAPTER 7 - CONCLUSIONS AND RECOMMENDATIONS

7.1 General aspects ..... page 323
7.2 Subgrid model and boundary conditions ..... " 325
7.3 Numerical methods and computational aspects ..... " 327
7.4 Recommendations for further work ..... " 330

REFERENCES ..... page 333

APPENDIX A - Definitions and main formulae of tensor calculus page 360 (A.1)

NOMENCLATURE

Note: only the most relevant and recurrent symbols were included here.

A^+	near-wall damping constant
A_p	diagonal coefficient in linearized equations
a	main flow direction in cross-corrugated heat exchangers
a_{nn}	off-diagonal coefficients in linearized equations
C_f	(Fanning) friction coefficient
C_μ	constant in Prandtl-Kolmogorov relation
c_p	specific heat at constant pressure
c_s, c_s^*	constants in sub-grid models
D, D^*	near-wall damping factors
D_e	hydraulic diameter (=4δ in a plane channel)
E, F	constants in logarithmic laws of the wall for u and T
F, F_i	body force
f	(D'Arcy-Weisbach) friction coefficient
G	filtering function
H	channel height
H_i	internal corrugation height in cross-corrugated heat exchangers
h	rib height
i, j, k	indices of the generic control volume (grid point)
I, I_i	convective-diffusive flux of a generic scalar
J	enthalpy
k	turbulent kinetic energy
$\tilde{k}$	unresolved (sub-grid) turbulent kinetic energy
L	channel length; sinusoid length (cross-corrugated geometry)
l	turbulence length scale
LETOT	Large Eddy TurnOver Time, δ/u_τ
m_p	local mass source residual
$\dot{M}$	overall mass flow rate
N_p	number of control volumes in grid
N_t	number of time steps
Nu	Nusselt number
Nu_{av}	average Nusselt number in cross-corrugated heat exchangers
n	number of LETOT's
p_{stat}	static pressure
p	apparent pressure, $p_{stat}+(2/3)\mu S_{kk}$ (=p_{stat} in incompr. fluids)
P	equivalent pressure, $p+(2/3)\rho k$ (in LES: $\hat{P} = \hat{p}+(2/3)\rho\tilde{k}$);
	corrugation pitch in cross-corrugated heat exchangers

P_1	pitch of transverse ribs in rib-roughened ducts
P^*	periodic component of P
$\mathbf{P}$, P_i	surface force
P_{ij}	total stress tensor
P_c	cell Peclet number, $u\,\Delta x/\Gamma$
$\mathbf{q}$, q_i	heat flux vector
q_w	wall heat flux
Re, Re_D	Reynolds number, UD_e/ν (based on hydraulic diameter)
Re_δ	Reynolds number, $U\delta/\nu$ (based on channel half-height)
S	generic source term
S_{ij}	strain rate tensor, $(\partial u_i/\partial x_j + \partial u_j/\partial x_i)/2$
S^2	quadratic invariant $2S_{ij}S_{ij}$
s_Q, s_0, s_m, s_p	various coefficients and terms of linearized equations
s	wall thickness in cross-corrugated heat exchangers
T	temperature
T_M	coefficient of proportionality between wall shear stress and near-wall parallel component of velocity
t	time
U	average velocity in channel
$\mathbf{u}$, u_i	local velocity
u, v, w	velocity components along x, y, z
u_τ	friction velocity, $(\lvert\tau_w\rvert/\rho)^{1/2}$
v_{random}	rms value of fluctuating velocity
W	width of the computational domain
x_i; x, y, z	physical-space coordinates
y	distance from nearest wall
y_T	thickness of thermal sublayer
y_v	thickness of viscous sublayer

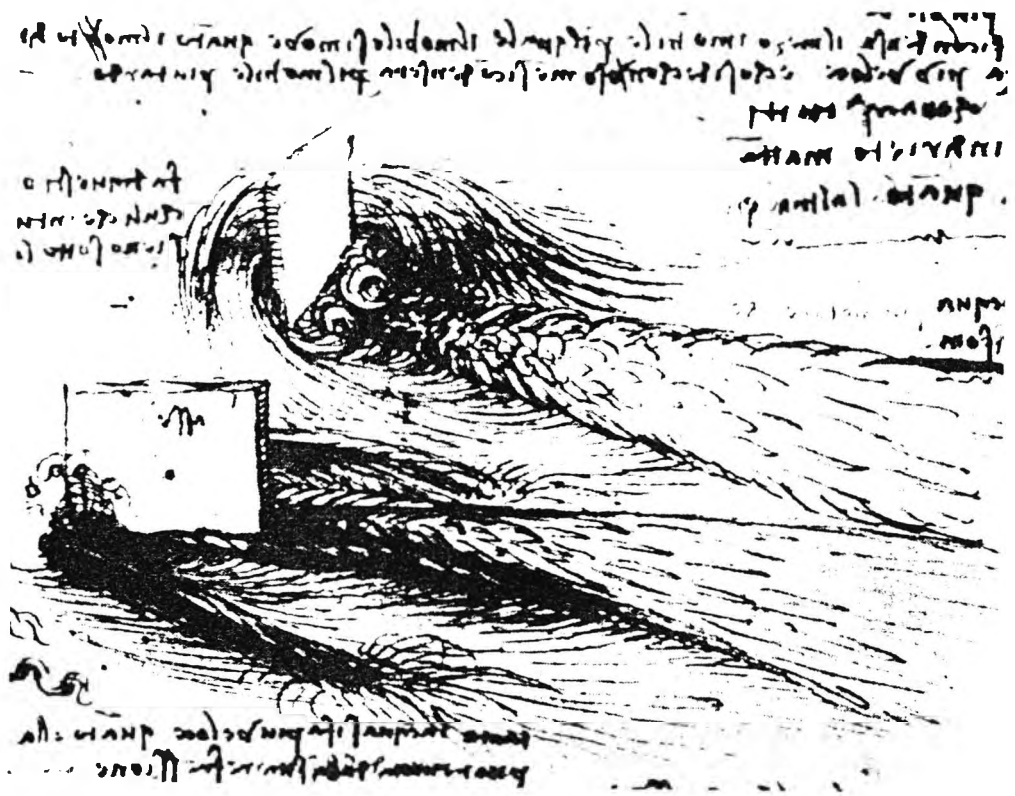
Greek letters

α	thermal diffusivity, $\lambda/(\rho c_p)$
α_s	sub-grid thermal diffusivity
ß	bulk viscosity
Γ	dynamic diffusivity of a generic scalar
δ	channel half-height, H/2
δ_{ij}	Kronecker delta
Λ	length scale in sub-grid models
Δx_i; $\Delta x, \Delta y, \Delta z$	dimensions of control volumes in grid

Δt	time step
ε	dissipation of turbulent kinetic energy
ε_M	total mass source residual
Θ	corrugation angle in cross-corrugated heat exchangers
κ	Von Karman constant (~0.42)
λ	thermal conductivity
μ	dynamic viscosity
μ_s	sub-grid dynamic viscosity
ν	kinematic viscosity, μ/ρ
ν_s	sub-grid kinematic viscosity
ξ	grid stretching factor along y
ρ	density
σ	Prandtl number, $c_p\mu/\lambda$
σ_s	sub-grid Prandtl number
σ_t	turbulent Prandtl number
σ_{ij}	anisotropic part of stress tensor
τ_w	wall shear stress
τ_0	equilibrium wall shear stress, $\delta\,\Delta p/\Delta x$
τ_{ij}	Reynolds stresses, $-\rho\overline{u_i'u_j'}$
$\tilde{\tau}_{ij}$	sub-grid Reynolds stresses, $-\rho\widehat{\tilde{u}_i\tilde{u}_j}$
ϕ	characteristic angle in "shifted" and "ejection" wall BC
ψ	stream function
ω	vorticity
ω_{ij}	vorticity tensor, $(\partial u_i/\partial x_j - \partial u_j/\partial x_i)/2$

Averages and fluctuations

Q	generic scalar
$\hat{Q}$	filtered value of Q
$\tilde{Q}$	unresolved (sub-grid) component, $Q-\hat{Q}$
$\overline{Q}$	time or ensemble average
Q'	fluctuation $Q-\overline{Q}$
Q'_{rms}	root mean square value of Q', $\overline{(Q'^2)}^{1/2}$
$\langle Q\rangle$	ensemble average over "homogeneous" directions
Q''	fluctuation $Q-\langle Q\rangle$
Q''_{rms}	root mean square value of Q", $\langle Q''^2\rangle^{1/2}$
$\overline{Q''_{rms}}$	time average of Q''_{rms}
$\langle\langle Q\rangle\rangle$	volume average over the whole computational domain



Leonardo da Vinci, two studies on water eddies caused by obstacles

"Observe the motion of the surface of the water, which resembles that of hair, which has two motions, of which one is caused by the weight of the hair, the other by the direction of the curls; thus **the water has eddying motions, one part of which is due to the principal current, the other to the random and reverse motion**"

[Leonardo da Vinci, 1510; transl. by U.Piomelli reported in Lumley, 1992]

CHAPTER 1 - INTRODUCTION

1.1 Turbulence

What is your substance, whereof are you made,
That millions of strange shadows on you tend?
[Shakespeare, Sonnet LIII]

Since the pioneering work of Osborne Reynolds [1883], over a century of efforts has been devoted by scientists and researchers all above the world to the understanding of one of the most complex and fascinating phenomena in nature, the turbulent motion of fluids. The British physicist Sir Horace Lamb said in 1932 "I am an old man now, and when I die and go to Heaven I would like to be enlightened on two subjects: quantum electrodynamics and turbulence. And I am rather optimistic about the former". Lamb's attitude was amply justified; sixty years later the questions still open on the turbulent motion of fluids are many.

Most fluid motions, both in Nature and under artificial conditions, are turbulent. There are good practical reasons to be interested in the problem. Much of the energy consumed by machines and devices in which fluid flow occurs is spent to overcome the resistance caused by turbulence; on the other hand, turbulence is often desirable in order to promote mixing and mass or heat transfer.

The definition of "turbulent" flow is often restricted to high-Reynolds number flows in which the small-scale motions become completely independent of the boundary conditions. More generally, a flow can be defined as turbulent whenever the flow variables exhibit a chaotic dependence on time. However, the notion of turbulence can be specified more rigorously only on the basis of recent achievements in the theory of dynamical systems and transition to chaos.

A full mathematical description of turbulence has long baffled theorists. Turbulence is characterized by unpredictable motions of the fluid; the key to this erratic and chaotic behaviour is "sensitivity to initial conditions", a term first introduced by Ruelle [1978] to describe systems in which small changes in initial conditions lead to large and unpredictable changes in the long-term evolution of the system. Two trajectories (either in the physical three-dimensional space or in the abstract phase-space) which start close to

each other do not remain close; the difference between them may grow exponentially in time so that they rapidly lose any relationship to each other. This means that computations of long-range behaviour will be seriously affected by small errors and uncertainties. Furthermore, when a trajectory in phase-space winds close to its initial point, its future evolution will, in general, be completely different from its past history; in that sense, no long-range pattern can be discerned. On the other hand, an experimentalist trying to reproduce the detailed behaviour of such a system will try in vain, for unavoidable small errors in the initial data (even in the absence of significant external noise) will conspire to produce a different pattern at each run.

Thus, both experimentally and computationally such a system will be described as 'chaotic', or 'irregular', and only in a statistical sense reproducibility will be attained. This is often mentioned as the 'butterfly effect', after the only apparently paradoxical remark made by Lorenz [1979] that a butterfly flapping its wings in Brazil may well produce large-scale effects on next month's weather in Texas, thus making precise long-range weather forecast an utopic goal!

Now, fluids are very complicated systems having many (or rather, infinite) degrees of freedom, and their behaviour in the appropriate phase space is difficult even to conceive, let alone to model and simulate accurately. Nevertheless, the question arises whether the basic mechanism underlying the observed 'chaotic' behaviour is one that does not require consideration of many degrees of freedom; as a matter of fact, certain simple dynamical systems, described by just three or few more differential equations, display a chaotic and erratic behaviour which is strongly reminiscent of turbulence in fluids and often possesses many of its essential features [Yorke and Yorke 1981].

One such model was studied by Lorenz [1963] in connection with the instability of free convection between parallel plates. Lorenz found that, under some severe approximations, the behaviour of the fluid would be described by a set of just three ordinary nonlinear differential equations involving a single basic controlling parameter R (related with a Rayleigh number). For R larger than a critical value, there are no stable steady or periodic solutions; computer experiments yield irregularly oscillating solutions, in which no long-range pattern can be identified, and which display several characteristics of turbulent fluid flows (including sensitivity to initial conditions, broad-range spectrum, and intermittency). Since Lorenz's

work, several more 'simple systems with complex behaviour' have been proposed, and their properties investigated, by different authors, see for example Nicolis and Prigogine [1987].

For 'simple' dynamical systems such as that described by the Lorenz equations, the behaviour of the system in phase space can be investigated directly by numerical simulations. For any given values of the parameters controlling the dynamical system, there is a more or less complicated region of the phase space that attracts all nearby states; starting from arbitrary initial conditions, the system will eventually end up on this set, wander through it and - given sufficient time - pass arbitrarily close to every point of the attractor. A rigorous definition of an attractor is given and discussed, for example, by Lanford [1981].

The geometric shapes of the Lorenz, and related, attractors have received considerable attention. Ruelle and Takens [1971] were the first to use the term 'strange attractor' for any attractor of a dynamical system which is i) bounded, ii) connected, and iii) looks 'strange', i.e. is neither a point (steady-state solution) nor a periodic orbit, or limit cycle (periodic solution). Considerable insight into the nature of such 'strange attractors' has come from the theory of fractal objects, first developed by Benoist Mandelbrot [1977]; strange attractors possess a fractional dimension and are self-similar at all scales. Techniques such as that of Poincare's 'return maps' [McDonough et al. 1984.a] can be applied in order to investigate their properties. The concept of 'structural stability' can be used to show that, in many cases, the topological nature (if not the fine details) of a strange attractor do not change if the equations describing the dynamical system are slightly perturbed; this implies that the behaviour of the system is qualitatively stable and thus will not be affected by details of the numerical procedure, or of the experimental technique, used to investigate it. A strictly related term is that of 'genericity'.

In this context, an important role is played by the theory of dissipative systems. These are systems possessing some sort of 'frictional' mechanism by which energy is dissipated, and kept in a dynamical-equilibrium state by some sort of 'energy' input from the environment (by contrast with conservative systems of Hamiltonian mechanics, which preserve the total energy even in the absence of exchanges with the environment). Only dissipative systems are structurally stable and thus possess an 'intrinsic' dynamic; by contrast, hamiltonian systems are structurally unstable, and thus not 'generic', as any small dissipative terms will change their long-term behaviour, i.e. the topological nature of their attractor in phase-space (for example, a weak

friction in a pendulum turns the attractor from a limit cycle into a fixed point, i.e. changes the system's asymptotic behaviour from periodical oscillations to rest in the equilibrium position). Also, it can be shown [Nicolis and Prigogine 1987] that only dissipative systems, which contract volume in phase-space, can possess strange attractors in the sense of Ruelle and Takens.

Starting basically from the strong analogy between the behaviour of the 'simple' dynamical systems discussed above and that of a fluid in turbulent motion, Ruelle and Takens [1971] suggested the following fundamental picture of turbulence:

"The object which accounts for turbulence is an attractor or a few attractors, of reasonably small dimension, embedded in the very large-dimensional state space of the fluid system. Motion on the attractor depends sensitively on initial conditions and this sensitive dependence accounts for the apparently stochastic time dependence of the fluid".

Indeed, it has been established that several partial differential equations possess global attractors which are embedded in finite-dimensional "inertial manifolds" of function space. On these manifolds, the system's dynamics are formally representable by finite sets of ordinary differential equations. This has been well proved for a variety of closed and (relatively) simple flow phenomena, including Rayleigh-Benard convection and Taylor-Couette flow [Swinney and Gollub 1981.a; Campbell and Rose 1983].

Although a rigorous mathematical proof that this reduction is possible for the three-dimensional Navier-Stokes equations does not exist yet, several attempts to reconduct turbulent phenomena to finite-dimensional dynamical systems have been presented in the recent literature. For example, following a suggestion by Lumley, Aubry et al [JFM **192**, 115-173, 1988] applied the orthogonal decomposition technique to the near-wall flow in a turbulent boundary layer; they expanded the instantaneous flow field in empirical eigenfunctions (shaped as streamwise rolls) and truncated the representation to obtain a low-dimensional set of just 10 ordinary differential equations. The dynamics of the system exhibited many of the empirically well known characteristics of near-wall turbulent flows, including intermittency and ejection-bursting events (see following sections).

Thus, the link between fluid turbulence and the chaotic behaviour of dynamical systems involving a finite number of degrees of freedom appears to be much more than a generic analogy.

Unfortunately, very recent results by Keefe et al [JFM **242**, 1-29, 1992] suggest that Ruelle and Takens were probably a bit too optimistic as regards the dimension of attractors of general turbulent flows. The authors limited themselves to turbulent plane Poiseuille flow at moderate Reynolds numbers; by conducting very long direct simulations and computing the spectrum of the associated Ljapunov exponents, they were able to show that this dimension cannot be far from 780! This, indeed, supports the view that turbulent flows do possess finite-dimensional attractors; but the huge dimension of these rules out the notion that the global dynamics of turbulent flows can be attributed to the interaction of "a few" degrees of freedom.

1.2 Transition to turbulence

Turbulence is the gateway through which large fluid masses in ordered motion march to their heat-death doom
[C.F. von Weizsäcker]

Although the quantitative study of fluid motion began over a century ago, and the equations governing this phenomenon are now well known, the transition from laminar to turbulent flow has been a rather enigmatic phenomenon until recently. The difficulty is in the instability of the system of nonlinear equations describing the mass, momentum and energy balance of the fluid. These equations can be linearized and solved for systems close to thermodynamic equilibrium conditions, but far from equilibrium the solution is not, in general, unique and cannot be computed exactly [Swinney and Gollub 1978].

For any fluid dynamic system, at sufficiently low Reynolds numbers a single stable solution, either stationary or periodic oscillatory, exists, towards which the system will tend asymptotically independent of the initial conditions. As the Reynolds number increases, a critical value Re_c is reached beyond which the solution becomes unstable and a new type of motion appears. The low-Reynolds number solution reflects the spatial and time symmetry of the boundary conditions; transition to the second type of motion is accompanied by the breaking of this symmetry. As the Reynolds number increases, the motion becomes irregular in space and exhibits a chaotic dependence on time (turbulence). Nevertheless, the system is still a deterministic one and is governed by the same equations holding in the laminar regime; paradoxical as this may seem, it is a consequence of the system nonlinearity that the governing equations can have a solution so complex as not to look like the result of a deterministic process.

The onset of turbulence in a fluid as the Reynolds number increases is preceded by the appearance of instabilities which generally occur without any apparent order in complex flows, but may exhibit a clearly recognizable and repeatable sequence in geometrically simpler situations. It has been clear for some time that, somehow, the superposition of these instabilities is responsible for the appearance of chaos and turbulence. Several experimental and theoretical studies have been devoted to the understanding of the link between instabilities and turbulence. The former include, for example, the investigations on Couette flow between coaxial cylinders initiated by Taylor in the late Twenties. The latter are based on the mathematical theory of the stability of dynamical systems, which includes linear and nonlinear analysis techniques. As the phenomenon of turbulence is intrinsically related to the nonlinear nature of the equations of motion, nonlinear methods are obviously the most appropriate; however, they present a formidable complexity even for systems undergoing a sequence of two instabilities.

One of the first theoretical scenarios for transition to turbulence was given by Landau [Landau 1944; Landau and Lifschitz 1959]. He started from the Navier-Stokes and continuity equations under the assumption of time-independent boundary conditions, assumed that for sufficiently low Reynolds numbers Re a stable steady-state solution $\mathbf{v}_0(\mathbf{x})$ existed, and investigated the stability of this steady flow as Re was increased. The deviation from steady flow, $\mathbf{v}_1(\mathbf{x},t) = \mathbf{v}(\mathbf{x},t) - \mathbf{v}_0(\mathbf{x})$, obeys differential equations which can be linearised if $\mathbf{v}_1$ is assumed to be small enough. Thus, by separation of variables one is left with solutions of the form:

$$\mathbf{v}_1(\mathbf{x},t) = \mathbf{v}_1(\mathbf{x}) \exp(i\gamma t) \qquad (1.1)$$

in which γ is a complex eigenfrequency, $\omega+i\sigma$. If all eigenfrequencies have positive imaginary parts, all deviations from steady flow die away with time and the steady flow is stable. For Re increasing beyond some critical value Re_1, one eigenfrequency, say $\omega_1+i\sigma_1$, may cross the real axis; in this case a time-dependent, oscillatory mode with frequency ω_1 will appear in the flow. Now, Landau assumed that, for Re further increasing beyond Re_1, a second critical value Re_2 would be reached at which the new (oscillatory) solution becomes in turn unstable to perturbations with a new characteristic frequency, say ω_2. Thus for $Re>Re_2$ one would have two sustained modes at frequencies ω_1 and ω_2, generally unrelated and thus incommensurable, corresponding to a quasi-periodic flow which would not exhibit any time periodicity and would

thus appear quite complex and unpredictable. As Re is further increased, more and more new frequencies ω_3, ω_4 etc. would enter the game, giving the flow a more and more complex, and apparently 'chaotic', behaviour. Landau also suggested that the intervals between successive critical Reynolds numbers would be smaller and smaller, in relation to the fact that the new modes would be progressively smaller in scale. Thus, a flow containing an arbitrarily high number of incommensurable modes would be obtained at still finite Reynolds numbers.

Suggestive as Landau's scenario may be, it should be observed that, according to this view, a turbulent flow - however complex - would not be sensitive to initial conditions in the sense of Ruelle and Takens. Moreover, its frequency spectrum would contain sharp peaks corresponding to the critical frequencies ω_1, ω_2 etc. [McDonough et al. 1984.a]. By contrast, as discussed in Section 1.1, turbulent flows observed in nature are sensitive to initial data, and possess a broad-band spectrum. In the language of dynamical systems, the attractor corresponding to Landau's notion would be a multi-dimensional torus in phase space, on which would lie all flow trajectories, decomposable - in principle - into cyclic, or periodic, orbits having incommensurable frequencies. Now, it has been shown [Li and Yorke 1975] that, while two-dimensional tori of this kind are structurally stable (in the sense discussed in Section 1.1), tori having three or more dimensions, i.e. containing three or more frequencies, are not, and are destroyed by small perturbations giving rise to the characteristic, entangled topology of 'strange attractors'. Thus, the quasi-periodic behaviour envisaged by Landau would not be structurally stable, or generic, and would not be observed, in general, in nature.

A different, though subtly related, picture of transition to turbulence is suggested by the behaviour of simple systems which display a route to chaos. The first to be examined was the 'miniature' system represented by the single difference equation:

$$x_{n+1} = r\, x_n\, (1-x_n) \qquad (1.2)$$

in which the subscript n may be thought to represent an instant of time. Feigenbaum [1978] found that this system has a fixed point for $r \leq 3$, and a limit cycle (i.e. an oscillatory solution of period 2) for $3 < r \leq 3.45$. For larger r, the period-2 solution is supplanted by a period-4 solution, and so on; stable solutions of period 2^k are successively replaced by solutions of period 2^{k+1}. The critical values of r at which this occurs are closer and

closer until, at $r>r_{\infty} \cong 3.57$, a completely chaotic behaviour is established. This behaviour is reminiscent of Landau's infinite sequence of transitions; here, however, the 'flow' at high values of r does not contain any periodic mode at all. Moreover, this complex behaviour is achieved by a system having only one degree of freedom, whilst Landau's theory calls for an infinite number of degrees of freedom. In phase-space terms, the limit cycle representing the system's behaviour for low r becomes eventually a strange attractor as r is increased, and does so by passing through a sequence of period doublings.

Although the above system is extremely simplified, it is now widely believed that the basic mechanisms of 'transition to chaos' involved, notably period doubling, are essentially the same in much more complex systems including fluids in motion. A sound reason for this belief is that the behaviour of Feigenbaum's system does not depend on the specific form of the RHS of Eqn.(1.2), but is much more universal; for example, the value of r_{∞} does not change if the quadratic function in (1.2) is replaced by any nonlinear function having the same general form. Thus, the nonlinearity and the topological nature of the system, rather than details of its dynamic, play the crucial role.

1.3 Coherent Structures in turbulent flows

> **And more, much more, than in my verse can sit,**
> **Your own glass shows you when you look in it**
> [Shakespeare, Sonnet CII]

During the last years, the concept of coherent structure has led to a more detailed and mechanistic description of the phenomena responsible for the generation and transport of turbulence. A recent and rather comprehensive definition of this includes any recognizable pattern, recurrent in a flow field [Perry, 1986]; in other terms, a coherent structure would be any region of the fluid in which a high degree of spatial correlation among some flow variables exists, and which is relatively persistent in time. The interest of theorists has been drawn towards coherent structures by relatively recent developments which have occurred in several, apparently unrelated, fields of the physical sciences and which can be grouped under the label of "order out of chaos" [Campbell and Rose 1983]. In this sense, the theory of coherent structures in turbulence is embedded in the broader theory of spatially-

organized "dissipative structures" [Nicolis and Prigogine 1987], and is interlaced with such fields as the theory of cellular automata and the so called "catastrophe theory".

A distinction can be drawn between near-wall and bulk-flow structures. An example of the latter are the large eddies associated with shear layer instabilities, Figure 1.1. Coherent structures typical of the near-wall region include hairpin vortices, bursts and streaks. Hairpin vortices are generated by the U-shaped distortion of spanwise rolls periodically created by shear in the wall region of a turbulent flow, Figure 1.2. By self-induction, the leading end of these U-shaped vortices tends to leave the wall; this in turn brings it into a higher-speed region of the fluid, resulting in a stretching of the vortex along the flow direction. The deformation proceeds until a breakdown of the roll occurs; this is associated with a sudden release of mechanical energy ("turbulence burst"), which has been shown to be responsible for most of the turbulence generation at the wall. In the region confined between the two branches of a hairpin vortex the streamwise velocity is relatively low and the fluid moves away from the wall. In a real wall-bounded turbulent flow, several parallel hairpin vortices exist at any instant on a wall, and a pattern of alternating high- and low-speed regions ("streaks") is established on it. The existence of these structures has been experimentally confirmed in different ways; for example, Figure 1.3 [Kline et al. 1967] shows a picture of streaks obtained by the hydrogen-bubble visualization technique.

Shortly before the turbulence burst associated with the breakdown of a U-shaped vortex, the velocity normal to the wall and directed away from it may reach very high values; this is referred to as an "ejection" event. On the other hand, following the vortex breakdown high-speed fluid from the bulk-flow region is attracted towards the wall by the sudden negative pressure surge associated with the dissipation of mechanical energy ("sweep-inrush" event). These microphenomena cause characteristic distortions in the cross-stream profiles of the main velocity component, and contribute largely to the resulting average drag. A detailed, though not very recent, review of experimental knowledge on wall turbulence is given by Hinze [1975], who also discusses the remarkable analogy between the phenomena occurring in the near-wall region of fully turbulent flows, and those concerning the transition of boundary layers from laminar to turbulent. A more updated survey is given by Banerjee [1992].

Head and Bandyopadhyay [1981], using advanced flow visualization techniques, have shown convincingly that wall turbulence basically consists of a "forest" of hairpin vortices. Perry and Chong [1982] and Perry et al. [1986]

have further developed this concept. By observing that a vortex line induces a three-dimensional, irrotational flow field around it (fluid-dynamic analogue of the Biot-Savart law of electromagnetism), they have developed techniques to derive the main flow field, the spatial distribution of turbulence intensity, and its spectrum, from a random distribution of hairpin vortices having suitable properties and an appropriate range of sizes. In this sense, the near-wall "skeleton" of hairpin vortices can be regarded as the "genetic code" of near-wall turbulence. Similar concepts have been developed by Hatziavramidis and Hanratty [1979].

Hairpin vortices, streaks and bursts are not the only structures identifiable in wall turbulence. Perry et al. [1986] have shown the existence of a small-scale eddy motion at a distance from walls, which contributes largely to the so called Kolmogorov inertial subrange ($k^{-5/3}$ portion of the turbulence energy spectrum, k being here the wave number). These "detached" structures are approximately isotropic and are the result of the breakdown of more active vortices "attached" to the walls. They do not contribute appreciably to the Reynolds stresses, but are responsible for a large fraction of the turbulence energy dissipation.

Besides the development of more and more sophisticated experimental techniques, a relevant contribution to the understanding of coherent structures has been given during the last years by direct computer simulations of turbulent flows. For example, Moin et al. [1985] reproduced hairpin vortices convincingly, and Azab and McLaughin [1987] simulated directly the near-wall layer by spectral methods, modelling the outer flow region by appropriate boundary conditions.

In parallel with the development of experimental and computational methods yielding large bulks of three-dimensional and instantaneous flow data, techniques have been developed for the processing of such databases and the identification of coherent spatial structures. These include statistical processing of the data by such sophisticated methods as conditional averaging [Komori et al. 1989] or stochastic estimation [Guezennec 1989], and flow visualization either by direct experimental techniques [Head and Bandhyopadhyay 1981] or by computer graphics [Delville et al. 1989].

Of course, these studies have primarily a theoretical relevance, as they shed light on the physical mechanisms of turbulence and, more generally, on the phenomena of spatial organization in dissipative structures. However, they are also of potential technological and engineering interest; for example, a better understanding of near-wall phenomena in turbulent flows may well allow the design of surfaces optimized for low drag or high heat transfer rates.

Surfaces bearing longitudinal riblets for surface-drag reduction are now in the stage of commercial exploitation [Noauthor 1990.b].

1.4 Turbulence modeling and Direct or Large-Eddy Simulation

A numerical procedure without a turbulence model stands in the same relation to a complete calculation scheme as an ox does to a bull
[P. Bradshaw]

In parallel with the theoretical developments described above, a fundamental role in the understanding of the turbulent motion of fluids has been played in the near past - and probably will be played with increasing importance in the future - by more and more powerful and fast computers. Our comprehension of turbulence has been growing during the last twenty years as computers, making more and more resources available in terms of storage and computing speed, have allowed and stimulated the development of new turbulence models and numerical methods for the study of complex fluid flow problems. In parallel with the increase of computational resources and of the scope of feasible analyses, there has been a continuing decrease of the cost of computations (while experimental studies have often increased in cost as more and more detailed and complex experiments were designed and performed).

Computers started to spread in the Sixties and are now undergoing an extraordinary evolution; similarly, computational fluid dynamics (CFD) was established as a discipline of its own in the same period and is now in a phase of formidable growth. The first applications of numerical fluid dynamics to turbulent flow problems of some complexity date back to the late Sixties. They were based on turbulence models now considered as routine tools or even obsolete; the problems afforded were mainly two-dimensional and stationary [Launder and Spalding, 1974]. Only recently fully three-dimensional and time-dependent simulations have become feasible. Three-dimensional capabilities have made it possible to study in a realistic fashion complex geometries as are often encountered in engineering (e.g., the flow in a nuclear reactor vessel or around a car body). The capability of time-dependent simulations has also had an outstanding relevance, as it has made it possible to study not only "true" transient flows but also oscillatory phenomena in flows which are stationary on the average (which include vibrations and fluid-structure

interactions, e.g. the oscillations of an airplane wing or of a tube bundle in a heat exchanger).

It would seem that the natural limit towards which this evolutionary processes tends is the direct simulation of turbulent flows. With this approach, the Navier-Stokes, continuity and transport equations governing the fluid motion would be solved directly in a three-dimensional, time-dependent fashion without any recourse to turbulence models. Thus, a question arises naturally: why not wait for the introduction of machines sufficiently fast and economical to allow the direct simulation of turbulent flows in the majority of the situations of physical and engineering interest, rather than investing time and resources in the search for models which will be inevitably outdated in a few years? The answer is in the inherent limitations of direct simulation, which will be discussed in detail in Section 2.2. Lomax [1982] commented that currently available computers allowed the treatment of grids having at most a number of grid points of the order of 64^3. Now, in order to afford by direct simulation a turbulent flow at a Reynolds number of the order of 10^5 it would be necessary to use - even for elementary geometries - a grid having a number of grid points of the order of 512^3, i.e. about three orders of magnitude larger (powers of two are often used to quantify the number of grid points, although there are good reasons to use them only if spectral methods and FFT techniques are employed). Moreover, the intrinsic geometrical complexity of several problems of engineering interest requires probably a further increment of about one order of magnitude in the number of grid points (1024^3).

As the typical CPU time required for a simulation increases more than linearly with the number of grid points, computers having a speed 5-6 orders of magnitude larger than those considered by Lomax would be required; of course, storage capabilities, data transmission speed and graphical processing power would have to increase similarly.

In the decade elapsed since Lomax's article (1982) computers have evolved very quickly; there has been an increase of perhaps an order of magnitude in storage and computing speed, and fluid dynamic simulations involving 128^3 or more grid points have appeared with some frequency in the literature. Some designers are thinking of a further 1000-fold increase in computer performances as a realistic goal to be attained within the end of the century [Corcoran 1991]. This would mean computing speeds of 1 Teraflop (10^{12} floating-point operations per second), storage capabilities of 1 Terabyte (10^{12} bytes, i.e. over 100 billions real numbers), and data communication speeds of 1 Terabaud (10^{12} bits per second). Such performances would be made possible by further

developments of existing technologies, such as gallium arsenide chips and optical-fibre transmission cables, and above all by new parallel architectures.

In principle, if these projects will turn into reality, grids including 512^3 ($\sim 10^8$!) points will become treatable, allowing direct simulations of turbulent flows at Reynolds numbers of 10^4-10^5. However, there are at least three good reasons to be sceptical. First, declared performances are often only peak performances; for a real code, the computing speed may decrease even by a factor 100 or more [Corcoran 1991]. Second, simulations requiring the fastest available supercomputers and CPU times of days or weeks are perhaps feasible for research and demonstration purposes, but certainly cannot be regarded as everyday computational tools for engineering. Finally, several problems of practical interest (for example weather forecasting and pollutant dispersion in the atmosphere or in the aquatic environment) involve Reynolds numbers much higher than 10^5 and are probably forever beyond the reach of direct simulation. Thus, it is almost certain that, despite the tremendous progress in computing performances achieved so far and expected in the near future, direct simulation will be mainly restricted to the theoretical investigation of transitional and low-Reynolds number turbulent flows at least for the next 20 or 30 years. Therefore, some kind of turbulence modeling will be required for most of the practical applications.

The great majority of current turbulence-modeling work involves time- (so called Reynolds-) averaging, associated with various consequent simplifications. In this only the mean field is resolved, with the entire eddy behaviour unresolved, and hence mathematically modelled. Time-averaging approaches tend not to work too well for transitional flows, and are at their best at high turbulence. Recent surveys of computational methods for complex turbulent flows, notably involving heat transfer, are given by Launder [1988], Patankar [1988] and Collins and Ciofalo [1991]. An ample review of turbulence models is due to Nallassamy [1987]. A survey of forced convection, including experimental techniques, is given by Pletcher [1988].

A second alternative to direct simulation, which does not present the limitation of being restricted to low Reynolds numbers, is the approach known as Large-Eddy Simulation (LES). As will be discussed in detail in Chapter 2, it basically consists of simulating directly the three-dimensional, time dependent turbulent motion of a fluid only down to a certain scale, while the

lower scales (called unresolved, or subgrid) are taken into account by appropriate subgrid models.

This approach is still in a development stage, and has been mainly used for the simulation of flows in simple geometries. A description of proposed subgrid models will be given in Section 2.4, and a survey of applications presented so far in the literature in Section 2.6. Most researchers using LES have chosen to develop "ad hoc" computer codes, or have adapted to LES, by the inclusion of subgrid-scale models, existing codes developed for direct turbulence simulations such as TURBIT [Grötzbach 1987], FDS [Fodemski et al. 1987], FORTY [Antonopoulos-Domis and Love 1978]. Generally, these are optimized for specific problems such as Poiseuille or Couette flow, flow in annular passages etc., and use fast and accurate numerical algorithms such as spectral methods and explicit time stepping [Orszag 1980], in order to keep storage and computing times as low as possible while working with very fine grids and thus attaining a high degree of numerical accuracy. Of course, this approach presents a serious drawback, i.e. the difficulty of extending it to more complex and general configurations, in particular to flows of direct engineering interest.

An alternative approach has been chosen in the present work. It consists of using a general-purpose code of the last generation, a simple but relatively "universal" subgrid model, i.e. Smagorinsky's [1963], and numerical methods which are far from being optimized for speed and accuracy but, on the other hand, can be extended without difficulties to complex geometries. When applied to simple flows this approach presents the drawback of heavier computational loads and less accuracy as compared with high-efficiency spectral codes. Such an application (flow between plane parallel plates, i.e. "plane channel"), which of course is mainly used as a benchmark, is presented and discussed in Chapter 4. On the other hand, simulations using this approach can be extended to relatively complex geometries where spectral codes show all their limitations and generally fail. Two applications of this kind (flow with heat transfer in a channel having one of the walls roughened by transverse ribs, and in a crossed corrugated geometry representative of rotary air preheaters) are shown and discussed in Chapters 5 and 6, respectively.

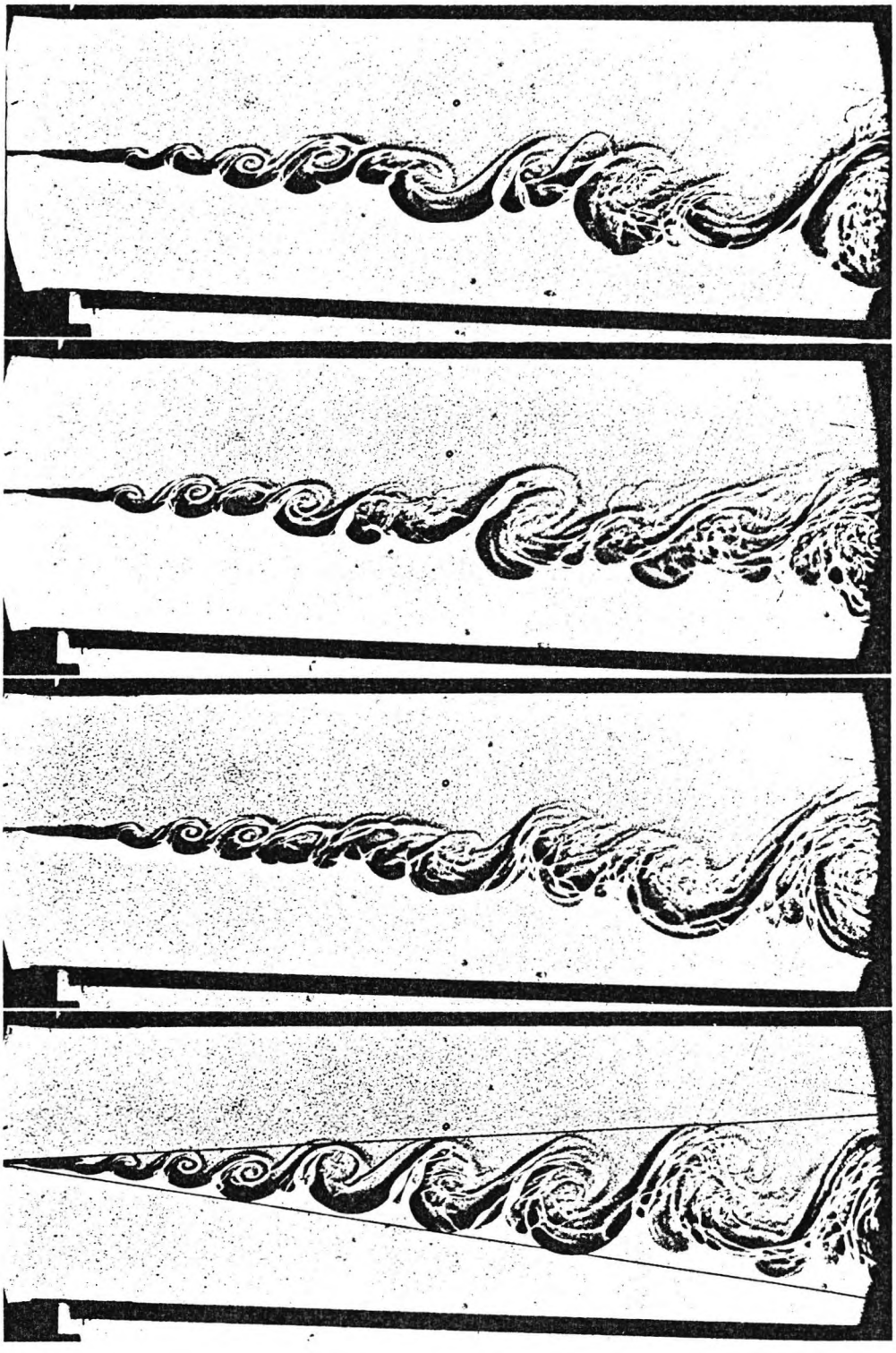


Figure 1.1 - Large eddies in a plane free mixing layer
[from Brown and Roshko, 1974]

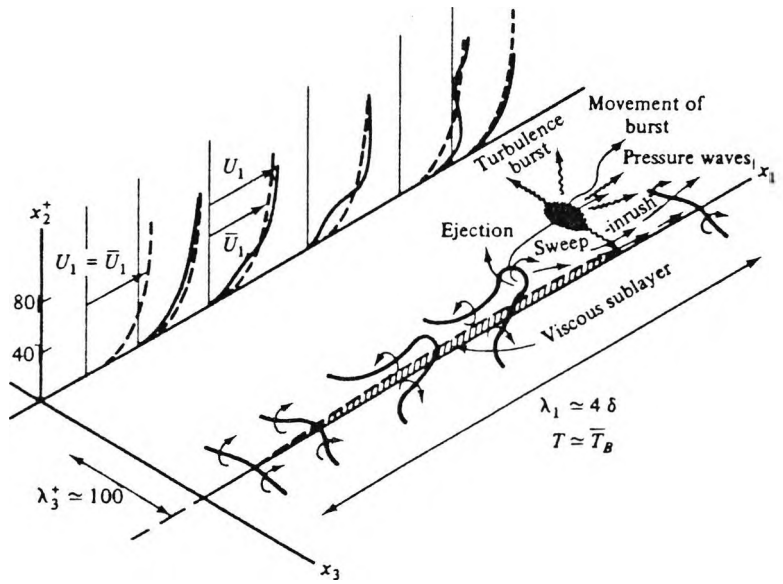


Figure 1.2 - Near-wall turbulence structure: hairpin vortices, ejection / sweep-inrush events, a turbulence burst and a low-speed elongated region (streak) are evidenced [from Hinze, 1975].

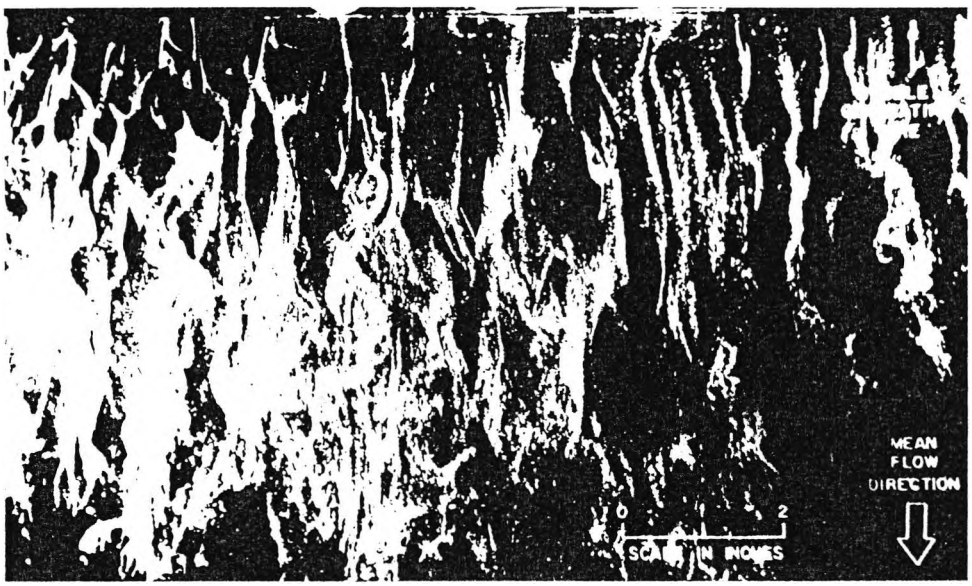


Figure 1.3 - Near-wall turbulence structure: streaks visualized by the hydrogen-bubble method [from Kline et al., 1967]

CHAPTER 2 - LARGE-EDDY SIMULATION: THEORETICAL FRAMEWORK AND STATE-OF-THE-ART

2.1 Governing equations

Rien n'est aussi pratique qu'une bonne theorie
[K. Levin]

2.1.1 Equations governing the fluid flow [Hinze 1975; Bradshaw 1978.b]

In the most general case of three-dimensional motion of a fluid, the flow field is specified by the velocity vector $\mathbf{u} = (u_1,u_2,u_3)$ or (u,v,w), by the pressure p and by the density ϱ, all functions of the three space coordinates x_1,x_2,x_3 (or x,y,z) and of time t.

In order to determine these five quantities, five equations are available:

a) the continuity equation;
b) three momentum equations;
c) a thermodynamic equation of state $f(\varrho,p,...)=0$.

This last equation may contain additional quantities such as the temperature T, for which the appropriate transport equations have then to be added to the system, see section 2.1.2.

a) The continuity equation expresses the balance per unit volume and per unit time between the mass which enters and exits a control volume, and the density variation in it. In the general case of unsteady flow of a varying-density fluid this is expressed by:

$$D\varrho/Dt + \varrho\,\mathrm{div}\mathbf{u} = 0 \qquad (2.1)$$

The symbol D /Dt denotes the 'substantial' derivative, which is the sum of a local and of an advective contribution:

$$D\varrho/Dt \equiv \partial\varrho/\partial t + \mathbf{u}\cdot\mathbf{grad}\,\varrho \qquad (2.2)$$

so that Eqn.(2.1) becomes:

$$\partial\varrho/\partial t + \mathbf{u}\cdot\mathbf{grad}\,\varrho + \varrho\,\mathrm{div}\mathbf{u} = 0 \qquad (2.3)$$

But the following vector identity holds:

$$\mathbf{u}\cdot\mathbf{grad}\,\varrho + \varrho\,\mathrm{div}\mathbf{u} \equiv \mathrm{div}(\varrho\mathbf{u}) \qquad (2.4)$$

so that Eqn.(2.1) can be written, using cartesian tensor notation and Einstein's convention of implicit summation over repeated indices:

$$\partial\varrho/\partial t + \partial(\varrho u_i)/\partial x_i = 0 \qquad (2.5)$$

For a constant-density flow this takes the simplified form:

$$\partial u_i/\partial x_i = 0 \qquad (2.6)$$

b) The momentum equations are derived from Newton's second law (mass*acceleration = total force acting on the fluid volume). Two classes of forces need to be considered:
- body forces (gravitational, inertial etc.);
- surface forces (pressure and friction).

If **F** and **P** are the body force and the surface force per unit volume, respectively, the momentum equations can be written in vector form as:

$$\varrho\,\mathrm{D}\mathbf{u}/\mathrm{D}t = \mathbf{F} + \mathbf{P} \qquad (2.7)$$

D**u**/Dt denotes the 'substantial' acceleration consisting, like the substantial derivative of density, of a local contribution $\partial\mathbf{u}/\partial t$ and of an advective contribution **u·grad u**. Here, **grad u** (or $\nabla\mathbf{u}$) stays for the triplet of vectors **grad** u_1, **grad** u_2, **grad** u_3; thus, **u·grad u** is the vector having components: $(\mathbf{u}\cdot\mathbf{grad}\,\mathbf{u})_i = \mathbf{u}\cdot\mathbf{grad}\,u_i$ (i=1,2,3).

More explicitly, the i-th component of the LHS of Eqn.(2.7) can be written, using again tensor notation and Einstein's convention on repeated indices:

$$\rho\, Du_i/Dt = \rho(\partial u_i/\partial t + \mathbf{u}\cdot\mathbf{grad}\ u_i) = \rho\,\partial u_i/\partial t + \rho u_j\,\partial u_i/\partial x_j$$
$$= \partial(\rho u_i)/\partial t - u_i\partial\rho/\partial t + \rho u_j\,\partial u_i/\partial x_j \qquad (2.8)$$

But, because of the continuity equation (2.5):

$$\partial\rho/\partial t = -\mathrm{div}(\rho\mathbf{u}) = -\partial(\rho u_j)/\partial x_j \qquad (2.9)$$

Substituting Eqn.(2.9) into Eqn.(2.8) one has:

$$\rho\, Du_i/Dt = \partial(\rho u_i)/\partial t + u_i\,\partial(\rho u_j)/\partial x_j + \rho u_j\,\partial u_i/\partial x_j$$
$$= \partial(\rho u_i)/\partial t + \partial(\rho u_i u_j)/\partial x_j \qquad (2.10)$$

This last form of Du_i/Dt is called the 'conservation' form of the substantial derivative; it has the property of leading to momentum balance expressions which are still valid exactly when written for finite volumes, and thus is usually preferred for finite volume - based numerical methods.

The body force $\mathbf{F} = (F_1, F_2, F_3)$ includes the gravity force and any fictitious (inertial) force to be introduced in momentum balances in non-inertial (e.g., rotating) reference frames. Fictitious forces may also be used in the simulation of periodic problems, see Chapters 4-6.

As to the surface forces, it can be shown by examining the equilibrium of a fluid volume that:

$$P_i = \partial P_{ij}/\partial x_j \qquad (2.11)$$

in which P_{ij} is the total stress tensor.

On the basis of Eqns.(2.10) and (2.11), Eqn.(2.7) can be written:

$$\partial(\rho u_i)/\partial t + \partial(\rho u_i u_j)/\partial x_j = \partial P_{ij}/\partial x_j + F_i \qquad (2.12)$$

(for each component). By letting:

$$P_{ij} = -p_{stat}\delta_{ij} + \sigma_{ij} \qquad (2.13)$$

in which $p_{stat} = -(1/3)\ P_{jj}$ (static pressure), σ_{ij} is the non-isotropic part of the stress tensor, and δ_{ij} is the Kronecker delta, one has:

$$P_i = - \partial p_{stat}/\partial x_i + \partial \sigma_{ij}/\partial x_j \qquad (2.14)$$

Therefore, Eqn.(2.12) can be written:

$$\partial(\varrho u_i)/\partial t + \partial(\varrho u_i u_j)/\partial x_j = - \partial p_{stat}/\partial x_i + \partial \sigma_{ij}/\partial x_j + F_i \qquad (2.15)$$

The forces acting on the surface of a fluid volume depend on the velocity field. It is an empirical matter to specify the relation between the stress tensor P_{ij} and the strain rate tensor:

$$S_{ij} = (\partial u_i/\partial x_j + \partial u_j/\partial x_i)/2 \qquad (2.16)$$

The attention will be restricted here to newtonian fluids, for which this relation can be assumed to be a simple linear proportionality. All gases and many liquids of practical interest belong to this class. In newtonian fluids, the stress-strain rate relation involves two scalar quantities, i.e. the viscosity μ and the so-called "second coefficient of viscosity" β :

$$\sigma_{ij} = 2 \mu S_{ij} + \beta \delta_{ij} S_{kk} \qquad (2.17)$$

Since the LHS of Eqn (2.17) is traceless, so must be the RHS; hence:

$$\beta = - \frac{2}{3} \mu \qquad (2.18)$$

Taking eqns (2.17) - (2.18) into account, the total stress tensor can be re-written as:

$$P_{ij} = - \left(p_{stat} + \frac{2}{3} \mu S_{kk} \right) \delta_{ij} + 2 \mu S_{ij} \qquad (2.19)$$

Of course, the term S_{kk} = div **u** vanishes in constant-density flow.

By substituting Eqn.(2.16) into (2.19) and the resulting expression into Eqn.(2.12) one has the Navier-Stokes equations:

$$\partial(\varrho u_i)/\partial t + \partial(\varrho u_i u_j)/\partial x_j = -\partial p/\partial x_i + \partial[\mu(\partial u_i/\partial x_j + \partial u_j/\partial x_i)]/\partial x_j + F_i \qquad (2.20.a)$$

in which:

$$p = p_{stat} + (2/3)\ \mu\ S_{kk} \qquad (2.21)$$

For incompressible fluids, one has of course $p = p_{stat}$. Eqn.(2.20.a) may also be written with the tensor S_{ij} 'split':

$$\partial(\rho u_i)/\partial t+\partial(\rho u_i u_j)/\partial x_j-\partial(\mu\partial u_i/\partial x_j)/\partial x_j = -\partial p/\partial x_i+\partial(\mu\partial u_j/\partial x_i)/\partial x_j+F_i \qquad (2.20.b)$$

or, in vector notation:

$$\partial(\rho\mathbf{u})/\partial t + \nabla(\rho\mathbf{uu}) - \nabla(\mu\nabla\mathbf{u}) = -\nabla p + \nabla[\mu(\nabla\mathbf{u})^T] + \mathbf{F} \qquad (2.20.c)$$

c) In principle, the density ρ can always be eliminated from the unknowns of the problems by using the equation of state. In the case of compressible fluids, it is a function of the pressure p; thus, by substituting the function $\rho(p)$ into the continuity equation, a differential equation in p is obtained having the general form:

$$\partial p/\partial t = F(p,\mathbf{u},t) \qquad (2.22)$$

and Eqns.(2.20)-(2.22) can be solved directly in the unknowns p and **u**.

In the case of incompressible fluids, the density ρ is no more a function of the pressure. It will be either a constant or a function of the temperature and, possibly, of other scalars such as concentrations; thus, it can still be eliminated from the unknowns of the problem, but the time derivative of pressure disappears from the continuity equation. Therefore, no equation of the form (2.22) can be written, describing how p varies with time; the pressure becomes an 'implicit' field specified by the condition that the velocities satisfying the momentum equations (2.12) or (2.20) also satisfy the continuity equation (2.5). Ideally, the pressure field propagates at infinite speed and adapts itself instantaneously to the velocity field. Of course, this requires the use of more sophisticated techniques to solve the coupled system of continuity and momentum equations, as will be discussed in Chapter 3. In the present work, only incompressible fluids will be considered.

2.1.2 Equations governing the transport of scalar quantities

In non-isothermal problems, the transport equation for enthalpy H has to be added to the fluid flow equations (2.1) and (2.20):

$$\partial(\rho H)/\partial t + \partial(\rho u_j H)/\partial x_j = - \partial q_j/\partial x_j + S_H \qquad (2.23)$$

in which S_H is a source term (power per unit volume), associated with internal heat generation, and q_j is the heat flux vector. For a fluid having a constant specific heat, $H=c_p T+\text{constant}$, and Eqn.(2.23) can be written:

$$\partial(\rho T)/\partial t + \partial(\rho u_j T)/\partial x_j = - (1/c_p)\partial q_j/\partial x_j + S_T \qquad (2.24)$$

in which $S_T = S_H/c_p$. More generally, the transport equation for a scalar quantity Q can be written:

$$\partial(\rho Q)/\partial t + \partial(\rho u_j Q)/\partial x_j = - \partial J_j/\partial x_j + S_Q \qquad (2.25)$$

in which J_j is the diffusive flux vector of Q and S_Q is a source term. Eqn. (2.23) is of course a special case of Eqn.(2.25), with $Q=H$, $J_j=q_j$ and $S_Q=S_H$. Also the momentum equations can be regarded as the transport equations of the scalar components of **u**; thus, also Eqns.(2.12) are special cases of Eqn. (2.25), with $Q=u_i$, $J_j=-P_{ij}$ and $S_Q=F_i$.

If the flux components J_j follow Fick's law:

$$J_j = - \Gamma \partial Q/\partial x_j \qquad (2.26)$$

(Γ being the molecular diffusivity of Q), then Eqn.(2.25) can be written:

$$\partial(\rho Q)/\partial t + \partial(\rho u_j Q)/\partial x_j = \partial(\Gamma \partial Q/\partial x_j)/\partial x_j + S_Q \qquad (2.27)$$

For the transport of heat, Fick's law is of course Fourier's law:

$$q_j = -\lambda \partial T/\partial x_j \qquad (2.28)$$

(λ being the thermal conductivity). Eqn.(2.24) can thus be written:

$$\partial(\rho T)/\partial t + \partial(\rho u_j T)/\partial x_j = \partial(\Gamma \partial T/\partial x_j)/\partial x_j + S_T \qquad (2.29)$$

in which $\Gamma = \lambda/c_p$ is the molecular thermal diffusivity. The ratio $\sigma = \mu/\Gamma$ is called Prandtl number if Γ refers to heat and Schmidt number if it refers to the concentration of some molecular species.

Fick's law (2.26) can be generalized as follows:

$$J_j = - \Gamma_{jk} \partial Q/\partial x_k \qquad (2.30)$$

in which Γ_{ij} is a diffusivity tensor. Such formulation is particularly useful to express the total (laminar + Reynolds, or subgrid) stresses in conjunction with higher-order closure models. The transport equation of a scalar Q, Eqn.(2.27), is then generalized as:

$$\partial(\varrho Q)/\partial t + \partial(\varrho u_j Q)/\partial x_j = \partial(\Gamma_{jk} \partial Q/\partial x_k)/\partial x_j + S_Q \qquad (2.31)$$

If Q is a passive scalar, i.e. a scalar which does not appear in the equations of motion (2.5) and (2.20), its transport equation (2.25) is linear in Q and its numerical solution does not ordinarily present special difficulties. On the other hand, if any term of the equations of motion depends on Q (as happens, for example, in free-convection problems when Q is the temperature T), Eqn.(2.25) becomes non-linear as the velocities u_j are (generally weak) functions of Q. Finally, if Q coincides with a velocity component, the transport equation (2.25) (which of course becomes one of the Navier-Stokes equations) is strongly nonlinear, and its numerical solution is exposed in general to all the difficulties of nonlinear equations including multiple solutions, sensitivity to initial conditions, and turbulence.

2.2 Direct simulation

Let him but copy what in you is writ,
Not making worse what Nature made so clear
[Shakespeare, Sonnet LXXXIV]

It is widely accepted that, at least for newtonian fluids, the Navier-Stokes equations, coupled with the continuity equation and, when appropriate, with the transport equations for temperature or other scalars, describe correctly the behaviour of the flow both under laminar and under turbulent conditions [Spalding 1978]. The difficulty - which, as will be shown, is not a simple matter of resources or of numerical methods - lies in the solution of these equations.

In order to solve directly the flow equations by any numerical method, the computational domain has to be spanned by some computational grid (spatial discretization), whose cells need to be smaller than the smallest significant structures to be resolved. Also, the simulation must be conducted by using

time steps Δt (time discretization) small enough to resolve the time behaviour of the various quantities.

As discussed in the Introduction, if the Reynolds number (i.e., the ratio between the inertial and the viscous forces acting on the fluid) is small enough, the flow is laminar. The significant spatial structures of the flow field are then of the same order of magnitude as the physical structures present in the computational domain (duct height, obstacle size, etc.). Also, if the boundary conditions and the forcing terms do not vary in time, the problem has always a stationary or a periodic solution (perhaps following a transient, depending on the initial conditions). Therefore, in this case it is generally possible to attain a sufficient space- and time-resolution, and to obtain computational results which are independent of the particular discretization used, and in good agreement with experimental data. It should be observed here that a laminar flow needs not to be 'simple' (in the intuitive sense); see for example the problem studied by Ciofalo and Collins [1988.a] (impulsively starting flow around a body with a backward-facing step), in which the solution - though purely laminar - includes transient vortices, wake regions and other details having a structure quite far from being 'simple'.

For higher values of the Reynolds number, the flow becomes turbulent. In this case, the flow field varies in a non-periodic fashion with time (even for constant boundary conditions and forcing functions), exhibits a sensitive dependence on the initial conditions, and lacks spatial symmetries (even if the problem presents geometrical symmetries). The spatial structures identifiable in the flow field ('eddies') cover a range of scales which extends from the scale of the physical domain down to that of the 'dissipative eddies', in which the kinetic energy of the eddy motion is eventually dissipated into heat by viscous effects. This interval of scales increases with the Reynolds number and, for fully turbulent flows, may include several orders of magnitude. Thus, although the governing equations are still describing correctly, at least in principle, the physical behaviour of the flow, their direct solution in the sense specified above becomes a task of overwhelming complexity.

In the following, quantitative estimates of the required storage and CPU time will be sketched for the direct simulation of turbulent flow in a specific geometry, i.e. a plane channel having half-height δ. This is the same problem that will be studied by Large-Eddy Simulation in Chapter 4, and can be considered as representative of a large class of thermofluid-dynamics problems. The geometry is sketched in Figure 2.1; the axes x, y and z are assumed to lie along the streamwise, cross-stream and spanwise directions, respectively, and

the flow is assumed to be periodic along x and z. The sizes of the computational domain, or 'box', along the periodic directions must be large enough for the correlations between fluctuating components to become negligible; this is equivalent to imposing that all relevant spatial structures must be 'captured' in the box. Measurements such as those by Comte-Bellot [1963] show that these minimum sizes are of the order of $L_x=4\delta$ and $L_z=2\delta$ (of course, $L_y=2\delta$ here). For similar reasons, the time duration of the simulation must include the lifespan of the longest-living flow structures; this is in general of the order of one 'Large-Eddy TurnOver Time' (LETOT), defined as δ/u_τ in which u_τ is the friction velocity. Thus, the simulation has to be extended to at least a few LETOT's. Longer simulations may be necessary, according to the initial conditions chosen, to allow for all numerical transients to die away and for a (statistically) steady-state to be attained.

A first, crude estimate of the number of grid points and of time steps necessary for a direct simulation follows directly from considering the Kolmogorov-Obukhov scales of dissipative eddies in locally isotropic turbulence, i.e. far from solid walls [Landau and Lifschitz 1959]:

length scale	$\lambda_o \approx \delta/Re_\delta^{3/4}$	(2.32.a)
velocity scale	$v_o \approx U/Re_\delta^{1/4}$	(2.32.b)
frequency scale	$\omega_o \approx (U/\delta)\, Re_\delta^{3/4}$	(2.32.c)
time scale	$t_o \approx (\delta/U)/Re_\delta^{3/4}$	(2.32.d)

in which U is the mean velocity and $Re_\delta=U\delta/\nu$ is the Reynolds number based on U and on the channel half-height δ. For this geometry the hydraulic diameter D_e is twice the channel height, i.e. 4δ, so that the corresponding Reynolds number is $Re_D = 4Re_\delta$.

By imposing the mesh size in all three directions to be of the same order of λ_o, and the time step of the same order of t_o, one has:

$$\Delta x, \Delta y, \Delta z \approx \delta\, Re_\delta^{-3/4} \qquad (2.33)$$

$$\Delta t \approx (\delta^2/\nu)\, Re_\delta^{-7/4} \qquad (2.34)$$

The overall number of grid points N_p follows from Eqn. (2.33):

$$N_p = (L_x/\Delta x)*(L_y/\Delta y)*(L_z/\Delta z) \approx Re_\delta^{9/4} \qquad (2.35)$$

The friction velocity u_τ is related to the (Fanning) friction coefficient $C_f = |\tau_w| / (\rho U^2/2)$ by:

$$u_\tau = (C_f/2)^{1/2} U \tag{2.36}$$

If C_f is estimated by using the Blasius correlation:

$$C_f = 0.056\ Re_\delta^{-1/4} \tag{2.37}$$

then one has:

$$u_\tau = 0.17\ Re_\delta^{7/8} \nu/\delta \tag{2.38}$$

and thus:

$$1\ LETOT = \delta/u_\tau = (\delta^2/\nu) Re_\delta^{-7/8} \tag{2.39}$$

$$N_t \approx LETOT/\Delta t \approx Re_\delta^{7/8} \tag{2.40}$$

Thus the number of grid points must increase as $Re_\delta^{9/4}$ and the number of time steps as $Re_\delta^{7/8}$. Although nothing can be said about the proportionality coefficients relating N_p and N_t to the appropriate powers of Re_δ on the basis of such a crude analysis, it is evident that the rapid increase of these parameters is an absolute obstacle to the direct simulation of high - Reynolds number turbulent flows, no matter the size and speed of available computers.

A more accurate estimate of the required values of N_p and N_t for a plane-channel flow can be made following the criteria discussed by Grötzbach [1987].
a) For directions normal to solid walls (y in this case), Grötzbach suggests that the viscous sublayer should be resolved by at least three grid points. Now, the sublayer thickness is:

$$y_v = y_v^+ \nu/u_\tau \tag{2.41}$$

Thus, by assuming $y_v^+ = 11$ and using Eqn.(2.38) for the friction velocity u_τ, the above condition can be expressed as:

$$\Delta y/\delta \leq 18\ Re_\delta^{-7/8} \tag{2.42}$$

Of course, if the computational grid is selectively refined near the walls, a somewhat larger value of Δy can be used in the bulk flow region.

b) As for the streamwise direction x, the Kolmogorov length scale, Eqn. (2.32.a), can be written [Landau and Lifschitz 1959] as:

$$\Lambda_o \approx (\nu^3/\varepsilon)^{1/4} \qquad (2.43)$$

in which ε is the turbulence energy dissipation rate. Grötzbach assumes that the mesh size along x can be somewhat larger than this scale:

$$\Delta x \leq 3 \div 5 \ (\nu^3/\varepsilon)^{1/4} \qquad (2.44)$$

Now, as the mesh spacing along x cannot depend on the distance from walls, the constraint on Δx is actually imposed by the highest value attained by ε along the cross-stream direction. Following the theory of equilibrium boundary layers [Launder and Spalding 1972; Hinze 1975] this occurs at the edge of the viscous sublayer ($y = y_v^+$) and is:

$$\varepsilon_{max} = 8 \ u_\tau^3/y_v \qquad (2.45)$$

By using Eqns.(2.38) and (2.41) for u_τ and y_v, Eqn.(2.45) may be written:

$$\varepsilon_{max} \approx 1.8*10^{-3} \ \nu^3 \ Re_\delta^{7/2}/\delta^4 \qquad (2.46)$$

From Eqns.(2.44) and (2.46) the following condition is obtained for Δx:

$$\Delta x/\delta \leq 18 \div 28 \ Re_\delta^{-7/8} \qquad (2.47)$$

It is noteworthy that the constraints on Δx, Eqn.(2.47), and on Δy, Eqn. (2.42), are comparable, although they were derived from quite different approaches. This is a consequence of turbulence being nearly isotropic at the smallest scales.

c) Finally, the spanwise direction z can be treated as the streamwise direction x if the computational box is bounded laterally by periodicity planes, and as the cross-stream direction y if it is bounded by solid walls. In the former case, one has:

$$\Delta z/\delta \leq 18 \div 28 \ Re_\delta^{-7/8} \qquad (2.48)$$

Criteria (2.42),(2.47),(2.48) may be summarized (a bit optimistically) as:

$$\Delta x/\delta = \Delta y/\delta = \Delta z/\delta \leq 28\ Re_\delta^{-7/8} \qquad (2.49)$$

Hence, the minimum total number of grid points is:

$$N_p = (L_x/\Delta x)*(L_y/\Delta y)*(L_z/\Delta z) \approx 7.7*10^{-4} Re_\delta^{21/8} \qquad (2.50)$$

for $L_x=4\delta$, $L_y=L_z=2\delta$. Eqn.(2.50) gives a dependence of N_p on Re_δ even more sensitive than Eqn.(2.35), but specifies a small proportionality factor.

As regards the time step, criterion (2.34) should be complemented by the Courant criterion. In fact, although this is a necessary stability requirement only when explicit time-stepping methods are used, yet it is generally considered as a more widely applicable accuracy requirement for complex flows. It may be written here as:

$$\Delta t < \Delta x/U \qquad (2.51)$$

which, taking Eqn.(2.49) into account, becomes:

$$\Delta t < 27\ (\delta^2/\nu)\ Re_\delta^{-15/8} \qquad (2.52)$$

This last criterion describes a more sensitive dependence of Δt on Re_δ than criterion (2.34), but actually becomes more stringent only at very large Reynolds numbers. Up to $Re_\delta \approx 10^{11}$ it is automatically satisfied provided that criterion (2.34) is followed. Thus, the time step can be chosen to be:

$$\Delta t = \text{constant} * (\delta^2/\nu)\ Re_\delta^{-7/4} \qquad (2.53)$$

in which the constant is ~1. In the following, the value 0.5 will be conservatively assumed.

In a simulation involving n LETOT'S, Eqns.(2.39) and (2.53) imply for the number of time steps:

$$N_t \approx 2\ n\ Re_\delta^{7/8} \qquad (2.54)$$

The values of N_p and N_t given by Eqns.(2.50) and (2.54), respectively, for the direct simulation of a plane-channel turbulent flow over n=10 LETOT's, are

summarized in Table 2.1 (columns 2 and 3) as functions of the Reynolds number Re_δ in the range $10^3 \div 10^4$ (column 1). The same table reports in column 4 corresponding estimates of the storage that would be required if the Harwell-FLOW3D code were used. It is expressed in Mwords, i.e. millions of real 8-byte locations, and is computed on the basis of about 100 words per grid point. Finally, estimates of the required CPU-time on a CRAY-2 computer for the same code are reported in column 5. They are computed by assuming the CPU time to be proportional to $N_p^{1.4}$ and to N_t, and to be about 1 second per time step for a grid having 10^4 nodes. All these assumptions are based on the author's previous experience with the Harwell-FLOW3D code [Ciofalo 1988.a, 1989.a, 1989.b]. Note that the Harwell CRAY-2 has 256 Mwords of in-core storage; for larger memory requirements out-of-core storage would have to be used, so that the reported CPU-time estimates should be multiplied even by several times.

Table 2.1 Estimated storage and CPU-time requirements for a direct simulation using Harwell-FLOW3D on a CRAY-2

Re_δ	N_p	N_t	Storage (Mwords)	CPU Time
1000	60000	4500	6	12 hours
1500	172000	6500	17	75 "
2000	365000	8250	36	275 "
2500	656000	10000	66	750 "
5000	$4*10^6$	19000	400	2 years
10000	$25*10^6$	35000	2500	50 "

By using Eqns. (2.50) and (2.54), storage and CPU-time requirements (for a 10-LETOT simulation) may also be expressed as:

$$\text{Storage} \approx 8*10^{-2} \; Re_\delta^{2.625} \text{ words} \qquad (2.55a)$$

$$\text{CPU (Cray-2)} \approx 0.9*10^{-9} \; Re_\delta^{4.545} \text{ seconds} \qquad (2.55b)$$

CPU-times should be multiplied by a factor 2-3 if, instead of a CRAY-2, the IBM-3090 200J of the University of Palermo Computing Centre (CUC) were used with the Vector Facility, and by a factor 5-6 if the same computer were used without exploiting the Vector Facility.

Table 2.1 shows that the storage requirements put an upper limit of about 4000 to the δ-Reynolds numbers affordable by direct simulation, provided that a very large computer such as the CRAY-2 were available. However, computing times become prohibitive at much lower Reynolds numbers.

If, instead of Harwell-FLOW3D, different computer codes and numerical methods were used, explicitly designed for direct or large-eddy simulation of plane-channel and similar flows, computing times could be reduced perhaps by a factor 100, and large savings could be achieved also in storage. However, due to the large exponent of Re_δ in Eqn.(2.55.b), the feasible Reynolds-number range would increase only by a factor 2 or 3; in any case, direct simulation would become unrealistic for $Re_\delta > 5000$, i.e. $Re_D > 20{,}000$. These values are still well below those encountered in most engineering applications.

2.3 Large-Eddy Simulation and spatial filtering

There are lies, damned lies, and statistics
[Mark Twain]

The example in Section 2.2 shows rather clearly that, even for a simple plane-channel flow, direct simulation of all scales of turbulence is feasible only at low Reynolds numbers, i.e. in the transitional regime, and is impossible in principle beyond some Reynolds number. This suggests naturally a simulation technique based on some decomposition of the flow field into large-scale and small-scale structures, the first being directly simulated in three-dimensional, time-dependent fashion, and the second (or rather their feed-back effects on the large-scale flow) being somehow modelled.

This approach is generally called 'Large-Eddy Simulation' (LES), a term introduced for the first time by Leonard [1974]. The rationale for Large-Eddy Simulation is that in a turbulent flow the large-scale structures, produced directly by the instability of the mean flow (shear or buoyancy effects), should be simulated directly, because 1) they are hard to model in a "universal" way, as they are highly problem-dependent and anisotropic; and 2) they are responsible for most of the transport of momentum, mass and scalars. On the other hand, the small-scale structures, produced by the energy-cascade process from larger eddies, are generally isotropic, depend little on the specific problem, and thus are much more amenable to be described by some "universal" model. Moreover, small eddies contribute little to heat and

momentum transport, so that a large-eddy simulation is expected to be little sensitive to the parameterization scheme used for them.

The computing effort required by large-eddy simulation is generally much higher than for conventional turbulence closure models, so that until a few years ago this approach has been practised on a significant scale only by few institutions and research centres provided with large supercomputing tools (in particular, the National Centre for Atmospheric Research and the Stanford University in the U.S., the Queen Mary College in the U.K. and the Kernforschungszentrum Karlsruhe in Germany). However, supercomputing facilities are becoming relatively widespread now, and LES is becoming a viable tool for turbulence research for an increasing number of scientists.

The basic principles of large-small scale decomposition and filtering, and the main related modelling problems, will now be briefly recalled and discussed. For the sake of clarity, the equations governing the flow and thermal fields for a Newtonian fluid are repeated below; source terms are omitted as they are not essential in the following discussion.

$$\partial\rho/\partial t + \partial(\rho u_i)/\partial x_i = 0 \qquad (2.5')$$

$$\partial(\rho u_i)/\partial t + \partial(\rho u_i u_j)/\partial x_j = -\partial p/\partial x_i + \partial[\mu(\partial u_i/\partial x_j + \partial u_j/\partial x_i)]/\partial x_j \qquad (2.20.a')$$

$$\partial(\rho T)/\partial t + \partial(\rho u_j T)/\partial x_j = \partial(\Gamma\, \partial T/\partial x_j)/\partial x_j \qquad (2.24.b')$$

In LES each quantity Q is decomposed as:

$$Q = \widehat{Q} + \widetilde{Q} \qquad (2.56)$$

Eqn.(2.56) is the analogue of the Reynolds-decomposition of a generic field into an average and a fluctuating component, which is the basis for all classical closure models of turbulence. However, a caret ($\widehat{Q}$) denotes here the large-scale (resolved) component, which is still time-dependent even in flows which are stationary in the average, while a tilde ($\widetilde{Q}$) denotes the small-scale, or 'sub-grid' (unresolved) component.

Following the general approach described by Leonard [1974], the large-scale components are the result of applying a filtering procedure to the local and instantaneous (unfiltered) quantities:

$$\widehat{Q}(\mathbf{x},t) = \int G(\mathbf{x},\mathbf{x}')\; Q(\mathbf{x}',t)\; d^3\mathbf{x}' \qquad (2.57)$$

where $Q = u_i$, p or T, and G is a normalized weight function, or filter. The integral extends (in principle) over the entire computational domain, and Q is still a continuous function, defined at each point in the domain and independent of the computational grid or discretization scheme used for the numerical computation of it. An example of filtered and unfiltered function is shown in Figure 2.2.

The equivalent of Eqn.(2.57) in transformed (wavenumber) space is:

$$\hat{Q}(\mathbf{x},t) = \int_{-\infty}^{+\infty} e^{i\mathbf{k}\mathbf{x}}\, \mathcal{G}(\mathbf{k})\, \mathcal{Q}(\mathbf{k},t)\, d\mathbf{k} \qquad (2.57')$$

in which $\mathbf{k} = (k_1, k_2, k_3)$ is the wavenumber vector, $\mathcal{Q}(\mathbf{k},t)$ is the transform of $Q(\mathbf{x},t)$ and $\mathcal{G}(\mathbf{k})$ is the transformed filtering function.

Several filters have been used by different researchers. Some of them are better expressed in physical space ($\mathbf{x}$), others in transformed wavenumber space ($\mathbf{k}$). For example, Lilly [1967], Deardorff [1970] and other early investigators used the "box", or "top-hat", filter, defined in physical space as:

$$G(\mathbf{x},\mathbf{x}') = \begin{cases} 1/\Delta^3 & \text{for } |x_i - x_i'| \le \Delta/2 \quad (i=1,2 \text{ and } 3) \\ 0 & \text{elsewhere} \end{cases} \qquad (2.58)$$

Δ being the characteristic filter width. Those using spectral methods and Fourier transforms, i.e. the Stanford group [Ferziger 1977] prefer to use the "gaussian" filter. It is defined in $\mathbf{x}$-space by:

$$G(\mathbf{x},\mathbf{x}') = \left(\frac{\sqrt{c/\pi}}{\Delta}\right)^n \exp\left[-(\sqrt{c}/\Delta)^n\, (\mathbf{x}-\mathbf{x}')^2\right] \qquad (2.59.a)$$

where c is a constant, Δ is the filter width and n is the number of dimensions to be filtered. For plane-channel flows and related problems, the Gaussian filter is applied only in the horizontal directions (i.e., n=2) and the finite differencing in the vertical direction implicitly supplies top-hat filtering. Following Kwak et al. [1975], c = 6 and Δ= twice the grid spacing along x and z (directions parallel to the walls). In $\mathbf{k}$-space, the same filter is defined by:

$$\mathcal{G}(\mathbf{k}) = \exp\left[-\Delta^2 k^2/(4c)\right] \qquad (2.59.b)$$

being $k^2 = k_1^2+k_2^2+k_3^2$. Finally, the "sharp cutoff" filter is given in **k**-space by:

$$\mathcal{G}(\mathbf{k}) = \begin{cases} 1 & \text{for } |k_i| < k_c \\ 0 & \text{for } |k_i| > k_c \end{cases} \qquad (2.60)$$

(i=1,2 and 3). In physical space, this filter is a damped sinusoid, with decreasing amplitude away from $\mathbf{x}'=\mathbf{x}$ [Leonard 1974]. The three filters described above are shown in Figure 2.3 both in physical (co-ordinate) space and in transformed (wavenumber) space.

By filtering the Navier-Stokes equations (2.20.a') one has:

$$\frac{\partial \rho \hat{u}_i}{\partial t} + \frac{\partial}{\partial x_j}(\rho \widehat{u_i u_j}) = -\frac{\partial \hat{p}}{\partial x_i} + \frac{\partial}{\partial x_j}\mu\left(\frac{\partial \hat{u}_i}{\partial x_j} + \frac{\partial \hat{u}_j}{\partial x_i}\right) \qquad (2.61)$$

with the problem of filtering the product $u_i u_j$. Considering that $u_i = \hat{u}_i + \tilde{u}_i$, one has:

$$\widehat{u_i u_j} = \widehat{\hat{u}_i \hat{u}_j} + \widehat{\hat{u}_i \tilde{u}_j} + \widehat{\tilde{u}_i \hat{u}_j} + \widehat{\tilde{u}_i \tilde{u}_j} \qquad (2.62)$$

This may be written:

$$\widehat{u_i u_j} = \hat{u}_i \hat{u}_j + L_{ij} + C_{ij} + \widehat{\tilde{u}_i \tilde{u}_j} \qquad (2.63)$$

where:

$$L_{ij} = \widehat{\hat{u}_i \hat{u}_j} - \hat{u}_i \hat{u}_j \qquad (2.64)$$

(so called "Leonard terms"); and:

$$C_{ij} = \widehat{\hat{u}_i \tilde{u}_j} + \widehat{\tilde{u}_i \hat{u}_j} \qquad (2.65)$$

(so called "cross terms").

The term $-\rho\widehat{\tilde{u}_i \tilde{u}_j}$ is the analogue of the generic Reynolds stress arising from the Reynolds-averaging of the Navier-Stokes equations, and is generally called unresolved, or subgrid, stress. If the Gaussian filter (2.59) is used, it can

be shown [Leonard 1974] that the "Leonard terms" can be expressed approximately by:

$$L_{ij} = \frac{\Delta^2}{24} \nabla^2(\hat{u}_i \hat{u}_j) \tag{2.66}$$

Similarly, the cross terms can be expressed approximately by:

$$\widehat{\tilde{u}_i \hat{u}_j} = \frac{\Delta^2}{24} \hat{u}_j \nabla^2 \hat{u}_i \tag{2.67.a}$$

$$\widehat{\hat{u}_i \tilde{u}_j} = \frac{\Delta^2}{24} \hat{u}_i \nabla^2 \hat{u}_j \tag{2.67.b}$$

Therefore, Eqn.(2.63) can be written:

$$\widehat{u_i u_j} = \hat{u}_i \hat{u}_j + \frac{\Delta^2}{24} [\nabla^2 \hat{u}_i \hat{u}_j + \hat{u}_i \nabla^2 \hat{u}_j + \hat{u}_j \nabla^2 \hat{u}_i] + \widehat{\tilde{u}_i \tilde{u}_j} \tag{2.68}$$

in which the only term left to be modelled is $\widehat{\tilde{u}_i \tilde{u}_j}$.

Note that, due to the existence of the 'Leonard' and 'cross' terms, one has $\widehat{u_i u_j} - \hat{u}_i \hat{u}_j \neq \widehat{\tilde{u}_i \tilde{u}_j}$ (in general). As discussed by Deardorff [1973.a] and Leonard [1974], the physical reason for this inequality is that in the turbulence spectrum there is no gap between the large and the small scales, but rather a continuous 'energy cascade' involving eddies of all intermediate scales.

The filtering techniques described above have been criticized by several authors. For example, Speziale [1985] has shown that computing Leonard's stresses explicitly while using an eddy-viscosity subgrid model violates Galilean invariance of the Navier-Stokes equations, and Piomelli et al. [1987] argue that using the length and velocity scales of the grid-sized eddies to parameterize subgrid-scale effects is inconsistent with the use of a Gaussian filter.

An approach alternative to the above filtering techniques, which allows to drop the (rather uncomfortable) Leonard and cross terms and to overcome the

above criticism, was proposed by Schumann [1975], but had been already practiced by Deardorff [1970.a foll.]. It is suitable for finite-volume / finite-difference based computational methods, and basically consists of replacing explicit filtering (prefiltering) by volume-averaging on each grid cell:

$$Q(\mathbf{x}) = \frac{1}{\Delta x_1 \Delta x_2 \Delta x_3} \int_{x_1-\Delta x_1/2}^{x_1+\Delta x_1/2} dx'_1 \int_{x_2-\Delta x_2/2}^{x_2+\Delta x_2/2} dx'_2 \int_{x_3-\Delta x_3/2}^{x_3+\Delta x_3/2} dx'_3 \; Q(\mathbf{x}') \qquad (2.69)$$

The application of this filter to the velocity components u_i leads to the following important properties:

$$\widehat{\hat{u}_i \hat{u}_j} = \hat{u}_i \hat{u}_j \qquad (2.70.a)$$

$$\widehat{\tilde{u}_i \hat{u}_j} = \widehat{\hat{u}_i \tilde{u}_j} = 0 \qquad (2.70.b)$$

The same approach can be applied to the temperature equation. As a result, Schumann's method leads to the following form of the equations governing the flow and thermal fields:

$$\frac{\partial \rho}{\partial t} + \frac{\partial}{\partial x_j}(\rho \hat{u}_j) = 0 \qquad (2.71)$$

$$\frac{\partial}{\partial t}(\rho \hat{u}_i) + \frac{\partial}{\partial x_j}(\rho \hat{u}_i \hat{u}_j) = -\frac{\partial \hat{p}}{\partial x_i} + \frac{\partial}{\partial x_j}\mu\left(\frac{\partial \hat{u}_i}{\partial x_j} + \frac{\partial \hat{u}_j}{\partial x_i}\right) - \frac{\partial}{\partial x_j}(\rho \widehat{\tilde{u}_i \tilde{u}_j}) \qquad (2.72)$$

$$\frac{\partial}{\partial t}(\rho \hat{T}) + \frac{\partial}{\partial x_j}(\rho \hat{u}_j \hat{T}) = \frac{\partial}{\partial x_j}\Gamma \frac{\partial \hat{T}}{\partial x_j} + \frac{\partial}{\partial x_j}(\rho \widehat{\tilde{u}_j \tilde{T}}) \qquad (2.73)$$

(subgrid density fluctuations were assumed to be negligible in order to derive the above equations). It has been shown by Antonopoulos-Domis [1981.b] that Schumann's method is not only simpler, but also more accurate (for a given filter width Δ) than methods based on "prefiltering" of the original equations.

The residual, or subgrid, stresses $\tilde{\tau}_{ij} = -\rho \widehat{\tilde{u}_i \tilde{u}_j}$ and the residual fluxes $\rho \widehat{\tilde{u}_j \tilde{T}}$ (which are the analogues of the Reynolds terms arising in time- or ensemble-averaged equations) contain unresolved terms and thus have to be expressed by means of a closure model. This is the task of the "subgrid models" which will be reviewed in the following Section.

2.4 Subgrid scale models for Large-Eddy Simulation

What one fool can do, another can

[Silvanus Thompson, 'Calculus made easy']

A survey of the subgrid-scale models for LES proposed and tested so far by various authors should not be separated from a discussion of their applications and of the numerical methods employed. However, for clarity of presentation, the main subgrid models will be classified and briefly described in this Section. Applications will be reviewed in more detail in Section 2.6, after a survey of the boundary conditions which will be given in Section 2.5.

2.4.1 Gradient-diffusion models

A large class of subgrid closure models are based on a gradient-diffusion hypothesis, similar to the Boussinesq hypothesis of conventional turbulence models. It consists of assuming the anisotropic part of the residual stress tensor $\tilde{\tau}_{ij}$ to be proportional to the resolved (large-scale) strain rate tensor $\hat{S}_{ij}$, i.e.:

$$\tilde{\tau}_{ij} - \frac{1}{3}\delta_{ij}\tilde{\tau}_{kk} = 2\rho\nu_s\hat{S}_{ij} \qquad (2.74)$$

in which:

$$\hat{S}_{ij} = \frac{1}{2}\left(\frac{\partial\hat{u}_i}{\partial x_j} + \frac{\partial\hat{u}_j}{\partial x_i}\right) \qquad (2.75)$$

($\nu_s = \mu_s/\rho$ is a kinematic subgrid viscosity, which has to be expressed by an appropriate model, and δ_{ij} is the Kronecker delta). If the subgrid turbulence energy (1/2) $\widehat{\tilde{u}_k\tilde{u}_k}$ is indicated by the symbol $\tilde{k}$, then the second term at the LHS of Eqn.(2.74) can be expressed as:

$$-\frac{1}{3}\delta_{ij}\tilde{\tau}_{kk} = \frac{2}{3}\delta_{ij}\rho\tilde{k} \qquad (2.76)$$

so that, substituting Eqn.(2.76) into Eqn.(2.74) and this into Eqn.(2.72); adding and subtracting the term (1/3) $\delta_{ij}\tilde{\tau}_{kk}$; and defining a modified pressure $\hat{P}$ including the kinetic term $\tilde{k}$:

$$\hat{P} = \hat{p} + \frac{2}{3}\rho\tilde{k} \tag{2.77}$$

the generic Navier-Stokes equation (2.72) can be written:

$$\frac{\partial}{\partial t}(\rho\hat{u}_i) + \frac{\partial}{\partial x_j}(\rho\hat{u}_i\hat{u}_j) = -\frac{\partial\hat{P}}{\partial x_i} + \frac{\partial}{\partial x_j}(\mu+\mu_s)\left(\frac{\partial\hat{u}_i}{\partial x_j} + \frac{\partial\hat{u}_j}{\partial x_i}\right) \tag{2.78}$$

For a constant-density fluid, Eqn.(2.78) can be simplified as:

$$\frac{\partial}{\partial t}(\hat{u}_i) + \frac{\partial}{\partial x_j}(\hat{u}_i\hat{u}_j) = -\frac{1}{\rho}\frac{\partial\hat{P}}{\partial x_i} + \frac{\partial}{\partial x_j}(\nu+\nu_s)\left(\frac{\partial\hat{u}_i}{\partial x_j} + \frac{\partial\hat{u}_j}{\partial x_i}\right) \tag{2.79}$$

Equations (2.71)-(2.78) are formally identical to the time-dependent version of the governing equations for turbulent flow based on conventional Boussinesq closure models such as the k-ε. In order to solve this set of equations, all that is needed is a closure relation expressing ν_s as a function of known (resolved) quantities.

As pointed out by Voke and Collins [1983.a], all proposed subgrid models belonging to the gradient-diffusion family can be summarized under the general form:

$$\nu_s = c\, l\, q \tag{2.80}$$

in which c is a dimensionless constant and l and q are a length and a velocity scale, respectively. They can be further classified as:

a) constant-ν_s model: $\nu_s = c_0$ (2.81.a)

b) 'strain' model: $\nu_s = c_1 l^2 \hat{S}$ (2.81.b)

c) 'vorticity' model: $\nu_s = c_2 l^2 \hat{\omega}$ (2.81.c)

d) unresolved energy model: $\nu_s = c_3 l\, \tilde{k}^{1/2}$ (2.81.d)

Bardina et al. [1983] list the same basic subgrid-viscosity models and include also some "hybrid" formulations obtained by linear combination of the above.

The first model can be used only for isotropic homogeneous turbulence, and of course reconducts LES to a direct simulation with an artificially reduced

Reynolds number. The second and third model can both be derived from the work of Smagorinsky [1963].

The 'strain' model (b) is by far the most popular subgrid model, and was developed also by Lilly [1966]; it is generally called 'Smagorinsky - Lilly' subgrid model. Note that it is a nonlinear model, as the subgrid viscosity linking the subgrid stresses with the large-scale strain rate $\hat{S}_{ij}$ is itself a function of $\hat{S}_{ij}$. The parameter l is a length scale and is generally related to the width of the filter used. In finite difference - finite volume simulations, especially when the Schumann volume-averaging approach is adopted, a sensible choice is to express l as the average cell size (cubic root of its volume); i.e.,

$$l = \bar{\Delta} \equiv (\Delta x_1 \Delta x_2 \Delta x_3)^{1/3} \qquad (2.82.a)$$

where the Δx_i's are the mesh sizes along the three directions. The quantity $\hat{S}$ is the quadratic invariant of the resolved strain rate tensor $\hat{S}_{ij}$:

$$\hat{S} = (2\, \hat{S}_{ij} \hat{S}_{ij})^{1/2} \qquad (2.82.b)$$

Eqn.(2.81.b) is more commonly written in the form:

$$\nu_s = (c_s \bar{\Delta})^2 \, (2\, \hat{S}_{ij} \hat{S}_{ij})^{1/2} \qquad (2.81.b')$$

The Smagorinsky-Lilly model can be derived by imposing equilibrium between energy transfer from large-scale to small-scale structures, and energy dissipation by the latter. A statistical derivation of this model from the Direct-Interaction Approximation (DIA) theory was given by Yoshizawa [1982, 1986], who also extended it to buoyancy-driven turbulence [Yoshizawa 1983].

A crucial issue is, of course, the choice of an "optimum" value for the constant c_s; the problem is discussed in Section 2.4.5.

Model (c) is a modified version of the more common Smagorinsky model (b), in which the parameter $\hat{S}$ is replaced by:

$$\hat{\omega} = (2\, \hat{\omega}_{ij} \hat{\omega}_{ij})^{1/2} \qquad (2.83)$$

$\hat{\omega}_{ij}$ being the resolved vorticity tensor:

$$\hat{\omega}_{ij} = \frac{1}{2}\left(\frac{\partial \hat{u}_i}{\partial x_j} - \frac{\partial \hat{u}_j}{\partial x_i}\right) \qquad (2.84)$$

This model was tested by Ferziger [1977] and was found to yield results comparable with those of the Smagorinsky-Lilly model (b). An advantage is that it gives a vanishing subgrid viscosity in regions of zero vorticity (irrotational flow). Of course, also this model is a nonlinear one.

Model (d) was initially proposed by Lilly [1967] and was developed independently by Schumann [1975] and Deardorff [1980]. Its application requires the knowledge of the subgrid turbulence energy $\tilde{k}$; this can be estimated by solving a transport equation for $\tilde{k}$, which is the analogue of the k transport equation to be solved in the k-ε and k-l turbulence models. For example, in his study of the atmospheric boundary layer, Deardorff [1980] solved the following sub-grid turbulence energy transport equation:

$$\frac{\partial \tilde{k}}{\partial t} + \frac{\partial}{\partial x_j}\hat{u}_j\tilde{k} = -\widehat{\tilde{u}_j\tilde{u}_k}\frac{\partial \hat{u}_j}{\partial x_k} + \frac{\partial}{\partial x_j}\nu_s\frac{\partial \tilde{k}}{\partial x_j} + S_B - \tilde{\varepsilon} \qquad (2.85)$$

in which S_B was a buoyancy-production term and $\tilde{\varepsilon}$ was the dissipation of subgrid turbulence energy. This was expressed in turn in terms of $\tilde{k}$ and of the length scale l as follows:

$$\tilde{\varepsilon} = c_\varepsilon \tilde{k}^{3/2} / l \qquad (2.86.a)$$

with:

$$c_\varepsilon = 0.19 + 0.51\, l/\bar{\Delta} \qquad (2.86.b)$$

Deardorff assumed (in the present notation) c_3=0.10, and defined the length scale l so that in highly turbulent, well mixed regions it coincided with the average mesh size:

$$l = \bar{\Delta} \qquad (2.87.a)$$

but in stably stratified, low-turbulence regions above the mixed layer was reduced according to:

$$l = 0.76\ (\tilde{k})^{1/2}\ (g/\vartheta_o\ \partial\vartheta_l/\partial y)^{-1/2} \qquad (2.87.b)$$

in which ϑ_l is a modified temperature (liquid water potential temperature) and ϑ_o a reference value for this.

The same subgrid model was used by Moeng [1984-1987] and Moeng and Wyngaard [1984-1988] to study turbulence in the planetary boundary layer. Horiuti [1985.a] and Yoshizawa and Horiuti [1985] derived a transport equation for the subgrid kinetic energy from statistical considerations and applied the resulting one-equation subgrid-energy model to the study of turbulent channel flows. The subgrid-energy model, and the form of the transport equation for $\tilde{k}$, are discussed also by Grötzbach [1987].

Also the transport equation (2.73), governing the temperature field, contains a term (the last at the RHS) made up by unresolved quantities. It consists of the divergence of the vector $\tilde{\mathbf{q}}$, or $\tilde{q}_i$ (unresolved, or subgrid, heat flux divided by the specific heat c_p):

$$\tilde{q}_i = \rho\widehat{\tilde{u}_i\tilde{T}} \qquad (2.88)$$

A gradient-diffusion assumption similar to that used for the subgrid stresses leads for $\tilde{q}_i$ to the expression:

$$\tilde{q}_i = -\Gamma_s \frac{\partial\hat{T}}{\partial x_i} \qquad (2.89)$$

in which $\hat{T}$ is the resolved temperature and $\Gamma_s = \rho\alpha_s$ the subgrid thermal diffusivity. By substituting Eqn.(2.89) into (2.73) one has the following form of the temperature transport equation:

$$\frac{\partial}{\partial t}(\rho\hat{T}) + \frac{\partial}{\partial x_j}(\rho\hat{u}_j\hat{T}) = \frac{\partial}{\partial x_j}(\Gamma+\Gamma_s)\frac{\partial\hat{T}}{\partial x_j} \qquad (2.90)$$

The subgrid thermal diffusivity Γ_s is generally expressed on the basis of the subgrid viscosity μ_s and of a 'subgrid Prandtl number' σ_s:

$$\Gamma_s = \mu_s / \sigma_s \qquad (2.91.a)$$

For constant-density fluids, the alternative form using kinematic viscosity and diffusivity is more appropriate:

$$\alpha_s = \nu_s / \sigma_s \qquad (2.91.b)$$

The issue will be discussed further in Section 2.4.5.

2.4.2 Non-Boussinesq models

A wider class of subgrid closure models can be obtained by dropping the gradient-diffusion hypothesis. Of course, this leads to more complex expressions for the subgrid stresses and fluxes $\tilde{\tau}_{ij}$, $\tilde{q}_{ij}$.

Deardorff [1974] used a subgrid stress/flux transport model, consisting of individual transport equations for each of the sub-grid stresses - much as in Reynolds-stress transport (RSM) closure for time- or ensemble-average based turbulence models. The model, once completed with heat transport and buoyancy terms, involved not less than seven constants to be 'tuned', and required many of the assumptions well known to RSM modellers in order to achieve closure. According to the author, this model required 2½ times more CPU time than a corresponding gradient-diffusion (Boussinesq) model. It is noteworthy that in later papers [Deardorff 1980, Moeng 1984] the NCAR group reverted to a simpler eddy-diffusivity approach. However, Deardorff had shown already in earlier work [1973.a] that both the subgrid-energy model and the Smagorinsky-Lilly 'strain' model can be formally derived as successive approximations from the full subgrid stress/flux transport model.

A similar second-order closure model, but based on algebraically approximated equations (and thus closely related to ASM closure models) was developed by Schumann [1975]. He started from the observation that the large-scale component of a scalar Q, obtained following a filtering or volume-averaging procedure, is still a function of space and time and can be decomposed into mean $\langle\widehat{Q}\rangle$ and fluctuating component $\widehat{Q}'' = \widehat{Q}-\langle\widehat{Q}\rangle$. $\langle\widehat{Q}\rangle$ can be thought to be either a long-term time average or an ensemble average; in particular, for the flow in a plane channel, an annulus or any other geometry presenting the appropriate symmetries, $\langle\widehat{Q}\rangle$ can be replaced by the average over planes or surfaces parallel to the walls. Now, the mean component $\langle\widehat{Q}\rangle$ is more anisotropic, and more sensitive to the boundary conditions and to the effect of solid walls, than the fluctuating component. Thus, instead of modelling the $\tilde{\tau}_{ij}$'s via a single subgrid viscosity as in the Smagorinsky model, Schumann split the resolved strain rate tensor $\widehat{S}_{ij}$ into mean $\langle\widehat{S}_{ij}\rangle$ and fluctuating

component $\hat{S}_{ij}-\langle\hat{S}_{ij}\rangle$, and assumed that the unresolved stresses $\tilde{\tau}_{ij}$ are the superposition of a 'locally isotropic' part, proportional to $\hat{S}_{ij}-\langle\hat{S}_{ij}\rangle$, and of an 'inhomogeneous' part proportional to $\langle\hat{S}_{ij}\rangle$. Moreover, he formulated in tensorial terms rather than in scalar terms the relation between the $\tilde{\tau}_{ij}$ and the $\hat{S}_{ij}$, and allowed for the effects of computational grid anisotropy. In the context of the volume-averaging (implicit filtering) procedure, the resulting model can be summarized as:

$$\tilde{\tau}_{ij}/\rho = -2\,\nu_{s,ij}\,(\hat{S}_{ij}-\langle\hat{S}_{ij}\rangle) - 2\,\nu_{s,ij}^{*}\,\langle\hat{S}_{ij}\rangle \qquad (2.92)$$

The 'locally isotropic' subgrid viscosity tensor is expressed as:

$$\nu_{s,ij} = c_2(F\tilde{k})^{1/2}C_{ij} \qquad (2.93)$$

in which F is the characteristic area (face of a control volume) over which the $\tilde{\tau}_{ij}$ are averaged; $\tilde{k} = \widehat{\tilde{u}_i\tilde{u}_i}/2$ is the subgrid kinetic energy, also averaged over F; c_2 is a constant loosely corresponding to the constant c_s of the Smagorinsky model; and the C_{ij} are the components of a geometric tensor introduced in order to account for the anisotropic effects associated with the computational grid.

As to $\nu_{s,ij}^{*}$, associated with the mean component of the strain rate tensor and thus strongly depending on the external boundary conditions, Schumann restricted his analysis to the flow in plane or annular channels; in this case, as mentioned above, $\langle\hat{u}_i\rangle$ and $\langle\hat{S}_{ij}\rangle$ are averages over planes or surfaces parallel to the walls and thus are functions of the coordinate y only (distance from the nearest wall). The only non-zero component of $\langle\hat{S}_{ij}\rangle$ is $\langle\hat{S}_{12}\rangle$, and the corresponding component of ν_s^{*} is:

$$\nu_{s,12}^{*} = l^2\,|\delta_2\langle\hat{u}_1\rangle| \qquad (2.94)$$

in which δ_2 is the finite-difference operator approximating the derivative along the cross-stream direction 2, and l is a mixing length expressed by:

$$l = \min[c_{10}F^{1/2},\ \kappa y] \qquad (2.95)$$

where c_{10} is a further constant and $\kappa = 0.42$ is the Von Karman cappa.

A similar ASM-like second-order closure model was presented recently by Schmidt and Schumann [1989].

A simplified version of Schumann's model was used by Moin and Kim [1982] in their well known simulations of plane-channel flow. They expressed the two subgrid viscosities ν_s, ν_s^* as simple scalars:

$$\nu_s = (c_s D \bar{\Delta})^2 \left[2(\hat{S}_{ij} - \langle\hat{S}_{ij}\rangle)(\hat{S}_{ij} - \langle\hat{S}_{ij}\rangle)\right]^{1/2} \qquad (2.96.a)$$

$$\nu_s^* = (c_s^* D^* \Delta_2)^2 \left[2 \langle\hat{S}_{ij}\rangle \langle\hat{S}_{ij}\rangle\right]^{1/2} \qquad (2.96.b)$$

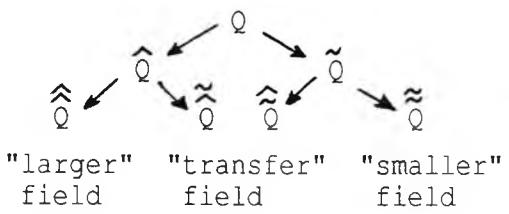
in which $c_s = c_s^* = 0.065$ (constants similar to the Smagorinsky c_s), D and D^* are Van-Driest damping factors accounting for near-wall effects (see next Section), $\bar{\Delta}$ is the characteristic filter width, and Δ_2 is the grid size in the direction normal to the walls.

Non-Boussinesq subgrid models such as those described above usually involve a relevant number of empirical constants and of 'ad hoc' assumptions; they behave very well for specific problems and simple geometries, such as boundary layers, plane channels and annuli, but are very difficult to generalize to different problems and complex configurations. For example, the models used by Schumann and Moin and Kim rely heavily on the possibility of averaging the various flow quantities over surfaces parallel to the walls, which of course would not be allowed if these surfaces were not periodic ("homogeneous") ones.

2.4.3 Multi-level models

Another approach to more refined subgrid models is based on considering more than two levels (i.e., resolved and subgrid, Eqn.(2.56)) in the decomposition of the flow field.

Bardina, Ferziger and Reynolds [1980, 1983] proposed a subgrid model based on a three-level decomposition. For any scalar Q, the repeated application of the filtering procedure generates the three-level hyerarchy summarized by the following scheme:



in which $\tilde{\hat{Q}}=\hat{Q}-\hat{\hat{Q}}$ and $\hat{\tilde{Q}}=\tilde{Q}-\tilde{\hat{Q}}$ are actually the same field, christened "transfer" field by the authors and including the larger eddies of the subgrid field, coincident with the smaller eddies of the resolved field. By assuming the energy cascade to occur always through the "transfer" field, Bardina et al. were able to show that a good approximation for the terms $R_{ij} = \widehat{\tilde{u}_i\tilde{u}_j} + \widehat{\tilde{u}_i\hat{u}_j} + \widehat{\hat{u}_i\tilde{u}_j}$ (including both the subgrid stresses and the 'cross' terms defined in Section 2.3) should be:

$$R_{ij} = \hat{u}_i\hat{u}_j - \hat{\hat{u}}_i\hat{\hat{u}}_j \qquad (2.97)$$

However, this model does not ensure a net energy transfer from larger to smaller scales. Thus, it was used only in linear combination with an eddy-viscosity model having the appropriate energy-transfer properties, so that the subgrid stresses (inclusive of 'cross' terms) were expressed by the "mixed" model:

$$\tilde{\tau}_{ij}-(1/3)\delta_{ij}\tilde{\tau}_{kk} = -2\rho\nu_s\hat{S}_{ij} + \rho c_r[R_{ij}-(1/3)\delta_{ij}R_{kk}] \qquad (2.98)$$

with the R_{ij}'s expressed by Eqn.(2.97), and c_r being a combination parameter to be 'tuned' by numerical experiments. The authors tested various combinations of the 'scale-similarity' model with eddy-dissipation models, compared results with full (direct) numerical simulations, and shown that their procedure gave better predictions than any eddy-viscosity approach, especially as regards comparisons at vector and tensor level.

The approach proposed by Bardina et al. was also tested and discussed by Horiuti [1989].

On similar concepts is based the "dynamic SGS model" proposed by Germano et al. [1991]. Basically, it attempts to locally calculating the eddy viscosity coefficient to reflect closely the state of the flow; this is done by sampling the smallest resolved scales and using this information to model the subgrid scales. Besides the grid filter G, a (broader) test filter G' is introduced; scales whose length is intermediate between the grid filter width and the test filter width contribute resolved turbulent stresses, which can be used to estimate the local and instantaneous value of the Smagorinsky 'constant' c_s.

In practice, the authors applied the model only to plane-channel flow, where c_s can be assumed to be a function of t and y (distance from wall) only. They shown that the model predicted the correct asymptotic behaviour of the subgrid viscosity at walls without the use of 'ad hoc' damping functions (see

following subsection), and gave results in better agreement with direct simulations than the basic Smagorinsky model.

2.4.4 Non-conventional approaches

An interesting approach to subgrid modeling, which attempts to found it on strange-attractor theory and which does not resort to formal averaging or filtering, is followed by McDonough and co-workers [McDonough et al. 1984.a; McDonough and Bywater 1986]. For each flow variable Q, they assume a standard additive decomposition of the same form as Eqn. (2.56):

$$Q = Q_o + Q^* \tag{2.99}$$

in which, however, Q_o may be assumed to correspond to the first few modes of a generalized Fourier representation, which can be accurately approximated globally via any standard discretization technique (finite difference, finite element, spectral), while the term Q^* is associated with the remainder of the Fourier series. The authors do not work directly on the full Navier-Stokes equations, but rather on their one-dimensional version known as Burgers' equation:

$$\frac{\partial u}{\partial t} + u \frac{\partial u}{\partial x} = - p_x + \nu \frac{\partial^2 u}{\partial x^2} \tag{2.100}$$

which formally contains all the kinds of terms appearing in the full Navier-Stokes equations (i.e. linear temporal and diffusive, nonlinear advective, and a forcing term corresponding to a pressure gradient). Also other authors, for example Love and Leslie [1979], had used Burgers' equation in place of the more cumbersome full Navier-Stokes equations to study and compare different subgrid models for LES.

By substituting Eqn.(2.99), written for u and p_x, into Eqn.(2.100), the original equation is separated into the equivalent coupled system:

$$\frac{\partial u^o}{\partial t} + u^o \frac{\partial u^o}{\partial x} + (1-\beta) \frac{\partial}{\partial x} (u^o u^*) - \frac{1}{Re} \frac{\partial^2 u^o}{\partial x^2} = - p_x{}^o \tag{2.101.a}$$

$$\frac{\partial u^*}{\partial t} + u^* \frac{\partial u^*}{\partial x} + ß \frac{\partial}{\partial x}(u^{\circ}u^*) - \frac{1}{Re}\frac{\partial^2 u^*}{\partial x^2} = - p_x^* \qquad (2.101.b)$$

in which $Re = 1/\nu$ and ß is an 'a priori' unknown parameter satisfying $0<ß\leq 1$. The authors observe that, in contrast to usual averaging or filtering procedures, this decomposition does not lead to Reynolds stress-like terms which ultimately must be modeled to close the system. On the other hand, the decomposition parameter ß, whose values are in general unknown, must be prescribed. The value ß=1 is chosen in the papers considered here; the authors mention that values for ß can be derived from the 'renormalization group' theory of LES formulated by Yakhot and Orszag [1985].

Now, McDonough et al. concentrate on the small-scale equation (2.101.b) and look for local solutions of this in an arbitrary interval $[x_i-h/2, x_i+h/2]$, h being the finite-difference grid spacing for the large-scale calculations. A solution is sought via representation by truncated Fourier series, leading to a system of ordinary differential equations in the time-dependent Fourier coefficients. The large-scale terms appearing in Eqn.(2.101.b) are treated as constants in this interval h, which is consistent with first-order large-scale spatial approximations. Arbitrary values are chosen for these large-scale fields and for the initial conditions, as well as for the 'Reynolds number' Re.

The resulting computed behaviour of $u^*(x,t)$ in h displays bifurcation sequences as a function of the parameters and subparameters representing the large-scale solutions. The use of a combination of techniques, including velocity time series, power spectral densities and Poincarè maps, confirms the existence of a strange attractor in the appropriate phase-space. In particular, as the 'bifurcation subparameter' p_x^* is varied for a fixed Re, a detailed sequence of bifurcations is identified in the computed small-scale solutions, which is reminiscent of the Ruelle-Takens [1971] picture of transition to turbulence and also similar to experimental results such as those obtained by Gollub and Benson [1980] for the Rayleigh-Benard problem. However, chaotic solutions appear at values of p_x^* well below that at which the final bifurcation to a strange attractor occurs, suggesting that here the sequence leading to turbulence may be more complex than in the Ruelle-Takens theory and may involve Feigenbaum period doubling [Feigenbaum 1980] and Pomeau-Manneville intermittency [Pomeau and Manneville 1980]. These results are noteworthy as they are obtained from a physical model (Burgers' equation) which, though still far from the full Navier-Stokes equations, is certainly

closer to them than the simple, discrete, few-equation systems considered by Feigenbaum, Lorenz or other authors, and on which Ruelle and Takens founded their view of transition to turbulence.

Detailed numerical solutions for the small-scale field u^* can now be fed back into the large-scale equation (2.101.a); the idea here is that the small-scale solution relative to a space interval h and to a time interval Δt has nothing special, and thus can be extended in space and time to the whole large-scale domain. Of course, this is equivalent to a subgrid model for LES. In other papers [McDonough et al. 1984.b] the authors extended their treatment to the temperature equation and to the one-dimensional equivalent of free-convection problems.

However, the authors did not generalize their study to the full three-dimensional Navier-Stokes equations, so that - for the time being - their results have mainly a theoretical relevance but cannot be directly transposed into subgrid model formulations.

2.4.5 Further aspects of subgrid modelling

There are several aspects of subgrid modelling which deserve a closer consideration. Some of these will be briefly scrutinised here, namely, near-wall damping, magnitude of the subgrid viscosity coefficient, energy backscatter, and subgrid Prandtl number. Of the issue of wall boundary conditions, a more detailed overview will be given in Section 2.5.

I. Near-wall damping

As in closure models based on time- or ensemble-averages, the wall region deserves special attention. In particular, the subgrid model has to account for the fact that the ~~total stresses do not~~ resolved strain rate does not vanish on walls, while the subgrid stresses do; hence, the subgrid viscosity ν_s or its more complex equivalents must vanish at the walls. This is related to the fact that on solid walls the large eddies dissipate their energy directly rather than by the usual energy cascade involving smaller and smaller eddies.

Wall effects can be partially taken into account by appropriately reducing, or 'damping', the length scale l in the proximity of walls. An approach common to conventional low-Reynolds number turbulence models is to use the Van Driest [1956] damping function:

$$D \equiv l/l_\infty = 1 - \exp(-y^+/A^+) \qquad (2.102.a)$$

where l_∞ is the value of l far from walls, y^+ is the distance from the nearest wall, expressed in 'wall units' (i.e., $y^+=y\,u_\tau/\nu$), and A^+ is a constant for which the value of 25 is generally used.

The damping function may be given the alternative form:

$$D \equiv l/l_\infty = 1 - \exp[-(y^+/A^+)^2] \qquad (2.102.b)$$

which has the property of yielding not only l=0, but also dl/dy=0 on the wall; this may be preferable for numerical reasons (i.e., to avoid sharp gradients of l).

A third damping function was suggested by Miner et al. [1989]:

$$D = [f_0 + (1-f_0)\,\{1 - \exp[-(y^+-y_0^+)/A^+]\}^2]^{1/2} \qquad (2.102.c)$$

with $f_0 = 0.04$, $y_0^+ = 8$.

The three profiles given for $D(y^+)$ by eqns.(2.102.a),(2.102.b),(2.102.c) are compared in Figure 2.4. Models (a) and (b) yield similar profiles, with the latter giving lower values of D for $y^+<A^+$ and higher values for $y^+>A^+$. Model (c) is characterized by a minimum at $y^+=y_0^+$, and thus yields relatively high values of D (i.e., less damping) within the viscous sublayer.

Taking near-wall damping into account, the Smagorinsky-Lilly subgrid model for ν_s, Eqn.(2.81.b'), can be re-written as:

$$\nu_s = (c_s D\bar{\Delta})^2\,(2\hat{S}_{ij}\hat{S}_{ij})^{1/2} \qquad (2.103)$$

in which D is given by one of the (2.102), or by some alternative formulation.

It should be observed that the use of the above near-wall damping functions requires some knowledge of the appropriate "inner" length scale ν/u_τ. For boundary-layer or plane-channel flows, this can be computed from the imposed streamwise pressure gradient or from the local or average wall shear stress without special difficulties (see Section 2.5 and Chapter 4). However, for flows in complex geometries (notably involving recirculation) u_τ may not be well defined and further assumptions would be required, see Chapters 5-6.

II. Magnitude of the subgrid eddy-viscosity coefficient

A much debated issue of LES is the magnitude to be attributed to the coefficient relating the subgrid viscosity to the length scale and strain rate, or equivalent quantities. The problem is most simply formulated in the

context of the Smagorinsky model, where it comes down to the choice of a value for the constant c_s.

Lilly [1966] determined that, for homogeneous isotropic turbulence with $\bar{\Delta}$ equal to the grid size and cutoff in the inertial subrange, one should have c_s=0.23. Values close to this were selected as optimum by Clark et al. [1979] on the basis of comparisons at scalar level with direct simulation results.

However, in most applications to flows with mean shear (see review in Section 2.6), smaller values of c_s were found necessary to avoid excessive damping of the resolved fluctuations. McMillan et al. [1980] used direct simulation results to show that c_s must decrease with increasing strain rates; similarly, in large-eddy simulations of the atmospheric boundary layer Deardorff [1970.b and foll.] found that the value 0.17 gave best results for neutral conditions, but a higher value (0.21) was better under unstable conditions, i.e. when buoyancy-generated turbulence prevails on shear-induced turbulence. The optimum choice of c_s is also discussed in Deardorff [1971].

In actual large-eddy simulations of channel flows, values of about 0.1 were found appropriate both by Deardorff [1970.a], who used only $\sim 10^4$ grid points, and by Piomelli et al. [1989], who used much finer grids. An even smaller value (0.065) was used by Moin and Kim [1982], who had up to $\sim 5*10^5$ grid points, for both the "locally isotropic" and the "inhomogeneous" constants c_s, c_s^* in Eqns.(2.96). This is in contrast with results of Mason and Callen [1986], who found that the value c_s=0.2 gave good predictions if the grid resolution was sufficiently fine, and concluded that lower values of c_s are required only if the numerical resolution is insufficient. The contrast may be partly due to the fact that Mason and Callen employed "synthetic" wall boundary conditions, i.e. wall functions, while Piomelli et al. resolved the viscous sublayer explicitly.

In conclusion, there is not much agreement on the magnitude of the subgrid viscosity coefficient. Values ranging from 0.065 to 0.23 have been claimed to be optimum by different authors, in unclear correlation with the flow conditions, the grid size and the numerical methods used. What can be said with some confidence is that c_s is of the order of 0.1, and is larger for isotropic and buoyancy-induced turbulence than for shear-generated turbulence; also, smaller values of c_s seem to be appropriate in the near-wall region than in the bulk flow. Modified Smagorinsky models, in which the 'constant' c_s was made a function of the local flow field, have been proposed and tested by Kobayashi et al. [1985.b] and Yoshizawa [1989]. Also the dynamic SGS model of Germano et al., mentioned in Section 2.4.2, goes along this direction.

The author's impression is that in real simulations both numerical damping and numerically-generated fluctuations are superimposed on 'true' subgrid effects, and tend to mask the separate influence of the subgrid viscosity coefficient. Stable and even realistic simulations of complex and recirculating flows at very high Reynolds number have been presented [Nishikawa et al. 1991], which used no subgrid model at all!

III. Energy backscatter

Most of the commonly used subgrid-scale models assume that the main function of subgrid scales is to remove energy from the large scales and dissipate it through the action of viscous forces. However, it has been known for some years that while, on the average, energy is indeed transferred from the large to the small scales ("forward scatter"), reversed energy flow ("backscatter") from the small scales to the large ones may also occur intermittently.

By post-filtering large databases from direct simulations of turbulent and transitional plane-channel flows, Piomelli et al. [1991] shown that backscatter may interest a large fraction of the grid points at any instant; in flows undergoing transition to turbulence even the net plane-averaged transfer may occur backward, especially in the near-wall region and during the early stages of the transition. The precise amount of backscatter was found to depend on the Reynolds number and on the filter used; whatever its magnitude, an accurate modelling of this phenomenon is in principle desirable in order to obtain accurate predictions of the resolved flow field, especially in transitional and non-equilibrium conditions.

However, as discussed by Piomelli et al., the nett energy transfer from small to large scales is given by the subgrid-scale dissipation $\varepsilon_{SGS} = \tilde{\tau}_{ij}\widehat{S}_{ij}$. In Smagorinsky-type models, $\tilde{\tau}_{ij} = -2\mu_s\widehat{S}_{ij}$ and thus $\varepsilon_{SGS} = -2\,\mu_s\widehat{S}_{ij}\widehat{S}_{ij}$, which is always negative. Thus, these models are absolutely dissipative, i.e. they can not predict backscatter. The "mixed model" of Bardina et al. [1980, 1983] and the "dynamic SGS model" of Germano et al. [1991] are capable of predicting backscatter and thus are more recommendable for transitional and non-equilibrium flows. For fully developed turbulent flows in channels, the correct modelling of backscatter does not seem to be as crucial, and absolutely dissipative models such as Smagorinsky's are (under this respect) quite acceptable.

IV. Subgrid Prandtl number

The 'subgrid Prandtl number' is the LES analogue of the 'turbulent Prandtl number' σ_t used in conventional gradient-diffusion closure models of turbulence. However, values consistently ranging from 0.7 to 0.9 have been proposed in the literature for this latter parameter, and can be theoretically justified on the basis of turbulence theory [Landau and Lifschitz 1959; Yakhot et al. 1987]. On the contrary, a broad range of values has been proposed in the LES literature for the subgrid Prandtl number, from 0.25 [Hunter et al. 1988] to 0.5 [Antonopoulos-Domis 1981.a] and 0.85 [Kobayashi et al. 1984, 1985.b]. Deardorff [1973.a] observed that pressure fluctuations at the sub-grid scale can inhibit momentum transfer relative to eddy transfer of scalar properties, thus making values of σ_s much less than 1 physically reasonable. In their large-eddy simulations of the planetary boundary layer, Deardorff and the NCAR group generally made σ_s a function of the local atmospheric stability, choosing values close to 1 in stably-stratified regions and smaller values in well mixed regions. For example, in Deardorff [1980] σ_s was expressed as:

$$\sigma_s \equiv \frac{\nu_s}{\alpha_s} = (1+21/\bar{\Delta})^{-1} \qquad (2.104)$$

with l given by Eqns.(2.87), and thus ranged from 1/3 to 1. Moeng and Wyngaard [1988] derived a value of about 0.4 from high-resolution simulations using a 96^3-grid. Alternative values for σ_s were tested in other NCAR works, see also Section 2.6.

Finally, it is to be observed that the efforts towards improved subgrid models should address not only the problem of a better representation of the subgrid terms, but also the formulation of criteria for the optimum choice of the 'cutoff' between large and small scales, i.e. of the grid size for a given problem. Currently, the finest grids compatible with the available computational resources are usually adopted; however, as faster and larger computational means become more common, the choice of optimum grid dimensions will probably acquire an increasing importance and will have to be based on detailed considerations on the turbulence spectra and the large-eddy size. This will probably constitute the true turning point towards the application of LES to problems of engineering interest.

2.5 Wall boundary conditions for Large-Eddy Simulation

Humpty Dumpty sat on a wall:
Humpty Dumpty had a great fall.
All the King's horses and all the King's men
Couldn't put Humpty Dumpty in his place again
[Lewis Carroll, 'Through the looking glass']

2.5.1 Local formulations

One of the most subtle problems of LES is the correct formulation of boundary conditions for the resolved fields on solid walls.

Let us consider first the hydrodynamic problem. Restricting our attention to finite-volume approximation methods, and with no essential loss of generality, the problem of imposing wall boundary conditions to the velocity field $\mathbf{u}$ basically consists of specifying the contribution carried to the momentum balance in a near-wall cell (control volume) by the face or faces which lie on a wall.

For the momentum balance in the direction normal to the wall, this is easily accomplished by imposing the normal component of $\mathbf{u}$ to vanish on the wall itself (this is a rather general condition and holds even for inviscid flows). On the other hand, for the directions tangential to the wall the problem can be restated as that of defining a relation between the velocity $\mathbf{u}_p$ at a near-wall grid point, and the local wall shear stress τ_w at the corresponding wall location.

The velocity $\mathbf{u}_p$ can always be decomposed into a component $\mathbf{u}_{par}$ parallel to the wall, and a component $\mathbf{u}_n$ normal to it (which in most cases will be very small, but not necessarily nil):

$$\mathbf{u}_p = \mathbf{u}_{par} + \mathbf{u}_n \qquad (2.105)$$

(see Figure 2.5). Without loss of generality, the relation between $\mathbf{u}_{par}$ and τ_w may be given the linear form:

$$\tau_{w,i} = - T_{M,i}\, u_{par,i} \qquad (2.106)$$

which applies separately to each component of τ_w and $\mathbf{u}_{par}$ along cartesian axes x_i; the $T_{M,i}$'s are temporarily unspecified coefficients (note that, in

general, the wall may be arbitrarily oriented with respect to the axes x_i so that all three components $\tau_{w,i}$ may be nonzero).

Now, if P lies in the viscous sublayer, the velocity profile can be assumed linear between P and P' (Figure 2.5) and the wall shear stress τ_w is simply given by:

$$\tau_w = - \mu \, u_{par} / y_p \qquad (2.107)$$

so that the three multipliers $T_{M,i}$ are equal and their common value is:

$$T_{M,i} = \mu / y_p \qquad (i=1,2,3) \qquad (2.108)$$

Thus, Eqn.(2.106) expresses a truly linear relation. In Eqn.(2.108), μ should be the laminar viscosity; as an alternative, the total (laminar + subgrid) viscosity $\mu_{tot} = \mu + \mu_s$ may be used instead. Eqn.(2.108) then becomes:

$$T_{M,i} = \mu_{tot} / y_p \qquad (i=1,2,3) \qquad (2.108')$$

Here, μ_s and μ_{tot} may be evaluated at P or, better, averaged over $\overline{PP'}$. However, the near-wall damping expressed by Eqns.(2.102) and similar ensures that μ_s is very small in the viscous sublayer, so that $\mu_{tot} \cong \mu$ and the two formulations (2.108), (2.108') are practically equivalent.

On the other hand, if P lies outside the viscous sublayer, i.e. in the fully turbulent region, the velocity profile in PP' cannot be assumed to be linear, so that Eqn.(2.107) does not hold. An alternative is to assume that the 'universal' logarithmic velocity profile holds in $\overline{PP'}$:

$$|u_{par}|^+ = (1/\kappa) \ln (E y_p^+) \qquad (2.109)$$

in which

$$u^+ \equiv u / u_\tau \qquad (2.110.a)$$

$$y^+ \equiv y \, u_\tau / \nu \qquad (2.110.b)$$

and

$$u_\tau \equiv (|\tau_w|/\rho)^{1/2} \qquad (2.111)$$

(friction velocity). In Eqn.(2.109), κ is the Von Karman constant ($\tilde{=}0.42$) and E is a constant linked to the nondimensional thickness of the viscous sublayer, y_v^+, by:

$$E = \exp(\kappa y_v^+) / y_v^+ \qquad (2.112)$$

A value of about 11 can be accepted for y_v^+; as a consequence, $E \tilde{=} 9.8$.

Writing for simplicity $u_{par} \equiv |\mathbf{u}_{par}|$, Eqns.(2.109)-(2.110) yield:

$$u_\tau = (\kappa u_{par}) / \ln(E y_p u_\tau / \nu) \qquad (2.113)$$

which can be used to compute u_τ iteratively, starting from any reasonable guess, if y_p and u_{par} are (locally) known. Once u_τ is computed, Eqn.(2.111) gives the modulus of the wall shear stress τ_w. Coherently with the assumption of 'universal' wall functions, τ_w can be supposed to be parallel to $\mathbf{u}_{par}$; the result is:

$$T_{M,i} = -\rho u_\tau \kappa / \ln(E y_p u_\tau / \nu) \quad (i=1,2,3) \qquad (2.114)$$

Eqns.(2.108) (to be used if P lies in the viscous sublayer) and (2.114) (to be used otherwise) are essentially identical to the approach proposed by Mason and Callen [1986] in their large-eddy simulations of plane-channel flow. Hence, they will be called "Mason-Callen boundary conditions", or "model a", in the following. Note that whether P does or does not lie in the sublayer can be simply verified by checking whether the following inequality holds:

$$u_{par} \leqslant \nu (y_v^+)^2 / y_p \qquad (2.115)$$

A major limit of this formulation is that it is based on the assumption that universal 'wall functions' hold locally and instantaneously (or, at least, on the average in the limited region included in a single control volume); this may be questioned in a truly turbulent flow, as it neglects the existence of the phase shift between the wall shear stress and the near-wall velocity, observed, among the others, by Hanjalić and Stosić [1983]. Also, the validity itself of 'universal' wall functions is questionable in complex flows, notably involving recirculation, as discussed by Ciofalo and Collins [1989.a]. On the other hand, the above approach is the only one that can be applied, at least

formally, to general geometries, as it is based entirely on local quantities and makes no use of "wall-averaged" or "channel-averaged" velocities and stresses. This quality is not shared by the formulations which will now be discussed.

2.5.2 Global formulations

A second possible approach to the formulation of wall boundary conditions (in the sense specified above) is based on assuming that 'universal' wall functions (including the linear velocity profile in the viscous sublayer) do not hold locally, but rather globally, i.e. on the average over the whole computational domain.

Several alternative formulations of this kind are reviewed, for example, by Piomelli et al. [1989] for the case of plane Poiseuille flow ("plane channels"). They will be discussed in the following in a form slightly more general than that used by Piomelli et al. (who do not consider the case of P lying in the viscous sublayer).

Model b - This is basically as proposed by Schumann [1975]. The local wall shear stress is expressed as:

$$\tau_w = - |\tau_o| \, u_{par} / U_p' \qquad (2.116)$$

in which τ_o is the "equilibrium" average wall shear stress along x, related to the driving streamwise pressure gradient $\Delta p/\Delta x$ by:

$$\tau_o = \delta \, \Delta p/\Delta x \qquad (<0) \qquad (2.117)$$

while U_p' is the corresponding near-wall velocity as given by the 'universal' wall functions, i.e.:

$$U_p' = \begin{cases} u_\tau^2 \, y_p / \nu & (\text{for } y_p^+ \equiv y_p u_\tau/\nu \leq y_v^+) \qquad (2.118.a) \\ (u_\tau/\kappa) \ln (E y_p u_\tau/\nu) & (\text{for } y_p^+ \equiv y_p u_\tau/\nu > y_v^+) \qquad (2.118.b) \end{cases}$$

The multipliers $T_{M,i}$ are equal also in this case, and are given by:

$$T_{M,i} = |\tau_o|/U_p' \qquad (i=1,2,3) \qquad (2.119)$$

(also, if x, y and z are the downstream, cross-stream and spanwise directions, respectively, the walls will be parallel to the xz plane and thus only $\tau_{w,x}$ and $\tau_{w,z}$ will be nonzero, while $\tau_{w,y}=0$ everywhere).

Of course, this formulation is particularly "comfortable" to use when the "driving" pressure gradient $\Delta p/\Delta x$ (and not the flow rate in the channel) is imposed as a known quantity, as in this case the multiplier T_M is also a known quantity and does not depend on the solution.

Note that, in general, the average of $u_{par,x}$ over planes parallel to the walls, $\langle u_{par,x} \rangle$, will not equal U_p' (the former quantity depends on the instantaneous computed flow field, while the latter is known "a priori"). As a consequence, Eqn.(2.116), the wall-averaged computed stress $\langle \tau_x \rangle$ along the main flow direction will not equal the "equilibrium" value τ_o, i.e. will not balance the imposed driving pressure gradient, and the flow rate will be free of varying during the simulation.

Model c - This is basically as proposed by Grötzbach [1987]. The local wall shear stress is expressed as:

$$\tau_w = - |\tau_o'| \, u_{par} / U_p \qquad (2.120)$$

which is formally very similar to Eqn.(2.116). However, here U_p is the mean near-wall velocity, as computed by averaging the values of $u_{par,x}$ (which are part of the solution) over planes parallel to the walls:

$$U_p = \langle u_{par,x} \rangle \qquad (2.121)$$

while τ_o' is the wall shear stress along x, satisfying the 'universal' profile for U_p; i.e., $\tau_o' \equiv \rho (u_\tau')^2$, where u_τ' satisfies:

$$U_p/u_\tau' = \begin{cases} y_p u_\tau'/\nu & (\text{for } y_p^+ \equiv y_p u_\tau'/\nu \le y_v^+) \qquad (2.122.a) \\ (1/\kappa) \ln (E y_p u_\tau'/\nu) & (\text{for } y_p^+ \equiv y_p u_\tau'/\nu > y_v^+) \qquad (2.122.b) \end{cases}$$

Eqns.(2.122), on the whole, should be regarded as a transcendent equation in u_τ' which is necessary to solve in order to compute τ_o' and thus to apply Eqn.(2.120). Also in this case, the multipliers $T_{M,i}$ are equal and are given by:

$$T_{M,i} = |\tau_o'|/U_p \qquad (i=1,2,3) \qquad (2.123)$$

Note that, in this case, $\langle \tau_{w,x} \rangle$ is equal to τ_o'. However, this in turn is not equal to $\delta \Delta p/\Delta x$; thus, as in the previous model, the wall shear stress does not balance the imposed pressure gradient and global equilibrium of the fluid is not ensured.

Model d - This was proposed by Piomelli et al. [1989] to take into account somehow the effect of the elongated structures which are found in the wall region of a turbulent channel flow. It is based on the assumption that the local wall shear stress is related not to the local near-wall (parallel) velocity, but to the near-wall velocity at a location shifted downstream by a length l_x. Thus, they may be called "shifted" wall boundary conditions. The wall shear stress is expressed by:

$$\tau_w = - |\tau_o'| \, u_{par}(x+l_x, y_p, z) / U_p \qquad (2.124)$$

in which τ_o' and U_p have the same meaning as in model (c), while l_x is related to the distance of near-wall points P from walls, y_p, by:

$$l_x = y_p \, \mathrm{cotg} \, \phi \qquad (2.125)$$

(see Figure 2.6). Piomelli et al. suggest a value of about 8°-13° for the characteristic angle ϕ. The multipliers $T_{M,i}$ are given by:

$$T_{M,i} = \frac{|\tau_o'|}{U_p} \frac{u_{par,i}(x+l_x, y_p, z)}{u_{par,i}(x, y_p, z)} \qquad (2.126)$$

In this case, the $T_{M,i}$'s may be different from each other; namely, $T_{M,x}$ may differ from $T_{M,z}$.

Model e - Also this model was proposed by Piomelli et al. [1989] to take into account the effect of the near-wall coherent structures of a turbulent channel flow. It is based on the assumption that the local wall shear stress is affected by "ejection" events (see Introduction) occurring at a location translated downstream by a length l_x. When fluid is ejected from the wall towards the centre of the channel, the main velocity (u) in the near-wall region decreases, thus reducing the gradient $|\partial u/\partial y|$ and the wall shear stress $\tau_{w,x}$ (in absolute value). The opposite occurs when fluid coming from the central regions of the channel is brought towards the wall by a "sweep-inrush"

event. Note that the spanwise wall shear stress, $\tau_{w,z}$, is not affected by these phenomena and thus can be computed as, for example, in model (d). The wall shear stress components are thus expressed as:

$$\tau_{w,x} = -|\tau_o'| + c \rho u_\tau \, v(x+l_x, y_p, z) \qquad (2.127.a)$$

$$\tau_{w,z} = -|\tau_o'| \, w(x+l_x, y_p, z) \, / \, U_p \qquad (2.127.b)$$

Piomelli et al. suggest a value of the order of 1 for the constant c. The multipliers $T_{M,i}$ may be different from each other, as in model (d), and are conveniently expressed by:

$$T_{M,x} = \frac{|\tau_o'|}{U_p} \frac{U_p}{u(x, y_p, z)} \left[1 - c \sqrt{\frac{\rho}{|\tau_o'|}} \, v(x+l_x, y_p, z) \right] \qquad (2.128.a)$$

$$T_{M,z} = \frac{|\tau_o'|}{U_p} \frac{w(x+l_x, y_p, z)}{w(x, y_p, z)} \qquad (2.128.b)$$

2.6 Applications presented in the literature

So all my best is dressing old words new,
Spending again what is already spent
[Shakespeare, Sonnet LXXVI]

2.6.1 Planetary boundary layer

Following the pioneering papers by Smagorinsky [1963] and Lilly [1966, 1967], an impressive amount of research work on Large-Eddy Simulation was carried out since the early 'Seventies at the National Centre for Atmospheric Research (NCAR) at Boulder [Deardorff 1970-1980; Sommeria 1976; Sommeria and Deardorff 1977; Deardorff and Willis 1984; Moeng 1984-1987; Moeng and Wyngaard 1984 - 1988].

This work was entirely in the context of Planetary Boundary Layer (PBL) research and included the development of numerical methods and models for subgrid momentum and scalar transport; their application to atmospheric

turbulence simulation; and the statistical and spectral analysis of the large databases thus produced. It will be briefly surveyed here; attention will be focussed on subgrid models and other numerical fluid dynamics aspects, but it should be kept in mind that the authors were primarily interested in geophysical and meteorological issues which, of course, are beyond the scope of this presentation.

The subgrid models and numerical methods tested at NCAR during the 'Seventies are surveyed in Deardorff [1973.a]. The computational model was based on a finite-difference, staggered-grid approach and used explicit time stepping. The leapfrog scheme was adopted in many applications, with some 'smoothing' every so many intervals to prevent decoupling of even/odd time steps; the Adams-Bashforth scheme was also tested and was found to be superior in computations based on complex subgrid models. At each time step, a Poisson equation was solved for the pressure in order to satisfy continuity. The second-order Arakawa scheme was used for the discretization of the advective terms; moreover, the grid was moved downstream with the mean wind velocity by a simple galilean transformation in order to reduce the associated truncation errors.

In all applications, periodic boundary conditions were used in the horizontal directions. At the upper boundary ("lid"), the vertical velocity v and the vertical derivatives of horizontal velocity components u, w, of temperature T and of other scalars (if any) were set to zero. At the surface (ground), v was set to zero while for u, w and T "true" wall boundary conditions were replaced by conditions on their second derivatives along y, imposed at the centre of near-surface cells (corresponding to a height of about 20 meters) and derivable from classical 'universal' profiles holding in the surface layer. Several subgrid models of increasing complexity were implemented and tested, ranging from the simple Smagorinsky-Lilly model to a full subgrid stress/flux transport model and to a subgrid energy model, all of which have been described in Section 2.4.

After a preliminary application to channel flow [Deardorff 1970.a], see next section, Deardorff simulated neutral and unstable planetary boundary layers [Deardorff 1970.b, 1970.c, 1970.d, 1972.a]. The computational domain had relative sizes of 4H * H * 2 or 4H (along x, y and z as defined in Figure 2.1), corresponding roughly to a height of 1 kilometer by a few kilometers across. The grid included 40 * 20 * 20 or 40 cells, totalling from 16,000 to 32,000. The large-scale momentum equations included Coriolis and buoyancy

terms, with the Boussinesq approximation; an additional transport equation was solved for the temperature, expressed as "virtual potential temperature" ϑ^* to account for vertical pressure gradient and moisture effects.

Subgrid terms were described by the Smagorinsky-Lilly model, Eqn.(2.101), with c_s=0.13 in the neutral case and 0.21 in unstable cases (characterized by higher turbulence levels). The magnitude of c_s is discussed in detail in Deardorff [1971]. Near-wall damping was not explicitly included, but c_s was set to a lower value (0.10) in all cases at the first near-surface grid points. The subgrid Prandtl number to use in the temperature transport equation was set to 1/2 in the neutral case and to the lower value of 1/3 in unstable cases; it was set to 1 in all cases at the first near-surface points.

Results presented included vertical profiles of various mean and resolved fluctuating quantities, for which good qualitative agreement with known PBL data was claimed. Turbulent structures, including thermal plumes and Ekman-like vortices, elongated in the downstream direction, were simulated with convincing realism. Note that these elongated structures, though superficially resembling the sublayer 'streaks' mentioned in the Introduction, have a different nature and are several orders of magnitude larger; in the atmospheric simulations considered here, sublayer structures would be by far too small to be resolved by any feasible grid (besides being ill-defined due to surface roughness). However, quantitative comparisons with field data were not presented in these early works. The required CPU time on a CDC 6600 was about 150 hours for four basic simulations, corresponding to some hours of real time.

In the above early studies the height of the computational domain contained just the PBL, and did not allow for effects of entrainment of overlying air into it. In further works [Deardorff 1974.a, 1974.b] this limitation was greatly alleviated by allowing the model height to exceed the PBL thickness by a comfourtable margin; the upper "lid" was placed at a height of 2 km, while the PBL height ranged from about 100 to 1500 m during diurnal growth. This required doubling the vertical number of grid points; grids having 40*40*40 cells (64,000 in total) were used. The horizontal 'box' sizes were 5*5 km. The numerical methods were as described above [Deardorff 1973.a]; the large-scale equations included now a transport equation for the humidity q.

The subgrid model was more complex than in the 1970-1972 studies; it was based on the solution of transport equations for each of the subgrid stresses and fluxes of potential temperature ϑ and moisture q. Details are given in Deardorff [1973.b]. Computed results included the evolution of vertical

profiles of all mean quantities, resolved fluctuations, and second moments. Field data from the experiment known as Wangara-day 33 (taken in Southeast Australia over flat terrain) were used for comparison; a satisfactory agreement was found.

More recent papers by Deardorff [1976, 1980] address the issue of turbulence structure in an atmospheric boundary layer capped by a deck of stratocumulus clouds. The set of large-scale equations employed was as in Deardorff [1974.a], i.e. momentum, temperature (expressed here as "liquid water potential temperature" , ϑ_l) and moisture. The subgrid model, however, was much simpler than in Deardorff [1974.a], being based on the 'subgrid energy' approach synthesized by Eqn.(2.81.d).

For the dissipation $\tilde{\varepsilon}$ appearing in the subgrid-energy transport equation (2.85), the expressions (2.86) were adopted; also, c_ε was increased by a factor of up to 3.9 near the surface to account for ground effects. The length scale l was computed by using Eqns.(2.87). Finally, Eqn.(2.92) was used for the subgrid Prandtl number appearing in the temperature transport equation.

The computational 'box' was 2 km in height, as in Deardorff [1974.a], and from 2*2 to 5*5 km across. The grid included 40^3=64,000 cells and the numerical methods were as described above. Seven test cases were simulated, differing in the presence or not of cloud capping, phase-change and cloud radiative cooling in the model, and in the values imposed for the turbulent heat and moisture fluxes.

The NCAR LES code was greatly improved by Chin-Hoh Moeng [1984]. Following the approach adopted by the Stanford group [Moin et al. 1978], she completely re-wrote Deardorff's code leaving the finite-difference discretization along the vertical direction (y), but replacing it with a pseudospectral method, based on Fourier-series expansion, along x and z. The numerical accuracy of the code was tested by simulating (without any subgrid model and auxiliary transport equations) the classical problem known as Taylor-Green vortex flow [Taylor and Green 1937].

The simulations for the Wangara-day 33 test case previously reported by Deardorff [1974.a,b] were then repeated using 32*40*32 nodes, a time step of 3 seconds, and basically the same 'subgrid energy' model as in Deardorff [1980], but with a gaussian filter and Leonard/cross terms explicitly computed along x and z. Some changes were also introduced in the large-scale transport equations for temperature and moisture; in particular, a 'liquid-water static energy' equation was introduced in place of a potential or virtual potential

temperature equation. Of course, a discussion of these aspects would be beyond the scope of the present review. The overall results were comparable with those of Deardorff [1974.a,b], the most apparent disagreement being in the vertical profiles of horizontal velocity variances.

The same model was also applied to the study of a stratus-cloud topped planetary boundary layer [Moeng 1986, 1987]. A grid of 40*40*40 nodes was used; particular attention was dedicated to the modelling of radiative cooling in the cloud deck and to the necessary modifications in the 'liquid-water static energy' transport equation.

The large databases of computational results produced by the above simulations were also analysed by Moeng and Wyngaard [1984, 1986] and by Fiedler and Moeng [1985]. The main purpose of these studies was to derive models of pressure and scalar variances/covariances for use in more conventional, second-order closure models of turbulence.

Moeng's pseudospectral code originally had all variables out of core except pressure, for which an elliptic (Poisson) equation had to be solved at each time step. The memory management allowed grids of up to 40^3 nodes on the NCAR CRAY-X-MP and was accomplished by a technique known as 'slab partitioning'. Replacement of this by a method called 'pencil partitioning' allowed also the pressure equation to be treated out-of-core, thus increasing the size of feasible grids to 96^3.

Simulations of the planetary boundary layer using this much finer grid are described by Moeng and Wyngaard [1988]. The time step was 1 second, and the sizes of the computational 'box' were 5*2*5 km (along x, y and z); thus, the cell sizes were about 50*20*50 m, well within the inertial subrange. This allowed a comparison of filters on the basis of the produced turbulence spectra; the authors concluded that a wave-cutoff filter, Eqn.(2.60), gave spectra closer to the theoretical (Kolmogorov) $k^{-5/3}$ trend in the inertial subrange than the gaussian filter (2.59). Also, wave-cutoff satisfies the requirements pointed out by Speziale [1985] and Piomelli et al. [1988], discussed in Section 2.4, and was thus judged to be markedly preferable.

In the same paper, from an analysis of the local balance of production and molecular destruction of subgrid temperature variance, the authors deduced a value of about 0.4 for the subgrid Prandtl number σ_s, although a somewhat smaller value (0.3) was preferred in the actual simulations. Finally, they re-examined the results of Deardorff [1974.b] and found some errors in the model constants used for subgrid scalar transport, probably accounting for the reported overpredictions of scalar variances.

As a final remark on the NCAR work, it should be stressed that Deardorff and his colleagues were interested in LES mainly as a tool for improving our understanding of planetary boundary layer physics. Thus, many of the choices regarding subgrid constants and other modeling details are often justified more on physical grounds than on the basis of rigorous turbulence-theory considerations, and may sometimes appear arbitrary to those not acquainted with PBL meteorology. However, the NCAR contributions to the development of LES are undoubtedly outstanding, and it is a pity that, due to the lack of communication channels between the geophysical-research and the engineering-research communities, they are relatively little known among numerical fluid dynamicists interested in engineering and general applications.

Large-eddy simulations of the planetary boundary layer were also conducted by Nieuwstadt and Brost [1986] under a collaboration between NCAR and the Dutch Meteorological Institute. They were furtherly developed in the Netherlands by Nieuwstadt and deValk [1987], who simulated the dispersion of buoyant and non-buoyant plumes in the atmospheric boundary layer. In these studies the finite-difference computational method, the subgrid model and the computational box were essentially as in Deardorff [1980].

A large-eddy simulation model for mesoscale meteorology (MESOSCOP) was also developed in Germany by Schumann et al. [1987] and applied to the simulation of mixing in the convective boundary layer in the absence of mean wind [Schmidt and Schumann 1989; Schumann 1989], a problem which is known as a very difficult one for conventional closure models of turbulence.

The subgrid model was of the ASM-type, in that subgrid momentum and heat fluxes were determined by algebraic relationships derived from second-order closure theories and involving the subgrid turbulence energy $\tilde{k}$, for which a separate transport equation was solved. The computational method was based on finite-difference approximations on equidistant staggered grids. Second-order difference schemes were used for the advective terms. Time integration was performed by the explicit Adams-Bashforth method.

Very fine grids, having up to 160*40*160 (x*y*z) cells, were used; with this number of cells, simulations required 65,000 seconds of CPU time for 2,800 steps (corresponding to some hours of real time) on a CRAY-X-MP. Out-of-core storage was necessary, and a "slab-partitioning" technique was used. The most relevant result was the prediction of coherent convective structures in the form of narrow and fast updraughts surrounded by larger and

slower downdraughts in a polygonal spoke pattern, similar to that observed under certain conditions in Rayleigh-Bènard convection and convincingly close to patterns actually observed in the convective boundary layer of the atmosphere.

Finally, spectral simulations of isotropic and stably-stratified turbulence, obtained with a resolution of 128^3 collocation points, were presented by Mètais and Lesieur [1989], and were compared with direct simulations for lower Reynolds numbers. Large-eddy simulations of the convective atmospheric boundary layer were also presented by Mason [1987] and Mason and Thomson [1987].

2.6.2 Basic geometries

Besides the atmospheric-turbulence studies described above, most LES applications presented so far in the literature regard basic geometries such as homogeneous turbulence, incompressible fluids flowing between plane parallel walls (Poiseuille flow) or in annular passages, and free convection in horizontal layers delimited by parallel plates (Rayleigh-Bènard convection). Some of the most significant examples will be surveyed in this subsection.

One of the earliest applications is due again to Deardorff of the NCAR at Boulder, who studied plane Poiseuille flow at 'infinite' Reynolds number using the Smagorinsky-Lilly subgrid model [Deardorff 1970.a]. The sizes of the computational box were 6δ, 2δ and 4δ along x, y and z, respectively (see Figure 2.1); a finite-difference grid having only 24, 24 and 14 cells along the same directions was used. Periodic boundary conditions were imposed along x and z, while conditions on the second-order cross-stream derivatives of u and w (compatible with 'universal' logarithmic velocity profiles) were imposed at a distance $\Delta y/2$ from the walls, as in the mentioned planetary boundary-layer simulations [Deardorff 1972.a foll.]. Also, the condition v=0 was imposed on the walls.

For the Smagorinsky constant c_s, Deardorff found an optimum value of about 0.1; corresponding cross-stream profiles of mean and fluctuating (resolved) velocities were compared with experimental data for high-Reynolds number channel flow [Laufer 1954, 1950] and a satisfactory qualitative agreement was found. Also, the near-wall structure of turbulence was reproduced with some realism, especially as regards elongated regions of

alternating low and high downstream velocity u (resembling the experimentally observed 'streaks', see Introduction). However, no quantitative assessment of streak spacing was possible, as the Reynolds number was unspecified and moreover was assumed so high that the viscous sublayer was not explicitly resolved.
As mentioned above, this study was preliminary to the planetary boundary layer simulations conducted at NCAR in the following years.

Large-eddy simulations of plane-channel flow were conducted at the Kernforschungszentrum Karlsruhe, W. Germany, by Schumann [1975], who used his subgrid model (2.92) with $\nu_{s,ij}$ and $\nu^{*}_{s,ij}$ expressed by Eqns.(2.93), (2.94) and a transport equation similar to Eqn.(2.85) resolved for the subgrid turbulence energy $\tilde{k}$. Schumann considered computational boxes having sizes 4δ to 8δ and 2δ to 4δ, respectively along x and z, and finite-difference grids including 16 to 64 cells along x, 16 to 64 along y and 8 to 16 along z. The wall boundary conditions were those summarized in Section 2.5, Eqns.(2.116) to (2.119). As usual in these simulations, periodicity conditions were imposed along x and z. Optimum values of 0.094 and 0.01 were found respectively for the constants c_2 and c_{10} of the model. Simulation results, once compared with experimental data by Laufer [1954, 1950] and Comte-Bellot [1965], exhibited an agreement much better than the earlier results by Deardorff [1970.a] mentioned above. However, Schumann used up to 10 times more grid points than Deardorff, so that it is not clear how much of the improvement can be attributed to the grid refinement rather than to the more complex subgrid model (containing, however, as many as 10 adjustable constants as compared to the single basic constant c_s of the Smagorinsky-Lilly model used by Deardorff).

Schumann applied the same model and methods also to the simulation of flow with heat transfer in annular passages, somehow representative of nuclear reactor subchannels; this is the first known application of large-eddy simulation to a problem of direct engineering interest.

Grötzbach [1988, 1990] developed Schumann's model and applied it to the simulation of Rayleigh-Bènard convection, a problem previously studied by the author using direct simulation [Grötzbach 1982]. The subgrid model and numerical methods developed by the Karlsruhe group are reviewed by Grötzbach [1986].

Work on LES, based on spectral or combined finite difference / spectral methods, was initiated since the 'Seventies at the Stanford University (Thermosciences Division, Department of Mechanical Engineering) in close

cooperation with the NASA-Ames Research Centre. The earlier steps of this work are reviewed by Ferziger [1977, 1981]. Spectral numerical methods, especially suitable for use with the ILLIAC-IV computer, were developed at NASA by Rogallo [1977, 1981] and applied to direct simulations of homogeneous turbulence. A combined finite difference - spectral technique, suitable for plane-channel flow, was devised by Kwak et al. [1975].

McMillan and Ferziger [1979] analysed various aspects of eddy viscosity models by comparing LES results with full simulations of turbulent flows, following a suggestion by Clark et al. [1979]. Their results indicated that eddy viscosity models correlated poorly with 'exact' subgrid stresses (tensor-level comparison) although the resolved fields were fairly predicted.

The same technique was used by Bardina et al. [1980, 1983]. They used spectral methods, in conjunction with very fine grids (from 64^3 to 128^3 nodes), to simulate homogeneous turbulent flows with and without mean shear. The authors tested various combinations of subgrid models, including the 'scale-similarity' approach described in Section 2.4.2, against the full simulations of homogeneous turbulent flow obtained by Rogallo [1977, 1981] and experimental results by Comte-Bellot and Corrsin [1971]; the best agreement with full simulations was given by a linear combination of their 'scale similarity' model with the Smagorinsky model, see Eqn.(2.98). The authors studied also the effect of rotation on turbulence structure and developed techniques to extract information on subgrid quantities from large-eddy simulation results ('defiltering').

The best known results of the Stanford group are probably those presented for plane Poiseuille flow by Moin and Kim [1982] (and previously by Moin et al. [1978] and Kim and Moin [1979]). They used the subgrid model summarized by Eqns.(2.96), which is a simplified version of Schumann's model in that it does not involve the explicit solution of a transport equation for the subgrid turbulence energy and uses simple scalar values for the subgrid viscosities ν_s, ν_s^*. The sizes of the computational domains were $\pi 2\delta$ to $\pi 4\delta$ along x and $\pi(2/3)\delta$ to $\pi\delta$ along z. A finite-difference approximation was used along the cross-stream direction y, and a spectral one, based on Fourier expansions, along the periodic directions x and z; the time-stepping method was explicit. No-slip conditions were imposed at the walls and Van Driest - like damping, Eqn.(2.102.a), was also used in the wall region. Very fine grids, having up to 64*64*128 points along x, y and z, were adopted in this study: the viscous sublayer $y^+<11$ was resolved by four grid points (selectively refined near the walls) for a Reynolds number, based on channel half-height, of about 15,000. The spanwise grid was also made very fine in order to improve the resolution

of the near-wall 'streaks'. The overall number of grid points exceeded 500,000 for some test cases.

Moin and Kim's study is still considered a "classic" in Large-Eddy Simulation. The computational results were in very good agreement with experimental data [Kreplin and Eckelmann 1979; Hussain and Reynolds 1975] as regards cross-stream profiles of mean quantities and (resolved) fluctuations. Near-wall 'streaks' were predicted with great accuracy, see Figure 2.7, although their spanwise spacing was still higher than indicated by experimental data (about 150-200 wall units against 100). The large databases produced by the above simulations were further analysed in successive works in order to search for coherent structures and to extract statistical and spectral information from them.

Further LES studies by the Stanford group regard stratified flows [Findikakis 1981], the effect of rotation on turbulence structure [Kim 1983], turbulence in uniformly-sheared layers [Moin et al. 1985], wall boundary conditions and model consistency in wall-bounded flows [Piomelli et al. 1988, 1989], and transitional flows [Piomelli et al. 1990].

In the U.K., the first LES studies were conducted by the 'Turbulence Unit' at the Queen Mary College [Love and Leslie 1977; Antonopoulos-Domis and Love 1978; Leslie and Quarini 1979]. Both finite-difference and spectral methods were developed and implemented on computer codes (FORTY, ECCLES, CHANEL) purposely written for direct and large-eddy simulation.

The case of isotropic turbulence, with special regard to the transport of passive scalars, was investigated by Antonopoulos-Domis [1981.a,b]. Large-eddy simulations of low-Reynolds number channel flow were presented by Gavrilakis et al. [1986]. Hunter et al.[1988] used spectral methods to simulate the growth of the thermal boundary layer in a channel having one of the walls heated for a Reynolds number of a few thousands. They worked out an analogy between the growth of a thermal layer with time following a step increase of the wall temperature, and its growth in space downstream of an abrupt change of the wall thermal conditions; the latter case had been studied by Antonia et al. [1977]. This analogy allowed comparison of LES results with real-time interferograms obtained in a wind tunnel [Lockett 1987] under not-fully developed conditions. Further simulations of developing turbulent boundary layers were presented by Tsai and Leslie [1990].

Voke [1989] used a multi-grid method, in conjunction with a subgrid model similar to that used by Moin and Kim [1982], to simulate turbulent flow in a plane channel at $Re_\delta \cong 3{,}000$. The sizes of the computational 'box' were $2\delta * 2\delta * \delta$

along x, y and z, respectively. The finest grid had up to 32*64*128 points and was used only every so many time steps, the computations being carried on on a much coarser grid during most of the simulation. This method allowed significant reductions of the required CPU time with no significant loss of resolution.

At the City University of London, Voke and Collins [1984.a] and then Fodemski et al. [1987] conducted large-eddy simulations of turbulent channel flow using spectral methods, based on Fourier expansions along the periodic directions and Chebychev expansions along the cross-stream direction [Voke et al. 1985]. An important feature of their computer code was the formulation of the governing equations in general coordinates [Voke 1982; Voke and Collins 1983.b, 1984.b]. This allowed the computational domain to be distorted in order to represent relatively complex geometries, including channels having one of the walls roughened by transverse ribs [Fodemski et al. 1986]. In order to avoid instabilities, a step-by-step deformation technique was developed, in which the solution for each geometry was used as initial condition for the further small geometry change. However, an unconditional numerical instability occurred whenever the steepness of the obstacles exceeded a certain limit.

In Japan, Horiuti [1982] used the Smagorinsky-Lilly model (2.81.b), with a near-wall damping function for the length scale and no-slip boundary conditions, to simulate incompressible plane-channel flow. A noteworthy result was the realistic prediction of near-wall turbulence 'bursts' and 'sweeps' of the kind discussed in the Introduction. Later [Horiuti 1985.a], the author replaced the Smagorinsky-Lilly model by his own one-equation subgrid-energy model; results from the two were compared in another paper [Horiuti 1985.b]. It was found, in particular, that the subgrid-energy model led to a better prediction of the spanwise streak spacing.

2.6.3 Complex geometries

Only a few large-eddy simulation studies are known for recirculating flows and (relatively) complex geometries such as rib-roughened channels, backsteps and jets.

LES results for the flow over periodic transverse square ribs at a Reynolds number of 11,000 were presented by Kobayashi et al. [1984.a]. They used a finite-difference approach, based on the SMAC method, to solve the time-dependent Navier-Stokes equations for the large-scale fields. Central

differencing in space, and the explicit Adams-Bashforth time stepping scheme, were adopted. The subgrid model was that of Smagorinsky; a quadratic function was used to model near-wall damping of the subgrid kinematic viscosity. Heat transfer was also simulated, using a value of 0.85 for the subgrid Prandtl number σ_s. The duct geometry was characterized by a rib pitch-to-height ratio (P_1/h) of 5, and by a rib height to channel height ratio (h/H) of 1/3.2. The computational domain included one pitch in the streamwise direction, and only 0.35 channel heights in the spanwise direction. Streamwise and spanwise periodicity was imposed. Prescribed values of the heat flux were assigned on each wall, including the top (smooth) wall of the channel. The computational grid included 40 points streamwise, 25 cross-stream and just 9 spanwise (about 9,000 points in total). The simulation covered just a fraction of a LETOT, resolved by very small time steps of about 10^{-3} D_e/U (maximum Courant number < 0.1). Results were presented in the form of cross-stream profiles of mean u velocity, resolved turbulence energy and resolved uv Reynolds stress, in addition to contour plots of the instantaneous pseudo-stream function and of the fluctuating rms v velocity on a spanwise "slice", and to average temperature profiles along the walls. The authors obtained a single recirculation "bubble" in the inter-rib region, in agreement with experimental evidence for the geometry considered [Mantle 1966]. However, only velocity and turbulence profiles near the smooth wall were quantitatively compared with experimental data of Laufer [1950, 1954]; the other predictions were only qualitatively discussed.

In a subsequent paper [Kobayashi et al. 1985.b] the authors introduced some modifications in the subgrid model and in the near-wall damping function. These changes basically consisted of making the constant c_s of the Smagorinsky subgrid model a decreasing function of the local "cell Reynolds number" (defined with respect to the local vorticity ω and mesh size $\bar{\Delta}$, as $\omega\bar{\Delta}^2/\nu$). This was claimed to improve the predictions, although it is not clear on what basis this conclusion was founded.

Non-periodic turbulent flow over a single square rib in a plane channel was simulated by Werner and Wengle [1989] by using the Smagorinsky-Lilly SGS model with c_s=0.1. Near-wall damping was partially taken into account by using for the length scale in Eqn.(2.81.b') the smaller value of $c_s\bar{\Delta}$ and κy, y being the distance from the nearest wall and κ the Von Karman constant (0.42). The rib height to channel height ratio, h/H, was 1/2. The Reynolds number, based on bulk upstream velocity and obstacle height, was 42,500 to match that of experiments by Dimaczek et al. [1988].

Fully developed outflow conditions were imposed. At the inflow section, the time-dependent flow field from LES results for fully-developed plane-channel flow was used. The computational domain included 4 rib heights upstream and 13 downstream of the rib. A finite-difference method was used, with very fine staggered and non-uniform grids having up to 160*64*64 nodes along the streamwise, cross-stream and spanwise directions, respectively. Central differences were used for the advection terms. The numerical integration in time proceeded in cycles of explicit steps starting with an Euler step, followed by approximately 50 leapfrog steps and ending with an averaging step. A time-lagged treatment was used for the diffusion terms. Pressure-velocity coupling was performed by a predictor-corrector scheme akin to SIMPLE. Statistics were collected over the (supposedly) "homogeneous" direction z parallel to the rib, and over 5.5 reference times (r.t.=2h/U), after a development phase of 7.5 r.t..

Very realistic mean and fluctuating velocity fields were obtained; with the finest grid used, the reattachment length downstream of the rib was ~7h, against an experimental value of ~7.6h (as measured from the middle of the rib); the flow separating from the leading edge of the rib did not reattach on its top surface, in agreement with experimental observations. Switching to a coarser grid (80*28*44 nodes), the reattachment length decreased to ~6.4h and the flow reattached (in the average) on the top surface of the rib. However, mean and fluctuating velocity profiles were little affected, and remained in close agreement with experimental results even in calculations with a significantly lower number of grid points. Strong three-dimensionality of the instantaneous flow was predicted, both in the impingement region (leading face of the rib) and in the reattachment and recovery regions downstream of the obstacle. The authors point out that this makes the use of z as "homogeneous", averaging direction much questionable.

Non-periodic flow over a backward-facing step was first predicted using LES by Schmitt and Friedrich [1987]. Also Morinishi and Kobayashi [1990] simulated the turbulent flow over a backward-facing step using a modified (varying-c_s) Smagorinsky model, based on the work of Yoshizawa [1989]. The Reynolds number, based on mean flow rate and step height, was $4.6*10^4$ and the expansion ratio was 1.5. Computational grids having up to 230*50*20 points were used, and 'artificial' boundary conditions, based on universal near-wall velocity profiles, were imposed. Predictions were compared with various experimental results presented in the literature, and a very good agreement was found both on reattachment length and on mean velocity and turbulence-intensity profiles

in the recirculation and redevelopment regions. Large-eddy simulations of backward-facing step flow were also presented by Silveira-Neto et al. [1991].

Gao et al.[1991] simulated the impingement of hot jets on a cold wall, representative of the "thermal striping" phenomenon occurring in sodium-cooled nuclear reactors, using a spectral code and the Smagorinsky subgrid-scale model.

Other applications of LES to complex geometries presented so far in the literature include recirculating jets [Baron and Laurence 1983], arrays of axial-symmetric jets [Rizk and Menon 1988, 1989] and periodic arrangements of cubes in a simulated atmospheric boundary layer [Murakami et al. 1987].

2.6.4 Summary and future developments

Excellent, though not very recent, reviews of LES work and its prospects are due to Ferziger [1977], Voke e Collins [1983.a], Yoshizawa [1987] and Grötzbach [1987]. An interesting discussion of LES applicability to engineering problems is presented by Collins and Voke [1983].

It is noteworthy that the first appearance of Large-Eddy Simulation in computational fluid dynamics was in connection with such an eminently practical problem as weather forecasting [Smagorinsky 1963]. Only successively did LES acquire the rather theoretical character which distinguishes, for example, the work of Leonard [1974]. On the face of the most recent developments both in computing and in modelling, it is probably time to re-examine the question whether LES can be considered mature as a computational tool for engineering problems. To this purpose, it is useful to consider the opinions expressed on this subject by some of the leading scientists in the field.

In his review paper on Large-Eddy Simulation [1977] Ferziger stated "...The method is more expensive computationally than other approaches in common use. However, our experience has shown that, at least for simple flows, good results can be obtained with a surprisingly small number of mesh points and, consequently, the method is more expensive than more conventional Reynolds stress modeling by only a factor of two or three in many cases. With continuing decrease in the cost of computation, we believe that this method has an excellent chance of becoming a computational tool for benchmarking and final design optimization". Later on in the same paper, he continued "...For the near-term future, large eddy simulations appear to promise the ability to test

models used in other types of simulation and to provide constants and other data required to make these computations successful...Over the long range, it is possible that LES methods will become a standard computational tool. Although they are likely to remain expensive, they could find use as final design check methods and as calibrators of day-to-day design tools".

In his survey and outlook paper on computational fluid dynamics, Chapman [1979] considered the issue of LES in the wider context of the future of CFD. He concluded that, if the actual trends in development of computer memory and speed were to prevail in the following decade, then large eddy simulations would be used in the late 1990's for investigations of the flow over complete practical aircraft configurations.

Collins and Voke [1983] went even a bit further. In their 1983 review paper - purposefully entitled 'The application of Large-Eddy Simulation to engineering problems' - they stated "...At some time in the future we may expect large-eddy simulation to become of direct relevance to engineering flows such as those encountered in nuclear reactor coolant problems", and added "...The general trend at present is towards simulations of greater complexity, and of greater practical interest to engineers". In the same paper, the authors pointed out that the most attractive feature of Large-Eddy Simulations appears to be "the relative model-independence of the results, i.e. their insensitivity to details of the subgrid modelling, which makes them attractively robust compared with the more traditional approach". For the same reason, they expressed a marked preference for simple sub-grid models: "...The results of both Schumann and Moin and Kim suggest that a simple SGS model is frequently adequate, and that additional layers of complexity may obscure the essential model-independence of the simulation results". We may add here that 'additional layers of complexity' in the model often carry with them additional potential sources of numerical errors, are difficult to implement in exactly the same way in different computer codes, and thus are not amenable to reliable benchmarking by different computors.

Collins and Voke also identified three main areas in which additional research was especially needed:

- complex geometries;
- heat transfer by turbulence;
- wall region of bounded flows.

The last problem was seen as "...particularly challenging for large-eddy simulation, since even very small eddies may be highly anisotropic, and therefore a correct sub-grid model is difficult to formulate".

Grötzbach [1987] expressed similar views: "One may expect that within the next decade the large eddy simulation method will partly take the place of the Reynolds models, especially as regards the calculation of complex two-dimensional and three-dimensional flows. For these problems more and more transport equations for the closure terms are used in the Reynolds models. In this way, however, the computational effort and the number of coefficients increase. Thus, the large eddy simulation method will become a promising alternative of comparable effectiveness but of much higher universality and reliability.". Moreover, he pointed out that the large eddy simulation technique promises to be especially useful in those applications where the fluctuating field variables are of direct interest, such as aerodynamic noise generation, fluid-structure interaction (for example in naval research), and alternating tensile stresses induced by thermal striping (for example in nuclear power plants).

Grötzbach also identified some of the major problems hindering extended applications of the method:

- the specification of turbulent inlet and outlet conditions for all those problems which are not amenable to the use of periodic boundary conditions;
- the wall approximations for high Reynolds number flows;
- the difficulties involved in code verification, as typical LES outputs are quasi-random in nature and can be compared with experimental data only on a statistical basis.

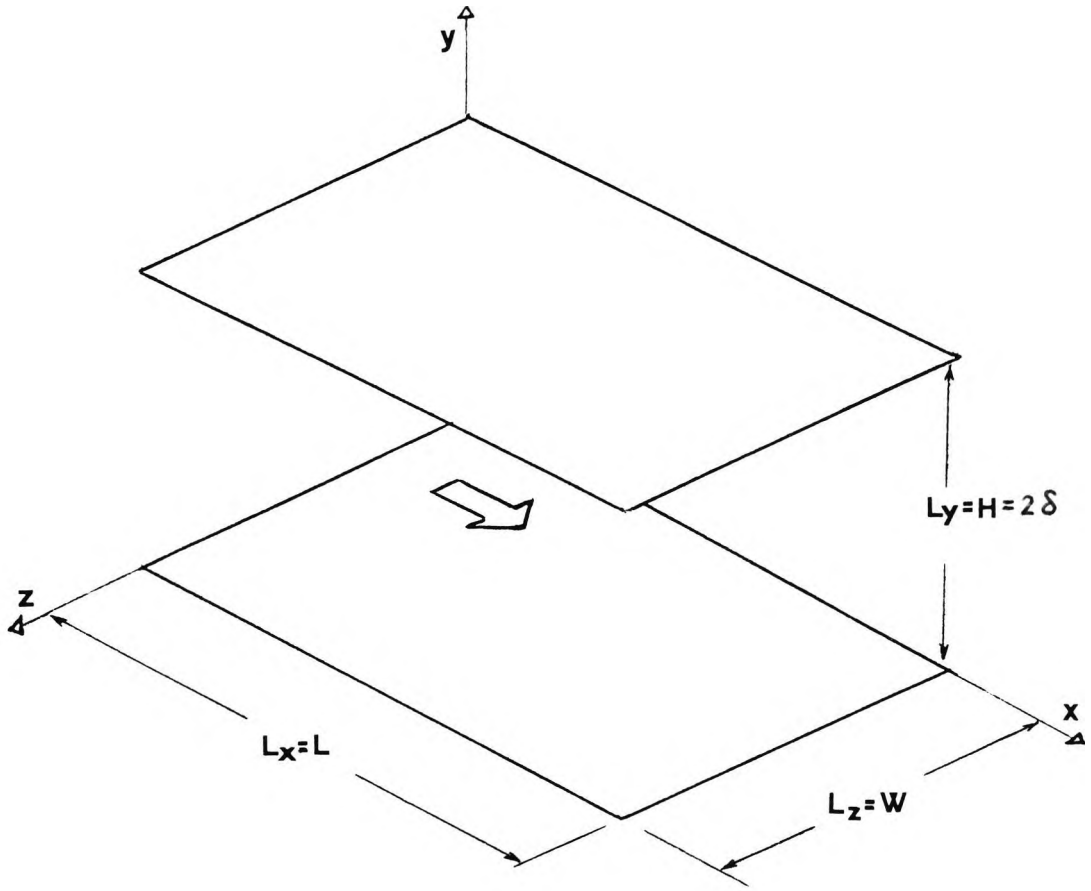


Figure 2.1 - Schematic representation of a plane channel

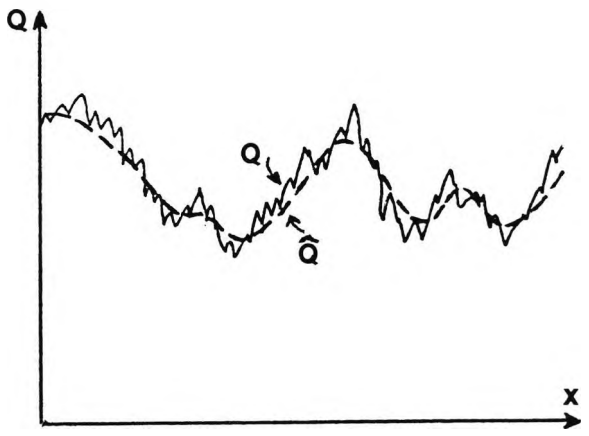


Figure 2.2 - Example of spatial filtering in one dimension

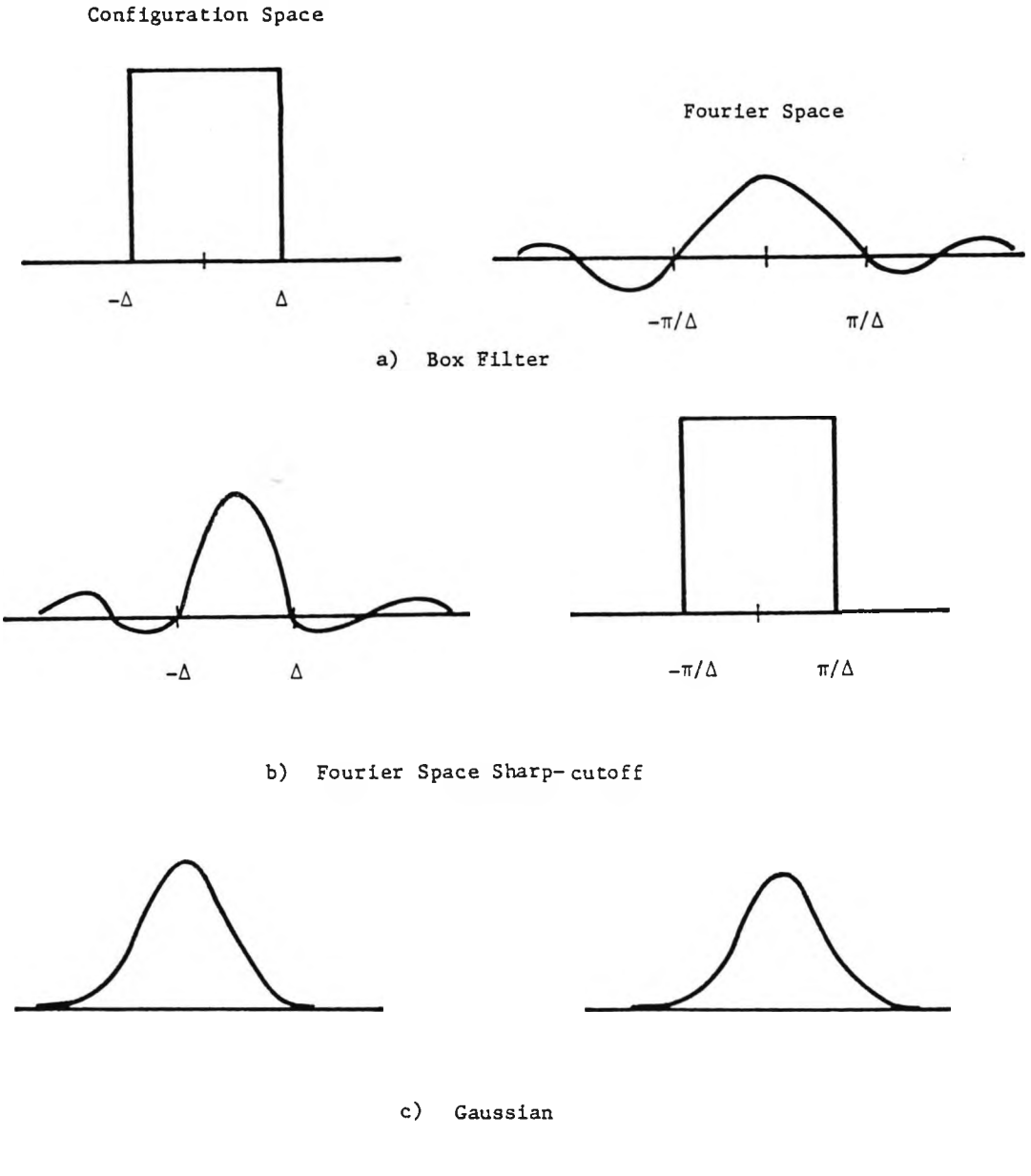


Figure 2.3 - One-dimensional filters in physical, or configuration, space (left) and transformed, or Fourier, space (right) [Ferziger 1981].
a: "top-hat", or "box", filter;
b: sharp-cutoff filter;
c: gaussian filter.

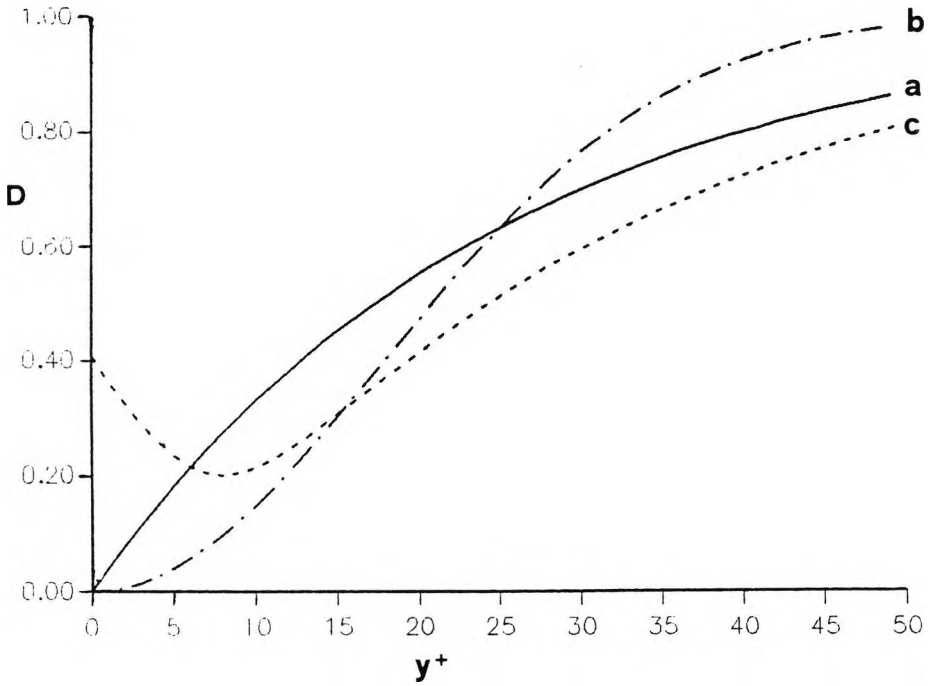


Figure 2.4 - Profiles of the near-wall damping function D.
a) VanDriest, Eqn.(2.102.a), with $A^+=25$
b) Modified VanDriest, Eqn.(2.102.b), with $A^+=25$
c) Miner et al., Eqn.(2.102.c), with $A^+=25$, $f_0=0.04$ and $y_0^+=8$

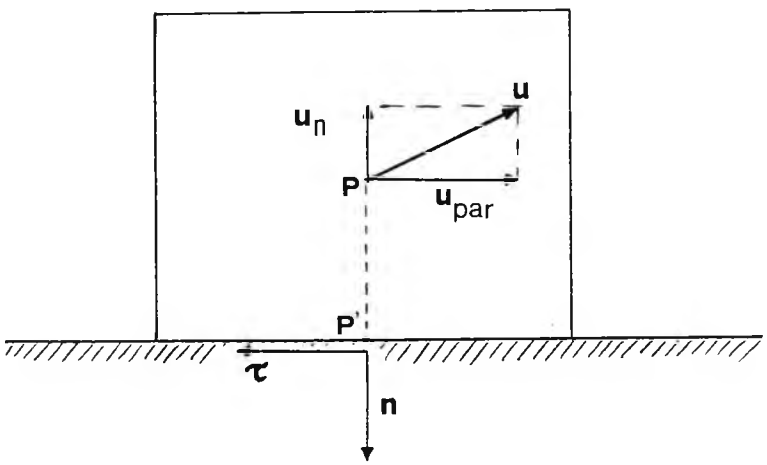


Figure 2.5 - Near-wall velocity and corresponding wall shear stress

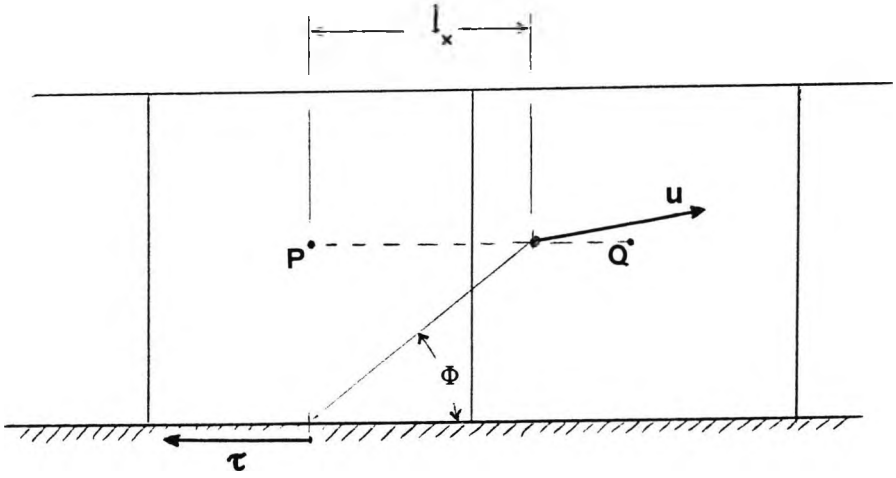


Figure 2.6 - Illustration of "shifted" and "ejection" wall boundary conditions

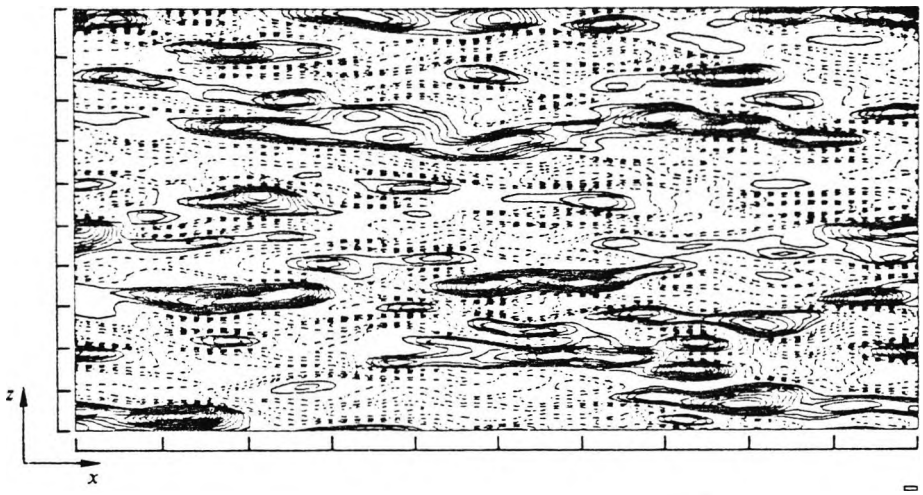


Figure 2.7 - Contours of u in the x-z plane at $y^+=6.26$ predicted by Moin and Kim [1982].

CHAPTER 3 - THE HARWELL-FLOW3D CODE AND ITS APPLICATION TO LARGE-EDDY SIMULATION

3.1 Code overview

Why to dedicate oneself to do badly
what has already been done well ?
[Abbè Dinouart, 'The art of being silent']

3.1.1 Introduction

Harwell-FLOW3D belongs to a family of thermofluid-dynamic computer codes which owe their existence mainly to work carried out at the Imperial College of London starting from the early Seventies. Other members of this family are, for example, TEACH [Gosman and Pun 1974]; TUFC [Cliffe et al. 1977]; Phoenics [Noauthor 1990.c]; and STAR-CD [Noauthor 1990.d]. They are all characterized by:

- finite difference / finite volume methods;
- solution of the primitive equations (Navier-Stokes);
- pressure-velocity coupling algorithms of the SIMPLE family;
- k-ε (and in some cases alternative, more advanced) turbulence models.

Some of these codes (e.g. Phoenics, FLOW3D, and STAR-CD) have fully three-dimensional, time-dependent capabilities and are commercially available as standard packages, which usually include:

- pre-processors, for the input of data in high-level language or menu form and for grid generation;
- a solver;
- post-processors, for the graphic presentation of the results;
- additional modules for the treatment of combustion, radiation etc.

The first release of FLOW3D [Wilkes et al. 1985; Jones et al. 1985, 1986] used a staggered and rectilinear grid (either in cartesian or cylindrical coordinates). After this preliminary release, the code was largely re-written as Harwell-FLOW3D, Release 2, to implement body-fitted coordinates [Burns et al. 1986.a, 1987.a, 1987.b]. The approach chosen was based on a structured, co-located (non-staggered) grid and on cartesian velocity components as the main flow unknowns, and used the Rhie and Chow [1983] algorithm to prevent

'chequerboard' oscillations. The mathematical treatment of the flow equations in general coordinates is described by Burns and Wilkes [1987] and will be summarized in Section 3.2. The last paper also presents the SIMPLE-family pressure-velocity coupling algorithms used by the code. Linear equation solvers, with special reference to conjugate-gradient methods, are discussed and compared by Kightley [1985] and Kightley and Jones [1985], and discretization schemes (including HUW and QUICK, see Section 3.2) by Thompson and Wilkes [1982]. These last features, as well as the treatment of porous regions, the handling of coupled conduction - convection problems, and the (k-ε) turbulence model with "wall functions", were retained from Release 1 with only minor changes. A novel feature was the allowance for compressible flow, with a transport equation for the fluid enthalpy and a user-modifiable equation of state. Like Release 1, the code was fully vectorized and was optimized for CRAY computers.

The reference manual for Release 2.1 is given by Burns et al.[1988.a]; this is the version of the code which was used for most of the large-eddy simulations described in the present work (Chapters 4 to 6).

While this work was in progress, the code's capabilities were being extended to include advanced ASM and RSM turbulence models [Clarke and Wilkes 1988, 1989; Wilkes and Clarke 1989]; new discretization schemes for the advection terms, like CCCT and CONDIF [Alderton and Wilkes 1988]; adaptive gridding [Hawkins and Kightley 1989]; combustion models [Wilkes et al. 1989] and coupling with radiation codes [Guilbert 1989]; and some (limited) two-phase flow capabilities [Lo 1987; Lo and Hope 1989]. The relative development work is summarized by Burns et al.[1988.b]. A version of the code including these advanced features, i.e. Release 2.3 [Noauthor 1990.a] was used for some large-eddy simulation runs for the plane-channel case (Chapter 4), with the main purpose of testing the alternative differencing schemes CONDIF and CCCT (described in Section 3.2.1). Finally, it has to be mentioned that a completely new version of Harwell-FLOW3D (Release 3), allowing multiblock grids, has recently been developed and has become commercially available in 1992.

In parallel with the development of the code proper, also pre- and post-processors were written for grid generation, data input and graphic presentation of computational results. A package for the generation of body-fitted grids using transfinite interpolation is described by Ingram et al. [1989]. The data necessary to specify problem and computational strategy may be supplied via a high-level command language, based on the Harwell facility INPROC [Winters and Jackson 1984], and described by Hanson et al.[1989] and

Jones and Hanson [1989]. Graphic post-processing of the results is normally performed on mainframes via the package OUTPROC, based on the TGIN language [Jackson and Winters 1989; Winters and Jackson 1989] and originally developed as part of the finite-element Harwell software ENTWIFE [Winters 1984]; also, surface plots can be produced by the program SURF3D, and simulated particle trajectories by the program RIP. Of course, FLOW3D may be interfaced with many other commercially available grid-generation and computer graphics packages. Finally, workstation versions of the code, including the post-processing software JASPER, have recently been developed. Currently, the software is commercially available from AEA Industrial Technology at Harwell.

In the present work little use was made of standard pre- and post-processing facilities. Problem specification and grid generation were performed via the appropriate user-frontend routines; this approach was chosen as being the most flexible and powerful, and thus more indicated for the non-standard problems involved in LES. The facility OUTPROC was found to be quite time-consuming for transient problems, and thus was used only to a limited extent. Fast, though somewhat crude, printer plots were produced at runtime by using the purposely-written routine QSHADE, described by Ciofalo [1988.b]; limited post-processing of the FLOW3D dump files was performed by using GDDM libraries (on IBM and Tektronics graphic terminals) or other simple graphics packages.

3.1.2 Applications and previous experience with the code

An updated survey of applications and validation tests for Harwell-FLOW3D is given by Jones [1991]. Since 1986 the author and his colleagues, both at the City University of London and at the University of Palermo, have tested and applied this code to a wide range of problems. They include:

- 2- and 3-D turbulent flow with heat transfer past a backward-facing step [Ciofalo and Collins 1988.c];
- 2-D turbulent flow with heat transfer past a double symmetric flat-duct expansion [Ciofalo and Collins 1988.b];
- 2-D isothermal, transient, laminar flow at high Reynolds number past a backstep [Ciofalo and Collins 1988.a];
- 2-D, laminar natural convection in complex enclosures [Ciofalo and Karayiannis 1989.a, 1989.b, 1990, 1991; Karayiannis et al. 1991, 1992];
- 3-D turbulent mixing in stirred tanks [Brucato et al. 1989, 1990];
- 3-D turbulence structure and pollutant transport in the atmospheric boundary layer [Provenzale 1991; Iannello 1992];

- 3-D laminar/turbulent flow and heat transfer in crossed-corrugated gas heat exchangers [Fodemski 1990; VV.AA. 1989 - 1992; Ciofalo, Collins and Perrone 1990, 1991; Ciofalo, Collins and Henry 1991; Henry et al. 1991];
- 2- and 3-D turbulent flow with heat transfer in ribbed ducts [Fodemski 1987, 1989; Fodemski and Collins 1988] and in multi-start helically-ribbed annuli [Henry and Collins 1989].

Most of the above studies, when appropriate, made use of the standard k-ε turbulence model. Modified wall functions were developed to improve predictions in recirculating flows [Ciofalo and Collins 1989.a]; their implementation in the code is described by Ciofalo [1988]. A low-Reynolds number model was also implemented and applied to flow and heat transfer in crossed-corrugated ducts [Ciofalo 1991]. The numerical methods used are reviewed and discussed by Collins and Ciofalo [1991] in the context of CFD application to transport processes. Preliminary large-eddy simulation results have been presented in previous papers, both for plane channels [Ciofalo, Fodemski and Collins 1988; Ciofalo 1989.a] and for rib-roughened channels [Ciofalo 1989.b; Ciofalo and Collins 1989.b, 1989.c, 1992]. They are based on the code modifications first described by Ciofalo [1988], which will be summarized in Section 3.3.

3.1.3 Brief description of Harwell-FLOW3D, Release 2

The main features of the code are summarized in Table 3.1.

Table 3.1 - Main features of Harwell-FLOW3D, Release 2

a) capabilities and physical models

Type of flow:	laminar / turbulent; steady / unsteady
	2 / 3-dimensional; incompressible / compressible
	isothermal / non-isothermal
	forced / natural convection
	(Boussinesq approximation or fully-varying ρ)
Turbulence models (standard):	k-ε (all releases); ASM / RSM (Rel. 2.3 foll.)
Grid:	rectilinear / general body-fitted
Physical-space Coordinates:	cartesian / cylindrical
Boundary conditions:	solid walls
	symmetry or periodicity surfaces
	inlet / outlet faces
	faces at imposed pressure
Further options:	solids / thin walls / porous regions
	heat conduction in solids
	additional scalar tranport equations
	adaptive grids (Rel. 2.3 foll.)
	combustion (Rel. 2.3 foll.)
	radiative heat transfer (via RAD3D code)

b) numerical methods

Pressure/velocity coupling:	SIMPLE / SIMPLEC / PISO / PISOC
Advection terms:	Central / Upwind / Hybrid upwind /
	2nd order upwind / 3rd order upwind
	CONDIF / CCCT (Rel. 2.3 foll.)
Linear equation solvers:	Line relaxation / Sweeping SIP /
	3-D Strongly Implicit Procedure (ST3D) /
	Conjugate Gradient (ICCG) / CG-squared

Some aspects will be briefly discussed here, namely:

- computational domain and structures which can be defined within this;
- code flow-chart;
- input/output subroutines;
- input/output files.

The generic computational domain of Harwell-FLOW3D, Release 2, is shown in Figure 3.1. It must be spanned by a three-dimensional body-fitted grid, generally non-orthogonal, including NI, NJ and NK volumes along the "intrinsic" directions I, J and K, respectively. The grid is specified by giving the coordinates of the control volume corners with reference to a cartesian, arbitrarily oriented frame Oxyz; these are stored in the 3-dimensional arrays XC(I,J,K), YC(I,J,K) and ZC(I,J,K). The generic control volume, which is an arbitrarily distorted "brick", is sketched in Figure 3.3; the numbering of the corners and of the centroid P is shown. The "intrinsic" directions are labelled U,D,N,S,E,W following the usual "compass rose" convention.

The computational domain includes a layer of "dummy" control volumes (corresponding to I = 1 or NI, J = 1 or NJ, K = 1 or NK) which surround the actual physical domain of interest and are used to impose the appropriate boundary conditions. It should be observed that two-dimensional problems are treated as three-dimensional ones with two symmetry or periodicity planes (see below).

Though the "intrinsic" directions I, J, K define a system of general coordinates, the cartesian velocity components u, v, w (defined with respect to the Oxyz frame) are used as the main flow variables (together with the pressure p and, if appropriate, with density and scalars). The cartesian reference frame may be replaced by a cylindrical one Orϑz; in this case, if the computational domain includes the axis, a special treatment is implemented to deal with the singular boundary "D".

Some of the internal or boundary 'structures' which can be defined include:

- **Solid regions** (either conducting or non-conducting);
- **Porous regions**.

These are both defined as sets of control volumes (CV's). For conducting solids, the thermal diffusivity tensor and (in transient problems only) the solid's density and specific heat need to be specified. For porous regions, the permeability tensor must also be supplied.

- **Thin surfaces** (impervious boundaries between fluid regions);
- Interfaces between **solid and fluid**;
- Interfaces between **dummy CV's and fluid**;
- Interfaces between **dummy CV's (or non-conducting solids) and conducting solids**.

These are defined as sets of control volume faces (for thin surfaces, both sides need to be specified), and the following interface or boundary conditions need to be set:

a) velocity boundary conditions (i.e., u, v and w on the wall); in Release 2.1, walls may be defined as "sliding", but must have a zero normal velocity component. This limitation does not apply to Releases 2.3 and following.
b) scalar boundary conditions; for example, for the temperature T these are given in the form $AT_w + Bq_w = C$, where T_w and q_w are the temperature and the heat flux on the wall. For interfaces involving conducting solids, the solid's conductivity in the direction normal to the wall must also be supplied. Of course, velocity boundary conditions are not required on interfaces between solid regions.

- **Dirichlet boundaries** ("inlets"): these are sets of CV's on a face of which the values of all flow variables (except p) must be specified;
- **Neumann boundaries** ("outlets"): these are sets of CV's on a face of which the normal derivatives of all flow variables (except p) must be specified; in the case of multiple outlets, it is possible to specify the flow rate, or fraction of the total flow rate, going through each of them;
- **Pressure boundaries**: these are sets of CV's on which the pressure p is specified;
- **Symmetry boundaries**: these may only be whole boundary surfaces U,D,N,S,E or W. In discrete terms, imposing symmetry is equivalent to imposing that, for any two control volumes lying on the two sides of the symmetry boundary, the velocity components normal to this have opposite values while the velocity components tangential to this, and all scalars, have identical values;
- **Periodicity boundaries**: these may only be couples of whole boundary surfaces U-D, N-S or E-W. In discrete terms, imposing (for example) U-D periodicity is equivalent to imposing on each variable Q the double condition $Q_{1,j,k} = Q_{NI-1,j,k}$ and $Q_{2,j,k} = Q_{NI,j,k}$.

The numerical methods used in Harwell-FLOW3D, Release 2 will be discussed in detail in Section 3.2. However, some remarks on the overall solution strategy can be made by observing the code's flow-chart, schematically shown in Figure 3.2. The three "nested" loops are relative to time stepping, "outer" iterations and "inner" iterations, respectively. N_t is the generic time step, N_{it} the generic "outer iteration", and N_{lin} the generic "inner" iteration of the linear equation solvers.

Time advancement, and the whole computation, is normally terminated when a prescribed number of time steps $N_{t,max}$ has been reached. With SIMPLE or SIMPLEC, the "outer" iterations are stopped either when a prescribed maximum number is reached, or when the overall residual mass source ε_M (which is the sum of the absolute values of all mass flow imbalances in control volumes, and thus expresses the amount by which continuity is <u>not</u> satisfied) falls below a prescribed value (SORMAX). Of course, when PISO or PISOC are used with a single iteration per time step, no such criterion applies. Finally, the "inner" iterations of the generic linear equation solver are stopped either after a prescribed number, or when the norm of the residual, $\|\mathbf{Ax-b}\|$, has been reduced to a suitable fraction of its initial value.

As mentioned above, for the present simulations the input to the code was given by using the appropriate user-frontend routines. They are listed in Table 3.2 below; the main purpose of each routine is indicated. Note that only periodic or wall boundary conditions were imposed, and that conduction in solids, compressibility, porous regions and many other capabilities of the code were not used.

Table 3.2 - User-frontend subroutines used for LES applications

GETDT	Time step
SETCON	Solid regions (conducting or non-conducting)
SETDIO	Control parameters for disk output
SETPER	Periodicity planes
SETPIO	Control parameters for printed output
SPEC	Miscellaneous: physical properties, control parameters, solution strategy
STFACE	Interfaces and velocity/scalar B.C.'s on them
USRBCS	Initial conditions
USRDIM	Problem dimensions and main options; storage allocation for work arrays
USRGRD	Grid (coordinates of control volume corners)
USRMON	User monitoring of various quantities
USRTRN	User-defined output at each time step

Besides the frontend subroutines listed above, the implementation of a subgrid model for Large-Eddy Simulation required subroutines USRVIS and USRDIF to be configured appropriately, and a set of auxiliary subroutines to be purposely written and added to the code. Moreover, the implementation of boundary conditions for LES required subroutines WALSHR and WALSTR to be modified, and in some cases (conditions "a" of Chapter 2) also subroutine SCMOM to be slightly changed and an extra subroutine (MASCAL) to be included in the code. These modifications will be discussed in detail in Section 3.3.

Finally, Table 3.3 lists the input / output files used by Harwell-FLOW3D. For each of them the I/O unit number, the corresponding FORTRAN variable used in the code, the "nickname" typically used to identify the file in the computing system, and the main purpose are indicated.

Some "extra" files were defined in the present study in addition to, or instead of, the "standard" ones. The file DATA was used to specify the input parameters, in conjunction with special versions of SPEC written for each of the main problems studied; it replaced the READ command-language file. The file MAT was used to allocate printer plots based on the routine QSHADE mentioned earlier. The file RESTART was used as dump/restart file instead of the "standard" file DUMP; it contains only the main flow variables (u,v,w,p,T)

strictly necessary for a restart while the "standard" dump file contains also convection coefficients, viscosity etc. and is considerably larger. This was necessary in order to minimize disk storage occupation as a large number of results were saved for successive post-processing. Note that, although grid-point (centroid) velocity components u,v,w do not satisfy continuity exactly, no significant "jump" or discontinuity was observed when using them to restart a simulation.

Table 3.3 Input/Output files

a) Input

No.	FORTRAN name	Nickname	Description
5	NREAD	READ	Input data in command language
12	NNEWS	NEWS	Informations for users
7	NIGRID	GRID	Grid
16	NRDISK	DUMP	Standard restart file
Extra files:			
51	NRGUES	RESTART	Simplified restart
13	NDATA	DATA	Input data read from SPEC

b) Output

No.	FORTRAN name	Nickname	Description
6	NWRITE	OUTPUT	Printer output
17	NWDISK	DUMP	Standard dump for OUTPROC or restart
20	NSOLVE	DIAG	Diagnostic messages
49	IOUN1	TOPL	Topological information for OUTPROC
Extra files:			
37	NMAT	MAT	Printer plots (shade maps)
52	NWGUES	RESTART	Simplified dump

3.2 Numerical methods

> **Mathematics is often regarded as the bread and butter of science. If the butter is omitted, the result is indigestion, loss of appetite, or both.**
> [Cundy and Rollett, Mathematical Models, 1961]

In this section the basic numerical methods implemented in Harwell-FLOW3D, Release 2, and used for the large-eddy simulations presented in the present work, will be briefly summarized. Three main topics will be covered:

- Finite-volume discretization of the governing equations on body-fitted, co-located grids, and resulting algebraic equations;
- Pressure-velocity coupling algorithms;
- Solution techniques for the linearised equations.

3.2.1 Finite-volume discretized equations

The basic transport equation of a scalar quantity Q has the form (2.27), which is repeated here for the reader's convenience:

$$\partial(\rho Q)/\partial t + \partial(\rho u_j Q)/\partial x_j = \partial(\Gamma\, \partial Q/\partial x_j)/\partial x_j + S_Q \qquad (3.1)$$

Note that this is written in a cartesian reference frame. The discretized form of Eqn.(3.1) on a finite-volume, co-located grid (i.e. a grid in which all variables are defined at the centroids of control volumes) will now be derived. The case of a steady-state problem will be considered first; the extension to transient problems will then be described.

The steady-state version of Eqn.(3.1) can be written in shorthand as:

$$\partial I_i/\partial x_i = S \qquad (3.2)$$

in which $S = S_Q$, and:

$$I_i \equiv \rho u_i Q - \Gamma\, \partial Q/\partial x_i \qquad (3.3)$$

are the components of a vector **I** representing the total (advective + diffusive) flux of the generic scalar Q.

By integrating Eqn.(3.2) on a generic control volume V such as that shown in Figure 3.3, centred in P, and using the Gauss theorem to transform the volume integral of a divergence into the surface integral of the corresponding normal flux, one is left with the approximate equations:

$$\Sigma\ (\mathbf{I}\ \mathbf{A})_{nn} = V\ \langle S\rangle_P \qquad (3.4)$$

in which the index nn (ranging from 1 to 6) refers to the faces d,u,s,n,w,e of the control volume; $\mathbf{A}_{nn}$ is the corresponding area vector, pointing outward; and $\langle S\rangle_P$ denotes the volume average of the source term S over V.

Note that the discretized equations (3.4) are derived making reference only to the "physical" space of the cartesian coordinates $x^i=x_i$, in which the computational grid is, in general, distorted. However, in order to work out a set of algebraic equations involving only values of the unknowns (velocity, scalars) and of the physical properties at the centroids "P" of control volumes, it is convenient to think of the grid in "physical" space x^i as generated by a smooth mapping from a regular, rectilinear grid of the "computational" space ξ^i (Figure 3.4). This allows one to use the powerful methods of absolute differential calculus (tensor calculus), briefly summarized in Appendix A. The coordinates ξ^i may be identified with the indices i,j,k labelling a control volume in the grid. In this approach (called "computational space approach" by Burns and Wilkes [1987]) the transport equations (3.2) are first transformed into the corresponding equations in computational space ξ^i prior to being discretized.

As discussed in Appendix A, Eqn.(3.3) for the total flux can be expressed in general coordinates ξ^i (and in contravariant components) by replacing:

- all cartesian components $u^i = u_i$ of the velocity vector by their generalized contravariant components u'^i;
- all partial derivatives $\partial Q/\partial x_i$ (cartesian components of the vector ∇Q) by the corresponding generalized contravariant components of ∇Q, i.e $g^{ij}\,\partial Q/\partial \xi^j$ (g^{ij} being the metric tensor).

The result is:

$$I'^i = \rho u'^i Q - \Gamma g^{ij}\,\partial Q/\partial \xi^j \qquad (3.5)$$

If the diffusivity Γ has a tensorial nature in physical space, as in Eqn. (2.31), then the last term should be replaced by $\Gamma^{ik} g^{kj}\,\partial Q/\partial \xi^j$. In both cases,

the product of the physical diffusivity Γ by the metric tensor is a tensor, generally not diagonal nor orthotropic. Thus, no additional complexity is actually introduced by considering a physically anisotropic (tensorial) diffusivity instead of a simple scalar.

Eqn.(3.2) can now be written in general coordinates by substituting the covariant divergence ∇_i for the ordinary divergence $\partial/\partial x_i$:

$$\nabla_i I'^i = S \tag{3.6}$$

or, using Eqn.(A.20) of Appendix A:

$$\frac{1}{\sqrt{g}} \frac{\partial}{\partial \xi^i} (\sqrt{g}\ I'^i) = S \tag{3.7}$$

Eqn.(3.7) can be further transformed by introducing the normal flux components $I_\perp^i$, see Appendix A. On the basis of definition (A.10) and of Eqn.(3.5), these are:

$$I_\perp^i = \rho u_\perp^i Q - \Gamma \sqrt{g} g^{ij} \frac{\partial Q}{\partial \xi^j} \tag{3.8}$$

so that Eqn.(3.7) can be written as:

$$\frac{\partial}{\partial \xi^i} I_\perp^i = \sqrt{g} S \tag{3.9}$$

This last equation is now discretized on the generic control volume of the grid in computational space ξ^i. The result is:

$$[I_\perp^1]_d^u + [I_\perp^2]_s^n + [I_\perp^3]_w^e = \langle \sqrt{g} S \rangle_P \tag{3.10}$$

As shown by Burns and Wilkes [1987], Eqn.(3.10) can be derived from (3.4) by approximating the volume V by the Jacobian determinant and the area vectors $\mathbf{A}_{nn}$ by the appropriate rows of the adjugate Jacobian matrix, see Appendix A.

Thus, in Eqn.(3.4) areas and volumes are more accurately expressed, especially for strongly distorted grids. On the other hand, Eqn.(3.10) lends itself more naturally to deriving an appropriate set of algebraic equations in the flow unknowns.

The finite difference representation of the terms appearing in the total normal flux components (3.8) has now to be specified. The average values of $I_{\perp}^{i}$ on faces nn can be expressed as:

$$(I_{\perp}^{i})_{nn} = (C^{i})_{nn} Q_{nn} - (D^{ij})_{nn} \left(\frac{\partial Q}{\partial \xi^{j}} \right)_{nn} \qquad (3.11)$$

in which, by comparison with Eqn.(3.8) and with the definition (A.10) of normal flux components:

$$(C^{i})_{nn} = [\rho \mathbf{u} \cdot \mathbf{A}^{(i)}]_{nn} \qquad (3.12.a)$$

$$(D^{ij})_{nn} = [\Gamma \sqrt{g} g^{ij}]_{nn} \qquad (3.12.b)$$

being i=1 for nn = d or u, 2 for nn = s or n, and 3 for nn = w or e.

The quantities $(C^{i})_{nn}$ (convection coefficients) are the same for all variables Q. They are computed by interpolating the velocities defined on control volume centroids, once at each outer iteration, or step, of the pressure-velocity coupling algorithm used, and are stored in the 4-dimensional array **CONV**(I,J,K,NWL), in which the indexes I,J,K specify the control volume in the grid, and the index NWL specifies the face u, n or e of the control volume. Thus, for example, the convection coefficient on the "u" face of the control volume i,j,k is $(C^{1})_{u}$ = **CONV**(I,J,K,1), shortly indicated as C_{u}, while the coefficient on the "d" face of the same control volume is $(C^{1})_{d}$ = -**CONV**(I-1,J,K,1), shortly indicated as $-C_{d}$.

The way in which centroid velocities are interpolated to yield face velocities is particularly critical; it is known that "naive" linear interpolation leads to 'chequerboard' oscillations and thus a special algorithm, based on suggestions by Rhie and Chow [1983], is used. This will be discussed later, after the main pressure-velocity coupling algorithms will have been introduced.

Getting back to Eqns.(3.10)-(3.12), the terms $G^{ij} = \sqrt{g} g^{ij}$ (geometrical diffusion coefficients) are purely geometrical quantities and thus, apart from the case of adaptive grids which will not be considered here, are computed

only once. They are stored in the 5-dimensional array **GDIFF**(I,J,K,NWL,INDEX) in which NWL spans, as above, the three faces u, n and e of each control volume and INDEX spans the three components of G^{ij} defined on that face. Finally, the physical diffusivity Γ is computed on each face nn by linear interpolation between control volume centroids, using physical-space weight factors which are computed once for all and stored in the 4-dimensional array **WFACT**(I,J,K,NWL). Further arrays **AREA**(I,J,K,NWL) and **VOL**(I,J,K) are used to store the face areas and the volumes of the computational cells. Thus, 19 real locations per control volume are required to store the necessary geometrical information. It is noteworthy that connection coefficients (or Christoffel symbols, see Appendix A) do <u>not</u> directly enter the final equations and thus need not to be stored (they would require 18 additional real locations per control volume).

The computational-space derivatives $\partial Q/\partial \xi^j$ on control-volume faces, appearing in <u>diffusive</u> terms of Eqn.(3.11), are always evaluated by central differences between adjacent grid points (control volume centroids). Much more critical is the finite-difference approximation of Q on control-volume faces in the <u>advective</u> terms of Eqn.(3.11). It is well known that more accurate schemes tend to be less "robust"; in particular, the use of central differencing for values of the "cell Peclet number" $Pe_c \equiv u\Delta x/\Gamma$ larger than 2 leads to loss of diagonal dominance in the matrix of the linearized transport equations (unless small time steps or underrelaxation factors are used), and may jeopardize the convergence of the iterative linear-equation solvers employed. Discussions of the problem may be found, for example, in Roache [1972.a,b], Leonard [1979] and Vreugdenhil [1989]. Ample reviews of alternative discretization schemes, devised to preserve both accuracy and "robustness", are given by Patankar [1988] and Collins and Ciofalo [1991].

In Harwell-FLOW3D, Release 2, a number of discretization methods are implemented, ranging from diffusive, simple upwind schemes through to bounded, quadratic upwind ones. The various schemes can be illustrated by writing, for example, the expression for Q_d (value of the generic scalar Q on the "down" face d) in terms of values of Q at neighbouring nodes (centroids of control volumes). The numbering of the nodes (i-1, i, i+1) will be assumed to follow the direction of the flow and, for the sake of simplicity, the grid will be assumed to be uniform and cartesian (Figure 3.5).

I. Central (CD):

$$Q_d = \frac{1}{2}(Q_D + Q_P) \qquad (3.13)$$

This scheme is formally second-order accurate, i.e. the truncation error associated to the discrete representation of Q_d (3.13) is proportional to $(\Delta x)^2$. As mentioned above, it is not "robust" and may lead to unphysical solutions for high cell Peclet numbers. However, Ciofalo and Collins [1988.a] used it succesfully up to $Pe_c = 10^3$ (in conjunction with small time steps) to compute a high-Reynolds number, transient, 2-D laminar flow. In that case, the linear equation solvers ST3D and ICCG (see below) were used for the transport and pressure-correction equations, respectively, and all the available pressure-velocity coupling algorithms (SIMPLE, SIMPLEC, PISO, PISOC) were tested. Thus, CD was used as the reference discretization method in all the large-eddy simulations described in Chapters 4-6. Only for the plane-channel case, Chapter 4, alternative schemes were also tested and compared.

II. Upwind (UD):

$$Q_d = Q_D \qquad (3.14)$$

III. Hybrid (HD):

$$Q_d = \begin{cases} Q_D & \text{for } Pe_c > 2 \quad (3.15.a) \\ \frac{1}{2}(Q_D + Q_P) & \text{for } Pe_c \leq 2 \quad (3.15.b) \end{cases}$$

These schemes are very "robust" and have always been widely used in engineering applications. The hybrid scheme may be slightly better, as central differencing is used where the cell Peclet number is low (for example, in recirculation regions and wakes); it is used as the default differencing scheme in Harwell-FLOW3D. However, both schemes are only first-order accurate and may introduce a large amount of "false", or numerical, diffusion, especially in the presence of high cell Peclet numbers and of large streamwise gradients of Q; in these cases, they lead to solutions which, although "realistic" and unaffected by spurious oscillations, are actually the solutions to a <u>different</u> problem. For example, Ciofalo and Collins [1988.a] shown that the use of hybrid differencing suppressed many physically relevant features of a complex laminar flow. First-order schemes such as UD and HD were shown to be too dissipative, completely suppressing turbulence, in preliminary LES studies

with FLOW3D by Gavrilakis [1987]. Thus, they were never used in the large-eddy simulations described here.

IV. Second-order upwind (HUW): $$Q_d = \frac{3}{2} Q_D - \frac{1}{2} Q_{DD} \qquad (3.16)$$

This, and the following, schemes are less compact than (I)-(III) due to the presence of the DD term. In three dimensions, the differencing "molecule", or "stencil", includes more points than P and the 6 immediate neighbouring nodes D,U,S,N,W,E, so that the matrix of linearized equations would include more than seven diagonals. In order to retain a compact matrix structure, which greatly simplifies the linear equation solvers, Eqn.(3.16) is re-written as:

$$Q_d = Q_D + \frac{1}{2} (Q_D - Q_{DD}) \qquad (3.17)$$

and the second term at the RHS is moved into the source term as a deferred correction. Details are given by Thompson and Wilkes [1982].

V. Quadratic upwind (QUICK): $$Q_d = \frac{3}{8} Q_P + \frac{6}{8} Q_D - \frac{1}{8} Q_{DD} \qquad (3.18)$$

This scheme, introduced by Leonard [1979], is formally third-order accurate. In order to retain, as above, the compact 7-diagonal matrix structure, it is re-written as:

$$Q_d = \frac{5}{8} Q_D + \frac{3}{8} Q_P + \frac{1}{8} (Q_D - Q_{DD}) \qquad (3.19)$$

with all terms at the RHS, except the first, being treated as sources.

VI. CCCT: $$Q_d = (\frac{3}{8} - \alpha) Q_P + (\frac{6}{8} + 2\alpha) Q_D - (\frac{1}{8} + \alpha) Q_{DD} \qquad (3.20)$$

This is basically the CCCT/SMART scheme of Gaskell and Lau [1987] and is a modification of the QUICK scheme which is bounded, thus eliminating the non-physical overshoots often reported of QUICK and similar high-order schemes. The parameter α is computed locally as a function of the curvature of Q. The deferred correction method is then used as with QUICK. Details are given by Alderton and Wilkes [1988].

VII. CONDIF: this is a modification of central differencing in which the matrix coefficients (of the linearized transport equations) corresponding to the advection terms are written in such a way as to be diagonally dominant, and upwind differencing is used at any points at which unphysical overshoots are likely to occur. This prevents the difficulties mentioned for central differencing, at the cost of considerable coding complications and extra-storage requirements. The scheme was introduced by Runchal [1987]; modifications were proposed by Hedberg [1989]. Details of the implementation are given by Alderton and Wilkes [1988].

Once the various terms have been properly discretized, the generic transport equation for the scalar Q takes the form:

$$(\Sigma\, a_{nn} + s_m)Q_P - \Sigma\, a_{nn}Q_{NN} - S' = \langle\sqrt{g}S\rangle_P \qquad (3.21)$$

in which:

Q_P is the value of Q at P and Q_{NN} the values of Q at the 6 neighbouring points D,U,S,N,W,E;

a_{nn} are matrix coefficients, the exact form of which depends on the discretization scheme used for the advection terms; for example, using hybrid differencing one has:

$$a_u = \max\,(\tfrac{1}{2}|C_u|,\, D_u) - \tfrac{1}{2}C_u \qquad (3.22.a)$$
$$a_d = \max\,(\tfrac{1}{2}|C_d|,\, D_d) + \tfrac{1}{2}C_d \qquad (3.22.b)$$

etc., while, using central differencing:

$$a_u = D_u - \tfrac{1}{2}C_u \qquad (3.23.a)$$
$$a_d = D_d + \tfrac{1}{2}C_d \qquad (3.23.b)$$

etc.;

s_m is the "mass source" term:

$$s_m = \Sigma\,(C^i)_{nn} = C_u - C_d + C_n - C_s + C_e - C_w \qquad (3.24)$$

which goes to zero (in incompressible flows) only for a fully-converged solution;

S' is a term which includes the effects of the non-orthogonality of the grid:

$$S' = \left[D^{12} \frac{\partial Q}{\partial \xi^2} + D^{13} \frac{\partial Q}{\partial \xi^3} \right]_d^u + \left[D^{21} \frac{\partial Q}{\partial \xi^1} + D^{23} \frac{\partial Q}{\partial \xi^3} \right]_s^n + \left[D^{31} \frac{\partial Q}{\partial \xi^1} + D^{32} \frac{\partial Q}{\partial \xi^2} \right]_w^e \quad (3.25)$$

and thus vanishes on cartesian (rectilinear) grids;

S is the "true" source term of Eqn.(3.7.a).

In order to increase the diagonal dominance of the linearized equations, it is convenient to linearize the source term itself by writing:

$$\langle \sqrt{g} S \rangle = s_Q + s_0 Q_P \quad (3.26)$$

so that, by letting:

$$s_P \equiv s_0 - s_m \quad (3.27.a)$$

$$a_P \equiv \Sigma a_{nn} - s_P \quad (3.27.b)$$

and also absorbing the extra terms S' due to non-orthogonality into the RHS, Eqn.(3.21) becomes:

$$a_P Q_P - \Sigma a_{nn} Q_{NN} = s_Q + S' = s'_Q \quad (3.28)$$

Now, the case of <u>transient</u> problems can be considered. The extra term $\partial(\rho Q)/\partial t$, which figures at the LHS of Eqn.(3.1), would still be present at the LHS of the space-discretized equation (3.28), which would thus take the form:

$$\partial(\rho Q_P)/\partial t + a_P Q_P - \Sigma a_{nn} Q_{NN} = s'_Q \quad (3.29)$$

If <u>implicit</u> time stepping is used, Eqn.(3.29) can be reconducted to the form (3.28) by modifying appropriately the coefficients and source term. In particular, if <u>fully implicit backward</u> time differencing is adopted, then Eqn.(3.29) is discretized in time as:

$$[(\rho Q_P) - (\rho Q_P)^{old}]/\Delta t + a_P Q_P - \Sigma a_{nn} Q_{NN} = s'_Q \quad (3.30)$$

in which the superscript "old" refers to the previous time step, while terms with no superscript are for the current time step. This can be written:

$$(\rho/\Delta t + a_P)Q_P - \Sigma\, a_{nn}\, Q_{nn} = s'_Q + (\rho/\Delta t)Q_P^{old} \qquad (3.31)$$

which, by letting:

$$\breve{a}_P \equiv \rho/\Delta t + a_P \qquad (3.32.a)$$

$$\breve{s}'_Q \equiv s'_Q + (\rho/\Delta t)Q_P^{old} \qquad (3.32.b)$$

becomes:

$$\breve{a}_P Q_P - \Sigma\, a_{nn}\, Q_{nn} = \breve{s}'_Q \qquad (3.33)$$

formally identical to the steady-state equation (3.28), except that terms containing the time step Δt have been included in the diagonal coefficient $\breve{a}_P$ and in the source term $\breve{s}'_Q$.

As an alternative, a time-centred treatment (Crank-Nicolson) can be used. By defining:

$$Q^* \equiv \tfrac{1}{2}\,(Q^{old}+Q) \qquad (3.34)$$

the discrete time-stepping equation corresponding to Eqn.(3.30) can be written in shorthand as:

$$\frac{Q^* - Q^{old}}{\Delta t/2} = F(Q^*) \qquad (3.35)$$

and of course can be treated in the same way as above to yield discretized equations similar to (3.33) for the "mid-point" field Q^*. Once Q^* is known, the values of Q at the new time step are computed by extrapolation from Q^{old} and Q^*:

$$Q = 2Q^* - Q^{old} \qquad (3.36)$$

The above discussion shows that Eqn.(3.28) can be assumed as the basic form of the discretized transport equation both in steady-state and in transient

problems. For simplicity, the symbol (˘) will be omitted from the terms s'_Q and a_P in the following.

In order to simplify the following discussion of pressure-velocity coupling algorithms, it is convenient to derive the specific form that the discretized transport equation (3.28) takes when Q is a velocity component u^i, i.e. when the original differential equation (3.1) is one of the Navier-Stokes equations (2.20.b). An examination of these last equations shows that now the source term S_Q in Eqn.(3.1) must be:

$$S_u i = - \frac{\partial p}{\partial x_i} + \frac{\partial}{\partial x_j} u \frac{\partial u_j}{\partial x_i} + F_i \qquad (3.37)$$

The discretization of the equations following the procedure described above leads now to [Burns and Wilkes 1987]:

$$a_P u^i{}_P - \Sigma a_{nn} u^i{}_{nn} = - A_i{}^j \partial p/\partial \xi^j + s'_u i \qquad (3.38)$$

in which, with respect to the generic scalar transport equation (3.28), the pressure-gradient contribution has been separated from the remaining source term at the RHS. The reason for this is that the pressure-gradient term plays a special role in pressure-velocity coupling algorithms, as will be discussed in the following sub-section. The terms $A_i{}^j$ are the cartesian components of the area vectors $\mathbf{A}^{(j)}$ (see Appendix A).

Eqn.(3.38) can be written succintly as:

$$a_P u^i{}_P = H(u^i) - \delta_i p + s' \qquad (3.39)$$

in which H( ) is a pseudo-linear operator (actually, it contains the convection coefficients C^i and thus the velocity components u^i themselves) and δ_i is just a shorthand for $A_i{}^j \partial/\partial \xi^j$.

3.2.2 Pressure-velocity coupling algorithms

As discussed, for example, by Collins and Ciofalo [1991], the solution of the governing fluid dynamic equations is especially critical in incompressible flow problems since transport equations of the form (2.20.b) (or equivalent discretized form (3.39)) can be written for the three velocity components, but not for the pressure p, which is the fourth flow variable. It behaves as an

"implicit" field, the values of which are determined by the condition that the velocities satisfying momentum balances, i.e. the Navier-Stokes equations, also satisfy mass balance, i.e. the continuity equation (2.5) (or its discretized form). In the finite-volume, co-located grid treatment used here, this is simply:

$$\Sigma\ (C^i)_{nn} = 0 \qquad (3.40)$$

being $(C^i)_{nn}$ the convection coefficients defined by Eqn.(3.12.a).

In most direct or large-eddy simulations presented so far in the literature, explicit time stepping is used. The new pressure field is computed by solving at each time step a Poisson equation, derived from the Navier-Stokes equations by imposing the (new) velocity field to be divergence-free. Basically, this technique can be traced back to the MAC method of Harlow and Welch [1965]. However, most recent general-purpose computer codes (including Harwell-FLOW3D) implement implicit time stepping (or steady-state) capabilities, and their pressure-velocity coupling algorithms are generally derived from the SIMPLE method first introduced by Patankar and Spalding [1972]. The basic characteristic of these algorithms is that a Poisson equation is solved for a pressure correction (P-C), rather than for the whole pressure field, and is coupled, generally in an iterative fashion, with momentum equations written using the last available pressure field. The SIMPLE method, together with its variants SIMPLEC [VanDoormal and Raithby 1984], PISO [Issa 1986; Issa et al.1986] and PISOC, are implemented in Harwell-FLOW3D and have all been tested by the author in large-eddy simulations. They will be shortly described in the following; the pressure correction method is reviewed, for example, by Connell and Stow [1986] and Latimer and Pollard [1989].

a) SIMPLE(C) algorithm

The i-th discretized momentum equation is Eqn.(3.39). If the exact pressure field p were known, the velocities u^i satisfying Eqn.(3.39) would automatically satisfy also the continuity equation (3.40) (provided that the convection coefficients $(C^i)_{nn}$ appearing in this were derived from the grid-point velocities u^i following the Rhie and Chow prescriptions, as will be discussed later). However, if a tentative pressure field p^* is substituted for p in Eqn.(3.39), this becomes:

$$a_p u^{i*}_p = H(u^{i*}) - \delta_i p^* + s' \qquad (3.41)$$

and is satisfied by an approximate velocity field u^{i*} which does not satisfy continuity, but gives a "residual mass source":

$$\Sigma\ (C^i)_{nn}{}^{*} = \dot{m}_P \neq 0 \qquad (3.42.a)$$

or, in terms of normal flux components:

$$\left[\rho u_\perp^{1*}\right]_d^u + \left[\rho u_\perp^{2*}\right]_s^n + \left[\rho u_\perp^{3*}\right]_w^e = \dot{m}_P \neq 0 \qquad (3.42.b)$$

The pressure and velocity fields satisfying <u>both</u> the (discretized) momentum equations and the (discretized) continuity equation will be given by the approximate fields u^{i*}, p^* plus "correction" terms u^{i}', p' (presumably small if p^* was a good approximation of the "exact" pressure field):

$$u^{i**} = u^{i*} + u^{i}' \qquad (3.43.a)$$

$$p^{**} = p^{*} + p' \qquad (3.43.b)$$

with:

$$a_P u^{i**}{}_P = H(u^{i**}) - \delta_i p^{**} + s' \qquad (3.44)$$

$$\Sigma\ (C^i)_{nn}{}^{**} = 0 \qquad (3.45.a)$$

Eqn.(3.45.a) can be written also in terms of normal flux components:

$$\left[\rho u_\perp^{1**}\right]_d^u + \left[\rho u_\perp^{2**}\right]_s^n + \left[\rho u_\perp^{3**}\right]_w^e = 0 \qquad (3.45.b)$$

By subtracting Eqn.(3.41) from (3.44), one has for the correction terms:

$$a_P u^{i}{}'_P = H(u^{i}') - \delta_i p' \qquad (3.46)$$

Now, the original SIMPLE procedure [Patankar and Spalding 1972] simply neglects the term $H(u^{i}')$ in Eqn.(3.46) in order to derive an explicit expression for the velocity corrections. However, VanDoormal and Raithby [1984] argued that $H(u^{i}')$ is of the same order as $a_P u^{i}{}'_P$, so that it is inconsistent to retain the latter while neglecting the former. Rather, they suggested to re-write Eqn.(3.46) after adding and subtracting the term $H(u^{i}{}'_P) = \Sigma\ a_{nn} u^{i}{}'_P$ at the RHS, which gives:

$$a_P u^{i\prime}{}_P = H(u^{i\prime}{}_P) + H(u^{i\prime}-u^{i\prime}{}_P) - \delta_i p' \qquad (3.47)$$

and then to neglect the term $H(u^{i\prime}-u^{i\prime}{}_P)$, which is indeed smaller than either $H(u^{i\prime})$ or $a_P u^{i\prime}{}_P$ since it involves only velocity <u>differences</u> between centroid (P) and faces (nn) of a control volume. Having thus simplified Eqn.(3.46), and taking into account the definitions of the operator H and of the terms $u^{i\prime}{}_P$, one has:

$$u^{i**} = u^{i*} - D\delta_i p' \qquad (3.48.a)$$

where:

$$D \equiv [a_P(1-\Sigma a_{nn}/a_P)]^{-1} = [a_P f_P]^{-1} \qquad (3.49)$$

(in which only the corrective factor $f_P = 1-\Sigma a_{nn}/a_P$ differentiates SIMPLEC from the original SIMPLE).

In terms of normal flux components $u^i_\perp$, using the general relationship between the $u^i_\perp$ and the u^i given in Appendix A, Eqn.(3.48.a) becomes:

$$u^{i**}_\perp = u^{i*}_\perp - \frac{1}{f_P} C^{ij} \frac{\partial p'}{\partial \xi^j} \qquad (3.48.b)$$

where :

$$C^{ij} \equiv A_k{}^i A_k{}^j / a_P \qquad (3.49')$$

Now, a pressure correction (P-C) equation is obtained by substituting Eqn.(3.48.b) into the continuity equation (3.45.b). Taking also Eqn.(3.42.b) into account, this gives:

$$b_P p'{}_P - \Sigma\, b_{nn}\, p'{}_{NN} = s'{}_P - \dot{m}_P \qquad (3.50)$$

in which the coefficients b_{nn} are given by:

$$b_{u,d} = (\rho C^{11}/f_P)_{u,d};\ b_{n,s} = (\rho C^{22}/f_P)_{n,s};\ b_{e,w} = (\rho C^{33}/f_P)_{e,w} \qquad (3.51.a)$$

$$b_P = \Sigma\, b_{nn} \qquad (3.51.b)$$

and the term s'_P absorbs the additional terms due to non-orthogonality, namely:

$$s'_P = \left[E^{12}\frac{\partial p'}{\partial \xi^2} + E^{13}\frac{\partial p'}{\partial \xi^3}\right]_d^u + \left[E^{21}\frac{\partial p'}{\partial \xi^1} + E^{23}\frac{\partial p'}{\partial \xi^3}\right]_s^n + \left[E^{31}\frac{\partial p'}{\partial \xi^1} + E^{32}\frac{\partial p'}{\partial \xi^2}\right]_w^e \qquad (3.52.a)$$

being:

$$(E^{ij})_{nn} \equiv (\rho C^{ij}/f_P)_{nn} = \left[\rho \frac{\sqrt{g}}{a_P f_P} G^{ij}\right]_{nn} \qquad (3.52.b)$$

(of course, in SIMPLE $f_P=1$).

Note the analogy of Eqns.(3.50) and related (pressure correction) with Eqns.(3.28) and related (scalar transport). The "deferred correction" method allows also in this case to move all cross derivatives to the RHS of the equation, leaving just a 7-point "molecule", or "stencil", i.e. a 7-diagonal matrix of linearized equations (for the P-C equation, the matrix is also symmetric and thus solvers of the conjugate-gradient family can be used, see subsection 3.2.3). However, as discussed by Burns and Wilkes [1987, p.19], in this case it is appropriate to update the source terms at each inner iteration of the linear equation solvers, rather than at each outer iteration as is sufficient for the transport equations. See Burns and Wilkes [1987] also for a discussion of the approximation consisting of dropping the off-diagonal components of C^{ij}, adopted by Rhie and Chow [1983].

The steps to be followed for the solution of the fluid flow (and scalar transport, if any) equations via the SIMPLE(C) algorithms can now be summarized. The sequence is identical for a steady-state problem and for the generic time step of a transient problem. In either case, initial estimates p^*, $u^{i(0)}$, $Q^{(0)}$ are required for the pressure, velocity and scalar fields; in a transient problem, these are simply given by the respective values at the previous time step. Now, for the generic iteration (called "outer" iteration to distinguish it from the "inner" iterations of linear equation solvers), one has the following predictor/corrector scheme:

I. Prediction step:

- compute all convection / diffusion coefficients and source terms on the basis of the most recent estimates of u^i, Q (taking transient terms into account if appropriate);

- solve linearized momentum equations (3.41) to obtain the flow field u^{i*}; re-compute convection coefficients using Rhie-Chow interpolation.

II. Correction step:

- evaluate residual mass source $\dot{m}_P$ (for each grid point) from Eqn.(3.42.a);
- solve pressure-correction equation (3.50) to obtain p';
- correct velocities by using Eqn.(3.48.a) and pressures by using Eqn.(3.43.b) to obtain updated velocity and pressure fields u^{i**}, p^{**} replacing u^{i*}, p^{*};

III. Scalar transport equations:

- update convection coefficients etc. and solve all scalar transport equations (if any).

IV. Convergence test:

- check convergence (by monitoring either the overall continuity error or the behaviour of some flow quantity along consecutive iterations); go back to step (I) for a new iteration or exit to new time step (or final output), as appropriate.

This reference scheme can be altered in several ways, for example by looping a number of times over hydrodynamic equations before solving any scalar transport equation, etc. The SIMPLEC simulations carried out in the present work followed the basic reference sequence given above. An important feature of SIMPLE(C) is that the linearized transport or P-C equations need not to be solved with great accuracy at the generic outer iteration, since they are only approximate equations which approach the "true" (discretized) equations only as the outer iterations proceed.

b) PISO(C) algorithm

This is a non-iterative technique, explicitly introduced by Issa [1986] for transient problems and based on two correction steps per time step. This leads to a Δt^2-accurate solution in just one cycle, but requires the linearized equations to be solved with great accuracy (unlike SIMPLE(C)).

Basically, the steps represented by Eqns. (3.41) to (3.52), leading to velocity and pressure fields u^{i**}, p^{**}, are like in SIMPLE(C). With respect to the original PISO algorithm [Issa 1986], a SIMPLEC-like modification (leading to a f_p-factor different from 1) may be used, yielding the PISOC version. A

second correction step is now performed; improved velocity and pressure fields u^{i***}, p^{***} are sought, satisfying both the momentum and the continuity equations:

$$a_P u^i{}_P^{***} = H(u^{i***}) - \delta_i p^{***} + s' \qquad (3.53)$$

$$\Sigma\ (C^i)_{nn}^{***} = 0 \qquad (3.54)$$

Subtracting Eqn.(3.44) from (3.53) one has:

$$a_P u^i{}''_P = H(u^i{}'') - \delta_i p'' \qquad (3.55)$$

in which $u^i{}'' \equiv u^{i***} - u^{i**}$ and $p'' \equiv p^{***} - p^{**}$ are second velocity and pressure corrections. Approximating $H(u^i{}'')$ by $H(u^i{}')$, Eqn.(3.55) gives for the second velocity correction:

$$u^{i***} = u^{i**} + \frac{1}{a_P} H(u^i{}') - \frac{1}{a_P} \delta_i p'' \qquad (3.56)$$

in which the first velocity correction $u^i{}'$ is known from the first correction step. Substituting Eqn.(3.56) into the continuity equation (3.54) and taking Eqn.(3.45.b) into account one has the second pressure correction equation:

$$b_P p''_P - \Sigma\ b_{nn}\ p''_{NN} = s''_P \qquad (3.57)$$

in which the coefficients b_P, b_{nn} are as defined earlier, Eqns.(3.51), and s''_P is a non-orthogonality term expressed as in Eqn.(3.52.a), but using p'' instead of p'.

Using the same notation introduced for SIMPLE(C), the algorithm PISO(C) can be summarized as follows:

I. Prediction step:

- this is like in SIMPLE(C). Starting from estimates p^*, $u^{i(0)}$, $Q^{(0)}$ for the pressure, velocity, and scalar fields (e.g., values at previous time step), all convection / diffusion coefficients and source terms are computed and the linearized momentum equations (3.41) are solved, yielding a velocity field u^{i*} having a residual mass source $\dot{m}_p$.

II. First correction step:

- this, too, is like the (single) correction step in SIMPLE(C). The pressure correction equation (3.50) is solved for p'; pressure and velocity fields are updated using Eqns.(3.43.b) and (3.48.a), yielding p^{**} and u^{i**}.

III. Second correction step:

- evaluate the term s''_p at the RHS of Eqn.(3.57); solve Eqn.(3.57) to obtain the second pressure correction p". Correct velocities by using Eqn.(3.56) and pressure by using $p^{***} = p^{**} + p''$.

IV. Scalar transport equations:

- as in SIMPLE(C), convection coefficients are updated using u^{i***} and all scalar transport equations are solved accordingly.

Since PISO(C) is a non-iterative algorithm, convergence tests need not to be performed and the computation simply moves to the next time step. Like for SIMPLE(C), several variants could be introduced into PISO(C), including a third correction step or using the algorithm as an iterative technique. For the large-eddy simulations presented in this work, these were not used and the basic procedure outlined above, with the PISOC (SIMPLEC-like) correction, was followed.

3.2.3 Rhie and Chow interpolation

As already mentioned, a crucial issue in the computation of the convection coefficients $(C^i)_{nn}$ is how the velocity components on control volume faces are interpolated from those defined at control volume centres (grid points). The "naive" approach would be to use linear interpolation in physical space; for example, the (cartesian) velocity component u^i on face "e" would be given by:

$$\overline{u^i}_e \equiv (1-W_e)u^i_P + W_e u^i_E \qquad (3.58)$$

involving the velocity components at grid points P, E and appropriate geometrical weight factors W_{nn}. However, it is well known [Patankar 1980] that this leads to so-called "chequerboard" oscillations in pressure and velocity. The reason is that pressure fields on even and odd cells actually cease to be coupled via the momentum equations; they may become completely independent and start "drifting" in the absence of any effective (numerical) corrective mechanism.

A common remedy is the use of staggered grids, in which each velocity component is defined at the centres of the faces normal to it; it was used, for example, in Release 1 of Harwell-FLOW3D [Jones et al.1985, 1986]. However, this approach may become quite cumbersome in the presence of nonorthogonal, body-fitted grids, and requires considerable storage. An alternative technique, which allows the use of co-located (i.e., non-staggered) grids whilst preventing "chequerboard" oscillations, was suggested by Rhie [1981] and Rhie and Chow [1983] and has been implemented into Harwell-FLOW3D, Release 2 as well as into other last-generation computer codes. It will be briefly summarized here.

The i-th discretized momentum equation (3.39) can be written at two adjacent grid points (control volume centroids), e.g. P and E, as follows:

$$a_P u^i_P + (\delta_i p)_P = [H(u^i)]_P + s'_P \qquad (3.59.a)$$

$$a_E u^i_E + (\delta_i p)_E = [H(u^i)]_E + s'_E \qquad (3.59.b)$$

while at the centre of face "e", lying between P and E, it becomes:

$$a_e u^i_e + (\delta_i p)_e = [H(u^i)]_e + s'_e \qquad (3.60)$$

The problem is to approximate solutions of Eqn.(3.60) from solutions of Eqns.(3.59.a) and (3.59.b). The method of Rhie and Chow consists of interpolating the whole LHS of Eqn.(3.60) instead of the term in u^i_e alone:

$$a_e u^i_e + (\delta_i p)_e \cong \overline{a_e u^i_e} + \overline{(\delta_i p)_e} \qquad (3.61)$$

i.e.,

$$u^i_e \cong \overline{u^i_e} + [\overline{(\delta_i p/a)_e} - (\delta_i p/a)_e] \qquad (3.62)$$

which, using normal velocity components $u^i_\perp \equiv A_j{}^i u^j$, and remembering the definition (3.49') of C^{ij}, can be written as:

$$u^i_{\perp e} \cong \overline{u^i_{\perp e}} + \overline{C_e{}^{ij}} \left\{ \left[\overline{\frac{\partial p}{\partial \xi^j}} \right]_e - \left[\frac{\partial p}{\partial \xi^j} \right]_e \right\} \qquad (3.63)$$

and, neglecting cross-derivatives:

$$u^i_{\perp e} = \overline{u^i_{\perp e}} + \overline{C_e{}^{ii}} \left\{ \left[\overline{\frac{\partial p}{\partial \xi^i}} \right]_e - \left[\frac{\partial p}{\partial \xi^i} \right]_e \right\} \qquad (3.64)$$

(no summation implied), in which all terms with overbars are computed on face "e" by linear weighted interpolation between points P and E, as in Eqn.(3.58), while $(\partial p/\partial \xi^i)_e$ is computed by central differencing in computational space from values of p at points P and E. Eqn.(3.64) must be used to compute all convection coefficients $(\rho u^i_\perp)_{nn} = (C^i)_{nn}$ prior to using them at any stage of the SIMPLE(C) or PISO(C) pressure-velocity coupling algorithms.

3.2.3 Solution techniques for the linearized equations

The discretization / linearization techniques described above lead, at the generic SIMPLE(C) iteration or PISO(C) step, to very large systems of linear equations having the general form:

$$\mathbf{A}\mathbf{x} = \mathbf{b} \qquad (3.65)$$

This may represent either a scalar transport equation of the form (3.28), including the momentum equations (3.41) or (3.53); or a pressure correction equation like (3.50) or (3.57). In the latter case only, the coefficient matrix is symmetric. In all cases, if the "deferred correction" technique described above is used, the matrix **A** contains only seven non-zero diagonals (in three-dimensional problems) and is efficiently stored as a (N*7) array (being N = NI*NJ*NK the overall number of control volumes in the grid). It is schematically shown in Figure 3.6; the control volumes are assumed to be ordered along the index:

$$IJK = I + (J-1)*NI + (K-1)*NI*NJ \qquad (3.66)$$

For such very large systems of linear equations, only iterative solution techniques are applicable. Practically all iterative methods (including the well known Jacobi, Gauss-Seidel and SOR algorithms) consist of replacing the original matrix **A** by an approximation **S** = **A** + **T** which is easier to invert; Eqn.(3.65) can be written:

$$\mathbf{Sx} = \mathbf{Tx} + \mathbf{b} \qquad (3.67.a)$$

which suggests the iterative approach:

$$\mathbf{S}x_{k+1} = \mathbf{T}x_k + \mathbf{b} \equiv \mathbf{b}' \qquad (3.67.b)$$

This last equation may also be written:

$$\mathbf{S}\delta_{k+1} = \mathbf{r}_k \qquad (3.67.c)$$

in which $\mathbf{r}_k \equiv \mathbf{b} - \mathbf{A}x_k$ is the residual at the generic iteration k, and $\delta_{k+1} \equiv x_{k+1} - x_k$ is the variation of the solution between consecutive iterations.

The various iterative methods differ mainly in the form chosen for the approximation matrix **S**. Several alternative techniques are implemented in Harwell-FLOW3D, Release 2; they include line relaxation (LRLX); Stone's Strongly Implicit Procedure (SIP), either in a 2-D, "sweeping" version (ST2 DSW) or in a fully 3-D form (ST3D); conjugate gradient method (CG), with alternative preconditioners; CG-squared (CGSQ). Among these, the methods adopted in the present work were ST3D for all transport equations and ICCG (conjugate gradient with incomplete Cholesky preconditioning) for the pressure-correction equation. They are briefly outlined in the following.

a) **ST3D**

This is a three-dimensional adaption of the "Strongly Implicit Procedure" originally introduced by Stone [1968] for two-dimensional diffusion or diffusion/ advection problems. It is based on choosing for **S** the form **LU**, being **L** and **U** a lower-triangular and upper-triangular matrices, respectively, which contain four diagonals each in the same positions where they appear in the original matrix **A**. Without loss of generality, the main diagonal of one of the triangular matrices, say **U**, can be chosen to be unitary, so that **L** and **U** altogether contain 7N coefficients and can be stored in a (N*7) array.

The elements of **L** and **U** could be determined by imposing that the product matrix **S** = **LU** coincide with **A** along the 7 non-zero diagonals of **A**; this leads, in fact, to a system of 7 equations in 7 unknowns coefficients for each row (i.e., for each grid point). The matrix **S** would also contain 4 extra diagonals which are of course absent from **A**. In practice, however, slightly modified definitions of **L** and **U**, involving a variable iteration parameter α, work better and allow a faster convergence. Details are given in the paper by Stone [1968] for the original, 2-D version but are not published for the 3-D version implemented in Harwell-FLOW3D.

As **S** = **LU**, the system (3.67.b) can be written:

$$\mathbf{LU}\delta_{k+1} = \mathbf{r}_k \qquad (3.67.d)$$

which, left-multiplying both sides by $\mathbf{L}^{-1}$, is transformed into:

$$\mathbf{U}\delta_{k+1} = \mathbf{V}_k \qquad (3.68.a)$$
$$\mathbf{L}\mathbf{V}_k = \mathbf{r}_k \qquad (3.68.b)$$

Being **L** and **U** triangular, Eqns.(3.68) are promptly solved in $\mathbf{V}_k$ and δ_{k+1} by forward or backward substitution.

b) **ICCG**

This is a conjugate-gradient method with incomplete Cholesky preconditioning [Kightley 1985] and is applicable only if the matrix **A** is positive (semi) definite and symmetric. Thus, it is used only for the pressure-correction equation occurring in any of the SIMPLE family algorithms.

Like any preconditioned-CG method, ICCG basically solves the following system, equivalent to (3.65):

$$\mathbf{ALy} = \mathbf{b} \qquad (3.69)$$

in which the change of variable $\mathbf{x} = \mathbf{Ly}$ has been performed. Left-multiplying both sides by $\mathbf{L}^T$ gives:

$$\mathbf{A'y} = \mathbf{b'} \qquad (3.70)$$

in which $\mathbf{A}' \equiv \mathbf{L}^T\mathbf{A}\mathbf{L}$ and $\mathbf{b}' \equiv \mathbf{L}^T\mathbf{b}$. Eqn.(3.70) is then solved by the conjugate-gradient method. The overall sequence of steps can be summarized as follows:

$$\mathbf{p}_k = \mathbf{A}\mathbf{d}_k \qquad (3.71.a)$$
$$\mathbf{x}_{k+1} = \mathbf{x}_k + \alpha_k \mathbf{d}_k \qquad (3.71.b)$$
$$\mathbf{r}_{k+1} = \mathbf{r}_k - \beta_k \mathbf{p}_k \qquad (3.71.c)$$
$$\mathbf{q}_{k+1} = \mathbf{P}^{-1}\mathbf{r}_{k+1} \qquad (3.71.d)$$
$$\mathbf{d}_{k+1} = \mathbf{q}_{k+1} + \beta_k \mathbf{d}_k \qquad (3.71.e)$$

in which $\mathbf{P} \equiv (\mathbf{L}^T\mathbf{L})^{-1}$ is the so called preconditioning matrix, and the coefficients α_k, β_k are given by:

$$\alpha_k = [(\mathbf{q}_k)^T\mathbf{r}_k] \,/\, [(\mathbf{d}_k)^T\mathbf{p}_k] \qquad (3.72.a)$$

$$\beta_k = [(\mathbf{q}_{k+1})^T\mathbf{r}_{k+1}] \,/\, [(\mathbf{q}_k)^T\mathbf{r}_k] \qquad (3.72.b)$$

The initial residual is $\mathbf{r}_0 = \mathbf{b} - \mathbf{A}\mathbf{x}_0$, and the initial values $\mathbf{q}_0 = \mathbf{d}_0 = \mathbf{P}^{-1}\mathbf{r}_0$ are used for $\mathbf{q}$ and $\mathbf{d}$. An initial guess $\mathbf{x}_0$ is required for the solution vector; this is generally zero for the pressure correction.

For $\mathbf{P} = \mathbf{I}$ the method becomes the standard CG; for $\mathbf{P} = \mathbf{A}$ it would converge in a single iteration, but Eqn.(3.71.d) would be equivalent to the original problem (3.65). In practice, the best choice for $\mathbf{P}$ is a matrix easy to invert and having the same "general structure" as the matrix $\mathbf{A}$. Alternative definitions of $\mathbf{P}$ are discussed by Kightley and Jones [1985].

It should be observed that, unlike "true" iterative techniques, CG methods converge to the exact solution in a finite number of steps $\leq N$ [Hager 1988]; however, this number is usually very large and iterations are terminated long before that by some suitable stopping criterion (usually, when the norm of the residual is reduced to a prescribed fraction of its initial value).

3.3 Implementation of a subgrid scale model and of boundary conditions

Personally I am not of an imaginative temperament-
very few Engineers are
[R.Kipling, "The Strange Ride of Morrowbie Jukes"]

3.3.1 Code modifications for the Smagorinsky-Lilly subgrid model

The Smagorinsky-Lilly subgrid model implemented in the code, with Van-Driest (or similar) near-wall damping, is summarized here for the reader's convenience:

$$\nu_s = l^2 \hat{S} \tag{3.73}$$

with:

$$l = c_s D \bar{\Delta} \tag{3.74}$$

and:

$$\hat{S} = (2\hat{S}_{ij}\hat{S}_{ij})^{1/2} \tag{3.75}$$

In Eqn.(3.74), the three terms c_s, D and $\bar{\Delta}$ represent respectively:

I. c_s: this is the main model constant, which the user is free to set; as mentioned in Chapter 2, values of the order 0.1 have been proposed in the literature.

II. D: this is a near-wall damping factor, which may be expressed by one of Eqns.(2.102). Their application requires, however, that the distance y from the nearest wall be expressed in 'wall units' as y^+. In general, it is convenient to write:

$$y^+ = Fy \tag{3.76}$$

being F an appropriate non-dimensionalizing factor. For plane channel flows, F is naturally expressed as:

$$F = u_\tau/\nu \tag{3.77}$$

being $u_\tau \equiv (|\tau_w|/\rho)^{1/2}$ the mean friction velocity; this can be in turn deduced from the imposed streamwise pressure gradient. However, for flows within complex boundaries, notably involving recirculation, the scaling factor F not

only becomes a function of the wall region considered, but can not in general be expressed by Eqn.(3.77); in fact, τ_w may well vanish at separation or reattachment points. In the context of k-ε turbulence modelling, for example, F (which is used to impose wall boundary conditions based on universal 'wall functions') may be expressed as:

$$F = c_\mu^{1/4} k_P^{1/2} / \nu \qquad (3.78)$$

being k_P the value of the turbulence energy k at the near-wall grid point P and c_μ=0.09 the Prandtl-Kolmogorov constant. More generally, the scaling factor F is proportional to the thickness y_v of the viscous sublayer, so that a good scaling of y is equivalent to a good knowledge of the distribution of this thickness along walls (also, ideas such as expressed by Ciofalo and Collins [1989.a] about a varying y_v^+ could be applied here). Finally, in the most general case F is a function of space and time, through its dependence on the instantaneous flow field.

III. $\bar{\Delta}$ is the average cell size, conveniently expressed as the cubic root of the volume of the generic computational cell:

$$\bar{\Delta} = V^{1/3} \qquad (3.79)$$

In Eqn.(3.75), $\hat{S}_{ij}$ is the (resolved) strain rate tensor, expressed by Eqn.(2.75). In the case of cartesian physical-space coordinates x,y,z, the following expression holds for $\hat{S}^2$:

$$\hat{S}^2 = 2[(\partial\hat{u}/\partial x)^2+(\partial\hat{v}/\partial y)^2+(\partial\hat{w}/\partial z)^2]+ [(\partial\hat{u}/\partial y+\partial\hat{v}/\partial x)^2+(\partial\hat{u}/\partial z+\partial\hat{w}/\partial x)^2+(\partial\hat{u}/\partial z+\partial\hat{w}/\partial y)^2] \qquad (3.80)$$

The appropriate modifications must be introduced if cylindrical coordinates r, ϑ, z are used instead. In Harwell-FLOW3D, the term S^2 is already used, for example, in the k-ε model to compute the generation of k due to shear; it is equivalent to the term (GEN/VIS) in subroutine GENTRB.

From the above formulation of the subgrid model, it is clear that the computation of ν_s requires, besides the two constants A^+ and c_s, the knowledge of the following quantities for each mass control volume n:

$\bar{\Delta}_n$ (average cell size);
y_n (distance from nearest wall);
F_n (appropriate scaling factor for y_n);
S_n ('Smagorinsky' term).

Since, in a general flow, F is a property of each 'wall element' (control volume face lying on a wall) rather than of each control volume n, it is convenient to introduce the integer array:

L_n (index of the 'wall element' nearest to each control volume n)

so that the appropriate scaling factor F_n for the control volume n can be expressed as $F(L_n) = F_l$. Now:

a) $\bar{\Delta}_n$ can be easily expressed in terms of the array **VOL**, and thus needs not to be stored;

b) y_n and L_n are geometrical quantities which do not change during the course of a transient. Hence, it is convenient to store them in the two permanent arrays:

y_n = **WDIST**(I,J,K); L_n = **LDIST**(I,J,K)

with I=1 to NI, J=1 to NJ, K=1 to NK and n=I+(J-1)*NI+(K-1)*NI*NJ.

As no memory allocation is provided in the standard version of the code for such arrays, it is convenient (in order to avoid any modifications in routines of higher 'hyerarchical' rank than USRVIS) to store them into suitable 'chunks' of the working arrays **WORK** and **IWORK**, defining the relative pointers IWDIST and ILDIST and increasing the free-space pointers IWRFRE, IWIFRE by NIJK = NI*NJ*NK when USRVIS is called for the first time.

c) F_l and $\hat{S}_n$ are quantities which vary (in general) during a transient. $\hat{S}_n$ is given by Eqns.(3.75) or (3.80), while, as discussed above, in the most general case F_l is also a function of the instantaneous flow field. Thus, it is convenient to recompute them each time the subroutine USRVIS is called, and to store them temporarily in the two arrays:

F_l = **FACTOR**(L) (L=1 to NCV, overall number of 'wall elements');
$\hat{S}_n$ = **SMAG**(I,J,K) (I=1 to NI, J=1 to NJ, K=1 to NK).

These two arrays are also stored in appropriate sections of the working array **WORK**.

Besides the arrays described above, some additional arrays are needed for the actual computation of **WDIST, LDIST** and of **FACTOR, SMAG**. They are also used temporarily and stored in 'chunks' of the array **WORK** (see below).

The flow-chart of the interaction between USRVIS and the auxiliary subroutines introduced for LES is sketched in Figure 3.7. A few comments are necessary:

a) Subroutine LES0 is called when USRVIS is called the first time. Note that in FLOW3D, Release 2.1 USRVIS is called twice during the initialization phase, first through the path:

MAIN → FLMAIN → FLOW3D → INIT → PROPS → CVIS → USRVIS

and then through the path:

MAIN → FLMAIN → FLOW3D → INIT → INTBCS → PROPS → CVIS → USRVIS;

LES0 is called only the first time, and a flag is set so that no further call is made. The task of LES0 is currently the computation of arrays **WDIST** and **LDIST**, which is accomplished through subroutine WALDST.

b) Subroutine LEST is called at each time step, and in the initialization phase. It is used to compute:

I. Array **FACTOR** (= F_l), through subroutine USRFCT. Currently, for all the geometries investigated here USRFCT computes a simple scaling factor u_τ/ν from the (imposed) pressure drop along the channel; in successive developments, a more sophisticated computation of F_l, based on the concepts expressed above, might be implemented.

II. Array **SMAG** (= $\hat{S}_n$) from Eqn.(3.80) or its equivalent for cylindrical coordinates. This requires a call to subroutine GRADV (and its auxiliary routines), already present in the code, in order to compute velocity gradients. Much code for this was taken from the standard subroutine GENTRB.

c) Subroutine LES, also called at each time step, computes the subgrid viscosity ν_s and the total viscosity (array **VIS**) from the computed values of F_l, y_n, S_n and L_n (see above formulae).

d) The computation of **LDIST** and **WDIST** is accomplished in WALDST by an outer loop on 'wall elements' l=1 to NCV, and an inner loop on control volumes n=1 to NI*NJ*NK. For each couple (control volume - wall element) WALDST computes the distance between the n-th grid point (centroid of control volume N) and the centroid of the l-th wall element. The coordinates of the former are computed, as usual in FLOW3D, by averaging the corner coordinates stored in arrays **XC, YC, ZC**; the coordinates of the latter are stored in the 'standard' arrays **XFACE, YFACE, ZFACE** and are 'extracted' with the aid of the integer lists **ILEN, IST, INC, NWLA**, much as in the standard subroutine WALYP. The minimum distance for each cell n is stored in **WDIST**, and the corresponding value of l is stored in **LDIST**. The method is valid for arbitrary geometries; of course, the computation of **WDIST** and **LDIST** could be made trivially for simple geometries such as a plane channel.

The following tables 3.4 to 3.7 summarize the exchanged parameters for all the auxiliary subroutines described above. Comments are added when appropriate.

Table 3.4 Computation of arrays WDIST, LDIST

in USRVIS:	in LES0:	in WALDST:
XC, YC, ZC	**XC, YC, ZC**	**XC, YC, ZC**
LM = **ILIST**(JTWS)	LM	LMAX
ILIST(JTWS to JTWS+NCV-1)	**LTWS**(2...)	**ILEN** (dim. LMAX)
	LTWS(LM+2...)	**IST** (" 3*LMAX)
	LTWS(4*LM+2...)	**INC** (" 3*LMAX)
	LTWS(7*LM+2...)	**NWLA** (" LMAX)
NCV = **ILIST**(JTWS+8*LM+1)	NCV	NCV
IWORK(ILDIST to ILDIST+NIJK-1)	**LDIST**	**LDIST** (dim. NIJK)
WORK (IWDIST to IWDIST+NIJK-1)	**WDIST**	**WDIST** (" NIJK)
	X	**X** (dim. NIJK)
	Y	**Y** (" NIJK)
WORK(IWDIST+NIJK to	**Z**	**Z** (" NIJK)
IWDIST+12*NIJK-1)	**XFACE**	**XFACE** (dim. 3*NIJK)
	YFACE	**YFACE** (" 3*NIJK)
	ZFACE	**ZFACE** (" 3*NIJK)

Remarks:

I. As **LDIST** and **WDIST** need to be stored permanently, free-location pointers IWIFRE and IWRFRE are increased by NIJK when USRVIS is called for the first time;

II. For the computation of **LDIST** and **WDIST** (in subroutine WALDST) the arrays **X, Y, Z** (containing the coordinates of control volume centroids) and **XFACE, YFACE, ZFACE** (containing the coordinates of face centroids) are used. In earlier versions of FLOW3D, Release 2, **X, Y** and **Z** could be stored permanently in their own locations by setting the option LGRID = .TRUE. in the main program; this, however, is no more possible in Releases 2.1 and following, so that the computation of **X, Y, Z** and their temporary storage in the first 3*NIJK free locations of WORK are provided for. The same holds for arrays **XFACE, YFACE, ZFACE,** which are stored in the next 9*NIJK locations.

Table 3.5 Computation of array SMAG

in USRVIS:	in LEST:	in GRADV:
-	0	IFLAG
XC, YC, ZC	**XC, YC, ZC**	**XC, YC, ZC**
U , V , W	**U, V , W**	**U , V, W**
TE, DEN, VIS	**TE, DEN, VIS**	**TE, DEN, VIS**
VOL, AREA, WFACT	**VOL, AREA, WFACT**	**VOL, AREA, WFACT**
	UGRAD	**UGRAD** (dim. 3*NIJK)
WORK(IGRAD to IGRAD+9*NIJK-1)	**VGRAD**	**VGRAD** (" 3*NIJK)
	WGRAD	**WGRAD** (" 3*NIJK)
WORK(ISMAG to ISMAG+NIJK-1)	**SMAG**	-
NCV = **ILIST**(JTWS+8*LM+1)	NCV	-
ILIST(JTDIR....)	**LTDIR**	**LTDIR**
ILIST(JTNEUM...)	**LTNEUM**	**LTNEUM**
ILIST(JTNEUP...)	**LTNEUP**	**LTNEUP**
ILIST(JTSYS....)	**LTSYS**	**LTSYS**
ILIST(JTPS.....)	**LTPS**	**LTPS**
ILIST(JTWS.....)	**LTWS**	**LTWS**
RLIST(JRLWS....)	**RLWS**	**RLWS**

Remarks:

I. Array **SMAG** is stored (temporarily) in the first NIJK available locations of **WORK**;

II. Arrays **UGRAD, VGRAD, WGRAD** are stored in the next 9*NIJK locations in **WORK**;

III. Arrays **TE, DEN, VIS** are just passed as dummy parameters to LEST and GRADV, but are not actually used.

Table 3.6 Computation of array FACTOR

in USRVIS:	in LEST:		in USRFCT:	
LM = **ILIST**(JTWS)	LM		LMAX	
		LTWS(2...)	**ILEN**	(dim. LMAX)
ILIST(JTWS to JTWS+NCV-1)	**LTWS**	**LTWS**(LM+2...)	**IST**	(" 3*LMAX)
		LTWS(4*LM+2...)	**INC**	(" 3*LMAX)
		LTWS(7*LM+2...)	**NWLA**	(" LMAX)
NCV = **ILIST**(JTWS+8*LM+1)	NCV		NCV	

Remarks:

I. Array **FACTOR** has a length NCV equal to the number of 'wall elements'. It is temporarily stored in the first NCV available locations of **WORK**.

II. Some remarks on the meaning of **FACTOR** and on its computations were sketched above. Like in WALDST, the same approach as in the 'standard' subroutine WALYP is used in USRFCT to scan the walls.

Table 3.7 Computation of subgrid and total viscosity

in USRVIS:	in LES:
WORK(IWDIST)	**WDIST** (dim. NIJK)
WORK(ISMAG)	**SMAG** (" NIJK)
WORK(IFACT)	**FACTOR** (" NCV)
IWORK(ILDIST)	**LDIST** (" NIJK)
VOL, VIS	**VOL, VIS**

Remarks:

I. The subgrid kinematic viscosity is computed directly according to formulae (3.73) and following. It is then multiplied by the density (stored in array **DEN**, and however constant in all the present simulations), and added to the laminar viscosity VISCOS (contained in the common block FLUPR); the result is stored in the array **VIS**;

II. Immediately after subroutine LES has returned **VIS** to USRVIS, all the temporary **WORK** space used is released.

The use and release of working space is summarized below:

a) First call of USRVIS only (before calling LES0):

I. NIJK locations are reserved in **IWORK** for array **LDIST**, and in **WORK** for array **WDIST**:

```
ILDIST = IWIFRE    ,        IWIFRE = ILDIST + NIJK
IWDIST = IWRFRE    ,        IWIFRE = IWDIST + NIJK
```

II. 12*NIJK locations are temporarily reserved in **WORK** (for arrays **X, Y, Z, XFACE, YFACE, ZFACE**) and are then released, in accordance with the scheme:

```
IWRSAV = IWRFRE
IWRFRE = IWRSAV + 12NIJK
...(CALL LES0)...
IWRFRE = IWRSAV
```

b) Before calling LEST and LES (generic call of USRVIS):

NCV+NIJK+9*NIJK locations are temporarily reserved in **WORK** (respectively for array **FACTOR**, for array **SMAG**, and for arrays **UGRAD, VGRAD, WGRAD**) and are then released:

```
IWRSAV = IWRFRE
IWRFRE = IWRSAV + NCV + 10*NIJK
...(CALL LEST)...
...(CALL LES )...
IWRFRE = IWRSAV
```

At each stage, the availability of workspace is checked and error messages are issued if this is not enough.

3.3.2 Code modifications for the subgrid heat transport

In all the present simulations, subgrid heat fluxes (2.88) were expressed by the simple gradient-diffusion assumption (2.89); i.e., a subgrid thermal diffusivity proportional to the subgrid viscosity, Eqn.(2.91.a), was used. The subgrid Prandtl number, σ_s, was provided as an input parameter. Thus, subgrid

heat transport was simply implemented by computing Γ_s from Eqn.(2.91.a) and adding this to the laminar diffusivity Γ in subroutine USRDIF to get the total thermal diffusivity (array **DIFF**).

3.3.3 Implementation of wall boundary conditions for LES

Alternative hydrodynamic boundary conditions for Large-Eddy Simulation were discussed in detail in Section 2.5; they were all tested for the plane channel case (Chapter 5). All these formulations can be reconducted to appropriate expressions for the multipliers $T_{M,i}$ linking the (cartesian) components of the wall shear stress, $\tau_{w,i}$ to the corresponding components of the velocity parallel to the wall at the near-wall grid point P, $u_{par,i}$. In some formulations (models (a), (b), (c) of Section 2.5) the three multipliers are identical, i.e. the wall shear stress τ_w is assumed to be proportional to u_{par}; the implementation of these simply required minor modifications to the formulae used for T_M in subroutines WALSHR and WALSTR. However, the implementation of models (d) ("shifted") and (e) ("ejection"), involving three different values for the $T_{M,i}$, required also slight modifications to subroutine SCMOM in order to 'split' T_M into three components before calling WALSHR. Finally, the implementation of model (a) ("Mason and Callen" boundary conditions) in the case of high Reynolds number (first near-wall grid point outside the viscous sublayer, i.e. 'synthetic' wall boundary conditions) requires the computational steps summarized by Eqns.(2.109) to (2.115); these were implemented in a separate auxiliary subroutine MASCAL, called in turn by WALSHR and WALSTR. Note that, for low Reynolds number flows (first grid point within the viscous sublayer) model (a) is identical to the ordinary no-slip conditions used in laminar flow, and no special modification to the existing subroutines would be required.

As regards the thermal boundary conditions at walls, in most simulations described in the present work the wall heat flux was imposed. Thus, the details of the treatment of heat transfer between wall and wall-adjacent control volume have no influence on the overall temperature field in the fluid, and affect only the temperature distribution on walls (computed by subroutine WALTHF). Minor modifications to WALTHF were necessary only in the case of high-Reynolds number flows, in order to implement log-law profiles coherent with those assumed for the flow field.

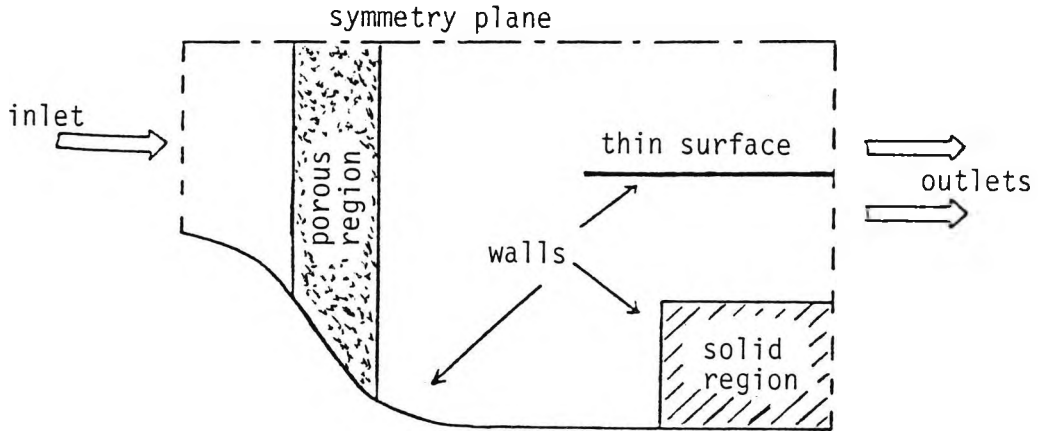


Figure 3.1 - Generic FLOW3D computational domain and structures which can be defined within it (a 2-D domain is shown for simplicity).

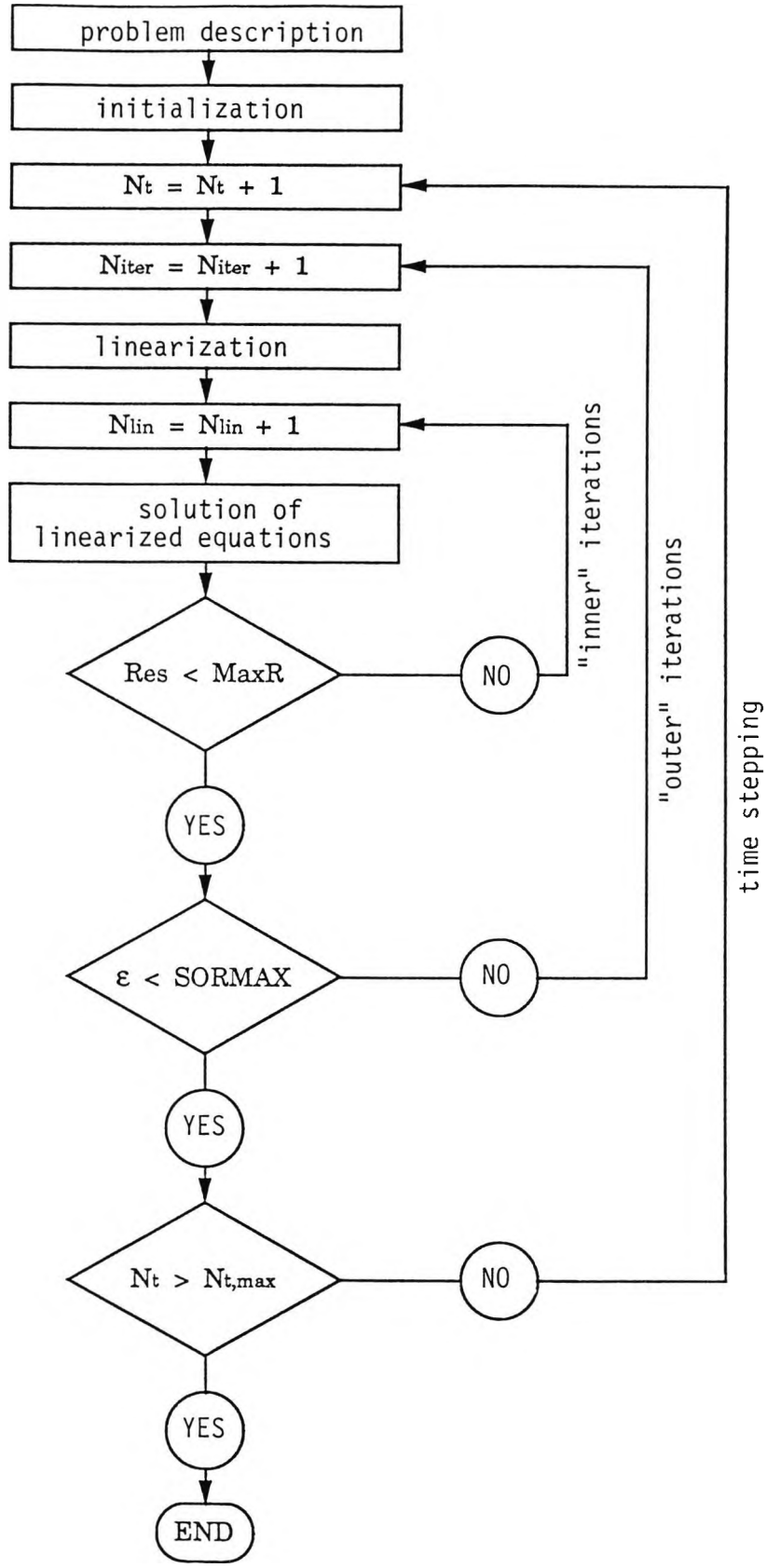


Figure 3.2 - Schematic flow chart of FLOW3D

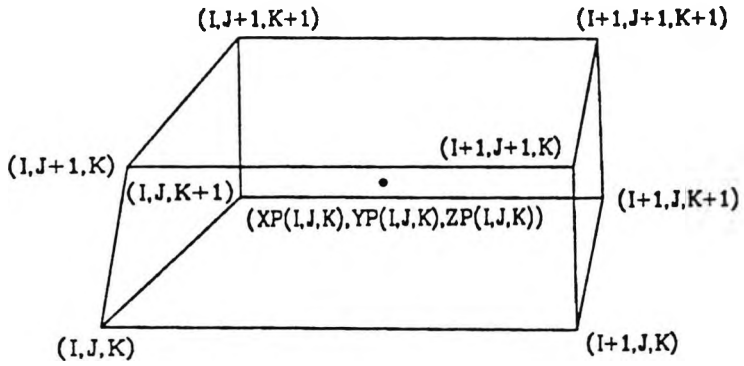


Figure 3.3 - Generic control volume. Indices of corners in the FLOW3D grid are shown. The usual "compass rose" nomenclature is used.

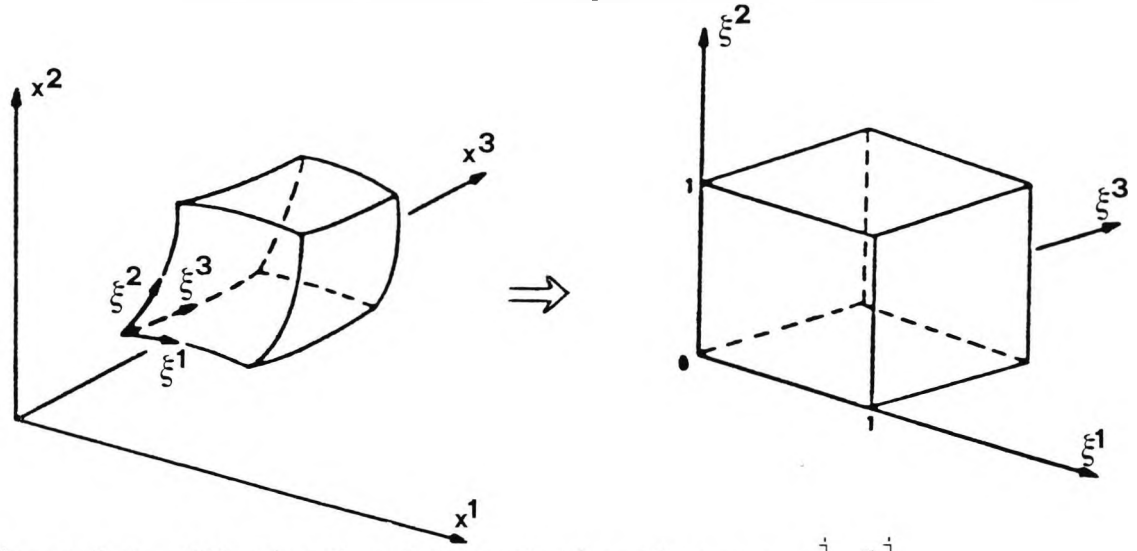


Figure 3.4 - "Physical" and "computational" spaces x^j, ξ^j.

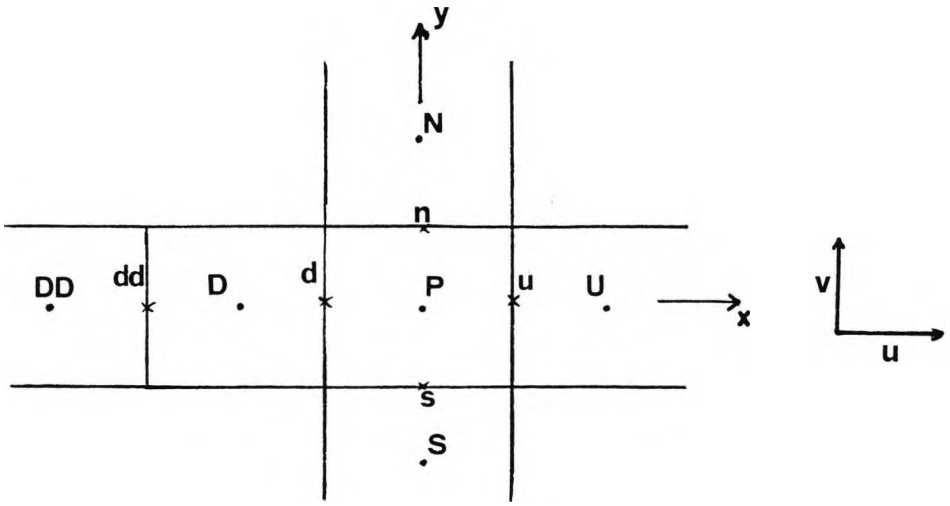


Figure 3.5 - Nomenclature of control volumes for discretization schemes.

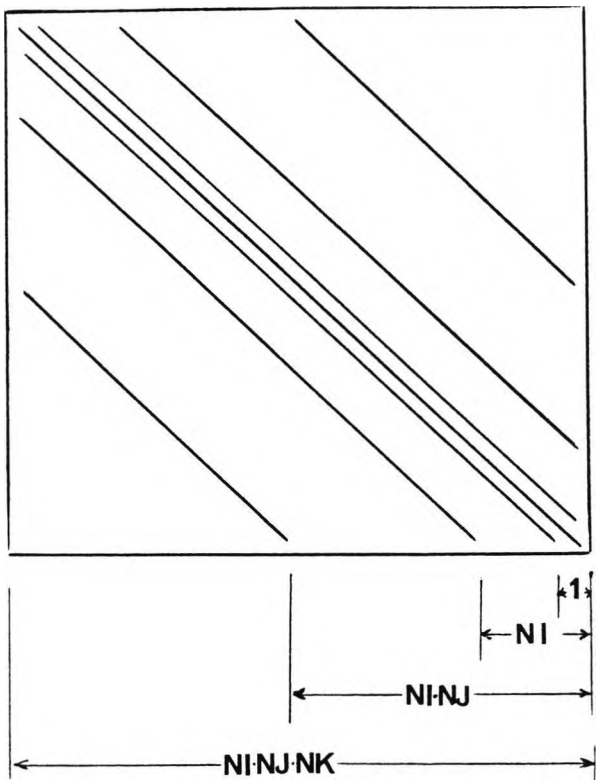


Figure 3.6 - Structure of the matrix **A** of linearized equations.

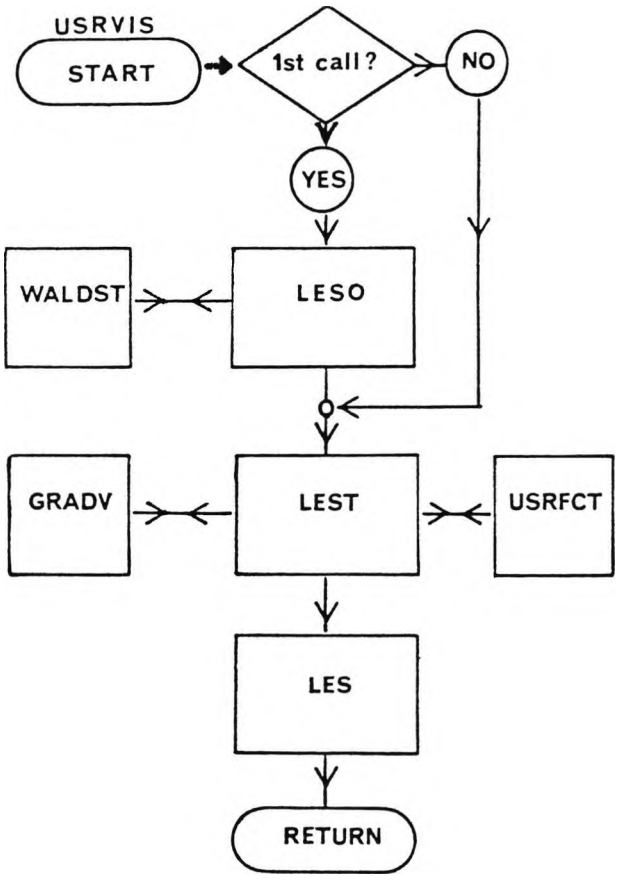


Fig.3.7 - Flow chart of subroutine USRVIS and auxiliary subroutines LES, LES0, LEST, USRFCT, WALDST used to compute subgrid viscosity.

CHAPTER 4 - APPLICATION TO TURBULENT FLOW WITH HEAT TRANSFER IN A PLANE CHANNEL

4.1 Introduction and literature review

> **If your pet theory of the universe is found to be contradicted by observation - well, these experimentalists do bungle things sometimes**
> [A.S. Eddington]

Experimental data for both mean and fluctuating velocities in turbulent channel flows have been obtainable for many years [Laufer 1954; Comte-Bellot 1963].

More recently, Kreplin and Eckelmann [1979] used hot-wire anemometry to measure the cross-stream profiles of mean velocity and of all three fluctuating components; the working fluid was oil, the duct had a rectangular cross-section with an aspect ratio of 3.59, the flow was practically fully-developed and the Reynolds number Re_δ, based on channel half-width and cross section-averaged velocity, was about 3000. Hussain and Reynolds [1975], using the same technique, measured only profiles of the mean velocity and of the streamwise fluctuation, but for a higher Reynolds number ($Re_\delta \cong 10,000$). The same quantities were measured by Nishino and Kasagi [1989] using Particle Image Velocimetry.

Experimental cross-stream profiles of mean and fluctuating velocities, once expressed in wall units as u^+, u^+_{rms} etc., see Eqns.(4.10) below, exhibit only a weak dependence on the Reynolds number. Since the friction coefficient decreases as Re^{-c}, with c close to 0.3 for moderate Reynolds numbers [Beavers et al.1971], a simple analysis shows that the <u>cross-section averaged</u> velocity, expressed in wall units u_τ as U^+, must increase as $Re^{c/2}$ (~ 0.15). However, the <u>peak</u> (centreline) value of u^+ is about 18 both in the experiments of Kreplin and Eckelmann [1979], for Re_δ=3,000, and in those of Hussain and Reynolds [1975], for Re_δ=10,000; thus, the increase in the average value is accompanied by an increasing flatness of the cross-stream u-profile, with little variation of the peak value.

Similarly, fluctuations do not exhibit a clear trend with Re. Among the three components, the streamwise fluctuation u^+_{rms} is the largest, with peaks of 2.3-2.8 near the walls; peak values of v^+_{rms} and w^+_{rms} are lower and close

to each other. Peaks of v^+_{rms} are the flattest and farthest from the walls. Turbulence becomes roughly isotropic in the central region of the duct.

There are no comparably accurate measurements of mean and fluctuating temperatures for thermally fully-developed non-isothermal flow. For example, the holographic-interferometry results of Lockett [1987] include real-time, span-averaged interferograms showing time-dependent 'thermal eddies' at Reynolds numbers of 10^4-10^5, but are for a thermal development length of a few channel heights. In fully-turbulent flow, the Nusselt number is expected to increase as $Re^{0.8}$, as, for example, in circular ducts. From Eqns.(4.10) below it follows that the cross-section averaged dimensionless temperature is expected to increase only as $Re^{0.05}$.

4.2 Model and methods

> **"Can you do Addition?" the White Queen asked.**
> **"What's one and one and one and one and one and one and one and one and one?"**
> **"I don't know" said Alice. "I lost count".**
> [Lewis Carroll, 'Through the looking glass']

4.2.1 Summary of governing equations and subgrid model

The filtered continuity, Navier-Stokes and energy equations, in which the fluid is assumed to be incompressible and the gradient-diffusion hypothesis is adopted for the subgrid terms, may be summarized as:

$$\frac{\partial \hat{u}_j}{\partial x_j} = 0 \tag{4.1}$$

$$\frac{\partial \hat{u}_i}{\partial t} + \frac{\partial}{\partial x_j}(\hat{u}_i \hat{u}_j) = -\frac{1}{\rho}\frac{\partial \hat{P}}{\partial x_i} + \frac{\partial}{\partial x_j}(\nu+\nu_s)\frac{\partial \hat{u}_i}{\partial x_j} \tag{4.2}$$

$$\frac{\partial \hat{T}}{\partial t} + \frac{\partial}{\partial x_j}(\hat{u}_j \hat{T}) = \frac{\partial}{\partial x_j}(\alpha+\alpha_s)\frac{\partial \hat{T}}{\partial x_j} \tag{4.3}$$

In the following, the caret (^) for 'resolved quantity' will be omitted. The modified pressure P includes the term $(2/3)\rho\tilde{k}$, see Eqn.(2.77).

The reference subgrid model used for the large eddy simulations of plane channel flow is the Smagorinsky-Lilly model with VanDriest near-wall damping, Eqns.(3.73)-(3.75), (3.79), (2.102.a); α is the molecular heat diffusivity ν/σ (with the Prandtl number σ=0.72) and α_s the corresponding subgrid diffusivity, expressed by Eqn.(2.91.b). The subgrid Prandtl number σ_s was made vary between 0.25 and 1 in the simulations.

4.2.2 Averages and fluctuations

The direct result of a simulation is the instantaneous resolved field of all scalar quantities Q (= u, v, w, p, T) on a three-dimensional grid, repeated at each time step. In order to interpret these results and compare them with experimental data or with other simulations, it is necessary to split the generic resolved field into an average and a fluctuating component via a statistical processing of the instantaneous results; this can be done in different ways. For any resolved scalar Q the following quantities can be defined:

Q	instantaneous local value;
$\langle Q \rangle$	instantaneous value, space-averaged (ensemble-averaged) over a plane parallel to the walls;
$\langle\langle Q \rangle\rangle$	instantaneous value, space-averaged over the whole volume of the computational domain;
$\overline{Q}$	local value, time-averaged over a given interval (number of time steps);
$\langle\overline{Q}\rangle = \overline{(\langle Q \rangle)} = \langle(\overline{Q})\rangle$	value of Q averaged over a plane and over a time interval.

Similarly, fluctuating (resolved) components can be defined as follows:

$Q' = Q - \overline{Q}$	instantaneous local fluctuation with respect to the time-averaged value;
$Q'' = Q - \langle Q \rangle$	instantaneous local fluctuation with respect to the plane-averaged (ensemble-averaged) value.

The corresponding root-mean-square (rms) values are:

$$Q'_{rms} = \sqrt{\overline{Q'^2}} = \sqrt{\overline{(Q - \overline{Q})^2}}$$

$$Q''_{rms} = \sqrt{\langle Q''^2 \rangle} = \sqrt{\langle (Q - \langle Q \rangle)^2 \rangle}$$

The latter will be extensively used, and indicated simply as Q_{rms}, in the following.

Moreover, space- or ensemble-averages of Q'_{rms}, $\langle Q'_{rms} \rangle$ and time-averages of Q''_{rms}, $\overline{Q''_{rms}}$, can be computed. Like $\overline{\langle Q \rangle}$, they are one-dimensional fields, functions only of the cross-stream coordinate y normal to the walls.

Similar average and rms values can be defined for wall quantities (pressure, shear stress, temperature, heat flux). Alternate definitions are, of course, possible.

4.2.3 Boundary conditions

The computational domain ('box') used for the **reference** simulations is sketched in Figure 4.1; a typical three-dimensional grid, having 32*16*16 control volumes and selectively refined in the near-wall regions, is shown in Figure 4.2. The sizes of the box are $L=8\delta$, $W=4\delta$ and of course $H=2\delta$, being δ the channel half-height, used as the main 'outer' length scale in the following. As discussed in Chapter 2, the choice of the box sizes is based on experimental results for the characteristic correlation lengths between fluctuations, e.g. Comte-Bellot [1963]. Periodic boundary conditions are imposed along the streamwise direction x and the spanwise direction z, while no-slip or synthetic wall boundary conditions are imposed at y=0 and y=H. The thermal boundary conditions are:

- **adiabatic upper wall** (y=H);
- **uniform heat flux** q on the **lower wall** (y=0).

As pressure P and temperature T are intrinsically non-periodic quantities, they are replaced by the respective periodic components P^*, T^*. By writing:

$$P = P^* + (dp/dx)x \qquad (4.4)$$

$$T = T^* + (dT/dx)x \qquad (4.5)$$

and substit. in Eqn.(4.2) (written for the streamwise direction 1=x) and in Eqn.(4.3), it is easy to show that these may be thought of as equations in P^*, T^*, provided the following source terms are added to their right hand sides:

$$S_u = - (dp/dx)/\rho = |dp/dx|/\rho \qquad (4.6)$$

$$S_T = - u(dT/dx) = - q/(2c_p\rho\delta)\ u/U \qquad (4.7)$$

in which u is the local instantaneous (resolved) velocity and U is the mean velocity, $\dot{m}/(\rho WH)$.

In Eqns.(4.6)-(4.7) the driving pressure gradient $|dp/dx|$ and the heat flux q (i.e. the temperature gradient dT/dx) are imposed as independent variables. The imposed pressure gradient can be used to derive the equilibrium wall shear stress:

$$\tau_o = \delta(dp/dx) \qquad (4.8)$$

and the corresponding equilibrium friction velocity:

$$u_\tau = (|\tau_o|/\rho)^{1/2} \qquad (4.9)$$

The various flow quantities can be made dimensionless with reference to u_τ as:

lengths (e.g., distance from wall)	$y^+ \equiv yu_\tau/\nu$	(4.10.a)
velocities	$u^+ \equiv u/u_\tau$	(4.10.b)
stresses (e.g., wall shear stress)	$\tau_w^+ \equiv \tau_w/(\rho u_\tau^2)$	(4.10.c)
pressures	$P^+ \equiv P/(\rho u_\tau^2)$	(4.10.d)
turbulence energy	$k^+ \equiv k/u_\tau^2$	(4.10.e)
temperatures	$T^+ \equiv (T_w-T)\rho c_p u_\tau/q$	(4.10.f)

In particular, Eqn.(4.10.a) is used to express y^+ in the near-wall damping functions (2.102). In Eqn.(4.10.f), T_w is the local instantaneous (resolved) wall temperature at the nearest wall location, so that $T^+=0$ at the heated wall and <u>increases</u> moving away from it. An alternative definition is:

$$T^{++} \equiv \rho T c_p u_\tau/q \qquad (4.10.g)$$

which, of course, <u>decreases</u> moving away from the heated wall.

The nominal mean velocity U^o, used as an initial condition, was chosen so that a given nominal Reynolds number $Re^o=U^oD_e/\nu$ was obtained (based on the hydraulic diameter $D_e = 2H = 4\delta$). The corresponding Reynolds number based on channel half-height was, of course, $Re_\delta^o=Re^o/4$. The driving pressure gradient to be used as source term in the streamwise Navier-Stokes equation was computed from:

$$|dp/dx| = (4C_f/D_e)\rho(U^o)^2/2 \qquad (4.11)$$

in which the (Fanning) friction coefficient C_f was expressed using the correlation given by Beavers et al. [1971] for low-Reynolds number turbulent flow in flat rectangular ducts:

$$C_f = 0.127*Re_D^{-0.3} \qquad (4.12)$$

4.2.4 Initial conditions

Two basic methods of setting the initial conditions were tested.

In both cases, for each plane y=constant parallel to the channel's walls, the values of each fluctuating velocity component (i.e. u-<u>, v and w) were randomly distributed over the grid points lying on that plane, following a normal distribution having zero mean and a prescribed standard deviation (also equal to the root-mean-square value of the distribution, $u_{rms}=<u''^2>^{1/2}$ etc.). The mean streamwise velocity, <u>, was prescribed for each plane, and of course both <v> and <w> were set to zero. Normal distributions having prescribed mean and standard deviation were generated by using the IMSL subroutines RNNOA, SSCAL and SADD.

The difference between the two methods was the following:

a) In the first approach, both <u> and u_{rms}, v_{rms}, w_{rms} were assumed to be uniform (i.e., independent of y). The value of <u> was set equal to the reference initial velocity $U^o=Re_\delta{}^o\delta/\nu$. The rms values were assumed to be proportional to the equilibrium friction velocity $u_\tau=(|\tau_o|/\rho)^{1/2}$:

$$u_{rms} = v_{rms} = w_{rms} = cu_\tau \qquad (4.13)$$

b) In the second approach, <u> and u_{rms}, v_{rms}, w_{rms} were assumed to be functions of y; their profiles were set on the basis of the experimental results of Kreplin ed Eckelmann [1979], appropriately scaled by u_τ.

Preliminary simulations evidenced that results were very little affected by the choice of conditions (a) vs. (b), as well as by the choice of the proportionality constant c in eqn.(4.13). Therefore, the simpler conditions (a), with c=1, were used throughout the following runs; of course, they amount to imposing an initial plug velocity profile, with superimposed isotropic random fluctuations. The choice c=1 gives for the resolved turbulence energy

$$k = \frac{1}{2} (u^2_{rms} + v^2_{rms} + w^2_{rms}) \qquad (4.14)$$

averaged over the whole channel and made dimensionless with reference to u_τ^2, i.e. as k^+, the initial value of 1.5, close to the experimental value of Kreplin and Eckelmann (~2).

It should be observed that neither conditions (a) or (b) satisfy continuity; this is not crucial for the solution algorithms used in Harwell-FLOW3D, as was preliminarily verified for non-LES transient simulations (see for example Ciofalo and Collins [1988.a]), but has some influence on the initial behaviour of the fluctuations, as discussed in the following section.

4.3 General issues

Clearly I cannot synthetize in a few lines,
especially in such a sunny day,
this rich and fascinating system
[Paul Feyerabend]

Some general aspects of the large-eddy simulations conducted will be discussed in this section, before presenting detailed results from reference cases and from the parametrical study which accompanied these. Three main issues will be considered, namely, the way in which a statistically steady state is attained; the effects of disequilibrium between the applied driving pressure gradient and the wall shear stress; and the dependence of computed flow statistics on the averaging technique used.

4.3.1 Numerical transient and restart

A critical issue of direct and large-eddy simulations is the way in which an artificially perturbed flow develops into a "truly" turbulent flow, and statistically steady-state conditions are established. The simplest indicator of the evolution of the simulated flow field is the channel-averaged resolved turbulence energy k, Eqn.(4.14), though of course several alternative quantities can serve as indicators.

The behaviour of k depends critically on the numerical methods used, on the initial conditions chosen, and on the subgrid model. As expected, the

influence of the Smagorinsky constant c_s was found to be particularly relevant in the present simulations. In Figure 4.2 the behaviour of k^+, starting from the pseudo-random initial conditions described in Section 4.2.4, is reported for Re^0=20,000, a 32*16*16 grid, and different values of c_s. The Crank-Nicolson time-stepping scheme was used here, with $t=0.01\delta/u_\tau$ (i.e., 1/100 LETOT's), and the pressure-velocity coupling algorithm was PISOC with a single iteration per time step.

The first stage of the transient is characterized by a rapid fall of k^+, which reaches values as low as 10^{-2} after about one LETOT. This can be interpreted as a consequence of the non-divergence-free initial conditions; as the velocity field is enforced to satisfy continuity by the pressure-velocity coupling algorithm (PISOC), most of the randomly assigned fluctuating components vanish. A low-turbulence phase follows, which may last up to several LETOT's as a boundary layer grows and vorticity is built up near the walls. The duration of this phase was found to increase with the number of control volumes in the computational grid (all the other conditions being the same).

For sufficiently low values of c_s, after some LETOT's the low-turbulence phase ends; k^+ increases rapidly, overshoots and then, if $c_s>0$ (i.e., if a subgrid dissipation mechanism is provided), stabilizes itself about a fairly uniform asymptotic value, with more or less broad fluctuations around this. For $c_s=0$ (no subgrid model), the low-turbulence phase is shorter; when this ends, k^+ overshoots to unrealistically high values, following which it does not exhibit a clear tendency towards an asymptotic stabilization, but rather continues (slowly) to increase. There is, however, no sudden 'burst' of the resolved fluctuations, which suggests that some <u>numerical</u> dissipation mechanism is at work.

On the other hand, for high values of c_s subgrid dissipation prevails on turbulence generation, and no transition occurs; the fluctuation energy is damped monotonically, and laminar flow is (incorrectly) predicted.

The instantaneous velocity components u, v, w and temperature T at a monitoring point located near a wall (y^+=20) are reported for the same transient at c_s=0.1 of Figure 4.2 in Figures 4.3(a) and (b). The <u>local</u> fluctuations <u>in time</u> follow more or less closely the behaviour of the <u>overall spatial</u> fluctuation intensity, summarized by the quantity k in Figure 4.2. After a relatively steady state is attained (say, after 10 LETOT's), the streamwise velocity u fluctuates with a time rms value, u'_{rms}, of about $3u_\tau$ around a time average of about $10u_\tau$. Both values are close to those obtained

by space-averaging u over planes parallel to the walls. Two main frequencies are identifiable, the first one (associated with the sharp peaks of u in Figure 4.3(a)) corresponding to a period of about $0.5\delta/u_\tau$ (1/2 LETOT), and the other to a period of about 5 LETOT's. The interval between consecutive sharp peaks encompasses several tens of time steps, which rules out numerical instabilities as the source of the fluctuations. The period of this more rapidly-varying fluctuation is comparable with the time required for the fluid to cross the channel from inlet to outlet, but also for a typical near-wall "streak" (see below) to travel its entire length over the monitoring point.

Similar remarks hold for the spanwise fluctuations, Figure 4.3(b), while the fluctuations of the cross-stream velocity v are much smaller in amplitude, due to the proximity of the wall, and apparently more broad-band in spectrum. Temperature fluctuations follow closely those of the main velocity, with maxima of T corresponding to minima of u and vice-versa.

In order to reduce the total duration of a simulation and to by-pass the (physically meaningless) low-turbulence stage, most simulations conducted in the course of the present study used as initial conditions the final (divergence-free) field produced by a preliminary c_s=0 simulation. Of course, only one such preliminary run was necessary for each computational grid tested. Each preliminary run was protracted long enough for the resolved turbulence energy k to go through the overshoot and to attain realistic, though not necessarily correct, values. This usually required 10 LETOT's (15 for the finest grids considered, e.g.~32^3 control volumes). The initial field thus obtained was adapted, if necessary, to Reynolds numbers different by that of the preliminary run by simply scaling up or down all velocities .

The restart technique was also used for runs in excess of the maximum CPU time compatible with overnight runs at CUC (12 hours). As mentioned in Chapter 3, in order to reduce the required disk storage only the velocity, pressure, and temperature fields were used to restart a run instead of the (more accurate) convection coefficients; nevertheless, no significant discontinuity in the computed quantities was ever observed across a restart, provided that no model parameter was changed.

4.3.2 Nonequilibrium effects

Figure 4.4 reports the time behaviour of the average resolved wall shear stress $\langle\tau_w\rangle$ (normalized by the equilibrium value τ_0) and of the average velocity U (in wall units) for c_s=0.08, a 32*16*16 grid, and Re^0=20,000. The simulation lasts 20 LETOT's starting from a few-LETOT preliminary run at c_s=0.

Following a numerical transient associated with the imposition of a non-zero value of c_s, which lasts about 10 LETOT's, the wall shear stress oscillates slightly around an asymptotic value which, however, is lower than that required to balance the imposed driving pressure gradient (dp/dx). As a consequence, the mean velocity in the channel, U, increases slowly as shown in the same figure.

A nice relation linking the long-term drift of the mean velocity U to the relative error in the wall shear stress $\langle\tau_x\rangle$ can be derived from simple dynamic considerations. From Newton's second law:

$$F = ma \tag{4.15}$$

In this case (see Figure 4.1):

$$F = (\langle\tau_x\rangle-\tau_0)\ 2LW \tag{4.16}$$
$$m = \rho LHW \tag{4.17}$$
$$a = dU/dt \tag{4.18}$$

so that eqn.(4.15) yields:

$$dU/dt = 2(\langle\tau_x\rangle-\tau_0)/(\rho H) \tag{4.19}$$

By expressing U in wall units as $U^+=U/u_\tau$ and t in LETOT's as $\Theta = tu_\tau/\delta = 2tu_\tau/H$, and taking Eqn.(4.9) into account, Eqn.(4.19) is transformed after some manipulations into:

$$dU^+/d\Theta = (\langle\tau_x\rangle-\tau_0)/|\tau_0| = \Delta\tau/|\tau_0| \tag{4.20}$$

i.e., the dimensionless acceleration of the fluid motion is equal to the relative error in the mean wall shear stress. For example, between 0 and 10 LETOT's $\langle\tau_x\rangle$, Figure 4.4, is underpredicted in absolute value by about 15%, i.e. $\tau/|\tau_0| = +0.15$; as a consequence, the average velocity U increases by about 0.15 wall units/LETOT (~1.5 wall units over LETOT's 0 to 10), as confirmed by Figure 4.4.

The above considerations also show that in large-eddy simulations of channel flow including only a few LETOT's (like the majority of those presented in the literature) even significant over- or under-predictions of the wall shear stress do not lead to a significant departure of the mean flow rate from that imposed in the initial conditions.

4.3.3 Averaging techniques; resolved and subgrid quantities

Figures 4.5 (a) to (d) compare instantaneous and time-averaged cross-stream profiles of the mean velocity, $\langle u \rangle$, and of the three rms fluctuations u_{rms}, v_{rms}, w_{rms} (defined as $u_{rms}=\langle (u-\langle u \rangle)^2 \rangle^{1/2}$ etc.). Results are expressed in wall units u_τ and time averages are taken over an interval of 10 LETOT's. The simulation is for $Re^0=20,000$, $c_s=0.08$ and a 32*16*16 grid. It is evident that instantaneous profiles exhibit strong irregularities and asymmetries, esp. in the fluctuating components. This is suggestive of large but short-lived structures occasionally determining high departures from mean values, particularly in near-wall regions. On the other hand, time averages are much more regular and symmetric, confirming that the averaging time is much larger than the lifespan of all significant flow structures (typically 1 LETOT).

Figure 4.6 reports cross-stream profiles of the various contributions to the principal stress (uv). Three contributions are shown:

- **resolved** Reynolds stress, $-\rho u''v'' = -\rho\langle (u-\langle u \rangle)(v-\langle v \rangle)\rangle$;
- **unresolved** (subgrid) stress, $-\rho\widehat{\tilde{u}\tilde{v}} = -\rho \nu_s \partial\langle u \rangle/\partial y$;
- **viscous** stress, $-\rho \nu \partial\langle u \rangle/\partial y$.

All quantities are normalized by the equilibrium wall shear stress, τ_0, and are time-averaged over 10 LETOT's. The simulation is for $Re^0=20,000$ and a 32*24*24 grid. Both the resolved and the subgrid stresses vanish on the walls, where ν_s and u'', v'' are equal to zero. The resolved stress peaks at $y/H \cong 0.12$ and 0.88, which is about 80 wall units from the walls; peaks of the subgrid stress are much lower (~1/2) and closer to the walls ($y^+\cong 20$). The unresolved stress is significant only in a narrow near-wall region. This tends to confirm that the grid resolution adopted here, though rather coarse, is sufficient to capture most of the turbulent stress in the resolved scale.

4.4 Detailed results for a reference case

The data with which the sciences start are concrete,
whereas the objectives they strive for are abstract
[Saadia Gaon, 'The book of beliefs and opinions'(ca.900 AD)]

4.4.1 Description of the test case and behaviour of k

Typical results are presented and discussed here for a reference 40-LETOT simulation at Re_δ=5000 (Re_D=20000), characterized by:

- Grid including 32*24*24 (x*y*z) volumes in the fluid, with selective refinement near the walls along the cross-stream direction y ($\xi=\Delta y_{min}/\Delta y_{max}$=0.2)
- Time step Δt=1/100 (LETOT) = $10^{-2}\ \delta/u_\tau$
- Crank-Nicolson time stepping scheme (option TPARM=0.5 in FLOW3D).
- Central differencing of advective terms
- Smagorinsky constant c_s=0.08
- subgrid Prandtl number σ_s=0.25
- Van Driest near-wall damping, eqn.(2.102.a), with A^+=25.

The locally-based wall boundary conditions presented as "model a" in Section 2.5 were used. Since, for the present Reynolds number and computational grid, the dimensionless distance of the first grid point from the wall, y_p^+, is ~4 (<11), these reduce themselves to ordinary no-slip boundary conditions, eqn.(2.108). Other computational details, periodic and initial conditions, and dimensions of the computational box, are as discussed in Section 4.2.

Selected results are presented in Figures 4.7 and following in dimensionless form, i.e., expressed in wall units according to Eqns.(4.10). Further results will be shown in the next sections, in discussing the results of the parametrical sensitivity analysis that was conducted.

Figure 4.7 reports the channel-averaged resolved turbulence, k, as a function of time. As in the example shown in Figure 4.3 (c_s=0.1), k decreases for some LETOT's to very low values ($k^+\cong$0.1); then it increases, exhibits a marked overshoot at about 22 LETOT's and eventually oscillates around the value k^+=2.5, in fair agreement with the experimental result of about 2 of Kreplin ed Eckelmann [1979]. The greater length of the low-turbulence phase with respect to the case in Figure 4.3, characterized by a coarser grid, should be observed.

4.4.2 Averages and fluctuations for the main fluid dynamic quantities

Figure 4.8(a) reports cross-stream profiles of the resolved streamwise velocity, u, averaged on planes parallel to the walls and over LETOT's 30 to 40, and expressed in wall units. k-ε predictions and experimental results of

Kreplin and Eckelmann [1979] ($Re_\delta \cong 3000$) and of Hussain e Reynolds [1975] ($Re_\delta \cong 10000$) are also reported for comparison purposes.

The centreline (maximum) velocity ($\overline{\langle u \rangle}^+_{max} \cong 20.5$) is overpredicted by 12% as compared with experimental data ($\langle u^+ \rangle_{max} \cong 18$). The profile of $\langle u \rangle$ exhibits a satisfactory symmetry and regularity.

Cross-stream profiles of resolved fluctuations $\overline{u_{rms}}$, $\overline{v_{rms}}$, $\overline{w_{rms}}$ are reported in Figures 4.8 (b) to (d). As above, quantities are time-averaged over LETOT's 30 to 40. Experimental results of Kreplin and Eckelmann and, for u_{rms} only, of Hussain and Reynolds, are reported for comparison purposes. LES predictions obtained by Moin and Kim [1982] using accurate spectral methods and a much higher resolution are also shown.

The comparison of numerical results with experimental data is, on the whole, satisfactory; the relative importance of the three fluctuating components upon overall turbulence levels is reproduced correctly, as are the peak and centreline values of each component. Predicted peaks of the cross-stream fluctuation, v_{rms}, are excessively low and far from walls, which may be due to the relatively poor resolution of the near-wall region.

The overview of predicted fluctuations is completed by the cross-stream profile of the resolved turbulence energy $\overline{\langle k \rangle}$, reported in Figure 4.8(e). Moin and Kim's results, experimental data and k-ε predictions are also shown. The present LES predictions compare favourably with the measurements of Kreplin and Eckelmann, better than k-ε predictions and actually better than Moin and Kim's results (which, however, are for a higher Reynolds number).

4.4.3 Temperature profiles and heat transfer

Cross-stream profiles of the resolved temperature $\overline{\langle T \rangle}^+$, made dimensionless according to eqn.(4.10.f) and averaged over planes parallel to the walls and over LETOT's 30 to 40, are shown in Figure 4.8(f). The three solid curves reported correspond to three values of the subgrid Prandtl number, σ_s (0.25, 0.5 and 1). As mentioned in Section 4.1, the literature is poor of experimental data for the present configuration (single-sided, fully developed heat transfer in plane channels). Therefore, the temperature profile computed by using the same code and the k-ε turbulence model was reported for comparison purposes (dashed line); for simple problems like the present one, k-ε predictions (based on 'wall functions' and on Jayatilleke's [1969] correlations) can be regarded as highly accurate.

It is evident from Figure 4.8(f) that the temperature profile is best predicted for the lowest value of σ_s (0.25); this, however, leads to undere-

stimating the temperature drop T^+ in the near-wall region. As discussed in Section 2.4, there is little agreement in the literature on the value of the subgrid Prandtl number σ_s; a value of 0.25, however, seems too low and difficult to justify on theoretical grounds. A cursory look at Figure 4.8(f) shows that the real problem is the overestimate of the temperature drop (i.e., underestimate of scalar transport) in the central (low-turbulence) region of the channel. As will be shown in the next Section, this is mainly an accuracy problem and can be overcome by refining the cross-stream grid, reducing the time step or replacing PISOC by the more accurate iterative algorithm SIMPLEC.

4.4.4 Instantaneous flow and temperature fields

An idea of the instantaneous simulated flow and temperature fields is given by Figures 4.9 to 4.11, which report shade plots of various quantites on selected 2-D slices of the computational domain at t=31 LETOT's (they were obtained by post-processing the computational results on a Macintosh personal computer). In these and the following graphs, the numerical values associated with the various grey patterns are also reported; they are all in wall units, as specified by Eqns.(4.10), except for the subgrid viscosity which is normalized by the laminar viscosity. Of course, all quantities are streamwise and spanwise periodic as imposed by the boundary conditions. The dimensions of the computational domain, L=8δ, W=4δ and H=2δ, correspond to L^+=2280, W^+=1140 and H^+=570 (wall units) on the basis of Eqn.(4.10.a).

Figure 4.9 shows instantaneous streamwise velocity, temperature, subgrid viscosity and pressure on a plane normal to the x-axis (main flow direction). The pseudo-chaotic character of the computed fields is evident. Low-velocity regions ("streaks") in the near-wall layer can be observed in Figure 4.9(a). They protrude up to $y^+ \cong 100$ into the bulk flow region and are spaced by about 200-250 wall units spanwise. Hot thermal plumes, closely corresponding to the low-speed regions, can be observed near the bottom wall in Figure 4.9(b). Regions of high subgrid viscosity, Figure 4.9(c), occur at $y^+ \cong 100$-150 and their spanwise location corresponds loosely to the low-speed streaks. The distribution of p, Figure 4.9(d), is characterized by high-pressure regions, protruding into the flow up to the midplane, and having no clear association with the velocity distribution.

Figure 4.10 refers to the plane J=2 ($y^+ \cong 4$) normal to the y-axis and close to the heated wall. The shade plot of u-velocity (a) confirms the presence of coherent structures, elongated in the streamwise direction x, having an average spanwise spacing of ~250 wall units. These structures

correspond to the "streaks" experimentally observed in turbulent near-wall flows [Kline et al. 1967] and reproduced in previous direct or large-eddy simulations [Moin and Kim 1982; Horiuti 1985; Azab and McLaughlin 1987], as discussed in Chapters 1 and 2. The spanwise streak separation observed experimentally is about 100-150 wall units; therefore, the present simulation overestimates this quantity about twice. As mentioned in Chapter 2, a comparable overestimate is reported by Horiuti [1982] using the Smagorinsky model for the unresolved scales; better predictions seem to be obtained using more sophisticated subgrid models, such as the one-equation, unresolved energy-model of Horiuti [1985.a,1985.b] or the two-component model of Moin and Kim [1982] (who, however, used also much finer grids than the present one, with up to 4 points in the viscous sublayer). The streamwise extent of the streaks observed in experiments (~1000 wall units) is fairly well reproduced. The prediction of near-wall streaks was found to be sensitive both to the computational grid and to the value of the Smagorinsky constant c_s, as will be discussed in the following Section.

The temperature distribution on the same plane $y^+ \simeq 4$ is reported in Figure 4.10(b). It presents similar elongated regions ('thermal streaks'), with higher temperatures corresponding to lower velocities and vice-versa. Figure 4.10(c) shows the distribution of the subgrid viscosity on the same plane; it mimics closely that of the velocity u, since higher values of u correspond to higher values of the strain-rate term S in Eqn.(3.73), and thus of the subgrid viscosity. The pressure shade plot in Figure 4.10(d) shows irregularly distributed low- and high-p spots, which are <u>not</u> elongated in the streamwise direction. This is in agreement with previous direct and large-eddy simulation results, see for example Moin and Kim [1982].

Finally, Figures 4.11(a) to (c) report instantaneous shade plots of u, T and ν_s on a plane normal to the spanwise direction z. In Figure 4.11(b), high-temperature plumes are evident, which interest mainly the boundary layer adjacent to the hot wall but occasionally protrude well into the bulk flow region and form an angle of about 45° with the wall.

The **time-evolution** of instantaneous velocity and temperature fields is documented in Figures 4.12 to 4.15.

Figure 4.12(a-c) shows shade plots of the streamwise velocity u on the plane J=2 ($y^+ \simeq 4$) parallel to one of the walls, respectively for t=31.1, 31.2 and 31.3 LETOT's. The motion of the streaks is evident; they move at a speed of about $5u_\tau$, corresponding to the mean streamwise velocity at the given distance from the wall. Similar plots are reported in Figure 4.13 for the temperature distribution on the same plane.

Figure 4.14 shows the evolution of the local instantaneous temperature T on a generic plane z=constant at consecutive instants t=31.1, 31.2 and 31.3 LETOT's, while Figure 4.15 refers to the instantaneous, but spanwise-averaged, temperature. The comparison of Figures 4.14 and 4.15 shows that, while the local temperature field exhibits broad spatial and temporal fluctuations, the corresponding span-averaged field is much more regular in space and varies little with time. The interest of such comparisons stems from the fact that experimental instantaneous temperature fields obtained by real-time interferometric techniques, such as those reported by Lockett [1987], see Figure 4.16, are inevitably averaged over the direction of the beam, which leads to a loss of information comparable with that observed here.

4.5 Influence of Reynolds number, model, grid and computational options

The first man knew him not perfectly,
no more shall the last find out
[The Ecclesiastes, on Wisdom]

In this section, the sensitivity of the results to the following parameters is investigated:

1 - Reynolds number;
2 - constant c_s of the Smagorinsky subgrid model;
3 - near-wall damping function, eqns.(2.102.a) to (2.102.c);
4 - computational grid;
5 - time step Δt, and
6 - time stepping scheme;
7 - pressure-velocity coupling algorithm;
8 - discretization scheme used for the advection terms.

Each of the above parameters was made vary individually around the values listed for the reference case examined in Section 4.4. However, in order to reduce the computing time required, coarser grids (having 32*16*16 or 32*24*16 volumes) were used as the reference ones in some cases. All simulations started from preliminary 'startup' runs using c_s=0.08 or c_s=0 and lasting a few LETOT's, as discussed in Section 4.3.1.

The 'Mason and Callen' wall boundary conditions ('local' formulation of Section 2.5.1) were used here; since the first grid point P lies within the

viscous-conductive sublayer ($y^+ < \sim 11$), they reduce themselves to ordinary no-slip conditions. More general wall boundary conditions will be compared in the following Section 4.6 both for low and high Reynolds numbers.

4.5.1 Reynolds number - dependence

Reynolds-number dependence was studied here only in the limited range Re^0=10,000 to 40,000. At higher Reynolds numbers, the reference grid resolution is not sufficient to have at least one point in the viscous sublayer, and wall boundary conditions switch to 'synthetic' ones. The associated changes in the solution cannot be regarded as 'Reynolds number - dependence', but rather involve the specific boundary formulation used (see Section 2.6). On the other hand, at lower Reynolds numbers the flow is not fully turbulent, and the use of the Smagorinsky model would not be appropriate.

Within the range examined, results are summarized in Figures 4.17(a) and (b). Cross-stream profiles of the mean velocity $\overline{\langle u \rangle}$ and of the mean temperature $\overline{\langle T \rangle}$ (expressed, as usual, in wall units, and time-averaged over 10 LETOT's) are reported for Re^0=10,000, 20,000 and 40,000 and for a 32*24*16 computational grid.

Results, once expressed in wall units, are little dependent on the Reynolds number. Predicted values of $\overline{U}^+$ (cross-section averaged velocity) and $\overline{\langle T \rangle}^+_{max}$ (wall-to-wall temperature drop) vary approximately as $Re^{0.12}$ and $Re^{0.06}$, respectively. As discussed in Section 4.1, the corresponding dependences suggested by experimental data are $Re^{0.15}$ and $Re^{0.05}$, respectively. Thus, the Reynolds number - dependence of these fundamental quantities is correctly predicted. However, it must be observed that the profile of $\overline{\langle u \rangle}$, Figure 4.17(a), tends to become unrealistically peaked (laminar-like) at low Reynolds number. Levels of the resolved fluctuations (not shown) were found to vary very little with Re.

4.5.2 Influence of the Smagorinsky constant

The issue of the optimum value of c_s in large-eddy simulations based on the Smagorinsky, and similar, models was discussed in Section 2.4.5. For the present simulations, the influence of c_s on the initial development of the solution, starting from pseudo-random and not divergence-free conditions, has been already discussed in Section 4.3.1 (and Figure 4.2). The results of a further parametrical study are discussed here; it regards 20-LETOT simulations

run with a 32*16*16 grid for c_s = 0 to 0.2. The results of a preliminary 20-LETOT simulation at c_s=0.08 were used in all cases as initial conditions. Results are presented in Figures 4.18(a) to (k).

The behaviour of k^+, Figure 4.18(a), is less influenced by the value of c_s than one may expect. For c_s=0 (no subgrid viscosity), k^+ does not diverge as t increases, but stabilizes itself around a value of about 4 (which is unrealistically high), although it exhibits a slightly increasing trend with small oscillations in time. A similar behaviour is obtained for c_s=0.04, with a smaller asymptotic value (about 3.3). On the other hand, for c_s=0.16 and 0.20, turbulence is rapidly damped and all fluctuations die away within ~20 LETOT's. A more complex behaviour is obtained for intermediate values of c_s (0.08, 0.12): the resolved turbulence energy oscillates broadly between 2 and 4 (case c_s=0.08) or 1.5 and 3.5 (case c_s=0.12).

Comparable results are obtained for the average wall shear stress $\langle\tau\rangle$, Figure 4.18(b). For small c_s, $\langle\tau\rangle$ exhibits rapid and small-amplitude oscillations; for high c_s, it does not fluctuate in time and, after an initial overshot, settles down to asymptotic values (markedly overpredicted only for c_s=0.20). Broader fluctuations are obtained for intermediate values of c_s. The behaviour of the average velocity U, Figure 4.18(c), is consistent with that of the shear stress. A marked decrease of U, due to the overprediction of $\langle\tau\rangle$, is obtained only for c_s=0.2.

Cross-stream profiles of mean quantities reveal more significant differences associated with different values of c_s. The subgrid viscosity, Figure 4.18(d), increases markedly with increasing c_s, though its rate of rise is less than quadratical (as would be suggested by Eqns.(3.73)-(3.74)) due to the associated fall in the resolved rate of strain, $\hat{S}$. Velocity profiles, Figure 4.18(e), are clearly wrong and laminar-like only for c_s=0.16 and 0.20, while they vary little between c_s=0 and 0.08. Temperature profiles, Figure 4.18(f), show that <u>resolved</u> turbulent transport of heat is practically absent in the bulk flow (central region of the duct) for c_s greater or equal to 0.12; on the other hand, for such high values of c_s the subgrid heat diffusivity α_s (proportional to ν_s through the subgrid Prandtl number σ_s) is so high that the overall temperature drop across the channel does not vary much as c_s varies.

Significant differences are shown by cross-stream profiles of velocity fluctuations, Figures 4.18(g) to (i). While values of c_s of 0.16 and 0.20 lead to an almost complete suppression of all three components, the effect of varying c_s between 0 and 0.12 is relatively little on the streamwise fluctuation ($\overline{u_{rms}}$), intermediate on the cross-stream fluctuation ($\overline{v_{rms}}$) and largest on the spanwise fluctuation ($\overline{w_{rms}}$). The last, in particular, attains realistic

values (as compared with experimental results, see for example Figure 4.8(d)) only in a narrow range of c_s-values around 0.08.

Finally, Figures 4.18(j) and (k) show the time-behaviour of the streamwise and spanwise velocity, respectively, at a monitoring point located near a wall (y^+=6, i.e. within the viscous sublayer) for different values of the Smagorinsky constant. For c_s=0 and 0.04, a broad-band fluctuating behaviour ("white noise") is obtained, and the amplitude of spanwise fluctuations is comparable with that of streamwise ones. On the other hand, for large values of c_s (0.16 and 0.20) fluctuations are completely suppressed. A more complex behaviour is obtained for intermediate values, especially for c_s=0.08; fluctuations of u, Figure 4.18(j), exhibit some intermittency characteristics and - as previously discussed in Section 4.3, Figure 4.3 - seem to contain two main frequencies, one of the order of $(0.5\ \mathrm{LETOT})^{-1}$ and a smaller one of the order of $(5\ \mathrm{LETOT})^{-1}$. Spanwise fluctuations, Figure 4.18(k), are much smaller and more broadly distributed in frequency.

Also the influence of c_s on the spatial structure of the flow field was found to be relevant. In Figures 4.19(a) to (d) shade plots of the streamwise (resolved) velocity u on the plane $y^+ \approx 20$ parallel to a wall are compared for four values of c_s (0, 0.04, 0.08, and 0.12). The 'streak' structure discussed in Section 4.4 is correctly obtained only for c_s=0.08; lower values of c_s yield an irregular structure with no dominant direction, while larger values yield a series of parallel stripes of alternating low and high u, covering the whole length of the channel. Apparently, for excessively low values of the Smagorinsky constant the resulting subgrid viscosity is not sufficient to establish the necessary correlation between fluctuating quantities, which results in a pseudo-random structure of the flow field. On the other hand, for large values of c_s the damping of the fluctuations approaches the critical value (close to 0.12 in the present case) which would completely suppress turbulence, resulting in strong time oscillations of the turbulence energy and in an excessive space correlation between fluctuating quantities.

The results of the above parametrical study on the influence of c_s can be summarized as follows:

- too large values of c_s (higher than ~0.12 for the present grid and numerical methods) lead to a complete suppression of turbulence;
- for c_s varying between 0 and 0.12, average quantities (such as k, U, $\langle T \rangle$) and cross-stream profiles of plane-averaged quantities (such as $\langle u \rangle$ and $\langle T \rangle$) are relatively little affected. A likely reason for this is that the discretization of the governing equations, despite the central differencing scheme

being used for the advection terms, introduces a certain amount of numerical diffusivity associated with the truncation errors, which adds itself to the 'physical' (laminar + subgrid) diffusivity and masks the effects of the subgrid model;

- at least three aspects of the simulated fields, however, are indeed sensitive to the value of c_s and thus should be considered for an optimum choice of this parameter:

1. the level of secondary (esp. spanwise) fluctuations;
2. the time structure of the fluctuations ("white noise" for $c_s<0.08$ versus intermittent behaviour with definite frequency contents for $c_s=0.08$);
3. the spatial structure of the near-wall flow field (irregular velocity distribution for low c_s, "streaks" for intermediate c_s and unrealistic longitudinal bands for high c_s.

4.5.3 Influence of the near-wall damping function

The influence of the near-wall damping model was studied by performing three 20-LETOT simulations (again on a 32*16*16 grid) using three different models for the function $D(y^+)$ which appears in Eqn.(3.74):

a) VanDriest function, eqn.(2.102.a), with $A^+= 25$;
b) Modified VanDriest function, eqn.(2.102.b), with $A^+= 25$;
c) Modified function proposed by Miner et al.[1989], eqns.(2.102.c) and (2.48), with $f_0=0.04$, $y_0^+=8$ and $A^+=25$.

The profiles $D(y^+)$ corresponding to the three above models were compared in Figure 2.4. For the present case, the damping factor at the grid point nearest to the wall ($y^+\cong 6$) is about 0.2 for models (a) and (c), while model (b) gives $D=0.05$.

Results are compared in Figures 4.20(a) to (c). The time behaviour of k^+, Figure 4.20(a), shows that functions (a) and (c) give similar results, thus confirming that what really matters is the value of D at the grid points nearest to the walls. When model (b) is used, turbulence levels decrease and the attainment of (statistically) stationary conditions is delayed. The mean velocity, Figure 4.20(b), is least overpredicted by employing model (c), while using model (b) the overestimate of $\langle u\rangle^+$ worsens with respect to model (a). Finally, longitudinal velocity fluctuations, Figure 4.20(c), are little affected by the near-wall damping function chosen.

In conclusion, results do not depart much from those obtained using the simple Van Driest function (2.102.a); the use of smaller damping factors near the walls (model b) delays the attainment of pseudo-stationary conditions and affects negatively the prediction of the average velocity profile. The peculiar profile of D predicted by model (c) in the laminar sublayer is obviously uninfluent as long as the latter is not finely resolved by the computational grid.

4.5.4 Influence of the computational grid

Once the dimensions of the computational box are chosen (they are $6\delta*2\delta*4\delta$ along x, y, z respectively in the present case), the finite-volume computational grid is characterized only by the number of control volumes in the fluid along the three directions (N_x, N_y, N_z) and/or by the degree of stretching of the control volumes near the walls along y ($\xi = \Delta y_{min}/\Delta y_{max}$). The grid is always uniform along x and z, coherently with the assumption of periodicity along these directions.

Here, the influence of the grid resolution was studied by varying individually N_x, N_y and N_z around the reference values of 32, 24 and 24, respectively, and running 20-LETOT simulations for c_s=0.08 and Re^0=20,000. In all cases, the initial conditions were obtained from preliminary 10-LETOT simulations at c_s=0, after rescaling mean velocities to U^+=17.5 and fluctuations to k^+=2.7. Of course, one such preliminary run was necessary for each grid studied.

The influence of the computational grid on the time behaviour of the volume-averaged resolved turbulence energy, k, is shown in Figure 4.21 for a) varying N_x (24-32-48); b) varying N_y (16-24-48) and c) varying N_z (16-24-32). On the whole, grid effects are small. An insufficient number of spanwise grid points, Figure 4.21(c), leads to a more irregular behaviour of k and delayes the attainment of (statistically) steady-state conditions. The overshoot of k is more pronounced for the finest streamwise grid, Figure 4.21(b). With a very fine cross-stream resolution (N_y=48) k does <u>not</u> decrease following the imposition of a non-zero value of c_s (as in all other cases), but rather peaks sharply to k^+=3.6; however, after about 5 LETOT's the corresponding line approaches the other ones and presents the same asymptotic behaviour.

The time behaviour of the wall-averaged shear stress, $\langle\tau\rangle$, obtained for different grids is reported in the same format in Figures 4.22(a) to (c). The influence of the computational grid on this quantity is indeed very small, at least in the range examined; with all combinations of grid points, $\langle\tau\rangle^+$ is

practically stabilized after about 10 LETOT's to values of 0.85-0.95, i.e. only slightly underpredicted with respect to Eqn.(4.12) for the current initial Reynolds number.

The time behaviour of the cross-section averaged velocity, U, is reported in Figures 4.23(a) to (c). Differences are larger here than for the wall shear stress, since the flow rate has a "memory" of the initial discrepancy in the value of $\langle\tau\rangle$ (LETOT's 0 to 10 in Figure 4.22). U increases in all cases, coherently with the generalized underprediction of $\langle\tau\rangle$ (see remarks on nonequilibrium effects in Section 4.3.2). The least effects are associated with varying the streamwise resolution, the largest with varying the cross-stream one.

The grid influence on cross-stream profiles of plane-averaged resolved quantities will now be examined. As usual, these profiles were also time-averaged over the last 10 LETOT's.

Figures 4.24(a) to (c) compare profiles of the subgrid viscosity $\overline{\nu}_s$, normalized by the laminar viscosity ν. Increasing the grid resolution along any direction reduces the values computed for $\overline{\nu}_s$, as expected from the Smagorinsky expressions (3.73)-(3.74) which involve directly the mean mesh size, $\overline{\Delta}$. Note also that excessively low resolutions (e.g. N_x=24 and esp. N_z=16) lead to irregular and non-symmetric profiles of $\overline{\nu}_s$.

Profiles of the mean velocity, $\overline{\langle u\rangle}$, are reported in Figures 4.25(a) to (c). They are little sensitive to the number of streamwise grid points, see graph (a); as regards the cross-stream resolution, graph (b), unrealistical centrally-peaked profiles are obtained only with the coarsest grid (N_y=16). Finally, increasing the spanwise resolution, graph(c), leads to a progressive reduction of the mean velocity towards profiles closer to the experimental results.

Profiles of the streamwise fluctuation, $\overline{u_{rms}}$, are compared in graphs (a)-(c) of Figure 4.26. As a rule, increasing the grid resolution along any direction leads to higher values of $\overline{u_{rms}}$ (especially in the near-wall peak regions), as a larger and larger fraction of the overall fluctuations is "captured" within the resolved scale (an exception is given by an excessively coarse spanwise grid, dotted line in graph(c), which leads to peaks of $\overline{u_{rms}}$ higher and farther from the walls). Similar results (increasing fluctuation levels for increasing grid resolution) are obtained for the main resolved Reynolds stress $\overline{\langle u"v"\rangle}$, Figures 4.27(a)-(c).

Finally, the influence of the grid on cross-stream profiles of the mean temperature $\overline{\langle T\rangle}$ is shown in Figures 4.28(a) to (c). The effects of N_x, N_y and

N_z are not monotonic; increasing the streamwise resolution, graph(a), leads to larger values of $\langle\overline{T}\rangle^+$, while opposite results are obtained by increasing N_y (b). The influence of the spanwise resolution (c) is negligible, at least for $N_z>24$.

The above study shows that the resolution adopted for the "reference" case of Section 4.4 (32*24*24 control volumes) is not sufficient to obtain completely grid-independent results: the solution is clearly still sensitive to a further increase of the number of control volumes, esp. along the cross-stream direction y. Refining the grid yields a general rise of resolved fluctuation intensities in the channel and a reduction of the mean velocity profile.

However, the residual grid dependence is surprisingly low; actually, realistic results are obtained even by very coarse grids having just 16 or 24 control volumes along each direction. Of course, further parametrical studies, in which computations were repeated for different Reynolds numbers and different amounts of grid stretching, would be required in order to clarify this issue fully.

4.5.5 Influence of the time step

The influence of the time step was studied by repeating 20-LETOT simulations for four different values of Δt:

a) Δt = 1/25 (LETOT)
b) Δt = 1/50 "
c) Δt = 1/100 "
d) Δt = 1/200 "

A 32*16*16 grid was used in all cases, the value of c_s was 0.08, and initial conditions were those generated by a preliminary 20-LETOT run with Δt=1/100th of a LETOT (reference value). Results are summarized in Figures 4.29(a) to (f).

The behaviour of the resolved turbulence energy, Figure 4.29(a), is similar for Δt=1/100 and 1/50, while k flattens down to an almost constant value for Δt=1/25. For Δt=1/200, a more regular behaviour is observed, though levels of k are much as for Δt=1/100, 1/50. The wall shear stress, Figure 4.29(b), is similar for Δt=1/200 to 1/50 while it is underpredicted for Δt=1/25. As a consequence, the average velocity U, Figure 4.29(c), increases

uniformly for this highest value of Δt, while very similar behaviours are predicted for the other time steps.

Cross-stream distributions of the mean velocity are reported in Figure 4.29(d). Profiles of $\overline{\langle u \rangle}$ are too high and laminar-like for $\Delta t=1/25$, acceptable for all other values of Δt, and decrease monotonically with the time step. Fluctuation profiles are deeply affected by Δt; the cross-stream component $\overline{v_{rms}}$, in particular (Figure 4.29(e)), is practically zero for the largest value of Δt, and there are still significant differences between predictions for $\Delta t=1/100$ and 1/200. As a consequence, profiles of the mean temperature (whose cross-stream transport depends strictly upon v") are sensitive to Δt and are grossly overpredicted for excessively high time steps, see Figure 4.29(f).

In conclusion, though predictions are already qualitatively correct for $\Delta t=1/50$, a significant residual time step-dependence is still observed for $\Delta t=1/100$, which corresponds to a maximum Courant number of ~1.

4.5.6 Influence of the time stepping scheme

The reference time stepping scheme used in all the above simulations (Crank-Nicolson) was compared here with the Euler Implicit, or Fully Implicit Backward, scheme (in Harwell-FLOW3D, the two schemes correspond to TPARM=0.5 and TPARM=1.0, respectively). As above, simulations were run for $c_s=0.08$ on a 32*16*16 grid, starting from the results of the same 20-LETOT simulation run for TPARM=0.5. The time step was 1/100th of a LETOT.

Results are summarized in Figures 4.30(a) to (c). It is evident that the use of the fully implicit scheme leads to a uniform fall (with no time oscillations) of the average resolved turbulence energy, Figure 4.30(a); consistently with this, the mean velocity $\overline{\langle u \rangle}$, Figure 4.30(b), and the mean temperature $\overline{\langle T \rangle}$, Figure 4.30(c), are grossly overpredicted (and, of course, tend to increase in time as k continues to fall). Similar results were obtained also for a time step twice smaller (1/200th of a LETOT).

It can be concluded that the implicit scheme damps excessively the turbulent fluctuations and thus must be avoided in large-eddy simulations.

4.5.7 Influence of the pressure-velocity coupling algorithm

All the simulations described above made use of the PISO pressure velocity coupling algorithm [Issa 1986], in the PISOC form based on the same improvements that were proposed for SIMPLE by VanDoormal and Raithby [1984].

The algorithm was used in the non-iterative form originally proposed by Issa, i.e. with a single cycle (including two pressure correction stages) per time step. Coherently, underrelaxation of velocities and temperature was not used (the absence of pressure underrelaxation is an inherent feature of PISOC). Note that the absence of multiple iterations rules out the use of nonorthogonal grids and of higher order differencing schemes, since these are dealt with by the "deferred correction" method described in Section 3.2.1.

As remarked by Issa, the use of PISO requires a high degree of accuracy in the solution of the linearized transport and pressure-correction equations at each cycle; here, the imposed residual reduction factor and maximum number of "inner" iterations were 0.01 and 100, respectively, for the transport equations (algorithm ST3D) and 0.005 and 250, respectively, for the pressure-correction equation (algorithm ICCG).

A comparison was conducted with the more widespread SIMPLE algorithm [Patankar and Spalding 1972], used in the SIMPLEC form [VanDoormal and Raithby 1984]. Being an inherently iterative technique, it was used with 10 iterations per time step, setting the underrelaxation factors for velocities and temperature to 0.7 and imposing residual reduction factors/maximum number of iterations of 0.1/10 (transport equations) and 0.05/25 (pressure-correction equation).

The test case considered was a 15-LETOT run characterized by Re^0=20,000, c_s=0.08 and 32*16*16 control volumes in the grid; initial conditions were generated by a preliminary PISOC simulation and no re-scaling of mean and turbulence quantities was used.

Results are shown in Figures 4.31(a) to (d). They include SIMPLEC predictions obtained with FLOW3D, Release 2.3 (a code release more advanced than Rel.2.1), as part of a code validation test. For reasons that were not clarified, the use of PISO or PISOC with a single cycle per time step led to divergence of the solution after a few time steps with this release of the code.

Figure 4.31(a) reports the evolution of the resolved turbulent kinetic energy, k. SIMPLEC and PISOC results do not exhibit relevant differences, save perhaps that the former, and more accurate, algorithm allows to attain statistically steady-state conditions slightly earlier than the latter. SIMPLEC results from Releases 2.1 and 2.3 are practically coincident for the first 4-5 LETOT's and then depart slightly from each other due to minor differences in the numerical methods used (e.g., in the preconditioning algorithm for the conjugate-gradient solver of the pressure correction equation). Predicted trends of the average velocity U and of the average wall shear stress $\langle\tau\rangle$ were

very similar for the two algorithms and code releases, and are not reported here.

Figure 4.3(b) shows cross-stream profiles of the mean velocity $\overline{\langle u \rangle}$, expressed as usual in wall units and time-averaged over the last 5 LETOT's. Again, differences between the two algorithms are little, though SIMPLEC yields a slightly flatter distribution. Similar remarks hold for the streamwise and spanwise fluctuations (not shown).

More significant differences are observed in the cross-stream fluctuation, Figure 4.31(c): SIMPLEC yields higher values of $\overline{v_{rms}}$ and a more regular profile of this quantity. Even larger differences, clearly associated with the above behaviour of $\overline{v_{rms}}$, are observed in the cross-stream profile of the mean temperature $\overline{\langle T \rangle}$, Figure 4.31(d) (based on the value 0.5 for the subgrid Prandtl number σ_s). SIMPLEC yields for $\overline{\langle T \rangle}^+_{max}$ (overall dimensionless temperature drop across the duct) values about 25% lower than PISOC; moreover, the cross-stream distribution of $\overline{\langle T \rangle}^+$ does <u>not</u> exhibit the (unphysical) large gradient in the bulk flow region observed in PISOC predictions, and thus approximates much better the (reference) k-ε profile reported, for example, in Figure 4.8(f) and allows the use of more realistic values for σ_s.

The above comparison shows that the loss of accuracy implied by the use of PISOC as a non-iterative algorithm has little consequences on <u>flow</u> quantities (average turbulence energy, average velocity), but more relevant implications for <u>scalar</u> quantities such as temperature (mainly due to the underprediction of cross-stream velocity fluctuations and thus of cross-stream turbulent scalar transport). On the other hand, the use of SIMPLEC (at least with the present number of outer iterations per time step, i.e. 10) implies CPU times about 2.5 times higher and was therefore limited, in the present study, to the cases in which it was strictly necessary (see below).

4.5.8 Influence of the spatial discretization scheme used for the advection terms

All the simulations described above were conducted by using the central differencing scheme (CDS) for the advection terms appearing in the Navier-Stokes and scalar transport equations. As discussed previously, there are signs that the overall solution procedure is still introducing numerical dissipation adding itself to the "physical" subgrid dissipation. Therefore, comparisons were made with the higher order QUICK scheme [Leonard 1979] and with its bounded version CCCT [Gaskell and Lau 1987; Alderton and Wilkes 1988]. They are both 3-point upwind schemes, formally granting third-order

accuracy and thus potentially more accurate than the (second-order) CDS scheme. Of course, testing schemes of the same, or lower, order than CDS would be useless as they cannot be more accurate and less dissipative.

A comparison is presented here for three 15-LETOT runs, respectively using CDS, QUICK and CCT. The grid had 32*16*16 control volumes, and initial conditions were generated by a preliminary 20-LETOT simulation using CDS. The Smagorinsky constant was 0.08. The SIMPLEC pressure-velocity coupling algorithm (with 10 iterations per time step) was used here; as mentioned in precedence, the use of higher-order differencing schemes, implying deferred correction of some advective contributions, would not be compatible with non-iterative algorithms such as PISO(C).

Results are summarized in Figures 4.32(a) to (f). Figure 4.32(a) shows the development of the average resolved turbulence energy k, both for the "startup", 20-LETOT, CDS run and for the following 15-LETOT CDS, QUICK and CCCT runs. The use of QUICK and CCCT yields higher levels of resolved turbulence, and a more irregular and intermittent behaviour of k. The evolution of the average velocity U and of the average wall shear stress $\langle\tau\rangle$ was very similar in the three cases and was not reported here. Cross-stream profiles of the mean velocity, $\overline{\langle u\rangle}$, are shown in Figure 4.32(b); these and the following cross-stream profiles were time-averaged over the last 5 LETOT's. CDS and QUICK profiles are very similar to each other, though the latter appears more irregular and less symmetric. CCCT yields larger values of $\overline{\langle u\rangle}$ and a markedly asymmetric profile. The mean temperature is reported in Figure 4.32(c); CCCT yields a large overprediction of $\overline{\langle T\rangle}^{+}$ while QUICK and CDS predictions are, again, similar.

Predictions relative to the resolved fluctuations are reported in Figures 4.32(d) to (f). Cross-stream profiles of $\overline{u_{rms}}$ are, on the whole, very similar, with slightly higher levels predicted by QUICK and CCCT. On the contrary, profiles of $\overline{v_{rms}}$ and $\overline{w_{rms}}$ predicted by using QUICK and CCCT are markedly different from the corresponding CDS results: they do not exhibit the characteristic central minimum presented by experimental data (see for example Figures 4.8(b) to (d)) and CDS predictions, are significantly lower, and are markedly irregular and asymmetric (especially for CCCT).

Figure 4.33 reports the behaviour of the volume-averaged resolved turbulence energy k obtained for two different values of c_s (0.08 and 0.16) using both CDS and QUICK. With either differencing scheme, the higher of the two c_s values does <u>not</u> allow sustained turbulence; the rate of damping of k is very similar for the two schemes, showing that QUICK is <u>not</u> significantly less dissipative than CDS.

The above results can be summarized as follows. The use of QUICK leads to slightly higher turbulence levels, while affecting little global flow rates, profiles of mean quantities such as <u> and <T>, and streamwise fluctuations. However, it leads to wrong profiles of cross-stream and spanwise velocity fluctuations, lacking the characteristic central depression observed in the experiments and correctly reproduced by using CDS. These features suggest that a significant fraction of the "resolved" fluctuations predicted by using QUICK is due to numerical effects ("wiggles"), often reported in association with this, and similar, high-order schemes. Substituting CCCT for QUICK leads to an excessive damping of cross-stream fluctuations, which in turns produces a gross overprediction of the temperature drop across the channel, while streamwise fluctuations are enhanced. Both QUICK and CCCT yield large time - fluctuations of the resolved turbulence energy and of instantaneous resolved fields, which do not average out over 5 LETOT's (yielding, in turn, irregular and asymmetric profiles of <u> and other mean quantities). In conclusion, neither of these higher-order schemes seems preferable to central differencing in large-eddy simulations.

4.6 Influence of wall boundary conditions

Truth is never pure, and rarely simple
[Oscar Wilde, 'The importance of being earnest']

The sensitivity of LES results to the alternative formulations (a)-(e) of wall boundary conditions described in Section 2.5 was studied both for Re^0=20,000 and for Re^0=100,000 using the same 32*24*24-volume computational grid as for the "reference" case of Section 4.4. In all cases, the PISOC algorithm, and the CDS scheme for the advection terms, were used. For model (e) ("ejection") the "adjustable" constants c and ϕ were set to 1 and 10°, respectively. Initial conditions were generated by running preliminary 20-LETOT simulations with wall boundary conditions of type (a) ("Mason and Callen") and rescaling velocities to the prescribed value of Re^0.

For the lower Reynolds number, the first near-wall grid points lie fully within the viscous sublayer, i.e. in the linear region of "universal" velocity (and temperature) profiles, and all the above formulations can be regarded as variants of no-slip boundary conditions. For the higher value of Re^0, the dimensionless distance of near-wall grid points from the wall is about 25, so that they lie in the turbulent (logarithmic) region of "universal" near-wall

profiles, and all the formulations tested here can be regarded as "synthetic" wall boundary conditions. Results are presented and discussed below.

4.6.1 Comparison of results for low Reynolds number (Re_o^0=5,000)

In this case, the dimensionless distances y^+ of the first near-wall points from the wall were about 4, 12 and 22 for J=2, 3 and 4 (and symmetric), respectively. The constant c_s was set to 0.08. Results are summarized in Figures 4.34 and 4.35.

Figure 4.34(a) reports the time behaviour of the average resolved turbulence energy, k. In all cases, this is similar to that observed in several previous examples: k falls slightly during the first few LETOT's (following the stepwise re-scaling of the velocity field), then rises and stabilizes itself around values between 2 and 3 after about 5 LETOT's. The results from the first four models are almost coincident during the first few LETOT's, then depart slightly from one another. Only the results from model (e) ("ejection") are markedly different since the beginning of the transient. The amplitude of the time-fluctuations of k is lowest for wall boundary conditions (a) ("Mason and Callen") and highest for wall boundary conditions (e) ("ejection").

Figure 4.34(b) reports the time behaviour of the mean wall shear stress, $\langle\tau\rangle$. In all cases, it remains slightly lower than the equilibrium value predicted on the basis of correlation (4.12). There are no large differences between the values predicted by using different wall boundary conditions. Again, only results from model (e) are appreciably different from the other ones: $\langle\tau\rangle$ is higher and exhibits oscillations having a small amplitude and a period of a few time steps. The behaviour of the cross-section averaged velocity U, shown in Figure 4.34(c), is consistent with that of the wall shear stress; all models predict a slight increase of U, with only marginal differences between the various results.

Cross-stream profiles of mean and fluctuating quantities (time-averaged over the last 10 LETOT's) are compared in Figures 4.34(d) to (f). All models give practically the same profile of mean velocity <u>. Slight differences can be observed between predictions of the mean temperature <T>; the largest values are predicted by boundary conditions (d) ("shifted") and the smallest by boundary conditions (e) ("ejection"). Profiles of the streamwise fluctuation u_{rms} show more pronounced differences; in particular, peak values are markedly higher for model (e) ("ejection"). Only minor differences are obtained in the cross-stream and spanwise fluctuations (not shown).

The distributions of the instantaneous velocity u on the near-wall plane

$y^+ \cong 4$, predicted using different wall boundary conditions, are compared in the form of shade plots in Figures 4.35(a) to (e). The "local" formulation (a) ("Mason and Callen") gives a "streak" pattern similar to that reported, for example, in Figure 4.10(a). Models (b) to (d) give similar patterns, but tend to produce broad and unphysical spanwise irregularities in the distribution of u. The "ejection" model (e) yields a regular streak pattern, superficially resembling that given by model (a) but actually characterized by much larger variations of the streamwise velocity (u varies between ~0 and ~16 wall units here, but only between ~2 and ~8 in case (a)).

In conclusion, the influence of wall boundary conditions is small, much as observed by Piomelli et al. [1989]. The only significant differences are obtained by using the "ejection" model (e), which (all other things being the same) gives higher values of the resolved fluctuations and a larger variation of the streamwise velocity over near-wall planes.

4.6.2 Comparison of results for high Reynolds number (Re_δ^0=25,000)

Here, the same grid and numerical methods were used as in the previous low-Reynolds number case. However, the Smagorinsky constant c_s was set to .1 since the choice c_s=.08 gave excessively high levels of the resolved fluctuations. The distances of the first near-wall points from the walls were about 16, 50 and 90 for J=2, 3 and 4 (and symmetric), respectively.

Results relative to the various formulations (a)-(e) of wall boundary conditions are summarized in Figures 4.36(a) to (f). Since the near-wall planes are well out of the viscous sublayer, the distribution of the streamwise velocity u does not exhibit the clear streak pattern observed in the low-Reynolds number case, and was not reported.

Many of the comments made on the low-Reynolds number results apply also to this high-Reynolds number case. Only a few remarks will be added here:

- On the whole, (statistical) equilibrium conditions are attained more rapidly than in the low-Reynolds number case (Figures 4.36(a)-(c)).
- As in the above case, the wall shear stress, Figure 4.36(b), is slightly underestimated by all models with respect to Eqn.(4.12)); as a consequence, the average velocity, Figure 4.36(c), is slightly overestimated.
- All models give again very similar cross-stream profiles of mean velocity and temperature, Figures 4.36(d) and (e).
- Model (e) ("ejection") yields higher values, and broader time - fluctuations, of k and $\langle T \rangle$; it also gives excessively high values of u_{rms}, with an unphysical inversion between the first two grid points.

In conclusion, both at low and high Reynolds number no strong reasons were found in favour of any of the boundary condition formulations tested; in particular, there was no clear advantage in using "global" formulations (b) to (e), applicable only to the present plane-channel geometry, rather than the more general "local" formulation of model (a). The "ejection" formulation (e) was the only yielding significant differences with respect to all the other models; despite some obvious drawbacks, like the wrong profile of u_{rms} at high Reynolds number (Figure 4.36(f)), it may be worth a more complete parametrical study in which, for example, the "adjustable" constants c, ϕ be made vary.

4.7 Conclusions

> **Reality is that which when you stop believing in it, it doesn't go away**
> [Philip K. Dick, 'V.A.L.I.S.']

The Smagorinsky-Lilly subgrid model was successfully implemented in the computer code Harwell-FLOW3D and applied to the large-eddy simulation of turbulent flow with heat transfer between infinite parallel plates (plane channel). Simulations were repeated for different Reynolds numbers; modeling details (near-wall damping, values of c_s and σ_s, wall boundary conditions); and computational methods (grid, time step and time-stepping scheme, pressure-velocity coupling algorithm, discretization of advection terms).

Profiles of mean and fluctuating velocities in good agreement with experimental data and previous, high-resolution, numerical simulations were obtained by using grids of 32*24*24 nodes, time steps of 1/100th of a LETOT, the Crank-Nicolson time advancement scheme, central differencing of the advection terms, the PISOC pressure-velocity coupling algorithm, and c_s=.08. Near-wall structures ("streaks") were qualitatively reproduced, although their spanwise spacing was larger than experimentally observed.

When a random (not divergence-free) field was used as the initial flow, resolved turbulence levels decreased rapidly, remained very low for a period of several LETOT's (increasing with the grid resolution), then overshot more or less markedly and finally stabilized themselves around values of ~2-3. When simulations started from a divergence-free flow, obtained by preliminary runs using the same computational grid, any stepwise variation of Re, c_s or other parameters resulted in shorter numerical transient and in a quicker recovery of (statistically) steady-state conditions.

Values of c_s larger than .12 resulted in a progressive decay of turbulent

fluctuations. Values smaller than .06 (including the limit case c_s=0, i.e. no subgrid model at all) resulted in unrealistically high values of the resolved velocity fluctuations, especially in the spanwise direction; moreover, they gave a "white-noise" spectrum of turbulent time-fluctuations. Also the near - wall distribution of the main velocity u was found to be sensitive to the value of c_s; qualitatively correct results ("streaks") were obtained only for c_s close to .08, while larger values yielded unrealistic "stripe" patterns, and smaller values gave irregular "patches" with no preferred orientation.

The accuracy of the results was clearly higher when SIMPLEC, with several iterations per time step, was substituted for PISOC; this was reflected, in particular, in the more correct prediction of cross-stream fluctuation levels and of cross-stream turbulent scalar transport, resulting in correct temperature profiles for a realistic value (.5) of the subgrid Prandtl number.

Reducing the number of grid points, especially in the cross-stream direction, resulted in a more or less marked overprediction of the average velocity (with a corresponding underprediction of the mean wall shear stress). However, refining the grid beyond the "reference" resolution (32*24*24) had little influence on mean quantities, while resolved fluctuation levels increased and the time behaviour of k and $\langle\tau\rangle$ became more regular.

Changing the time step between 1/50th and 1/200th of a LETOT had little influence on the solution; larger values resulted in fluctuation damping. Also the use of fully implicit backward time stepping (in place of the Crank - Nicolson scheme) led to suppression of turbulence.

Advection-term discretization schemes of higher order than CDS (namely, QUICK and CCCT) were tested. Results were disappointing: these schemes turned out to be <u>not</u> less dissipative than CDS, while contributing numerical oscillations ("wiggles") superimposed on "true", physical fluctuations, which resulted in wrong cross-stream profiles of v_{rms} and w_{rms} (lacking the characteristic minimum in the central region of the channel) and in large time-fluctuations of the average resolved turbulence energy k.

Finally, alternative wall boundary conditions were tested both for a low - Reynolds number flow (near-wall grid points in the viscous sublayer) and for a high - Reynolds number case (near-wall points in the fully turbulent region, i.e. 'synthetic' wall boundary conditions). Significant differences with respect to the reference formulation (a) were obtained only by using the "ejection" boundary conditions of Piomelli et al. [1989]; on the whole, however, none of the models appeared clearly superior to the others. In particular, "global" formulations, which present the shortcoming of being applicable only to plane-channel flows, did not behave better than the "local" formulation (a), which can be extended, in principle, to all geometries.

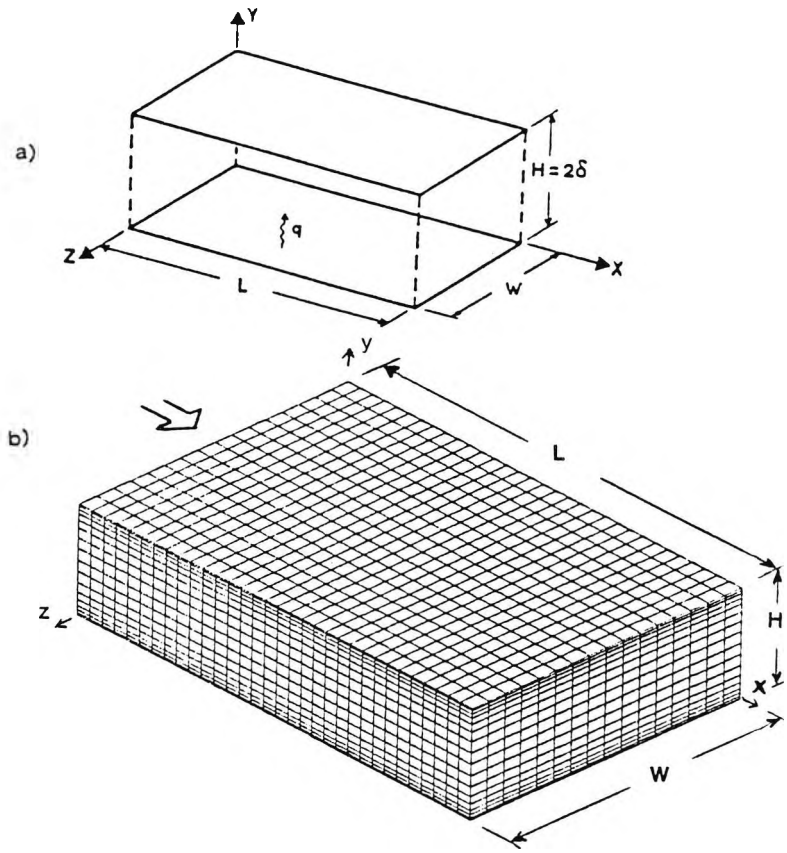


Figure 4.1 - Plane channel: computational box (a) and typical 3-D grid having 32*16*16 control volumes (b)

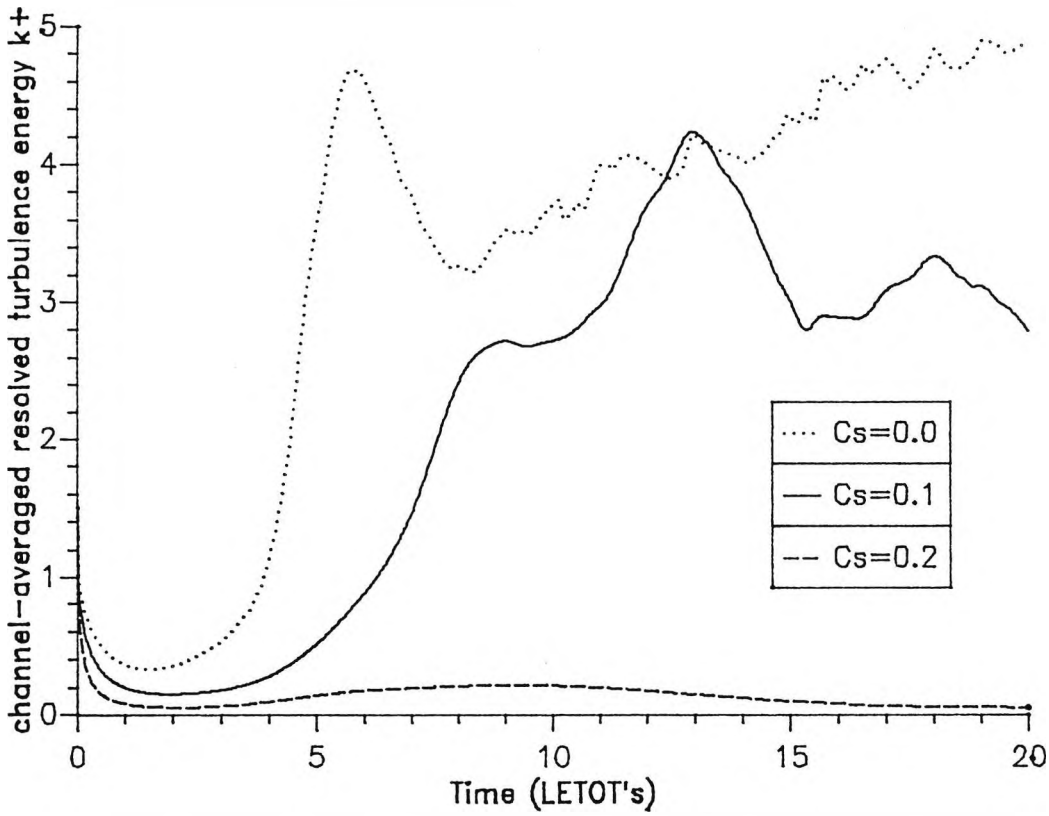


Figure 4.2 - Plane channel: initial behaviour of k for different values of c_s

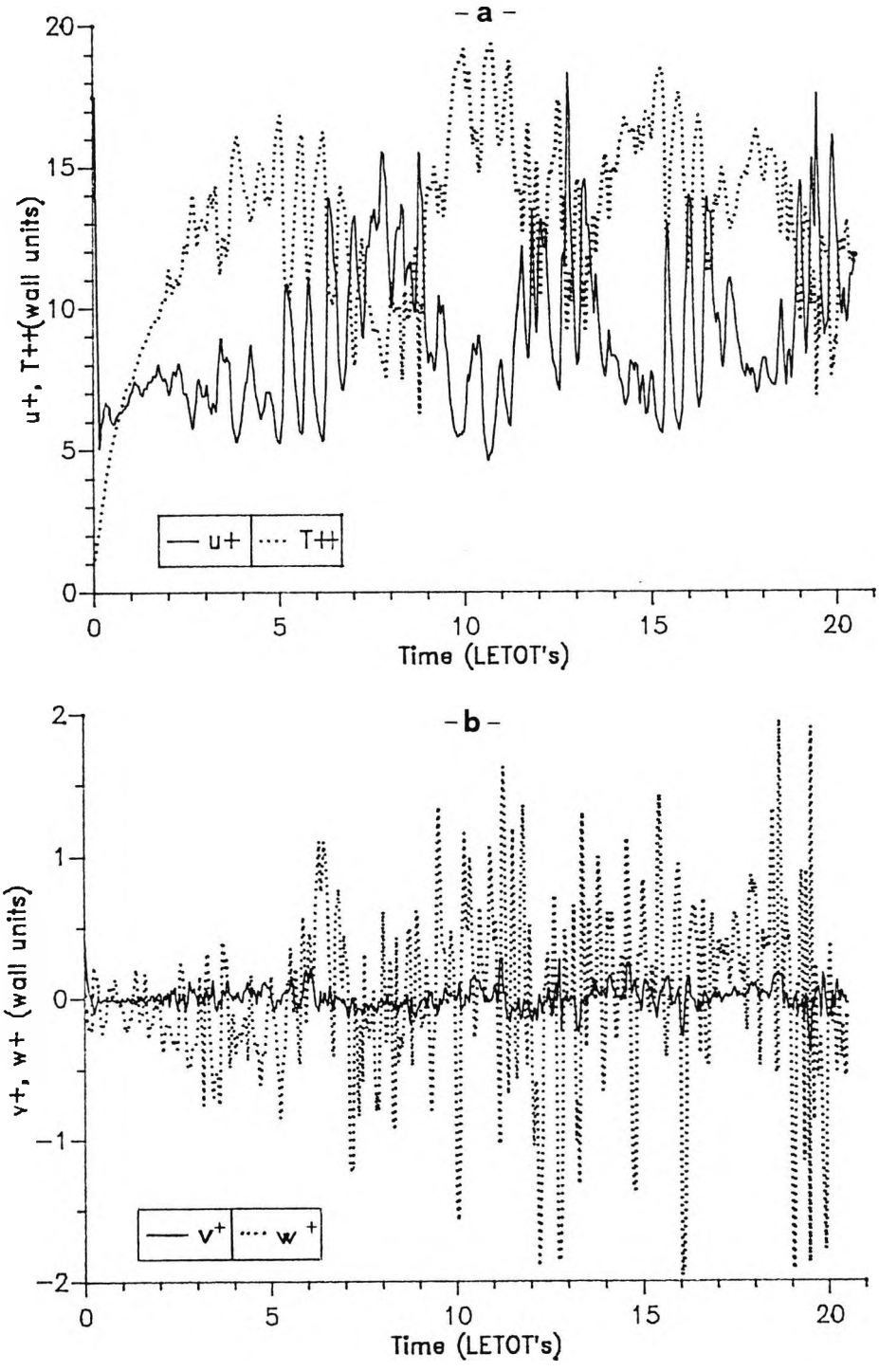


Figure 4.3 - Time behaviour of the three velocity components u,v,w and temperature T at a monitoring point (y^+=20) for the case c_s=0.08 in Figure 4.2. All quantities are expressed in wall units. (a): u^+ and T^{++}; (b): v^+ and w^+.

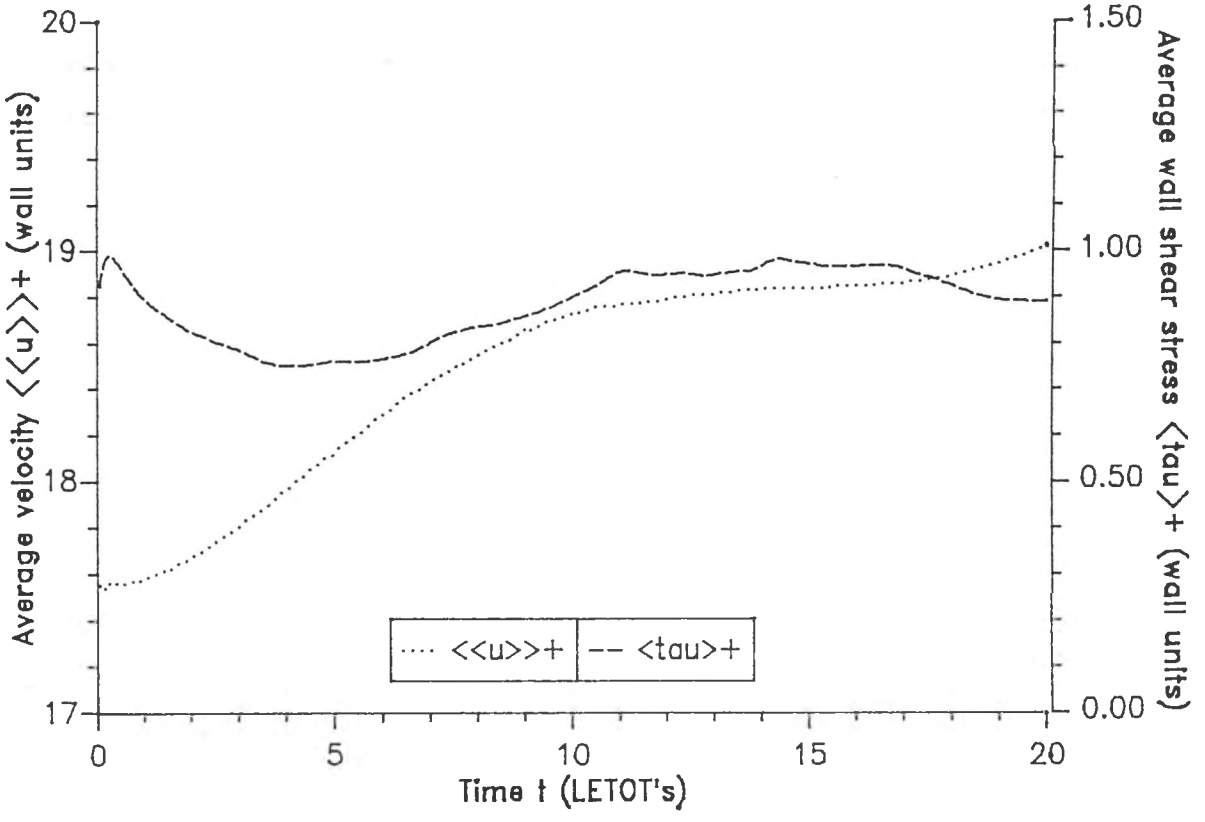
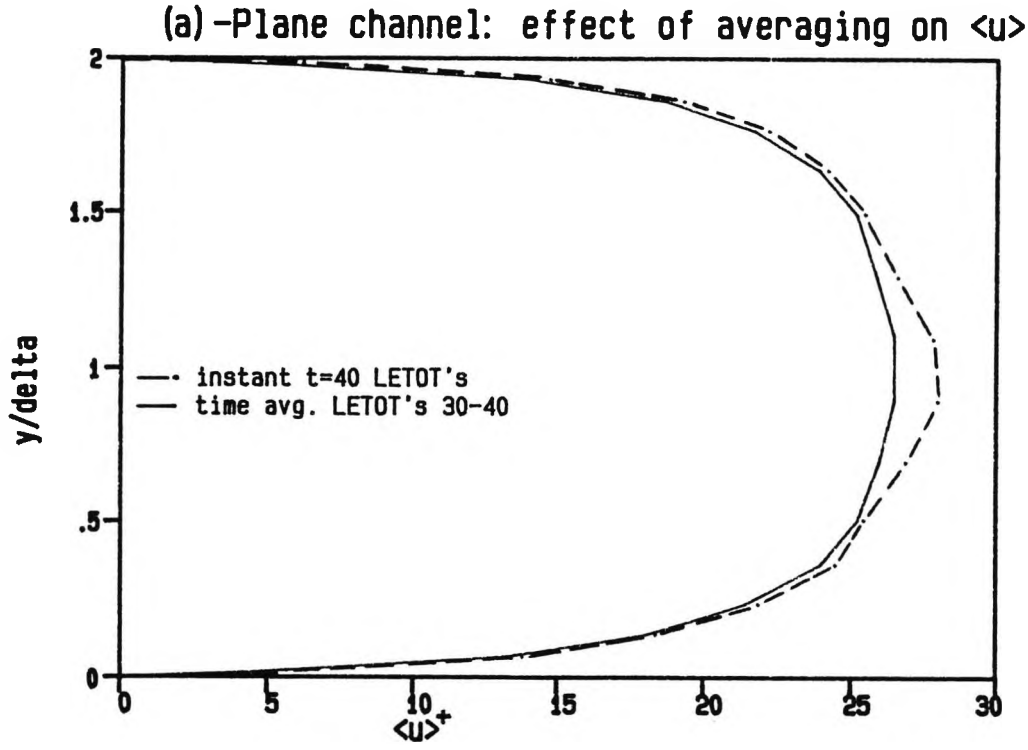


Figure 4.4 - Plane channel: disequilibrium effects. Behaviour of the mean wall shear stress $<\tau$ and of the average velocity U (Re^0=20,000, 32*24*24 grid)



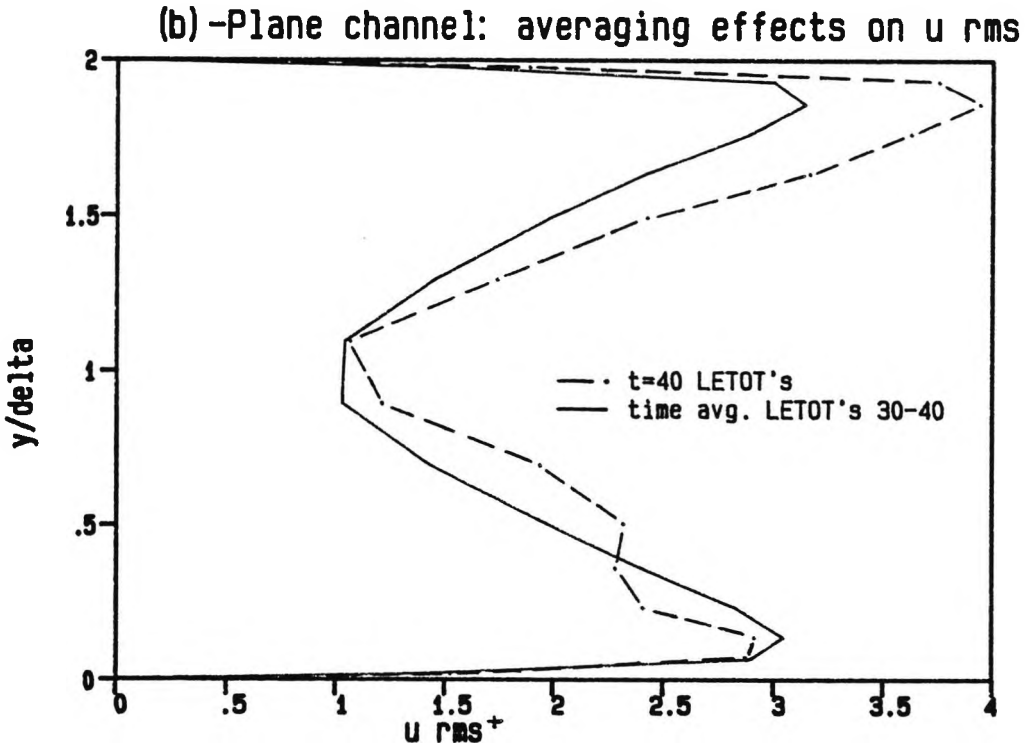
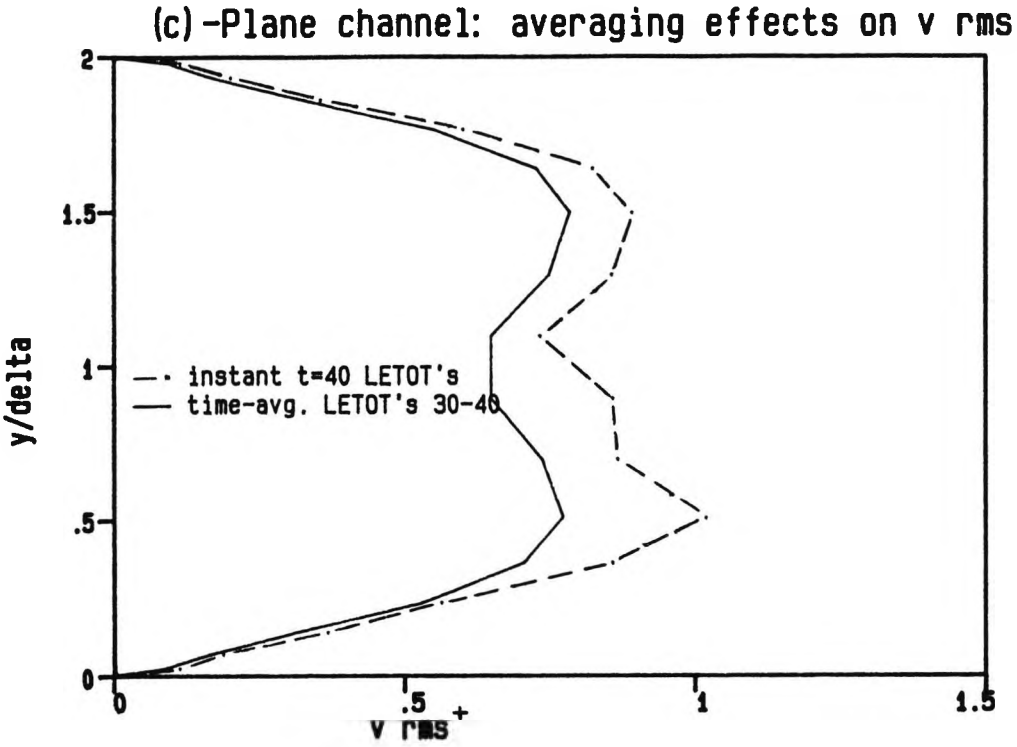


Figure 4.5 - Plane channel (Re^0=20,000, 32*16*16 grid)

a) instantaneous versus time-averaged cross-stream profile of <u>

b) instantaneous versus time-averaged cross-stream profile of u_{rms}



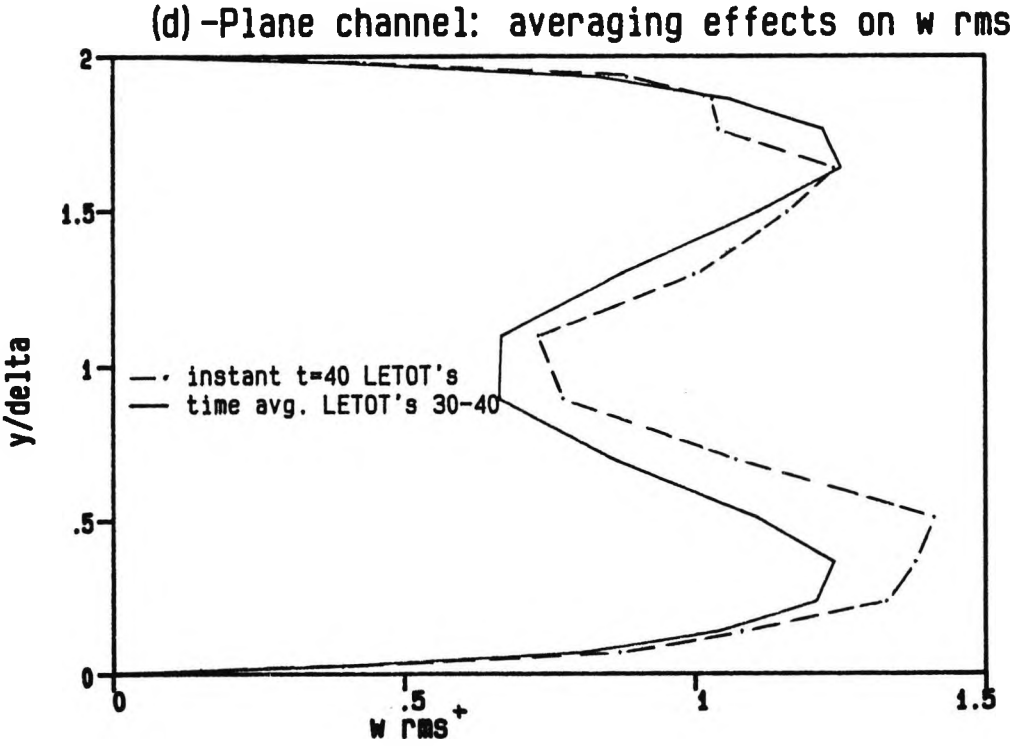


Figure 4.5 - (cont.'d)

c) instantaneous versus time-averaged cross-stream profile of v_{rms}

d) instantaneous versus time-averaged cross-stream profile of w_{rms}

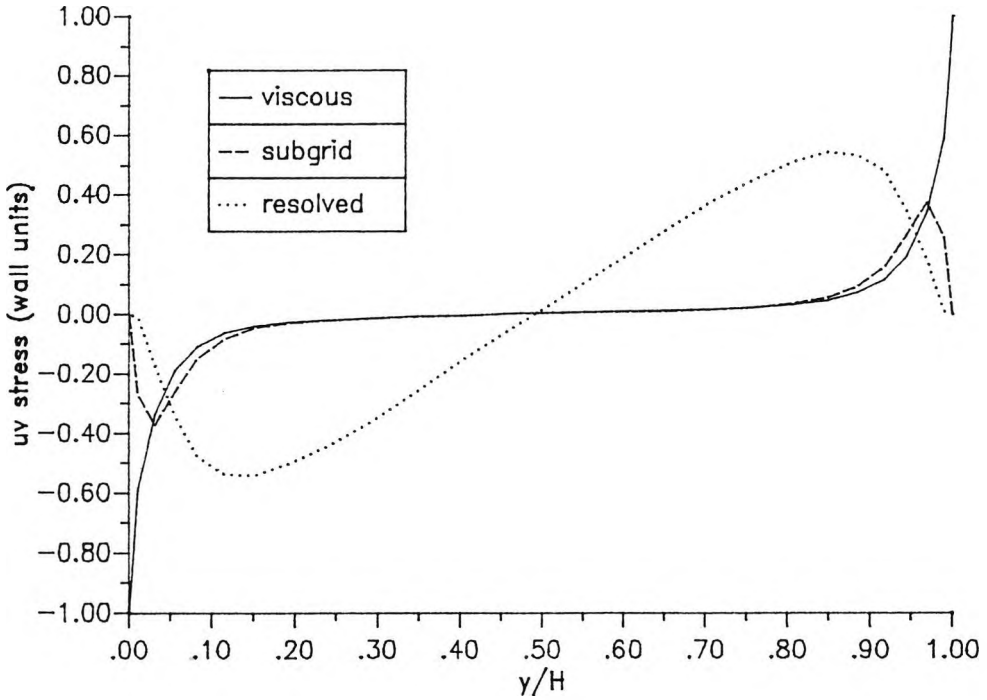


Figure 4.6 - Plane channel (Re^0=20,000, c_s=0.1, 32*24*24 grid): cross-stream profiles of the various contributions to the main (uv) stress.

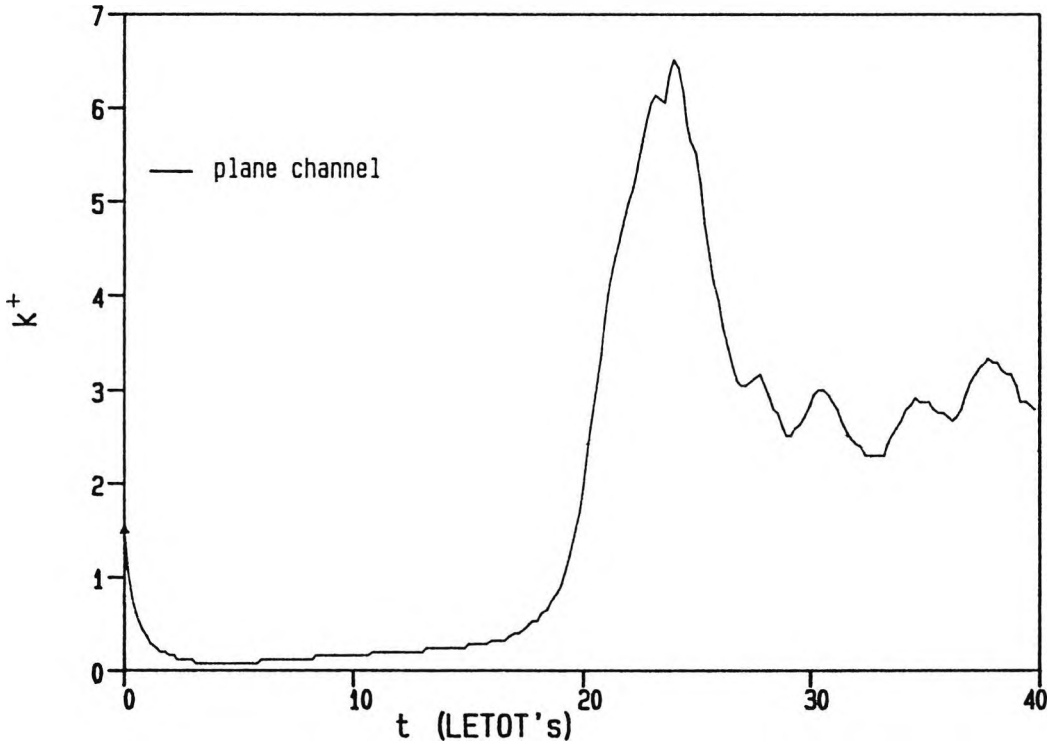


Figure 4.7 - Plane channel (reference case): behaviour of the volume-averaged resolved turbulence energy k

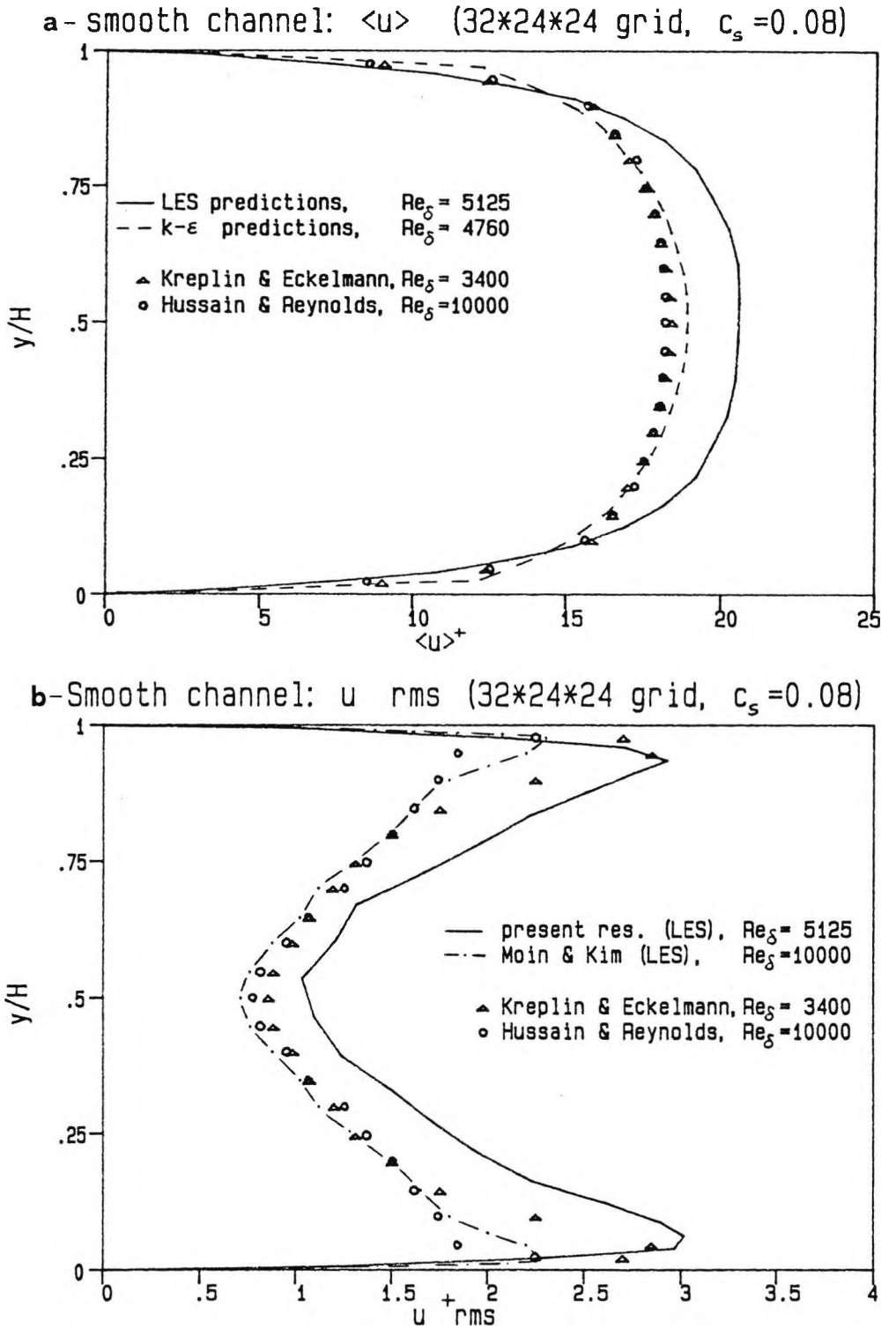
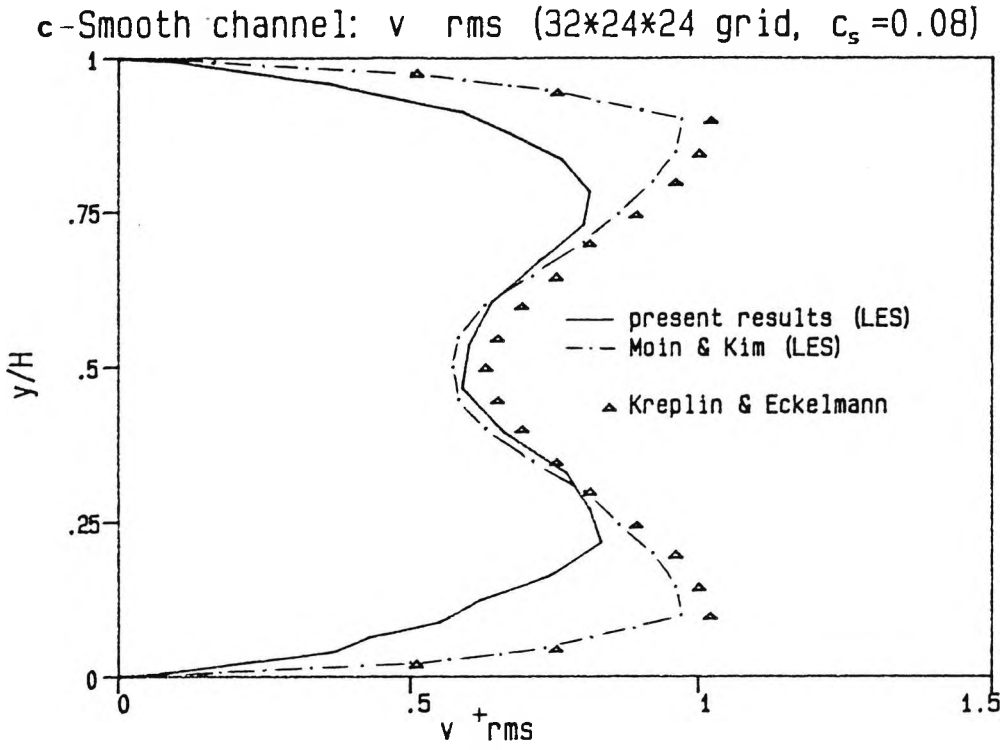


Figure 4.8 - Plane channel (reference case):

a) comparison of computed and experimental profiles of $\overline{<u>}$

b) comparison of computed and experimental profiles of $\overline{u_{rms}}$

Values of the δ-Reynolds number are indicated.



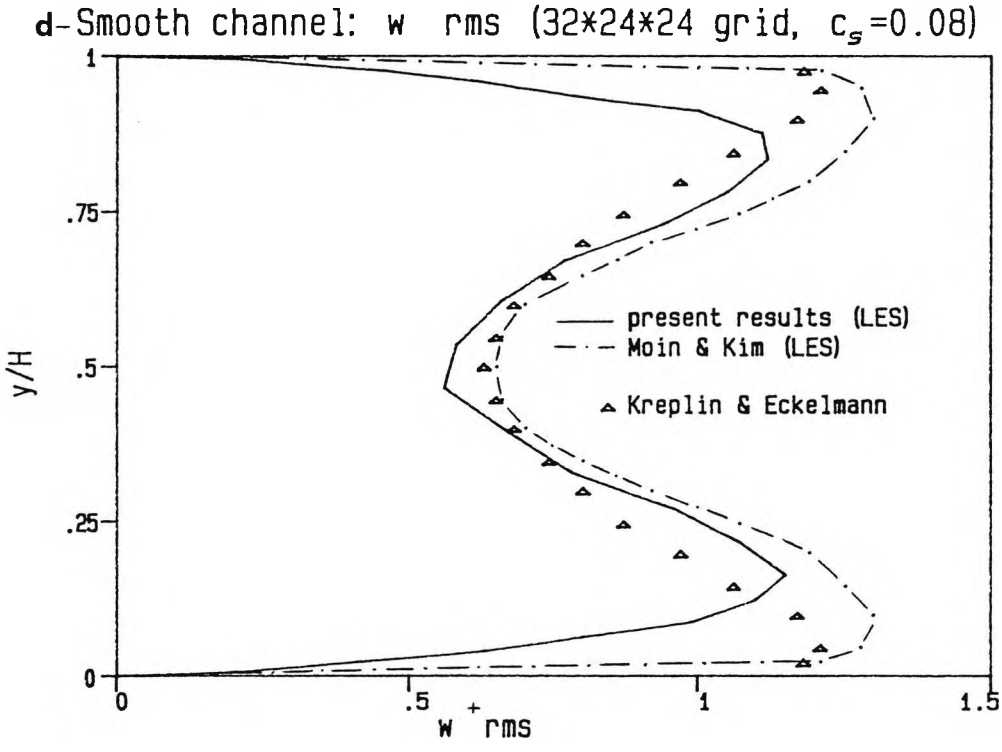


Figure 4.8 - (cont.'d):

c) comparison of computed and experimental profiles of $\overline{v_{rms}}$

d) comparison of computed and experimental profiles of $\overline{w_{rms}}$

Values of the δ-Reynolds number are indicated.

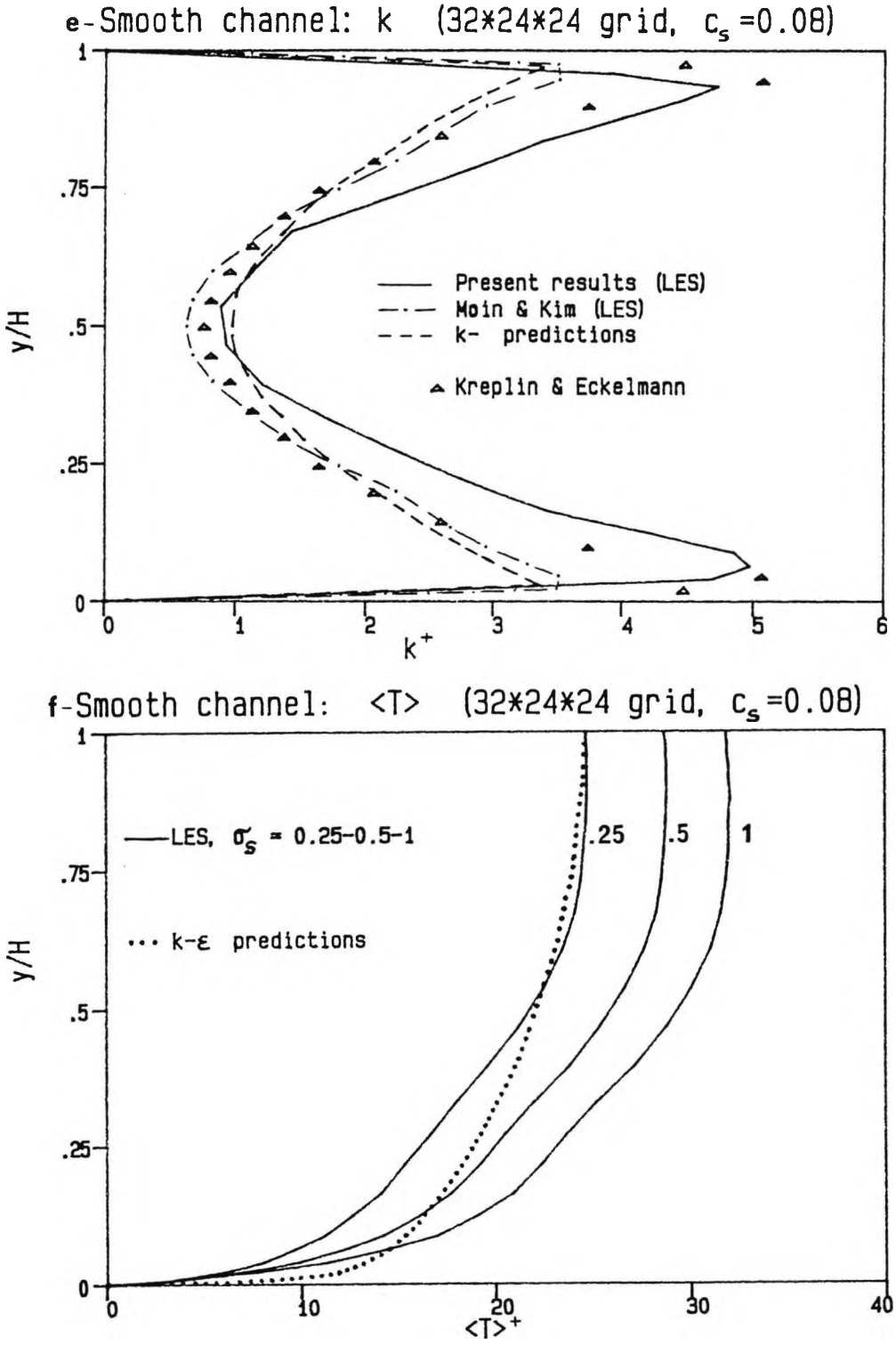


Figure 4.8 - (cont.'d):

e) comparison of computed and experimental profiles of <k>

f) cross-stream profiles of $\overline{\langle T\rangle}^+$ for different values of σ_s, and comparison with k-ε predictions.

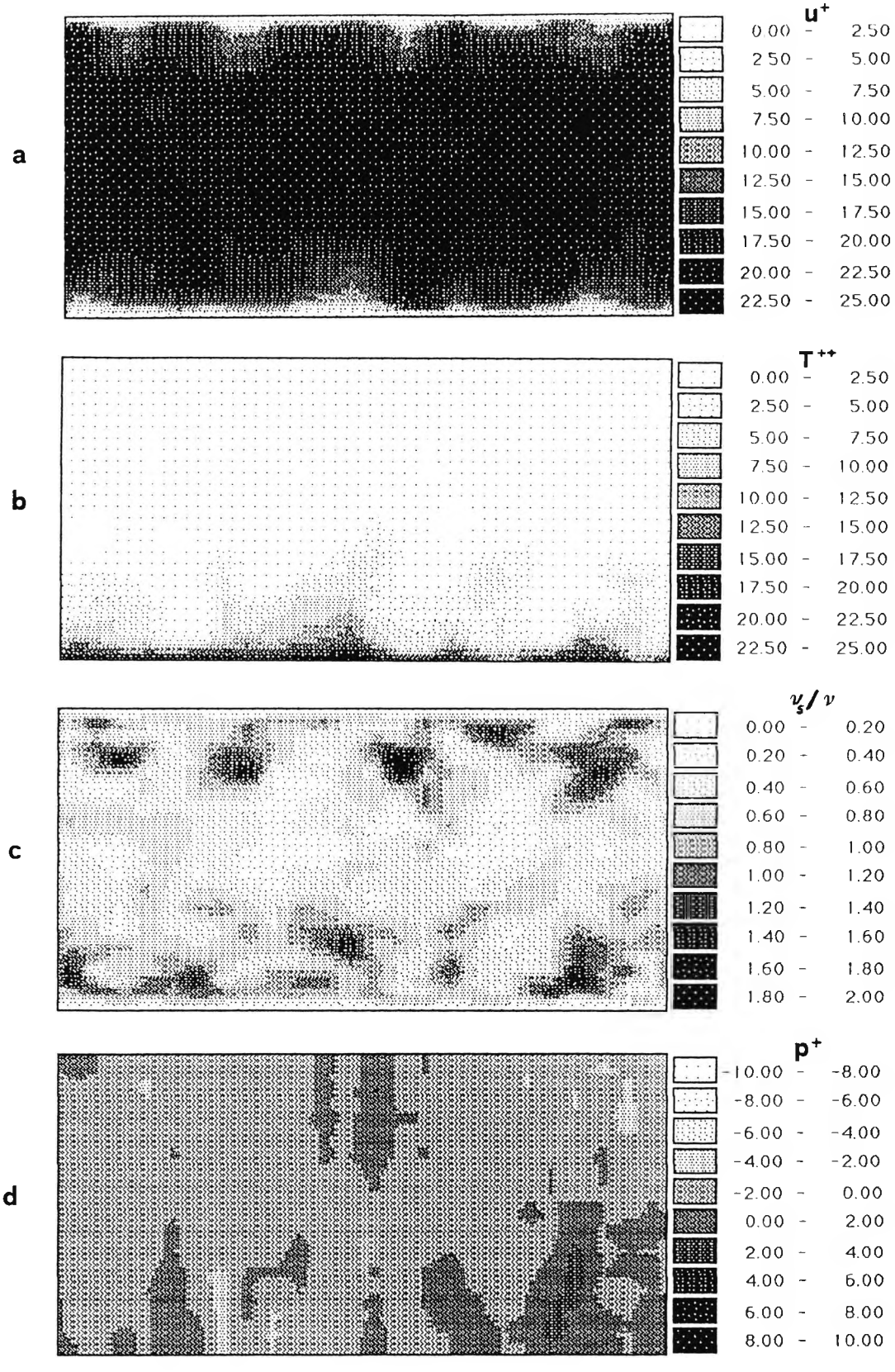


Figure 4.9 - Plane channel (reference case): shade plots of instantaneous velocity (a), temperature (b), subgrid viscosity (c) and pressure (d) on a plane normal to the main flow direction x.

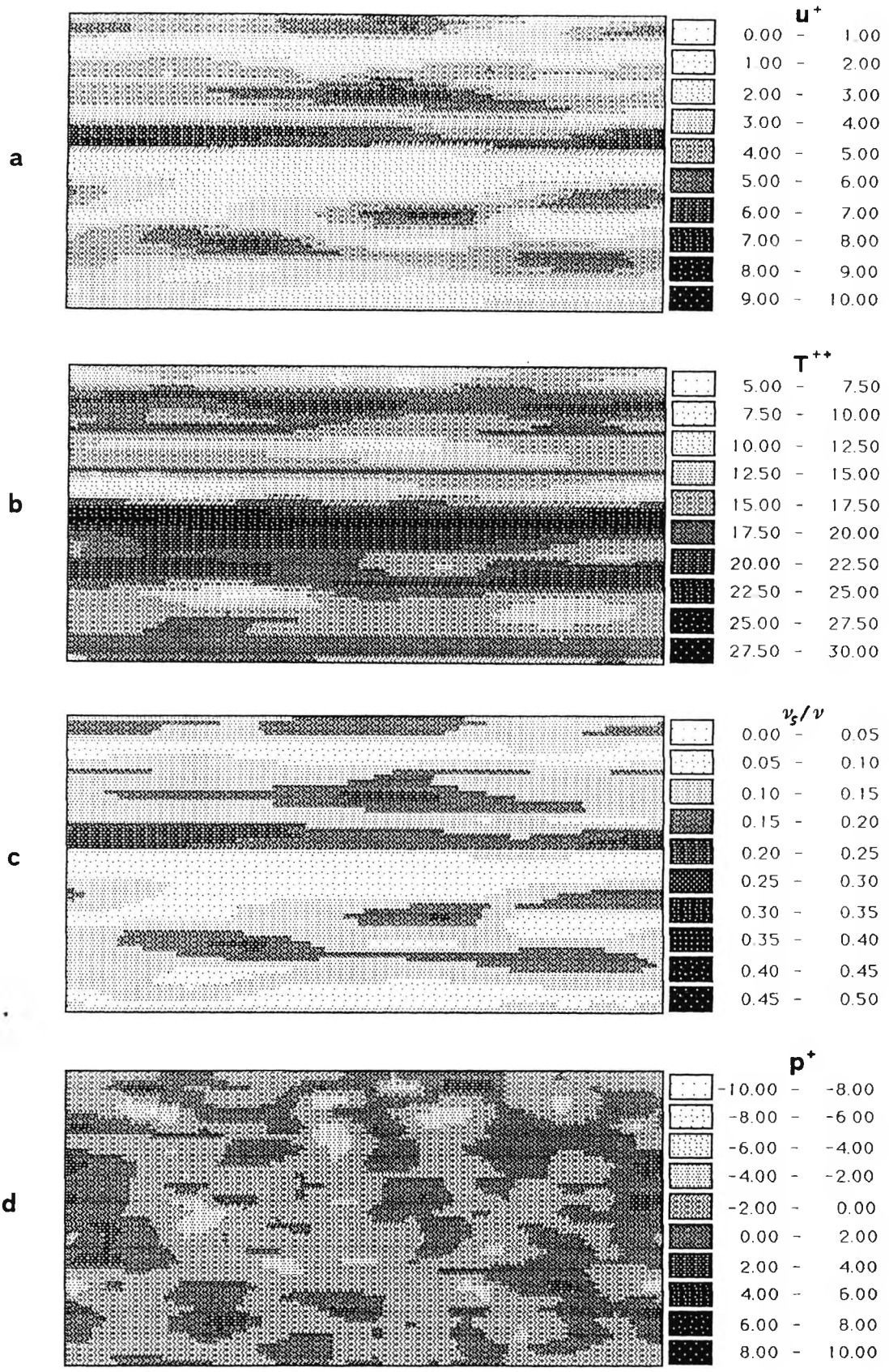


Figure 4.10 - Plane channel (reference case): instantaneous velocity (a), temperature (b), subgrid viscosity (c) and pressure (d) on the plane $y^+ \cong 4$ parallel to the heated wall.

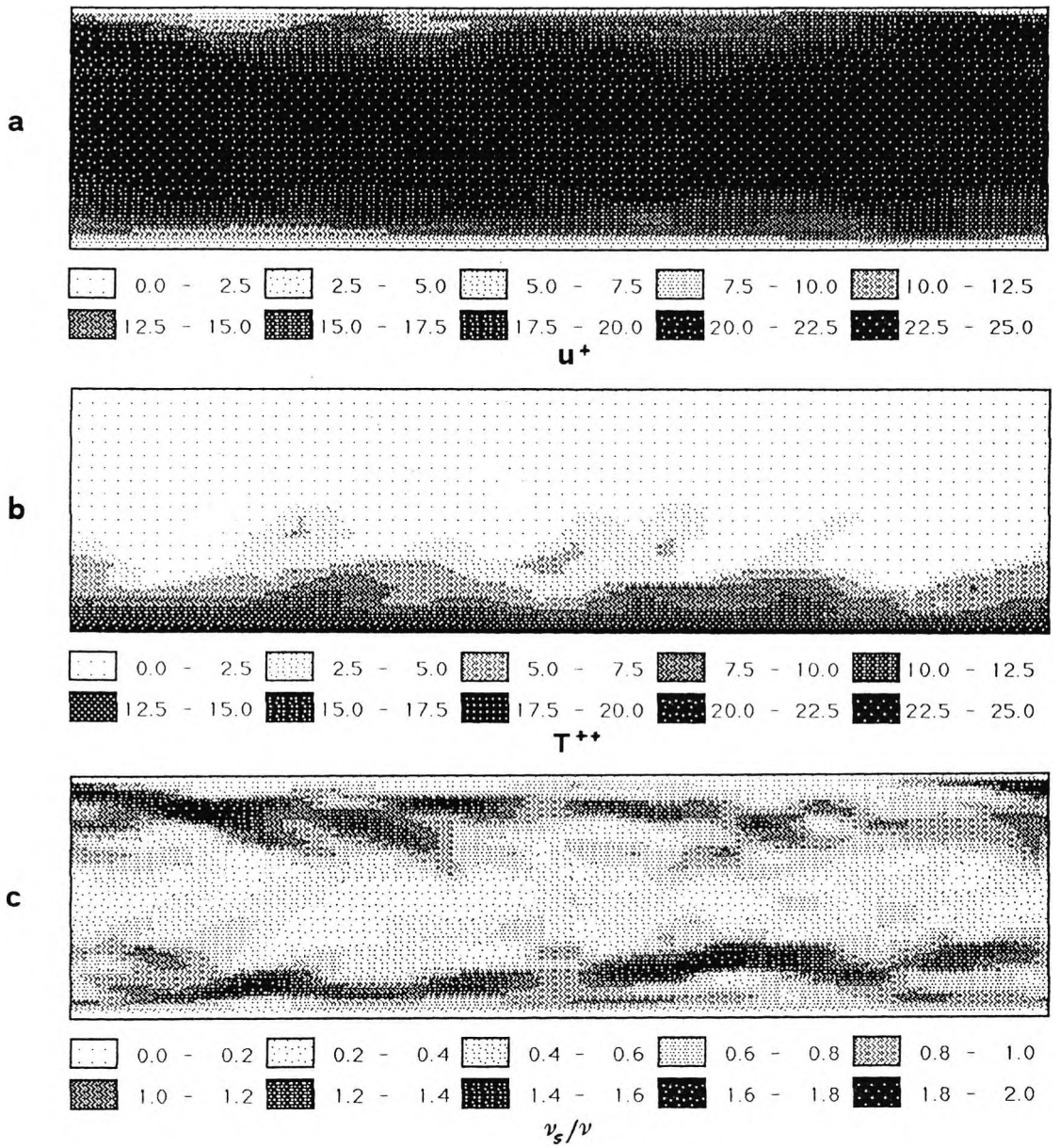


Figure 4.11 - Plane channel (reference case): instantaneous velocity (a), temperature (b), subgrid viscosity (c) on a plane normal to the spanwise direction z.

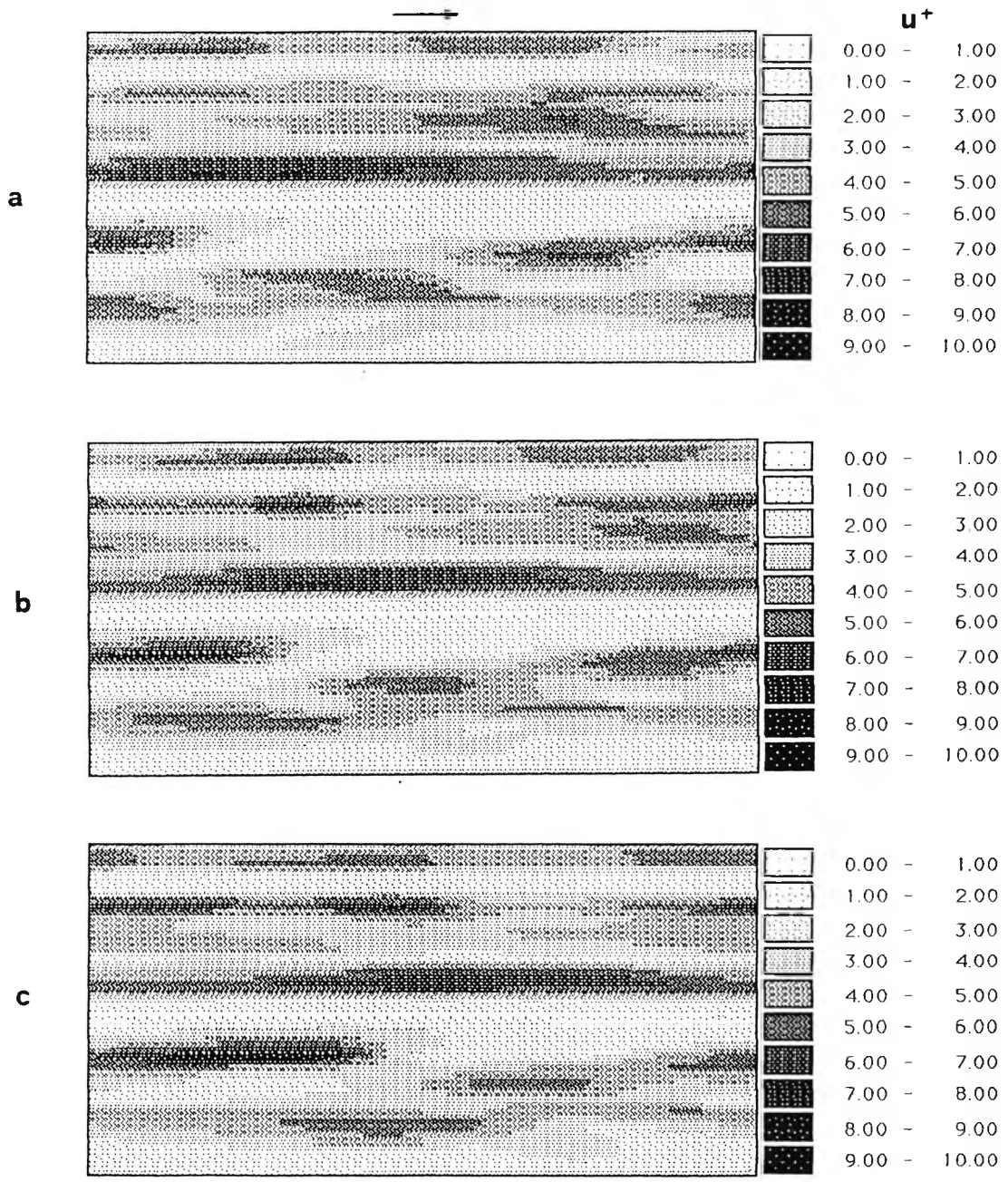


Figure 4.12 - Plane channel (reference case): evolution of the streamwise velocity u on the plane $y^+ \simeq 4$ parallel to the heated wall
a) t=31.1; b) t=31.2; c) t=31.3 (LETOT's)

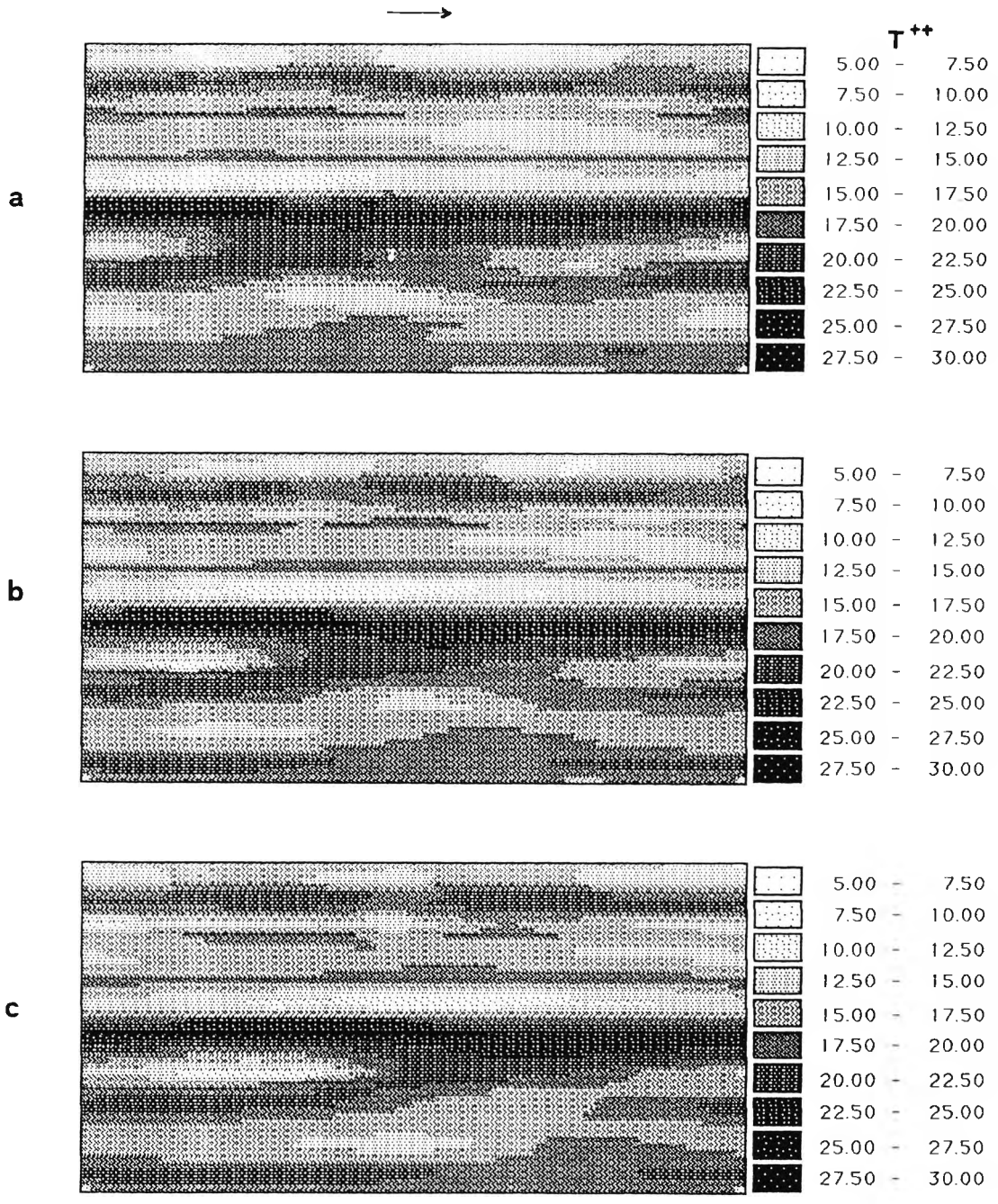


Figure 4.13 - Plane channel (reference case): evolution of the temperature T^{++} on the plane $y^{+}=4$ parallel to the heated wall
a) t=31.1; b) t=31.2; c) t=31.3 (LETOT's)

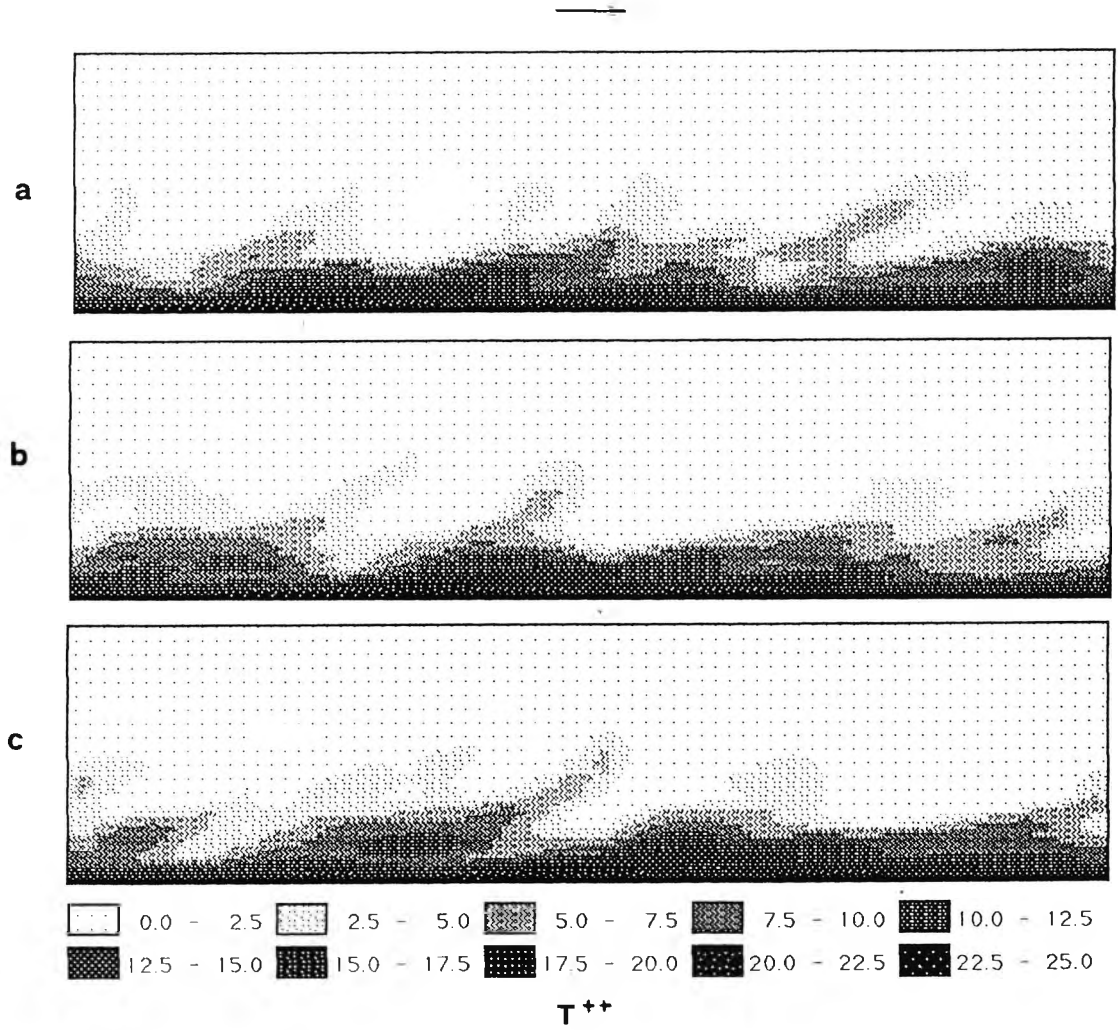


Figure 4.14 - Plane channel (reference case): evolution of the temperature T on a plane normal to the spanwise direction z
a) t=31.1; b) t=31.2; c) t=31.3 (LETOT's)

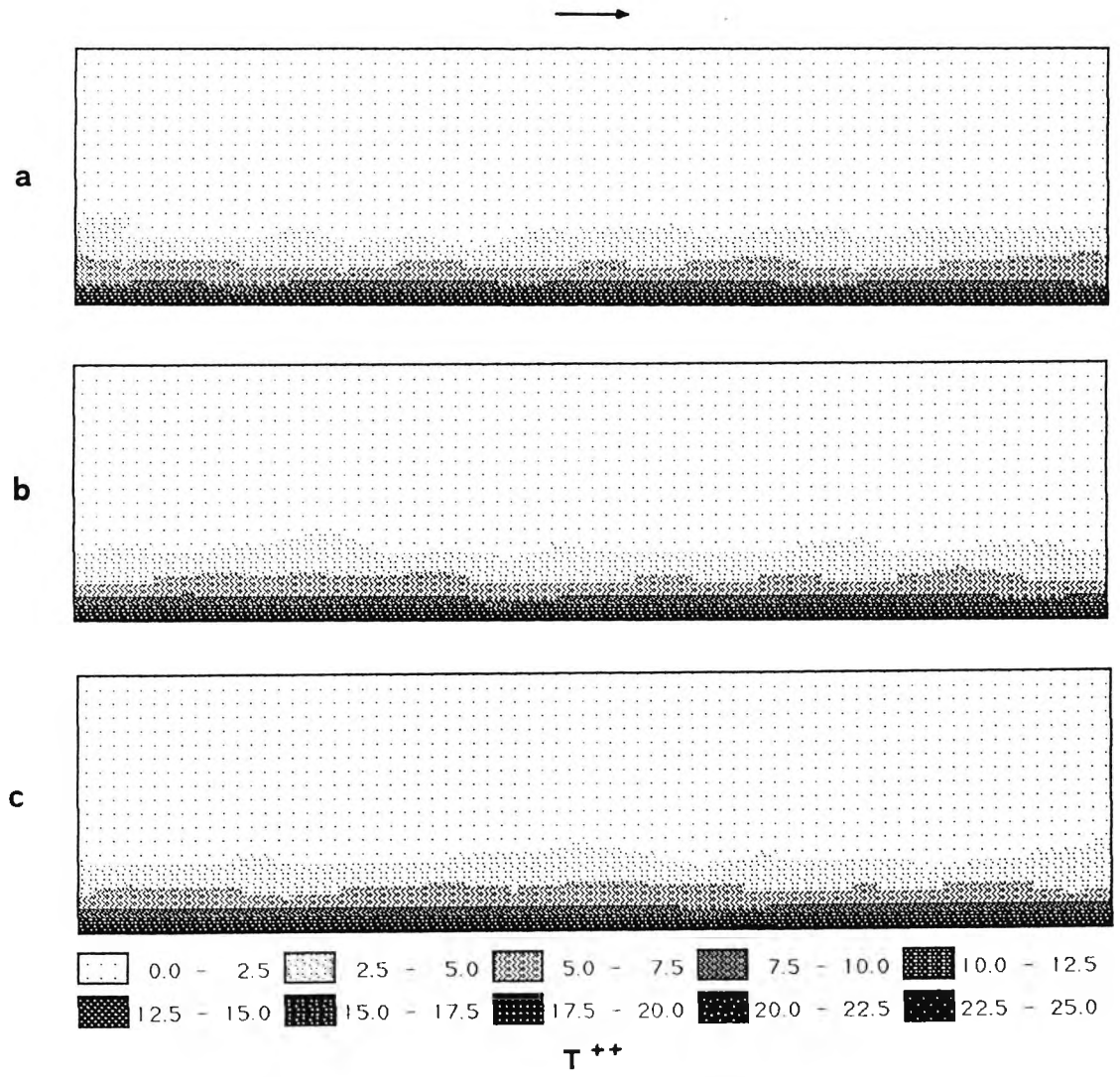


Figure 4.15 - Plane channel (reference case): evolution of the spanwise-averaged temperature
a) t=31.1; b) t=31.2; c) t=31.3 (LETOT's)

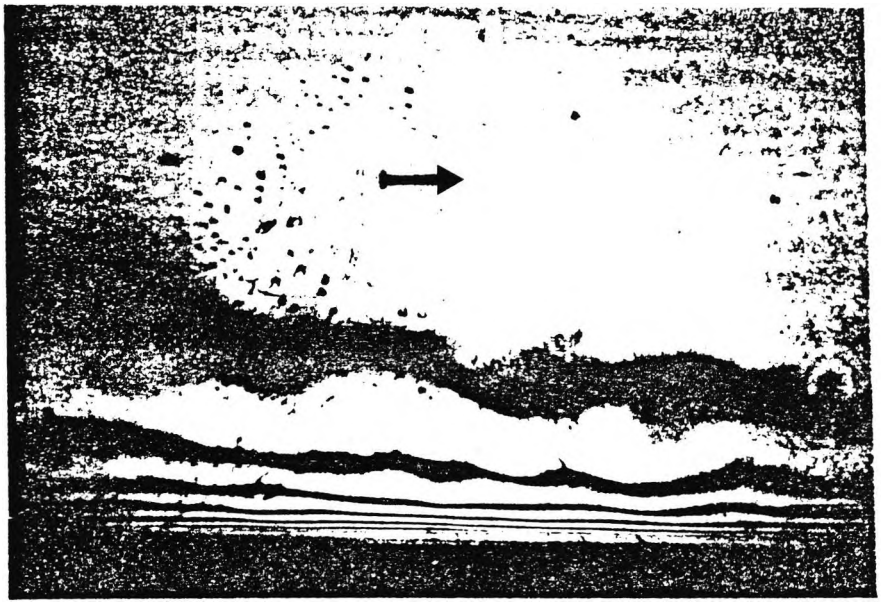


Figure 4.16 - Instantaneous, span-averaged temperature distribution obtained by Lockett [1987] for Re_{δ}=5,000 using holographic interferometry.

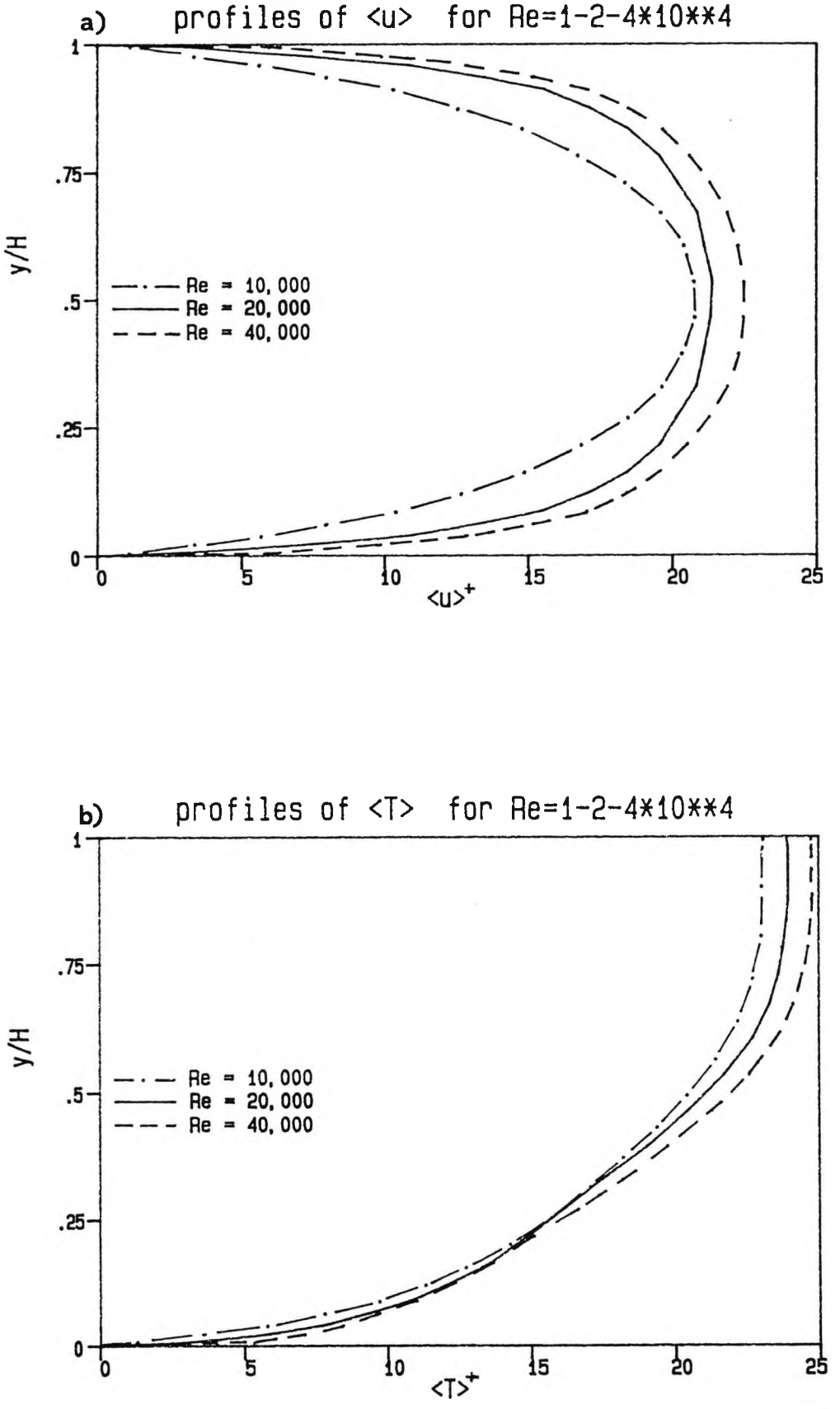


Figure 4.17 - Plane channel: comparison of cross-stream profiles of $\overline{\langle u \rangle}$ (a) and $\overline{\langle T \rangle}$ (b) for different Reynolds numbers and a 32*16*16 grid.

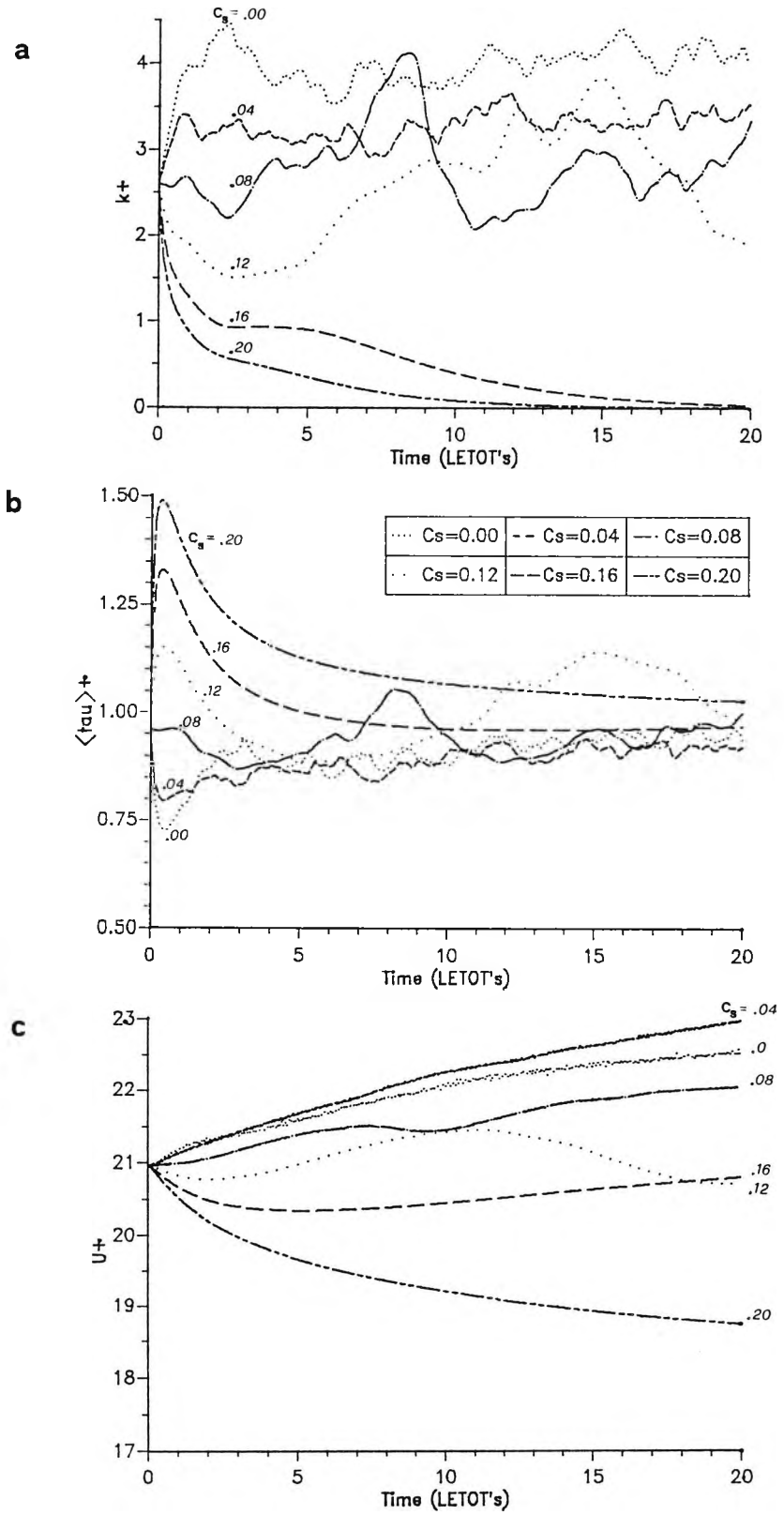
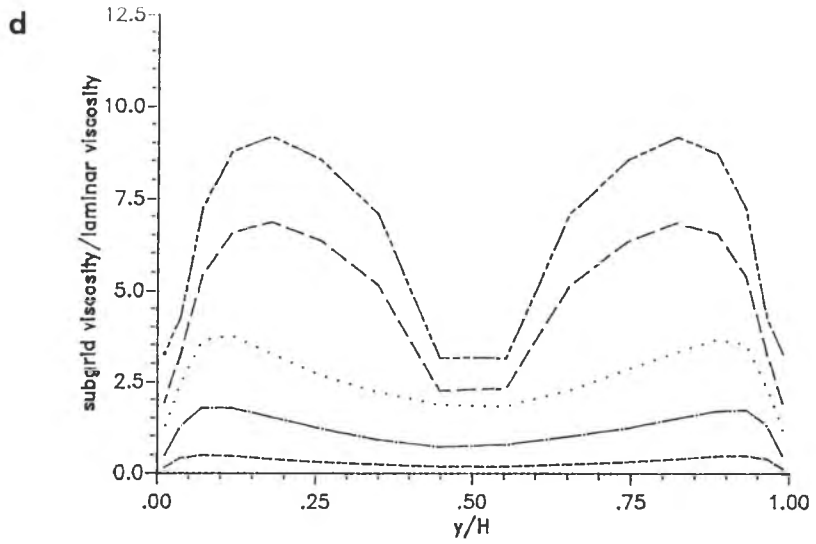


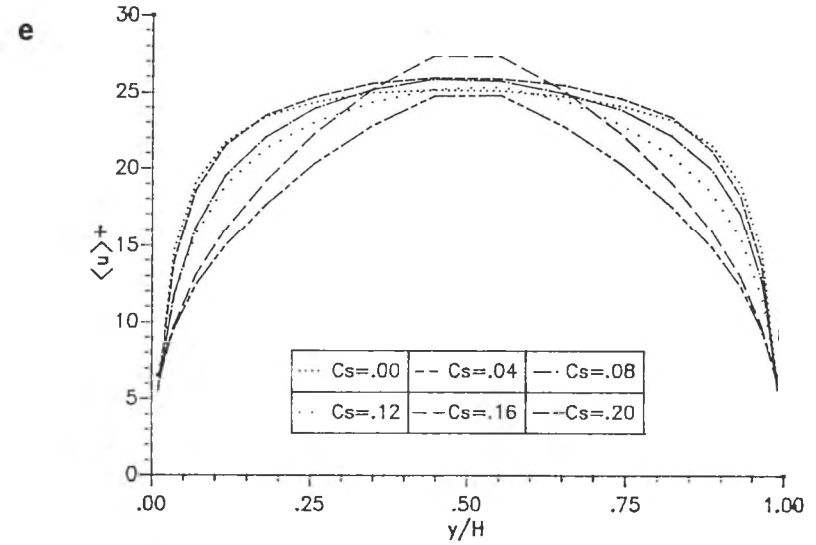
Figure 4.18 - Plane channel: influence of the Smagorinsky constant c_s.

a) evolution of the volume-averaged resolved turbulence energy k

b) evolution of the mean wall shear stress <τ>

c) evolution of the cross-section averaged velocity U





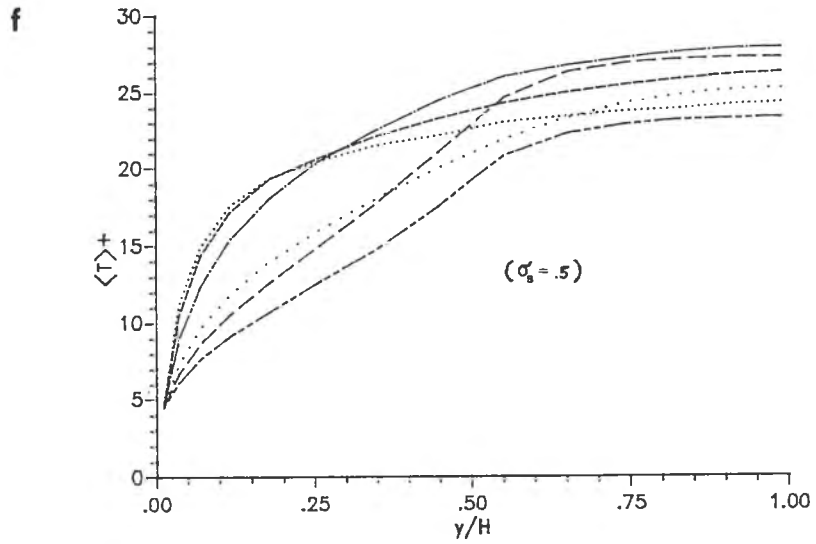


Figure 4.18 - (cont.'d)

d) cross-stream profiles of the subgrid viscosity $\overline{\langle \nu_s \rangle}$

e) cross-stream profiles of the mean velocity $\overline{\langle u \rangle}$

f) cross-stream profiles of the mean temperature $\overline{\langle T \rangle}$

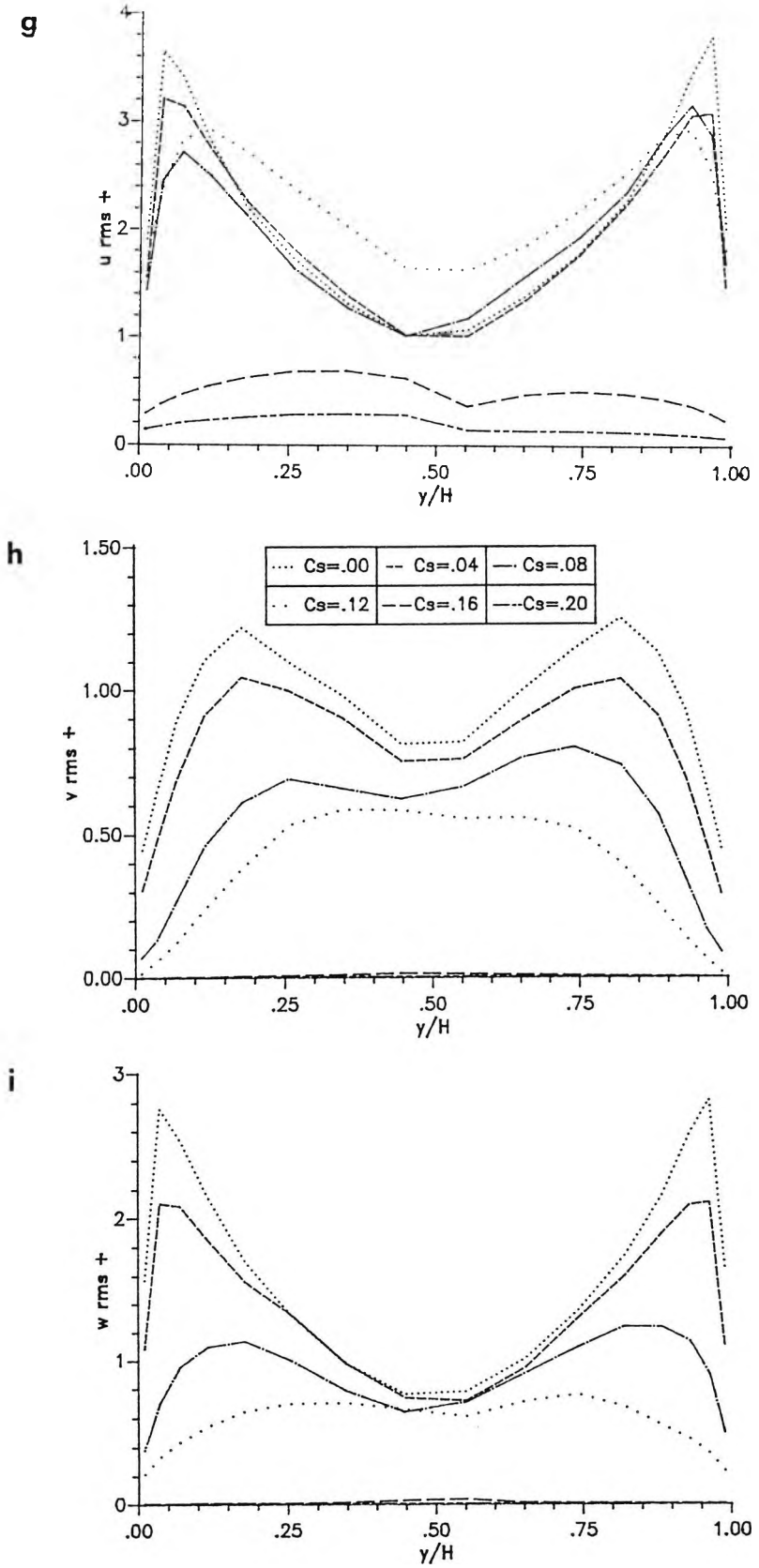


Figure 4.18 - (cont.'d)

g) cross-stream profiles of the streamwise fluctuation $\overline{u_{rms}}$

h) cross-stream profiles of the cross-stream fluctuation $\overline{v_{rms}}$

i) cross-stream profiles of the spanwise fluctuation $\overline{w_{rms}}$

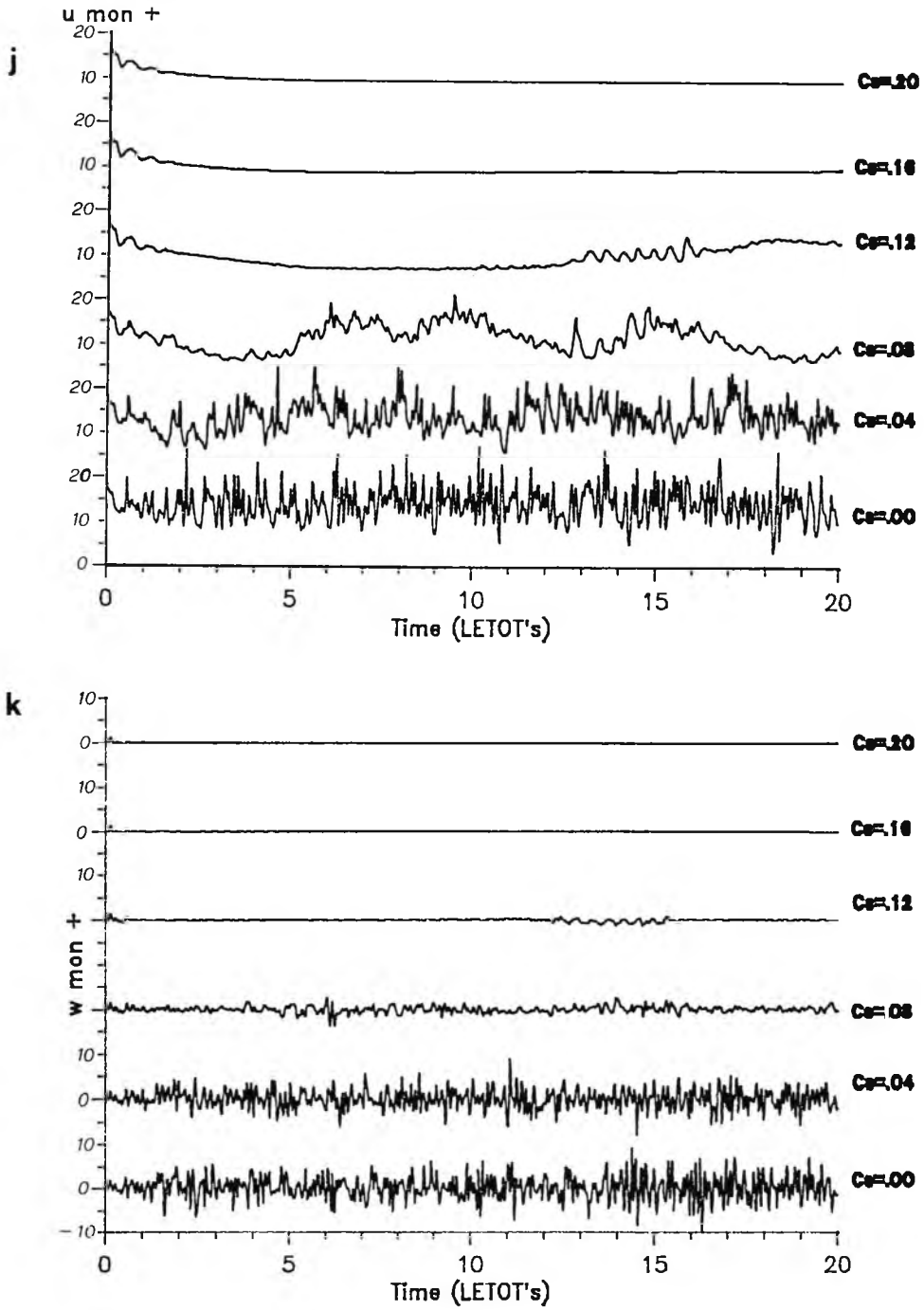


Figure 4.18 - (cont.'d): time behaviour of the streamwise (j) and spanwise (k) velocities at a monitoring point located near a wall ($y^+ \cong 6$).

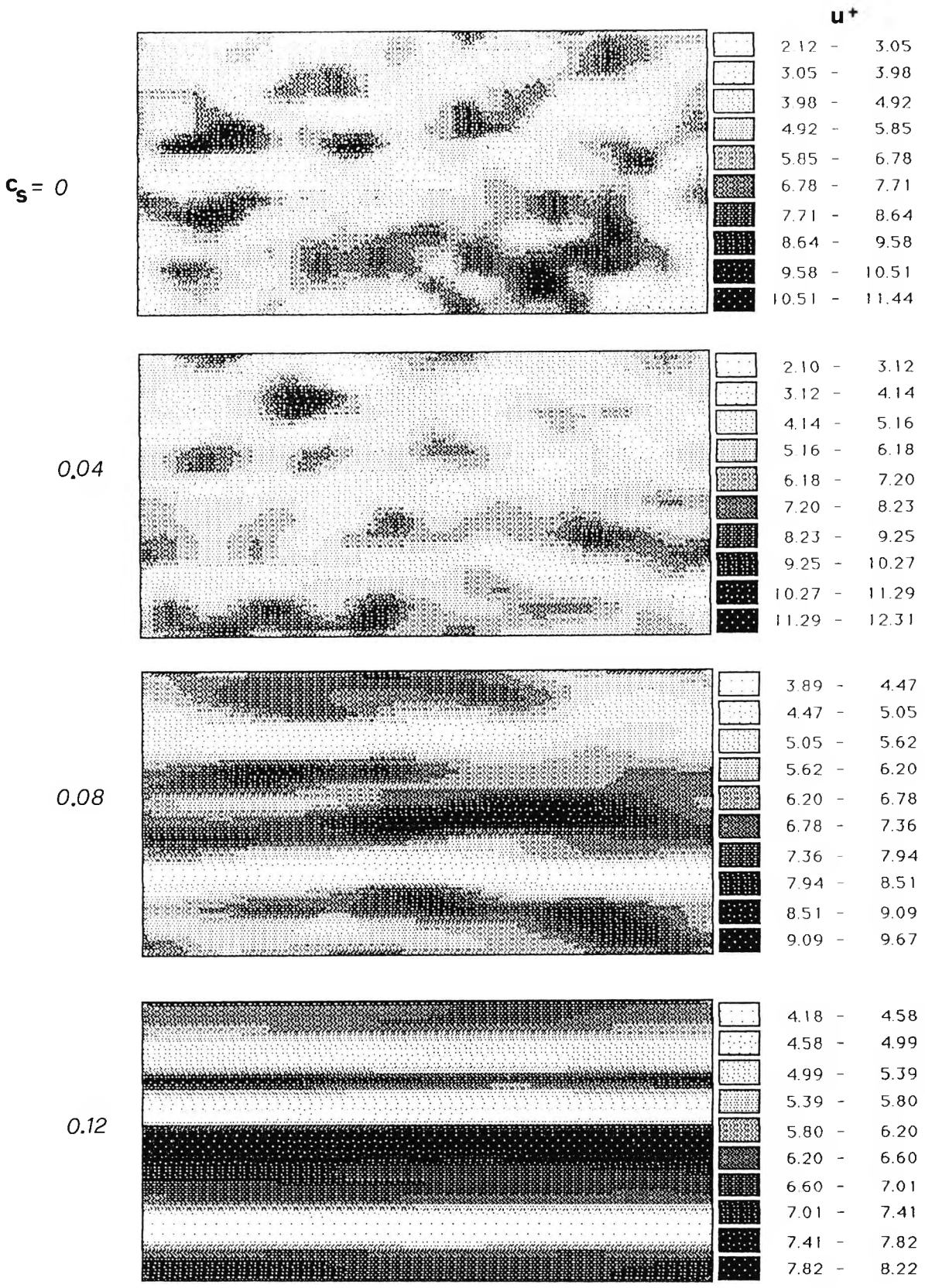


Figure 4.19 - Plane channel: influence of the Smagorinsky constant. Shade plots of the streamwise velocity u on the plane $y^+ \simeq 20$ close to a wall for different values of c_s.

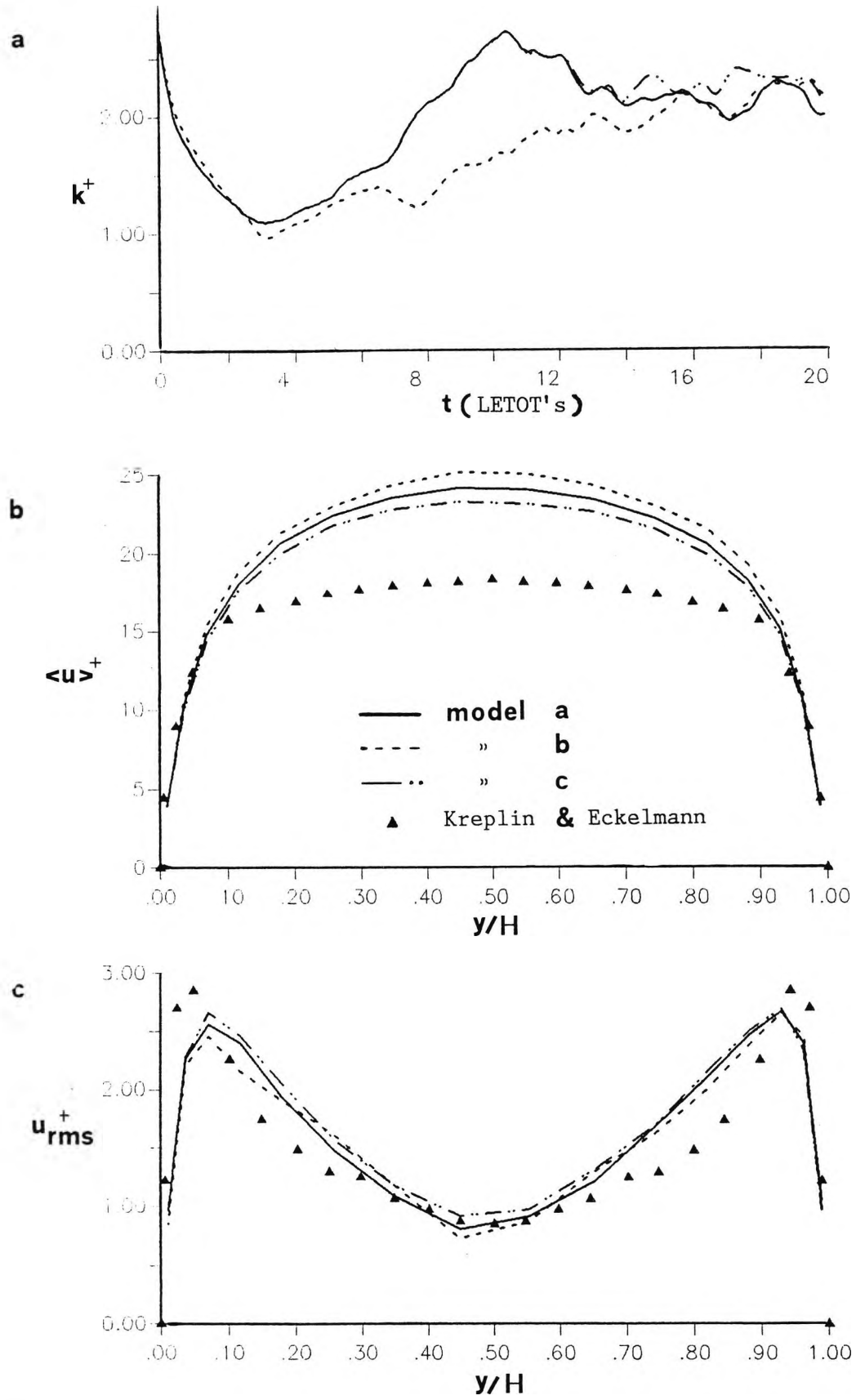


Figure 4.20 - Plane channel: influence of the near-wall damping function D.

a) time-behaviour of the average resolved turbulence energy k

b) cross-stream profiles of the mean velocity $\overline{\langle u \rangle}$

c) cross-stream profiles of the streamwise fluctuation $\overline{u_{rms}}$

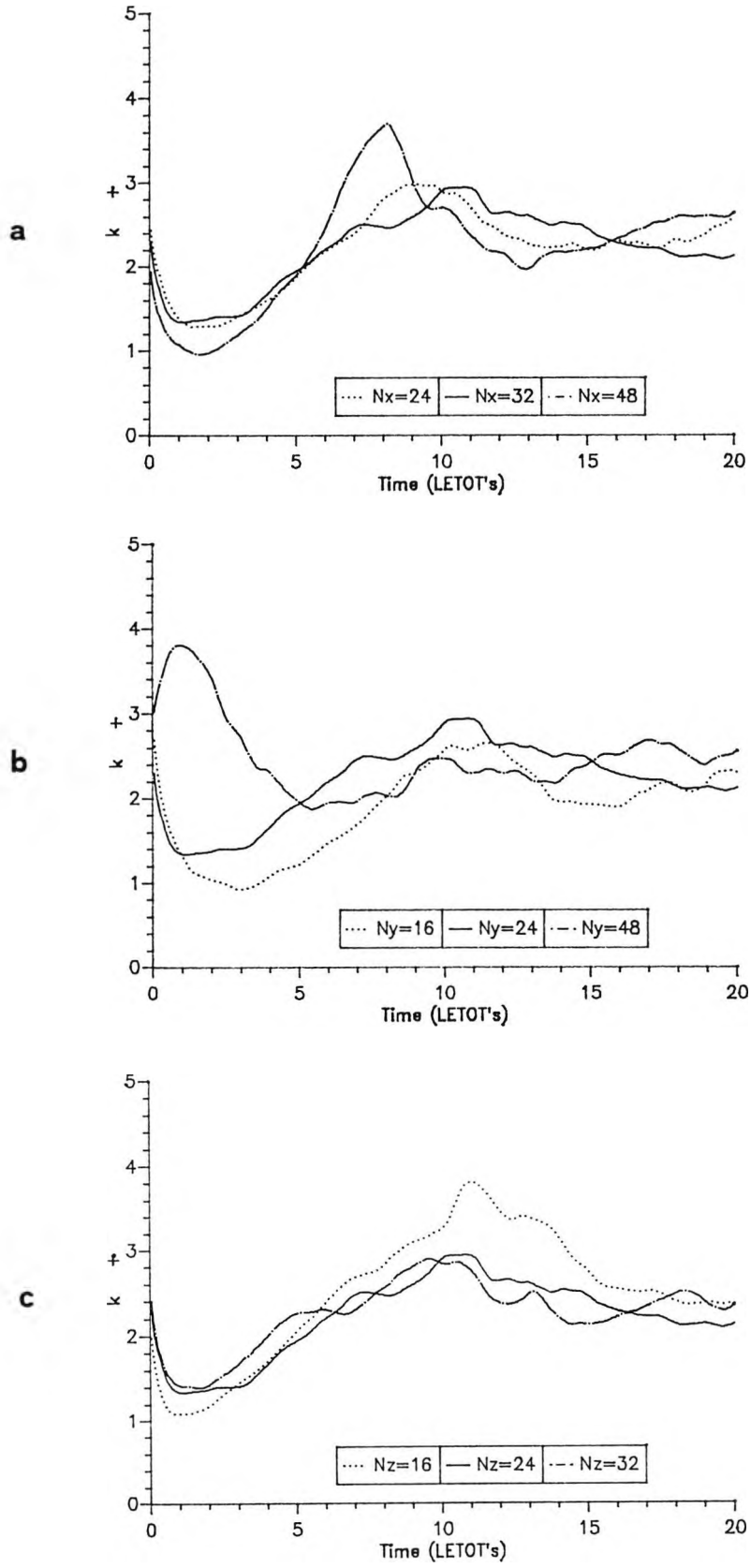


Figure 4.21 - Plane channel: influence of the computational grid. Behaviour of the average resolved turbulence energy k for a) varying N_x; b) varying N_y; c) varying N_z.

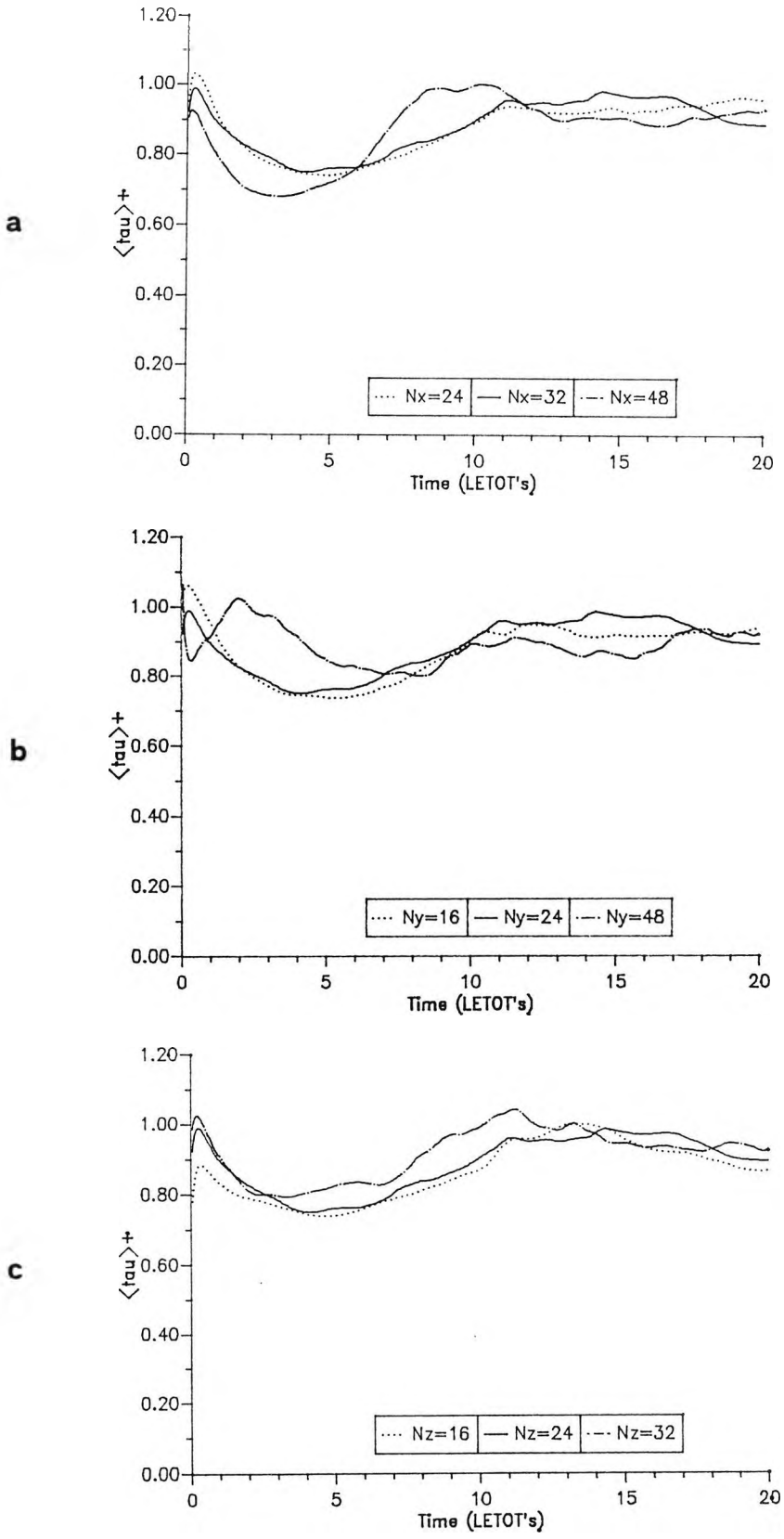


Figure 4.22 - Plane channel: influence of the computational grid. Behaviour of the mean wall shear stress $\langle \tau \rangle$ for a) varying N_x; b) varying N_y; c) varying N_z.

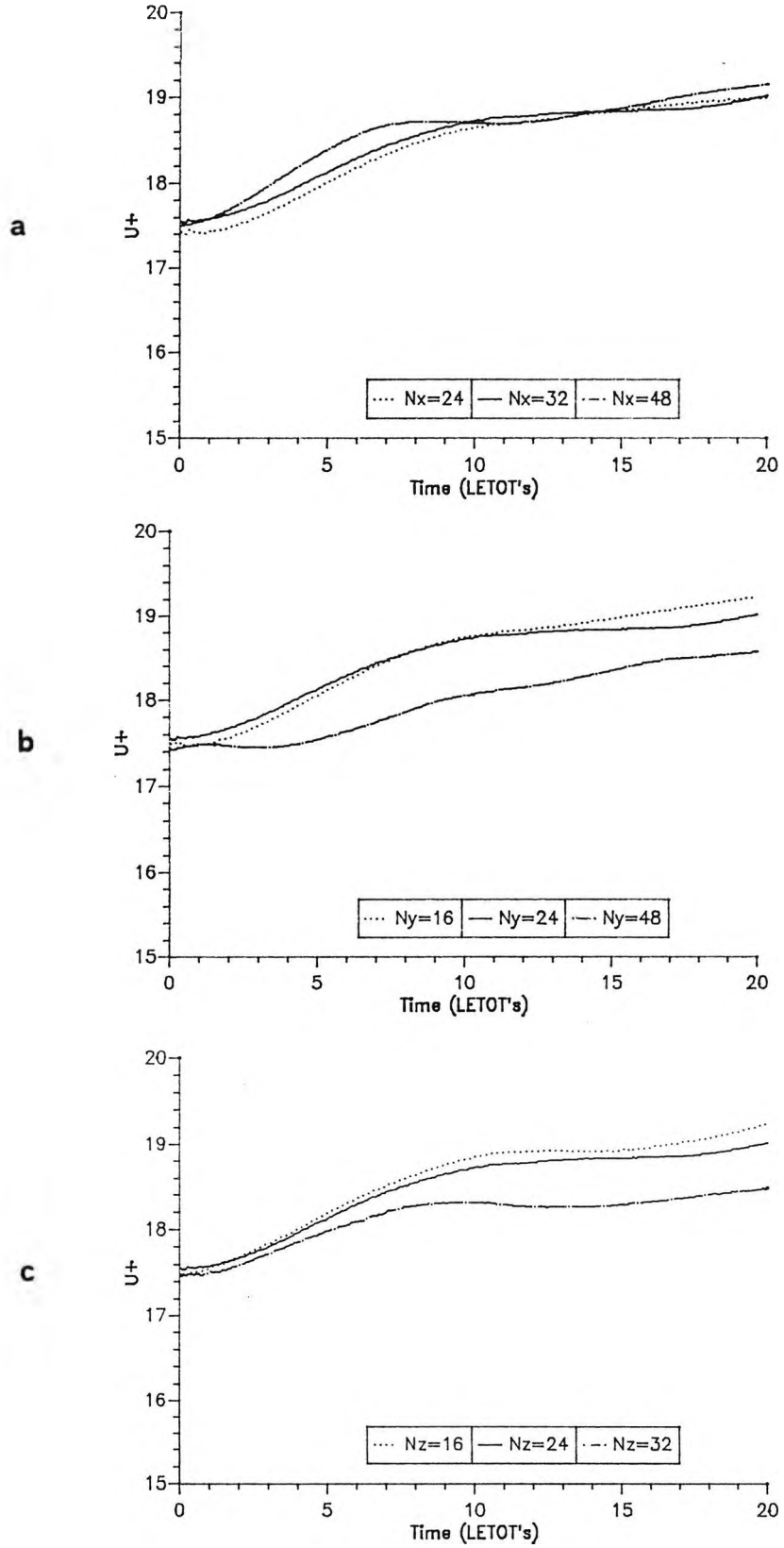
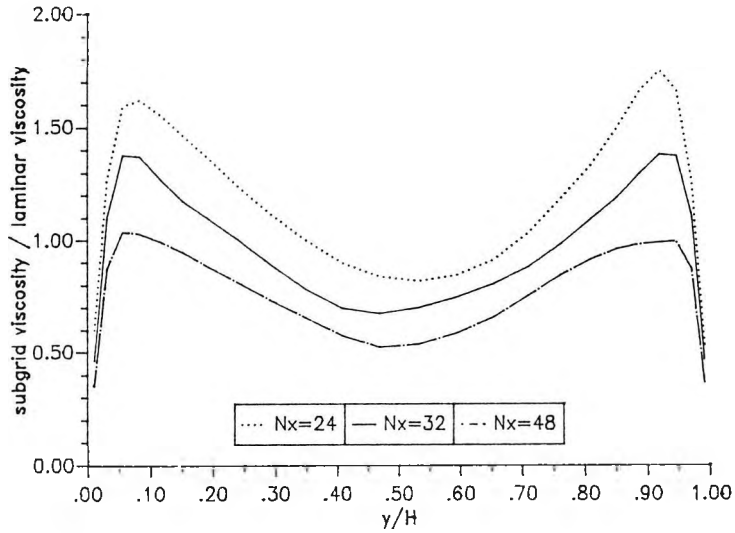
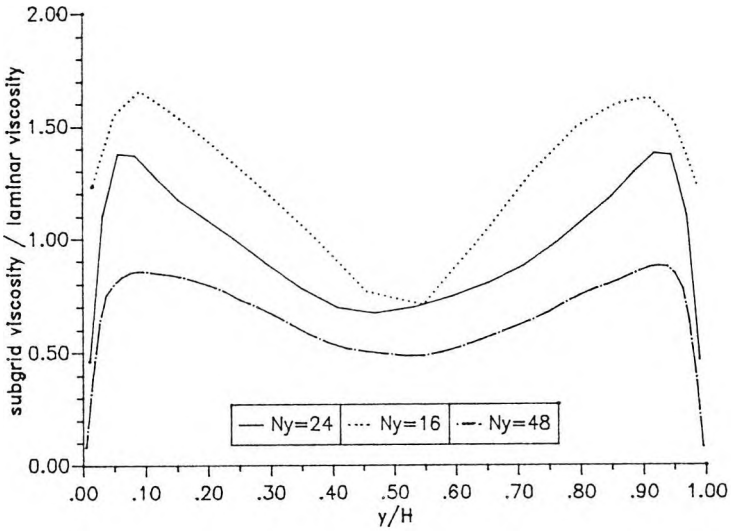


Figure 4.23 - Plane channel: influence of the computational grid.
Behaviour of the average velocity U for
a) varying N_x; b) varying N_y; c) varying N_z.

a



b



c

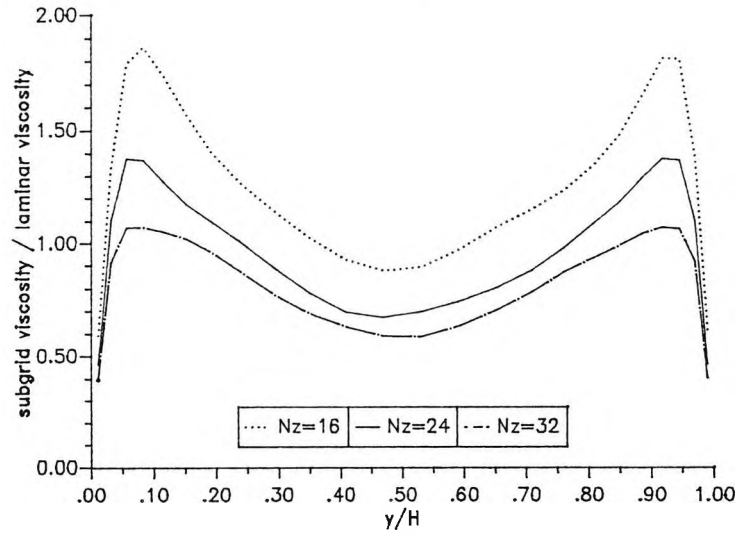


Figure 4.24 - Plane channel: influence of the computational grid. Cross-stream profiles of the subgrid viscosity $\overline{<\nu_s>}$ for a) varying N_x; b) varying N_y; c) varying N_z.

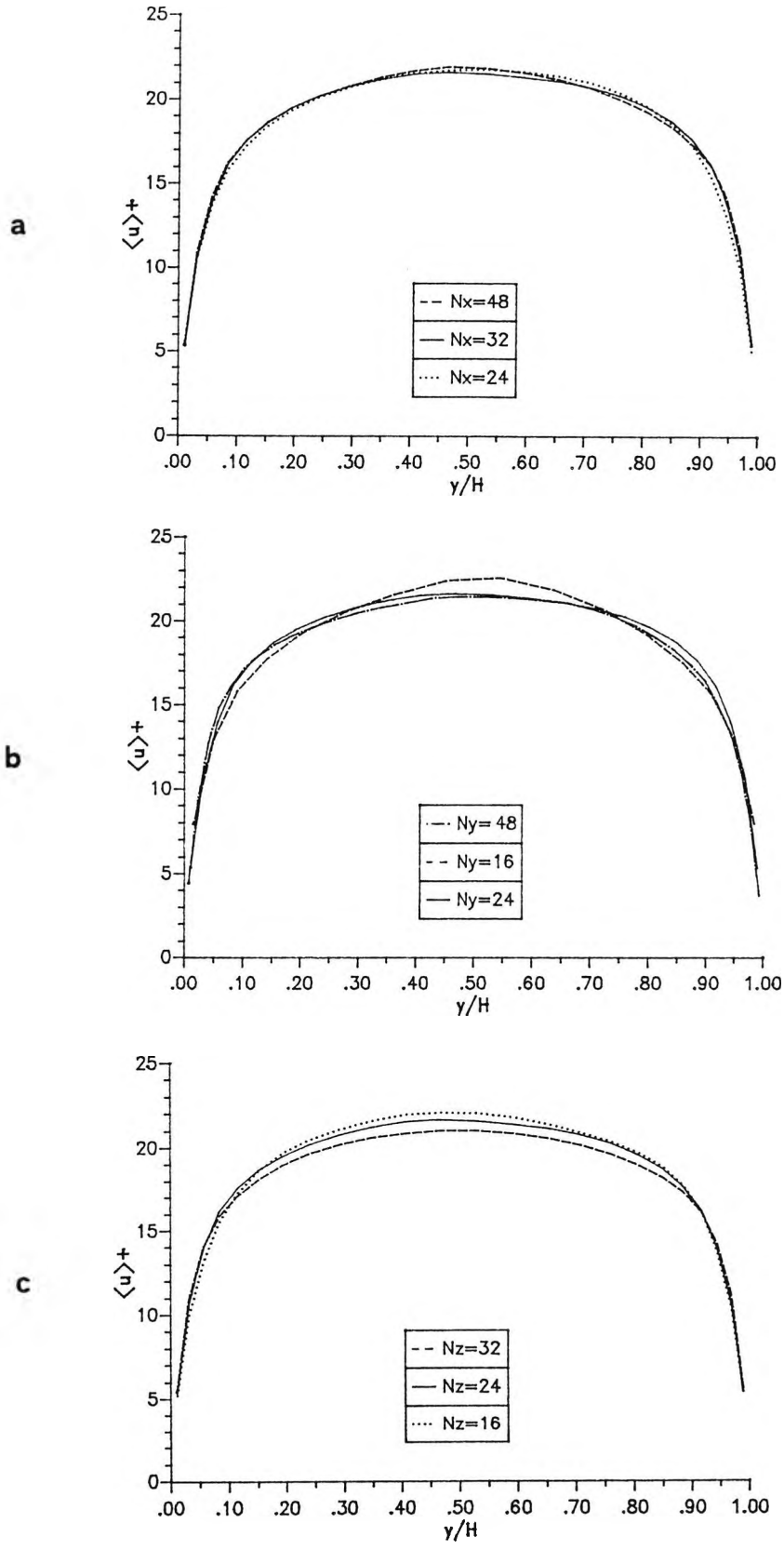


Figure 4.25 - Plane channel: influence of the computational grid. Cross-stream profiles of the mean velocity $\overline{\langle u \rangle}$ for a) varying N_x; b) varying N_y; c) varying N_z.

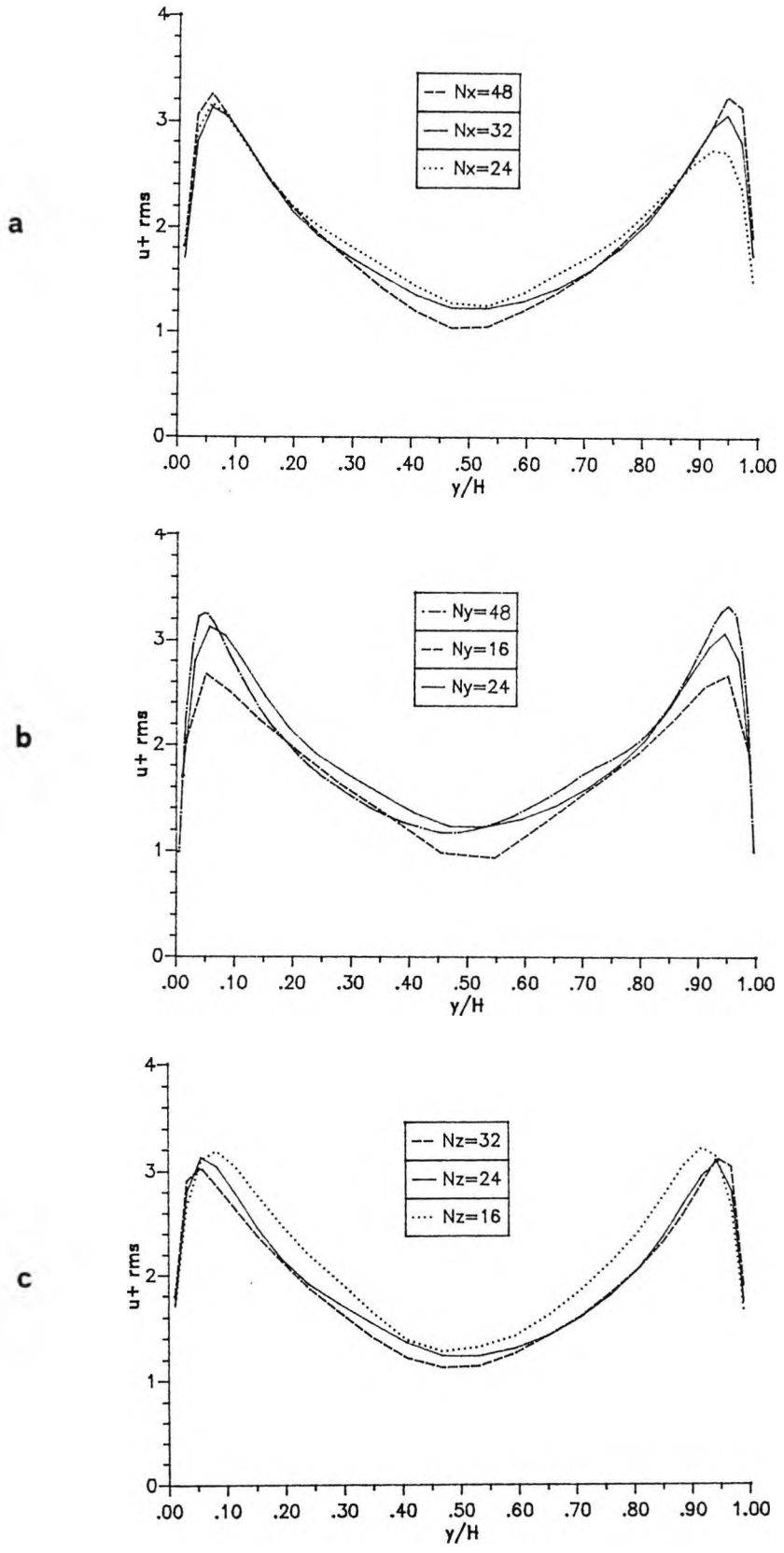


Figure 4.26 - Plane channel: influence of the computational grid. Cross-stream profiles of the streamwise fluctuation $\overline{u_{rms}}$ for a) varying N_x; b) varying N_y; c) varying N_z.

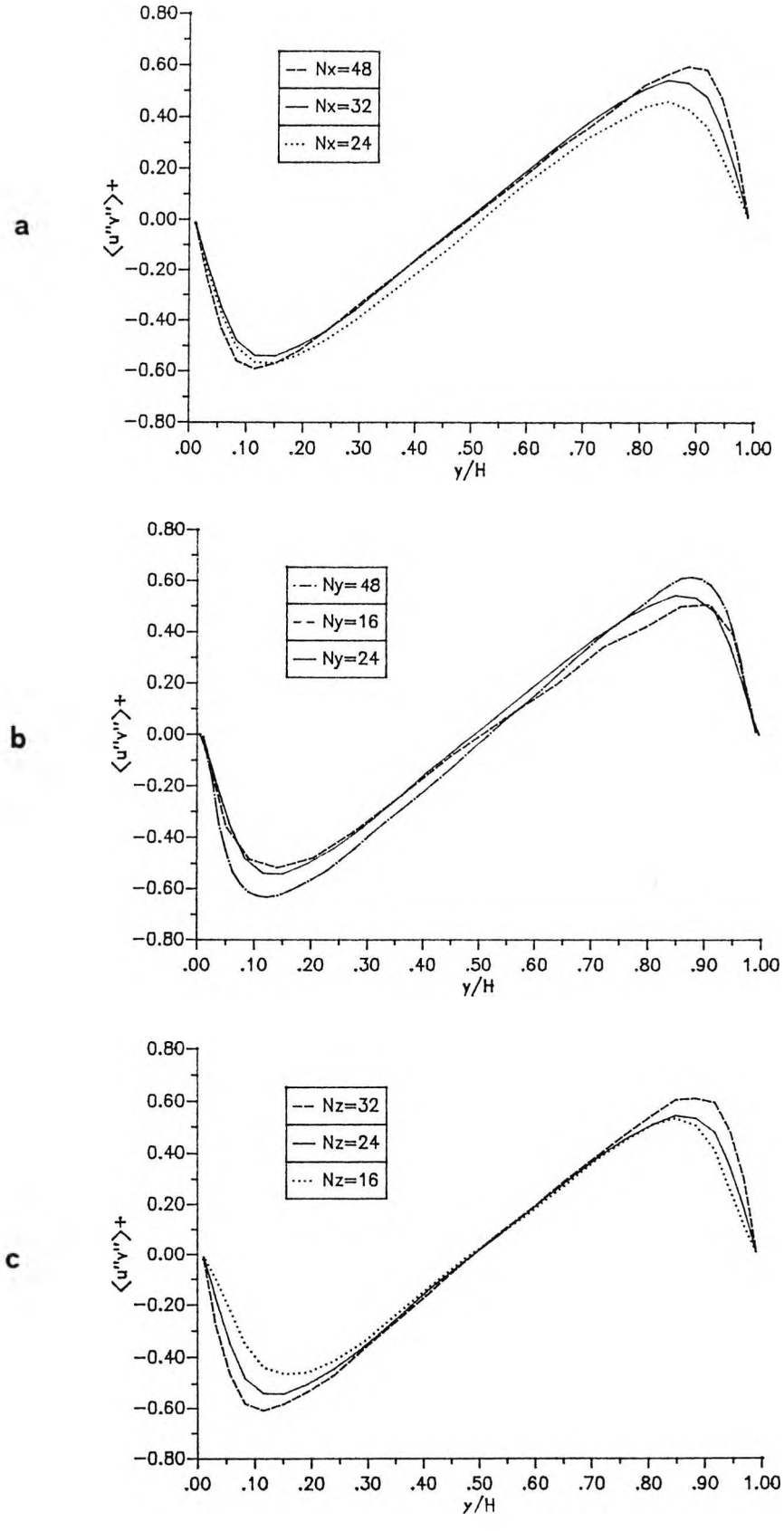


Figure 4.27 - Plane channel: influence of the computational grid. Cross-stream profiles of the Reynolds stress $\overline{\langle u''v'' \rangle}$ for a) varying N_x; b) varying N_y; c) varying N_z.

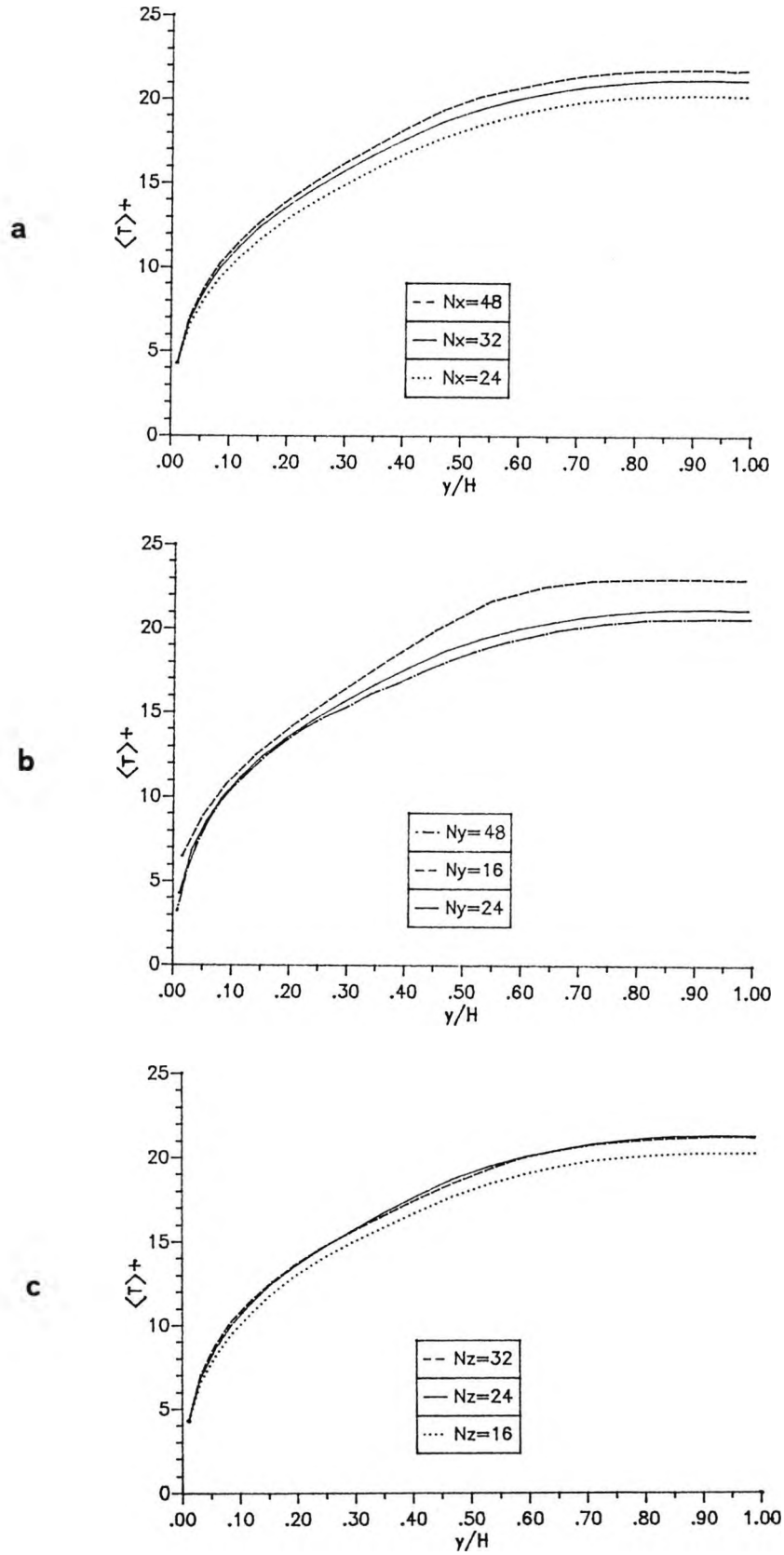


Figure 4.28 - Plane channel: influence of the computational grid. Cross-stream profiles of the mean temperature $\overline{\langle T \rangle}$ for a) varying N_x; b) varying N_y; c) varying N_z.

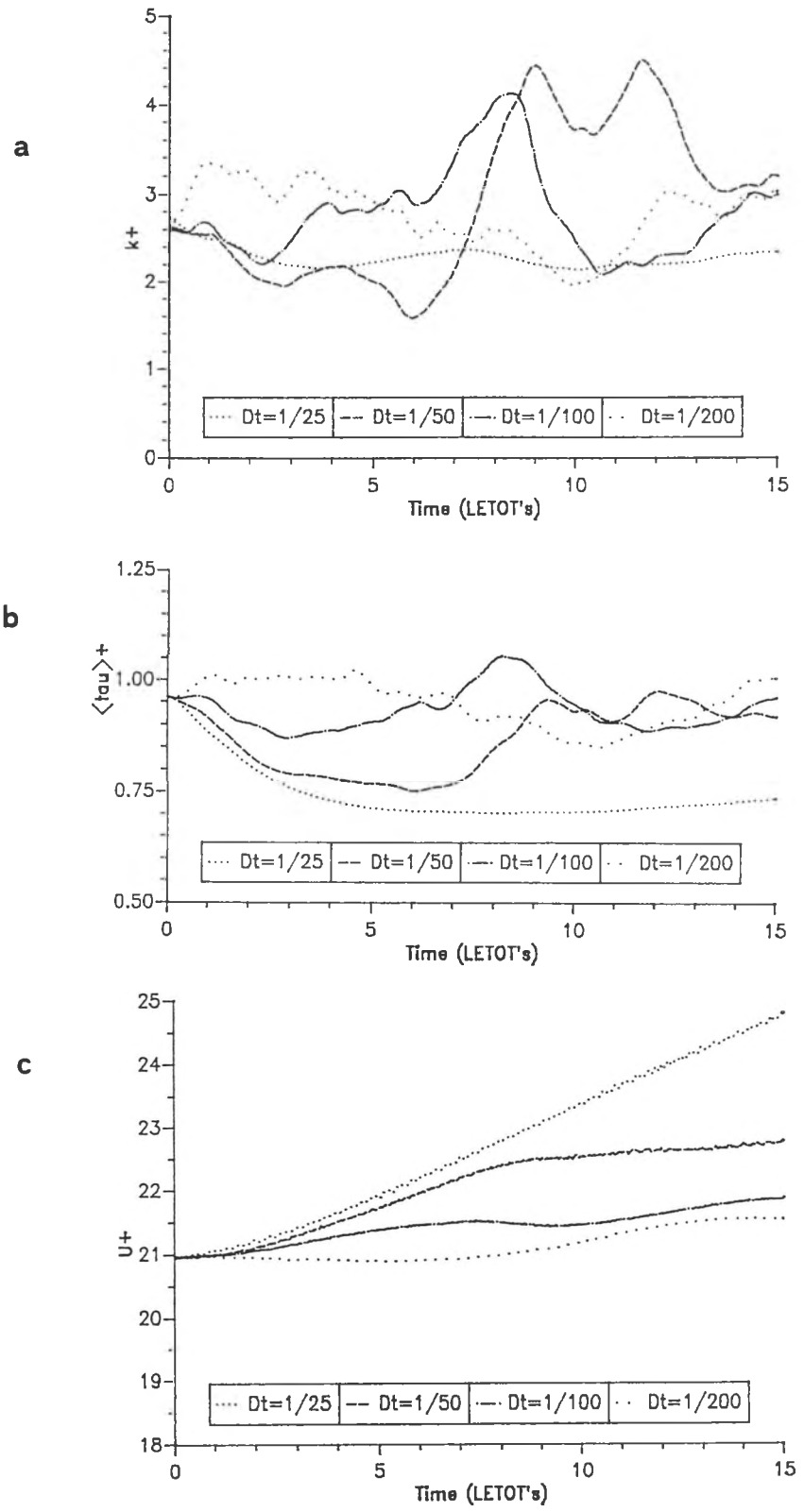
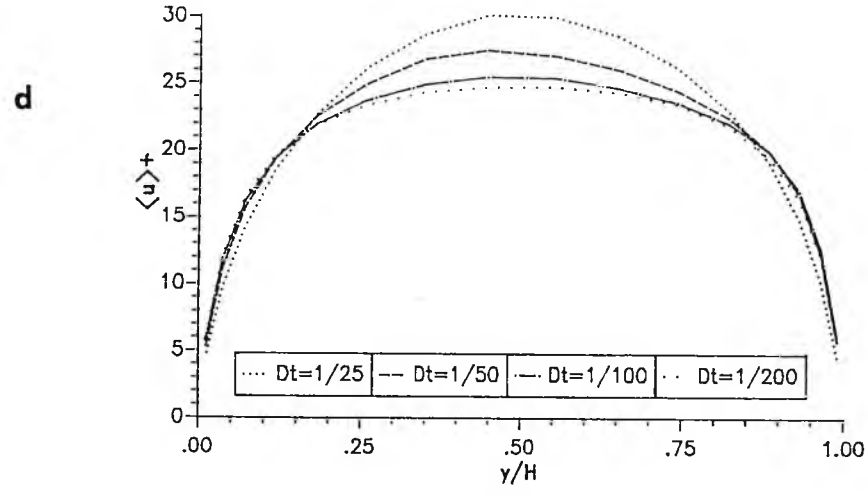


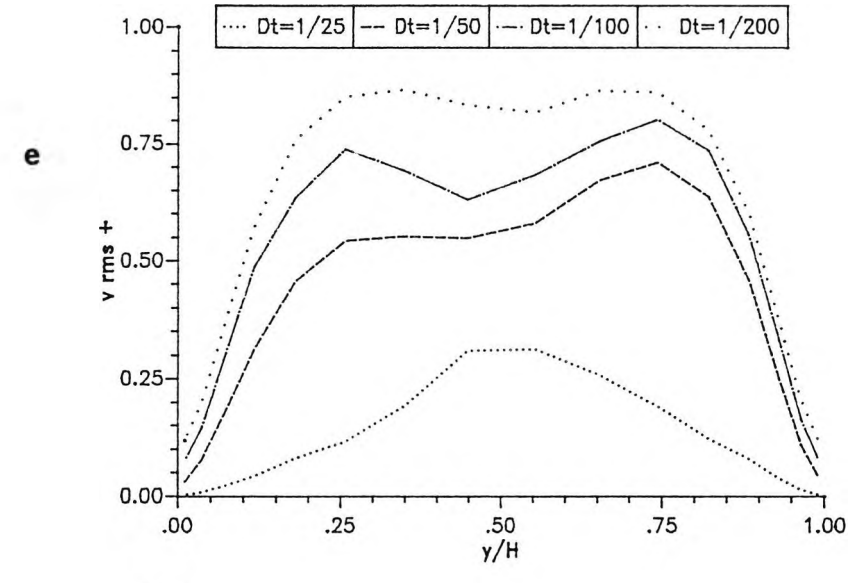
Figure 4.29 - Plane channel: influence of the time step.

a) behaviour of the average resolved turbulence energy k

b) behaviour of the mean resolved wall shear stress <τ>

c) behaviour of the average velocity U





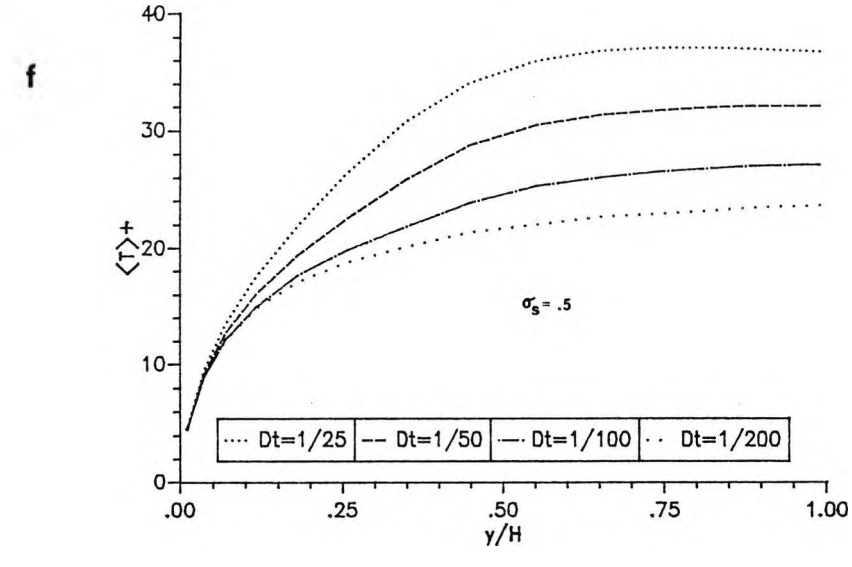


Figure 4.29 - (cont.'d)

d) cross-stream profiles of the mean velocity $\overline{\langle u \rangle}$

e) cross-stream profiles of the cross-stream fluctuation $\overline{v_{rms}}$

f) cross-stream profiles of the mean temperature $\overline{\langle T \rangle}$ for σ_s=0.5

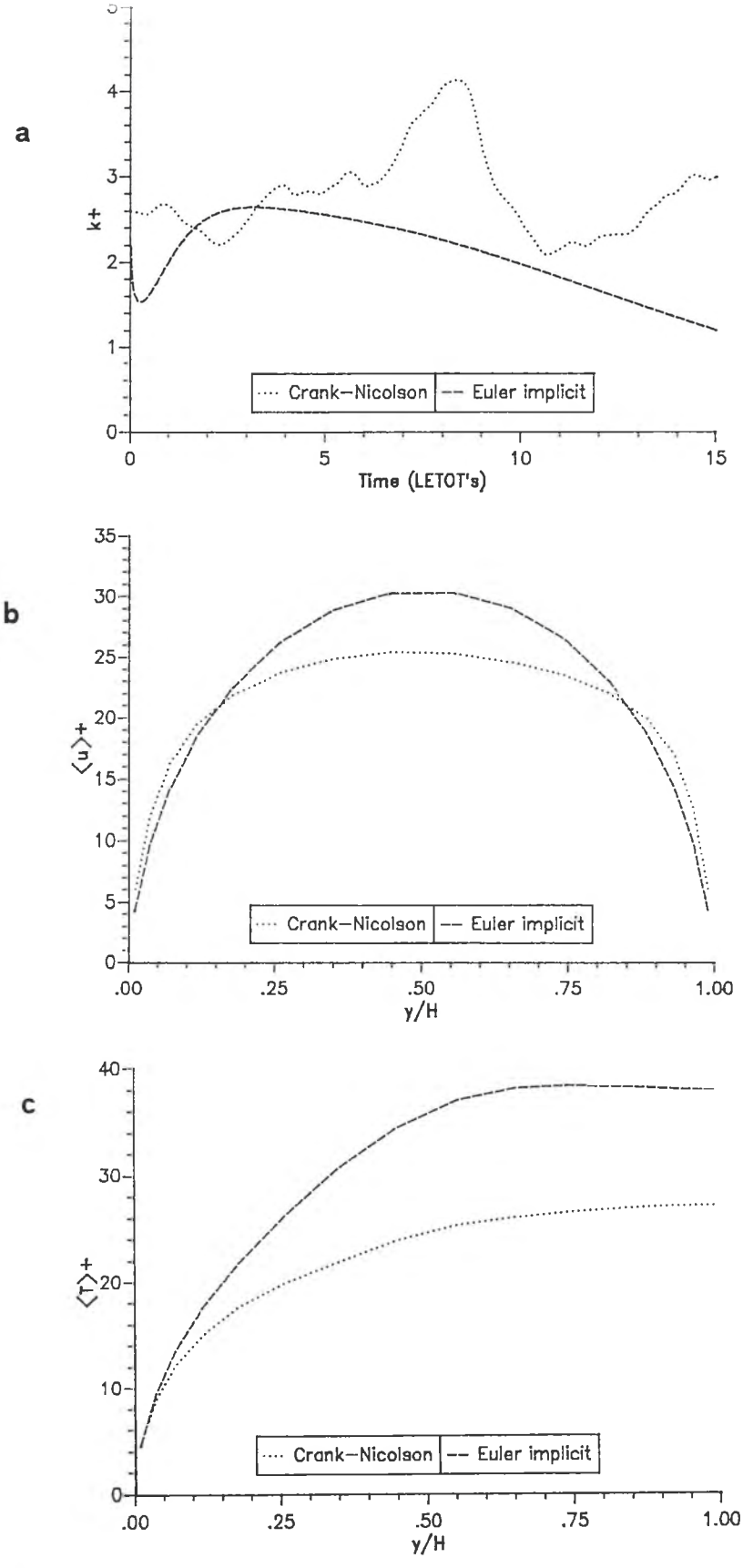


Figure 4.30 - Plane channel: comparison of time-stepping schemes.
a) behaviour of the average resolved turbulence energy k
b) cross-stream profiles of the mean velocity $\overline{\langle u \rangle}$
c) cross-stream profiles of the mean temperature $\overline{\langle T \rangle}$

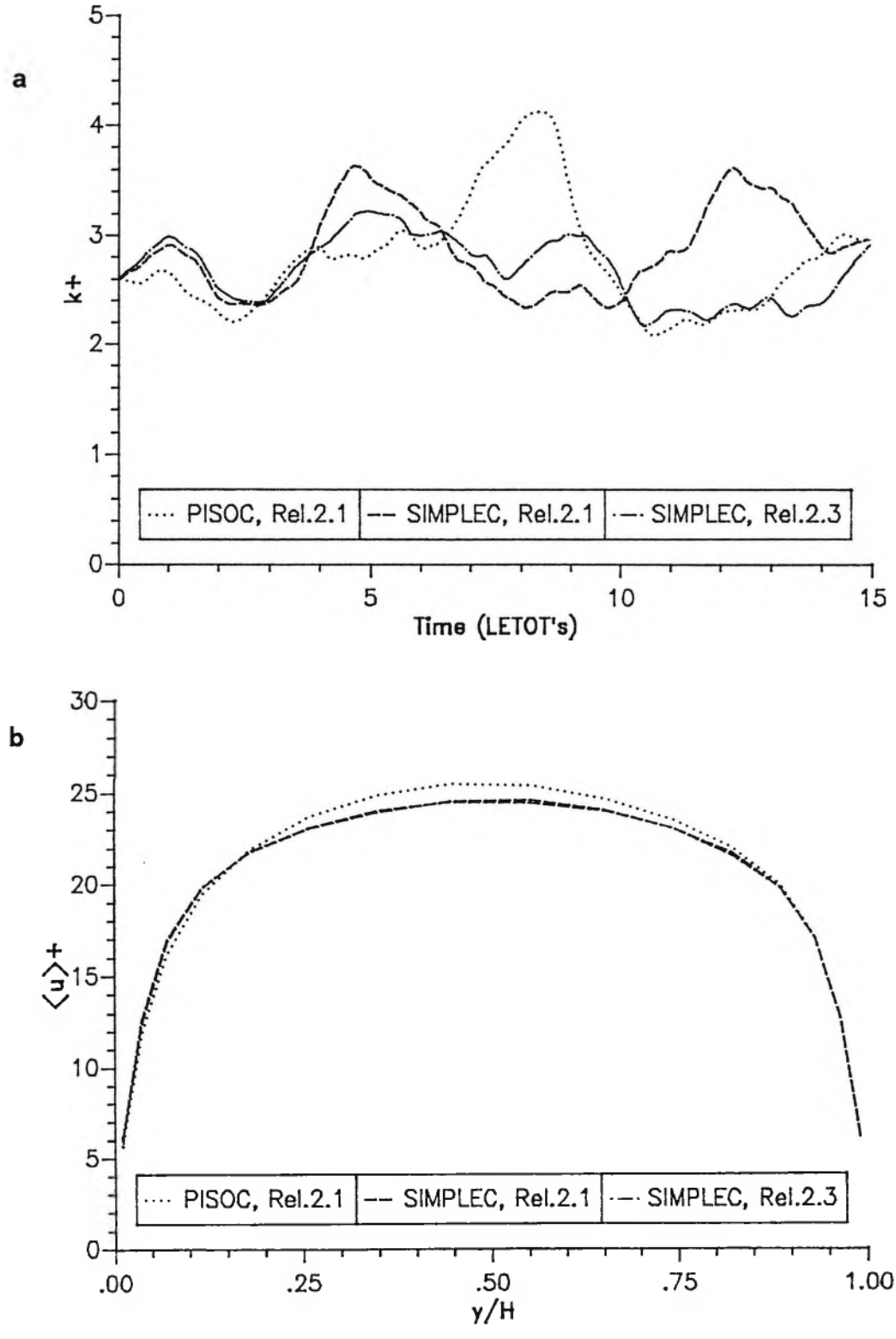
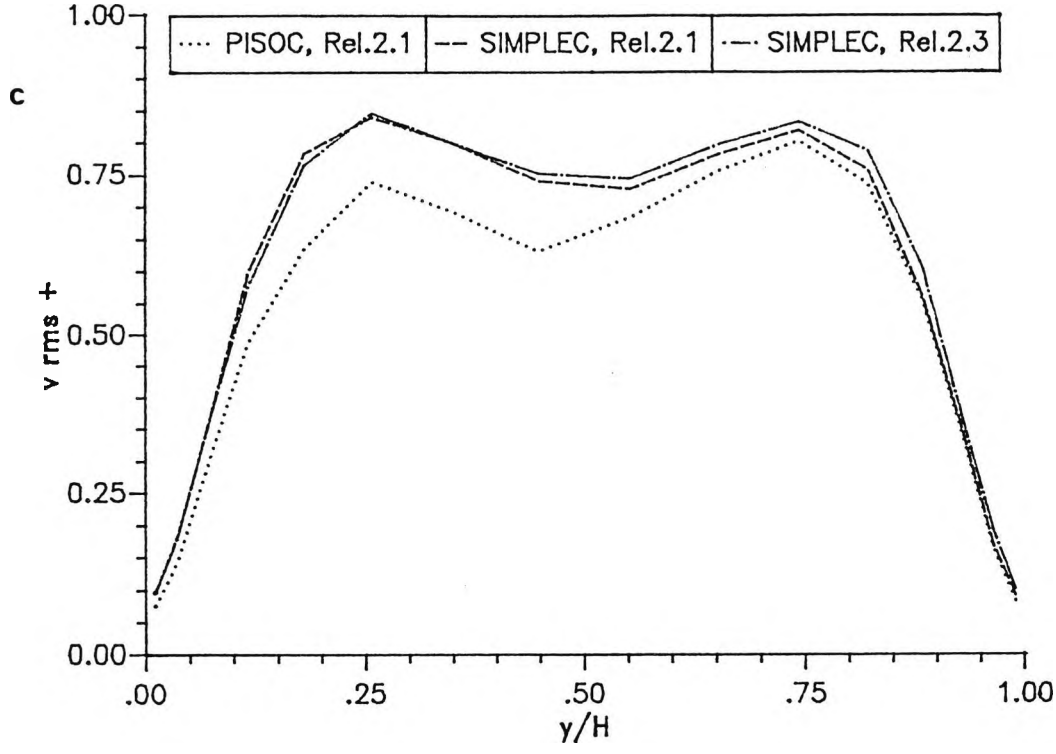


Figure 4.31 - Plane channel: comparison of pressure-velocity coupling algorithms and code releases (Re^0=20,000, 32*16*16 grid).
a) evolution of the average resolved turbulence energy k
b) cross-stream profiles of the mean velocity $\overline{\langle u \rangle}$



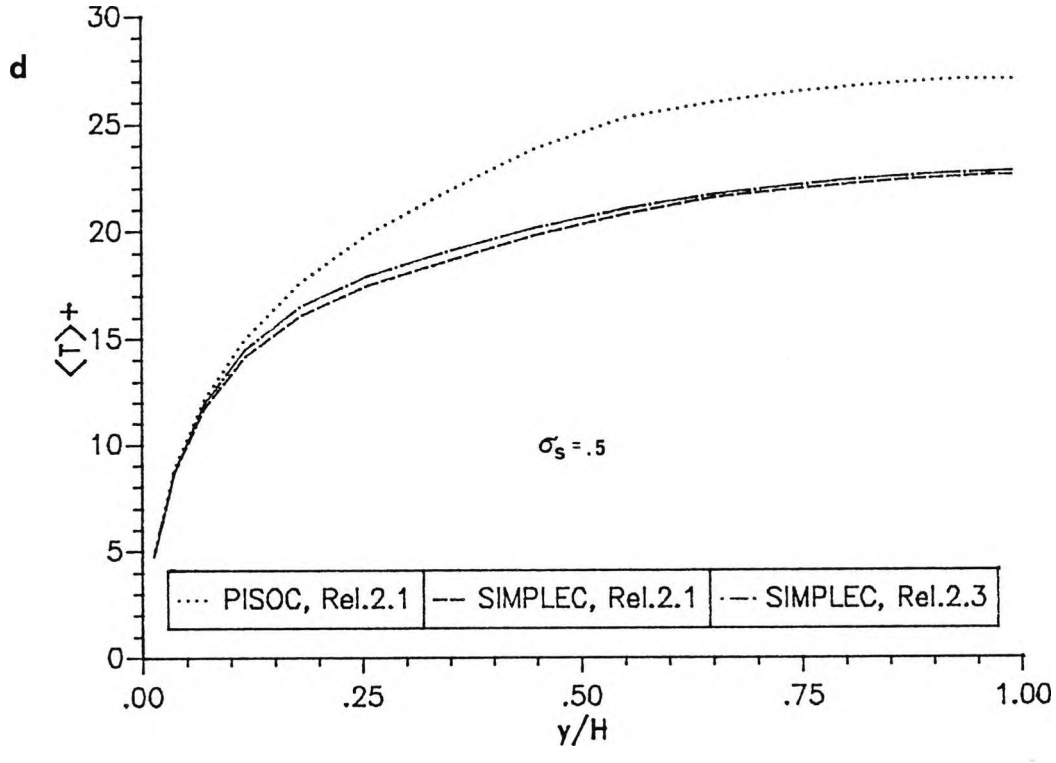


Figure 4.31 - (cont.'d)

c) cross-stream profiles of the cross-stream fluctuation $\overline{v_{rms}}$

d) cross-stream profiles of the mean temperature $\overline{\langle T \rangle}$ for σ_s=0.5

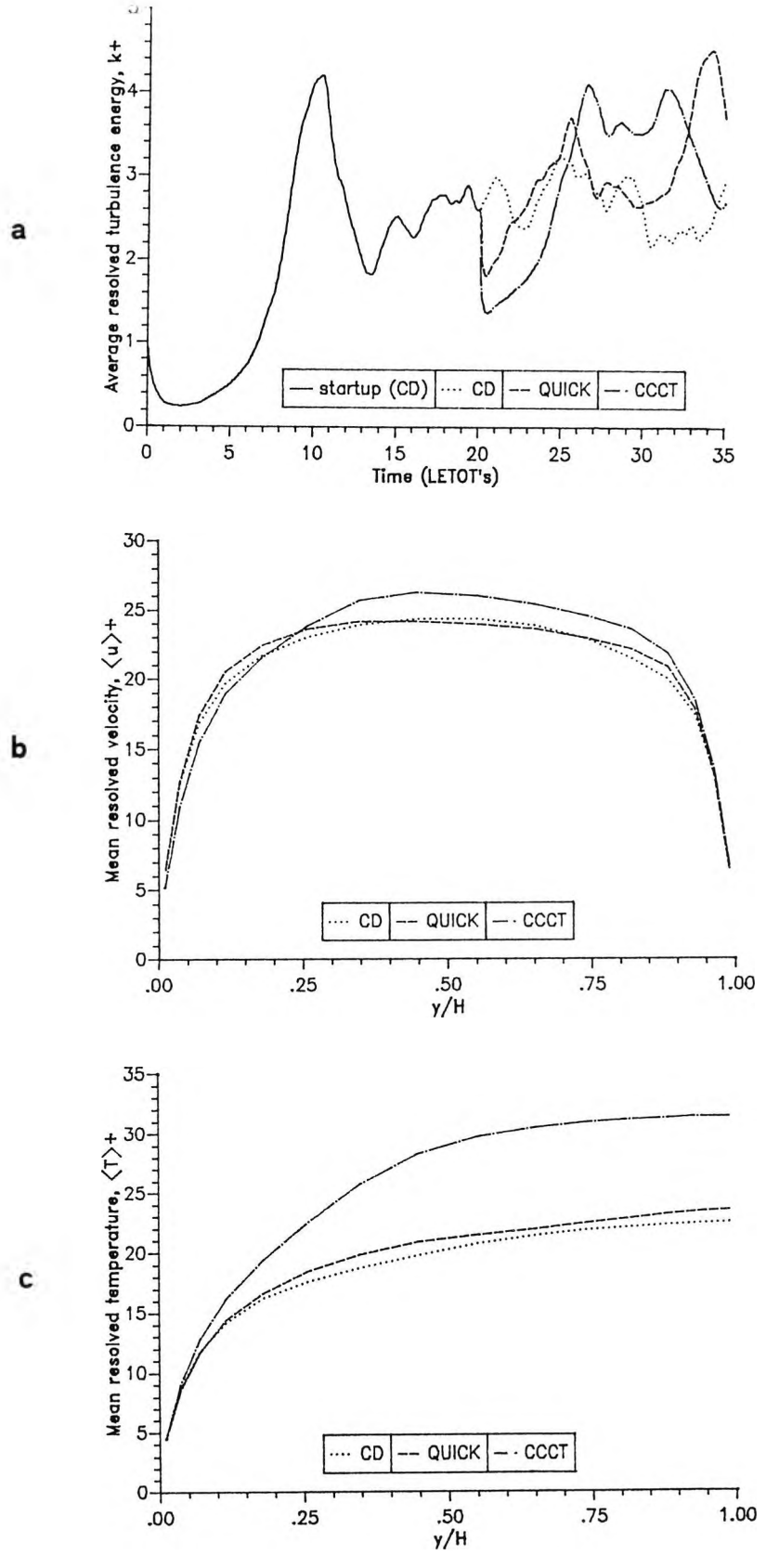


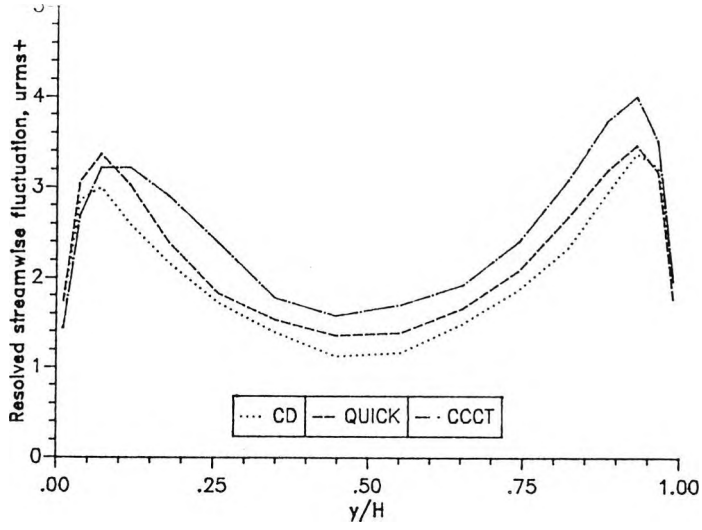
Figure 4.32 - Plane channel: influence of the discretization schemes used for the advection terms (Re^0=20,000, 32*16*16 grid, SIMPLEC).

a) behaviour of the average resolved turbulence energy k

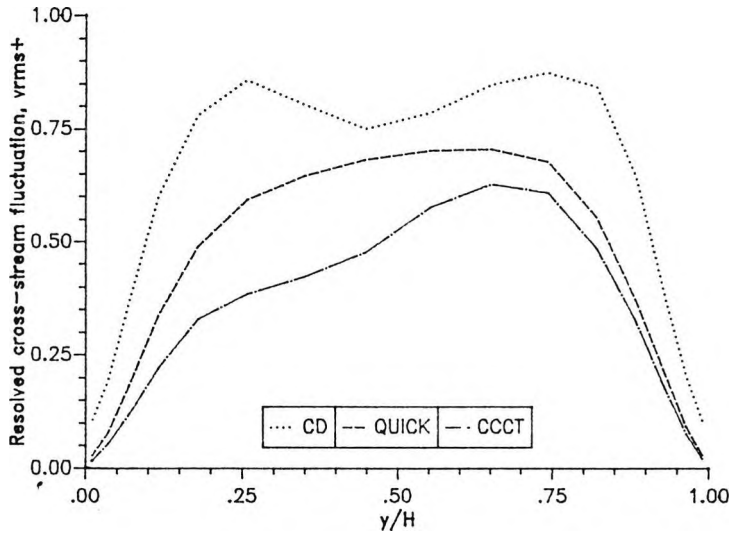
b) cross-stream profiles of the mean velocity $\overline{\langle u \rangle}$

c) cross-stream profiles of the mean temperature $\overline{\langle T \rangle}$ for σ_s=0.5

d



e



f

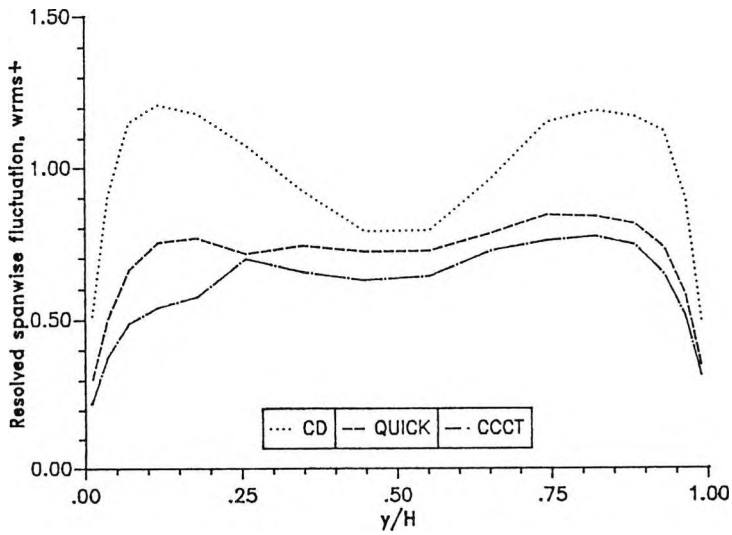


Figure 4.32 - (cont.'d)

c) cross-stream profiles of the streamwise fluctuation $\overline{u_{rms}}$

b) cross-stream profiles of the cross-stream fluctuation $\overline{v_{rms}}$

c) cross-stream profiles of the spanwise fluctuation $\overline{w_{rms}}$

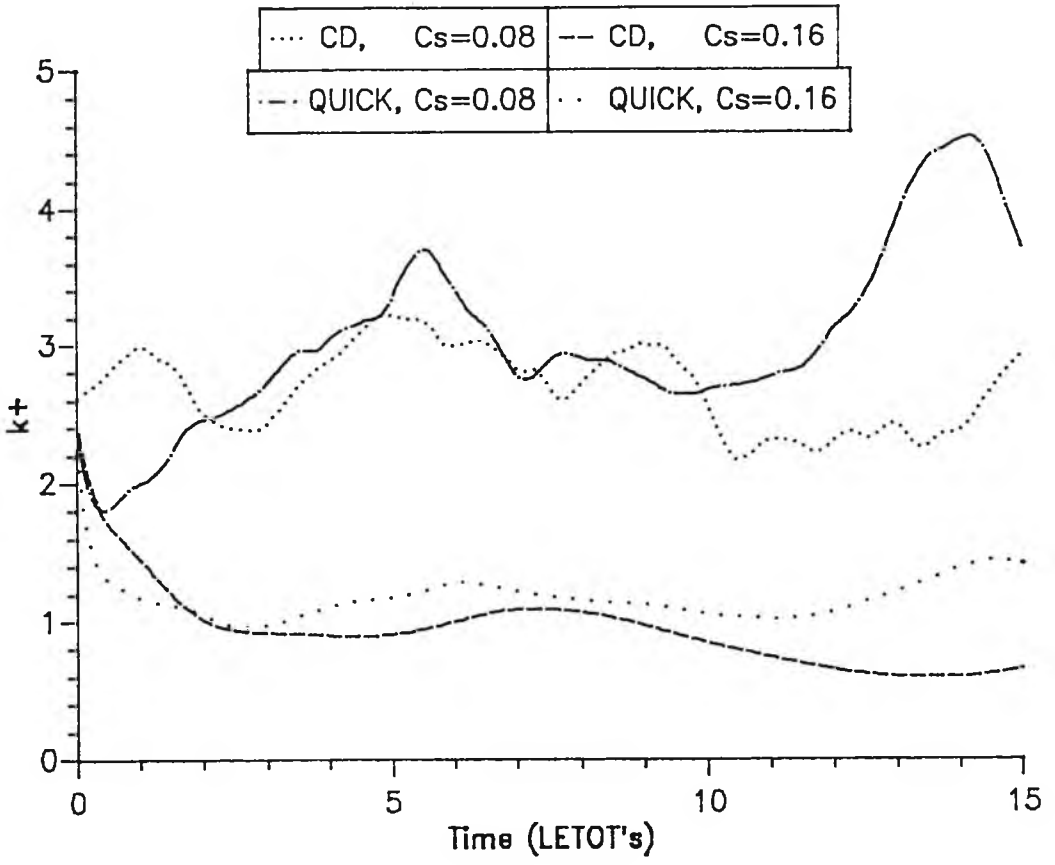


Figure 4.33 - Plane channel: time behaviour of the average resolved turbulence energy k for c_s=0.08 and 0.16 using the CDS and QUICK discretization schemes for the advection terms (Re^0=20,000, 32*16*16 grid, restart from a 20-LETOT run using CDS and c_s=0.08).

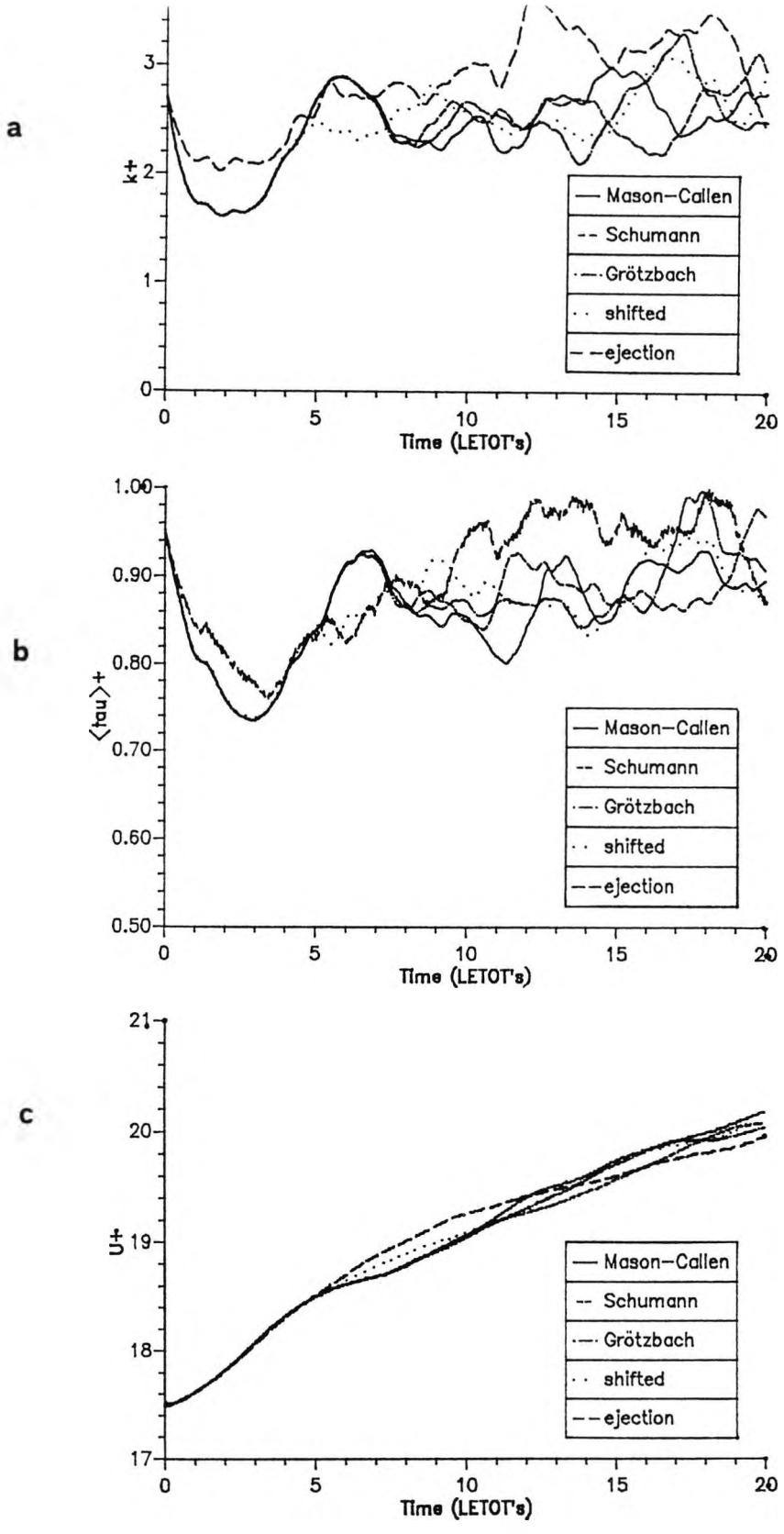
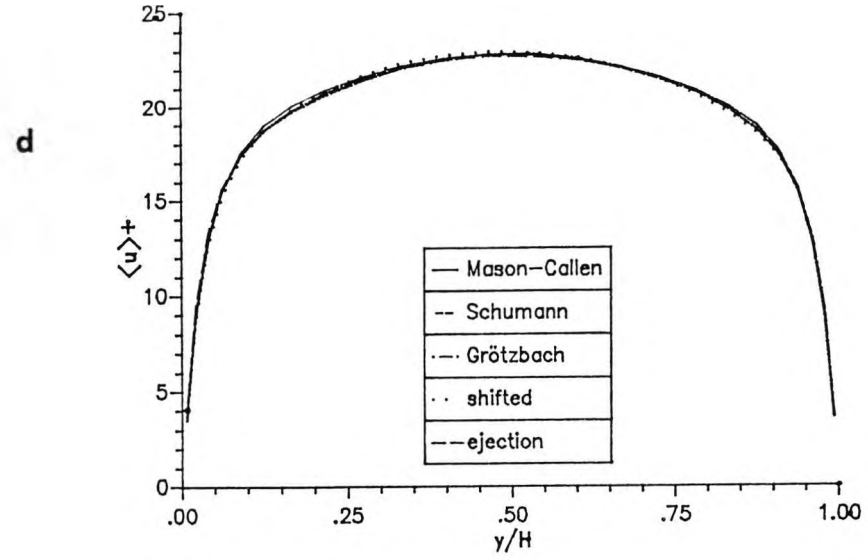


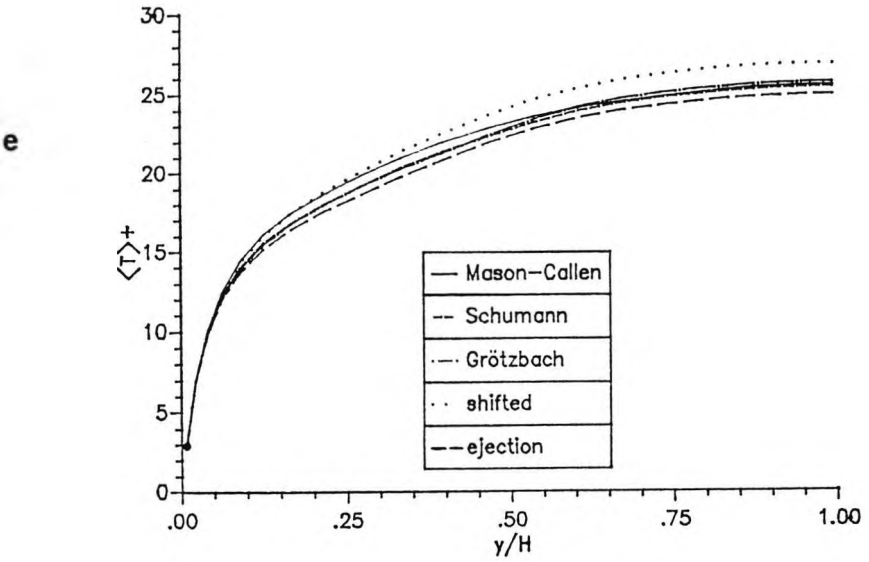
Figure 4.34 - Plane channel: comparison of different formulations of the wall boundary conditions (Re^0=20,000, 32*24*24 grid, c_s=0.08, PISOC)

a) behaviour of the average resolved turbulence energy k

b) behaviour of the mean wall shear stress <τ>

c) behaviour of the average velocity U





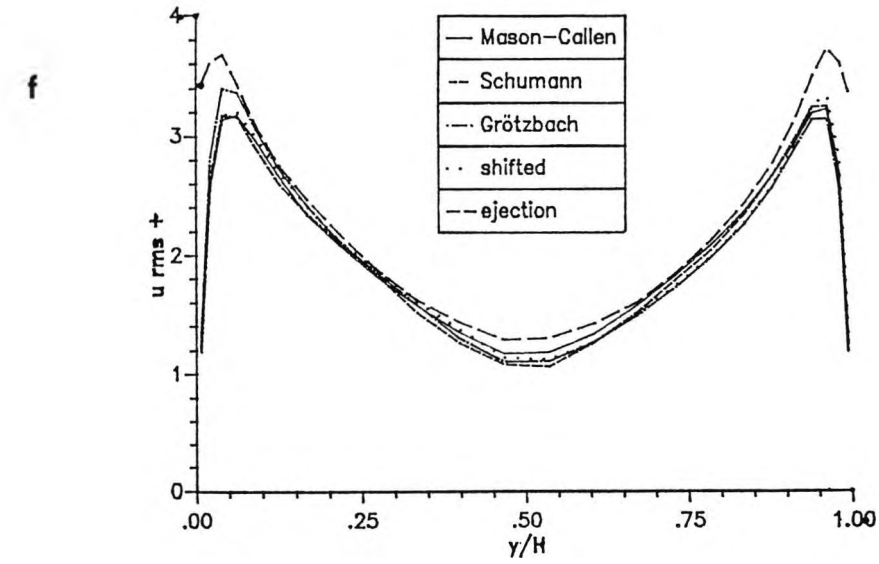


Figure 4.34 - (cont.'d)

d) cross-stream profiles of the mean velocity <u>

e) cross-stream profiles of the mean temperature <T>

f) cross-stream profiles of the streamwise fluctuation u_{rms}

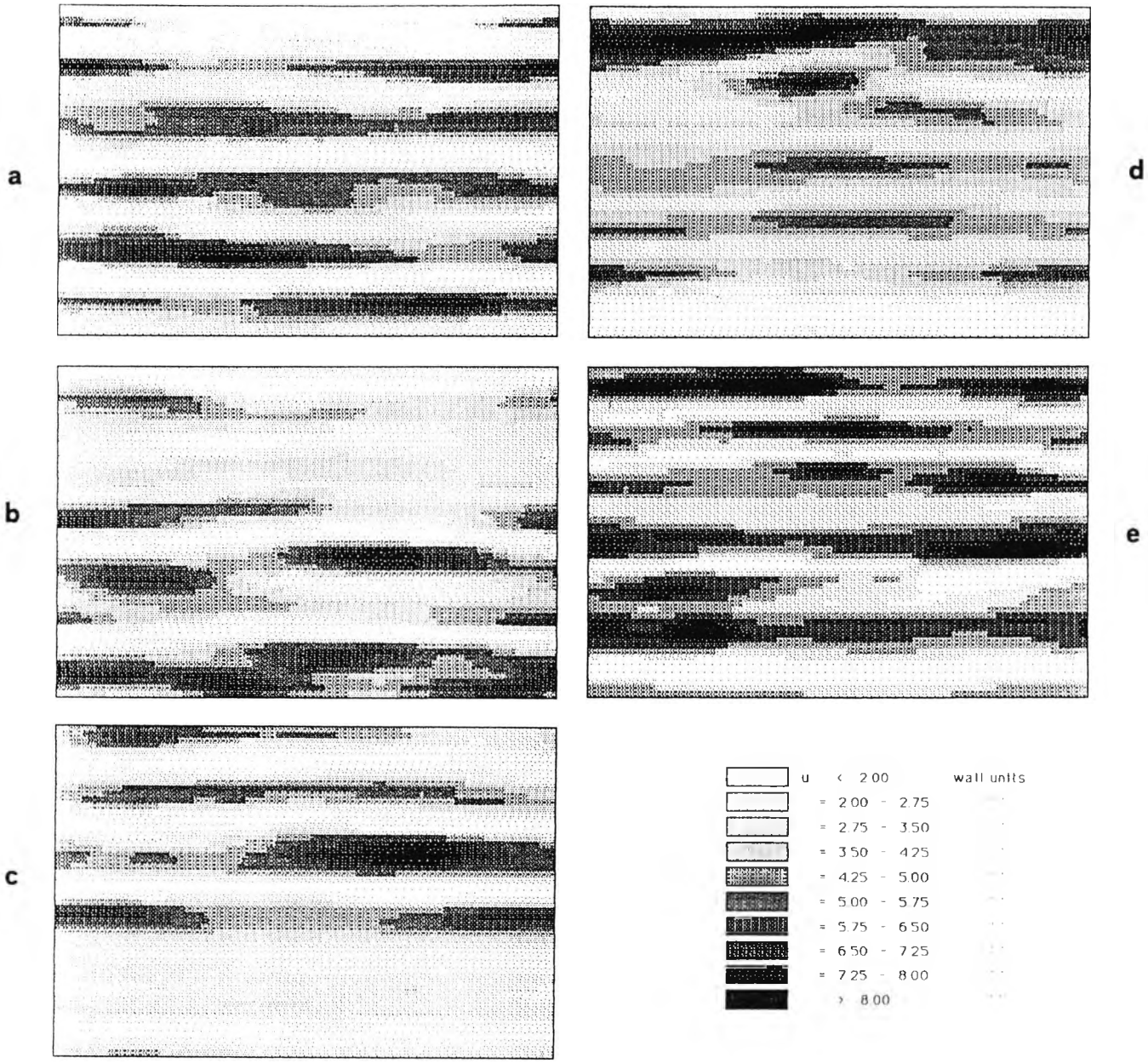


Figure 4.35 - Shade plots of the instantaneous velocity u on the plane $y^+ \cong 4$ obtained using different wall boundary conditions (low-Re case).

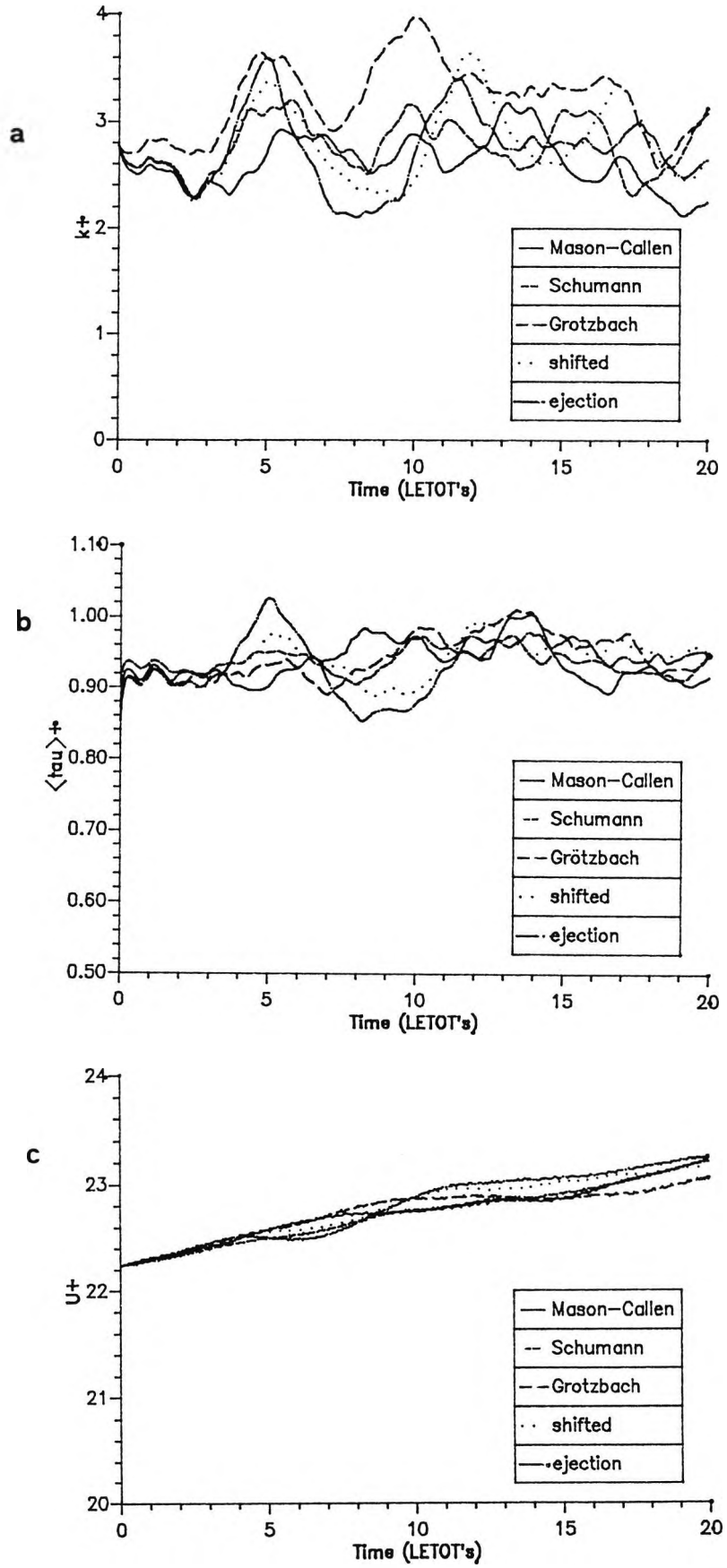


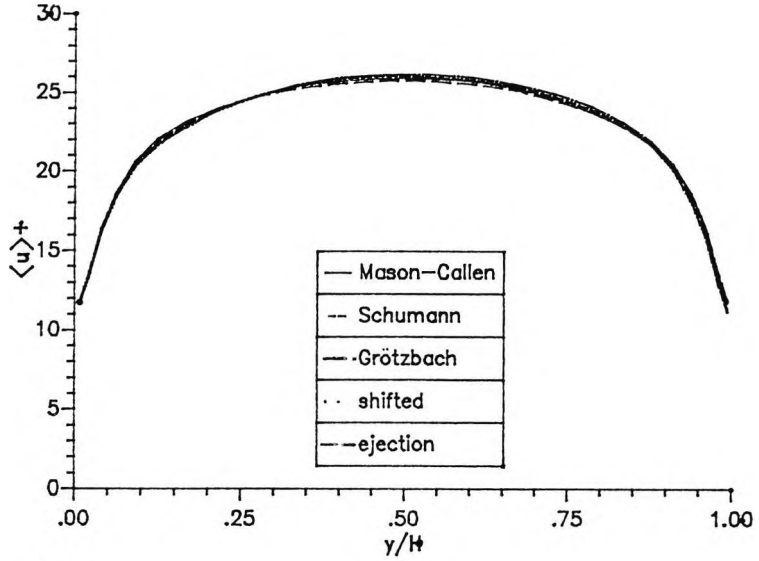
Figure 4.36 - Plane channel: comparison of different formulations of the wall boundary conditions (Re^0=100,000, 32*24*24 grid, c_s=0.08, PISOC)

a) behaviour of the average resolved turbulence energy k

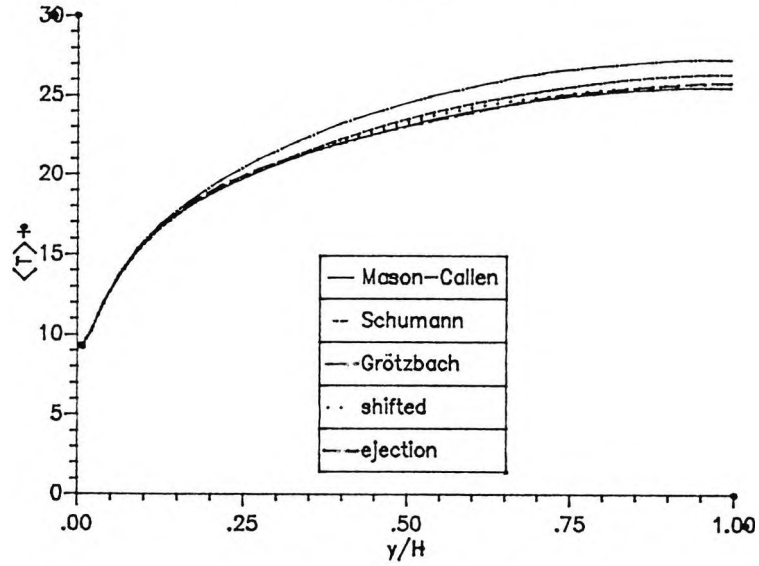
b) behaviour of the mean wall shear stress $\langle\tau\rangle$

c) behaviour of the average velocity U

d



e



f

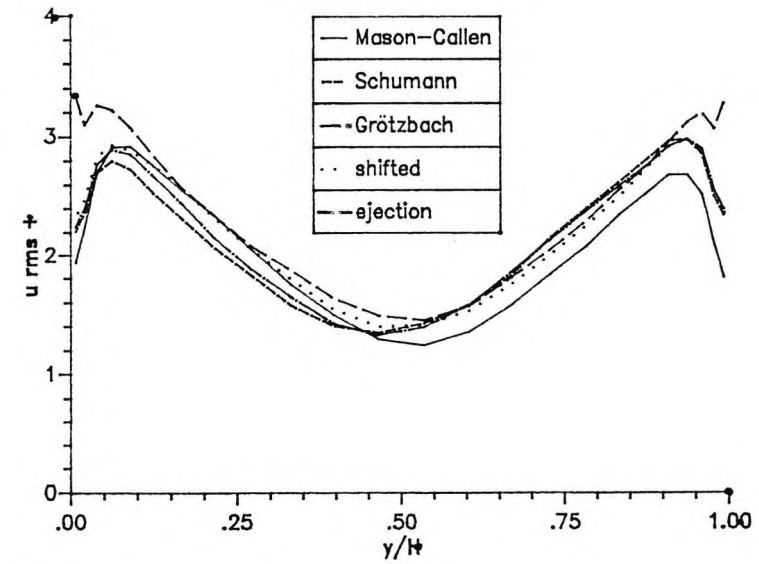


Figure 4.36 - (cont.'d)

d) cross-stream profiles of the mean velocity <u>

e) cross-stream profiles of the mean temperature <T>

f) cross-stream profiles of the streamwise fluctuation u_{rms}

THIS PAGE LEFT BLANK

CHAPTER 5 - APPLICATION TO TURBULENT FLOW WITH HEAT TRANSFER IN A RIBBED CHANNEL

5.1 Introduction and literature review

To say they err I dare not be so bold,
Although I swear it to myself alone
[Shakespeare, Sonnet CXXXI]

Turbulence promoters have been widely used in engineering to enhance heat transfer or mixing; see Nakayama [1982] for a brief review of the subject. Periodic square ribs on one wall of a plane duct can be considered as representative of a more general class of turbulence promoters; they are also a basic geometry for the study of recirculating flows with separation and reattachment, and thus have been extensively studied both experimentally and numerically.

5.1.1 Experimental results

Early experimental data on fluid flow over transverse ribs were obtained in the mid-Sixties in connection with the development of high-efficiency heat transfer surfaces for gas-cooled nuclear reactors. Mantle [1966] presented flow visualization data for air flowing over transverse ribs at different pitch-to-height ratios, P_1/h, from about 5 to 15. He found that no reattachment occurred for $P_1/h < 6.6$. Kacker [1971] measured the wall pressure distribution around ribs having $P_1/h = 7.2$ in an air flow at a Reynolds number of about 10^5, in order to estimate the increase in frictional pressure drop induced by the ribs.

Several subsequent studies focussed on a single rib protruding from one wall of a duct. Durst and Rastogi [1979] presented data obtained by Laser-Doppler Anemometry (LDA) for the mean and fluctuating streamwise velocities in a water flow at a Reynolds number of about $3.2*10^4$ over a square rib. In addition, smoke filament flow visualization results were presented. The channel blockage ratio (rib height to channel height, h/H) was very high (0.5). The authors obtained also computational results for this geometry, see next section. In a successive paper [Durst and Rastogi 1980] the same authors described also flow visualization results obtained for the air flow at a

Reynolds number of about $3*10^5$ over a rib; the channel blockage ratio, h/H, was made vary from 0.5 to almost zero. A strong inverse dependence of the reattachment length x_R on h/H was observed; it increased from 8 rib heights for h/H = 0.5 to 15 rib heights for h/H -> 0. This may be due in part to the adverse pressure gradient downstream of the rib (increasing with increasing h/H), which should cause the separated shear layer to spread thus reducing the apparent reattachment length. A second possible reason for the effect of the blockage ratio on x_R is that for low values of h/H the streamlines are strongly tilted upwards by the obstacle, so that reattachment occurs far downstream, while for higher h/H the presence of the opposite smooth wall prevents significant streamline tilting and reattachment occurs earlier. Durst and Rastogi studied also the influence of the rib aspect ratio, and found that for thin ribs (fences) the reattachment length was higher than for square ribs. The reason is again related to the slope of the streamlines separating from the leading edge of the obstacle.

Crabb et al. [1981] presented measurements of mean and fluctuating streamwise velocities and turbulence spectra obtained by combining LDA and hot-wire techniques. Data on the wall static pressure, and helium-bubble flow visualization results, were also included. The geometry was a single square rib with h/H = 1/12.8; the fluid was air, and the Reynolds number was $4.17*10^5$. The authors found a reattachment length of about 12.3 rib heights, and detected a counter-rotating corner eddy located below the main recirculation region and about 2 rib heights long. Results were also presented for a flat rib; the reattachment length was found to be shorter than for the square rib, consistent with the results of Durst and Rastogi [1980] discussed above. The authors also found a strongly anisotropic turbulence structure and commented that this could hardly be represented by eddy-viscosity turbulence models.

Finally, LDA results for various surface-mounted obstacles, including a single transverse square rib in a plane channel, were presented by Dimaczek et al. [1989].

Periodic ribs are the subject of the following papers.

Hanjalić and Launder [1972] conducted hot-wire measurements of mean and fluctuating velocities over the cross-section of a rectangular channel having one wall roughened by transverse square ribs; they also estimated the distribution of turbulent kinetic energy and dissipation rate. The Reynolds number was about $1.5*10^5$ and the working fluid was air. The main interest of the authors was in the effects of the channel asymmetry on the overall

turbulence structure, and measurements were not extended in the region close to the ribs or between them.

Humphrey [1979] and Humphrey and Whitelaw [1980] used LDA to measure mean and fluctuating streamwise and cross-stream velocities, and Reynolds stresses, for the turbulent flow of water in a square duct at a Reynolds number of $2.6*10^4$; one of the walls was roughened by tranverse square ribs of pitch-to-height ratio = 10. The blockage ratio of the channel was h/H = 0.1. The experimental technique used allowed measurements to be taken very close to the walls and to the ribs. A very strong turbulence anisotropy was observed.

Lawn [1976] presented hot-wire measurements for the air flow over transverse square ribs having $P_1/h = 7.2$. The Reynolds number was $2.3*10^5$. Data included mean and fluctuating streamwise velocities, estimates of the turbulent kinetic energy distribution, full-field pressure distribution, and wall shear stress. The blockage ratio of the wind tunnel was very small (about 1/25). Lawn found a reattachment length (size of the main recirculation bubble downstream of each rib) as low as 2.3 rib heights; flow re-separation occurred about one rib height upstream of the next rib.

Drain and Martin [1985] studied the flow of water in a flat rectangular duct having periodic square ribs with $P_1/h = 7.2$ and h/H = 1/5. The Reynolds number was $5.7*10^4$. LDA was used to measure mean and fluctuating streamwise and cross-stream velocities and Reynolds stresses. The reattachment length was found to be about 4.3 rib heights. This value was much higher than that reported by Lawn (2.3). A possible reason for this broad disagreement is that Lawn's data were for a higher (about 4 times) Reynolds number; the reattachment length in related geometry, such as backsteps, is known to decrease, to a certain extent, with increasing Reynolds numbers. A second reason may be a difference in the free-stream turbulence level; reattachments lengths are known to decrease with increasing values of this quantity. However, these effects are small and cannot account entirely for a difference of almost twice. Moreover, the blockage ratio in Drain and Martin's experiments was much higher than in Lawn's, and - at least for single ribs, see above - several experimental results suggest that the reattachment length should be <u>lower</u> for higher blockage ratios. Thus, some measurement error has to be hypothesized for at least one of the data sets proposed; comparison with overall results for single and multiple ribs suggests that Lawn's reattachment length results are, for some reason, seriously defective.

Further experimental results obtained by LDA for the flow field in ribbed channels are due to Bates et al. [1983] ($P_1/h = 7.2$, h/H = 1/5, Re = $5*10^4$);

Kobayashi et al. [1985] (P_1/h = 5, h/H = 1/3.2, Re = $3.8*10^4$ to $1.6*10^5$); and Cocking and Dalzell [1984].

Heat transfer data for ribbed ducts are less numerous than fluid flow data. Early results are due to Wilkie [1966], who measured the heat transfer coefficient and the wall pressure for air flowing in a cylindrical duct having square ribs on its wall; the Reynolds number was about $2*10^5$. Two different pitch-to-height ratios (7.2 and 15) were tested; the former value gave larger enhancement of heat transfer. The Nusselt number distribution along the ribbed wall was derived from mass transfer experiments by Williams and Watts [1970]. Heat transfer and pressure drop data were obtained on an air rig by Warburton [1972].

Watts and Williams [1981] measured local heat transfer coefficients using the copper-foil technique for a pitch-to-height ratio of 7, a blockage ratio of 1/8, and Reynolds numbers ranging from $7.7*10^4$ to $1.5*10^5$. They obtained the Nusselt number profile along the entire ribbed wall (rib faces included) under fully developed thermal conditions.

Sparrow and Tao [1983] used the naphtalene sublimation technique to measure the local mass transfer coefficient in flat rectangular ducts having one of the main walls roughened by transverse obstacles of circular cross section (rods). The duct Reynolds number was made vary between 10,000 and 45,000, the rod diameter to duct height ratio, d/H, between 0.082 (1/12) and 0.164 (1/6), and the rod pitch to diameter ratio, P_1/d, between 9.15 and 36.6. For the cases closest to the conditions investigated in this study, i.e. P_1/d=9.15 and adiabatic opposite (smooth) wall, they found that the Sherwood number increased with the Reynolds number as $Re^{0.63-0.64}$ and was little affected by d/H. The friction factor decreased as $Re^{-0.3}$ (i.e., as in smooth rectangular ducts) for d/H=1/12, but only as $Re^{-0.2}$ for d/H=1/6; at a Reynolds number of 20,000 it was about 50% higher for d/H=1/6 than for d/H=1/12. These results, although derived for rods, should be applicable (at least qualitatively) also to square ribs.

Han et al. [1978] investigated the effect of square ribs on heat transfer and pressure drop in flat ducts at Reynolds numbers of 3,000 - 20,000. P_1/H varied between 5 and 20, h/H between 1/15 and 1/5; non-transverse ribs and other cross-section shapes were also studied. These results cannot be directly compared with the present simulation as the test duct had ribs on <u>both</u> the main walls. The same applies to a later investigation by Han [1984], who considered a duct of square cross section and extended the investigation to Re=10^5.

Finally, heat transfer results have been obtained at the City University of London for ribbed channels by using holographic interferometry [Lockett 1987; Lockett and Collins 1990]. The most promising feature of this technique is that real-time interferograms can be obtained and the motion of 'thermal eddies' can be recorded and analysed; this in turn may give information on the flow field and its turbulence structure. However, it must be remembered that interferometry can give only spanwise-averaged results, in which many local features of the flow and temperature fields are inevitably smoothed away or cancelled.

5.1.2 Computational results

Several predictive studies, based on conventional turbulence models (especially the two-equation k-ε model), are known for the flow and heat transfer over transverse ribs.

As regards single ribs, Durst and Rastogi [1979] compared their own measurements with computational results. They used the k-ε model, as implemented in the TEACH code, to simulate the flow in the approaching and recirculation regions, and a three-equations turbulence model, based on the boundary-layer equations and implemented in the GENMIX code, in the redevelopment region downstream of reattachment. 45 cross-stream grid points were used. Reattachment lengths were severely underpredicted compared with flow-visualization and LDA results. Heat transfer predictions were also included; however, they were not compared with experimental data. In a subsequent paper [Durst and Rastogi 1980] the same authors compared their reattachment length data with predictions based on the standard k-ε model and on modified formulations, incorporating the curvature corrections proposed by Militzer et al. [1977] and by Launder et al. [1977]. The latter allowed reattachment lengths to be correctly predicted or even slightly overpredicted, while the standard k-ε model underpredicted x_R by ~30%. The curvature-correction of Militzer et al. behaved not as well as that of Launder et al.

Periodic rib flow was computed by Wilkes et al. [1980] and Wilkes and Firth [1981] by using the standard k-ε model with wall functions and the TUFC code. The geometry was characterized by a pitch-to-height ratio of 7.2 and symmetry conditions were imposed to the flow at some distance from the ribbed wall. The Reynolds number was 10^5. Results were compared with experimental data of Kacker [1971], Hanjalic and Launder [1972], and Lawn [1976]. The most serious limitation was a severe (40%) overprediction of the pressure drop for

a given flow rate as compared with Lawn's data. Strangely enough, the reattachment-length data of Lawn were correctly reproduced; however, as discussed above, these are somewhat contradictory with respect to the generality of results for this geometry, so that some underprediction inherent in the k-ε simulations of Wilkes probably compensated for an equivalent underestimate of x_R in Lawn's data.

Heat transfer predictions for the same geometry and Reynolds number were presented by Wilkes in a following paper [1981]. Experimental data of Watts and Williams [1981] for the Nusselt number were underpredicted by about 40% on the average. Also, the fine details of the streamwise Nusselt number profile were not correctly reproduced; the k-ε model yielded an almost flat Nusselt number over the whole inter-rib region. Some improvement in pressure drop and Nusselt number predictions was obtained by using the near-wall model of Chieng and Launder [1980] instead of the standard near-wall treatment employed in the TEACH and TUFC codes. Computations were also repeated simulating the heat conduction in the solid wall instead of imposing the wall heat flux; "hot-spots" disappeared but general levels of the Nusselt number did not change appreciably.

Flow and heat transfer predictions for the pitch to height ratio 7.2 were obtained also by Fodemski [1987, 1989] and Fodemski and Collins [1988.b], who used the standard k-ε model with wall functions and the finite-difference code FLOW3D, Releases 1 and 2. Apart from a different treatment of streamwise periodicity and other minor differences, both the method and the results were comparable with those of the above mentioned studies by Wilkes and Wilkes and Firth. However, relatively lower Reynolds numbers (10^4-10^5) were investigated, and three-dimensional simulations, using 53*59*10 grid points, were also presented. Results were compared, but only qualitatively, with experimental heat transfer data based on holographic interferometry [Lockett 1987].

Further k-ε simulations of the flow and heat transfer over periodic ribs were presented by Gosman et al. [1979] for an axisymmetric geometry. They used the TEACH code and compared predictions with experimental data of Mantle [1966] and Wilkie [1966]. The reattachment length, as usual, was underpredicted, and computations indicated a maximum of the average Nusselt number for a pitch-to-height ratio of about 4, against the widely accepted experimental value of 7.2.

k-ε predictions were also presented by Kobayashi et al. [1985.a], and compared with large-eddy simulation results, for a pitch-to-height ratio of 5, a blockage ratio of 3.2, and Reynolds numbers in the range $3.8*10^4$ to $1.6*10^5$. A very fine grid (80*50 points) and a finite-difference, time-dependent

approach were used. However, no comparison with experimental data was provided.

As discussed in Section 2.6.2, large-eddy simulations of the flow with heat transfer over periodic transverse square ribs were presented by Kobayashi et al. [1984, 1985.b]. Direct and large-eddy simulations of the flow with heat transfer over periodic obstacles were also presented by Voke and Collins [1984.a] and by Fodemski, Voke and Collins [1986, 1987]. The latter simulations were successful only as far as the steepness of the obstacles did not exceed a certain limit; thus, no results were obtained for square ribs. An interesting aspect of these predictions was the "flapping" of the shear layer separating from the trailing rib edge, with a characteristic period of the order of one LETOT; it is still not clear, however, whether this was a "physical" or a purely numerical effect. None of the above LES studies included quantitative comparisons with experimental data. Werner and Wengle [1989] presented LES predictions for the flow over a single rib and compared their results with measurements of Dimaczek et al. [1989].

Finally, the author's own LES results for a ribbed-channel geometry have been partially presented in some previous reports and papers [Ciofalo 1989.b; Ciofalo and Collins 1989.b, 1989.c, 1992].

5.1.3 Summary and correlation of experimental results

On the basis of these studies, it is generally accepted that the best results in terms of heat transfer enhancement are obtained for values of the pitch to height ratio, P_1/h, of about 7. In this case, the highest local heat transfer rates are attained at two distinct locations, significantly both involving flow impingement or reattachment:

a) the corner between the leading edge and the top surface of each rib;
b) the region (located approximately 4-5 rib heights downstream of each rib) where the shear layer separating from the rib reattaches on the smooth surface of the wall.

The former of these peaks is generally the higher, but it interests only a small fraction of the overall heat transfer surface. The latter peak is broader and involves a larger surface, thus contributing more substantially to the mean heat transfer coefficient.

For smaller values of the pitch to height ratio a single recirculation bubble is formed in the cavity between consecutive ribs and heat transfer is impaired. On the other hand, for larger values of P_1/h the beneficial effect of the ribs is excessively "diluted" over the entire heated wall.

The dependence of pressure drop and heat transfer rates on the relative rib height was investigated by Rapier [1977] for the case $P_1/h = 7.2$. According to his correlations, with respect to a smooth channel the presence of transverse square ribs on a wall causes the friction coefficient to increase by a factor:

$$M_p = 1 + 115\ h/D_e \qquad (5.1)$$

and the average heat transfer coefficient by a factor:

$$M_T = 2.4 + 20\ h/D_e \qquad (5.2)$$

in which h is the rib height and D_e is the hydraulic diameter of the channel. As regards the dependence of the same quantities on the Reynolds number, the results of Sparrow and Tao [1983], relative to transverse rods having $P_1/d=9.1$ and moderate Reynolds numbers (10,000-45,000), suggest that in artificially roughened ducts the mean Nusselt number should increase as $Re^{0.63-0.64}$; the exponent is thus lower than that expected in a smooth channel (0.8) and close to the value (2/3) often reported for the heat transfer coefficient in reattachment regions of separated shear layers [Ciofalo and Collins 1989.a]. Also, the friction factor should vary as $Re^{-0.2}$, i.e. with the exponent typical of smooth ducts at very high Reynolds numbers.

It can be easily shown that, according to these results, the channel-averaged velocity U and temperature T in a ribbed duct, once made nondimensional according to Eqns.(4.10) as U^+ and T^+, should vary roughly as $Re^{0.1}$ and $Re^{0.25}$, respectively.

5.2 Model and methods

> **As I see it, mere aesthetics doesn't pay dividends. I should like my models to be beautifully effective, and predictive. But the real goal is the understanding of a situation.**
> [Prof. W. Taylor]

5.2.1 Computational domain and boundary conditions

The computational domain used for the final large-eddy simulations of the ribbed-channel is shown in Figure 5.1. As for the plane-channel case (Chapter 4), periodic boundary conditions are imposed along the streamwise direction (x) and the spanwise direction (z); the sizes of the box are $L = 6\delta$ streamwise, $W = 4\delta$ spanwise, and of course $H = 2\delta$ cross-stream, δ being the channel half-height. For the plane-channel case, this choice of the box size can be justified by correlation-length considerations based on experimental data. However, comparable results are not available for the ribbed geometry; thus, the choice is somewhat arbitrary and can be justified only 'a posteriori' on the basis of the computational results.

The values chosen for the pitch-to-height ratio of the ribs P_1/h, and for the blockage ratio of the channel, h/H, were 7.2 and 1/4.8, respectively. The former value, as discussed in Section 5.2, is the one of greatest engineering interest, as it has consistently been found empirically to yield the greatest enhancement of heat transfer rates. The size of the computational box is such that it includes two complete pitches; this allows direct testing of flow periodicity and improves statistics on computed quantities. A reduced computational domain, including only one rib and thus having $L = 3\delta$, was also used for grid- and Reynolds number - dependence assessment, see section 5.3.

As streamwise periodicity is imposed, the computed pressure and temperature fields cannot be the "true" ones, but periodic fields P^*, T^* related to P and T by the same Eqns. (4.4)-(4.5) valid for the plane channel case. Source terms, given by Eqns. (4.6)-(4.7), are added at the RHS of the streamwise momentum and temperature equations (4.2), (4.3).

As in the plane channel case, the pressure drop per unit length $|dp/dx|$ is imposed, while the flow rate (and thus the Reynolds number) follows as a result of the computation. The mean wall shear stress τ_o is defined by Eqn. (4.8), and the corresponding mean friction velocity u_τ can be computed as $(|\tau_o|/\rho)^{1/2}$. This can be used to define dimensionless quantities by Eqns. (4.10.a-g). However, in a ribbed channel τ_o is the mean shear stress on the

smooth wall but not on the ribbed wall. Thus, scaling y by u_τ/ν in Eqn. (4.10.a) is somewhat inappropriate, although it is the simplest available choice.

5.2.2 Initial conditions

Initial conditions are imposed much as in the plane channel case. The nominal mean (cross section - averaged) velocity u^o is determined so that the nominal Reynolds number, based on D_e (the hydraulic diameter, given by 4δ here) equals Re^0. The required pressure gradient dp/dx is determined by using Eqn.(4.11); in this, the friction coefficient C_f is expressed using the friction multiplier proposed by Rapier, Eqn.(5.1), and the correlation of Beavers et al., Eqn.(4.12), for the corresponding smooth channel. Thus:

$$C_f = (1 + 115\ h/D_e) * (0.127 * Re_D^{-0.3}) \qquad (5.3)$$

The required pressure drop turns out to be 13 times higher in the ribbed duct ($h/D_e = 1/9.6$) than in the plane channel for a given Reynolds number.

Now, the mean velocity u (along x) is set equal to u^o, and mean v and w are set equal to zero; random u, v and w fluctuations, having rms values equal to u_τ, are distributed normally in the channel in order to 'trigger' turbulence. The exact form of the initial conditions, however, has almost no influence on the flow development after some time. The initial temperature is set equal to zero throughout the channel.

5.2.3 Subgrid model, numerical methods and boundary conditions

As in the plane-channel simulations, the subgrid model used here was the Smagorinsky-Lilly model (2.103), with the Van-Driest damping function (2.102.a). The value 0.08 was used for the Smagorinsky constant c_s throughout the simulations. The subgrid Prandtl number σ_s, used in Eqn.(2.91.b) to express the subgrid thermal diffusivity α_s, was 0.25.

The algorithm PISOC was adopted for pressure-velocity coupling, and the methods ST3D and ICCG for the solution of the linearized transport and pressure-correction equations, respectively. Underrelaxation parameters, residual reduction factors etc. were as discussed for the plane-channel simulations in Chapter 4. Only Crank-Nicolson time-stepping was used.

The hydrodynamic wall boundary conditions were those described as method 'a' in Section 2.5.1 and based on the formulation by Mason and Callen [1986].

As discussed in Section 2.5, this is the only formulation among those considered which can be extended (at least formally) to general geometries including reverse-flow regions, like the present one.

However, in order to avoid introducing additional complications, only moderate Reynolds numbers (<40,000) were considered here. Thanks to selective grid refinement, the near-wall grid points (control volume centres) lay within the viscous sublayer defined by $y^+<11$ (at least as far as y^+ was computed from Eqn.(4.10.a) as in a plane channel, using the friction velocity based on the mean wall shear stress τ_0). Thus, the wall boundary conditions reduced themselves to ordinary 'no-slip' conditions, i.e. a linear profile was assumed for u and T between the wall and the first near-wall point.

The thermal boundary conditions were as follows:

a) the top wall was adiabatic;

b) on the bottom wall, a constant heat flux q was assumed on the horizontal wall between ribs, but a value q/3 on each face of a rib. Thus, the total heat input into the channel was the same as for the plane duct.

5.2.4 Grid, time step and statistics

A typical computational grid used for the ribbed channel had 48*24*24 (x*y*z) volumes. Grids were selectively refined near the walls, and uniformly spaced along z. A slice of the grid on a plane z=constant is shown in Figure 5.2. The dependence of the results on the number of grid points will be discussed in Section 5.3.

The time step was 1/100 of a LETOT (δ/u_τ); this choice is based on the experience gained from the plane channel, Chapter 4. Simulations lasted 40 LETOT's, i.e. 4000 time steps. The maximum cell Peclet number (defined as $u\Delta x/\nu$) was $\sim 10^3$ and the maximum Courant number ($u\Delta t/\Delta x$) was ~1.

Mean and fluctuating components of the (resolved) flow and temperature fields were computed by processing instantaneous fields as described for the plane-channel case. However, for any scalar Q, <Q> denotes here the space-average over the duct's span rather than over planes parallel to walls (which are not homogeneous ensembles); similarly, $Q"_{rms}$ is the root-mean-square fluctuation of Q about <Q>, etc. Apart from this, the meaning of all averaging symbols is as for the plane channel, see also Nomenclature. Note that in the ribbed channel <Q>, $Q"_{rms}$ etc. are two-dimensional fields (functions of x and y), whilst in the plane channel they are one-dimensional fields, functions of the cross-stream coordinate y only.

5.3 Results and discussion

The object of studying complex flows
is to be able to predict them
[P. Bradshaw]

5.3.1 Turbulence energy and flow rate

The behaviour of the channel-averaged resolved turbulence energy k is shown in Figure 5.3 for Re° = 20,000 (48*24*24 grid). For comparison purposes, the behaviour of k in a plane channel is also reported for the same size of the computational box and a 32*16*16 grid.

For the ribbed channel, the low-turbulence phase is much shorter than for the plane channel (~1 LETOT), no overshoot occurs, and an asymptotic behaviour is established after a few LETOT's.

The instantaneous Reynolds number increased slowly starting from the initial (nominal) value of 20,000. The exact behaviour of both k and Re was found to be sensitive to the constant c_s and to the grid used. For the ribbed channel, the final Re (LETOT's 30-40) was ~26,600, i.e. the flow rate was overpredicted by ~30% with respect to correlation (5.3). The corresponding δ-Reynolds number was ~6650.

5.3.2 Grid dependence

For the ribbed channel, the investigation of grid-dependence was more difficult than for the smooth channel. The 48*24*24 grid shown in Figure 5.2 is close to the upper limits allowed by CPU time and storage (the CRAY-2 at Harwell would have allowed, in principle, grids having up to ~10^6 volumes, but only a limited CPU-time budget was available on it; on the other hand, on the IBM 3090 of the University of Palermo Computing Centre the time allowance was larger but only 16 Mbytes of storage were available).

Due to these limitations, the sensitivity study was conducted by varying individually the number of streamwise, cross-stream and spanwise grid points, N_x, N_y and N_z, in the range 16 to 32 for all directions, but for a "reduced" computational domain including only one complete rib pitch. The number of spanwise points, N_z, was found here to have little influence on the results in the range examined. For varying N_x and N_y, results are summarized in Figures 5.4 and 5.5, respectively; cross stream profiles of $\overline{\langle u \rangle}$ and $\overline{u''_{rms}}$, expressed

in wall units, are reported for the channel cross section midway between consecutive ribs, section A in Figure 5.2.

Figures 5.4 - 5.5 suggest that 24 cross-stream and streamwise points (per pitch) are sufficient to give a basically grid-independent flow field, including the backflow (recirculation) region downstream of a rib. An insufficient streamwise resolution (N_x=16) results in failure to predict backflow at section A, Figure 5.4(a), and in unrealistically high fluctuations near the smooth wall, Figure 5.4(b). The cross-stream resolution appears to be less critical, Figure 5.5.

Comparison between simulations for a single rib and for two consecutive ribs did not evidence any significant difference in the results. However, final simulations were run for the two-rib domain shown in Figure 5.1 in order to improve statistics and to check the existence of streamwise structures extending over more than one rib pitch.

5.3.3 Reynolds number dependence

Reynolds number - dependence was investigated in the restricted range Re° = 10,000 to 40,000, for the reasons discussed in Section 5.2.3. Results are summarized in Figure 5.6. Cross-stream profiles of $\overline{\langle u \rangle}$ and $\overline{\langle T \rangle}$, expressed in wall units using Eqns.(4.10), are shown for the section midway between consecutive ribs. It is clear that, once made dimensionless, mean fields are little influenced by the Reynolds number. Predicted values of u^+ and T^+ vary both as $Re^{0.10}$, approximately; as discussed in Section 5.1.2, experimental results suggest for these quantities a dependence as $Re^{0.10}$ and $Re^{0.25}$, respectively. Thus, the Reynolds number - dependence of pressure drop is correctly predicted, while heat transfer rates do not follow the ~2/3-law typical of recirculating flows, but rather the 0.8-law of boundary-layer and smooth-duct flows.

For the ribbed channel, an additional parameter which influences the flow and thermal fields is the blockage ratio, h/H. Due to the necessity of having an adequate cross-stream resolution in the rib region, and to limitations on the overall grid size, values of h/H significantly less than the 'reference' one (1/4.8) could not be investigated in the present study. The flow and thermal fields in the proximity of a rib, as well as the shear stress, pressure and temperature distributions on the bottom wall, should be little affected by h/H. However, it is clear that comparison with experimental results obtained for different values of this ratio has only a qualitative nature.

5.3.4 Instantaneous fields

In the following, we concentrate on results for h/H = 1/4.8, Re° = 20,000 and a 48*24*24 grid, covering two ribs. An overall view of the instantaneous (resolved) flow and temperature fields is given by Figures 5.7 to 5.10.

Figure 5.7(a) shows the instantaneous velocity field on two planes normal to the main flow direction x (sections A and B of Figure 5.2). Vectors are (v,w); some contours of u are superimposed. Figure 5.7(b) shows the instantaneous velocity field on a plane (y^+ = 11) close to the ribbed wall. Here, vectors are (u,w), and contours of v are superimposed. Large eddies rotating in the x-z plane (i.e., strong three-dimensionality of the flow) and intense backflow regions near the leading sides of the ribs, are the most apparent features.

Figure 5.8 is an instantaneous map of the shear stress on the bottom wall; black cells are those in which $\tau_w < 0$, i.e. forward (direct) flow occurs. The main reattachment regions at ~2/3 of the distance between ribs appear "patchy", which confirms the strong three-dimensionality of the flow. This feature is in qualitative agreement with the results of Werner and Wengle [1989] discussed in Section 2.6 (which, however, were for non-periodic flow over a single rib). Almost continuous black stripes downstream of each rib indicate that stable counter-rotating corner eddies occur below the main recirculation regions.

Figure 5.9 is a temperature map of the ribbed wall at the same instant, t=40 LETOT's. Here, black regions are those where the wall temperature is lower than the plane average, i.e. higher heat transfer occurs. These are concentrated both in the proximity of reattachment areas and immediately upstream of each rib.

Figure 5.10 (a,b) shows instantaneous velocity and temperature fields at t = 40 LETOT's on an arbitrary plane z = constant. Only the region near one rib is shown.

The evolution of the instantaneous flow and temperature fields can be appreciated by looking at Figures 5.11-5.13.

Figure 5.11 shows shade plots of the instantaneous resolved streamwise velocity u on the plane y^+=30 parallel to the bottom (ribbed) wall, respectively for t=40.00, 40.02, and 40.04 LETOT's. Darker regions correspond to forward flow, lighter regions to backflow. The "patchy" nature of the reattachment region, already indicated by the wall shear stress map in Figure 5.8, is confirmed by these plots.

The evolution of the resolved temperature on the same plane, and at the same time instants, is reported in Figure 5.12. Here, dark shades correspond to hot fluid (i.e., low heat transfer rates) and are localized mainly in the regions immediately downstream of each rib.

Figure 5.13 shows shade plots of the instantaneous resolved spanwise velocity w on a plane normal to the z axis, again for t=40.00, 40.02 and 40.04 LETOT's. The main recognizable structure is a region of high w, presumably associated with a large streamwise vortex having its axis at about 45° with respect to the main flow direction. The existence of such structures confirms the strong three-dimensionality of the flow.

5.3.5 Effects of space/time averaging

The effect of spanwise-averaging and time-averaging on the predicted temperature field is shown in Figure 5.14 (a-c). The top graph (a) is a shade-plot of the temperature field on the plane z = W/2 at the instant t = 40 LETOT's; some isotherms are depicted for purposes of clarity, and large irregular thermal structures are clearly visible. The central graph (b) is a plot of the spanwise-averaged field at the same instant; large thermal eddies present in graph (a) have been smoothed away by spanwise-averaging. Similar isotherm patterns are recorded by taking interferograms, which inevitably average the temperature field over the channel span [Lockett and Collins 1990]. The problem of extracting information about the flow structure from similar interferograms, taken in real time, was discussed in Chapter 4 for the case of plane-channel flow, and can be introduced for this more complex configuration; LES methods are a promising approach to the solution of such problems. Finally, graph (c) (bottom) is averaged in time over LETOT's 30 to 40. Smoothing effects are even more pronounced than in the span-averaged graph. The resulting time-averaged temperature field (or rather its span-average) is what would be recorded by long-exposure interferograms or similar techniques. Note that at the present Reynolds number of 20,000, and for the flow of air in a wind tunnel 5 cm in height, one LETOT corresponds to $5*10^{-2}$ s, i.e. the averaging time of graph (c) would correspond to just 0.5 seconds of real time.

The effect of averaging on the computed velocity u can be appreciated by considering Figure 5.15, in which cross-stream profiles are reported for the two section A and B of Figure 5.2. The following quantities are represented:
- local and instantaneous velocity, u, at t=40 LETOT and z=W/2;
- spanwise-averaged and instantaneous velocity, <u>, at t=40 LETOT's;

- local and time-averaged velocity, $\overline{u}$, at z=W/2 (time averages are over LETOT's 30 to 40);
- spanwise- and time-averaged velocity, $\overline{\langle u \rangle}$.

The local instantaneous velocity presents, especially at section B, an irregular profile. Spanwise-averaged profiles are smoother, but still exhibit residual irregularities (the averaging ensemble includes only 24 values). Time-averaged profiles are much more regular, and differ little from span- and time-averaged ones.

A similar comparison is shown in Figure 5.16 for the streamwise velocity fluctuation. Three quantities are shown:
- space rms fluctuation, u''_{rms}, defined as $\langle (u-\langle u \rangle)^2 \rangle^{1/2}$;
- time rms fluctuation, u'_{rms}, defined as $[\overline{(u-\bar{u})^2}]^{1/2}$;
- time-average of the space fluctuation u''_{rms} over LETOT's 30 to 40, $\overline{u''_{rms}}$.

The first quantity exhibits a rather irregular profile; its time-average, however, is remarkably close to the local, time-rms fluctuation. All profiles share some distinguished features, such as the sharp maximum observed immediately over the rib top in Figure 5.16(b).

The effect of the various averages on wall quantities can be appreciated, for example, by considering Figure 5.17. In it, the whole simulated streamwise length of the channel, including two rib pitches, is represented. The abscissa is the distance ξ travelled along the ribbed wall following the sides of the ribs; it is made dimensionless with respect to the rib height h. The quantities shown are τ_w (local instantaneous resolved streamwise wall shear stress), as computed at z = W/2 and t = 40 LETOT's; $\langle \tau_w \rangle$ (span-averaged instantaneous stress); and $\overline{\langle \tau_w \rangle}$ (span- and time-averaged stress, the time-average being made over 10 LETOT's). The local and instantaneous profile exhibits strong space fluctuations; moreover the profiles relative to the two rib pitches differ markedly from each other. Span-averaging reduces the irregularities and makes the profiles over the two pitches closer to each other. Finally, span- and time-averaging produces a smooth and periodic profile, repeating itself almost exactly over the two pitches. Similar remarks hold for the wall pressure and for the wall temperature or Nusselt number.

5.3.6 Mean wall quantities

The following Figures 5.18 to 5.20 report wall quantities ($\overline{p_w}$, $\overline{\tau_w}$ and $\overline{Nu}$). LES results are averaged at each streamwise location over the channel span, and further averaged in time over LETOT's 30 to 40. Moreover, the profiles

relative to the two rib pitches included in the computational domain are averaged to improve the statistical quality of the results. The abscissa in Figures 5.18-5.20 is defined as in Figure 5.17.

Figure 5.18 reports streamwise profiles of the wall pressure, made dimensionless with respect to $\frac{1}{2}\rho(u_{max})^2$ (in which u_{max} is the maximum velocity in the channel). The mean streamwise pressure gradient is subtracted from results, so that only the periodic component of the pressure is actually shown. The pressure is arbitrarily set to zero in the position midway between two consecutive ribs. k-ε predictions obtained by the author using Harwell - FLOW3D, and experimental data of Kacker [1971], obtained for Re = 50,000 in a channel having H/h = 8, are also reported in a similar form for comparison. Taking into account the above remarks on comparisons with different geometries and Reynolds numbers, the qualitative agreement with experimental data is encouraging, generally comparable with that obtained by the k-ε model, and much better in the region of the leading side of the rib.

Figure 5.19 shows similar profiles of the wall shear stress in the streamwise direction, $\langle\overline{\tau_w}\rangle$. k-ε results are also reported for comparison. No accurate experimental data seem to have been reported in the literature for this quantity. Values are normalized to τ_0, i.e. the mean, or nominal, wall shear stress. Values of $\langle\overline{\tau_w}^+\rangle$ differ broadly from k-ε predictions; the LES wall shear stress profile indicates that reattachment occurs about 4 rib heights downstream of each rib, and is followed by a short direct-flow region and then by re-separation ~1.5 rib heights upstream of the consecutive rib. A counter-rotating corner eddy is also clearly indicated by negative values of $\langle\tau_w\rangle$ downstream of a rib. These results, especially as regards the reattachment length, are in agreement with experimental findings for comparable pitch-to-height and blockage ratios. Drain and Martin [1985] reported a reattachment length of 4.3 h for $P_1/h = 7.2$, $h/H = 1/5$ (practically coincident with the values used in the simulation). k-ε computations underpredict severely this important parameter, giving ~3h in the present case.

Figure 5.20 shows span- and time-averaged profiles of the Nusselt number, defined here as:

$$Nu = \frac{q}{T_w - T_a} \frac{D_e}{\lambda} \qquad (5.4)$$

in which T_w is the wall temperature and T_a the cross-section averaged fluid temperature. Profiles are normalized to the corresponding averaged value $\overline{Nu}_a$ to facilitate comparison with:

a) k-ε results, obtained with Harwell-FLOW3D for the same pressure drop and channel geometry;
b) experimental results of Watts and Williams [1981], obtained by the copper foil technique in a channel having h/H = 1/8 at Re = 82,000;
c) experimental results of Lockett [1987], obtained by holographic interferometry in the City University wind tunnel (having h/H = 1/9.5) at Re $\cong$ 30,000.

The LES predictions present many features that agree with experimental data, and differ from k-ε results. The overall streamwise profile of $\overline{Nu}$, with an absolute sharp maximum shortly upstream of each rib and a secondary flat maximum at 2/3 of the distance between ribs (i.e., in the reattachment region) is correctly reproduced. Note also the relative minimum shortly downstream of the rib, probably in correspondance with backflow separation (edge of a counter-rotating eddy). This graph should be compared with the instantaneous temperature map in Figure 5.9. These features are totally missing in the k-ε predicted profile, which appears practically flat over the whole inter-rib gap.

As experimental data were obtained for different ratios of rib height to duct height (h/H) and for different Reynolds numbers, the levels and the average values of the Nusselt number cannot be compared directly with LES predictions on a quantitative basis. However, some comparison can be drawn if values of Nu are scaled to the present h/H (1/4.8) and Re (26,600) by using Rapier's [1977] results in the form:

$$Nu = \text{const.} * Re^{2/3} * (2.4 + 10\ h/H) \qquad (5.5)$$

k-ε results for Nu can be scaled using the same law; in fact, k-ε simulations (for the same pressure drop as in LES) give a Reynolds number of 21,000, in good agreement with correlation (5.3). Results are summarized in Table 5.1. It shows that, within the limits of validity of Eqn.(5.5), LES predicts a value of Nu comparable with both k-ε and experimental results.

Table 5.1 Comparison of mean Nusselt number (scaled)

	LES	k-ε	Watts & Williams [1981]	Lockett [1987]
h/H	1/4.8	1/4.8	1/8	1/9.5
Re	26,600	21,000	82,000	30,000
Nu (scaled)	154	150	140	142

5.3.7 Mean flow and temperature fields, and resolved fluctuations

Cross-stream profiles of mean velocity and temperature are reported in Figure 5.21 for the two streamwise positions A and B indicated in Figure 5.2; they are in dimensionless form and are compared with k-ε predictions obtained using Harwell-FLOW3D for the same pressure drop.

On profiles of $\overline{\langle u \rangle}$ the most relevant disagreement is in the consistently higher value of bulk velocity, and in the backflow region predicted by LES, but not by the k-ε model, midway between ribs (section A). Profiles of $\overline{\langle T \rangle}$ agree fairly well on section B but LES predictions are lower (i.e., heat transfer rates are higher) at section A.

Cross-stream profiles of the three fluctuating velocity components and of the total resolved turbulence energy are reported in Figure 5.22 for the same two sections A,B. Profiles of k predicted by the k-ε model are also shown for comparison purposes. Turbulence levels agree on the whole with k-ε predictions; the most relevant difference is in the sharp peak predicted by LES just over the rib top, graph (b), and mainly associated with a peak in $u"_{rms}$.

Cross-stream profiles of the mean streamwise velocity and of the streamwise fluctuation, computed by LES for h/H = 1/4.8 and Re^{O} = 20,000, are reported in Figure 5.23 for the two streamwise locations A and B. They are compared with experimental results of Bates et al. [1983] and of Drain and Martin [1985], obtained for h/H = 1/5 and Reynolds numbers of ~50,000 and 64,000, respectively. For the mean velocity only, also k-ε predictions based on the TUFC code are reported from Drain and Martin [1985]. Profiles are normalized to the mean velocity over the rib top, or to its square.

Experimental profiles of the mean velocity confirm that the main recirculation region extends beyond one-half of the distance between consecutive ribs. This is correctly predicted by LES, while k-ε results show no backflow at section A. The experimental streamwise fluctuation profile at section B exhibits a sharp peak just above the rib top, which is qualitatively predicted

by LES but not by the k-ε model. On both sections A and B, LES overpredicts turbulence levels in the bulk flow region. The disagreement between the two available sets of experimental results as regards the fluctuation intensity near the smooth wall should also be noticed.

5.4 Conclusions

Book both my wilfulness and errors down,
And on just proof surmise accumulate
[Shakespeare, Sonnet CXVII]

Large-eddy simulations were performed using Harwell-FLOW3D for the flow and heat transfer in a channel having one of the walls roughened by transverse square ribs. The Reynolds number varied between 10,000 and 40,000. The Smagorinsky-Lilly subgrid model was used, with Van-Driest near-wall damping and no-slip boundary conditions at the walls. Just three arbitrary constants were involved, namely c_s (0.08), A^+ (25) and σ_s (0.25).

Satisfactorily grid-independent results were obtained using 24 volumes downstream (per rib pitch), 24 cross-stream and 24 or even less spanwise. For a computational domain including two complete rib pitches (33,800 overall control volumes), simulations lasting 10 LETOT's were sufficient to reach statistical equilibrium and fair statistics, and required about 30' of CPU time on a CRAY-2.

This study is one of the first based on LES presented so far for a complex geometry involving flow separation, reattachment, and recirculation. Statistically stationary conditions were reached after a few LETOT's. The mean flow rate was overpredicted as compared with experimental correlations and also k-ε simulations, and so were turbulence levels in the bulk flow region. However, the overall flow structure and many fine features of the mean and fluctuating fields were in good qualitative agreement with existing experimental data. Certain flow features were correctly predicted by LES but absent from k-ε simulations, notably involving recirculation (e.g., reattachment length and peaks of Nu).

A noteworthy feature of the results was the strong three-dimensionality of the flow. As discussed also by Werner and Wengle [1989], this makes the use of the spanwise direction z as 'homogeneous', averaging direction questionable; in future works on this geometry, statistics should be obtained only with reference to time without such 'homogeneity' assumptions.

The simulations failed to predict correctly the Reynolds number - dependence of the Nusselt number. This may depend on the relatively poor resolution of the near-wall region; also the adequacy of the 'subgrid Prandtl number' concept is questionable in recirculating flows. However, it must be observed that in such flows even well established turbulence models, such as the k-ε, fail to reproduce the correct Reynolds number - dependence of heat transfer rates.

Perhaps surprisingly, the overall quality of the predictions, for example regarding the establishment of statistical equilibrium, was higher for this relatively complex geometry than for the simpler plane-channel flow considered in Chapter 4. However, a turbulent flow between simple boundaries may be quite complex in its internal structure, while in a geometrically complex domain the flow characteristics are more heavily dominated by the geometry and may well be relatively easier to predict with reasonable accuracy. A well known example of this in external flows is separation over sharp corners as opposed to separation from smooth surfaces. It should also be considered that for basic geometries (like plane channels, pipes, or annuli), a very large amount of experimental information is available and has been used through the years to 'tune' standard turbulence models, such as the k-ε, while for more complex geometries, especially involving separated flow regions, most existing turbulence models present some drawback and LES can be more competitive.

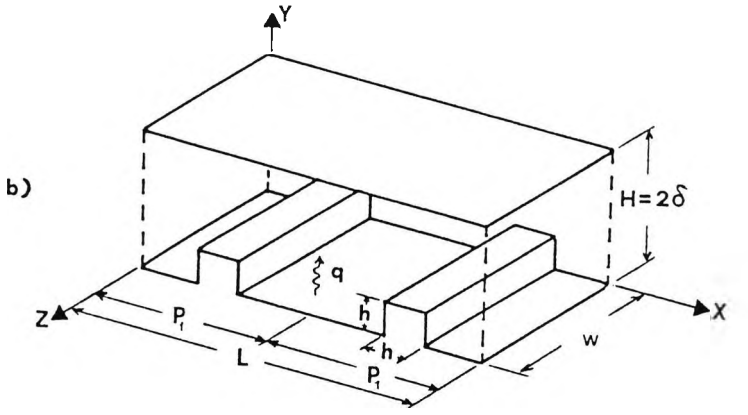


Figure 5.1 - Ribbed channel: schematic of the computational domain.

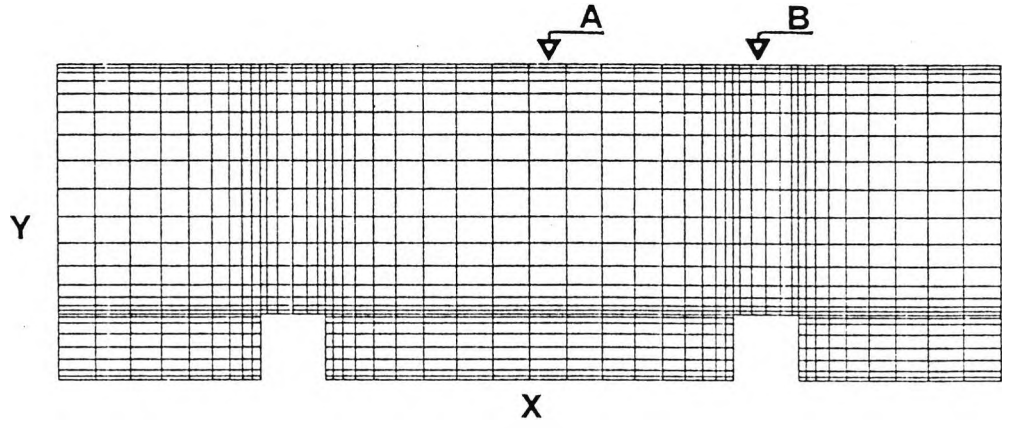


Figure 5.2 - Ribbed channel: computational grid

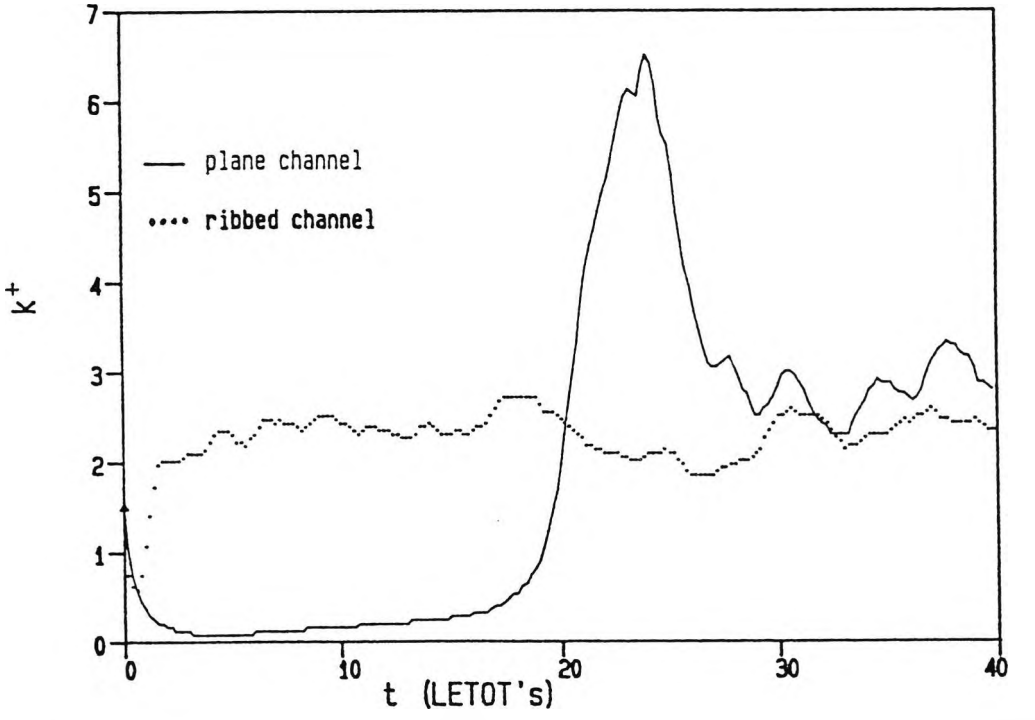


Figure 5.3 - Ribbed channel: average resolved turbulence energy as a function of time for Re^0=20,000.

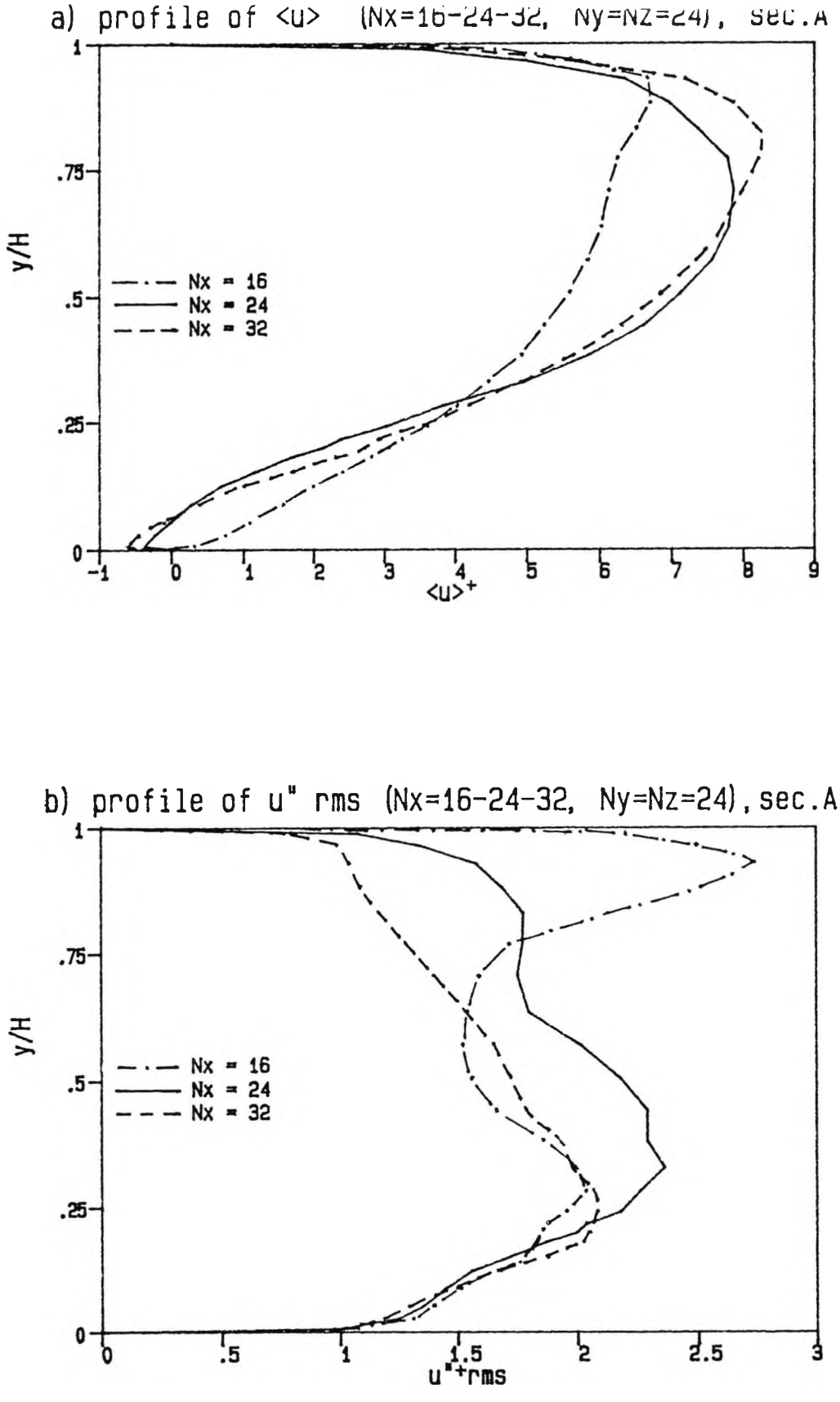
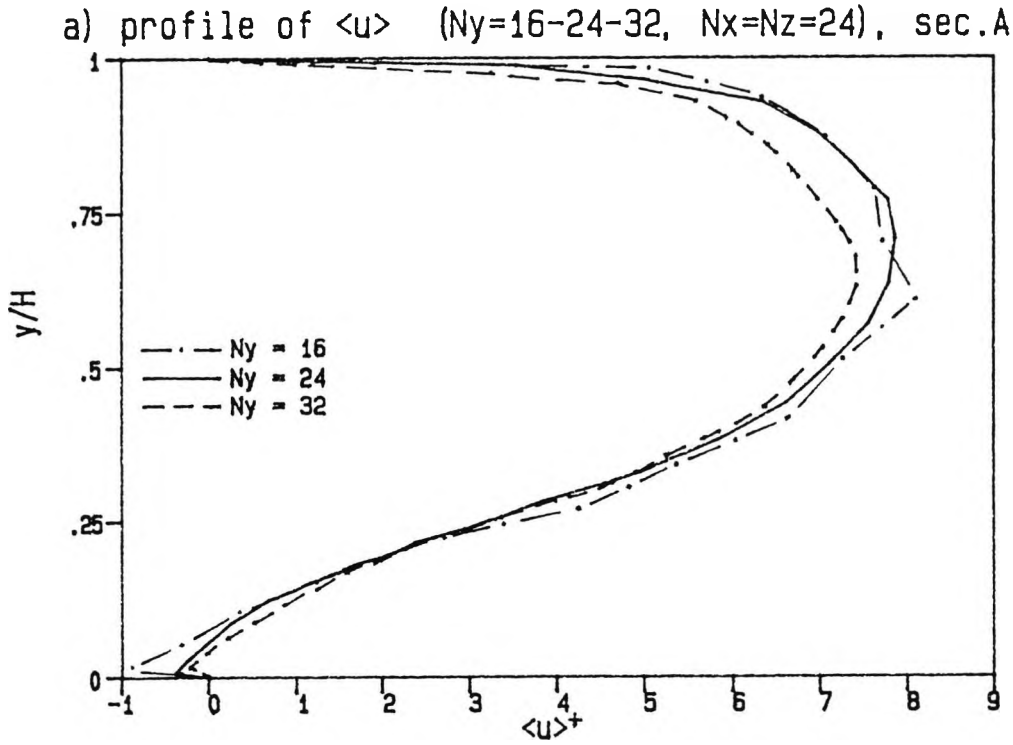


Figure 5.4 - Ribbed channel: comparison of cross-stream profiles of $\overline{\langle u \rangle}$ and $\overline{u''_{rms}}$ at section A of Figure 5.2 for N_x varying from 16 to 32 and $N_y=N_z=24$ ($Re^0=20,000$).



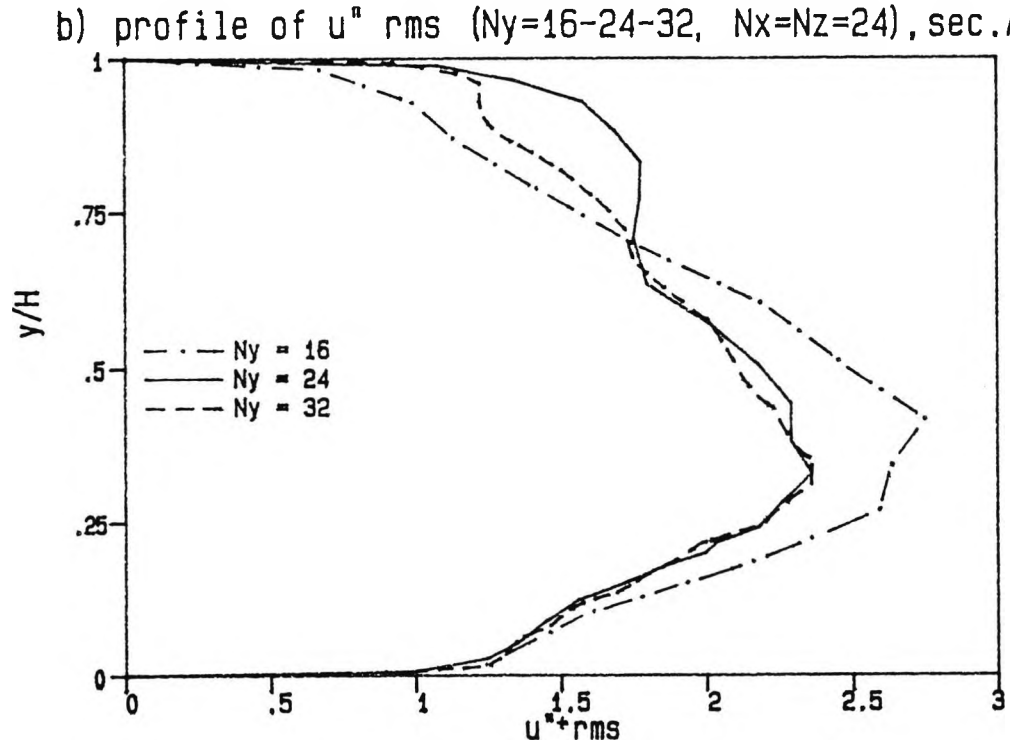


Figure 5.5 - Ribbed channel: comparison of cross-stream profiles of $\overline{\langle u \rangle}$ and $\overline{u''_{rms}}$ at section A of Figure 5.2 for N_y varying from 16 to 32 and $N_x=N_z=24$ ($Re^0=20,000$).

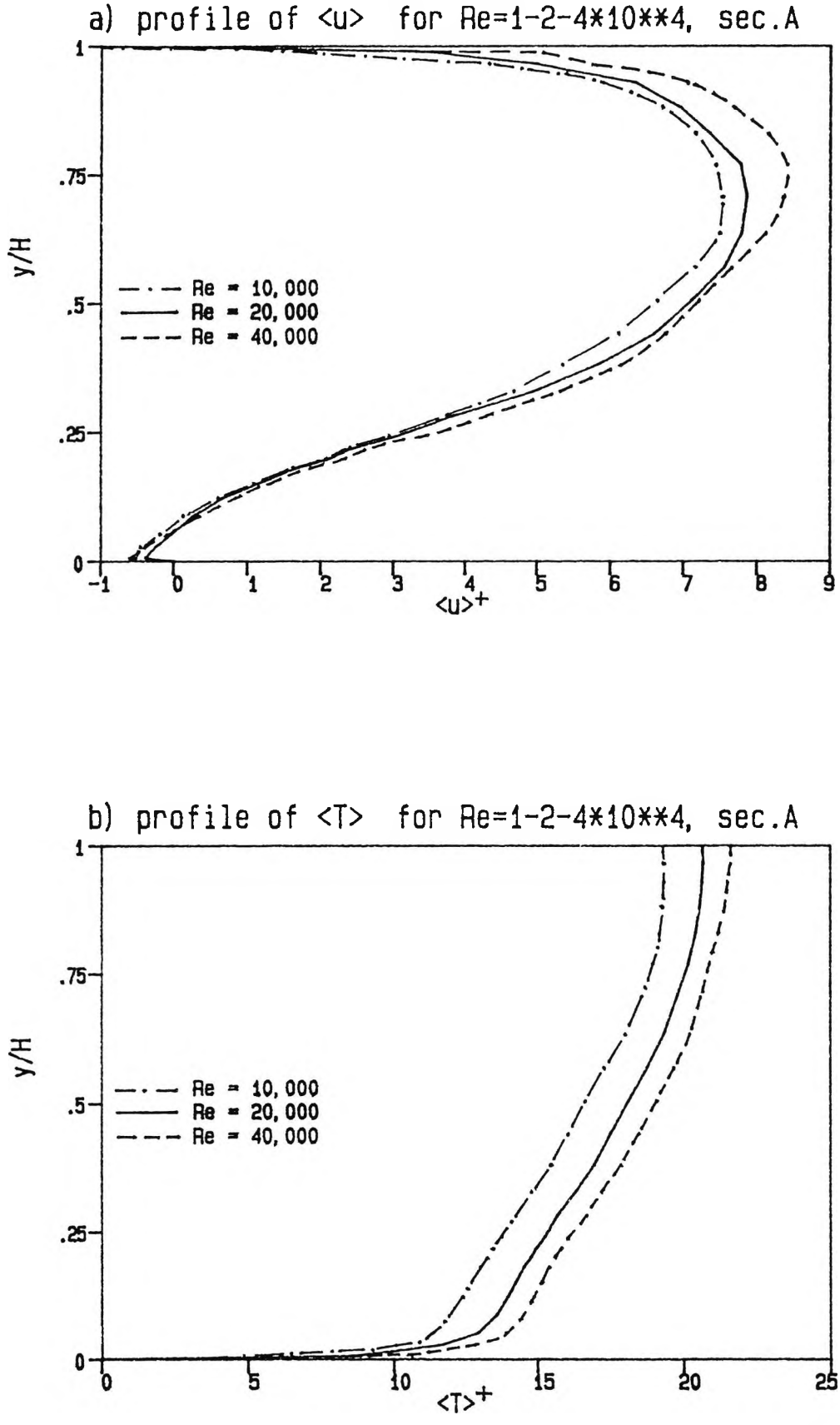


Figure 5.6 - Ribbed channel: comparison of cross-stream profiles of $\overline{\langle u \rangle}$ and $\overline{\langle T \rangle}$ at section A of Figure 5.2 for different Reynolds numbers and a 24^3-volume computational grid.

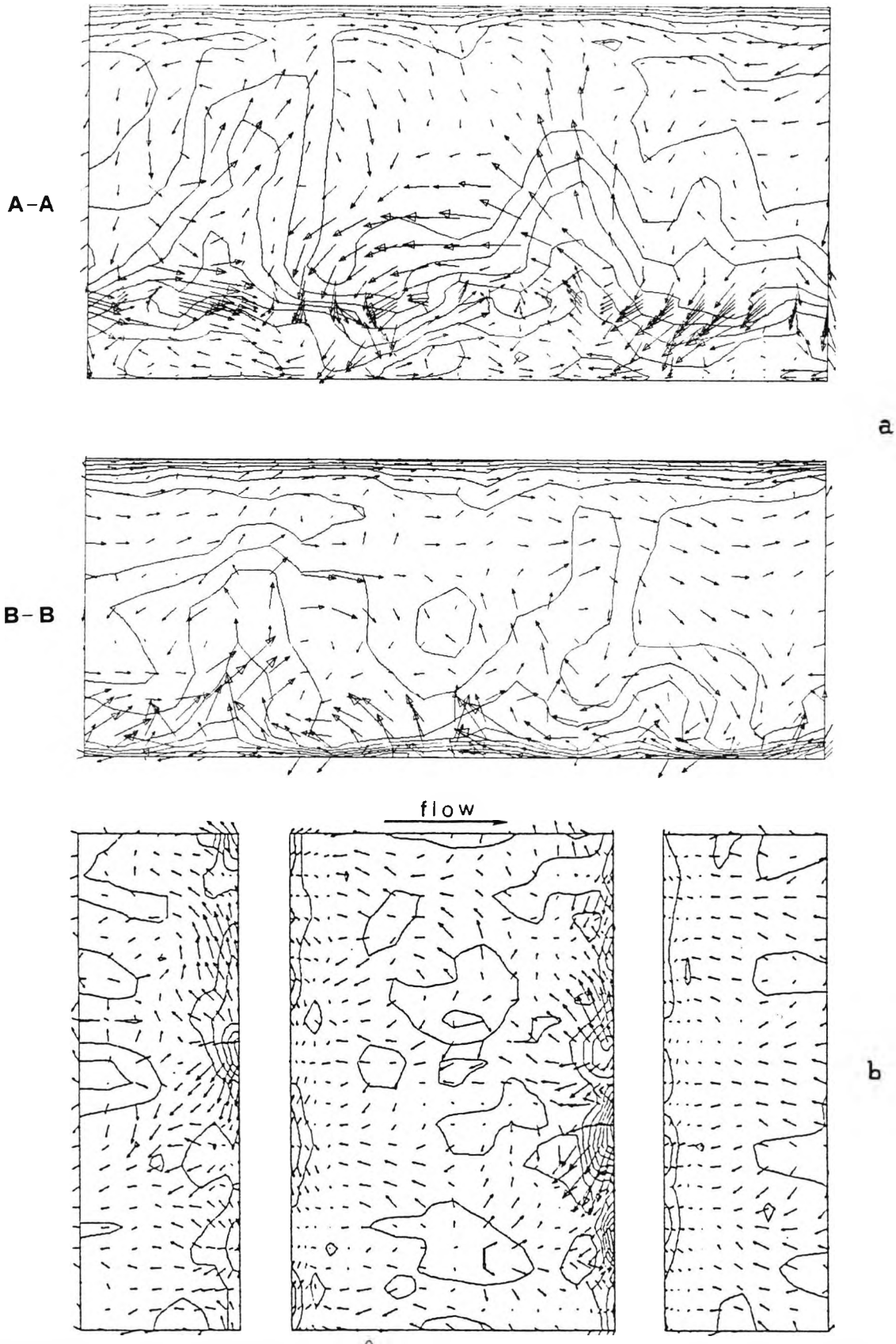


Figure 5.7 - Ribbed channel (Re^{0}=20,000): instantaneous velocity field on
a) planes normal to the main flow direction, sections A and B
(vectors v-w, contours of u);
b) plane y^{+}=10 parallel to the ribbed wall
(vectors u-w, contours of v).

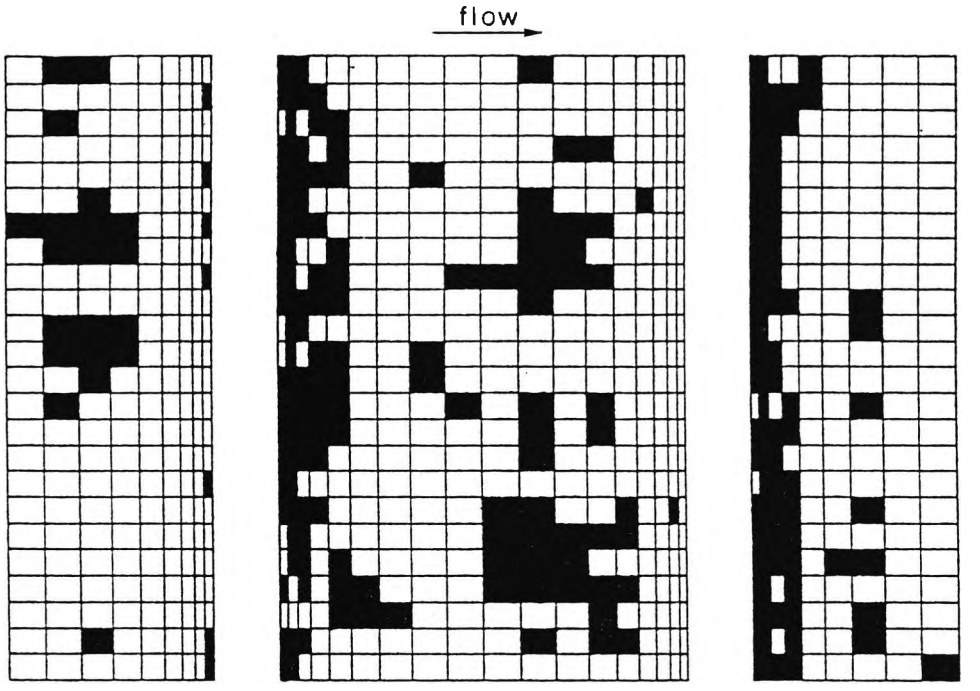


Figure 5.8 - Ribbed channel (Re^0=20,000): instantaneous shear stress map on the ribbed wall (dark cells indicate τ_x<0, i.e. forward, or direct, flow).

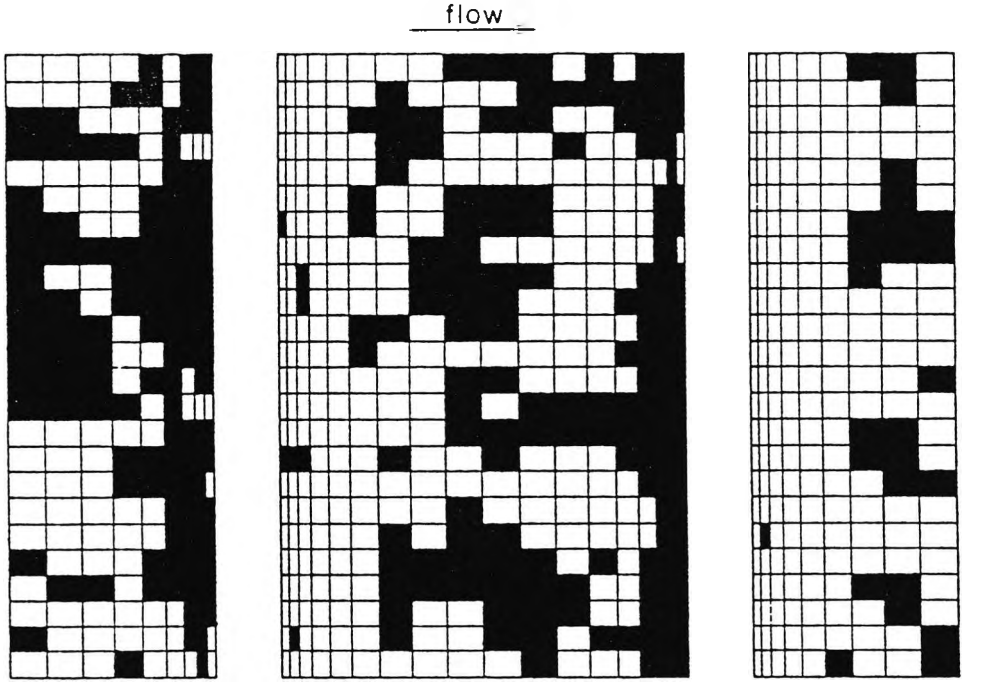
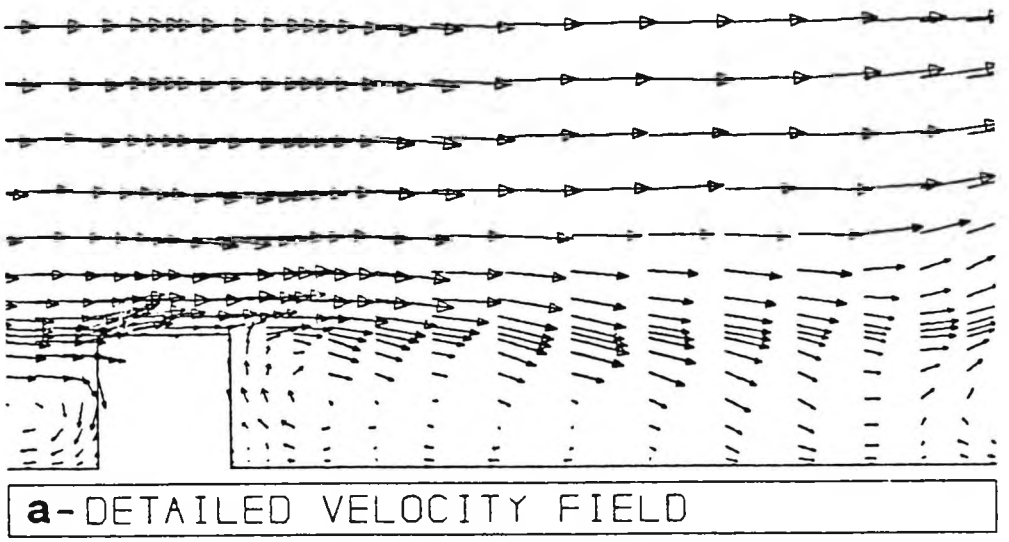


Figure 5.9 - Ribbed channel (Re^0=20,000): instantaneous temperature map on the ribbed wall (dark cells indicate T_w<T_{wa}, i.e. Nu>Nu_a).



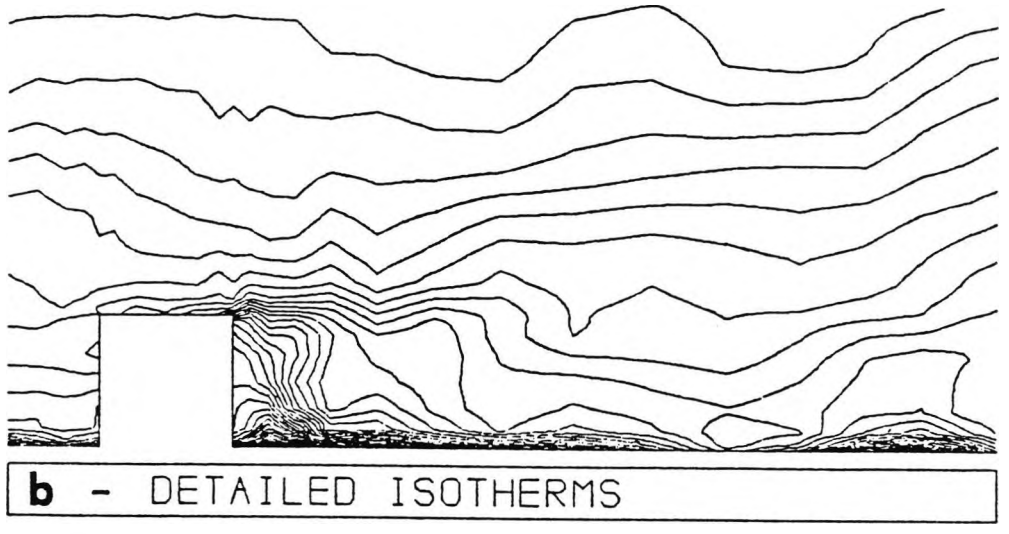


Figure 5.10 - Ribbed channel (Re^{0}=20,000): instantaneous temperature and velocity fields near a rib on a plane normal to z.

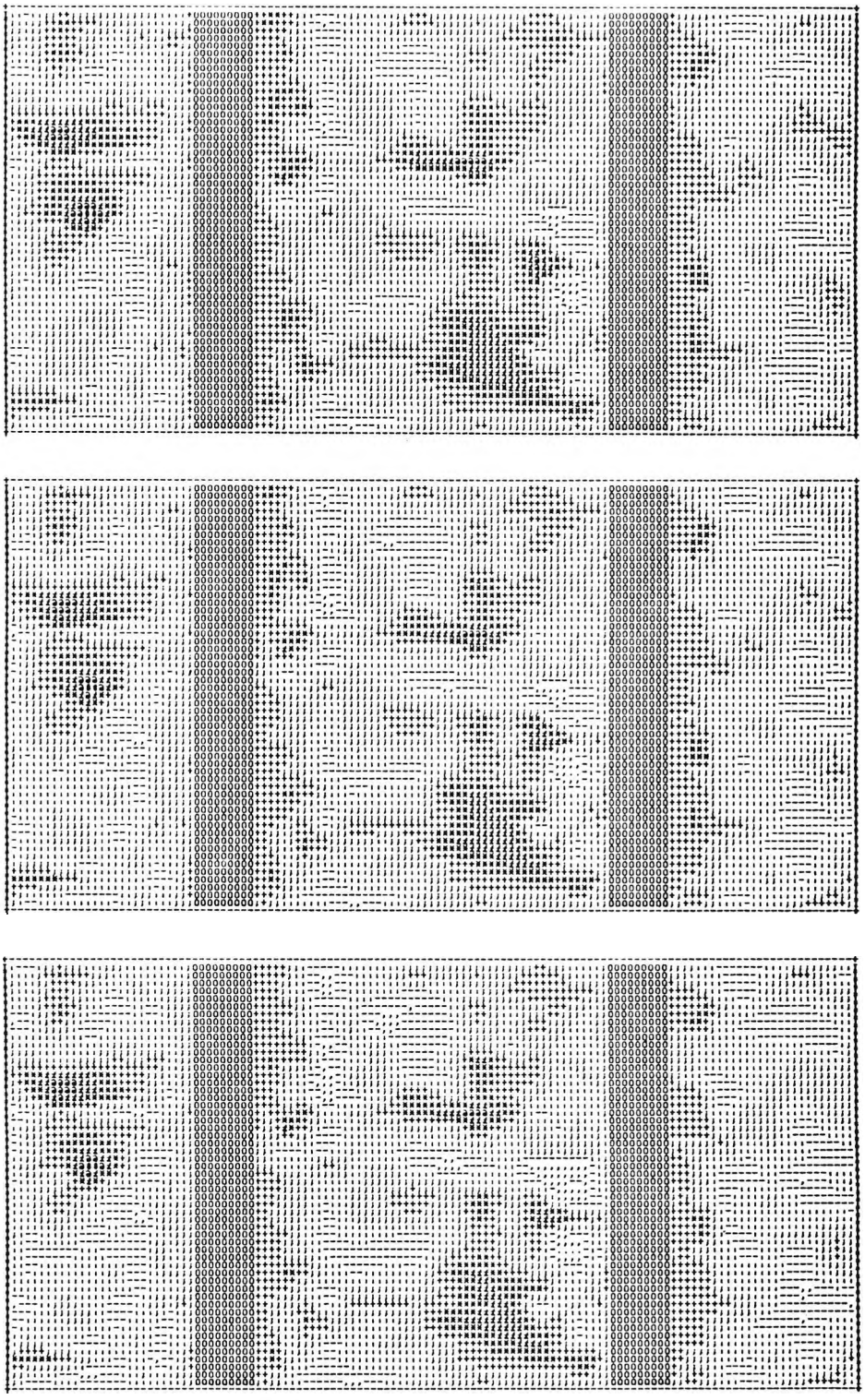


Figure 5.11 - Ribbed channel (Re^{0}=20,000): shade plots of the instantaneous resolved streamwise velocity u on the plane y^{+}=30 parallel to the ribbed wall for t=40.00, 40.02 and 40.04 (LETOT's).

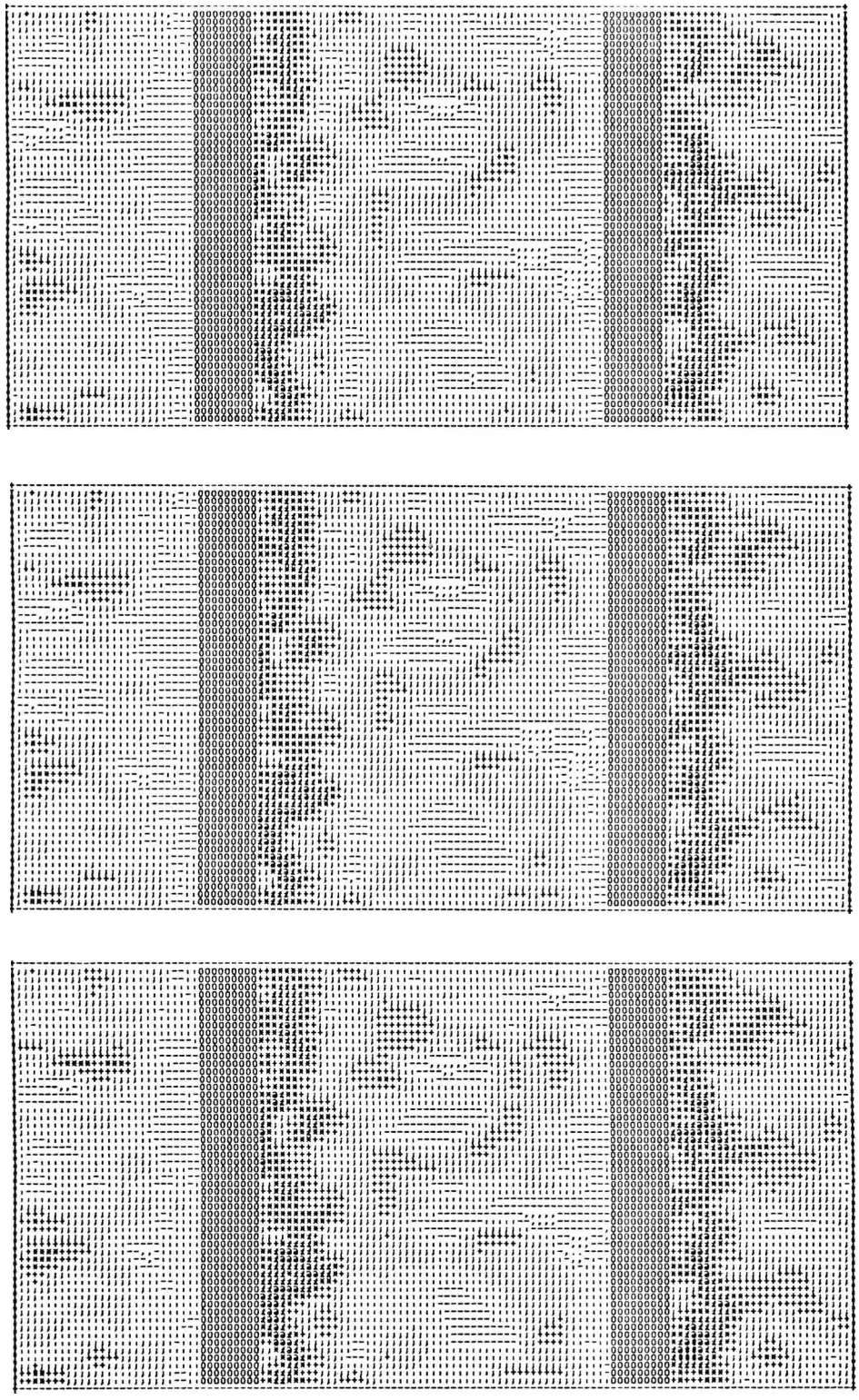


Figure 5.12 - Ribbed channel (Re^{0}=20,000): shade plots of the instantaneous resolved temperature T on the plane y^{+}=30 parallel to the ribbed wall for t=40.00, 40.02 and 40.04 (LETOT's).

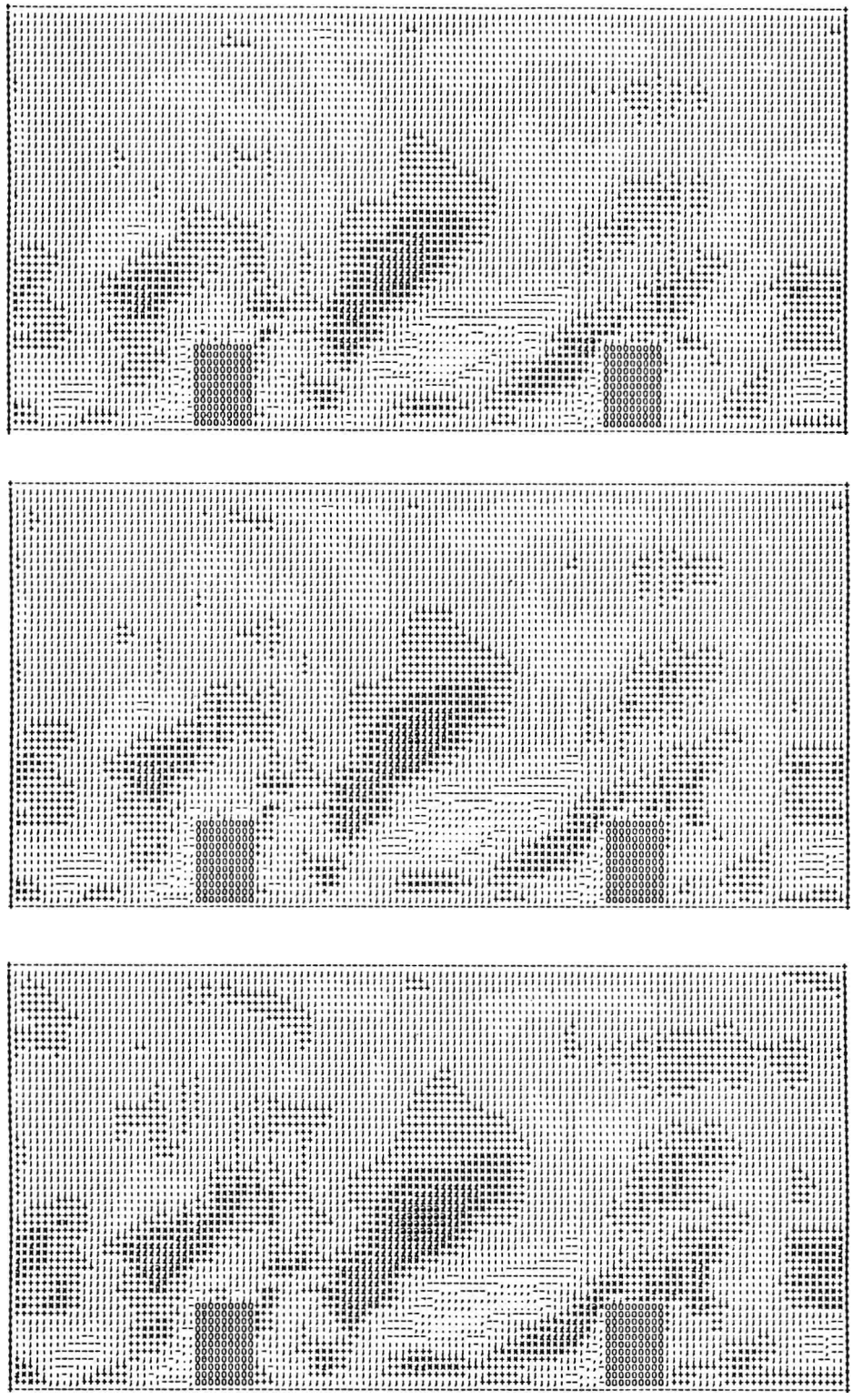


Figure 5.13 - Ribbed channel (Re^0=20,000): shade plots of the instantaneous resolved spanwise velocity w on a plane normal to the z axis for t=40.00, 40.02 and 40.04 (LETOT's).

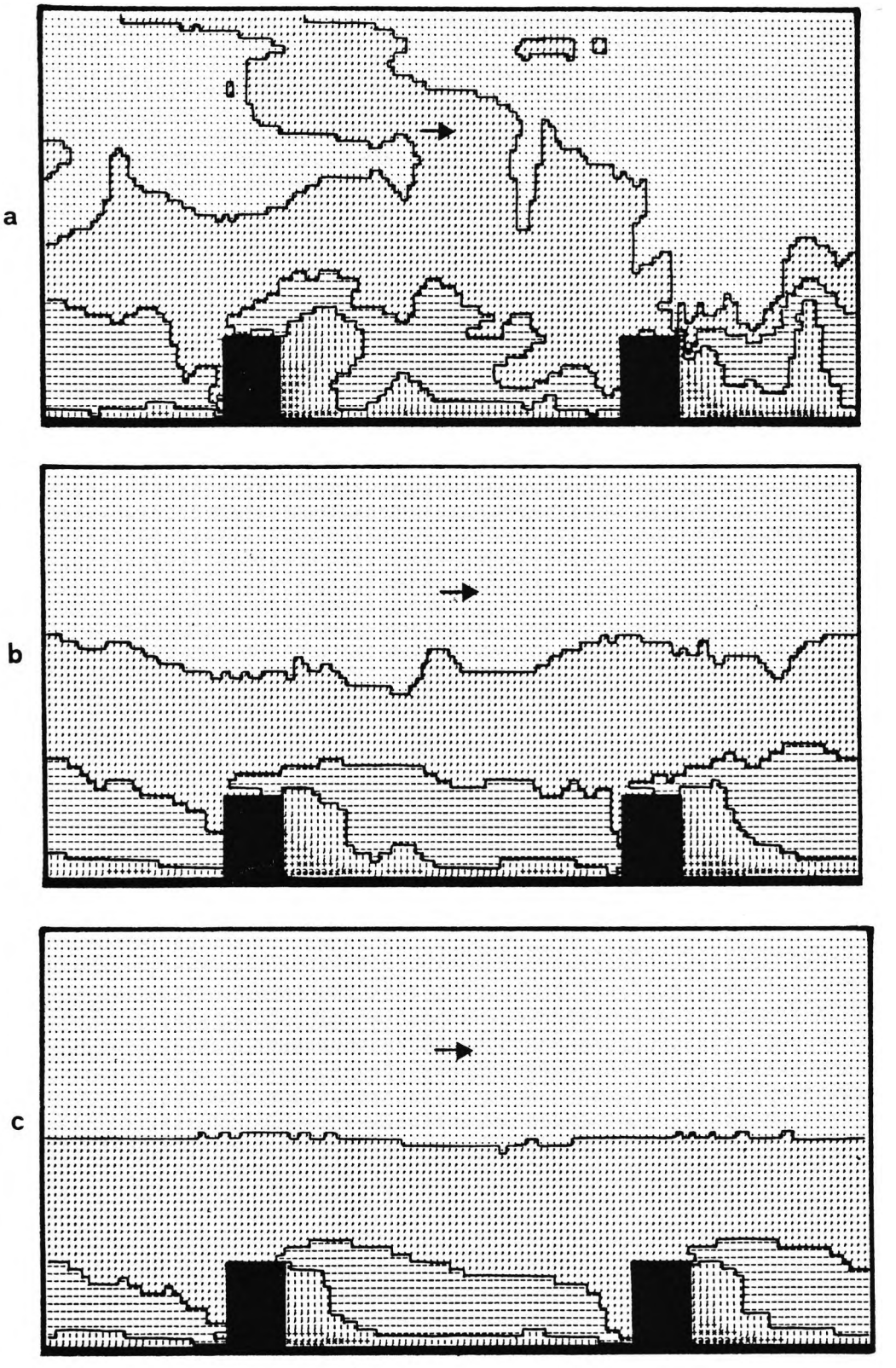


Figure 5.14 - Ribbed channel (Re^{0}=20,000): temperature distribution (interval between consecutive isotherms ≃3.5 wall units).

a) z=W/2, y=40 LETOT's

b) span-average, t=40 LETOT's

c) z=W/2, time-average over LETOT's 30 to 40

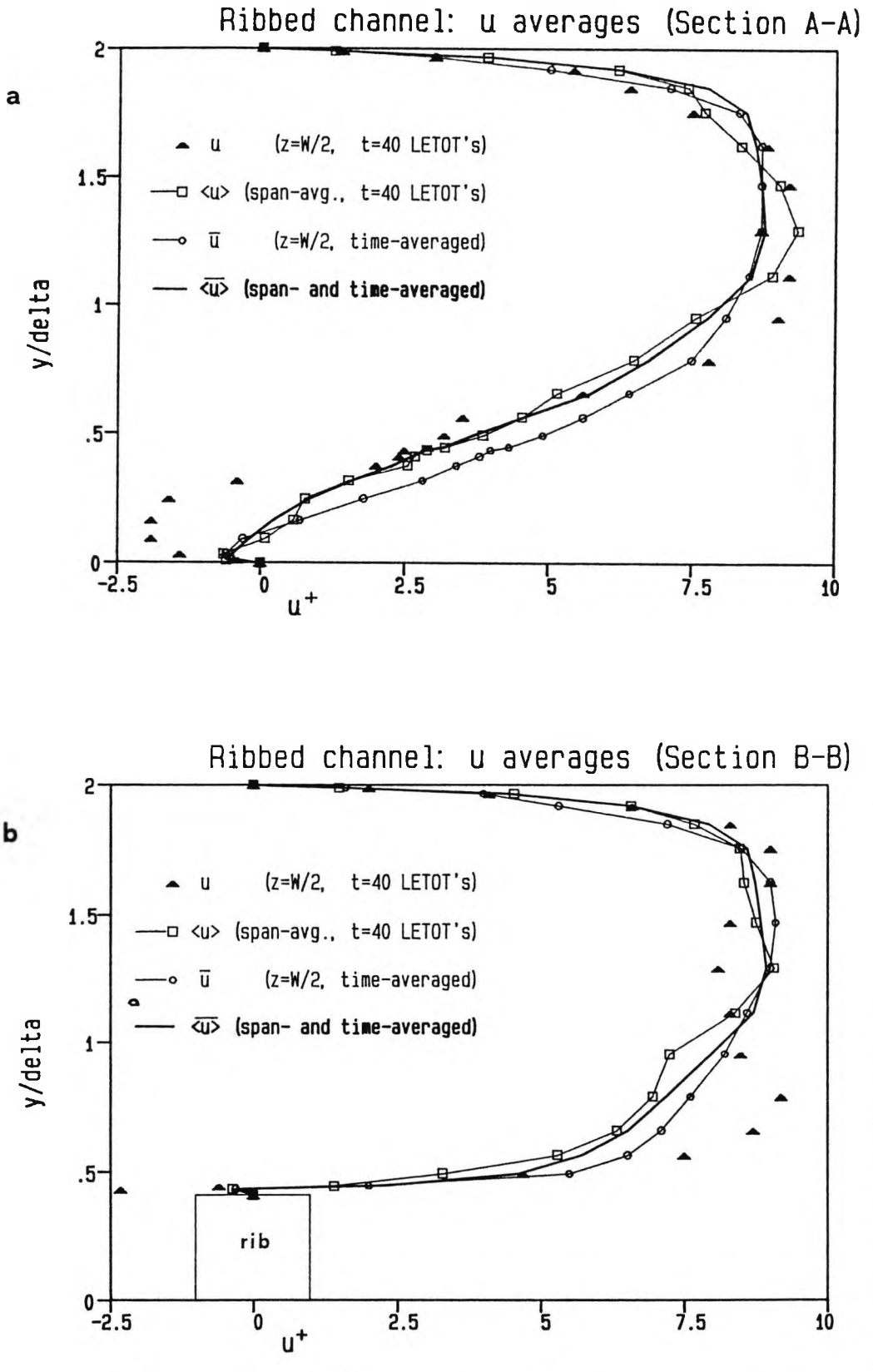


Figure 5.15 - Ribbed channel (Re^0=20,000): comparison of instantaneous and local cross-stream profiles of the velocity u with various averaged profiles
a) section A-A; b) section B-B

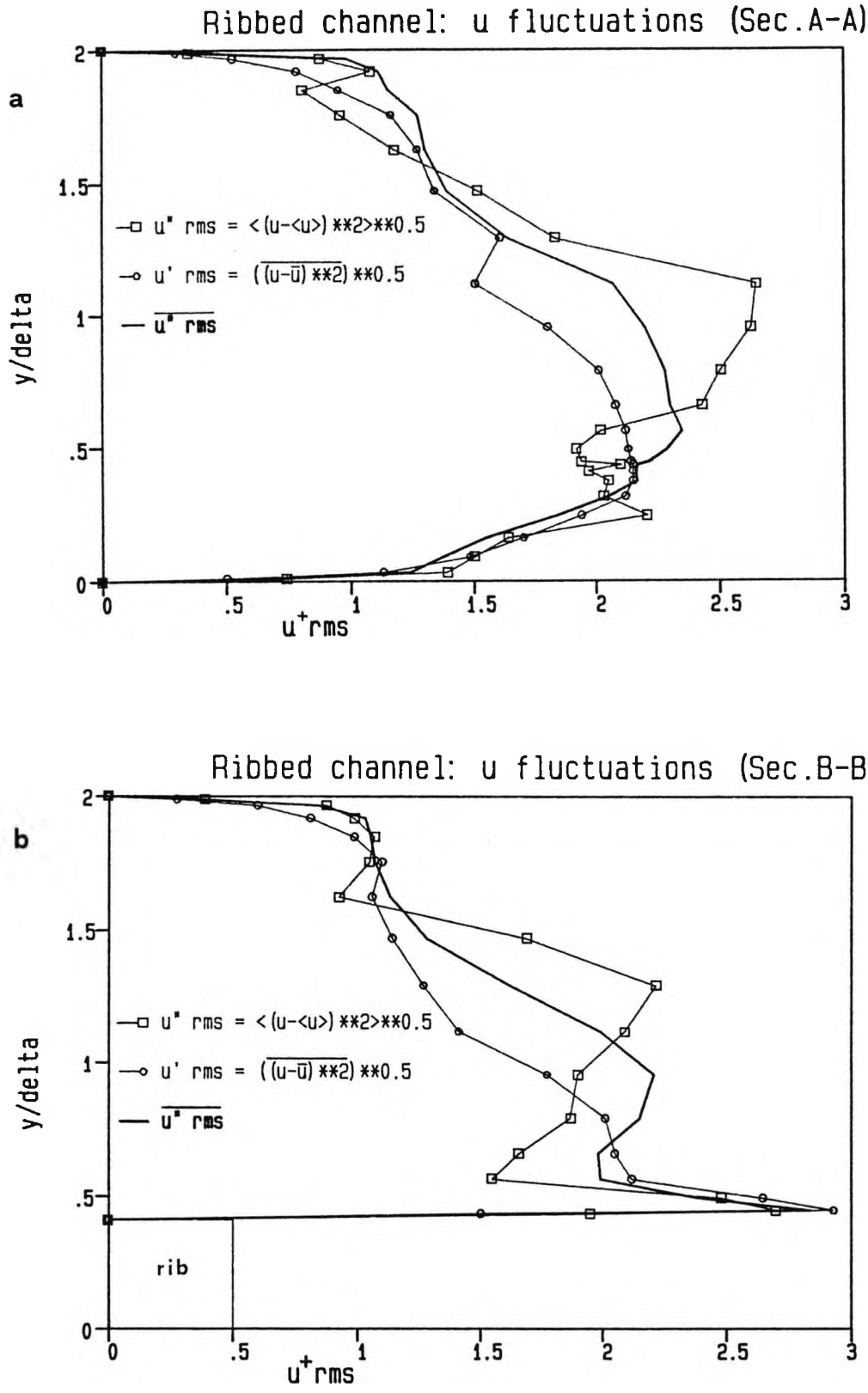


Figure 5.16 - Ribbed channel (Re^0=20,000): comparison of cross-stream profiles of the resolved streamwise fluctuation u_{rms} obtained by different statistical techniques
a) section A-A; b) section B-B

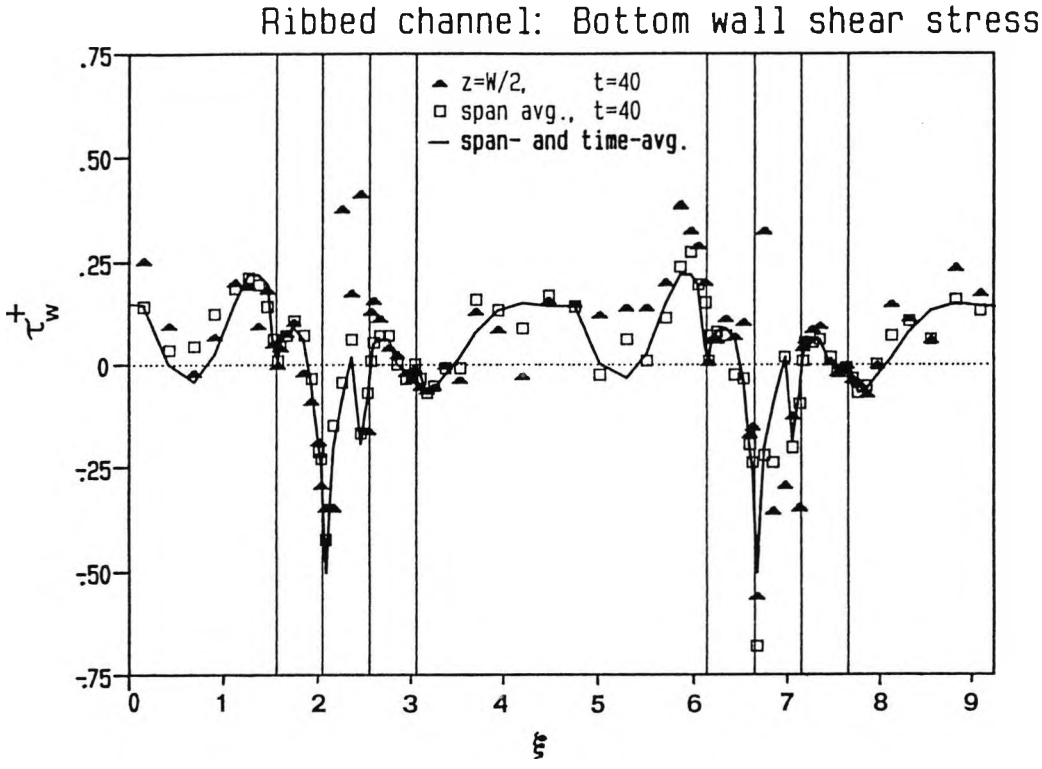


Figure 5.17 - Ribbed channel (Re^0=20,000): effect of span- and time-averaging on the computed shear stress along the ribbed wall.

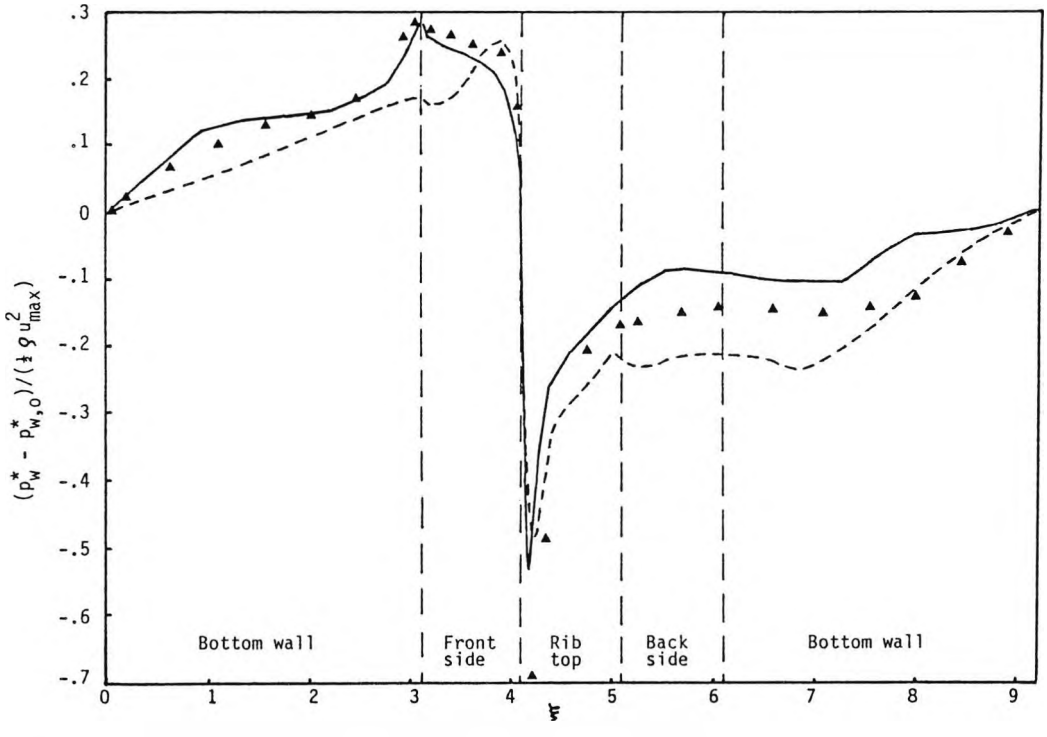


Figure 5.18 - Ribbed channel: profiles of the static pressure along the ribbed wall.

——— Present predictions (LES, h/H=1/4.8, Re=26,600)

– – – k-ε predictions (h/H=1/4.8, Re=20,000)

▲ Experiments (Kacker 1971, h/H=1/8, Re=50,000)

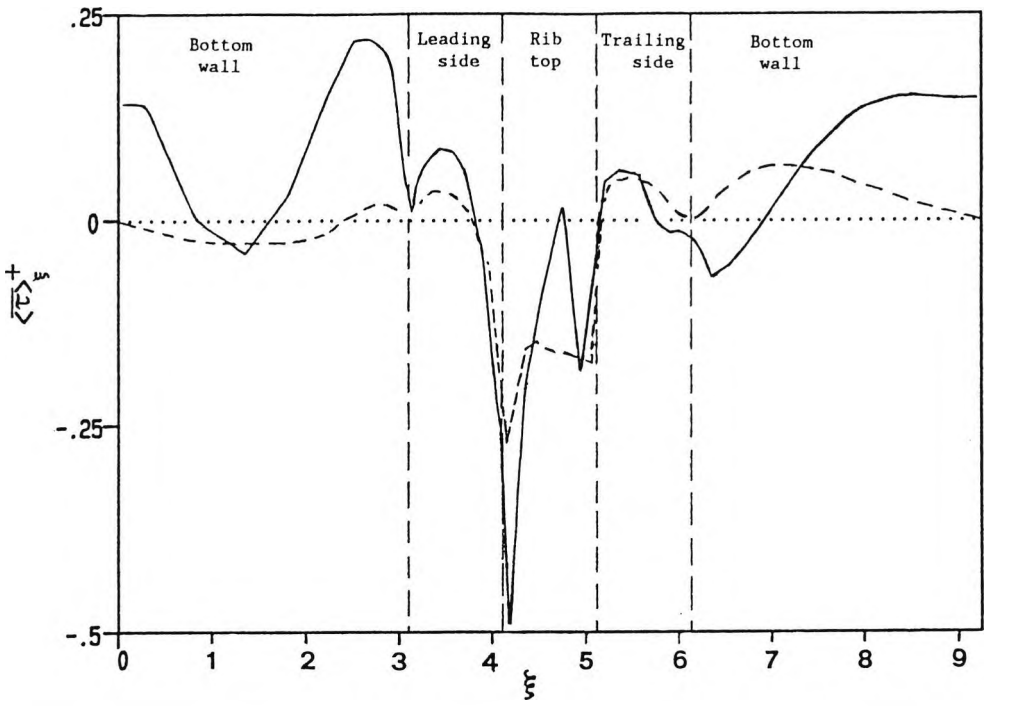


Figure 5.19 - Ribbed channel: profiles of the shear stress in the direction along the ribbed wall.

——— Present predictions (LES, h/H=1/4.8, Re=26,600)

– – – k-ε predictions (h/H=1/4.8, Re=20,000)

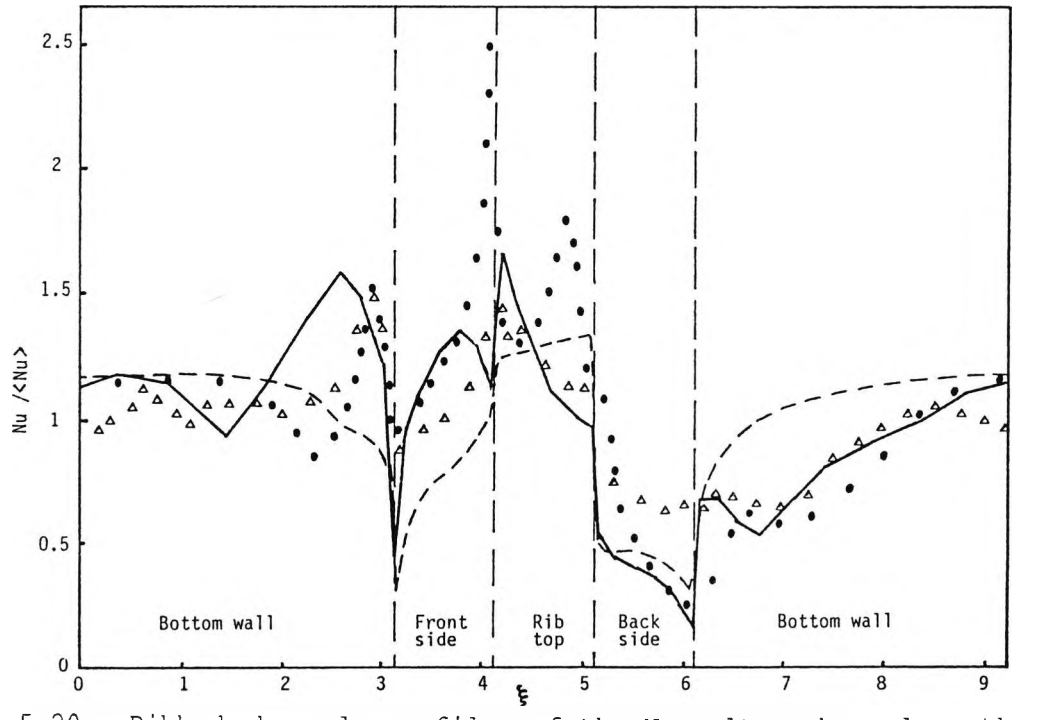


Figure 5.20 - Ribbed channel: profiles of the Nusselt number along the ribbed wall.

——— Present predictions (LES, h/H=1/4.8, Re=26,600)

– – – k-ε predictions (h/H=1/4.8, Re=20,000)

• Experiments (Lockett 1987, h/H=1/9.5, Re=30,000)

△ Experiments (Watts et al.1981, h/H=1/8, Re=82,000)

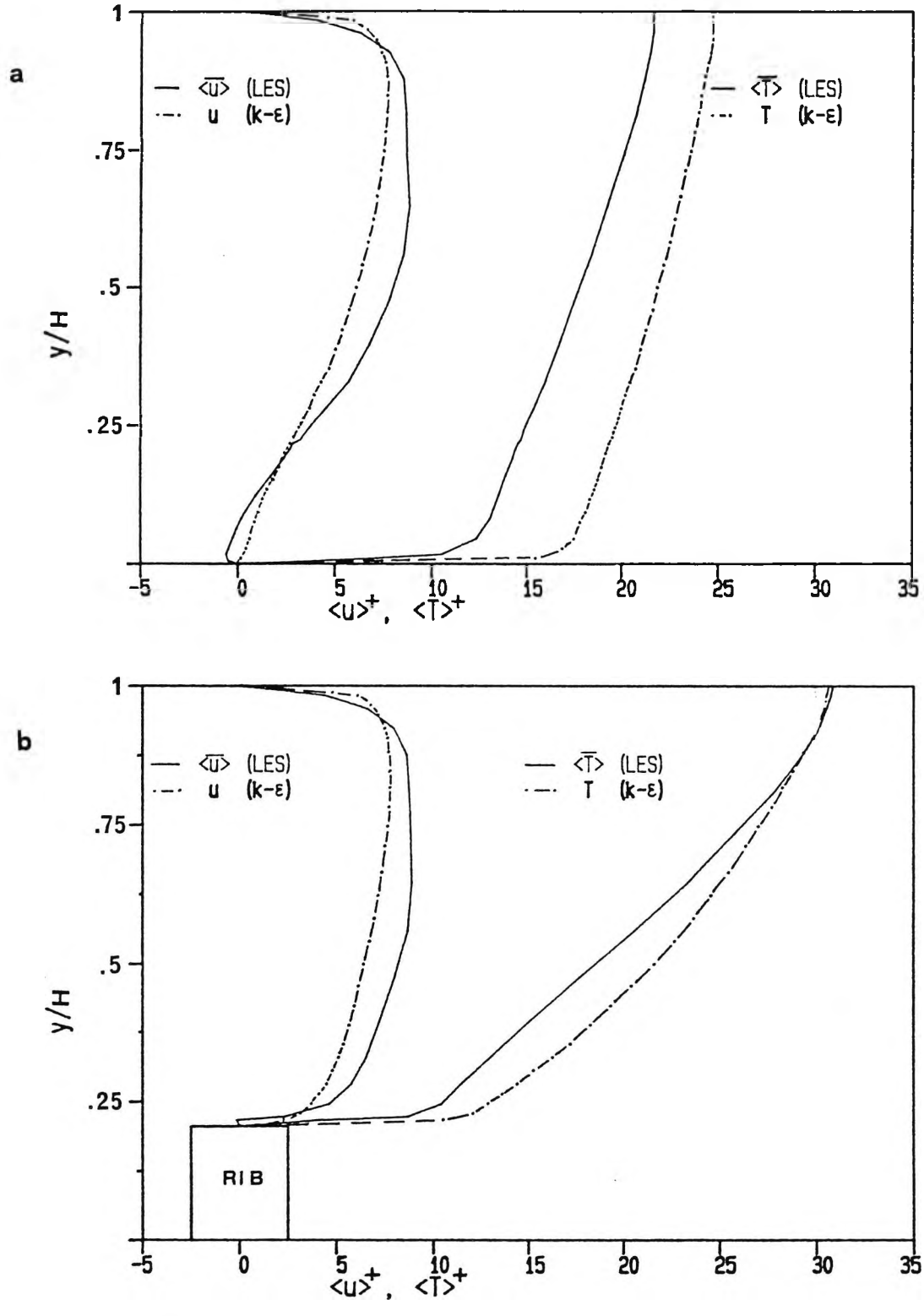


Figure 5.21 - Ribbed channel: cross-stream profiles of mean u and T at the two sections A and B of Figure 5.2.

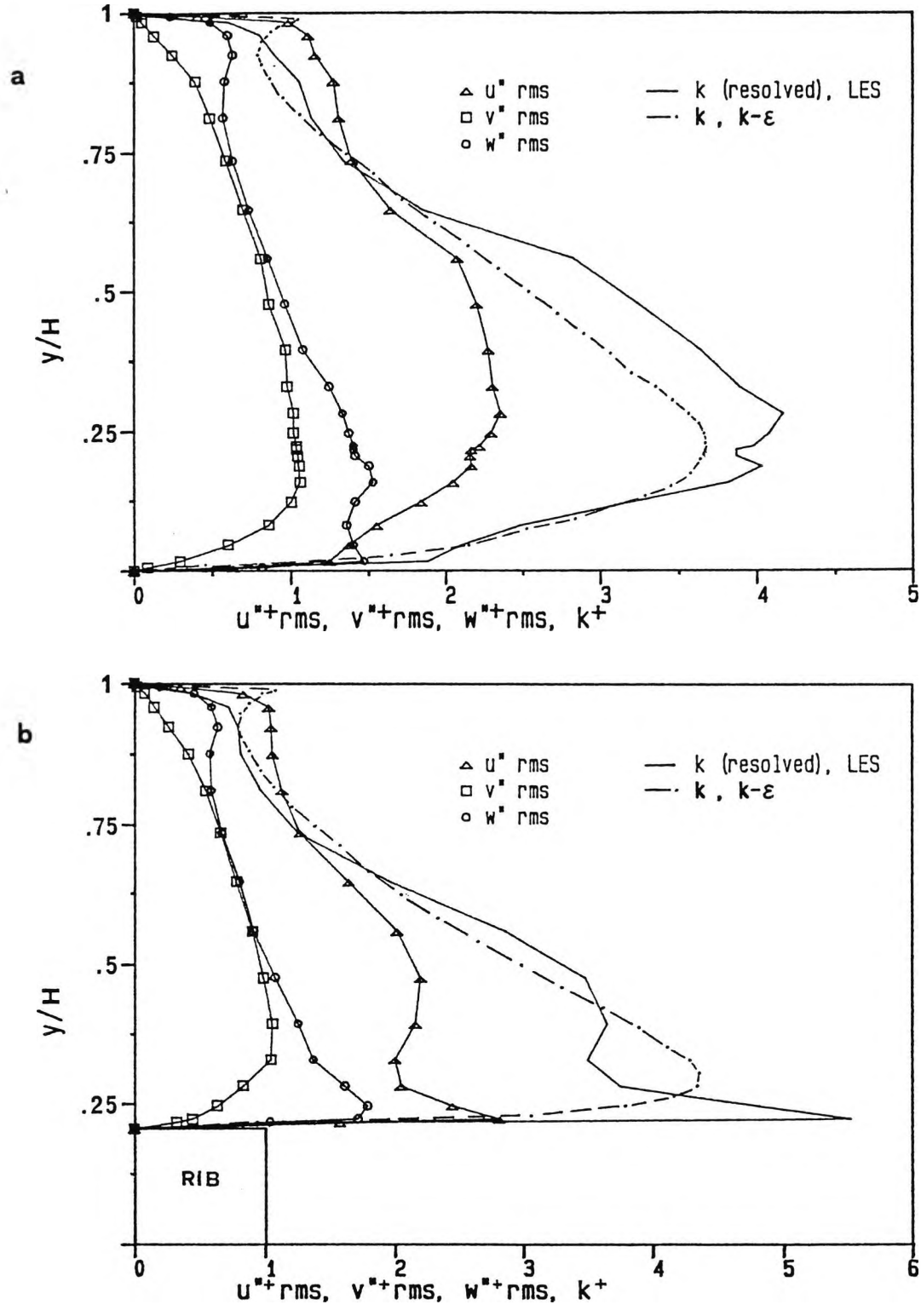


Figure 5.22 - Ribbed channel: cross-stream profiles of velocity and temperature fluctuations at the two sections A and B of Figure 5.2

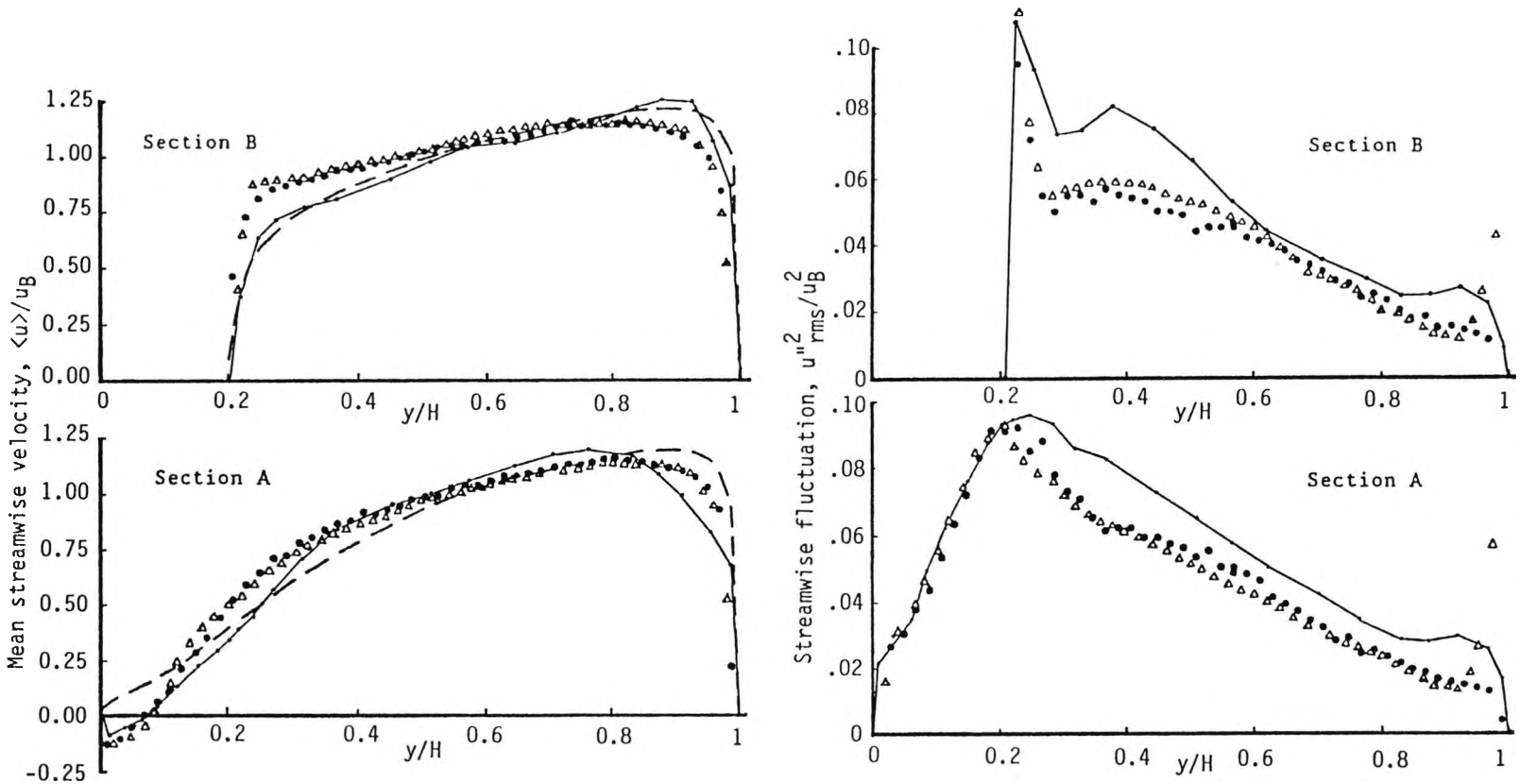


Figure 5.23 - Ribbed channel: computed and experimental cross-stream profiles of mean and fluctuating streamwise velocity. Values are normalized to the average velocity over a rib, u_B.

——— Present predictions (LES, h/H=1/4.8, Re^{O}=40,000)

- - - k-ε predictions using the TUFC code [Drain and Martin 1985]

△ Experiments (Drain & Martin 1985, h/H=1/5, Re=64,000)

● Experiments (Bates et al. 1983, h/H=1/5, Re=50,000)

CHAPTER 6 - APPLICATION TO TURBULENT FLOW WITH HEAT TRANSFER IN A CROSSED CORRUGATED HEAT EXCHANGER GEOMETRY

6.1 Introduction and literature review

> **Air heaters may not be the most glamorous of items in a modern power plant, but they are nonetheless essential for its efficient and economical operation**
> [Chojnowski and Chew, 1978]

6.1.1 Rotary regenerators

Compact heat exchangers are found in almost every field of engineering, from energy production to transport technology. In particular, air preheaters are essential components of fossil-fuelled power plants [Chojnowski and Chew 1978; Chew 1985]. Typically, they cool the flue gases leaving the final water-heating stage (economizer) from ~300°C to ~100°C, and deliver warm air at ~250°C to the furnace. In a 500-MWe unit, the air heaters may recover some 100 MW of low-grade heat, thus increasing substantially the overall plant efficiency. Moreover, preheating the combustion air makes the use of lower-grade fuels possible and, in coal-fired plants, provides the means of drying the fuel.

Air heaters can be classified into direct transfer - type exchangers, or recuperators, and storage-type exchangers, or regenerators. The latter are cheaper and more compact, and are generally preferred on large modern plants. Regenerators rely on the heat-storage capacity of a matrix of closely packed corrugated steel plates, which is exposed alternately to the hot flue gases and to the cool combustion air. In the Ljungström design, the matrix rotates between stationary ducts, while in the Rothemühle design the matrix is stationary and rotating hoods distribute the two streams through it (Figure 6.1). The two designs are essentially equivalent; the heat storage matrix is built in the form of a squat cylinder (Figure 6.2), typically having a vertical axis, a diameter of ~10 metres, and a depth of ~2. Two such units serve a 500-MWe boiler; each of them is crossed by flue-gases and air flow rates of the order of 200 m^3/s, with speeds of 3-6 m/s. The surface-to-volume ratio can be as high as 5-600 m^2/m^3.

The theory of rotary regenerators dates back to Nusselt [1927] and has been extended, for example, by Hausen [1976]. Computer simulations of the

overall behaviour of regenerators appeared as early as in the late 'Sixties [Wilmott 1969]. Design criteria are discussed in handbooks such as that by Rohsenow et al. [1986]. However, the models used in the above - and similar - works assume that convective heat transfer coefficients are somehow known. More generally, the optimum design of these devices requires the knowledge of heat transfer and friction coefficients, and of their dependence upon the corrugation geometry and the operating conditions.

The main performances required of an air heater are high heat transfer rates, low pressure drops, and moderate fouling (or, better, moderate sensitivity of heat transfer and pressure drop to fouling). These performances depend mainly on the geometrical design of the heat transfer elements. Several arrangements have been used or proposed, differing mainly in the shape and size of the corrugations formed by the steel plates; some of them are shown, for example, in Figure 6.3 (a-d) [Chew 1985].

However, the various corrugation designs have been developed mainly on an empirical basis. Although both operational and laboratory data are available, they do not cover the full range of shapes, sizes and operating conditions (in particular, Reynolds numbers) as would be required for an optimization study. Moreover, data are generally available in the form of overall performances (average heat transfer coefficient, global pressure drop), and the phenomena which cause these (flow patterns, transition to turbulence ...) are not well understood. Therefore, it would be of considerable value to supplement available bulk data by local flow and heat transfer measurements and three-dimensional numerical simulations; such studies should allow to characterize the dependence of overall performances on fluid flow patterns and regimes (laminar-transitional-turbulent), thus leading to optimized designs which could hopefully result in significant financial advantages.

On the basis of the above considerations, a comprehensive experimental and predictive research programme was carried over jointly by Marchwood Engineering Laboratories (PowerGen, UK) and the City University of London (with parallel work by the present author at the Department of Nuclear Engineering, University of Palermo). The design chosen in this study is the so called "crossed corrugated", sketched in Figure 6.4. In this, closely packed plates, bearing sine-wave corrugations, delimit open flow passages which intersect one another at an angle Θ; a complex flow and temperature field is established which, especially for moderate values of Θ, may result in high heat transfer rates with still moderate pressure losses. The reason for the choice of this geometry is twofold: first, this is known to be a high-performance design and is actually used on some modern plants; second, it is

relatively easy to model and to investigate numerically. Within this design, the geometry of the heat exchange matrix is basically specified by two dimensionless parameters only, i.e. the corrugation angle Θ and the pitch-to-height ratio P/H (a minor role is played by the wall thickness to corrugation height ratio, s/H).

6.1.2 Corrugation geometry and computational domain

Although the exchangers themselves are substantial pieces of engineering equipment, they are composed of a large number (of the order of 10^7!) of nominally identical, small geometrical elements. For the crossed corrugated design of Figure 6.4, a unitary cell can be identified as sketched in Figure 6.5(a). Each cell has two inlets (W,D) and two outlets (E,U) and can be chosen as the computational domain. The projection of the cell on the midplane of the plates is shown in Figure 6.5(b), while the section C-C parallel to the bottom corrugation is shown in Figure 6.5(c) and the cross-section N-N normal to the top corrugation is shown in Figure 6.5(d). Most predictive results will be presented in the form of vector and shade plots of computed quantities on these three "slices", or on the top surface of the unitary cell. The orthogonal frame Oxyz used in the simulation is also reported in Figure 6.5.

The geometry of the heat exchange matrix is completely specified by the parameters P, H, s and Θ indicated in Figure 6.5. All relevant geometrical quantities can be derived from these as described below.

First, from Figure 6.5 it follows that H_i=H-s and T=P/sinΘ. The overall cross-sectional area normal to the main flow direction is:

$$A_c = T \sin(\Theta/2)\, H_i = P\, H_i \sin(\Theta/2) / \sin\Theta \qquad (6.1)$$

The reference velocity, v_r, can be defined as the ratio of the mass-flow rate $\dot{M}$ crossing the unitary cell to the cross-sectional area A_c times the density ρ:

$$v_r = \dot{M} / (\rho A_c) \qquad (6.2)$$

The (internal) volume of the cell is:

$$V = 2\,(T\, H_i/2)\, P = P^2\, H_i / \sin\Theta \qquad (6.3)$$

The solid-fluid interfacial area ("wetted" area) in the unitary cell is:

$$S = 2\ T\ L = 2\ P\ L\ /\ \sin\Theta \tag{6.4}$$

in which L is the length of the arc of sinusoid having pitch P and amplitude $H_i/2$. It can be shown that, under the assumption of perfectly sinusoidal corrugations, one has:

$$L = 2\ P\ E(\alpha,\pi/2)\ /\ (\pi\ \cos\alpha) \tag{6.5}$$

in which E is the elliptic integral of the second kind:

$$E(\alpha,\beta) = \int_0^{\beta} [1-\sin^2\alpha\ \sin^2\beta']^{1/2}\ d\beta' \tag{6.6}$$

and the angle α is given by:

$$\alpha = \arcsin\left\{(\pi H_i/P)\ /\ [1 + (\pi H_i/P)^2]^{1/2}\right\} \tag{6.7}$$

The hydraulic diameter can be defined as four times the cell volume V divided by the cell "wetted" area S. Finally, D_e and v_r can be used to define the Reynolds number:

$$Re = v_r\ D_e\ /\ \nu \tag{6.8}$$

The most relevant performance parameters of the exchanger are the <u>head loss per unit length</u> (in the main flow direction a) and the <u>average heat transfer coefficient</u>.

In fully-developed flow, the former quantity is simply the mean pressure drop between the inlet faces (D,W) and the outlet faces (U,E), divided by the length Δa (this is <u>not</u> true in developing flow , e.g. in the entrance region of the exchanger). The head loss can be made nondimensional by defining the <u>equivalent friction coefficient</u>:

$$f = |\Delta p|\ D_e\ /\ (\rho\ \Delta a\ v_r^2\ /\ 2) \tag{6.9}$$

The <u>local</u> heat transfer coefficient can be defined in dimensionless form, i.e. as a local Nusselt number, as:

$$Nu = q_w\ D_e\ /\ (\lambda(T_w-T_f)) \tag{6.10}$$

in which q_w and T_w are the local wall heat flux and wall temperature, T_f is the average (mixing) fluid temperature, and λ is the thermal conductivity of the fluid. An obvious definition of the average Nusselt number is:

$$<Nu> = \frac{1}{S} \int_S Nu \, dS \qquad (6.11.a)$$

A more engineering-like definition, however, is:

$$Nu_{av} = <q_w> D_e \; / \; (\lambda(<T_w>-T_f)) \qquad (6.11.b)$$

in which brackets <> denote surface averages. It is easily shown that:

$$<Nu>/Nu_{av} = \begin{cases} <T_w-T_f> <(T_w-T_f)^{-1}> & (\text{unif. } q_w) \\ 1 & (\text{unif. } T_w) \end{cases} \qquad (6.12)$$

so that $<Nu>=Nu_{av}$ for uniform-wall temperature conditions, but not otherwise (in particular, for uniform-wall heat flux conditions). If heat (mass) transfer occurs only on one of the walls, <Nu> should be defined as the average of Nu over the active surface only.

If the effect of conduction in the solid wall is neglected, the performance parameters f and Nu_{av} depend solely on the geometrical parameters Θ and P/H_i, on the Reynolds number, and on the Prandtl number.

6.1.3 Literature review

Very few experimental results have been published in the literature for corrugated geometries equal or similar to that described above. No detailed flow field measurements have been reported, and heat transfer characteristics have been investigated mainly by mass transfer techniques, using the analogy between mass and heat transfer.

Following early work by Okada et al. [1972], Rosenblad and Kullendorff [1975] and Zogg [1972] (this last dealing with triangular corrugations), Focke et al. [1985] used an electrochemical mass transfer method, the so called diffusion-limited current technique (DLCT), to determine local mass transfer coefficients on one of the walls of a test section including several tens of unitary cells. Of course, the working fluid was water. The pitch to height ratio was P/H=2; the Reynolds number ranged from $\sim 10^2$ to $\sim 10^5$, and the corrugation angle from 0° (corrugations parallel to each other and to the flow) to 180° (corrugations parallel to each other but orthogonal to the flow). Mass transfer results were reported as average Colburn j-factor

$j=Sh/(Re\ Sc^{1/3})$, being Sh the Sherwood number (mass-transfer analogue of the Nusselt number) and Sc the Schmidt number (analogue of the Prandtl number). Values of the equivalent friction factor f, measured by wall pressure tappings, were also reported. The authors observed a monotonic rise of both the equivalent friction coefficient f and the Colburn j-factor for the corrugation angle Θ increasing from 0 to ~160°. Beyond this value, f and j decreased slightly and presented a local minimum at Θ=180° (it has to be observed that the conditions for Θ=180° are <u>not</u> univocally defined in general, since they depend on the phase shift between the lower and upper plates; this was zero in the above experiments). The observed rise was much more pronounced for the pressure drop than for the mass transfer rate; for example, for Θ increasing from 30° to 160°, f increased by about 20-30 times, while j increased by only 2-2.5 (depending on the Reynolds number).

One of the most interesting results of this study was the behaviour of f and j as functions of Re for different values of the corrugation angle Θ. For Θ=0, transition from laminar to turbulent flow was clearly indicated by a steep increase in f and j for Re=6,000-10,000. As Θ increased, the transition became smoother and occurred at lower Reynolds numbers; no clear transition could be identified any more for Θ>60°.

In a later paper, Focke and Knibbe [1986] described the use of the electrode-activated pH method, with o-cresolphthalein as the indicator, to visualize flow patterns between cross-corrugated plates. The geometry was the same as in the above study; the authors limited their investigation to low Reynolds numbers (10 to 1000) and included the case of the two plates forming two <u>different</u> angles with respect to the main flow direction.

Gaiser and Kottke [1989.a, 1989.b, 1990] investigated the dependence of Nu and f on the corrugation angle Θ in the range 60° to 160° for pitch-to-height ratios of 1.78 and 7.12 and a Reynolds number of 2000. The working fluid was air, and the test section included over a hundred unitary cells, so that practically fully-developed conditions were attained. Local mass transfer coefficients were measured by using the chemical reaction, coupled with a colour reaction, between a first reactant added in gaseous form to the air and a second reactant absorbed in wet paper coating one of the walls. The authors reported maps of the local heat (mass) transfer coefficient and plots of the average Nusselt number and of the equivalent friction factor as functions of Θ. Under comparable conditions, results were in good agreement with those measured by Focke et al. [1985] and by other authors [Okada et al. 1972; Zogg 1972].

6.1.4 Previous experimental and computational work

a) experimental measurements

Experiments were carried out at the City University using a purposely modified blow-down, low-turbulence wind tunnel. The test section consisted of a couple of PVC plates, bearing corrugations about twice the size of those in a typical rotary regenerator. The plates were mounted at an angle Θ so as to include about 6-7 unitary cells streamwise and 10-12 spanwise. The top plate had its lower (i.e. inner, or air) side coated by a sheet of thermochromic liquid crystals (TLC), while a uniform temperature was provided on its upper (i.e. outer, or water) side by a constant-temperature water bath.

The liquid crystals had an event temperature range of 27.0 to 29.6°C. In the actual measurements, only the green colour band (corresponding to a TLC temperature $T_g = 28.3 \pm 0.075$°C) was used, as it is the brightest and sharpest. The air temperature T_f was kept fixed at about 45°C, while the temperature T_b of the water bath was changed stepwise between ~13°C and 28°C. For each value of T_b, the resulting steady-state colour pattern was recorded and analysed by a "true-colour" image-processing system; the associated Nusselt number was computed from:

$$Nu = \frac{1}{R} \frac{T_g - T_b}{T_f - T_g} \frac{D_e}{\lambda} \qquad (6.13)$$

in which R is the overall thermal resistance of the corrugated plate + TLC package. By letting T_b vary, a series of contours of Nu were thus obtained. <Nu> was computed by automatically averaging Nu over the "active" surface (top wall). Since the experimental conditions approach uniform-wall temperature ones, <Nu> is very close to Nu_{av} here.

The air velocity along the corrugations was measured by a thin Pitot-static probe, and the "reference" velocity v_r was estimated from this. The wall pressure distribution was measured by a micromanometer and pressure tappings, ~.5 mm in diameter, located along the "crests" and "troughs" of the top corrugated plate, and was used to compute the equivalent friction coefficient f.

Reference values and ranges investigated for the basic parameters which characterize the corrugation geometry are summarized in Table 6.1. The surface-to-volume ratio for the reference geometry is $S/V \cong 280$ m^2/m^3.

Table 6.1 - Basic parameters characterizing the experimental geometry

Parameter	Symbol	Reference value	Range
Wall thickness	s	0.075 cm	-
Sinusoid length	L	3.70 "	-
Pitch/height ratio	P/H	3.66	3.66, 2.84, 2.41, 2.07
Corrugation angle	Θ	36°	30°- 80°
Reynolds number	Re	2450	1000 - 7000

Complete results from the above investigation have been reported in a series of confidential reports [VV.AA. 1989-1992]; selected results have also been presented in unclassified reports or at different conferences and meetings, e.g. by Stasiek and Collins [1991], Shand [1990], Ciofalo et al. [1991.a, 1991.b].

b) numerical predictions

Under typical operating conditions, in a rotary regenerator of the type studied the Reynolds number ranges from ~1500 to 3000. Thus, transitional and weakly turbulent flow is expected, which - as it is well known - is very hard to predict by conventional turbulence models.

In former predictive studies [Ciofalo et al.1990, 1991], it was decided to investigate the Reynolds number-dependence of the main performance parameters by considering a broad range of Reynolds numbers (from 10^2 to 10^4), and obtaining laminar solutions up to Re=3000 and k-ε turbulent solutions at higher Reynolds numbers, with some overlapping of the two ranges. A correction procedure was also developed to take somehow into account the errors arising from the application of the high-Reynolds number form of the k-ε model to situations in which the near-wall grid points inevitably lay within the viscous sublayer (unless very coarse grids were used). This approach was expected to yield upper and lower bounds for the heat transfer and pressure drop coefficients in the intermediate, and most interesting, range. Also, by comparison with experimental data, it was expected to assist in characterizing features and effects of the transition to turbulence.

Typical results for the reference geometry in Table 6.1 are summarized in Figures 6.6(a) and (b) for the friction coefficient and the average Nusselt

number, respectively; they are, indeed, strongly suggestive of transitional flow. The experimental slope of Nu_{av} vs. Re appears to be even higher - in the whole range investigated - than that predicted by the k-ε model, whilst the experimental slope of f vs. Re appears lower. On the other hand, the experimental angle-dependence of both f and Nu_{av} is much higher than that predicted by either method. Actually, most of the angle-dependence seems to be associated with the influence of the corrugation angle on the Reynolds number at which transition occurs, rather than with "true" turbulence promotion.

Further predictive studies were conducted by using a low-Reynolds number turbulence model, very similar to that proposed by Lam and Bremhorst [1981] and purposely implemented in Harwell-FLOW3D, Release 2 [Ciofalo 1991]. Results were presented, for example, by Ciofalo et al. [1992]. The experimental Reynolds number - dependence of both f and Nu_{av} was predicted much better than by the above approaches, though some discrepancy persisted, especially in the angle-dependence of these parameters. Some of these results will be compared with the present LES predictions in Section 6.3.

6.2 Model and methods

> **Typical large computers perform a floating multiply in about 240 μs ...**
> **The main or fast memories have capacities of 500 to 100,000 words ...**
> [W.C.Sangren, 'Digital Computer and Nuclear Reactor Calculations', 1960]

6.2.1 Grid generation

Whatever the computational approach used, the computational domain (unitary cell) sketched in Figure 6.5 has first to be spanned by a body-fitted grid of hexahedral control volumes. For the sake of generality, the grid should include both the fluid region and the solid (wall) region, although the latter provision is strictly required only if coupled conduction-convection problems are to be treated (this was not done here). Also, a layer of "dummy" control volumes, surrounding the body, has to be included in order to impose boundary conditions, as required by the discretization method implemented in Harwell-FLOW3D, Release 2 (see Chapter 3).

The grid is completely specified by assigning the coordinates of the corners of the control volumes in the (cartesian) reference frame Oxyz, and storing them in the three-dimensional arrays **XC**(I,J,K), **YC**(I,J,K), **ZC**(I,J,K). The indices I,J,K can be regarded as discrete values of inner (generalized)

coordinates; with reference to Figure 6.5(a), the index I runs from face D ("Down") to face U ("Up"), the index K from face W ("West") to face E ("East") and the index J from bottom to top (directions S, "South" and N, "North"). A control volume is specified by the three indices I,J and K, while **XC**(I,J,K) etc. can be regarded as the (cartesian) coordinates of the (D,S,W) corner of the volume itself (see Figure 2.2). The three indices range from 1 to NI, NJ and NK, respectively, when labelling a control volume, and from 1 to NI+1, NJ+1 and NK+1, respectively, when labelling a corner. It should be observed that the constant-I surfaces are planes parallel to each other only in the upper portion of the body (y>0) and the constant-K surfaces only in the lower portion (y<0); they become curved surfaces in the opposite half of the body. The constant-J surfaces are all curved, except the one for J=NJ/2+1 which coincides with the midplane y=0.

Although grid-generation packages are available both for FLOW3D and as general-purpose software, a purposely-built routine was used here. It follows an approach first suggested by Fodemski and Collins [1989] and takes advantage of the fact that the computational domain can be mapped smoothly onto a cube and is symmetric for a 180°-rotation around the "a" axis (main flow direction). The grid generation can thus be split into two subtasks:

- generation of a two-dimensional, body-fitted grid on a face (say,"D");
- translations and reflections of this to generate a three-dimensional grid spanning the entire body.

a) - Generation of a two-dimensional auxiliary grid

Consider the face labelled D ("Down") in Figure 6.5(a). A local system of coordinates ξ,η can be introduced in the plane of this face. For symmetry reasons, only one half of the face needs to be considered. Moreover, we can separate the task of generating a body-fitted grid in the fluid region from that of adding the necessary control volumes in the solid wall and dummy volumes around the body.

Figure 6.7 shows the left half of a face I=constant on the physical plane ξ-η (a) and on the transformed plane K-J (b). In order to avoid degeneration of control volumes, it was found convenient [Fodemski 1990] to replace the original geometry (sinusoid OQEB) with the modified geometry shown (piecewise line OO_1QEB). This requires the choice of a value for $\overline{OO_1}$; the assumption $\overline{OO_1}=\overline{OD}=s$ (wall thickness) seemed to be appropriate. This slight departure from the "true" geometry is not expected to affect flow and heat transfer results to any significant extent.

Now, a body-fitted 2-D grid spanning the region O_1QEBAO_1 is generated as follows. First, point E is arbitrarily located on the line O_1B (the choice $\xi_E=(2/3)T/2$ turned out to be effective). The grid points lying on the boundary O_1EBA are then prescribed by subdividing the two tracts O_1A and EB (lines J=constant) into N_ξ even intervals, and the two tracts O_1E and AB (lines K=constant) into N_η, also even, intervals. Finally, the coordinates of the inner grid points (corners of control 'volumes') are computed by the simple iterative procedure:

$$\xi_{K,J}=\frac{1}{8}(\xi_{K-1,J-1}+\xi_{K,J-1}+\xi_{K+1,J-1}+\xi_{K-1,J}+\xi_{K+1,J}+\xi_{K-1,J+1}+\xi_{K,J+1}+\xi_{K+1,J+1}) \quad (6.14a)$$

$$\eta_{K,J}=\frac{1}{8}(\eta_{K-1,J-1}+\eta_{K,J-1}+\eta_{K+1,J-1}+\eta_{K-1,J}+\eta_{K+1,J}+\eta_{K-1,J+1}+\eta_{K,J+1}+\eta_{K+1,J+1}) \quad (6.14b)$$

i.e. by computing the grid point coordinates at each iteration as the average of those of the 8 neighbouring points at the previous one. With reference to Figure 6.7, the initial values of the inner point coordinates to use in Eqns.(6.14) can be assumed to be:

$$\xi_{K,J} = \overline{OO_1} + \overline{O_1A}\ (K-K_1)\ /\ N_\xi \quad (6.15.a)$$

$$\eta_{K,J} = \overline{AB}\ (J-J_1)\ /\ N_\eta \quad (6.15.b)$$

i.e., the "starting" grid is the uniform rectangular grid spanning the rectangle $O_1E'BA$.

This method is similar to that proposed by Amsden and Hirt [1973]; however, in Amsden and Hirt the boundary points move towards their final positions during the iterative process, while here they are placed in their final positions from the beginning. It is easy to see that solving Eqns.(6.14) is equivalent to solving numerically a Laplace equation for ξ,η. Preliminary numerical experiments showed that the results were almost identical if the "diagonal" points (K-1,J-1 etc.) were not included in the averages, thus reducing the 8-point formulae (6.14) to simpler 4-point formulae. The method converges in a few iterations (e.g., 50 for the relative variation of all ξ's and η's between two consecutive iterations to fall below 10^{-6} if $N_\xi=N_\eta=14$), and has never exhibited stability problems.

A typical result of the above grid generation method is shown in Figure 6.8(a) for $N_\xi=N_\eta=14$, $N_w=1$. It should be observed that the wall-fluid interface O_1EB is a constant-K line in the tract O_1E, but is a constant-J line in the tract EB, see Figure 6.7.

In order to add control volumes in the solid wall and "dummy" control volumes, the outer wall profile, line DFC in Figure 6.7(a), is approximated by a sinusoid of slightly different pitch, and slightly shifted, with respect to the basic sinusoid OQEB. The wall thickness s is subdivided into N_w layers, and an additional layer is generated around the body by means of algebraic formulae. Details are cumbersome and will not be given here. Finally, the half-grid can be reflexed around its right boundary to yield the complete grid spanning a constant-I slice of the upper part of the computational domain., as shown in Figure 6.8(b). The boundary values of the two indices K and J are also reported; here:

$$NJ = 2(N_\eta + N_w + 1) \tag{6.16.a}$$

$$NK = 2(N_\xi + N_w + 1) \tag{6.16.b}$$

The 2-D grid on the "slice" shown includes NK * NJ/2 cells.

b) - Generation of the three-dimensional grid

The "assemblage" of a complete three-dimensional grid spanning the computational domain is now simply accomplished by translating the 2-D grid of Figure 6.8(b) along the I-direction to span the upper half of the body, and then upturning, rotating and translating it along the K-direction to span the lower half. The resulting 3-D grid has NI=NK and NJ volumes along the I, K and J directions respectively, see Eqns.(6.16). Final formulae for the coordinates of the control volume corners in the Oxyz reference frame of Figure 6.5(a), following the usual FLOW3D conventions, are:

Region y > 0 - For I=1 to NI+1, J=NJ/2+1 to NJ+1, K=1 to NK+1:

$$XC(I,J,K) = \xi_{K,J-NJ/2}\sin\beta + \xi_{I,1}\cos\beta \tag{6.17.a}$$

$$YC(I,J,K) = \eta_{K,J-NJ/2} \tag{6.17.b}$$

$$ZC(I,J,K) = \xi_{K,J-NJ/2}\cos\beta + \xi_{I,1}\sin\beta \tag{6.17.c}$$

Region y $\leqslant$ 0 - For I=1 to NI+1, J=1 to NJ/2, K=1 to NK+1:

$$XC(I,J,K) = \xi_{K,1}\sin\beta + \xi_{I,NJ/2+2-J}\cos\beta \tag{6.18.a}$$

$$YC(I,J,K) = \eta_{I,NJ/2+2-J} \tag{6.18.b}$$

$$ZC(I,J,K) = \xi_{K,1}\cos\beta + \xi_{I,NJ/2+2-J}\sin\beta \tag{6.18.c}$$

in which ß = π/4-Θ/2.

For the "reference" geometry of Table 6.1, a typical resulting 3-D grid (including solid and "dummy" volumes) is shown in Figure 6.9(a). The solid wall is evidenced. As $N_\xi=N_\eta=14$, $N_w=1$, it follows from Eqns.(6.16) that for this grid NI=NJ=NK=32. Two "slices" of the same grid are shown (without "dummy" cells) in Figures 6.9(b,c). They lie on the midplane y=0 and on the plane C-C parallel to the bottom corrugation, respectively.

6.2.2 Subgrid model and turbulence statistics

The Smagorinsky-Lilly subgrid model, widely described in Chapters 2 (theory) and 3 (implementation), was used. The constant c_s was set to 0.08, i.e. to the value which gave the best results in plane- and ribbed-channel simulations. However, some cases, including different Reynolds numbers, were run with no subgrid model ($c_s=0$, i.e. as direct simulations), a comparison of the results is given in Section 6.3.1.

For the present geometry, it is not possible to identify "homogeneous" directions along which to build representative ensemble statistics (these were planes parallel to the walls for the plane channel in Chapter 4 and lines parallel to the ribs for the ribbed channel in Chapter 5). Thus, quantities such as <Q> or Q" (see Nomenclature) could not be defined; instead, mean and fluctuating components were defined with reference to time, i.e. as time averages $\bar{Q}$ and time fluctuations $Q'=Q-\bar{Q}$.

By analogy with the plane-channel case, the LETOT was defined here as δ/u_τ, being δ a conventional channel half-height, defined as $D_e/4$ (the hydraulic diameter is defined in Section 6.1.3 for the present geometry), and u_τ a conventional friction velocity equal to $(|\tau_o|/\rho)^{1/2}$, with $|\tau_o|=\delta|\Delta p|/\Delta a$ (i.e., δ times the mean pressure gradient along the main flow direction "a"). For the reference geometry of Table 6.1 and a Reynolds number of 2450, 1 LETOT is equal to $\sim 1.25*10^{-2}$ s. Simulations were usually protracted for 5 LETOT's; this includes a "startup" period of 3 LETOT's, necessary for the influence of initial conditions to die away and a (statistically) steady state to be attained, followed by a period of 2 LETOT's over which time averages and other statistics were taken.

6.2.3 Boundary and initial conditions

For the present simulations, the inlet-outlet faces D,U,W,E of Figure 6.5(a) were assumed to be periodic surfaces, i.e. surfaces on which the flow

variables repeat themselves periodically from face D to U and from face W to E. This approach is appropriate to simulate the flow and temperature fields in the generic cell of the exchanger, far downstream from intakes, in which fully developed flow and thermal conditions can reasonably be assumed to have been attained.

As usual, the intrinsically non-periodic quantities p (pressure) and T (temperature) must be replaced by their periodic components p^*, T^* (i.e., "true" p and T plus a term varying linearly along the main flow direction "a"). Pressure losses have to be balanced by adding to the right-hand side of the momentum equation (4.2), written for the x- and z- directions, the source terms (driving pressure gradients):

$$F_x = F_z = |\Delta p| \; / \; (\sqrt{2}\, \varrho\, \Delta a) \qquad (6.19)$$

Similarly, heat input into the fluid has to be balanced by adding to the right-hand side of the energy equation (4.3) the "sink" term:

$$S_T = - \frac{(u+w)}{\sqrt{2}\, \Delta a\, \dot{M}\, c_p} \int_S q_w \, dS \qquad (6.20)$$

in which u and w are the cartesian velocity components along x and z, respectively.

Note that previous laminar and k-ε simulations were run by imposing the required value of the Reynolds number, Re^o, and adjusting the driving pressure gradient $|\Delta p|$ in Eqn.(6.19) at each SIMPLEC iteration according to the actual Reynolds number Re. The result was a damped oscillation (along the "iteration axis") of both Re and $|\Delta p|$, slowly converging to a steady state. However, in the present time-dependent, large-eddy simulations it was preferred to avoid the introduction of such artificial fluctuations; thus, the pressure drop was imposed while the Reynolds number was left free of varying in time as a result of the computation. Sensible initial flow rates were chosen on the basis of the experimental results and of preliminary simulations.

Alternative flow boundary conditions, consisting of defining faces D and W as <u>inlets</u> (Dirichlet boundaries) and the opposite faces U and E as <u>outlets</u> (Neumann boundaries), were used in previous (laminar and turbulent) steady-state simulations. This approach, repeated for a number of unitary cells in series, was more suitable for the simulation of <u>developing</u> flow (e.g., entrance effects in the experimental rig). However, this was not attempted here; as it is well known, the direct or large-eddy simulation of

non-periodic flows raises considerable problems, particularly related to the necessity of building a suitable time-dependent inlet flow.

As regards the thermal boundary conditions at the solid walls, both in the test rig and in a real exchanger the true conditions are somewhat intermediate between uniform-T_w and uniform-q_w. Two different sets of thermal wall boundary conditions were used here: the first (uniform-heat flux conditions) were chosen as being the simplest and most universal to run a reference case, for which detailed computational results will be presented in Section 6.3.2, and to conduct a parametrical study on the influence of computational options and physical parameters. The second (mixed conditions) were used to compare results with experimental measurements; they approximated better the experimental conditions and consisted of setting:

$$q_w = (T_b - T_w)/R \qquad \text{on the top wall} \qquad (6.21.a)$$

$$q_w = 0 \qquad \text{on the bottom wall} \qquad (6.21.b)$$

in which, as was described in Section 6.1.4, R is the overall thermal resistance of the corrugated plate+liquid crystal package, and T_b is the (uniform) temperature of the water bath (assumed here to be 20.5°C).

Predicted Nusselt numbers, and their dependence upon the Reynolds number and the corrugation angle, were little affected by the particular conditions chosen (see also Section 6.3.5). It should be observed that, in periodic flow simulations, the integral at the right-hand side of Eqn.(6.19) has to be computed explicitly at each iteration and time step if uniform-temperature or "mixed" conditions are used, while it becomes a known constant under uniform wall heat flux assumptions.

The solid wall was regarded as non-conducting in the present simulations, and the boundary conditions were directly specified at the fluid-wall interface. Further remarks on this choice are to be found in Section 6.3.5.

Initial conditions consisted of setting in the upper and lower duct of the unitary cell a plug velocity profile $v_r/\cos(\Theta/2)$, parallel to the corresponding corrugation, and superimposing on this random fluctuations having spatial-rms values u_{rms}, v_{rms}, w_{rms} (as computed over the whole cell volume) proportional to the "conventional" friction velocity u_τ, defined in Section 6.2.2. The proportionality constant was just 1 in most cases. As previously observed for plane and ribbed channels, the resulting starting flow field does not satisfy continuity; however, this is not a critical drawback for the flow solvers used here (i.e., the SIMPLEC algorithm), and a

divergence-free flow field, still containing significant three-dimensional fluctuations, is generated after a few time steps.

6.2.4 Time stepping, pressure-velocity coupling and spatial differencing

On the basis of the previous LES experience with different geometries (Chapters 4 and 5), Crank-Nicolson time stepping was chosen, and time steps in the range $0.5\text{-}2*10^{-2}$ LETOT's were tested (see Section 6.3.1 for a comparison of the results).

As to the pressure-velocity coupling algorithm, the present body-fitted grids require deferred correction of the non-orthogonality terms (see Chapter 3) and thus prevents the use of PISO or PISOC in a non-iterative fashion. Since there is no significant advantage in using PISO(C) with multiple iterations per time step, the more reliable SIMPLEC algorithm was used. The maximum number of iterations per time step was set to 10, and underrelaxation factors of 0.65 (velocities, viscosity) and 0.75 (temperature) were commonly used. As usual, the linear equation solvers ST3D (transport equations) and ICCG (pressure-correction equation) were selected, with a maximum of 10 and 25 "inner" iterations, respectively. Central differencing was used for the advection terms.

6.2.5 Programming and computational aspects

Release 2.1 of Harwell-FLOW3D, in the FORTRAN-frontend input mode, was used. Besides the LES modifications described in Chapter 3, minor 'ad hoc' modifications were implemented in order to compute local and average wall heat transfer coefficients, to input the data in an easy-to-use format, and to process the instantaneous results into time-averages and fluctuations. A purposely written subroutine, called in turn by USRGRD, was used for the grid generation; it makes dynamic use of the working arrays **WORK** and **IWORK** in order to save storage.

All simulations were run on the IBM 3090-200J of the University of Palermo Computing Centre (CUC). Since Extended-Memory facilities have been recently implemented, allowing up to 64 Mbytes of in-core storage, it was possible to test finer grids (up to 42^3 control volumes) than those used for the plane and ribbed channel simulations in Chapters 4 and 5. No use was made of the Vector Facility since the code compiled with the "Vector" option gave troubles at runtime. Typical CPU times were about 150 seconds per time step with a computational grid having 32^3 control volumes, and 240 seconds per time

step with 42^3 volumes. Most simulations were protracted for only five LETOT's (250 time steps); even so, typical values of the CPU time ranged from 10 to 16 hours, i.e. close to the maximum which can be realistically afforded.

As has been previously remarked, standard graphic post-processors (e.g. the OUTPROC package) are not suitable for the treatment of time-dependent, three-dimensional results, since they would require the handling and storage of very large files. Moreover, they cannot generally handle time-averaged or fluctuating fields. Thus, results were dumped only for selected slices of the computational domain and were post-processed by purposely-written simple programs, based on GDDM software (used with a Tektronics graphic terminal) and on Apple-Toolbox software (used with a Macintosh-LC personal computer).

6.3 Results and discussion

> **By carefully constructing a model and watching it on a computer we can demonstrate the emergence of form out of chaos, and shape from what had been erratic**
> [C.A.Whitney, 'Random Processes in Physical Systems']

6.3.1 General aspects and sensitivity analysis

a) Influence of the subgrid model

The time-behaviour of the three velocity components u,v,w along x,y,z (see Figure 6.5) at a monitoring point located near the centre of face U (outlet of the upper corrugation) is reported in Figure 6.10 (a-c) for the reference case (i.e., Θ=36°, Re^{O}=3000) as computed with and without a subgrid model, i.e. for c_s=0.08 (large-eddy simulation) and c_s=0 (direct simulation).

In both cases, it is possible to identify a short initial transient (less than 1 LETOT) during which the initial fluctuation amplitude decreases markedly, and the effect of initial conditions is rapidly "forgotten". This is followed by a longer transient (2-3 LETOT's) during which mean velocities develop towards asymptotic values; note that, although the flow rate as a whole decreases, the velocities at the monitoring point increase as a fully-developed velocity field is gradually developed. After about 3 LETOT's, one can assume that statistically steady (ergodic) conditions have been attained. The corresponding fluctuations are clearly larger and more irregular for the case c_s=0 (no subgrid model, i.e. direct simulation). In either case, however, they exhibit the same general behaviour, with a sharp dominant frequency **F** of

about 7 LETOT^{-1}. As it is particularly clear for the c_s=0.08 case, u and w components oscillate out of phase by about 180°, which is strongly suggestive of quasi-periodic oscillations of the velocity direction, with small changes in amplitude, at the monitoring point considered here. This conclusion is supported by the examination of consecutive instantaneous velocity vector plots for the same test case, see examples in Section 6.3.2.

The Reynolds number, averaged over LETOT's 3 to 5, is about 2450 both for c_s=0 and for c_s=0.08; thus, there is no significant difference between LES and DS as far as the equivalent friction coefficient is concerned (in both cases, f=0.069).

The time-behaviour of the instantaneous average Nusselt number Nu_{av} for Θ=36° and different Reynolds numbers, computed either by LES (c_s=0.08) or by DS (c_s=0), is reported in Figure 6.11(a). In all cases, Nu_{av} decreases rapidly for 2-3 LETOT's as wall thermal boundary layers grow starting from the initial, uniform temperature conditions; asymptotic values are practically attained after 3 LETOT's. The influence of the subgrid model increases markedly with the Reynolds number; there are almost no differences between LES and DS results for Re=776, while for Re=4250 the predicted Nusselt number is ~10% higher if a subgrid model is used. A similar behaviour was observed for the equivalent friction factor.

The above results may be summarized by saying that the use of a subgrid model yields smaller and more regular velocity fluctuations; its influence on overall quantities such as the friction coefficient and the average Nusselt number becomes significant only for Re>2-3000 and is otherwise negligible.

The behaviour of the instantaneous average Nusselt number for Re^o=3000 and increasing corrugation angles is reported in Figure 6.11(b). It shows that, while values of Nu_{av} increase markedly with Θ, practically asymptotic values are always attained after about 3 LETOT's. This supports the restriction of the transient duration to 5 LETOT's and the use of the period between 3 and 5 LETOT's as the time-averaging interval.

b) Grid- and time step-dependence

The behaviour of the instantaneous average Nusselt number Nu_{av} for Θ=36°and Re^o=3000 is reported in Figure 6.12(a) as computed by using three progressively finer grids having 24^3 (13824), 32^3 (32768), and 42^3 (74088) control volumes, respectively. Differences are clearly negligible for the two finest grids.

The pressure distributions on the top wall of the unitary cell (time averaged over LETOT's 3 to 5 and normalized by $|\tau_o|$), obtained with the three

above grids for the same reference case, are compared in Figure 6.13 (a-c). Note that pressure is the flow variable most sensitive to computational methods and numerical accuracy. Again, while the results obtained with the coarsest grid are clearly different (and probably affected by spurious spatial oscillations, or "wiggles"), the results from the two finest grids differ only in minor details.

The above comparisons support the use of the intermediate (32^3-volume) grid as the reference one for the parametrical study whose results will be summarized in the following Sections.

The instantaneous Nusselt number computed for the reference case by using two values of the time step (1/100 and 1/50 of a LETOT) are compared in Figure 6.12(b). Results are barely distinguishable, which justifies the use of the larger of the two values as the standard one in all the following simulations.

6.3.2 Detailed results for the reference case

Velocity vector plots in the midplane y=0 for Θ=36°, Re°=3000 (Re=2450), computed by a 32^3-volume grid for Δt=1/50 (LETOT) and c_s=0.08 (**reference case**), are reported in Figure 6.14.

Graph (a) refers to the time-averaged velocity field (the time averaging having been made over LETOT's 3 to 5). It shows, as expected, velocities directed almost everywhere along the main flow direction, with higher fluid speeds in the central region, and is on the whole very similar to that obtained by using a low-Reynolds number turbulence model for the same conditions [Ciofalo et al. 1992]. Graph (b) refers to the instantaneous field at t=4.2 LETOT's; it shows how the fluid "meanders" about the main flow direction, the largest oscillations being found in the central region of the unitary cell. Oscillations are clearly induced by the instability of the "spiral" shear-layer which is established between the two streams flowing in the upper and lower corrugation. The corresponding fluctuating (i.e., instantaneous minus time-averaged) velocity field is shown in graph (c) (note the different velocity scale).

Corresponding vector plots, but for the slice C-C in Figure 6.5 (parallel to the bottom corrugation), are reported in Figure 6.15 (a-c). Significant instantaneous velocity fluctuations can be observed.

Vector plots of the in-plane velocity field in the cross-section N-N of Figure 6.5, normal to the top corrugation, are reported in Figure 6.16. Both the time-averaged (a) and the instantaneous (b) fields are shown (at different

scales). Vectors in the bottom region would be very large at the present scale (and would not show any interesting detail), so that they were not drawn.

The time-averaged flow field shows clearly the presence of swirl in the upper duct, induced by the fluid stream flowing in the lower one. Swirling flow in a similar geometry was predicted and visualized also by Henry and Collins [1991] from laminar and standard k-ε simulations; their results, however, exhibited a single central swirl cell, while in the present LES ones the main circulation cell is shifted to the right (i.e., along the flow direction in the bottom duct), and a secondary circulation cell is clearly visible on the left. The (time-averaged) swirl intensity is rather low; typical velocities in Figure 6.16(a) are less than one tenth the reference velocity v_r. Thus, it is unlikely that the swirl has any significant influence on the pressure-drop and heat-transfer characteristics of the corrugated geometry.

The instantaneous velocity field in section N-N, Figure 6.16(b), exhibits large velocity fluctuations near the midplane; no clear circulation cell can be identified.

Selected time-averaged scalar fields in the midplane are shown for the reference case in Figure 6.17 (a-c): the pressure p^*, normalized by the "conventional" reference stress $|\tau_o|$; the temperature T^*, normalized by $T_\tau=q_w/(\rho c_p u_\tau)$; and the subgrid viscosity μ_s, normalized by the laminar viscosity μ. The same time-averaged scalars are shown in Figure 6.18 (a-c) for the slice C-C parallel to the bottom corrugation. It must be kept in mind that p^* consists of what is left of the pressure field once the mean pressure gradient $(-|\Delta p|/\Delta a^* a$, "a" being a coordinate aligned with the main flow direction) has been subtracted; thus, p^* is periodic between the inlet and outlet faces of the unitary cell (D-U, W-E in Figure 6.5). Also, in LES it includes the kinetic term $(2/3)\rho\tilde{k}$, $\tilde{k}$ being the unresolved turbulence energy. Similar remarks hold for T^*, which is only the periodic component of the "true" temperature T.

Note how the lowest pressures, graphs (a), are attained near the "throat" of the lower duct. The temperature distribution, graphs (b), exhibits a characteristic "hot curl" near the midplane on the left, shortly downstream of the region where highest heat transfer rates occur. The subgrid viscosity, graphs (c), is largest about the midplane, i.e. within the "spiral" shear-layer occurring between the upper and lower fluid streams. Note that, for the present Reynolds number, corrugation angle and grid resolution, small

values of the subgrid viscosity are obtained; μ_s is less than 0.5μ over most of the midplane, and less than 0.15μ over most of the computational domain.

An idea of the time-evolution of scalar fields in the midplane is given by Figures 6.19 (pressure) and 6.20 (temperature). Both figures show three consecutive "frames" corresponding to t=4.0, 4.2 and 4.4 LETOT's, respectively; the interval between two consecutive "frames" (1/5 of a LETOT) was resolved by 10 time steps in the simulation. Note that temperature fluctuations are advected downstream by the mean flow, while pressure fluctuations are not.

Time-averaged distributions of pressure p^*, wall shear-stress intensity $|\tau|$ and (local) Nusselt number Nu on the top wall are reported for the reference case in Figure 6.21 (a-c). Both p^* and $|\tau|$ are normalized by $|\tau_o|$.

The close similarity between the surface distributions of $|\tau|$ and Nu should be observed; under the present conditions, both quantities are concentrated mostly on the right edge of the top wall, and exhibit a marked maximum near the trailing corner of the unitary cell. A secondary maximum is also visible near the centre of the right edge.

A vector plot of the instantaneous wall shear stress field on the top wall (at t=4 LETOT's) is shown for the same case in Figure 6.22. The concentration of stress on the right edge, especially in the upper (i.e., downstream) end, can be clearly seen.

The time-evolution of surface quantities is suggested by Figures 6.23 (wall pressure), 6.24 (wall shear stress intensity) and 6.25 (local Nusselt number). As in Figures 6.19 and 6.20, instantaneous fields are shown for t=4.0, 4.2 and 4.4 LETOT's, i.e. every 0.2 LETOT's (10 time steps). Note how also instantaneous distributions of $|\tau|$ and Nu maintain a close similarity, and how both quantities can occasionally attain local values much higher than the corresponding time-averages.

6.3.3 Influence of the Reynolds number

The increasing influence of the subgrid model as the Reynolds number increases was discussed in Section 6.3.1. As expected, the relative amplitude of velocity fluctations increases with the Reynolds number in the present transitional range. Figure 6.26 (a-c) compares the behaviour of the three velocity components u,v,w at the centre of face U (outlet of the upper corrugated duct) as computed for $\Theta=36°$ and Re=776, 2450, and 4130. For this corrugation angle, at the lowest Reynolds number fluctuations die away almost

completely, and laminar flow is predicted. The intermediate Reynolds number is the "reference" case, fully examined in the above Section. At the highest Re, fluctuations are considerably larger; also, it becomes possible to distinguish in the time evolution of the velocities a first stage (LETOT's 0-3) during which they are irregular and relatively low, and a second (fully-developed ?) stage in which they attain larger values and become more regular (quasi-periodic) with a dominant frequency F. The corresponding Strouhal number, defined as $F\delta/u_\tau$ (number of periods in one LETOT) and clearly associated with the frequency of vortices such as those in Figure 6.14(b), is ~7 at all Reynolds numbers for this Θ.

The increase of the (relative) fluctuation amplitude with Re is confirmed by Figures 6.27 and 6.28, in which instantaneous velocity fields obtained at t=4 LETOT's for the three above Reynolds numbers and Θ=36° are compared for the midplane and section C-C, respectively.

The influence of the Reynolds number on the swirling flow in the cross section N-N is evidenced in Figures 6.29 and 6.30, which show velocity vector plots of the instantaneous and time-averaged flow fields, respectively, for the three above values of Re. The latter figure shows that, as the Reynolds number increases, the swirl intensity - even once normalized by the reference velocity - increases significantly. Also, the swirl centre moves towards the centre of the duct. The secondary circulation cell on the left is almost completely absent at the lowest Reynolds number, while its position and relative intensity do not vary much between Re=2450 and Re=4130.

The influence of Re on time-averaged surface quantities is documented in Figures 6.31-6.33 (all for the top wall and Θ=36°). Figure 6.31 is relative to the pressure field; it shows that, as the Reynolds number increases, the high-pressure region near the upper-right corner of the cell grows, and pressure maxima (even once normalized by $|\tau_o|$) increase. Figure 6.32 shows tha wall shear-stress intensity $|\tau|$, normalized as usual by $|\tau_o|$; as Re increases, $|\tau|$decreases in the central region but increases in the edge region where maxima are located, i.e. the distribution of $|\tau|$ becomes more peaked. Finally, Figure 6.33 reports the local Nusselt number; similar remarks hold, i.e. the distribution of Nu becomes less and less uniform as Re increases.

The above results can be summarized by saying that increasing Reynolds numbers yield larger (relative) velocity fluctuations, a stronger swirl, and more peaked distributions of pressure, shear stress intensity and local heat transfer coefficient on the walls. The variation of f and Nu_{av} with Re was studied in detail only for Θ=37°; results will be reported in Section 6.3.5, where they will be compared with experimental wind-tunnel data.

6.3.4 Influence of the corrugation angle

Figure 6.3.4 (a-c) reports the behaviour of the three velocity components at the usual monitoring point (centre of face U), as computed for Re^{O}=3000 and Θ=36°, 48° and 60°, respecively. The large increase of the fluctuation amplitude with Θ is quite evident. The dominant frequency F of the velocity fluctuations, once expressed as a Strouhal number $F\delta/u_{\tau}$ (periods per LETOT), decreases with Θ from ~7 (Θ=36°) to ~6 (Θ=48°) and ~5 (Θ=60°).

The instantaneous velocity fields in the midplane at t=4 LETOT's, obtained for the three above values of Θ and Re^{O}=3000, are compared in Figure 6.35 (a-c). As Θ increases, the region interested by large flow oscillations spreads considerably; for Θ=36° only a narrow central "meandering" region can be observed, while for Θ=60° almost the whole midplane is interested by large oscillations. Similar plots are reported in Figure 6.36 (a-c) for section C-C (parallel to the lower corrugation).

The swirl patterns in the cross section N-N computed for Re^{O}=3000 and Θ=36°, 48° and 60° are compared in Figures 6.37 (instantaneous flow) and 6.38 (time-averaged flow). Both figures show, as expected, a large increase of the swirl intensity with the corrugation angle. The time-averaged fields in Figure 6.38 show that, as Θ increases, the secondary flow pattern in the cross section becomes increasingly complex; for Θ=60°, up to four distinct circulation cells, two of which counter-rotating, can be observed.

The influence of the angle on time-averaged surface quantities is documented in Figures 6.39 (pressure), 6.40 (shear stress intensity) and 6.41 (local Nusselt number). As usual, p^{*} and $|\tau|$ are normalized by the "conventional" reference stress $|\tau_{o}|$. The examination of Figures 6.39 and 6.40 shows that, as Θ increases, the downstream high-pressure region spreads whilst the edge high-stress region shrinks (the fraction of the cell pressure drop $|\Delta p|$ due to wall shear stress decreases, while the fraction due to bulk dissipation increases). The region near the right edge interested by high values of Nu, Figure 6.41, becomes more elongated, while overall Nusselt numbers levels increase significantly (note the different scales in Figure 6.41).

The dependence of f and Nu_{av} on Θ was studied in detail only for Re^{O}=3000; results will be presented, and compared with wind-tunnel data, in the following Section 6.3.5.

6.3.5 Comparison with experimental data

Selected LES results are compared here with experimental data from the wind-tunnel measurements mentioned in Section 6.1 [VV.AA. 1989-1992, notably Report No.10 by J.Stasiek and M.W.Collins, 1992].

As anticipated in Section 6.2, for this comparison uniform heat flux thermal boundary conditions at the walls were replaced by "mixed" conditions, Eqns.(6.21), which are more appropriate to approximate the actual conditions realized in the test section. However, they do not take into account the coupling of convection with heat conduction in the wall, and thus the thermal inertia of the latter; this would have required the explicit simulation of conduction in the solid wall, which presents some unsolved difficulties for periodic flow due to the particular structure of the computational grid. In the real test section, the effect of the wall inertia is to completely suppress wall temperature fluctuations, since the wall time constant (of the order of $s^2/\alpha \cong 5$ seconds for the PVC plates) is much larger than the dominating period of the fluctuations (of the order of $(1/7)\delta/u_\tau \cong 2*10^{-3}$ seconds for Re=3000). This is confirmed by the fact that no significant time-fluctuation of the wall temperature distribution (indicated by the liquid crystal colour) was ever observed in the test section once steady-state conditions had been reached.

The experimental and predicted (time-averaged) distributions of the local Nusselt number on the top (active) wall are compared in Figure 6.42 for Θ=37°, Re=3900 and in Figure 6.43 for Θ=60°, Re=2400. There is some uncertainty in the experimental Reynolds numbers since total flow rates (i.e., cross-section averaged velocities) in the corrugated ducts were not directly measured but rather inferred from the peak velocity, measured by a Pitot-static probe. Simulations were conducted using a 32^3-volume grid and setting c_s=0.08.

For both corrugation angles, the experimental Nusselt number distribution is qualitatively well reproduced by the simulations (even in some details which might look at first sight as unreproducible idiosyncracies of the experimental method!). Peak values of Nu tend to be overpredicted, while the central flat minima are slightly underpredicted. On the whole, the agreement is better than that obtained by any other computational approach tested so far, including the use of a low-Reynolds number turbulence model [Ciofalo et al. 1992].

For Θ=37°, the predicted average Nusselt number, computed as in the experiments (i.e., as the surface-average <Nu> of the local values on the top wall) is ~26.5, while the experiments give~27.5. For Θ=60°, <Nu>(predicted)≅30 and <Nu>(experimental)≅29. Thus, in both cases the average Nusselt number is predicted very well. Note that predicted values of <Nu> are close within a few

percent to those computed for Nu_{av} from Eqn.(6.11.b); these, in turn, are only slightly lower (less than 5%) than the values of Nu_{av} computed under uniform-wall heat flux conditions for the same geometries and Reynolds numbers (for uniform-heat flux conditions <Nu> is rather ill-defined and may differ significantly from Nu_{av}).

The Reynolds number - dependence of the predicted equivalent friction factor and average Nusselt number was investigated in the range 1000-7000 for a corrugation angle of 37°. Results are reported, and compared with experimental data, in Figure 6.44. Computational results obtained using laminar-flow assumptions, the standard k-ε model, and a low-Reynolds number k-ε model, are also shown. On the whole, LES predictions reproduce satisfactorily the observed Reynolds number dependence and lie very close to those obtained by the low-Re model; f is slightly overpredicted at the lowest Reynolds numbers and slightly underpredicted at the highest, while <Nu> is slightly overpredicted in the whole range, with the exception of the case Re=2500. The overall behaviour of laminar and standard k-ε predictions is not satisfactory, as was previously shown for the whole range of Θ and Re in Figure 6.6.

The dependence of f and <Nu> on the corrugation angle Θ for Re=3000 is shown in Figure 6.45. As above, experimental data, LES predictions, and results from steady-state laminar, standard k-ε, and low-Re k-ε computations, are reported. Values of the friction factor predicted by LES are very close to the low-Reynolds number k-ε results, and lie slightly below the experimental values (the largest discrepancy is observed for Θ=48°). The Θ-dependence of f seems to be reproduced better by LES. Values of <Nu> are predicted much better by LES than by the low-Reynolds number turbulence model, which tends to underpredict <Nu> over the whole range studied. Note the completely wrong Θ-dependence predicted for <Nu> by the standard k-ε model, and the strong underprediction obtained by assuming the flow to be laminar.

6.4 Conclusions

But these particulars are not my measure;
All these I better in one general best
[Shakespeare, Sonnet XCI]

Three-dimensional, time-dependent flow and temperature fields, and bulk head loss and heat transfer performances, were computed for a crossed-corrugated

geometry in a range of Reynolds numbers and corrugation angles. A computational domain (unitary cell) was defined, and its geometrical and thermal-hydraulic characteristics were derived. A method for the generation of a body-fitted grid was developed. The continuity, Navier-Stokes and energy equations were solved either directly or using the Smagorinsky-Lilly subgrid model, with c_s=0.08 and σ_s=0.5. Simulations were run for fully-developed flow by setting periodic boundary conditions at the inlet and outlet faces. At the walls, no-slip boundary conditions for the flow field, and either uniform-heat flux or "mixed" conditions for the temperature field, were imposed.

Most simulations were run for 5 LETOT's, defined in the text, of which the last two were used to compute time-averaged quantities. A sensitivity study showed that grids having 32 control volumes along each direction, and time steps of 1/50 of a LETOT, gave satisfactorily independent results. The use of a subgrid model for the unresolved scales led to slightly smaller and more regular velocity fluctuations; its influence on predicted bulk performances (time-averaged friction coefficient and mean Nusselt number) was found to be significant only above Re=2500.

The detailed examination of instantaneous velocity fields and of the time-behaviour of velocity components at monitoring points showed that most of the flow fluctuations arise from the instability of the "spiral" shear layer existing between the two fluid streams flowing in the upper and lower corrugated ducts, and are associated with large vortices localized about the midplane and lying roughly parallel to it. The frequency F of these vortices, once made dimensionless as a Strouhal number $F\delta/u_\tau$, depends only on the corrugation angle and decreases from ~7 to ~5 as Θ increases from 36° to 60°. The relative intensity of the fluctuations increases both with Θ and with Re; for Θ=36°, an almost completely laminar flow is predicted only for Re<1000.

A weak swirling flow exists in each of the two ducts; its relative intensity increases both with Θ and with Re. Moreover, as Re increases the swirl centre moves from the downstream side of each duct towards the centre; for Θ=36°, a secondary (but co-rotating) circulation cell exists near the upstream edge of each duct. Increasing the corrugation angle makes the swirl pattern increasingly complex; up to four circulation cells can be identified in the cross-section of a duct for Θ=60°.

The distribution of the local Nusselt number on an active wall is very similar, especially at low angles, to that of the wall shear stress intensity; both exhibit larger values on the downstream edge of the wall and flat minima in the central region of the duct. The corresponding distributions remain similar, but become more peaked, when the Reynolds number increases.

Increasing corrugation angles lead to larger regions of intense heat transfer, while the relative importance of the wall shear stress in determining the overall pressure drop decreases.

Predictive results, with special regard to the surface distribution of Nu and to the Reynolds number- and angle- dependence of f and <Nu>, were compared with experimental wind-tunnel measurements. The agreement was very satisfactory, comparable (and under some respects superior) to that obtained by a low-Reynolds number turbulence model.

Due to the relatively fine grids required, to their non-orthogonal nature, and to the use of SIMPLEC as the pressure-velocity coupling algorithm, computing times were significantly larger than those mentioned for the plane and ribbed channel in Chapters 4 and 5. Typical 5-LETOT simulations, with a 32^3-volume grid and $\Delta t=1/50$ (LETOT), required about 10 hours of CPU on the IBM 3090-200J at the University of Palermo Computing Centre. However, these CPU requirements are only **2-3** times larger than those typical of a fully-converged steady-state simulation using a low-Reynolds number turbulence model on the same grid, and of course - besides being more accurate - provide a much larger insight into the nature and the behaviour of the flow and thermal fields.

Further predictive work on this subject should include the extension of the study to a wider range of geometrical parameters; the testing of alternative and more sophisticated subgrid models; and the development of graphic capabilities for an easier post-processing and a better understanding and comparison of the results.

As mentioned in Section 6.1, the present predictive study was paralleled by an experimental wind-tunnel research programme at the City University of London. The experiments for the sine-wave, crossed corrugated geometry, have just been concluded; it is now expected to extend the investigation to alternative corrugation geometries and shapes. Hopefully, the numerical simulation of these problems, including DS and LES predictions, will continue to assist in the planning, the assessment and the interpretation of the experiments.

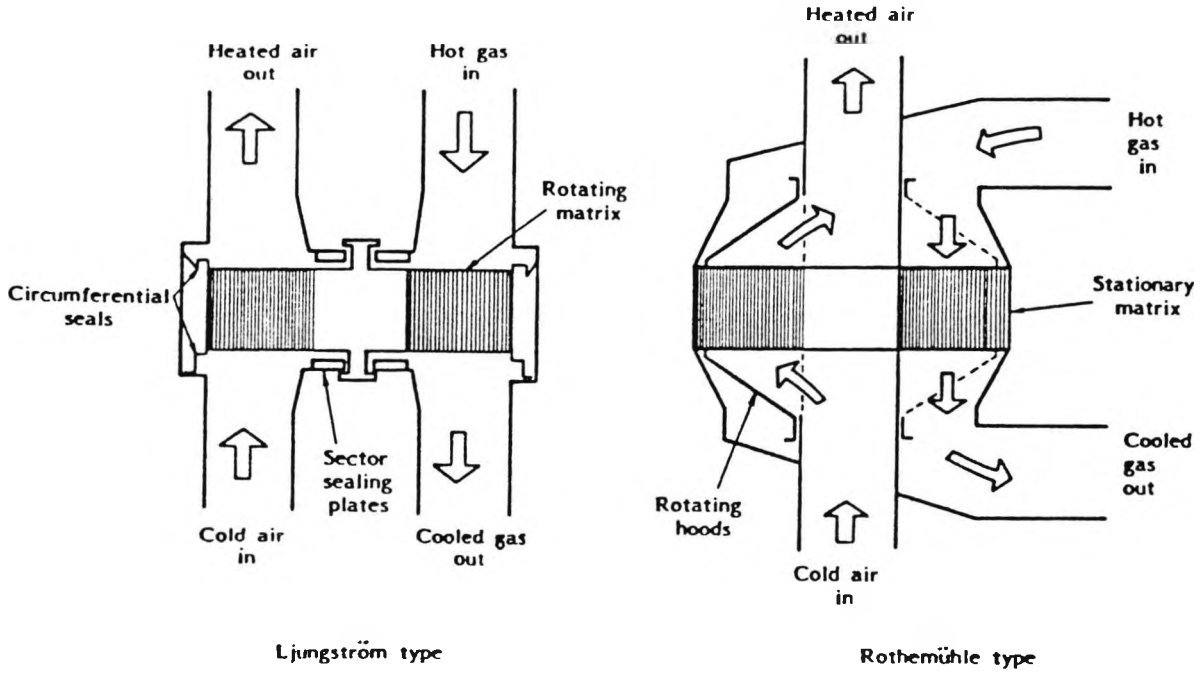


Figure 6.1 - Comparison of Ljungström and Rothemühle designs for rotary regenerators.

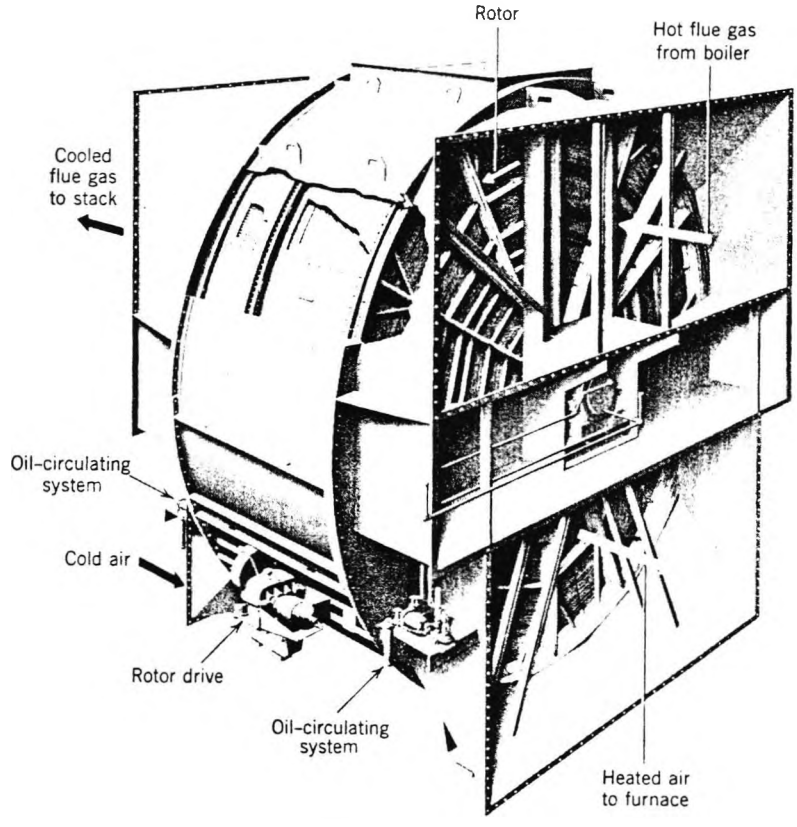
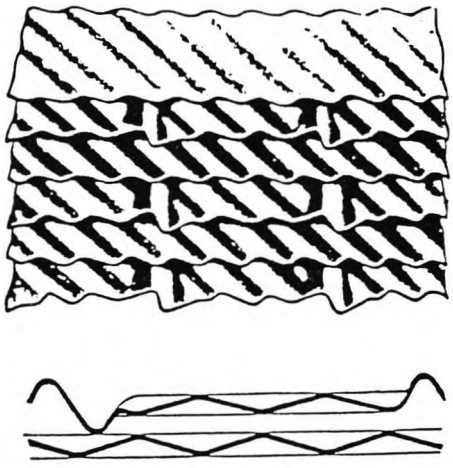
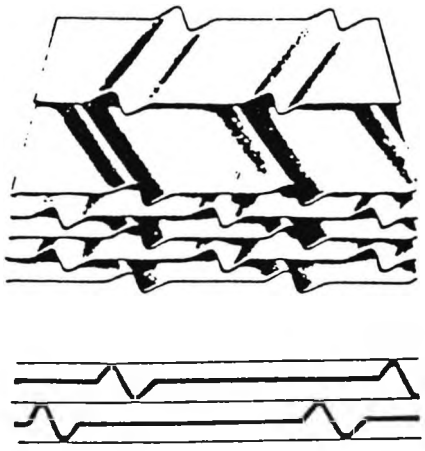


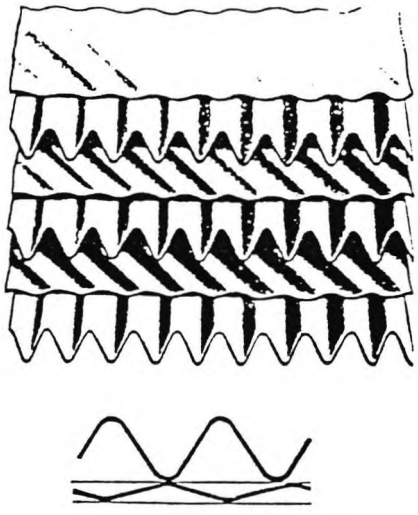
Figure 6.2 - Perspective view of a Ljungström rotary regenerator.



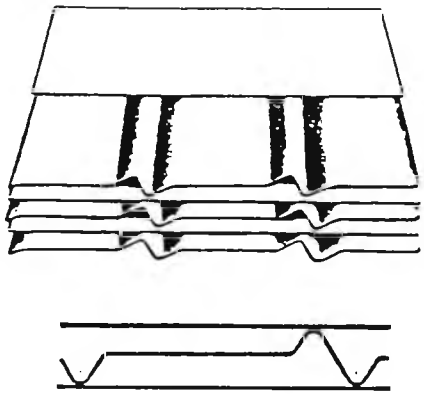
Double Undulated (DU)



Flat Notched Crossed (FNC)



Corrugated Undulated (CU)



Notched Plain (NP)

Figure 6.3 - Alternative corrugation designs for rotary regenerators.

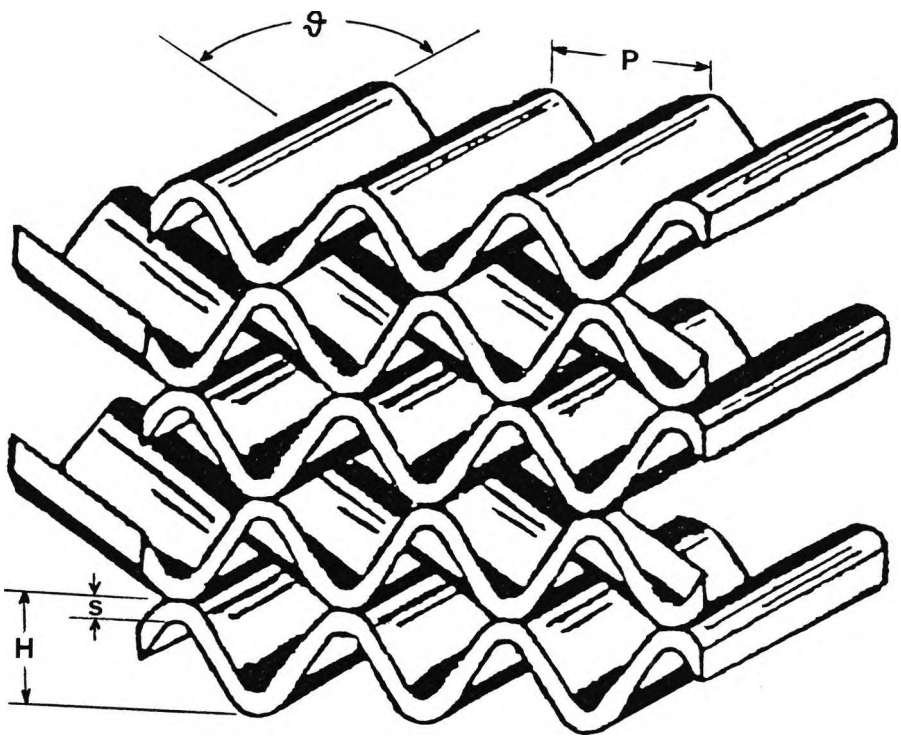


Figure 6.4 - Crossed corrugated heat transfer elements.

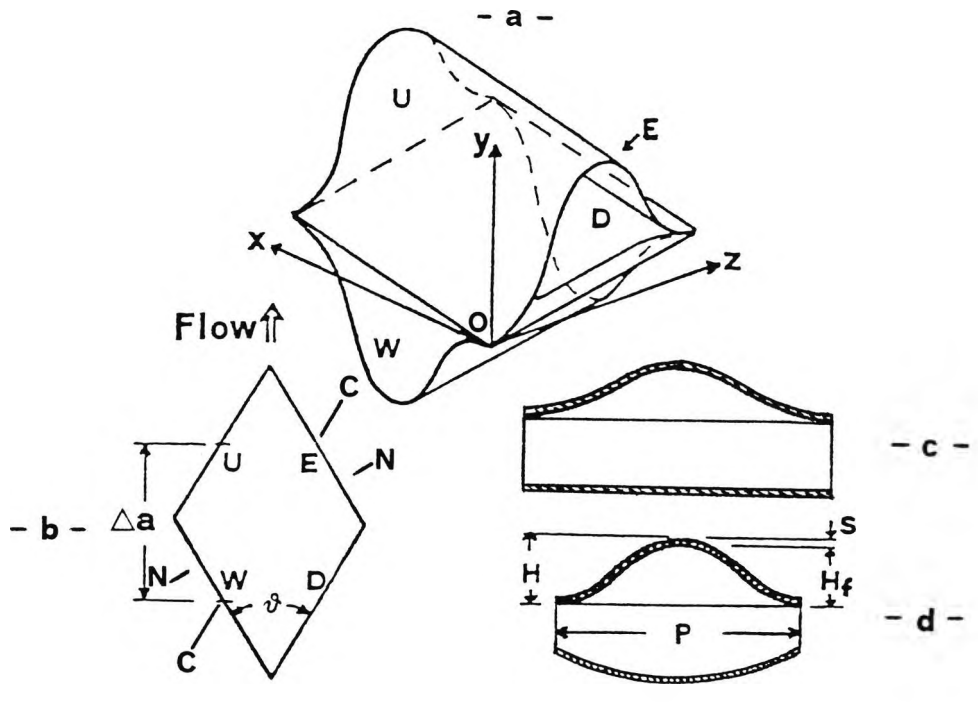


Figure 6.5 - Unitary cell (computational domain):
a) perspective view; b) midplane y=0;
c) section C-C parallel to the bottom corrugation;
d) cross-section N-N normal to the top corrugation.

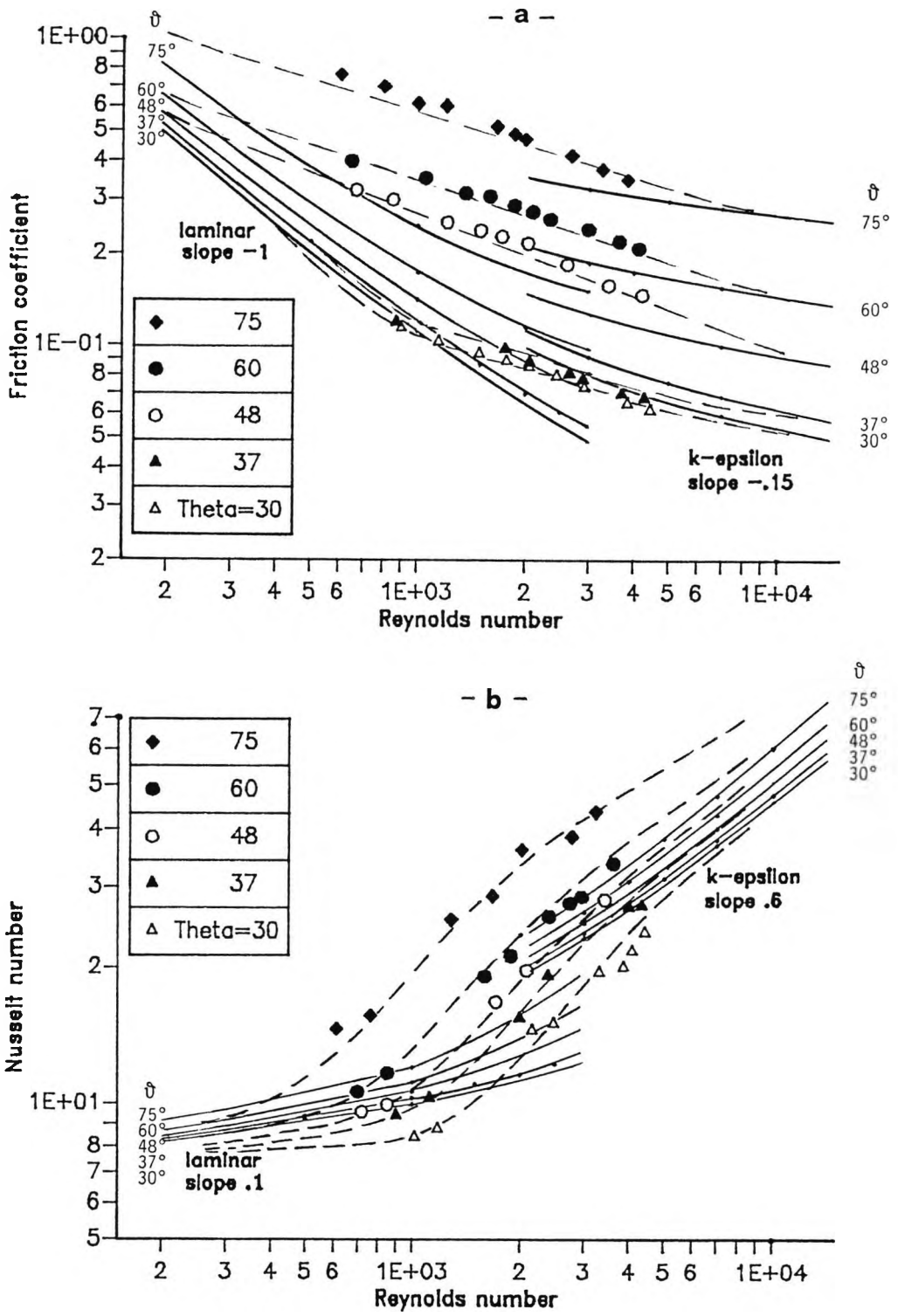


Figure 6.6 - Equivalent friction coefficient (a) and average Nusselt number (b) as functions of the Reynolds number for P/H_1=4 and different corrugation angles. Experimental results are compared with laminar and turbulent predictions.

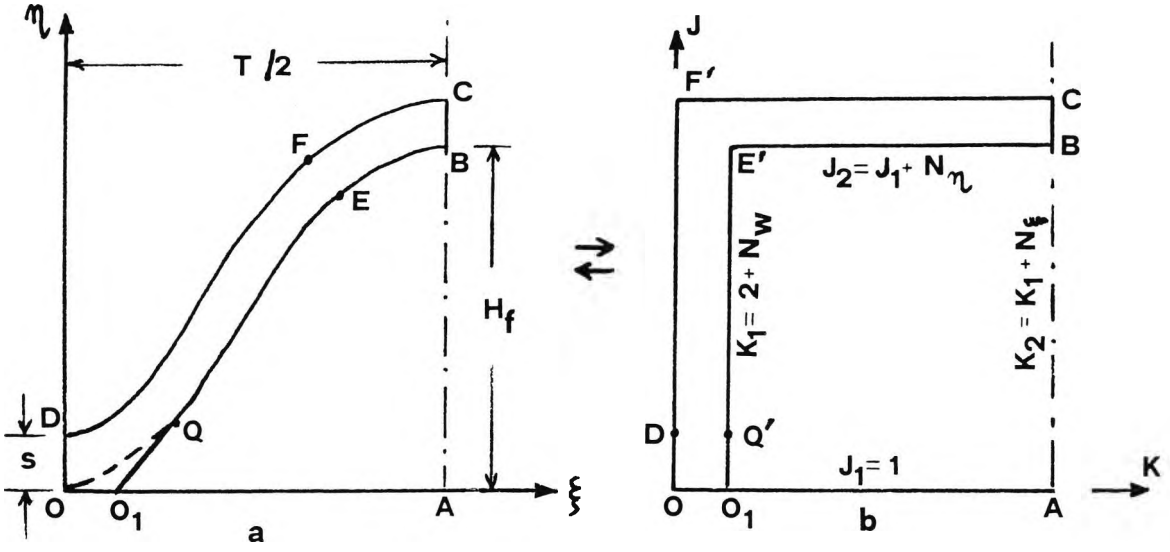


Figure 6.7 - Half-face I=constant and its equivalence to a rectangular domain having the same topology.
a) physical plane ξ-η ; b) transformed plane K-J

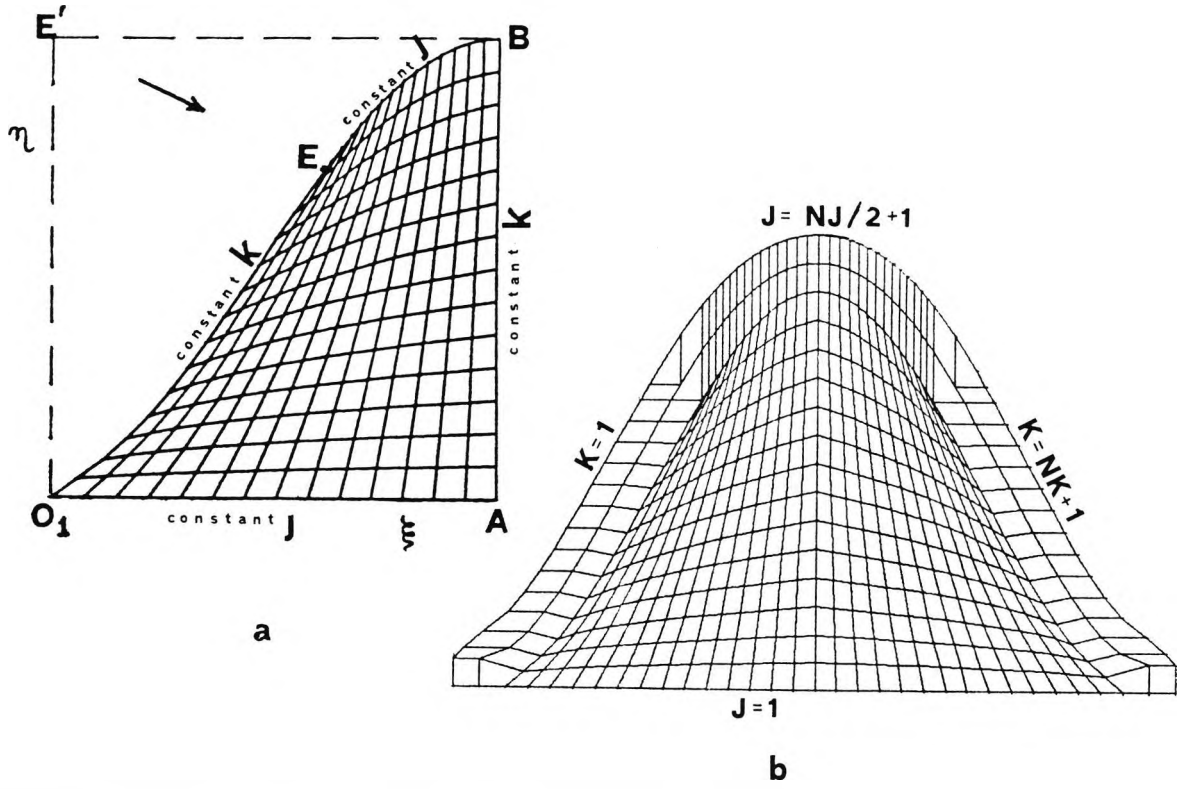


Figure 6.8 - 2-D auxiliary grid on a constant-I plane:
a) half-grid in the fluid region for $N_\xi = N_\eta = 14$, $N_W = 1$;
b) complete reflexed grid; extremal values of indices K and J are reported.

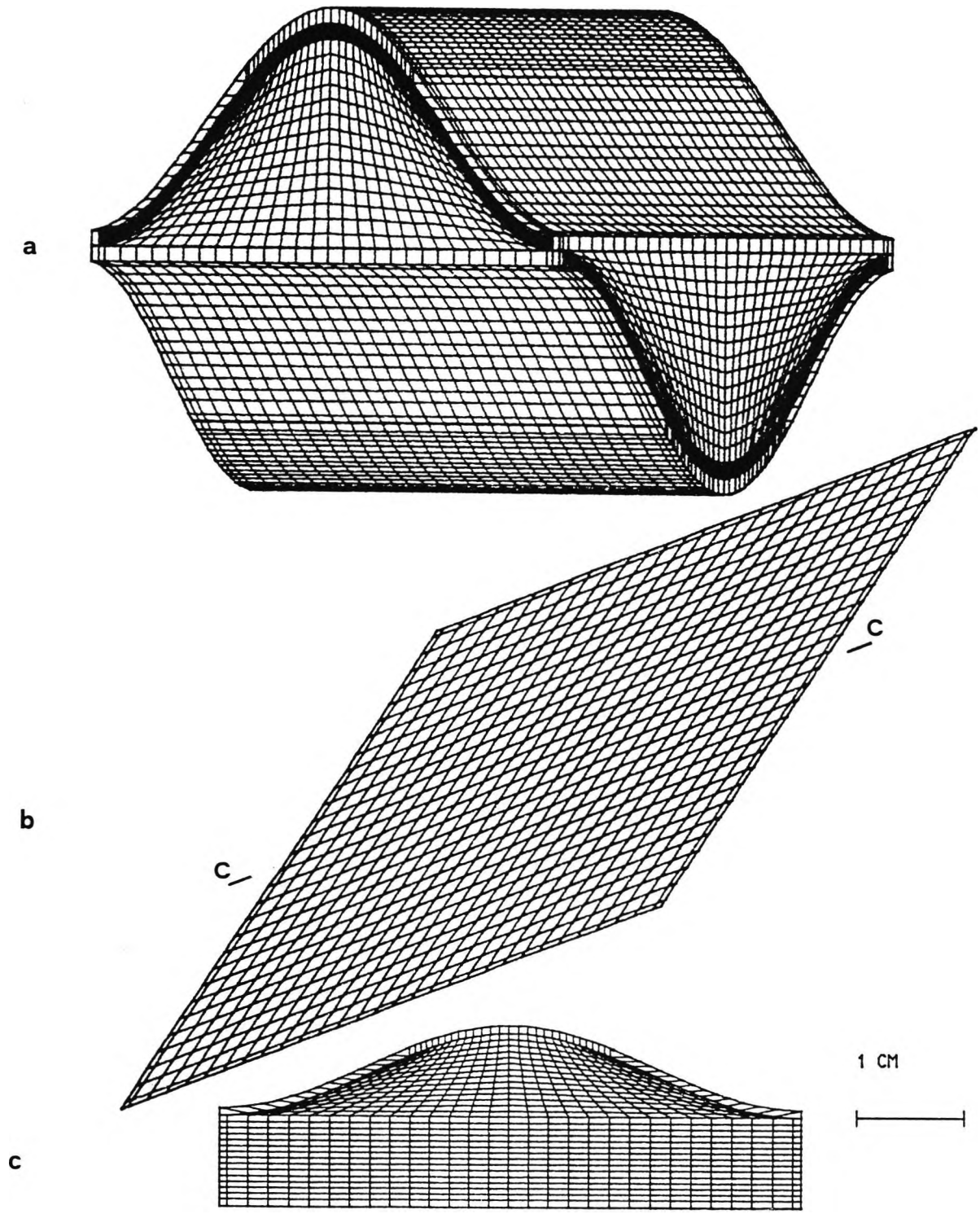


Figure 6.9 - Example of a three-dimensional grid for $N_\xi = N_\eta = 14$, $N_w = 1$:
a) perspective view; b) slice y=0 (midplane);
c) slice C-C parallel to the bottom corrugation.

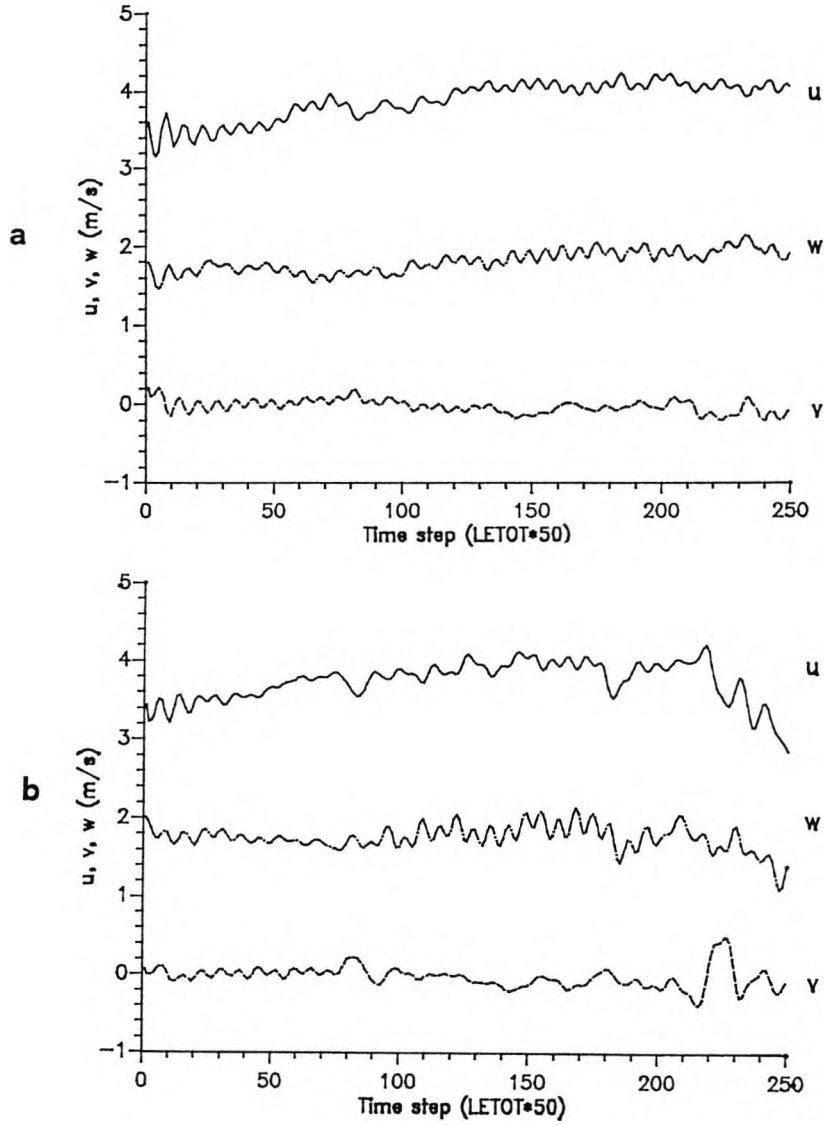


Figure 6.10 - Behaviour of the three velocity components u,v,w at a monitoring point located near the centre of face U, see Figure 6.5, for P/H_i=4, Θ=36° and Re^O=3000:
a) c_s=0.08 (LES); b) c_s=0 (DS).

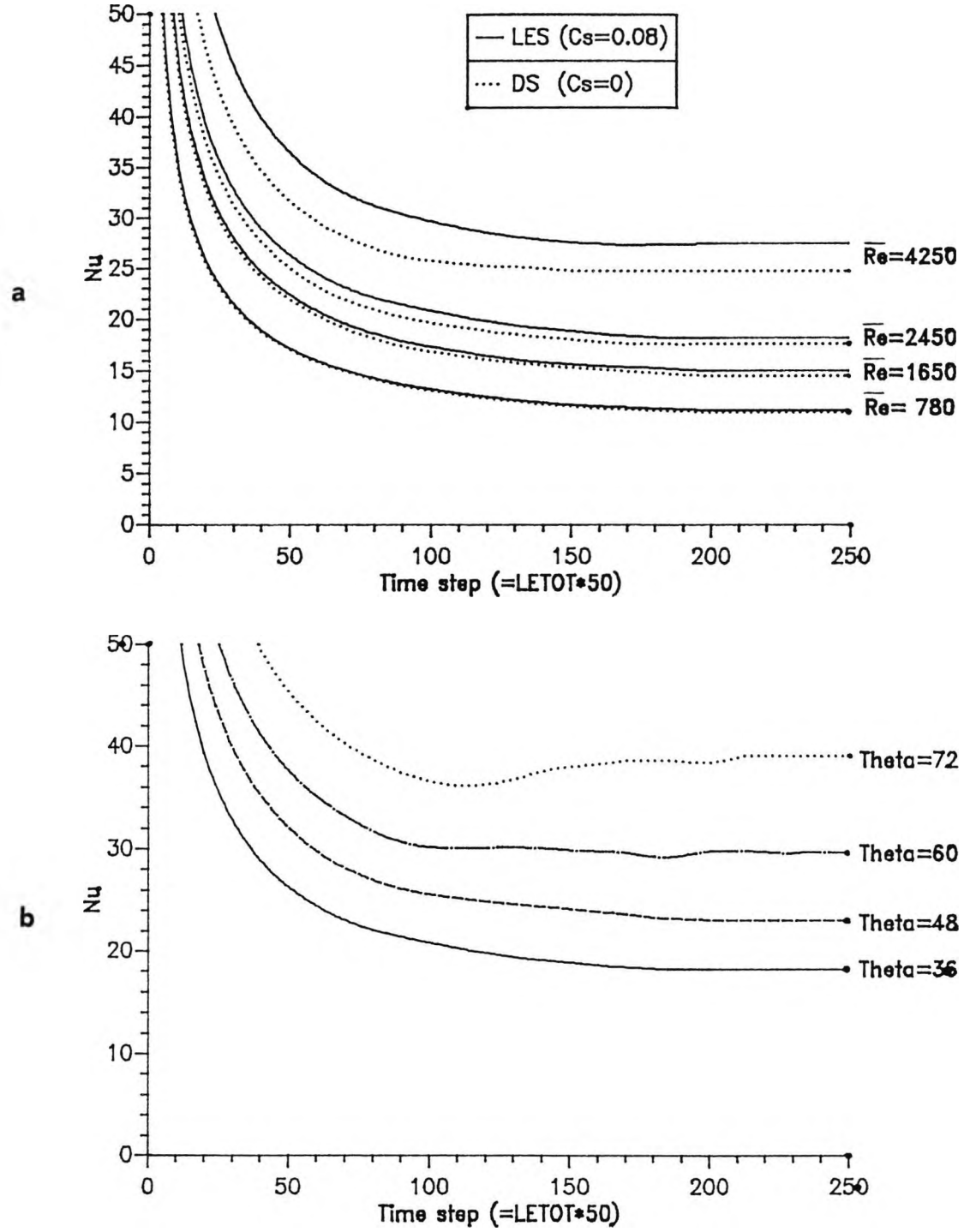


Figure 6.11 - Behaviour of the average Nusselt number (starting from a uniform+random temperature field) for $P/H_1=4$ and:
a) different Reynolds numbers, $\Theta=36°$, $c_s=0.08$ or 0;
b) different corrugation angles, $Re^{\circ}=3000$, $c_s=0.08$.

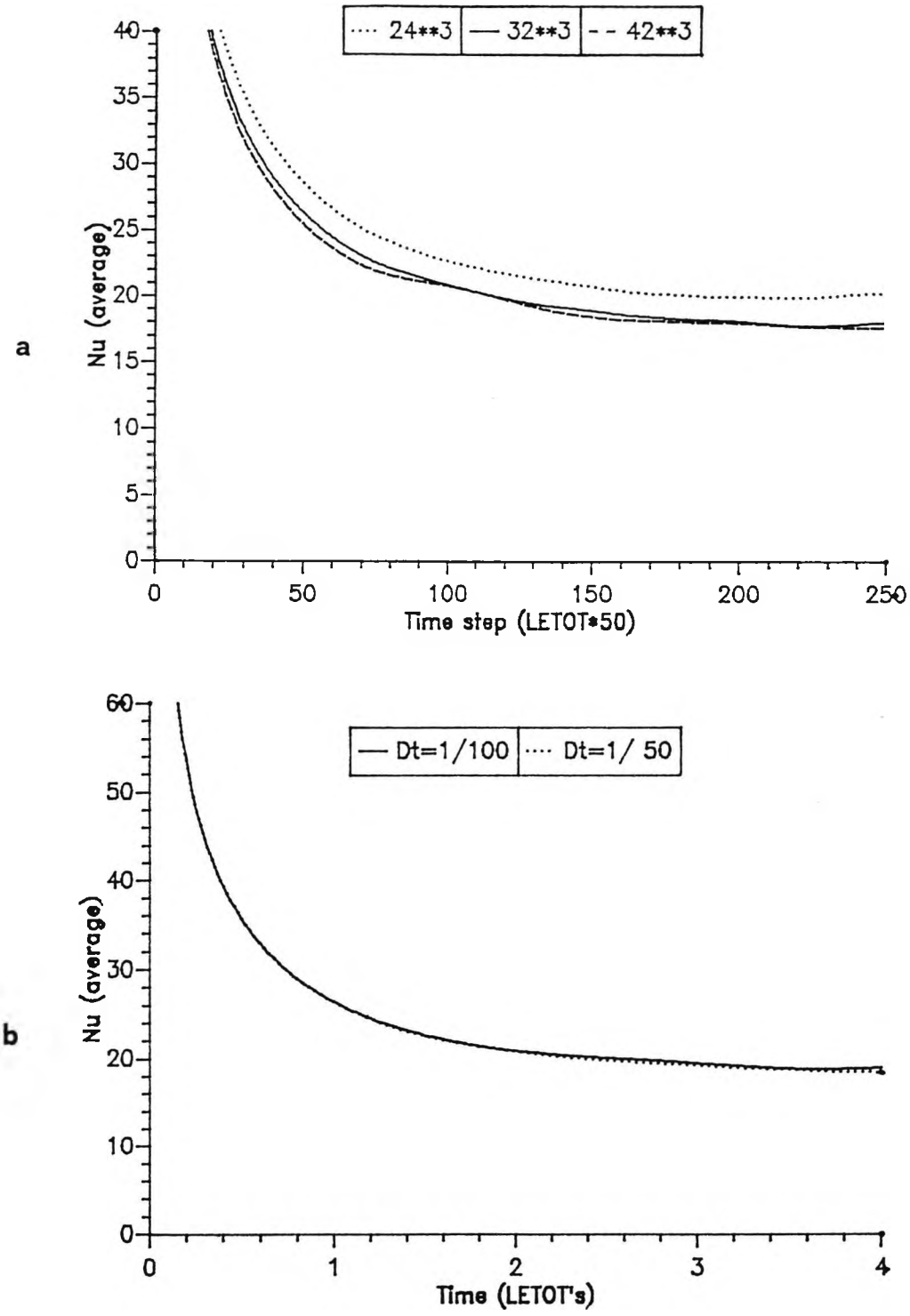


Figure 6.12 - Behaviour of the average Nusselt number for $P/H_1=4$, $\Theta=36°$, $Re^{O}=3000$, $c_s=0.08$, computed by:
a) three different grids having 24^3, 32^3, 42^3 control volumes;
b) two different time steps (1/100 and 1/50 of a LETOT).

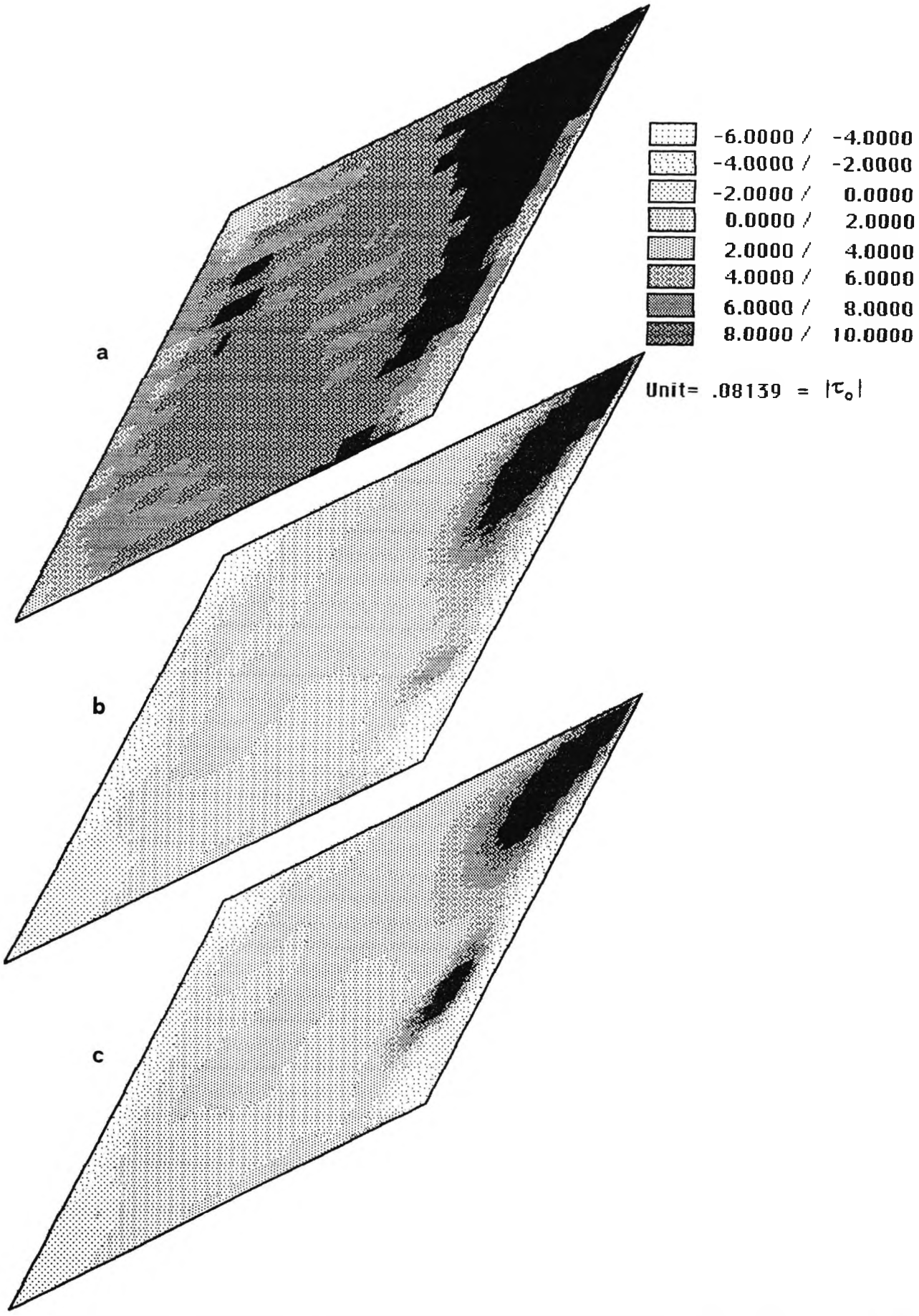


Figure 6.13 - Time-averaged pressure distribution on the top wall for $P/H_i=4$, $\Theta=36°$, $Re^{\circ}=3000$, $c_s=0.08$, computed by progressively finer grids: a) 24^3 volumes; b) 32^3 volumes; c) 42^3 volumes.

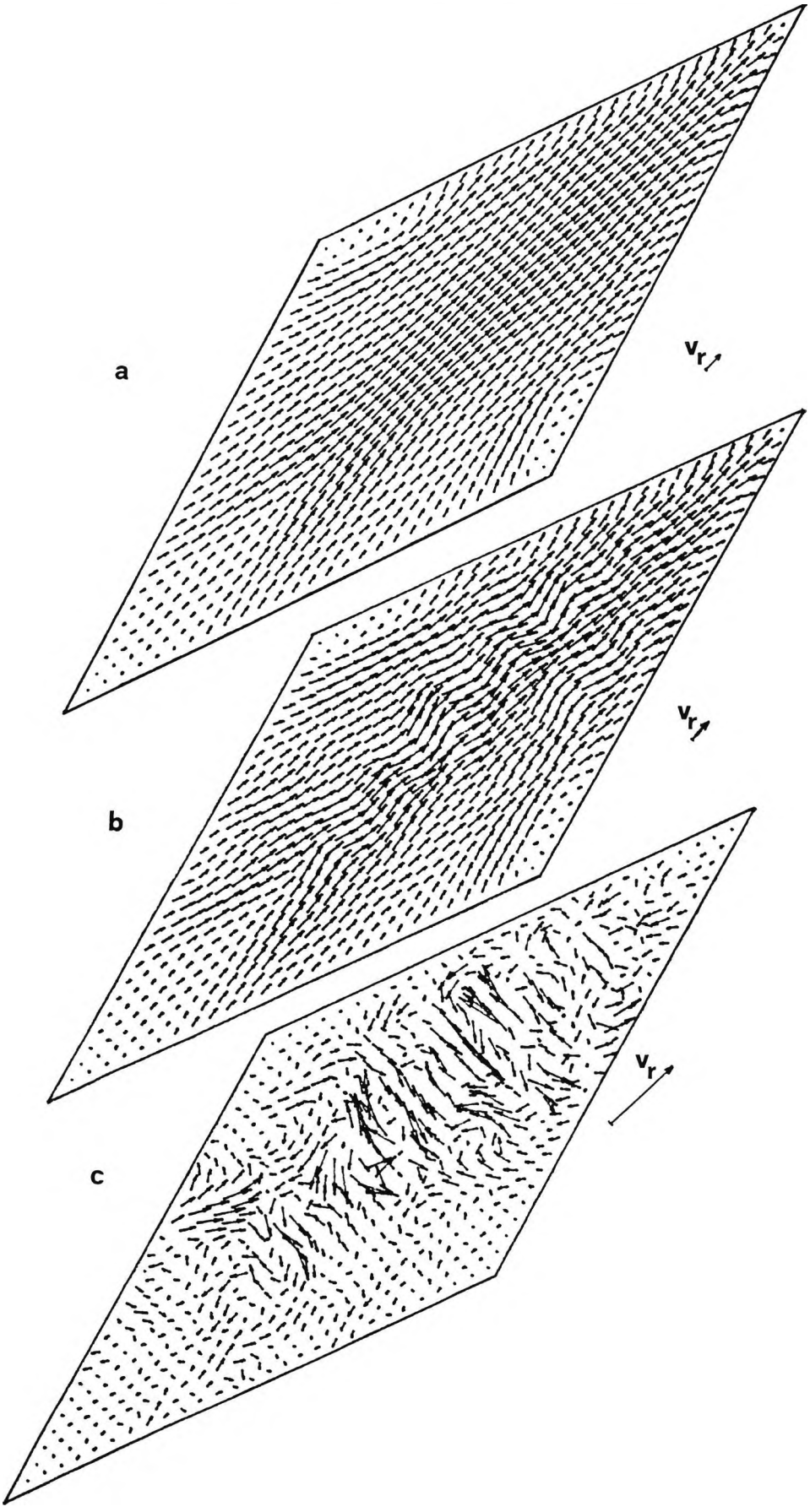


Figure 6.14 - Reference case (P/H_1=4, Θ=36°, Re°=3000): <u>time-averaged</u> (a), <u>instantaneous</u> (b) and <u>fluctuating</u> (c) velocity field in the midplane (t=4.2 LETOT's). The reference velocity v_r is shown.

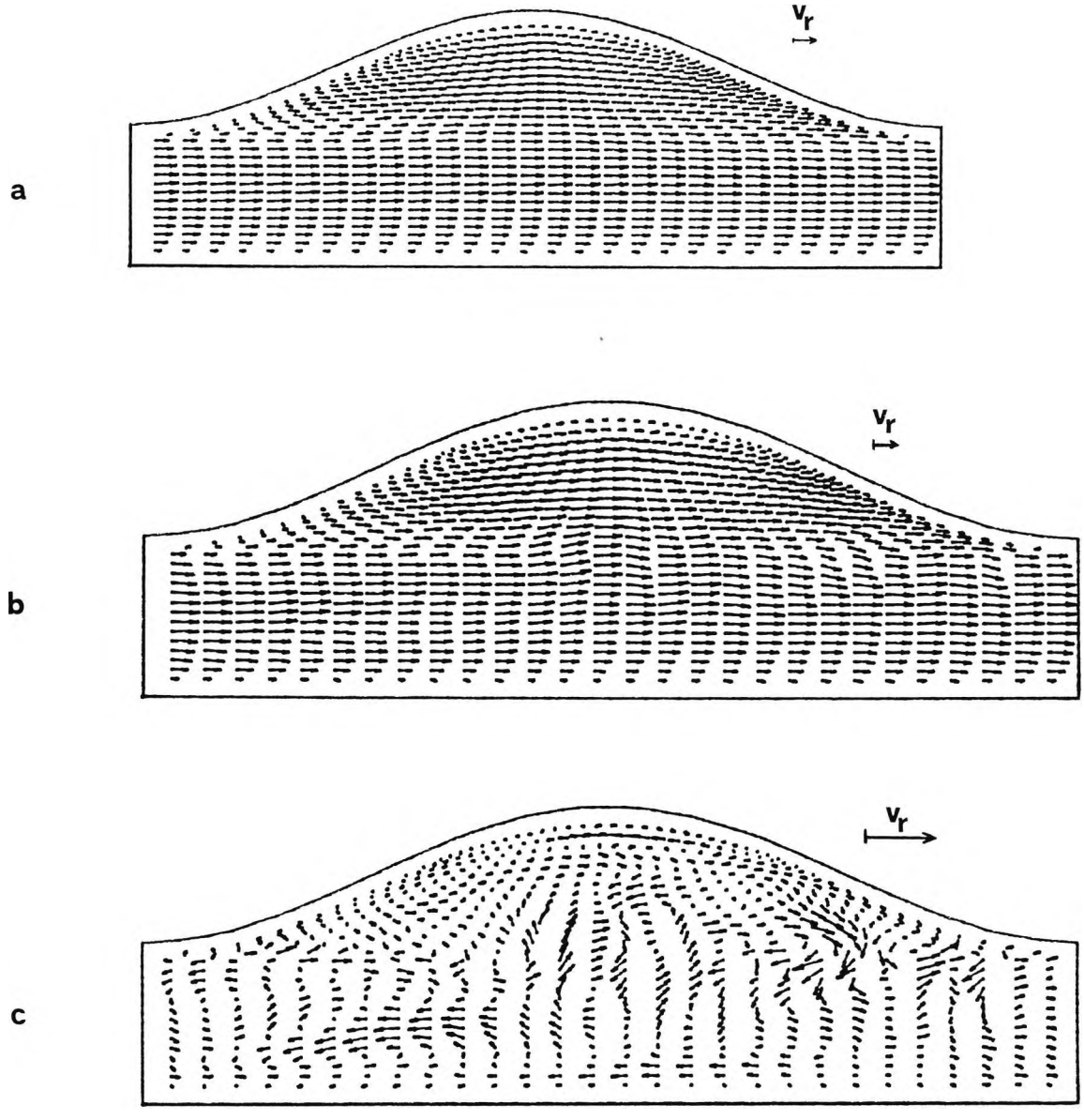


Figure 6.15 - Reference case (P/H_1=4, Θ=36°, Re°=3000): time-averaged (a), instantaneous (b) and fluctuating (c) velocity field in section C-C (t=4.2 LETOT's). The reference velocity v_r is shown.

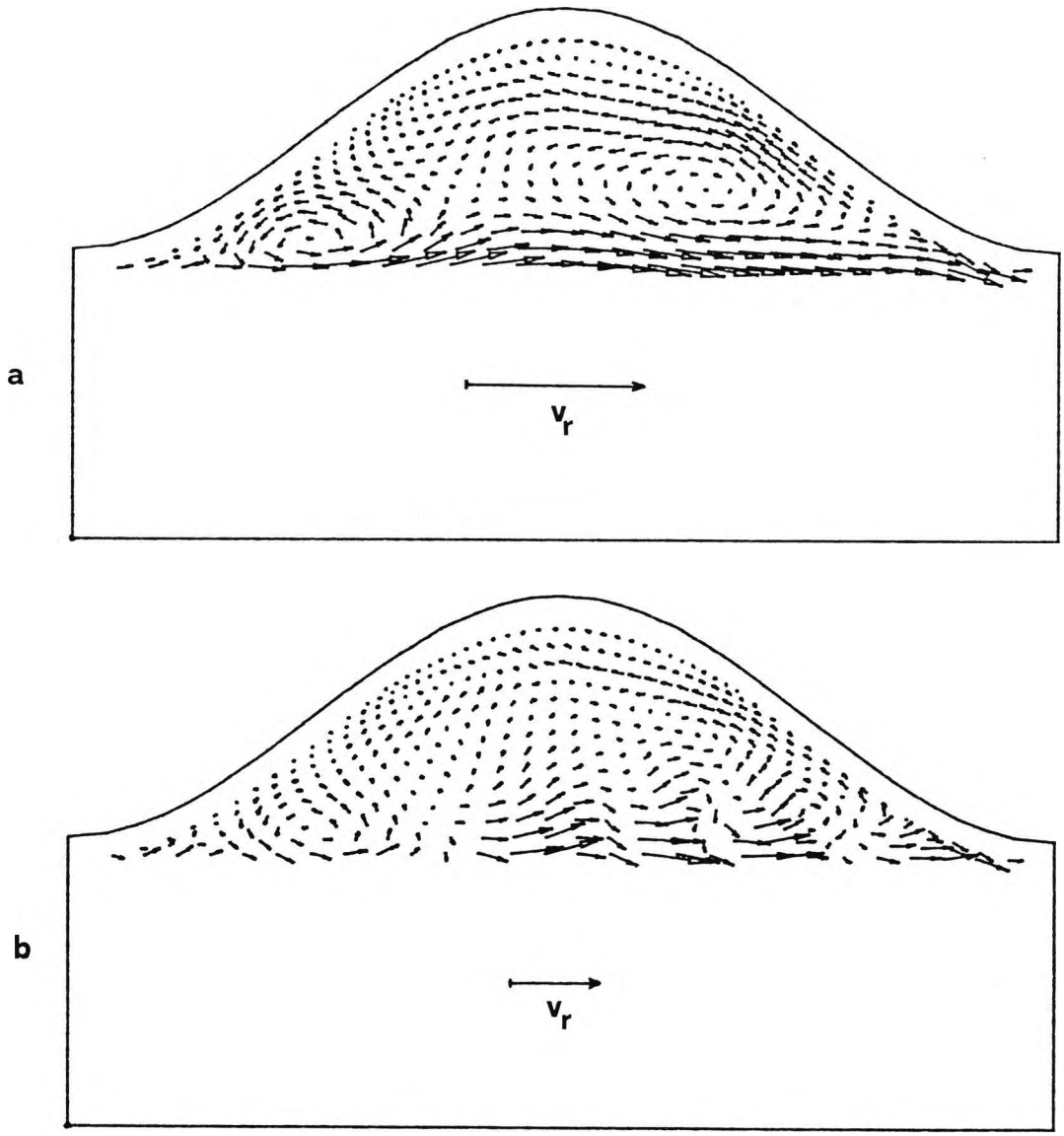


Figure 6.16 - Reference case ($P/H_1=4$, $\Theta=36°$, $Re^{\circ}=3000$): time-averaged (a) and instantaneous (b) velocity field in section N-N (normal to the top corrugation), showing swirling flow. Vectors in the lower half of the computational domain were not drawn. The reference velocity v_r is shown.

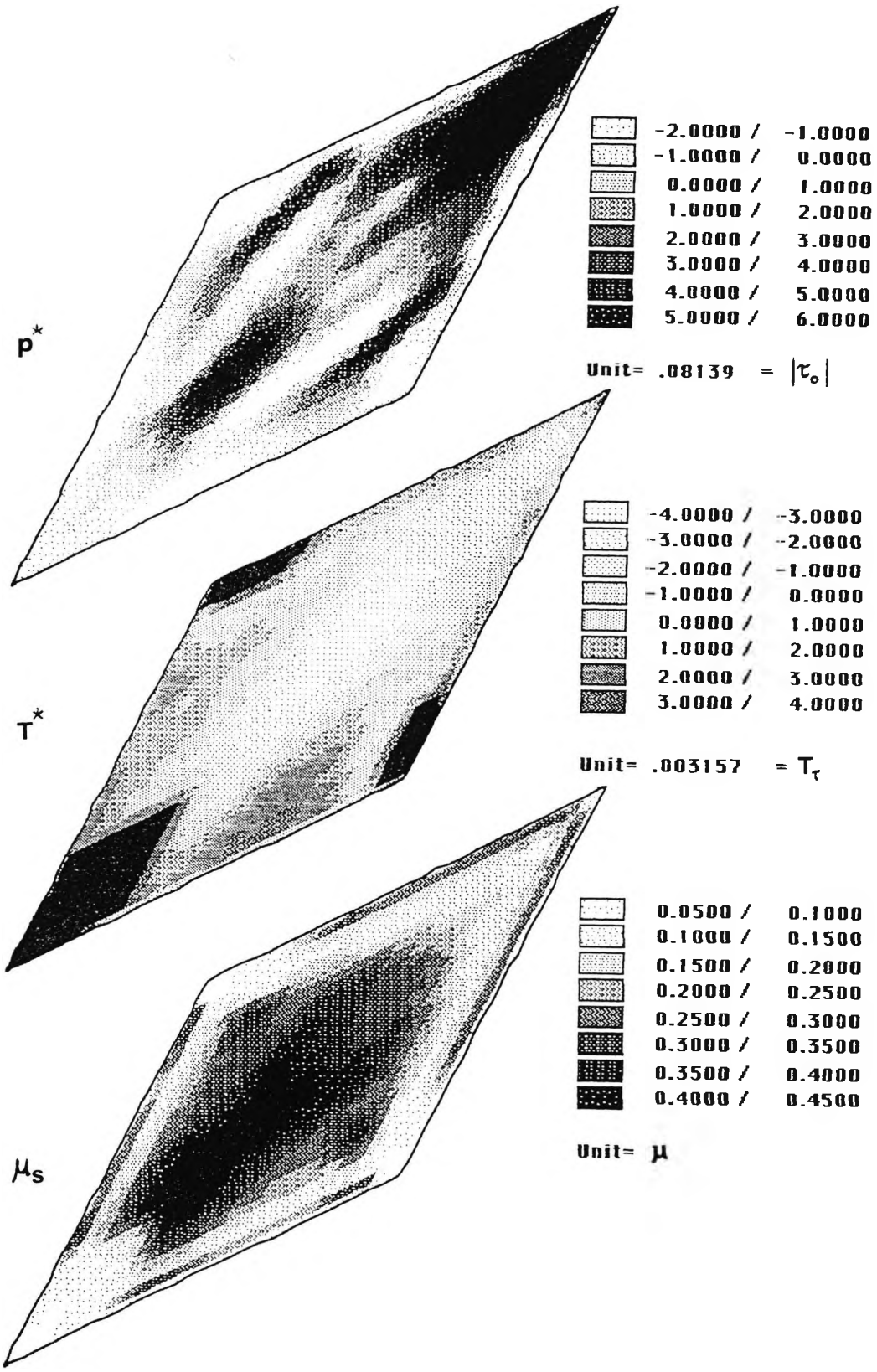


Figure 6.17 - Reference case (P/H_1=4, Θ=36°, Re^{O}=3000): time-averaged dimensionless pressure p^*, temperature T^* and subgrid viscosity μ_s in the midplane. Grey scales and normalization units are shown.

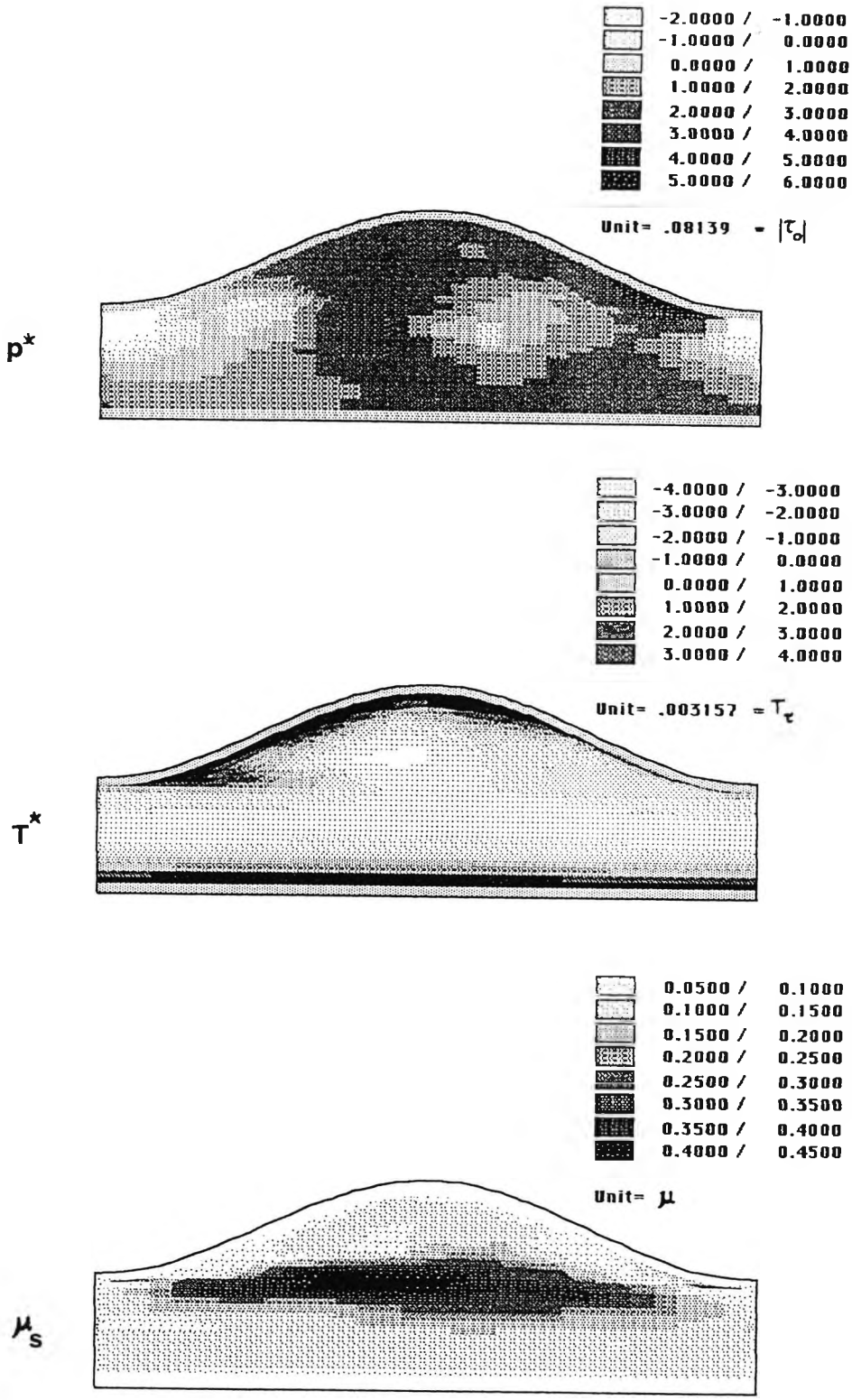


Figure 6.18 - Reference case (P/H_1=4, Θ=36°, Re°=3000): time-averaged dimensionless pressure p^*, temperature T^* and subgrid viscosity μ_s in section C-C. Grey scales and normalization units are shown.

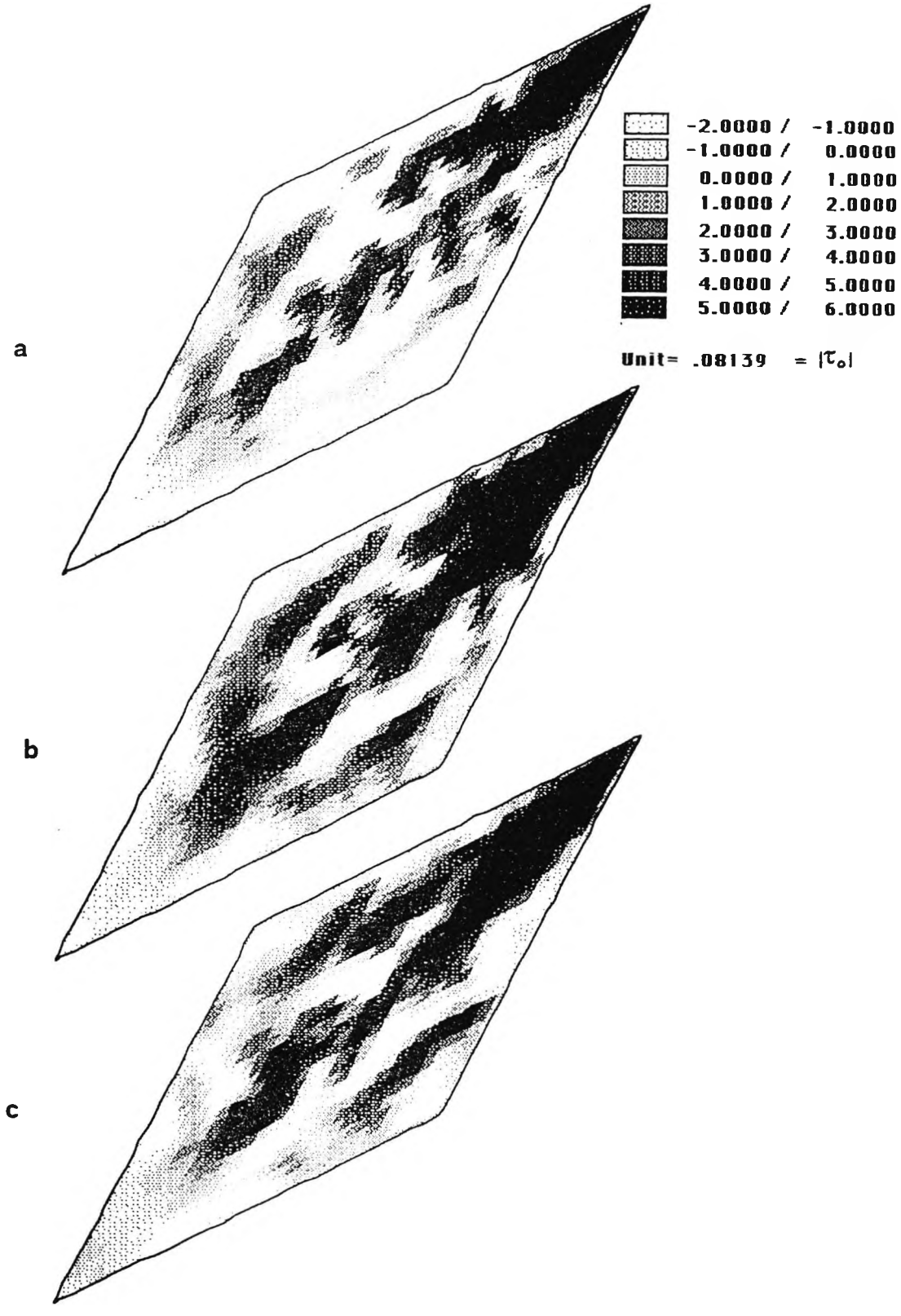


Figure 6.19 - Reference case (P/H_i=4, Θ=36°, Re^{O}=3000): instantaneous dimensionless pressure field in the midplane. Grey scales and normalization units are shown.
a) t=4.0 b) t=4.2 c) t=4.4 (LETOT's).

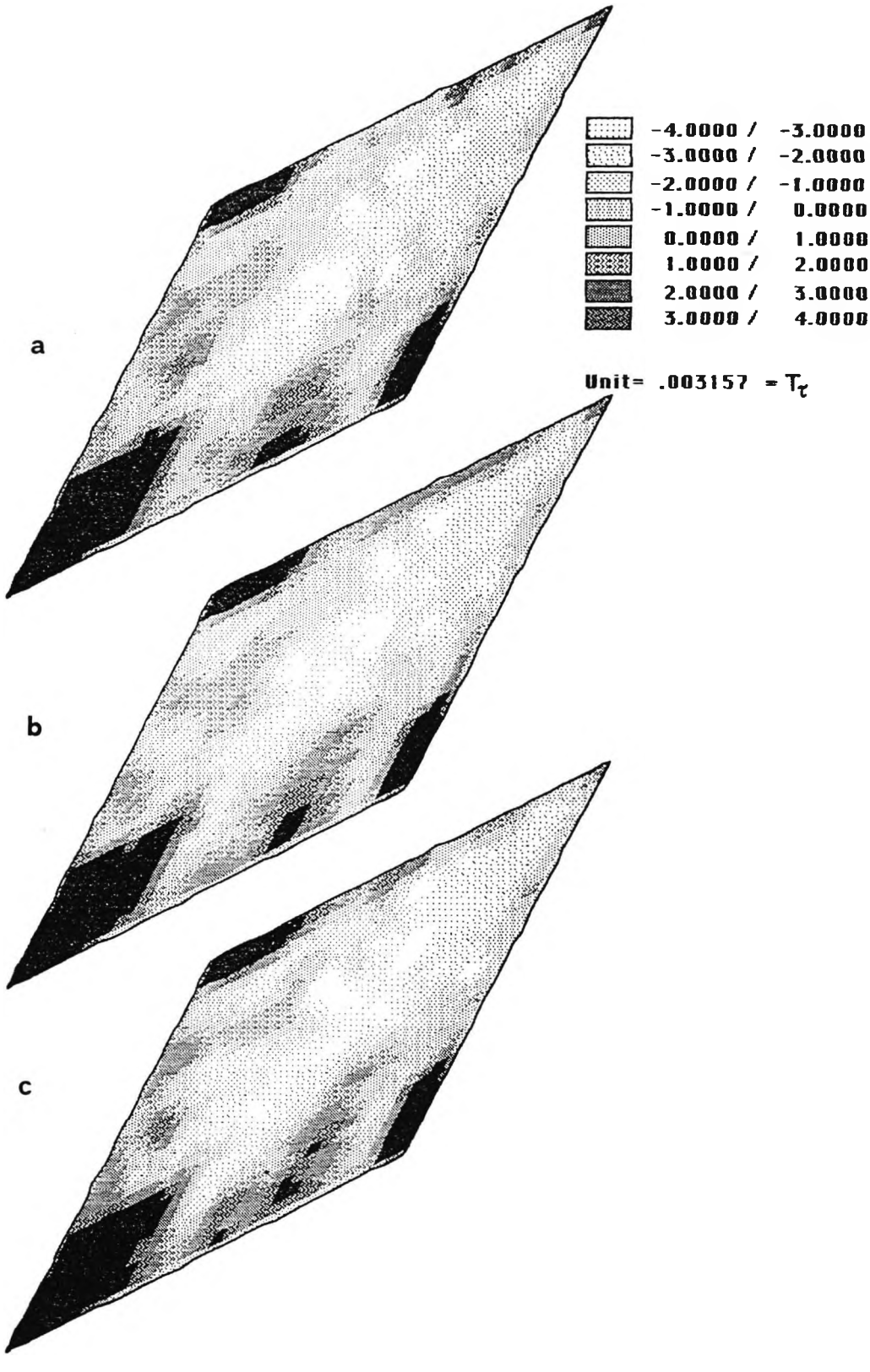


Figure 6.20 - Reference case (P/H_i=4, Θ=36°, Re°=3000): instantaneous dimensionless temperature field in the midplane. Grey scales and normalization units are shown.
a) t=4.0 b) t=4.2 c) t=4.4 (LETOT's).

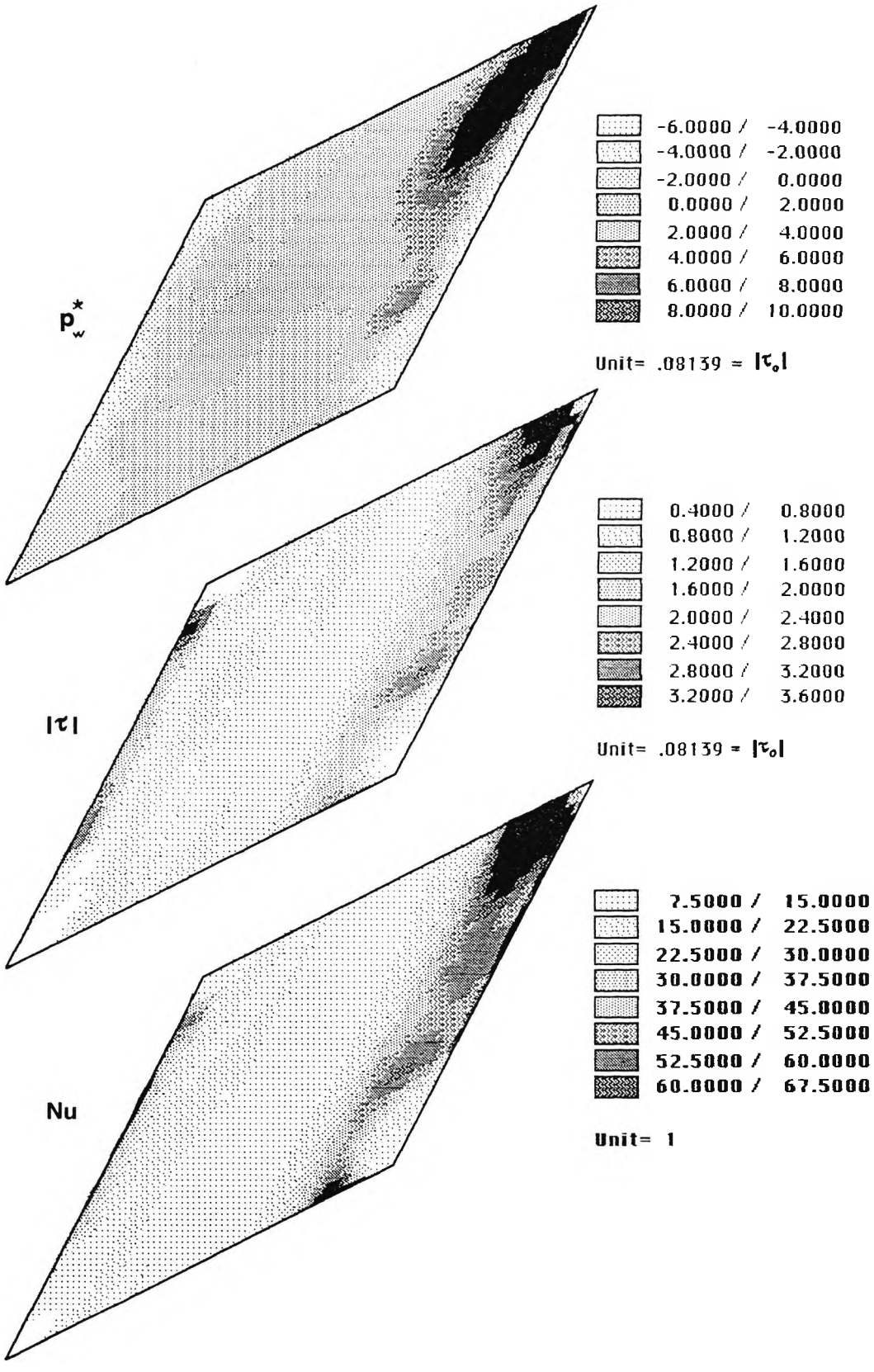


Figure 6.21 - Reference case (P/H_i=4, Θ=36°, Re°=3000): time-averaged dimensionless pressure p^*_w, shear-stress intensity $|\tau|$ and Nusselt number Nu on the top wall. Grey scales and normalization units are shown.

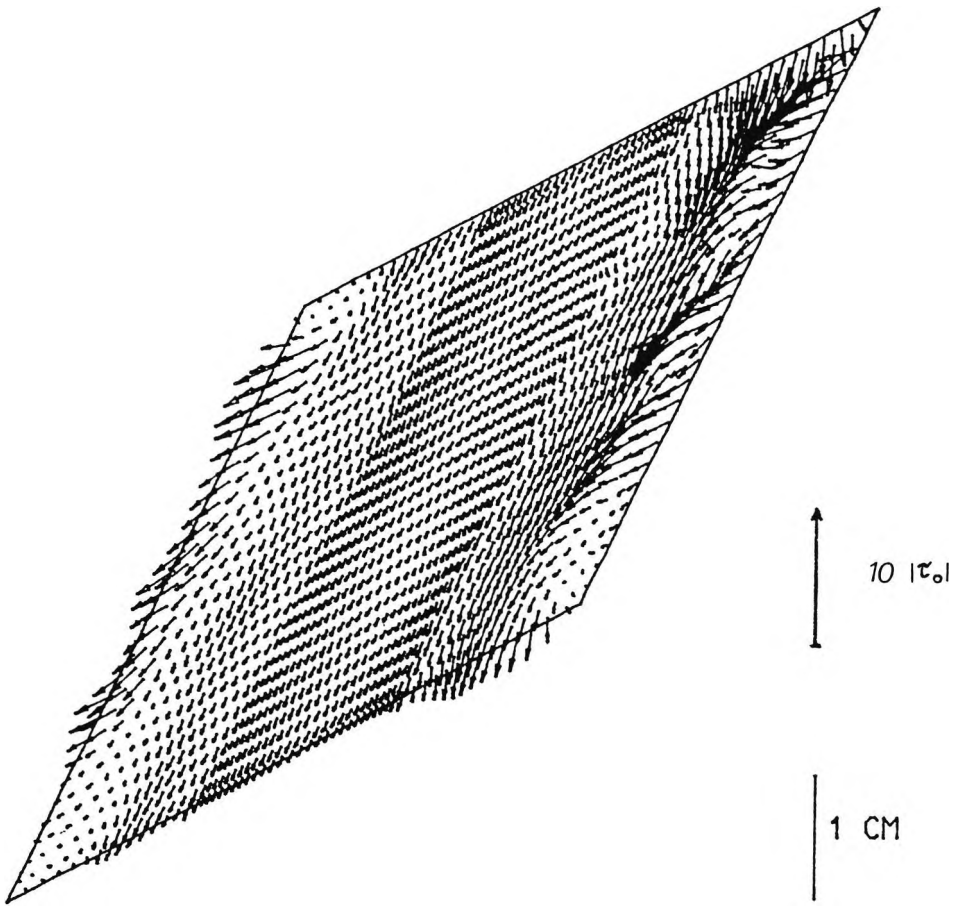


Figure 6.22 - Reference case (P/H_i=4, Θ=36°, Re^O=3000): vector plot of the instantaneous stress field on the top wall at t=4.2 LETOT's. The reference stress τ_o is shown.

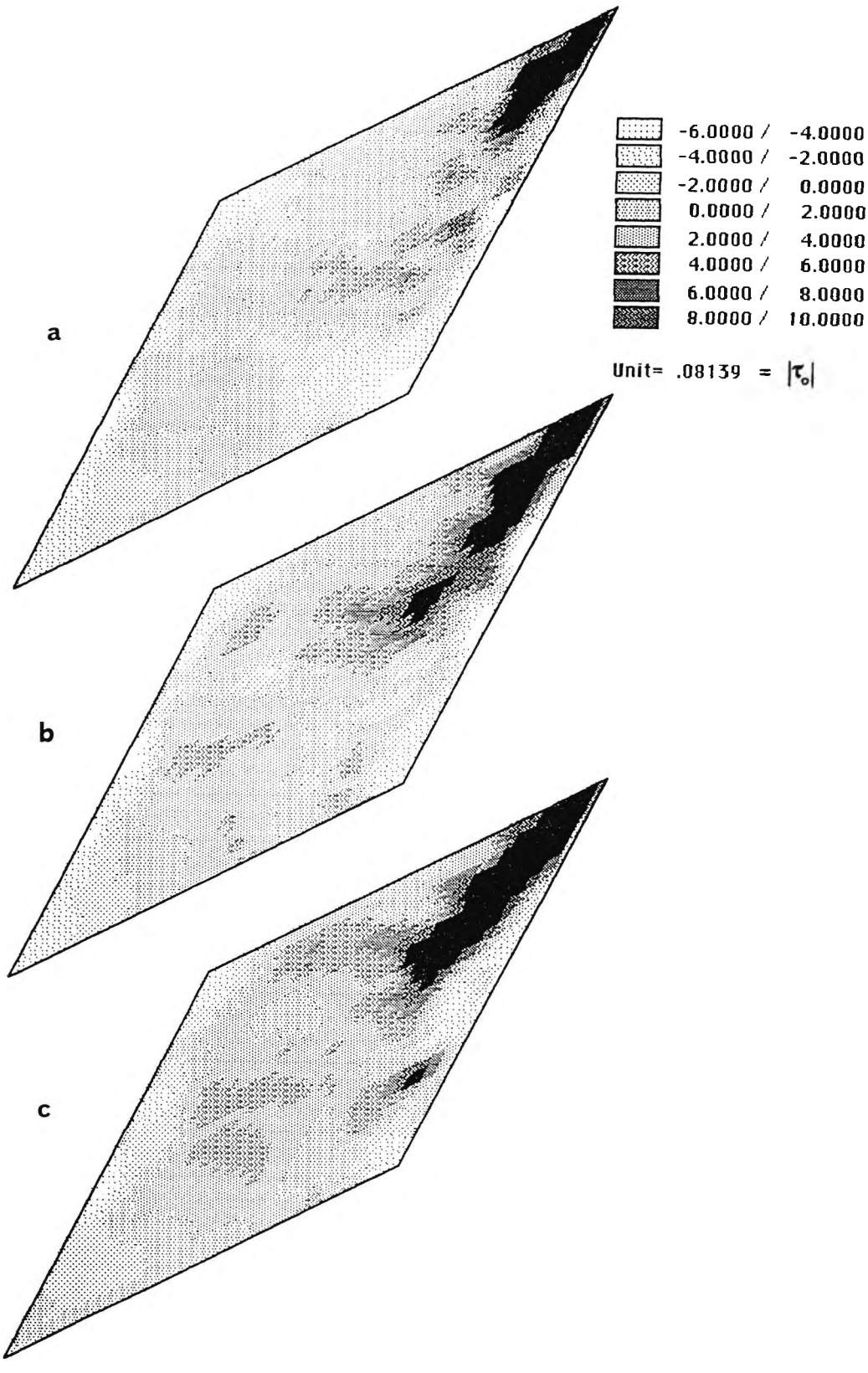


Figure 6.23 - Reference case (P/H_1=4, Θ=36°, Re°=3000): instantaneous dimensionless pressure on the top wall. Grey scales and normalization units are shown.
a) t=4.0 b) t=4.2 c) t=4.4 (LETOT's).

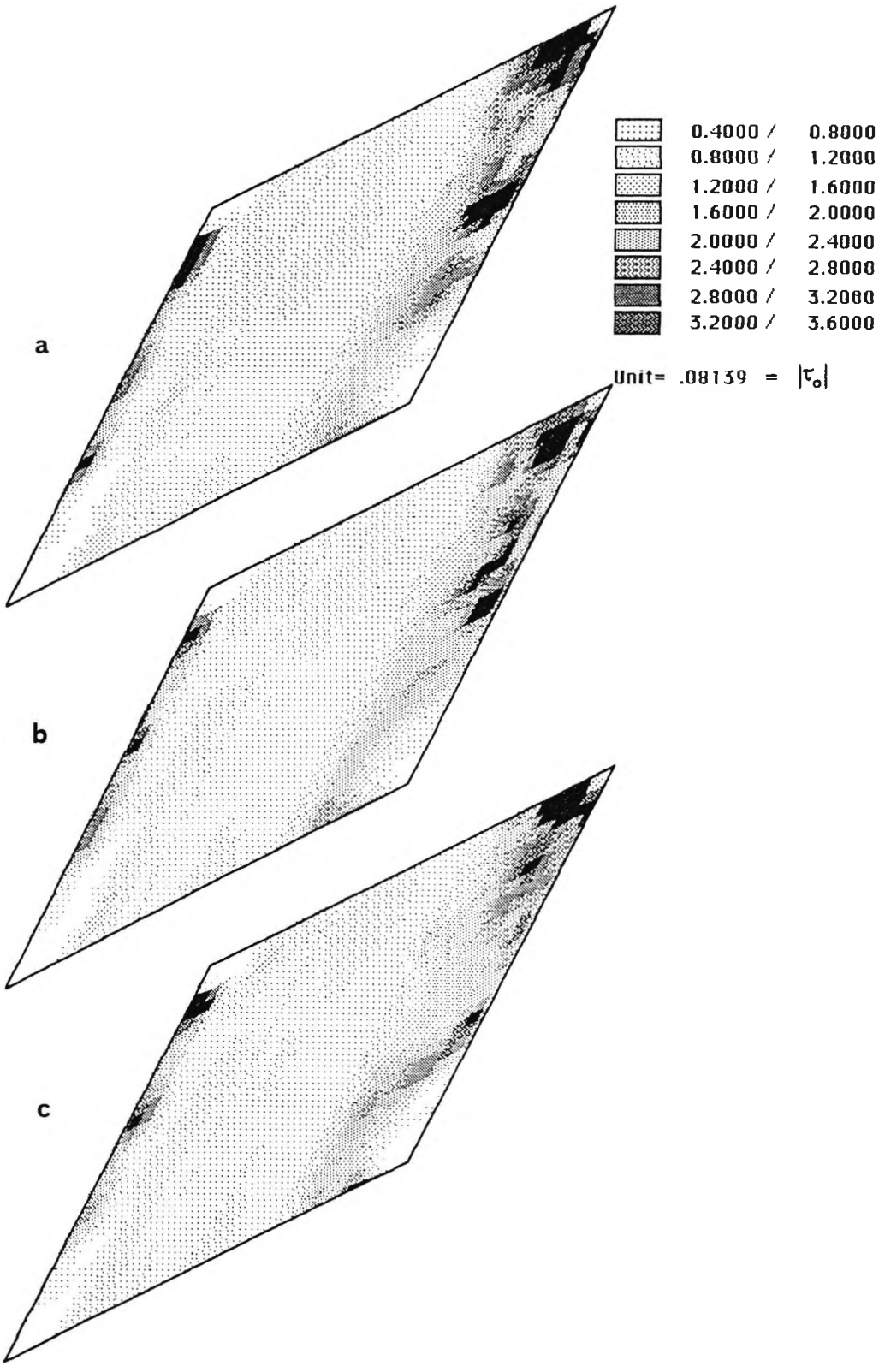


Figure 6.24 - Reference case (P/H_i=4, Θ=36°, Re^{O}=3000): instantaneous dimensionless shear-stress intensity on the top wall. Grey scales and normalization units are shown.
a) t=4.0 b) t=4.2 c) t=4.4 (LETOT's).

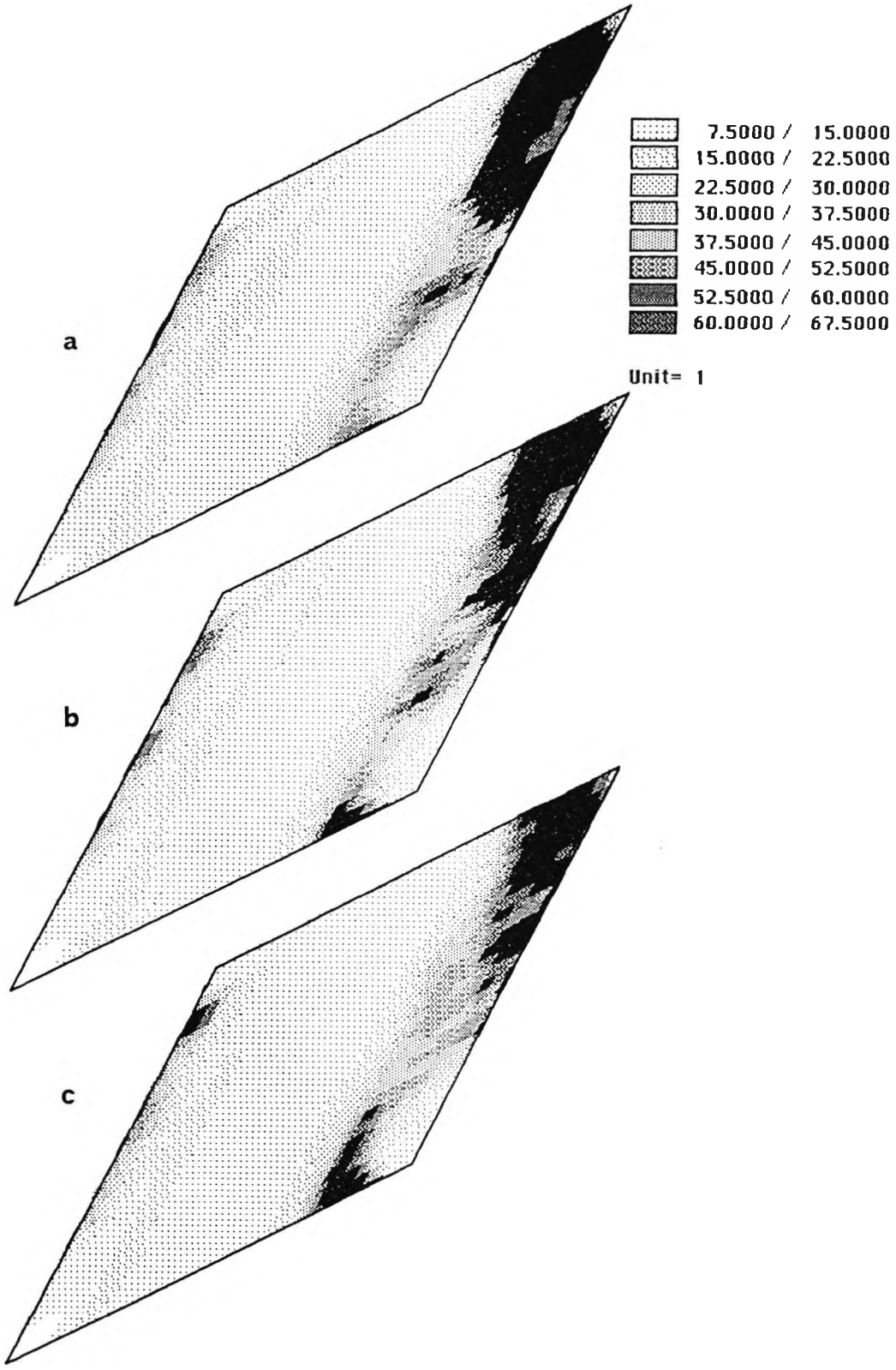


Figure 6.25 - Reference case (P/H_1=4, Θ=36°, Re°=3000): instantaneous Nusselt number on the top wall. Grey scales are shown. a) t=4.0 b) t=4.2 c) t=4.4 (LETOT's).

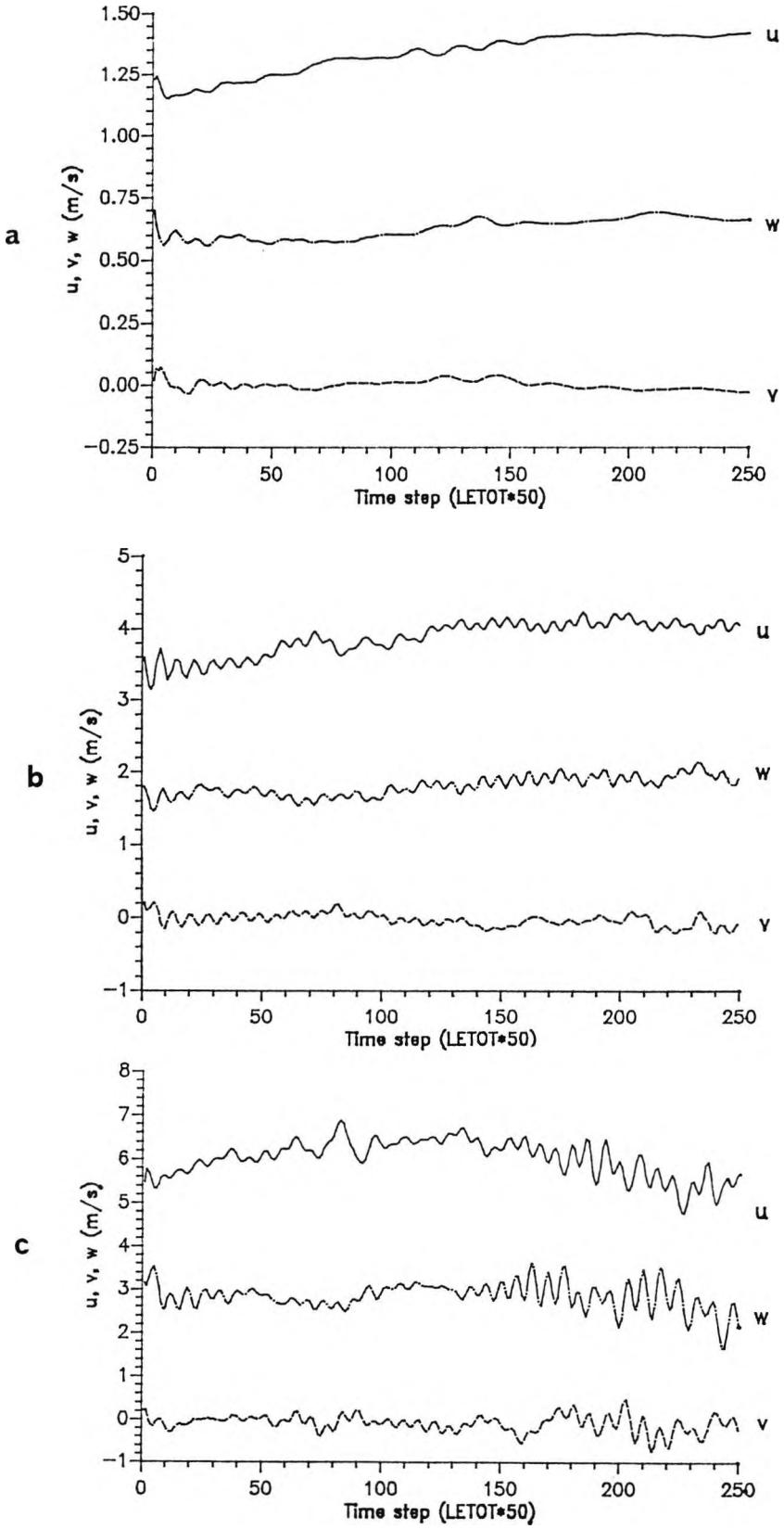


Figure 6.26 - Behaviour of the three instantaneous velocity components u,v,w at centre of face U for Θ=36° and increasing Reynolds numbers: a) Re=776 b) Re=2450 c) Re=4130

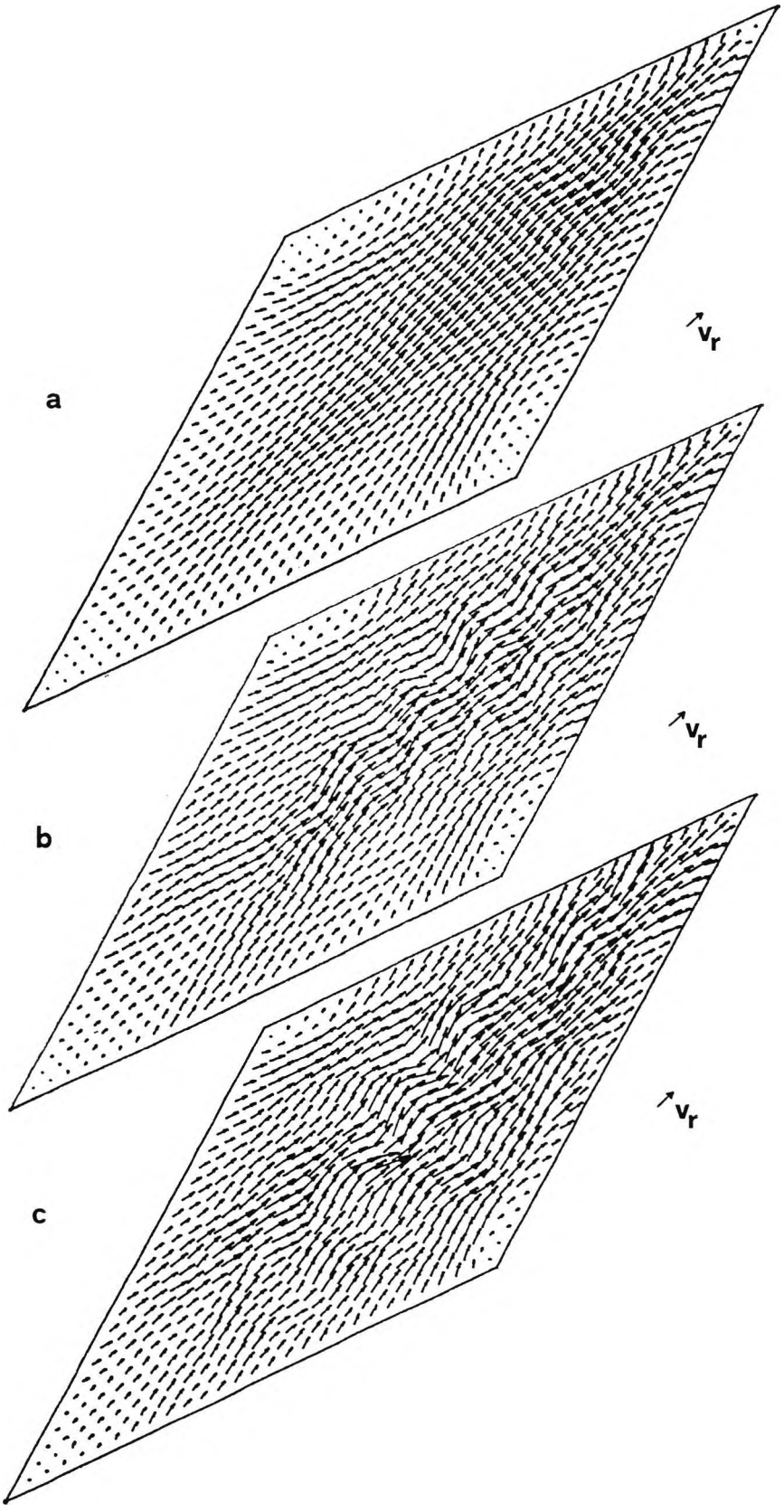


Figure 6.27 - Instantaneous velocity field in the midplane at t=4 LETOT's for Θ=36° and increasing Reynolds numbers. The reference velocity v_r is shown.

a) Re=776 b) Re=2450 c) Re=4130

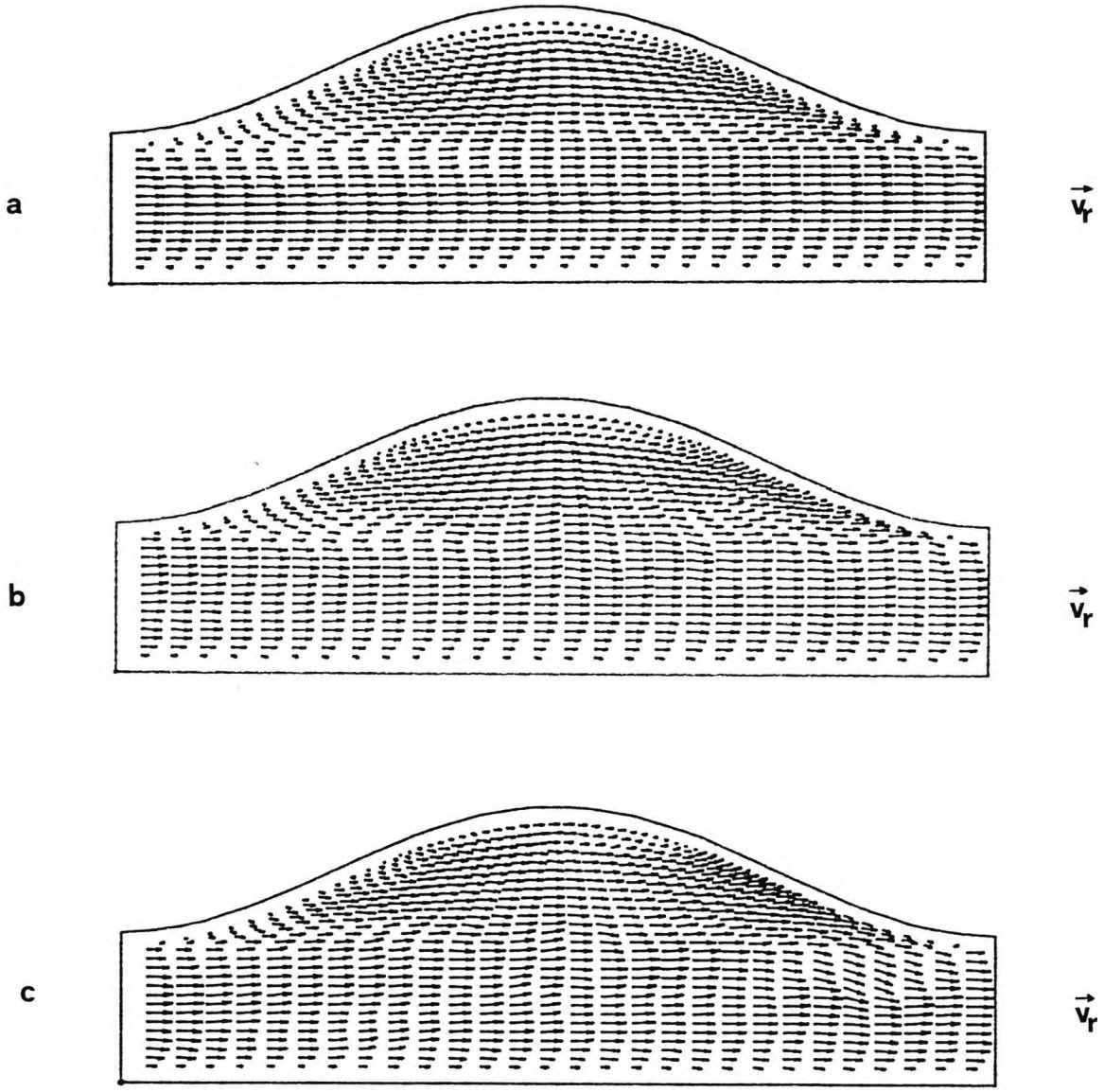


Figure 6.28 - Instantaneous velocity field in section C-C at t=4 LETOT's for Θ=36° and increasing Reynolds numbers. The reference velocity v_r is shown.

a) Re=776 b) Re=2450 c) Re=4130

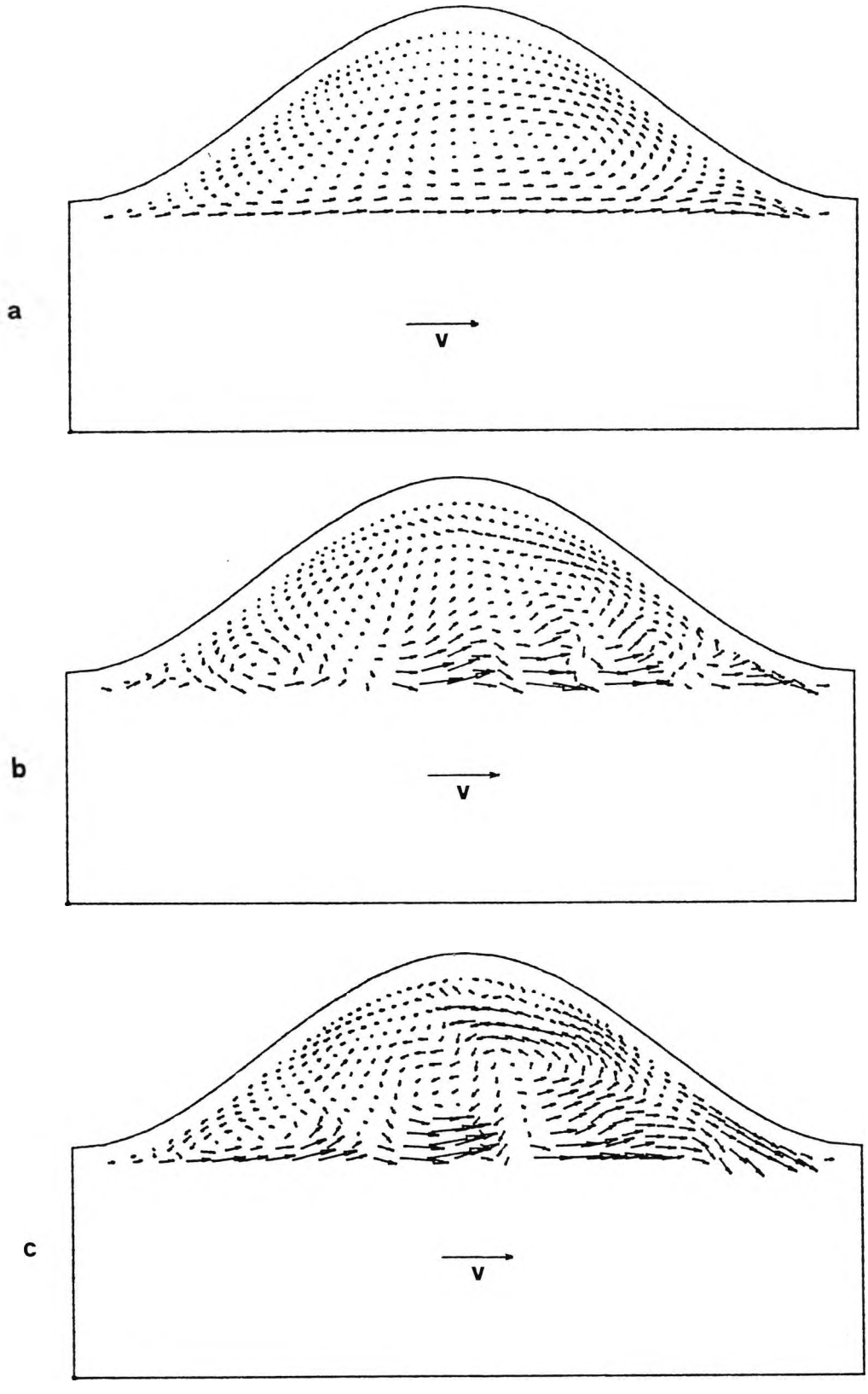


Figure 6.29 - Instantaneous velocity field in section N-N at t=4 LETOT's for Θ=36° and increasing Reynolds numbers. The reference velocity v_r is shown. Vectors in the bottom half were not drawn.
a) Re=776 b) Re=2450 c) Re=4130

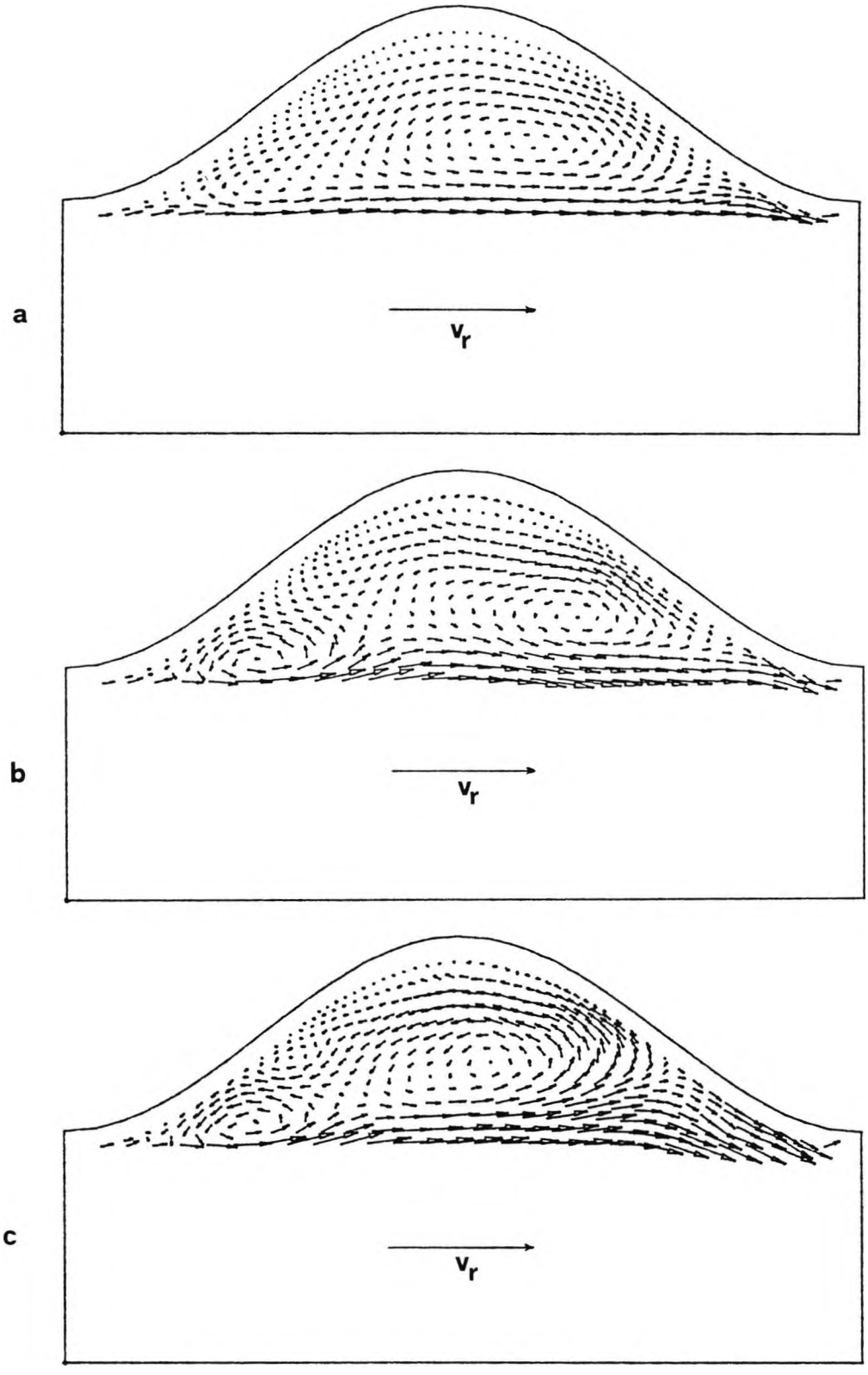


Figure 6.30 - Time-averaged velocity field in section N-N at t=4 LETOT's for Θ=36° and increasing Reynolds numbers. The reference velocity v_r is shown. Vectors in the bottom half were not drawn.
a) Re=776 b) Re=2450 c) Re=4130

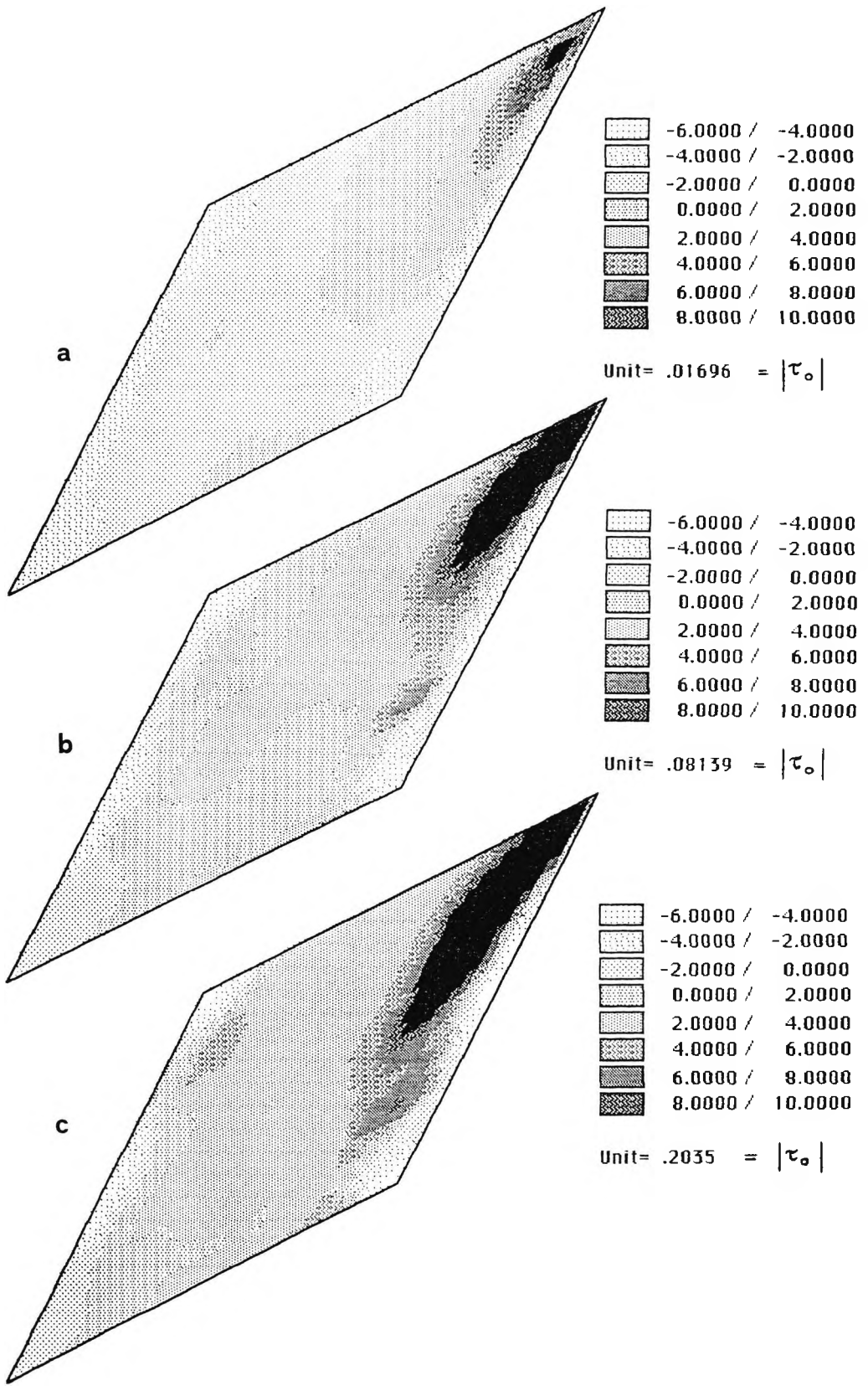


Figure 6.31 - Time-averaged dimensionless pressure on the top wall for $\Theta=36°$ and increasing Reynolds numbers. Grey scales are shown. p^* is normalized by the reference stress $|\tau_o|$.
a) Re=776 b) Re=2450 c) Re=4130

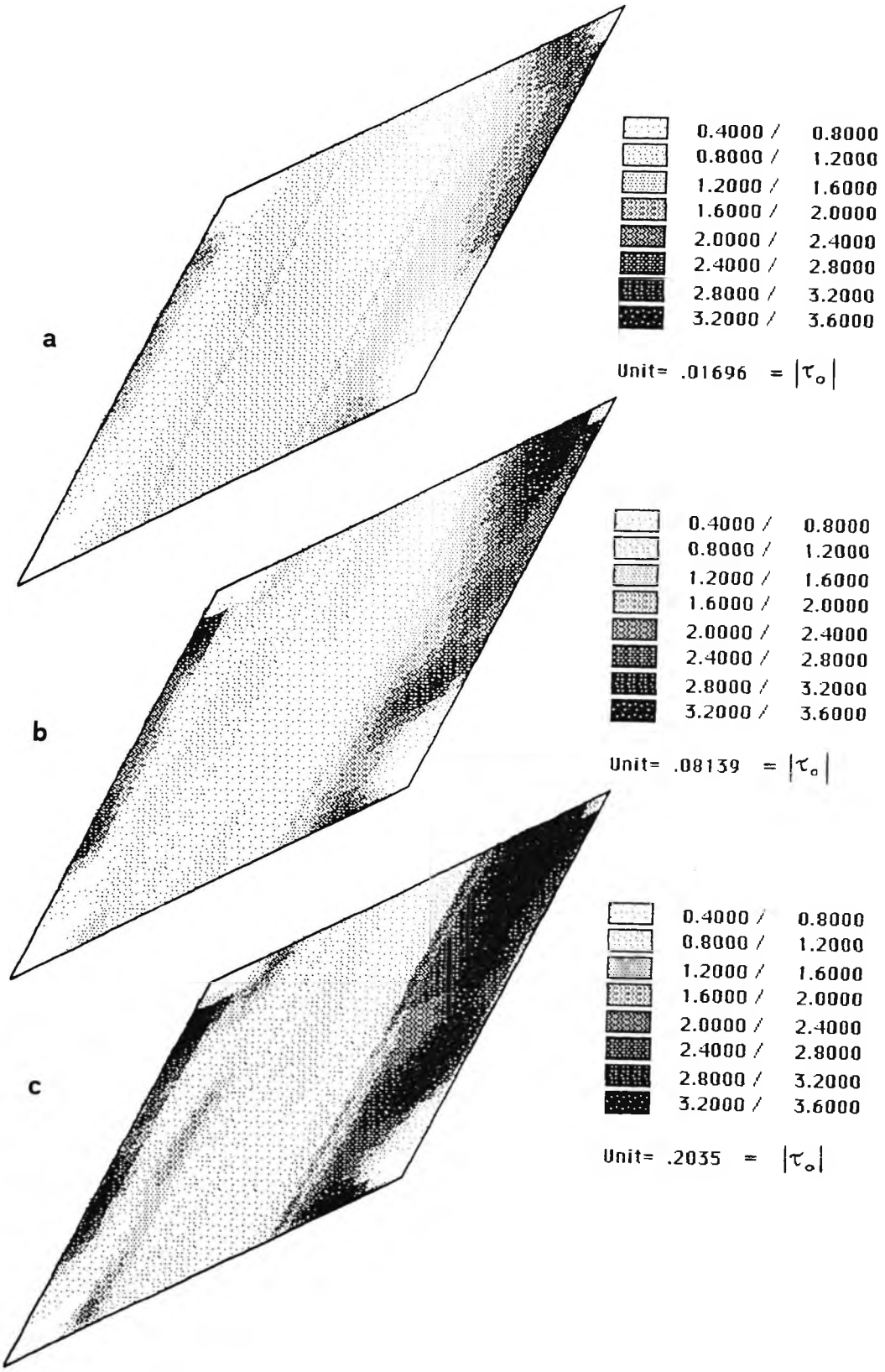


Figure 6.32 - Time-averaged dimensionless shear-stress intensity on the top wall for $\Theta=36°$ and increasing Reynolds numbers. Grey scales are shown. $|\tau|$ is normalized by the reference stress $|\tau_o|$.
a) Re=776 b) Re=2450 c) Re=4130

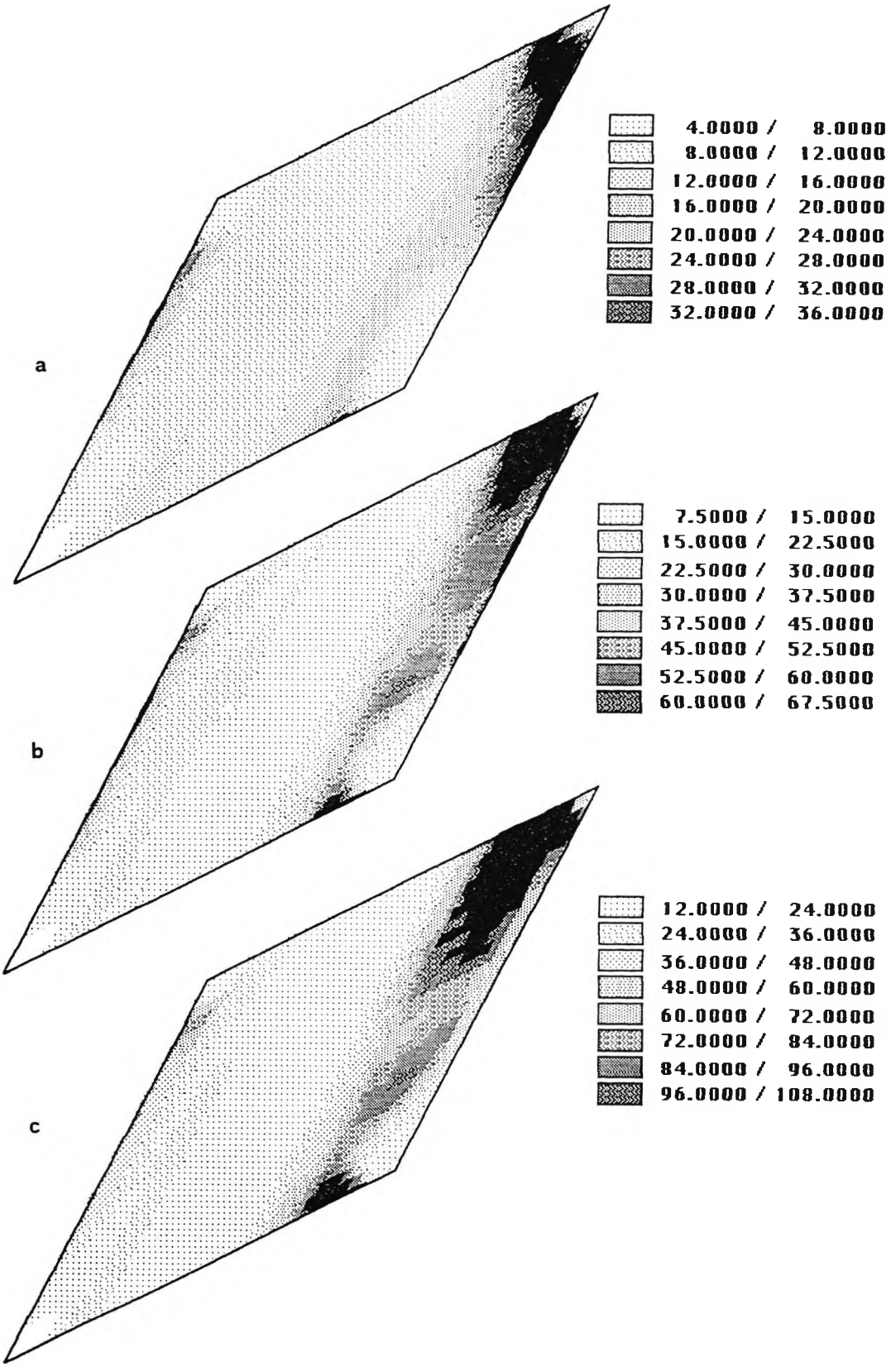


Figure 6.33 - Time-averaged Nusselt number on the top wall for $\Theta=36°$ and increasing Reynolds numbers. Grey scales are shown.
a) Re=776 b) Re=2450 c) Re=4130

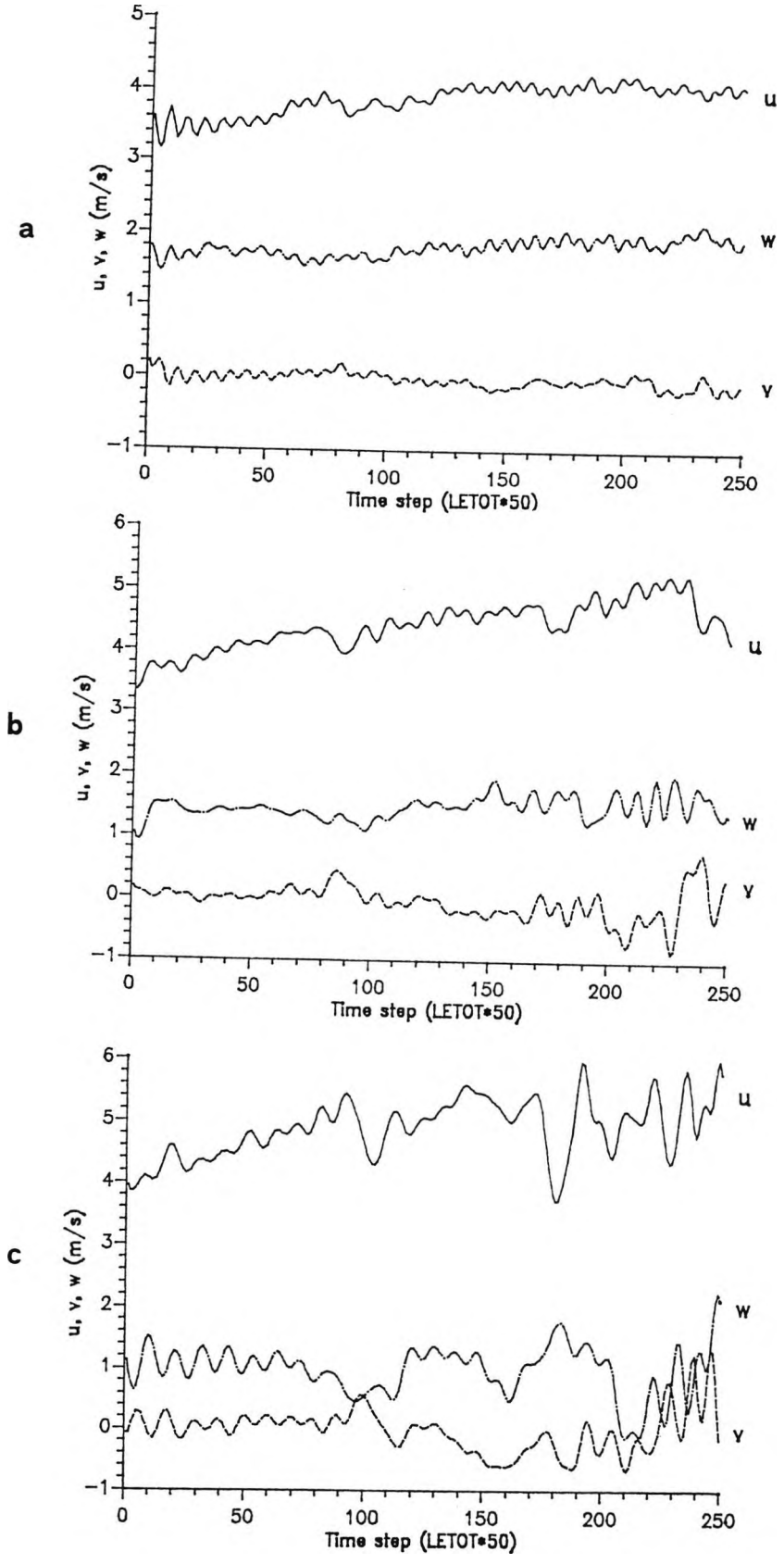


Figure 6.34 - Behaviour of the three instantaneous velocity components u,v,w at centre of face U for Re°=3000 and increasing angles:
a) Θ=36° b) Θ=48° c) Θ=60°

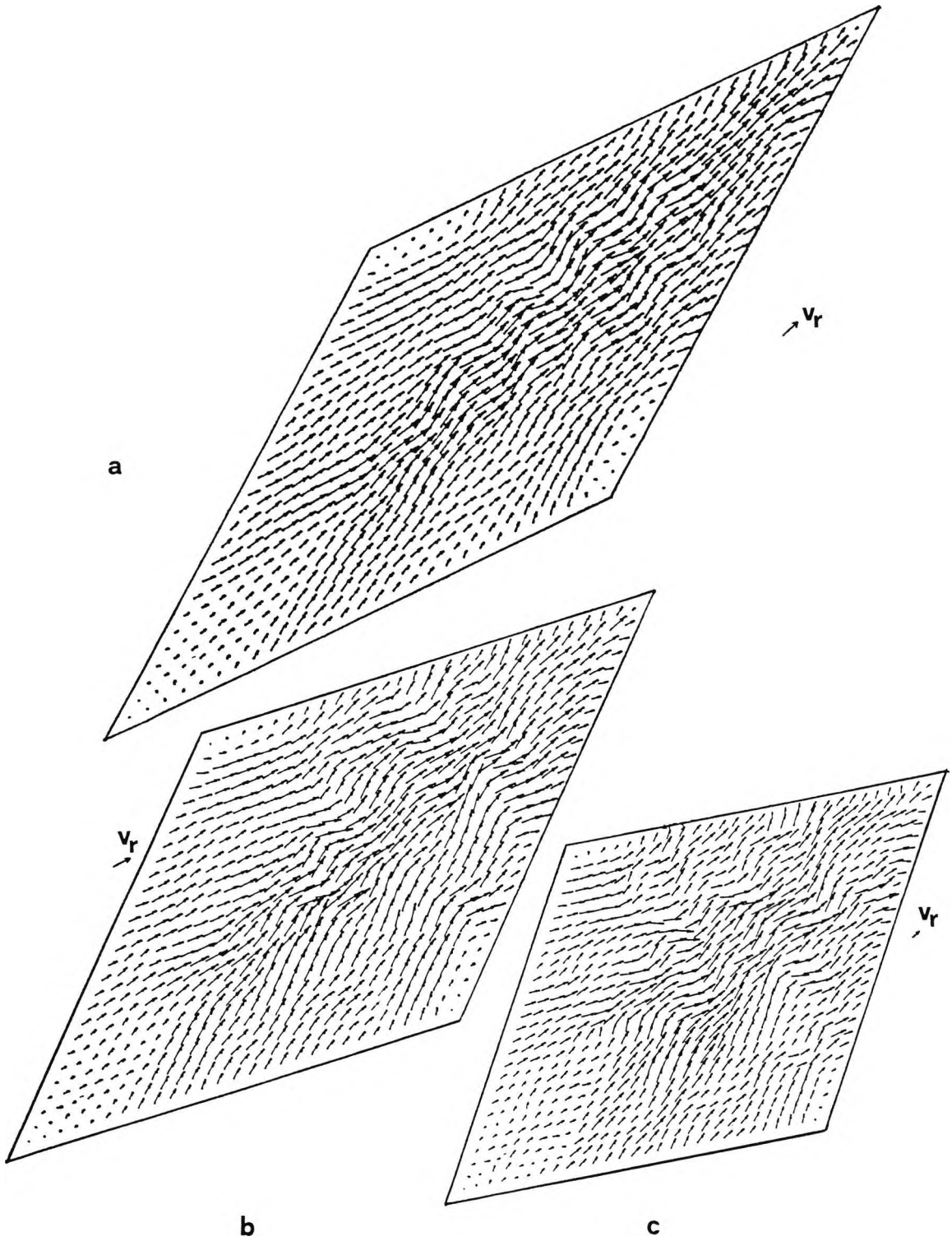


Figure 6.35 - Instantaneous velocity field in the midplane at t=4 LETOT's for Re°=3000 and increasing angles. The reference velocity v_r is shown.

a) Θ=36° b) Θ=48° c) Θ=60°

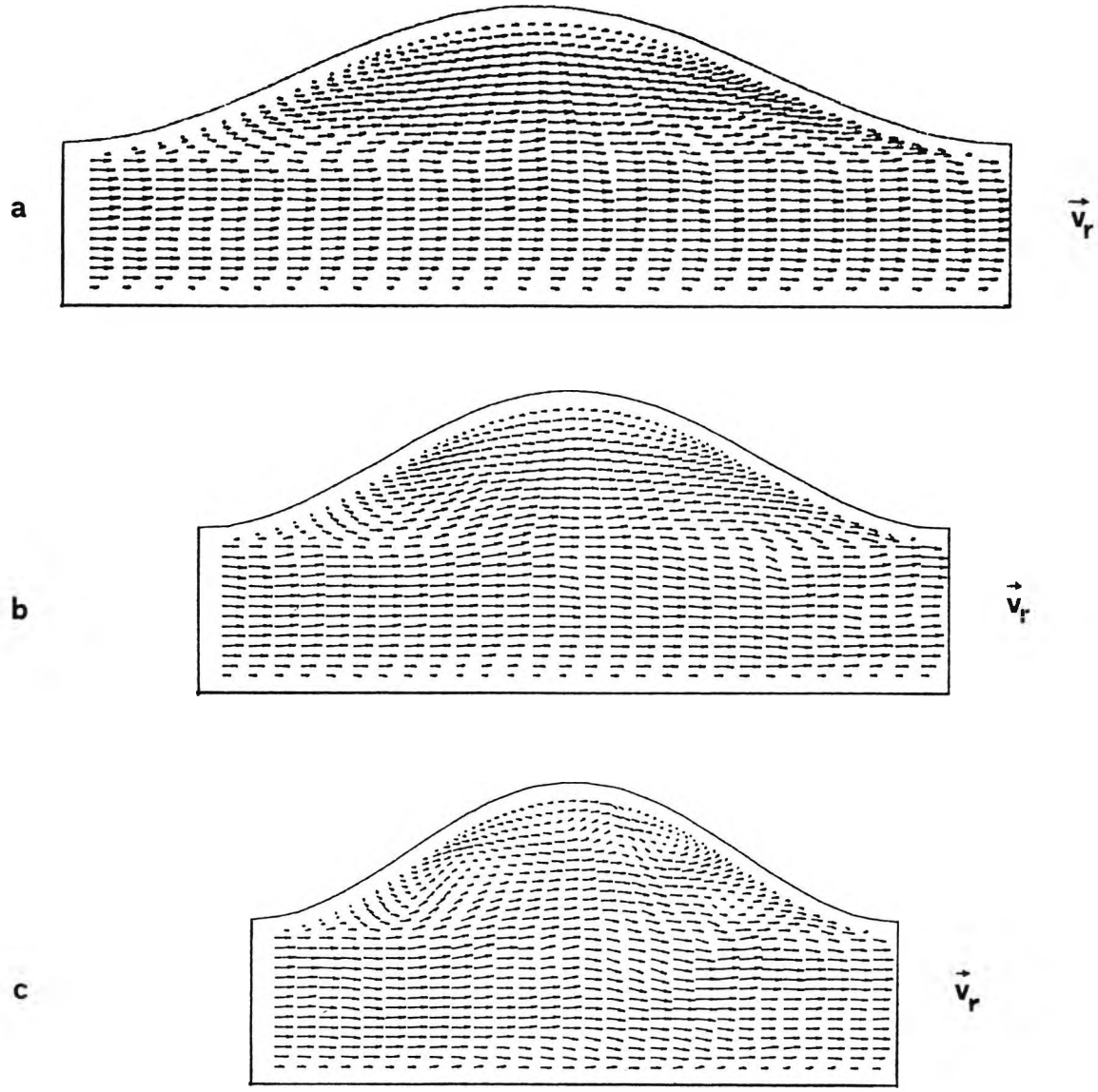


Figure 6.36 - Instantaneous velocity field in section C-C at t=4 LETOT's for Re°=3000 and increasing angles. The reference velocity v_r is shown.

a) Θ=36° b) Θ=48° c) Θ=60°

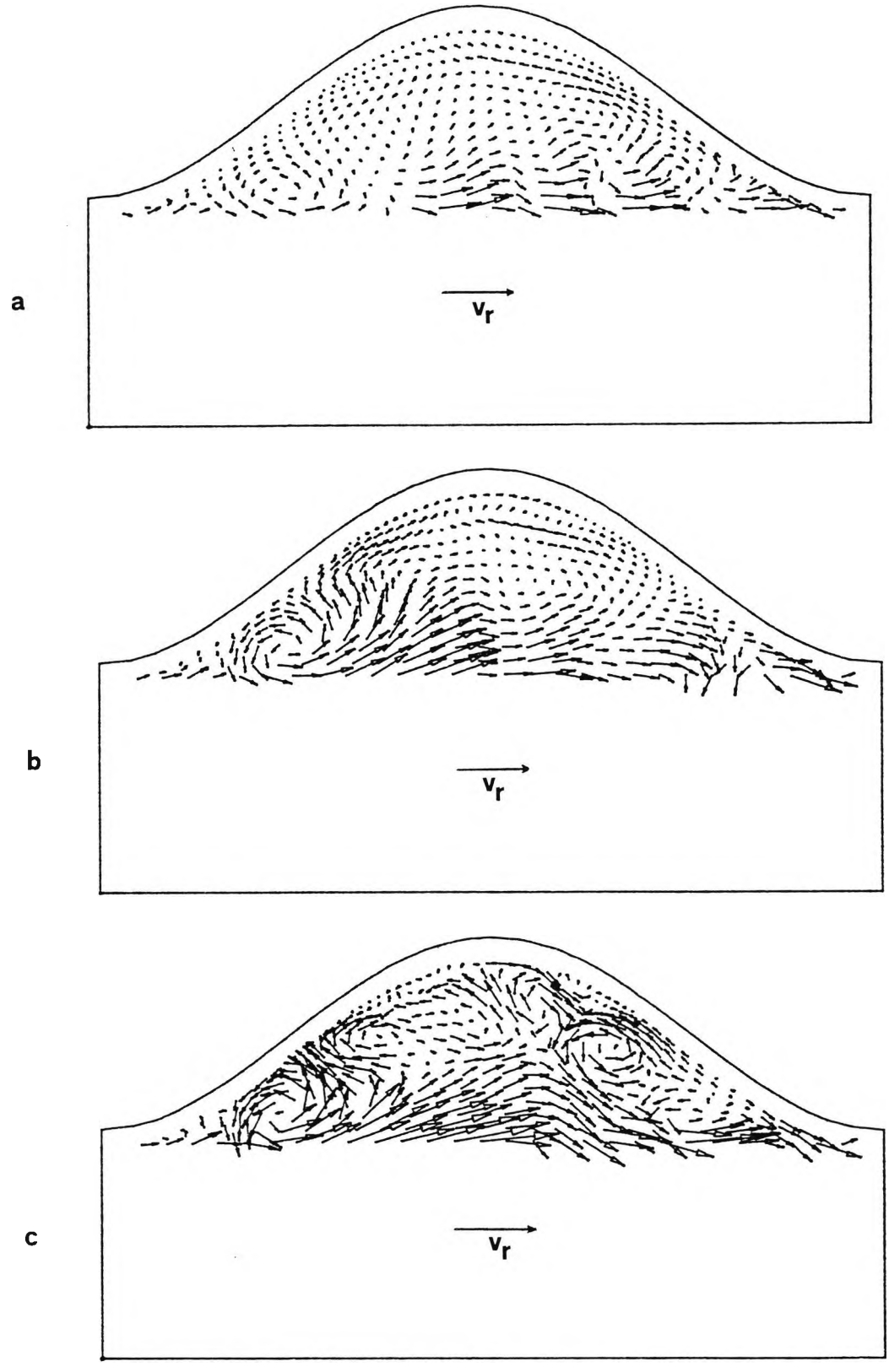


Figure 6.37 - Instantaneous velocity field in section N-N at t=4 LETOT's for Re°=3000 and increasing angles. The reference velocity v_r is shown. Vectors in the bottom half were not drawn.
a) Θ=36° b) Θ=48° c) Θ=60°

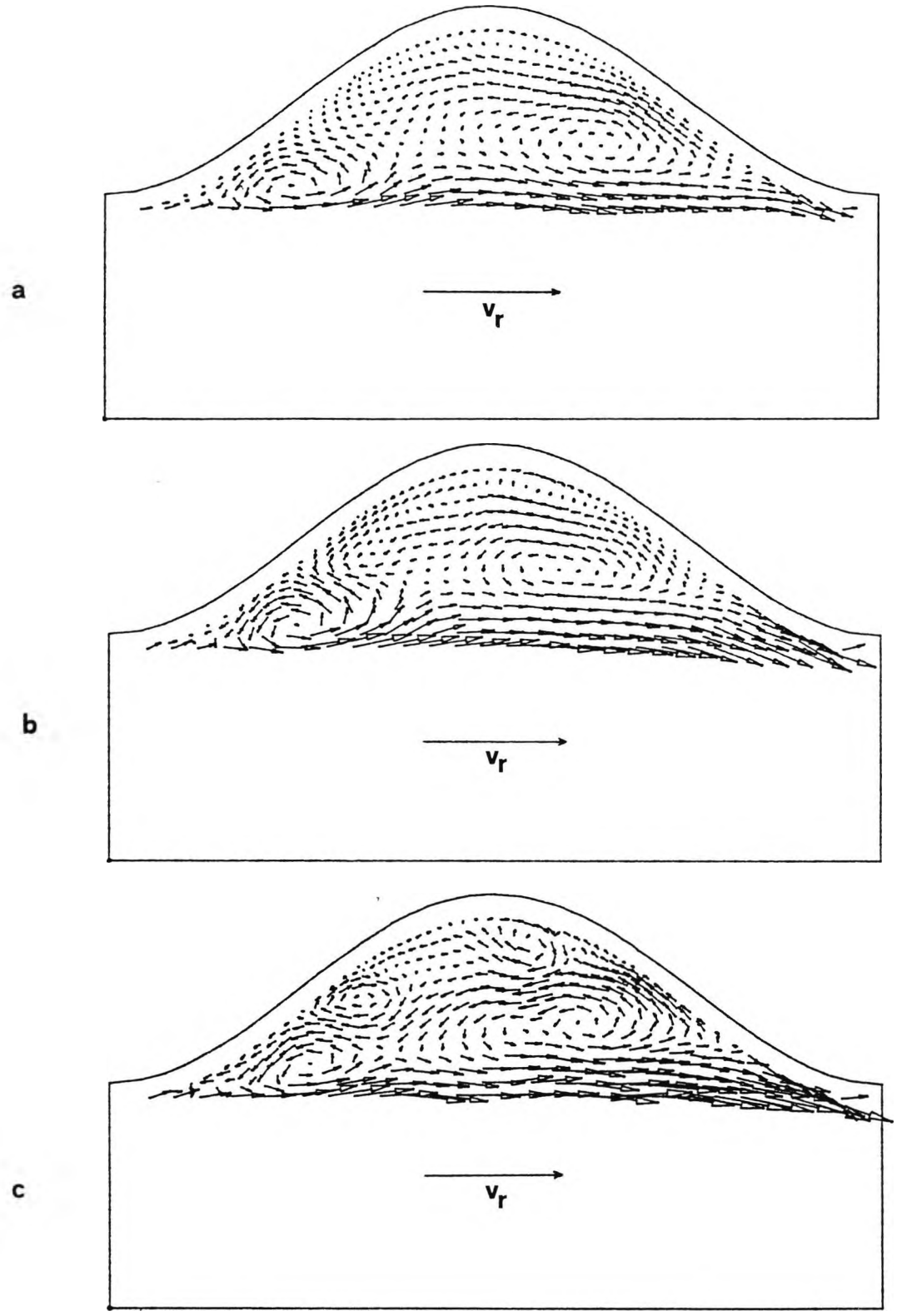


Figure 6.38 - Time-averaged velocity field in section N-N at t=4 LETOT's for Re°=3000 and increasing angles. The reference velocity v_r is shown. Vectors in the bottom half were not drawn.
a) Θ=36° b) Θ=48° c) Θ=60°

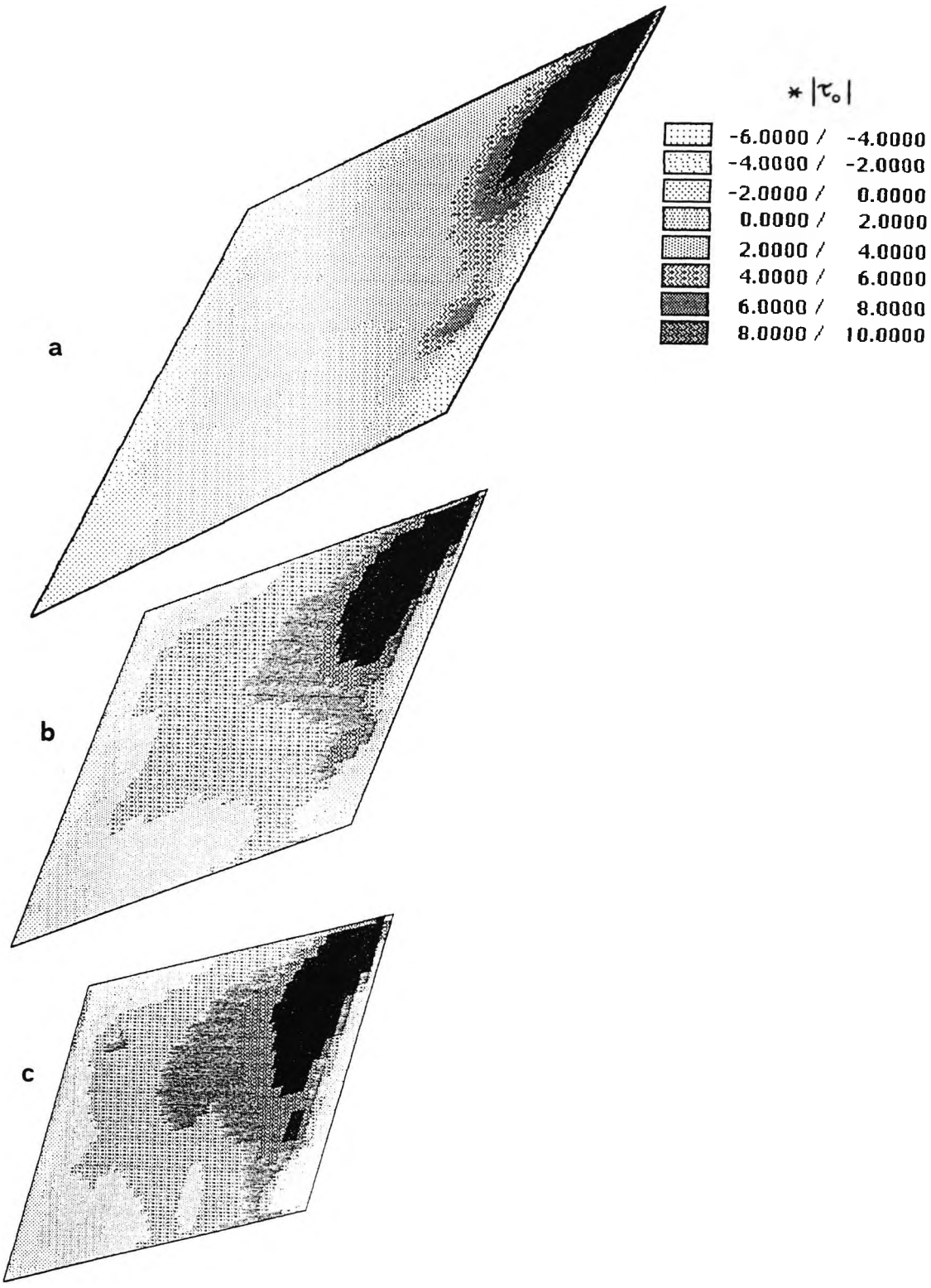


Figure 6.39 - Time-averaged dimensionless pressure on the top wall for Re°=3000 and increasing angles. Grey scales are shown. p^* is normalized by the reference stress $|\tau_o|$.
a) Θ=36° b) Θ=48° c) Θ=60°

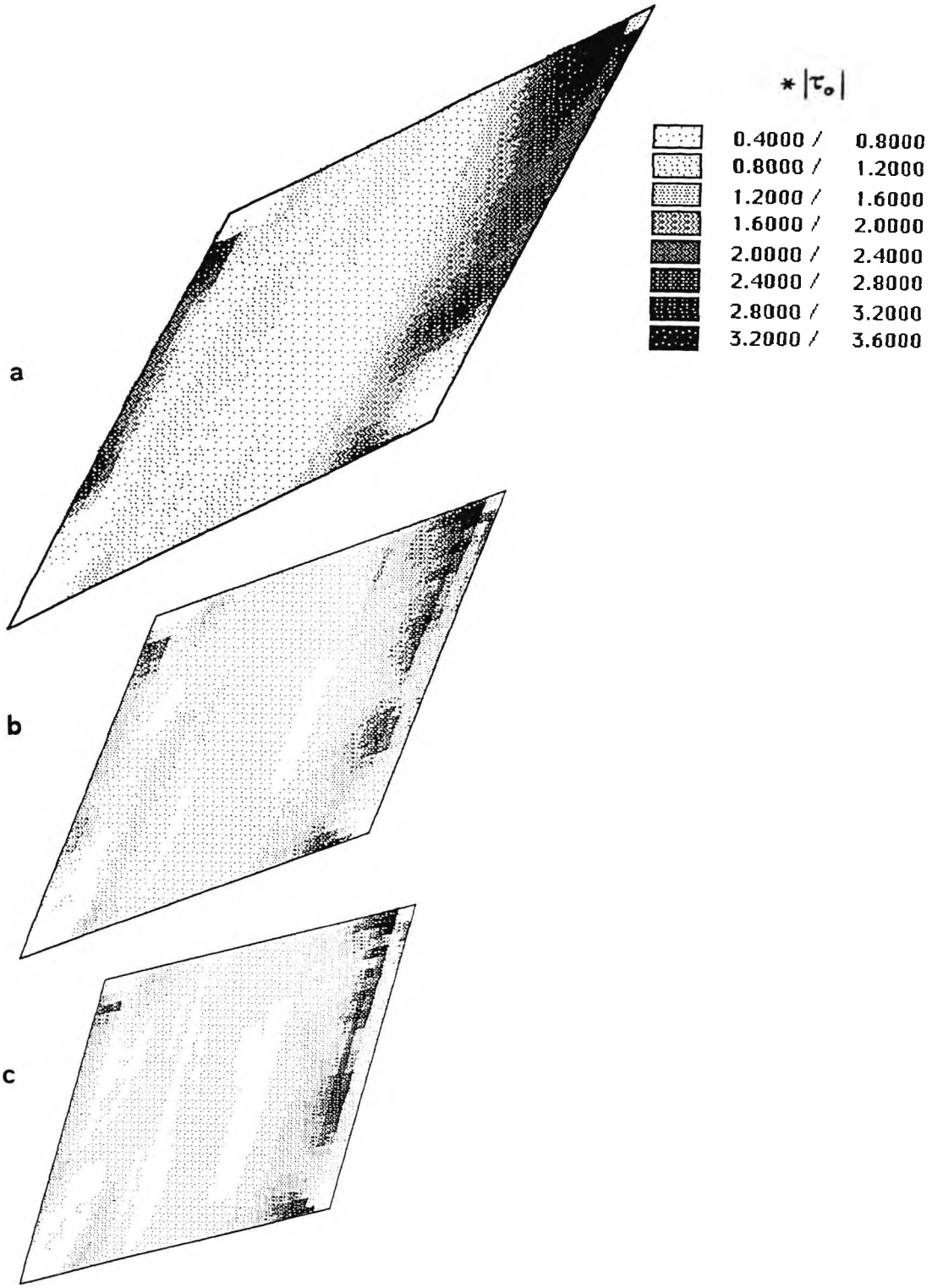


Figure 6.40 - Time-averaged dimensionless shear-stress intensity on the top wall for Re°=3000 and increasing angles. Grey scales are shown. $|\tau|$ is normalized by the reference stress $|\tau_o|$.
a) Θ=36° b) Θ=48° c) Θ=60°

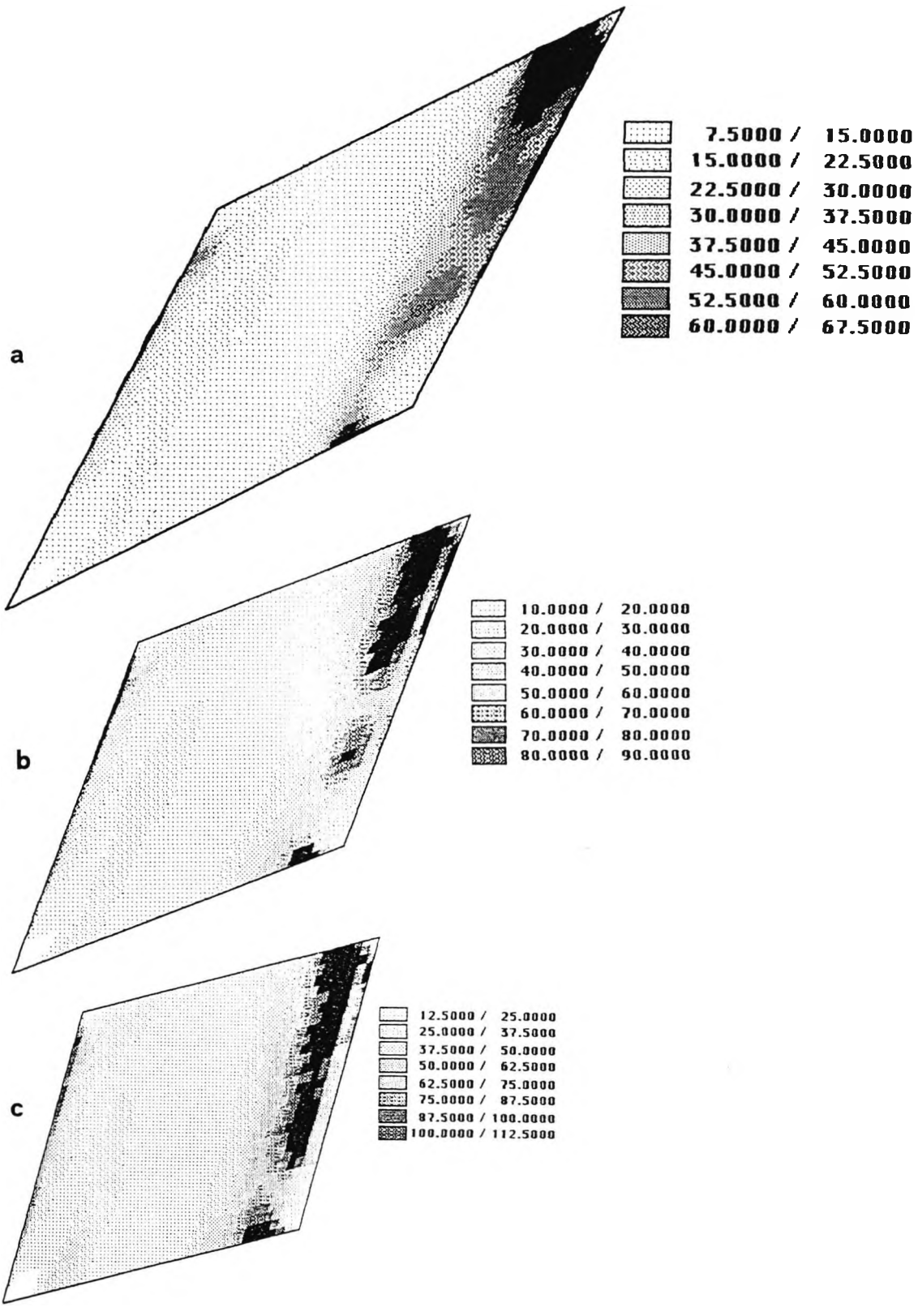


Figure 6.41 - Time-averaged Nusselt number on the top wall for Re^{O}=3000 and increasing angles. Grey scales are shown.
a) Θ=36° b) Θ=48° c) Θ=60°

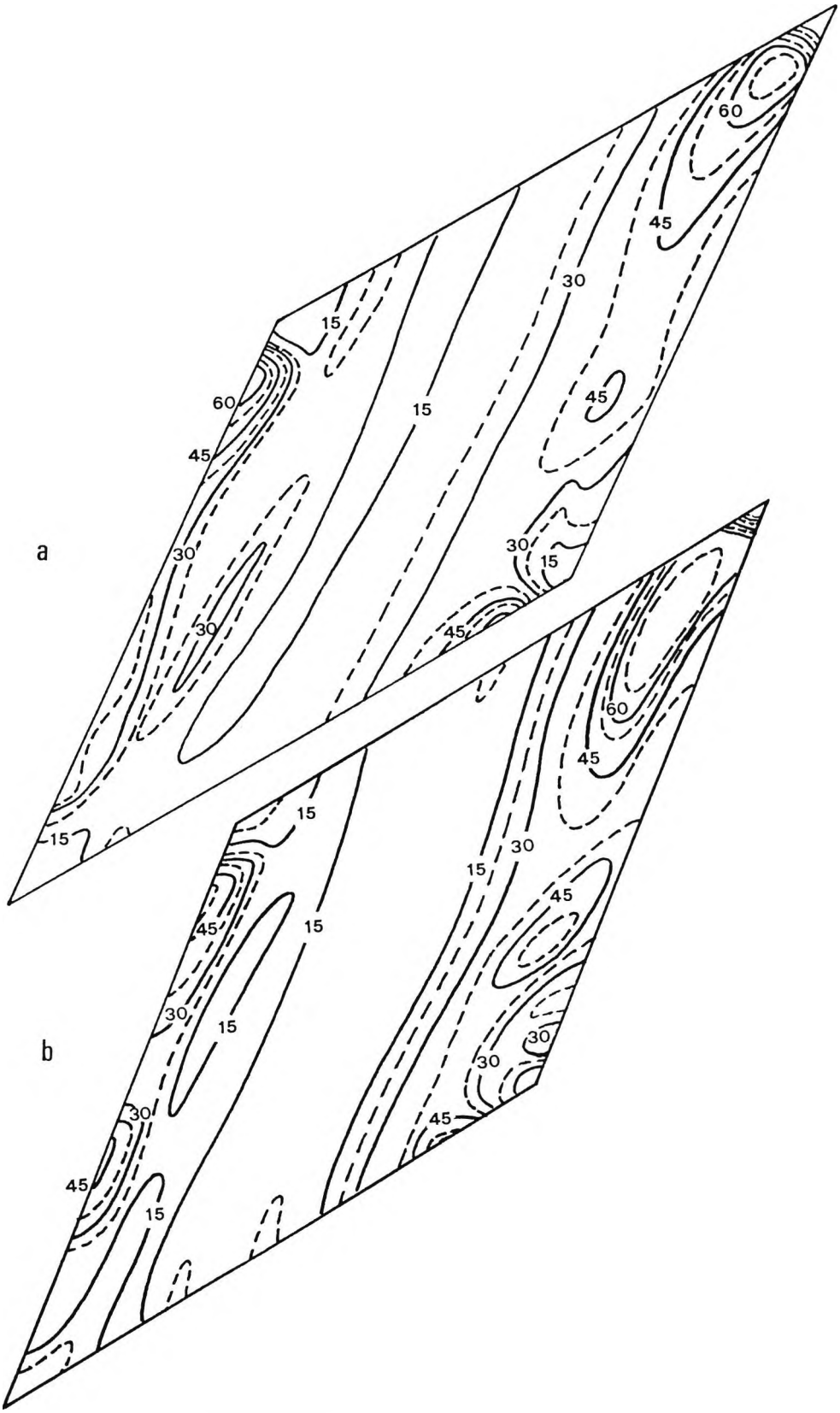


Figure 6.42 - Experimental (a) and predicted (b) Nusselt number distribution on the top wall for Re≅3900 and Θ=37°.

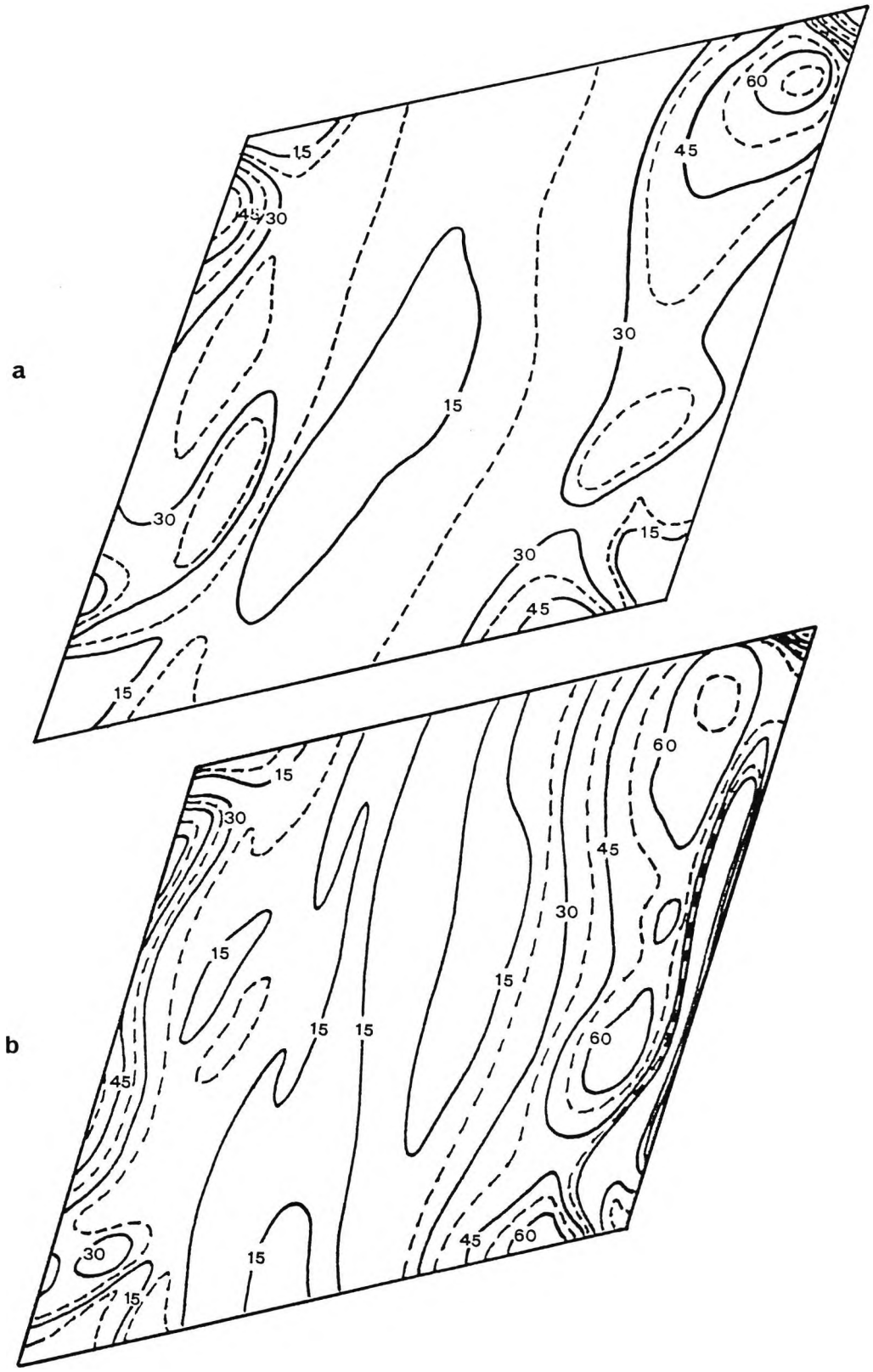


Figure 6.43 - Experimental (a) and predicted (b) Nusselt number distribution on the top wall for Re≅2400 and Θ=60°.

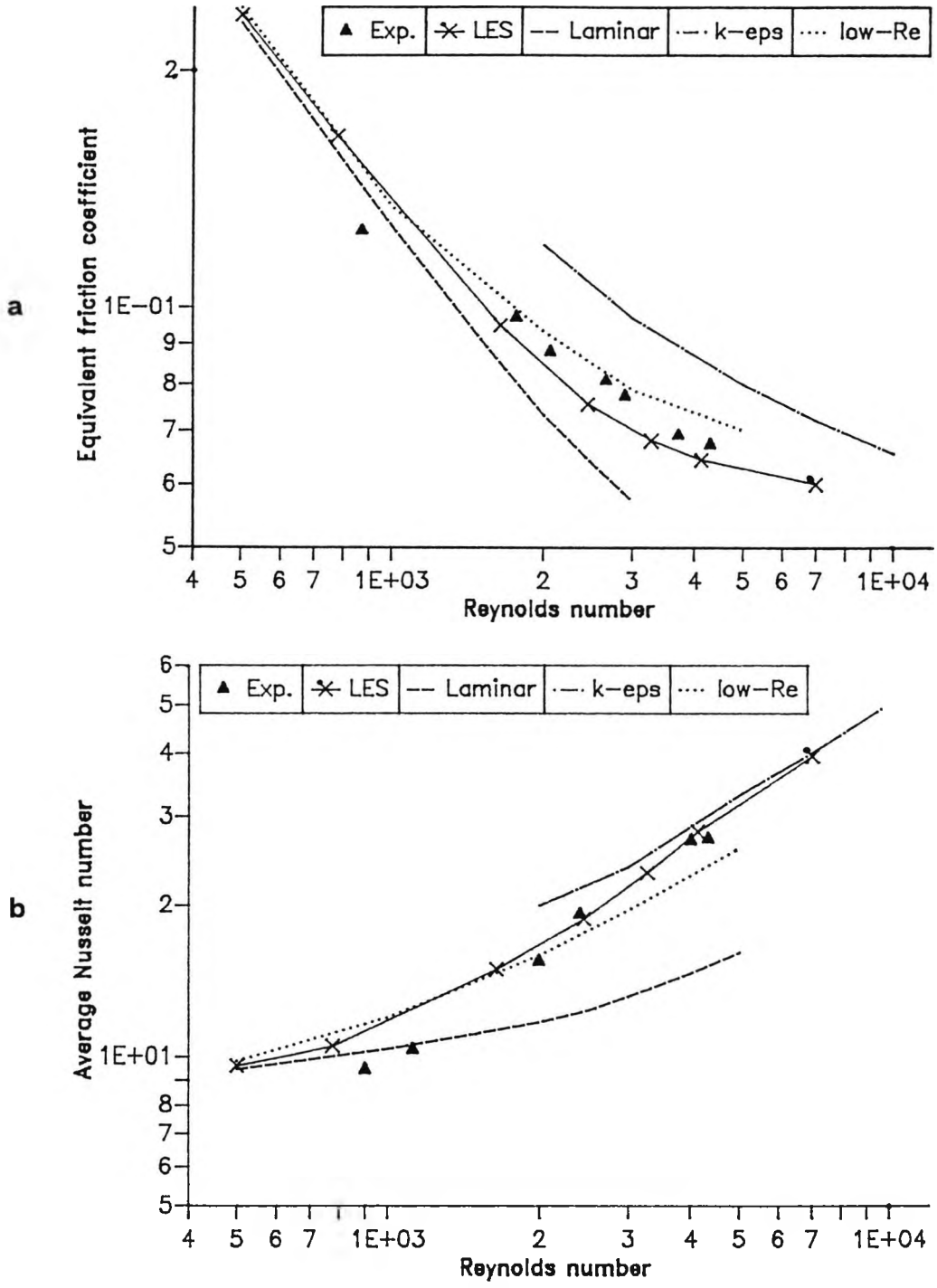


Figure 6.44 - Predicted vs. experimental equivalent friction coefficient (a) and average Nusselt number (b) as functions of the Reynolds number for Θ=37°. Predictions from large-eddy simulations and from steady-state laminar, standard k-ε and low-Reynolds number turbulent computations are reported.

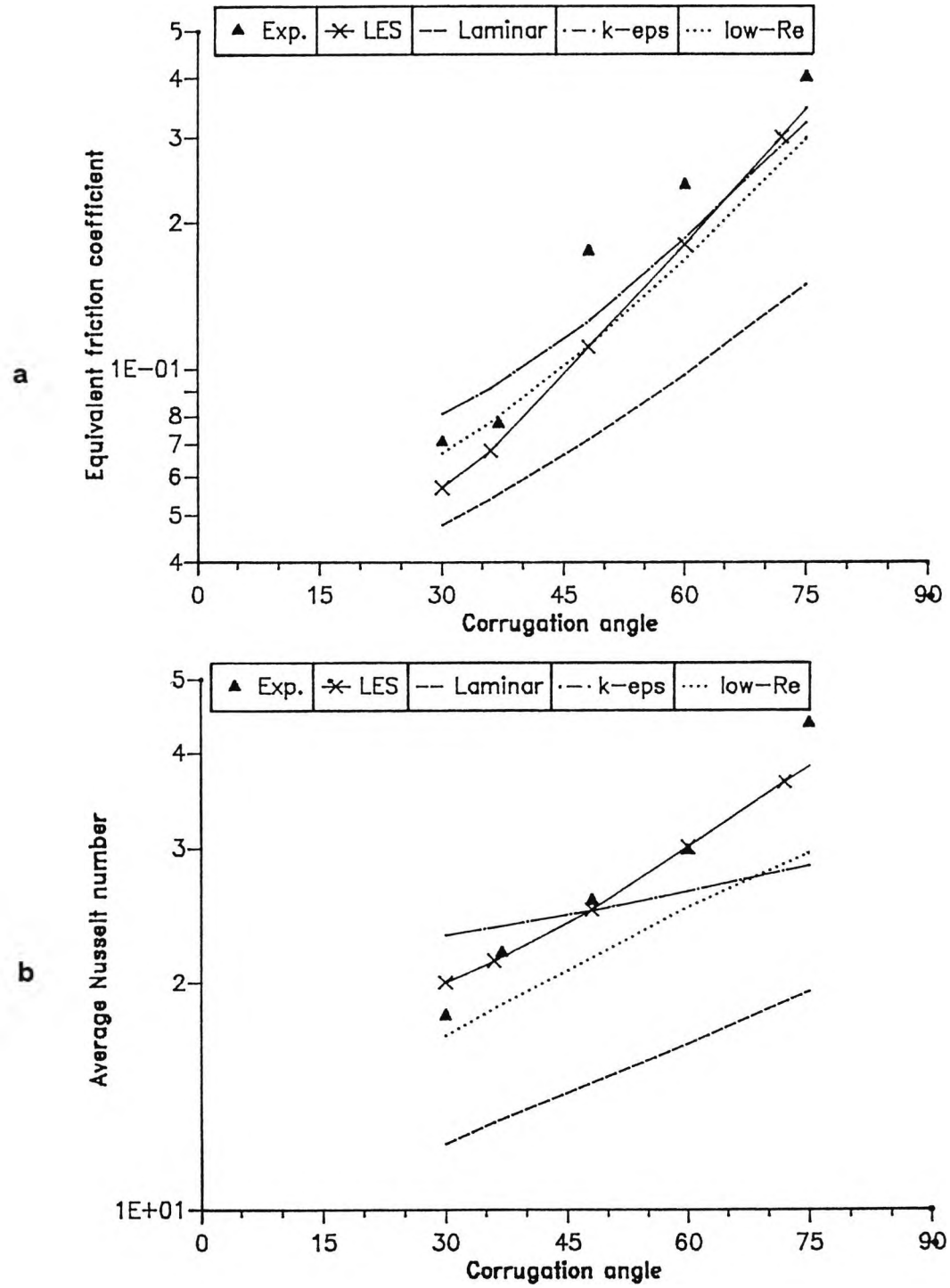


Figure 6.45 - Predicted vs. experimental equivalent friction coefficient (a) and average Nusselt number (b) as functions of the corrugation angle for Re=3000. Predictions from large-eddy simulations and from steady-state laminar, standard k-ε and low-Reynolds number turbulent computations are reported.

CHAPTER 7 - CONCLUSIONS AND RECOMMENDATIONS

> **God keep me from ever completing anything. This whole book is but a draught - nay, but the draught of a draught. Oh, Time, Strength, Cash, and Patience !**
> [H.Melville, "Moby Dick"]

7.1 General aspects

The main purpose of the present work was to demonstrate the feasibility of LES flow and heat transfer predictions for both simple and complex (recirculating) flows using a general-purpose code, a simple subgrid model and relatively coarse grids. This purpose was essentially reached; satisfactory 20-LETOT simulations required about 6 hours of CPU time for the plane-channel flow (with 34*26*26=22,984 overall grid points) and about 9 hours for the ribbed duct (50*26*26=33,800 grid points) on an IBM 3090-200J computer, used in scalar mode, and from 5 to 10 times less on a CRAY-2 computer. Analysis of the behaviour of the solution for the latter problem (see for example Figure 5.3) shows that much shorter simulations (10 LETOT's) are sufficient in this case to get independence from initial conditions and satisfactory statistics. Comparable CPU times, but for shorter transients (5 LETOT's), were required for the third problem, i.e. the crossed-corrugated geometry, using a 32^3-node grid.

For the simplest flow studied (**smooth channel**) several high-quality LES predictions are known. The present simulations suffered mainly from insufficient resolution of the computational domain, which resulted in a slight overprediction of the mean velocity and temperature profiles, and in a more significant overprediction of the streak spacing near the walls. Turbulence quantities, however, were predicted satisfactorily and coherent near-wall structures were qualitatively reproduced.

For the two more complex flows, the present study is among the first presented so far. Statistically stationary conditions were reached in both cases after a few LETOT's. In the **ribbed channel**, the mean flow rate was overpredicted as compared with experimental correlations, and so were turbulence levels in the bulk flow region; however, the overall flow structure and many fine details of the mean and fluctuating flow field were in good qualitative agreement with existing experimental data. Certain flow features were correctly predicted by LES but not by the k-ε model, notably involving recirculation. For the **crossed corrugated** geometry, the study was limited to

transitional and weakly turbulent conditions (Re=500-7000); the subgrid model had a significant influence on the results only for Re>2500, and played a minor role at lower Reynolds numbers. LES results were comparable with those obtained by using a low-Reynolds number turbulence model, and even better in reproducing the experimental Reynolds number- and angle-dependence of friction and heat transfer, and the surface-distribution of the local Nusselt number. Moreover, they included complex flow patterns - especially concerning swirl - which were not predicted by any other approach (unfortunately, experimental data are not available to validate these).

As a rule, predictions concerning geometrically complex flows were found somewhat easier to obtain than those for the smooth channel, in that (statistically) steady-state conditions were attained earlier, results were less grid- and time step-dependent, and the comparison with conventional closure models was more favourable. Although this conclusion may look surprising, it is just a consequence of the fact - already mentioned in Section 5.4 - that in geometry-driven problems the overall flow and thermal fields, and related quantities such as the heat transfer and friction coefficients, are less sensitive than in a geometrically simple problem to the accuracy with which the fine details of the flow (e.g., in the near-wall regions) are resolved. A remarkable consequence of this is that the ability of a numerical procedure to predict accurately basic flows should not necessarily be regarded as a measure of its applicability to complex flows of engineering interest.

Finally, it should be stressed that all the results presented in this work were obtained by using a very simple model, containing only a few 'adjustable' parameters (i.e. the Smagorinsky constant c_s, the VanDriest constant A^+ and, only for heat transfer predictions, the subgrid Prandtl number σ_s).

As regards the comparison with conventional turbulence models, it should be observed that the main point at issue is not whether LES performs "better" than these (e.g., the k-ε). The amount of information provided by a three-dimensional, time-dependent simulation of a turbulent flow is incomparably larger than that given by any time-average based turbulence model; under some circumstances, this may well overcome the disadvantage of a less accurate prediction of some mean property of the flow, especially as far as the simulation is used as a tool to assist our understanding of the physical mechanisms involved.

7.2 Subgrid model and boundary conditions

Throughout this work, the only subgrid model used was that of **Smagorinsky - Lilly**, as described by Eqn.(2.103). It was first proposed for planetary atmospheric circulation problems, i.e. in a context where the term "subgrid" applies to scales of the order of 100 Km, and can be derived with sensible approximations only under the assumption of equilibrium between the energy transfer from large to small scales, and the energy dissipation by the latter. Thus, it is an "absolutely dissipative" model, incapable - as mentioned in Section 2.4.5 - of predicting energy backscatter from small to large scales, and suitable (in principle) only for high-Reynolds number, fully turbulent flows. In addition to this, of course, it is a gradient-diffusion model and thus cannot predict subgrid Reynolds stresses not aligned with the corresponding large-scale strain rates.

Considering all this, the Smagorinsky - Lilly model would seem to be sadly unfit to moderate - Reynolds number, wall bounded flows such as those studied in the present work. As a matter of fact, however, this model has been widely applied to such flows, as reviewed in section 2.6. Though various shortcomings have been described, and various alternative models have been proposed and applied to specific problems, no simple alternative, applicable to general geometries, is at hand. Modified two-component models, such as those used by Moin and Kim [1982] and later by Voke [1989] and other authors, are based on ensemble-averages which can be defined only for plane channels and strictly related geometries. Similarly, varying-c_s models, such as proposed by Kobayashi et al. [1985.b] or by Morinishi and Kobayashi [1990], depend too much on the specific geometry considered. The subgrid stress transport model developed by the NCAR group [Deardorff 1973.b] is exceedingly complex for general use and inevitably involves a host of rather dubious "free" constants; significantly, the same authors reverted to simpler models in later studies. Probably, the only models which have given some clear proof of being superior to the Smagorinsky model, while retaining a sufficient universality and simplicity, are the one-equation subgrid energy - transport models derived first by Schumann [1975] and, in similar forms, by Deardorff [1976, 1980] and Horiuti [1985.a]. However, even these models contain geometry-dependent parameters and can not be simply extended to geometries different from those for which they were originally optimized.

As to the main "free" parameter of the model, i.e. the **Smagorinsky constant** c_s, its effect was studied here only for the smooth-channel flow in Chapter 4, for which reliable reference results were available for comparison. It was found that letting c_s vary had a significant influence only on the near-wall flow structure and on turbulence spectra, while affecting only weakly the overall flow and temperature fields. The value of 0.08 was selected as the most adequate, and was successively applied with satisfactory results, with no "ad-hoc" re-optimization, to the different and more complex geometries studied. This figure is well within the range of values proposed in the literature, as discussed in Section 2.4.5(II).

Alternative **near-wall damping functions** were tested for the same smooth-channel case. No large difference was found in the results, so that the simple and widely used VanDriest function, Eqn.(2.102.a), was used for all the geometries studied.

Subgrid heat transport was modelled in all cases through a simple gradient diffusion model, involving a single "free" constant (the **subgrid Prandtl number** σ_s). An early optimization of this parameter, based on PISOC runs for the plane channel [Ciofalo and Collins 1992] led to the low value σ_s=0.25, which is rather unrealistic and close to the lower end of the range of values proposed in the literature. The combination PISOC / σ_s=0.25, however, was used for all the ribbed-channel simulations in Chapter 5. Later, however, a more detailed parametrical study evidenced that temperature profiles and heat transfer coefficients are particularly sensitive to the numerical accuracy attained, and that simulations based on the SIMPLEC algorithm, with several iterations per time step, gave the best heat transfer results for σ_s=0.5, which is a more realistic value about in the middle of the literature range. The combination SIMPLEC / σ_s=0.5 was used for the later simulations concerning the smooth channel (Chapter 4) and for the crossed-corrugated geometry (Chapter 6).

The above remarks throw a shade of suspicion on the various "physical" considerations that have been proposed to account for each of the broadly scattered values of σ_s in the literature, as surveyed in Section 2.4.5(IV). It is well possible that, once numerical accuracy problems were overcome, these would converge to a single figure, perhaps close to that generally accepted for the "turbulent Prandtl number" σ_t (0.8-0.9).

For the smooth channel only, a number of alternative formulations of the **wall boundary conditions** were implemented and compared. In particular, the various

formulations described by Piomelli et al.[1989] were re-cast so as to apply both to low Reynolds numbers (resolved sublayer) and to high Reynolds numbers (unresolved sublayer, i.e. true "synthetic" wall boundary conditions). Note that in LES, even in the former case, wall boundary conditions do not simply collapse to no-slip conditions, since the strain rate-stress proportionality may still be assumed to hold either locally or globally, with many variants in the details. However, in both cases no significant influence on the results was observed, so that a clear preference was expressed for the "local" formulation of Section 2.5.1 (similar to that proposed by Mason and Callen [1986]) which offers the great advantage of being applicable, unlike all the rival models, to general geometries.

The **initial conditions** for all the cases studied were simply generated by superimposing random and isotropic velocity fluctuations, of the order of the friction velocity u_τ, on a plug velocity profile. Though the resulting starting flow field was not physically realizable for an incompressible fluid, as it was not divergence-free, the flow solvers did not have any troubles in dealing with this and in turning the flow into a divergence-free one within a few time steps.

In the smooth-channel case only, an undesired consequence of the enforcement of continuity was that most of the initial fluctuations were damped out, leaving a low-turbulence flow which in turn took a long time to develop again sustained and statistically stationary turbulence levels. It is well possible that, by using a divergence-free initial field, the low-turbulence stage could be bypassed, thus greatly reducing the required transient duration and the associated CPU time (such flows can be generated by building an appropriate pseudo-random vector velocity potential and computing its curl).

On the other hand, for the two geometrically complex flows of Chapters 5 and 6 the enforcement of a divergence-free flow was not associated with any significant suppression of turbulent fluctuations, so that the initial conditions used here appear quite acceptable for these problems.

7.3 Numerical methods and computational aspects

The numerical methods used throughout the present study were all chosen among the standard ones implemented in the Harwell-FLOW3D (Release 2) code, as described in Section 3.2 and in Appendix A.

As regards the **pressure-velocity coupling algorithm**, the earliest simulations conducted (which include most of the smooth-channel runs in Chapter 4 and all the ribbed-channel runs in Chapter 5) made use of the PISOC method in its non-iterative form (1 "iteration" per time step). The residual reduction factors required to stop the "inner" iterations of the linear-equation solvers were set to 0.01 for ST3D (transport equations) and 0.005 for ICCG (pressure correction equation). The corresponding maximum allowed numbers of iterations were set to 100 and 250, respectively. Of course, no underrelaxation was used.

However, a subsequent comparison with SIMPLEC (used with 10 iterations per time step, residual reduction factors of 0.1 (ST3D) and 0.05 (ICCG), and maximum numbers of iterations of 10 and 25, respectively) for the smooth-channel case evidenced a clear superiority of the latter algorithm: statistical stationarity was attained earlier, the overprediction of the mean velocity profile was reduced, and fluctuation profiles closer to experimental values were obtained. The most relevant difference, however, was the large reduction of the temperature drop in the central region of the channel allowed by the use of SIMPLEC, clearly related to the larger values predicted for the cross-stream velocity fluctuations $v"_{rms}$. As a consequence, as was mentioned in Section 7.2 above, the best agreement with reference data for the temperature profile and the heat transfer coefficient was obtained for a larger and more realistic value of the subgrid Prandtl number σ_s (0.5) than required by PISOC.

Moreover, the use of PISO(C) in a non-iterative form is incompatible with all situations requiring the "deferred correction" approach described in Section 3.2; these include nonorthogonal grids and higher-order differencing schemes. Finally, it has to be mentioned that using PISOC non-iteratively with a later version (Release 2.3) of the same code led to a rapid divergence of the instantaneous velocities after 30-50 time steps, although up to that point the solution was practically coincident with the (stable) one obtained using the reference code (Release 2.1). The reason for this has remained, so far, unexplained despite much consulting with the (patient!) code developers.

For all the above reasons, SIMPLEC was selected as the most accurate and reliable algorithm for all the subsequent simulations, including a part of the smooth-channel runs in Chapter 4 and all the corrugated-geometry runs in Chapter 6. A price had to be paid, however, in that computing times increased about 2.5 times with respect to PISOC (with the above mentioned iteration-control parameters).

As to the **differencing schemes** used for the advection terms, most simulations were based simply on the central scheme (CDS). For testing purposes only, some plane-channel runs were repeated using the higher-order schemes QUICK and CCCT. These comparisons were made using the code release 2.3, and, of course, the iterative SIMPLEC method.

As discussed in Section 4.5.8, results were disappointing. Both QUICK and (especially) CCCT yielded low and asymmetric profiles of the secondary fluctuations $v"_{rms}$, $w"_{rms}$; CCCT also led to a gross overprediction both of the mean velocity and of the mean temperature drop across the channel. With both algorithms, unrealistically high time-fluctuations of the resolved turbulence energy were obtained.

Thus, central differencing appeared to have no real competitors for this kind of simulations. It may be mentioned that the highest values of the Peclet cell number Pe_c (= $u\Delta x/\alpha$) were about 10,000 for the plane-channel simulations (high-Reynolds number cases in Section 4.6.2), about 5000 for the ribbed channel simulations and about 500 for the crossed-corrugated geometry. These figures are indeed quite high for central differencing to be used; nevertheless, the use of moderate time steps and the robustness of the linear equation solvers were sufficient to prevent instability problems.

The **time-step** values used in most simulations ranged from 1/200 to 1/50 of a LETOT (defined in the text for the different geometries). In this range, the observed time-dependence of the results was not large, though a residual difference could still be observed in the smooth-channel case between the results for 1/100 and 1/200 (Section 4.5.5). For this geometry only, also a very coarse time step of 1/25 of a LETOT was tested, and was found to damp (though not completely) the turbulent fluctuations.

With the grids commonly used (having 32 or 48 cells in the downstream direction), a time step of 1/50 (LETOT) corresponds to a maximum Courant number ($u\Delta t/\Delta x$) decreasing from about 2 for the smooth channel to 1 for the ribbed channel and 0.5 for the crossed-corrugated geometry (independent of the Reynolds number). Since the use of an explicit method would typically require Courant numbers of 0.3-0.5, it is clear that the advantage of using the present, implicit approach (as far as the time step is concerned !) decreases in the same order for the three above geometries. Needless to say, an explicit method would require much less computing effort per time step. Actually, the advantage of using implicit methods is expected to be very little in direct or large-eddy simulations in general, since - independent of stability

considerations - the Courant number must be kept small in order to capture the time-fluctuations of the flow field and to get sustained turbulence.

It has to be mentioned that for all the problems studied simulations were successful only when Crank-Nicolson time-stepping was used. The fully-implicit backward method, which was tested both for the plane channel and for the crossed corrugated geometry, led in both cases to a severe damping of the fluctuations even when the time step was reduced to 1/200 of LETOT, and thus was discarded as too dissipative for large-eddy simulations.

Finally, as regards the **computational grids** employed, many relevant remarks (concerning the cell Peclet number, the Courant number, the wall boundary conditions etc.) have been implicitly made in the above sections. The "reference" grids had 32*24*24 volumes along the streamwise, cross-stream and spanwise directions, respectively (excluding the "dummy" external ones) in the smooth-channel case, 48*24*24 for the ribbed channel and 32*32*32 for the crossed corrugated geometry. In the last case, at Re<2000 and moderate corrugation angles (37-48°) three cells lay in the viscous sublayer $y^+<11$ over most of the walls; as discussed by Chapman [1979] and Grötzbach [1986], under these conditions also direct turbulence simulations should be reliable, which was confirmed by the fact that very little difference in the results was obtained when the Smagorinsky constant c_s was set to zero. However, for the other two geometries, at the Reynolds numbers investigated the grids had only one near-wall volume lying in the viscous sublayer and, in the high-Reynolds number plane-channel simulations of Section 4.6.2, there was no cell in the sublayer.

7.4 Recommendations for further work

In the following, some areas are indicated in which, to the author's opinion, validation and development efforts should be concentrated and applications look more promising.

a) The extension of the simulations to **non-periodic geometries**. Streamwise and spanwise periodicity assumptions, used throughout the present work, are clearly the simplest to deal with in large-eddy simulations; however, they greatly reduce the field of the applications and cut out such interesting problems as the flow over isolated obstacles (including backsteps, circular duct expansions etc.) and entrance effects in pipes or exchangers.

While fully-developed outflow conditions are probably adequate enough in most cases, the generation of suitable, time-dependent inflow conditions is much more difficult. The few authors who have presented non-periodic large eddy simulations [Schmitt and Friedrich 1987; Morinishi and Kobayashi 1990; Silveira-Neto et al. 1991; Werner and Wengle 1989] have recurred in most cases to preliminary, fully-developed (periodic) flow simulations from which a single "slice", normal to the main flow direction, was extracted, stored for all consecutive time steps and successively used as the inflow condition for the non-periodic problem. Of course, this requires a considerable amount of extra computing time; for long transients, also the necessary disk storage may become a problem. It is possible that, for strongly geometry-driven flows such as those considered in Chapters 5 and 6, the exact spatial and spectral distribution of the inlet velocities would not be relevant, and that satisfactory time-dependent inflow conditions can be prescribed by some suitable simple law.

b) The development and validation of **better subgrid models.** These should maintain the universality of the Smagorinsky-Lilly model while improving over this as regards not only the description of subgrid mechanisms, but also the resulting quality of the large-scale predictions. As discussed previously, this does not look like an easy task; one-equation models, based on a transport equation for the subgrid turbulence energy, are probably the most promising.

c) The application to **transitional flows** (which include a host of problems of direct engineering interest concerning heat exchangers, free-convection etc.). The results in Chapter 6 confirm that for these problems the direct or large eddy simulation approach may well give results better than conventional "low-Reynolds number" turbulence models even when relatively coarse grids, and somewhat inadequate physical models, are employed. Moreover, in complex geometries for which even conventional simulations should be run in three dimensions, the extra computing effort required by DS and LES may really be very low and - to the author's opinion - more than payed for by the much larger wealth of information that can thus be gained.

Finally, two remarks on numerical aspects seem to be appropriate.

First, for the reasons discussed above, the implementation of **explicit time-stepping** capabilities would be greatly beneficial in large-eddy

simulations and should be sought if the application of general-purpose, flexible codes to LES is regarded as a promising area.

Secondly, the development and testing of more advanced physical models (including subgrid models) would not make much sense if it were not accompanied by a detailed investigation of the **accuracy** of the numerical methods employed; as discussed above in these conclusions, many drawbacks that were regarded, at first sight, as inherent shortcomings of the models used turned out to be rather a consequence of numerical inaccuracies, and to vanish once better algorithms or finer resolutions were adopted. Of course, this is true in general for numerical fluid dynamics, but is particularly true for the three-dimensional, time-dependent simulations to which this work is dedicated.

REFERENCES

Alderton, J.H. and Wilkes, N.S. (1988) Some Applications of New Finite Difference Schemes for Fluid Flow Problems, Harwell Report AERE-R 13234, 1988.

Amsden, A.A. and Hirt, C.W. (1973) A Simple Scheme for Generating Curvilinear Grids, J. Comp. Phys., Vol.11, pp.348-359, 1973.

Antonia, R.A., Danh, H.Q. and Prabhu, A. (1977) Response of a Turbulent Boundary Layer to a Step Change in Surface Heat Flux, J. Fluid Mech., Vol.80, pp.153-177, 1977.

Antonopoulos-Domis, M. (1981.a) Large Eddy Simulation of a Passive Scalar in Isotropic Turbulence, J. Fluid Mech., Vol.104, pp.55-79, 1981.

Antonopoulos-Domis, M. (1981.b) Aspects of Large Eddy Simulation of Homogeneous Isotropic Turbulence, Int. J. Num. Meth. in Fluids, Vol.1, pp.273-290, 1981.

Antonopoulos-Domis, M., and Love, M.D. (1978) The Finite Difference Schemes used in LES code FORTY, Queen Mary College Report EP 6032, London, 1978.

Arter, W., Fletcher, D.F. and Selden, A.C. (1988) Flow Simulations for a Glow Discharge Laser, UKAEA Report CLM-R 288, Culham Lab., November 1988.

Aytekin, A. and Berger, F.P. (1979) Turbulent Flow in Rectangular Ducts with Low Aspect Ratios Having One Rough Wall, Nuclear Energy, Vol.18, No.1, pp.53-63, 1979.

Azab, K.A. and McLaughlin, J.B. (1987) Modeling the Viscous Wall Region, Phys. Fluids, Vol.30, No.8, pp.2362-2373, Aug. 1987.

Bardina, J., Ferziger, J.H. and Reynolds, W.C. (1980) Improved Subgrid-Scale Models for Large-Eddy Simulation, Procs. AIAA 13th Fluid & Plasma Dynamics Conference, AIAA Paper No.80-1357, 1980.

Bardina, J., Ferziger, J.H. and Reynolds, W.C. (1983) Improved Turbulence Models Based on Large Eddy Simulation of Homogeneous Incompressible Turbulent Flows, Report No.TF-19, Thermosciences Division, Dept. of Mechanical Engineering, Stanford University, Stanford, CA, USA, May 1983.

Baron, F. and Laurence, D. (1983) Large Eddy Simulation of a Wall-Bounded Turbulent Jet Flow and of a Homogeneous Shear Flow, Procs. 4th Symposium on Turbulent Shear Flows, Karlsruhe, FRG, Sept. 12-14, 1983 (Preprints, pp.4.7-4.12).

Bates, C.J., Yeoman, M.L. and Wilkes, N.S. (1983) Non-Intrusive Measurements and Numerical Comparison of the Axial Velocity Components in a Two-Dimensional Flow Channel for a Backward-Facing Step and a Rib-Roughened Surface, Harwell Report AERE-R 10787, May 1983.

Beavers, G.S., Sparrow, E.M. and Lloyd, J.R. (1971) Low Reynolds Number Turbulent Flow in Large Aspect Ratio Rectangular Ducts, ASME J. of Basic Engng., Vol.93, pp.296-299, June 1971.

Bègue, C., Cardot, B., Parès, C. and Pironneau, O. (1990) Simulation of Turbulence with Transient Mean, Int. J. for Numer. Meth. in Fluids, Vol.11, pp.677-695, 1990.

Beyer, W.H., ed. (1987) Handbook of Mathematical Science, CRC Press, Boca Raton, Florida, 2nd ed., 1987.

Biringen, S. (1990) Numerical Simulation of Nonlinear Structures in Channel Flow Transition, AIAA Journal, Vol.28, No.2, pp.365-367, Feb.1990 (Technical Note).

Biringen, S. and Reynolds, W.C. (1981) Large Eddy Simulation of the Shear-Free Turbulent Boundary Layer, J. Fluid Mech., Vol.103, pp.53-63, 1981.

Boussinesq, J. (1877) Mem. pres. par div. savants a l'acad. sci. Paris, Vol.23, p.46, 1877.

Bradshaw, P. (1975) Review - Complex Turbulent Flows, ASME J. of Fluids Engineering, Vol.97, pp.146-154, June 1975.

Bradshaw, P., ed. (1978.a) Turbulence, 2nd Edition, Springer-Verlag, Berlin, 1978.

Bradshaw, P. (1978.b) Introduction - Chapter 1 in 'Turbulence', P. Bradshaw, ed., Springer-Verlag, Berlin, 2nd Edition, 1978.

Briscolini, M., Maggiore, M., Melli, P., Piccolo, F., Santangelo, P., Succi, S., Vitaletti, M. and Zecca, V. (1989) Fluid Dynamics Research at IBM ECSEC, ERCOFTAC Bulletin III, pp.7-10, 1989.

Brown, G.L. and Roshko, A. (1974) On Density Effects and Large Structures in Turbulent Mixing Layers, J. Fluid Mech., Vol.64, Part 4, pp.775-816, 1974.

Brucato, A., Ciofalo, M., Grisafi, F. and Rizzuti, L. (1989) Application of a Numerical Fluid Dynamics Software to Stirred Tank Modelling, Procs. Int. Workshop 'Supercomputing Tools for Science and Engineering', Pisa, Italy, 4-7 Dec. 1989.

Brucato, A., Ciofalo, M., Grisafi, F. and Rizzuti, L. (1990) Computer Simulation of Turbulent Fluid Flow in Baffled and Unbaffled Tanks Stirred by Radial Impellers, Procs. Int. Conf. 'Computer Applications to Batch Processes' (CATB '90), Cengio, Italy, 28-30 March 1990.

Burgers, J.M. (1948) A Mathematical Model Illustrating the Theory of Turbulence, Adv. in Appl. Mech., Vol.1, pp.171-199, 1948.

Burns, A.D. and Wilkes, N.S. (1987) A Finite-Difference Method for the Computation of Fluid Flows in Complex Three-Dimensional Geometries, Harwell Report AERE-R 12342, July 1987; see also updated version, October 1989.

Burns, A.D., Ciofalo, M., Clarke, D.S., Gavrilakis, S., Hawkins, I.R., Jones, I.P., Kightley, J.R. and Wilkes, N.S. (1988) Progress with the Harwell-FLOW3D Software for the Prediction of Laminar and Turbulent Flow and Heat Transfer, 1987-1988, Procs. HTFS 20th Anniversary Conference, Research Symposium, Loughborough University, Loughborough, U.K., 19-23 Sept. 1988 (Harwell Report AERE-R 13148, 1988).

Burns, A.D., Ingram, D., Jones, I.P., Kightley, J.R., Lo, S. and Wilkes, N.S. (1987) FlOW3D: The Development and Application of Release 2, Harwell Report AERE-R 12693, June 1987 (1987 HTFS Res. Symp.).

Burns, A.D., Jones, I.P., Kightley, J.R. and Wilkes, N.S. (1987) The Implementation of a Finite Difference Method for Predicting Incompressible Flows in Complex Geometries, Harwell Report AERE-CSS 204, 1987.

Burns, A.D., Jones, I.P., Kightley, J.R. and Wilkes, N.S. (1988) Harwell-FLOW3D, Release 2.1 - User Manual, Harwell Report AERE-R (Draft), Aug. 1988; see also by same authors: Harwell-FLOW3D, Release 2 - User Manual, Harwell Report AERE-R (Draft), July 1989.

Burns, A.D., Wilkes, N.S., Jones, I.P. and Kightley, J.R. (1986) FLOW3D: Body-Fitted Coordinates, Harwell Report AERE-R 12262, June 1986 (1986 HTFS Res. Symp.).

Campbell, D. and Rose, H., eds. (1983) Order in Chaos (Proceedings of the International Conference on Order and Chaos, Center for Nonlinear Studies, Los Alamos, 24-28 May 1982) - Physica 7D, 1983.

Celenligil, M.C. and Mellor, G.L. (1984) Numerical Solution of Two-Dimensional Turbulent Separated Flows Using a Reynolds Stress Closure Model, ASME J. of Fluids Engng., Vol.107, pp.467-476, Dec. 1985.

Chapman, D.R. (1979) Computational Aerodynamics Development and Outlook, AIAA Journal, Vol.17, pp.1293-1313, Dec. 1979

Chew, P.E. (1985) Rotary Air Preheaters on Power Station Boilers, Proc. Institute of Energy Symposium 'Waste Heat Recovery and Utilisation', Portsmouth, U.K., September 1985.

Chieng, C.C. and Launder, B.E. (1980) On the Calculation of Turbulent Heat Transport Downstream from an Abrupt Pipe Expansion, Numer. Heat Transfer, Vol.3, pp.189-207, 1980

Chojnowski, B. and Chew, P.E. (1978) Getting the Best Out of Rotary Air Heaters, CEGB Research Journal, May 1978, pp.14-21.

Ciofalo, M. (1988) Algorithms and Auxiliary Routines for FLOW3D, Release 2, TFERC Res. Memo. No. TF/03/88/01, The City University, London, 1988.

Ciofalo, M. (1989.a) Computation of Turbulent Recirculating Flows with Heat Transfer Using FLOW3D - Progress Report, January-April, 1988 (Large-Eddy Simulation), TFERC Res. Memo. No. TF 89/01/01, The City University, London, 1989.

Ciofalo, M. (1989.b) Computation of Turbulent Recirculating Flows with Heat Transfer Using FLOW3D - Progress Report, September-October, 1988 (Large-Eddy Simulation II), TFERC Res. Memo. No. TF/01.06.89, The City University, London, 1989.

Ciofalo, M. (1991) Implementation of a Low-Reynolds Number Turbulence Model for the Harwell-FLOW3D Code (Release 2), and Preliminary Application to Flow and Heat Transfer Problems, TFERC Report (No.9 of [VV.AA.1989-1992]), The City University, London, November 1991.

Ciofalo, M. and Collins, M.W. (1988.a) Time-Dependent Numerical Simulation of the Starting Flow of an Incompressible Fluid Past a Backward-Facing Step,

Proc. AGARD Symposium 'Validation of Computational Fluid Dynamics', Lisbon, Portugal, 2-5 May, 1988, Paper No.37.

Ciofalo, M. and Collins, M.W. (1988.b) Predictive Study of Turbulent Fluid Flow and Heat Transfer Past a Double Symmetric Flat Duct Expansion, Procs. 2nd Nat. UK Heat Transfer Conf., Glasgow, UK, 14-16 Sept. 1988 - Mechanical Engineering Publications, London, 1988, Vol.2, pp.1057-1074.

Ciofalo, M. and Collins, M.W. (1988.c) Predictive Study of Heat Transfer to an Incompressible Fluid Past a Downstream-Facing Step in Turbulent Flow, Int. J. of Heat and Technology, Vol.6, No.3-4, pp.8-33, 1988 (Pres. at 5th Nat. Conf. of UIT, Turin, Italy, June 1987).

Ciofalo, M. and Collins, M.W. (1989.a) k-ε Predictions of Heat Transfer in Turbulent Recirculating Flows Using an Improved Wall Treatment, Numer. Heat Transfer, Part B, Vol.15, pp.21-47, 1989.

Ciofalo, M. and Collins, M.W. (1989.b) Large-Eddy Simulation of Turbulent Flow in Plane and Rib-Roughened Channels, Numerical Methods in Laminar and Turbulent Flow, Vol.6, part 2, C. Taylor et al., eds, Pineridge Press, Swansea, U.K., 1989, pp.1869-1882 (Procs. 6th Int. Conf. held at Swansea, UK, July 1989).

Ciofalo, M. and Collins, M.W. (1989.c) Predictions of Heat Transfer for Turbulent Flow in Plane and Rib-Roughened Channels Using Large Eddy Simulation, Proc. 7th Nat. Conf. of the UIT (Unione Italiana di Termofluidodinamica), Florence (Italy), 15-17 June 1989, pp.57-71.

Ciofalo, M. and Collins, M.W. (1992) Large-Eddy Simulation of Turbulent Flow and Heat Transfer in Plane and Rib-Roughened Channels, Int. J. Numer. Methods in Fluids, Vol.15, pp.453-489, 1992.

Ciofalo, M. and Karayiannis, T.G. (1989.a) Natural Convection in a Rectangular Partitioned Cavity, Procs. 7th Nat. Conf. of UIT (Unione Italiana di Termofluidodinamica), Florence, Italy, 15-17 June 1989.

Ciofalo, M. and Karayiannis, T.G. (1989.b) Convective Heat Transfer in a Vertical Square Cavity with Partitions at the End Walls, Procs. Eurotherm Seminar 'Natural Convection in Enclosures', Harwell, U.K., 7-8 Dec. 1989.

Ciofalo, M. and Karayiannis, T.G. (1990) Convective Heat Transfer in a Vertical Rectangular Cavity with Partitions at the End Walls, Heat Transfer 1990 (Procs. 9th Int. Heat Transfer Conf., Jerusalem, Israel, 19-24 August 1990), Paper 16-TR-03, Vol.5, pp.297-303.

Ciofalo, M. and Karayiannis, T.G. (1991) Natural Convection Heat Transfer in a Partially- or Completely-Partitioned Vertical Rectangular Enclosure, Int. J. of Heat and Mass Transfer, Vol.34, No.1, pp.167-179, 1991.

Ciofalo, M. and Perrone, G. (1990) Laminar and Turbulent Fluid Flow and Heat Transfer Predictions in Crossed Corrugated Rotary Regenerators, Dipartimento di Ingegneria Nucleare, Università di Palermo, Quaderno 3/90, Palermo, Italy, July 1990.

Ciofalo, M., Collins, M.W. and Henry, F.S. (1991) Laminar and Turbulent Flow and Heat Transfer in Crossed Corrugated Heat Exchangers, Procs. 7th Int. Conf. Numerical Methods for Thermal Problems, Stanford University, Stanford, CA, USA, July 8-12, 1991 (Numerical Methods in Thermal Problems, Vol.7, Part 1, J. Lewis et al., eds, Pineridge Press, Swansea, UK, 1991, pp.622-638).

Ciofalo, M., Collins, M.W. and Perrone, G. (1990) Laminar Flow and Heat Transfer Predictions in Cross-Corrugated Rotary Regenerators, Procs. 8th Nat. Conf. of the UIT (Unione Italiana di Termofluidodinamica), Ancona, Italy, 29-30 June 1990.

Ciofalo, M., Collins, M.W. and Perrone, G. (1991) Turbulent Flow and Heat Transfer Predictions for Cross-Corrugated Rotary Regenerators, Procs. EUROTECH-Direct 91, Thermofluids Engineering, Birmingham, U.K., 2-4 July 1991, paper C413/041.

Ciofalo, M., Fodemski, T.R. and Collins, M.W. (1988) Large Eddy Simulation of Turbulent Flow and Heat Transfer in Plane Channels, Procs. 6th Nat. Conf. of the UIT (Unione Italiana di Termofluidodinamica), Bari, Italy, 9-11 June 1988, pp.37-54.

Ciofalo, M., Perrone, G., Stasiek, J. and Collins, M.W. (1992) Numerical and Experimental Study of Flow and Heat Transfer in Cross-Corrugated Rotary Regenerators, Procs. 10th Nat. Conf. of the UIT (Unione Italiana di Termofluidodinamica), Genoa, Italy, 25-27 June 1992, pp.75-86.

Clark, R.A., Ferziger, J.H. and Reynolds, W.C. (1979) Evaluation of Subgrid-Scale Models Using an Accurately Simulated Turbulent Flow, J. Fluid Mech., Vol.91, part 1, pp.1-16, 1979; also: Report No.TF-9, Thermosciences Division, Department of Mechanical Engineering, Stanford University, Stanford, CA, USA, 1977.

Clarke, D.S. and Wilkes, N.S. (1988) The Calculation of Turbulent Flows in Complex Geometries Using an Algebraic Stress Model, Harwell Report AERE-R 13251, Aug. 1988.

Clarke, D.S. and Wilkes, N.S. (1989) The Calculation of Turbulent Flows in Complex Geometries Using a Differential Stress Model, Harwell Report AERE-R 13428, April 1989.

Cocking, S.J. and Dalzell, W. (1984) Two Component Velocity Measurements on Turbulent Flow in a Ribbed-Wall Flow Channel and Comparison with a Turbulent Energy - Dissipation Model, Harwell Report AERE-R 11231, 1984.

Coleman, G.N., Ferziger, J.H. and Spalart, P.R. (1990) A Numerical Study of the Turbulent Ekman Layer, J. Fluid Mech., Vol.213, pp.313-348, 1990.

Collins, M.W. and Ciofalo, M. (1991) Computational Fluid Dynamics and Its Application to Transport Processes, J. Chem. Tech. and Biotech., Vol.52, pp.5-47, 1991.

Collins, M.W. and Voke, P.R. (1983) The Application of Large Eddy Simulation to Engineering Problems, Heat and Technology, Vol.1, N.1, pp.36-55, Aug. 1983.

Comte-Bellot, G. (1963) Contribution a l'etude de la turbulence de conduite, Doctoral Thesis, Univ. of Grenoble, France, 1963 [in French].

Comte-Bellot, G. (1965) Ecoulement turbulent entre deux parois parallele, Publ. Sci. Minist. Air Fr.419, 1965 [in French].

Comte-Bellot, G. and Corrsin, S. (1971) Simple Eulerian Time Correlation of Full- and Narrow-Band Velocity Signals in Grid-Generated 'Isotropic' Turbulence, J. Fluid Mech., Vol.48, No.2, pp.273-337, 1971.

Connell, S.D. and Stow, P. (1986) The Pressure Correction Method, Computers & Fluids, Vol.14, No.1, pp.1-10, 1986.

Corcoran, E. (1991) Calcolatori Superveloci, Le Scienze [it. ed. of Scientific American], No.271, pp.82-92, 1991.

Cousteix, J. and Hondeville, R. (1985) Turbulence and Skin Friction Evolutions in an Oscillating Boundary Layer, Procs. 5th Symposium on Turbulent Shear Flows, Cornell University, Ithaca, NY, USA, Aug. 7-9, 1985 (Preprints, pp.18.7-18.12).

Crabb, D., Durao, D.F.G. and Whitelaw, J.H. (1981) Velocity Characteristics in the Vicinity of a Two-Dimensional Rib, Proc. 3rd Symp. Turb. Shear Flows, Davis, CA, USA, Sept. 9-11, 1981 (Preprints, pp.16.6-16.10).

Dang, K. and Roy, P. (1985) Direct and Large Eddy Simulation of Homogeneous Turbulence Submitted to Solid Body Rotation, Procs. 5th Symposium on Turbulent Shear Flows, Cornell University, Ithaca, NY, USA, Aug. 7-9, 1985 (Preprints, pp.17.1-17.6).

Deardorff, J.W. (1970.a) A Numerical Study of Three-Dimensional Turbulent Channel Flow at Large Reynolds Numbers, J. Fluid Mech., Vol.41, Part 2, pp.453-480, 1970.

Deardorff, J.W. (1970.b) A Three-Dimensional Numerical Investigation of the Idealized Planetary Boundary Layer, Geophys. Fluid Dynamics, Vol.1, pp.377-410, 1970.

Deardorff, J.W. (1970.c) Preliminary Results from Numerical Integration of the Unstable Planetary Boundary Layer, J. Atmos. Sci., Vol.27, pp.1209-1211, 1970.

Deardorff, J.W. (1970.d) Convective Velocity and Temperature Scales for the Unstable Planetary Boundary Layer and for Rayleigh Convection, J. Atmos. Sci., Vol.27, pp.1211-1213, 1970.

Deardorff, J.W. (1971) On the Magnitude of the Subgrid Scale Eddy Coefficient, J. Comp. Phys., Vol.1, pp.120-133, 1971.

Deardorff, J.W. (1972.a) Numerical Investigation of Neutral and Unstable Planetary Boundary Layers, J. Atmos. Sci., Vol.29, pp.91-115, Jan. 1972.

Deardorff, J.W. (1972.b) Parameterization of the Planetary Boundary Layer for Use in General Circulation Models, Monthly Weather Review, Vol.100, pp.93-106, 1972.

Deardorff, J.W. (1973.a) Three-Dimensional Numerical Modeling of the Planetary Boundary Layer, in 'Workshop on Micrometeorology', D.A. Haugen, ed., Am. Met. Soc., Boston, 1973, Chapter 7, pp.271-311.

Deardorff, J.W. (1973.b) The Use of Subgrid Transport Equations in a Three-Dimensional Model of Atmospheric Turbulence, ASME J. of Fluids Engng., Vol.95, pp.429-438, 1973.

Deardorff, J.W. (1973.c) An Explanation of Anomalously Large Reynolds Stresses Within the Convective Planetary Boundary Layer, J. Atmos. Sci., Vol.30, pp.1070-1076, 1973.

Deardorff, J.W. (1973.d) Simulation of Turbulent Channel Flow, ASME J. of Fluids Engng., Vol.95, p.429, 1973.

Deardorff, J.W. (1974.a) Three-Dimensional Numerical Study of the Height and Mean Structure of a Heated Planetary Boundary Layer, Boundary-Layer Meteorology, Vol.7, pp.81-106, 1974.

Deardorff, J.W. (1974.b) Three-Dimensional Numerical Study of Turbulence in an Entraining Mixed Layer, Boundary-Layer Meteorology, Vol.7, pp.199-226, 1974.

Deardorff, J.W. (1976) On the Entrainment Rate of a Stratocumulus-Topped Mixed Layer, Quart. J. Roy. Meteor. Soc., Vol.102, pp.563-582, 1976.

Deardorff, J.W. (1980) Stratocumulus-Capped Mixed Layers Derived from a Three-Dimensional Model, Boundary-Layer Meteorology, Vol.18, pp.495-527, 1980.

Deardorff, J.W. and Willis, G.E. (1984) Further Results from a Laboratory Model of the Convective Planetary Boundary Layer, Boundary-Layer Meteorology, Vol.32, pp.205-236, 1984.

Delville, J., Bellin, S., Garem, J.H. and Bonnet, J.P. (1989) Analysis of Structures in a Turbulent Plane Mixing Layer by Use of a Pseudo-Flow Visualization Method Based on Hot-Wire Anemometry, in "Advances in Turbulence 2", H.-H.Fernholz and H.E.Fiedler, eds., Springer-Verlag, Berlin, 1989, pp.251-256 (Procs. 2nd European Turbulence Conference, Berlin, Aug. 30 - Sept. 2, 1988).

Demuren, A.O. (1985) False Diffusion in Three-Dimensional Flow Calculations, Computers & Fluids, Vol.13, pp.411-419, 1985.

Dimaczek, G., Tropea, C. and Wang, A.B. (1989) Turbulent Flow Over Two-Dimensional Surface-Mounted Obstacles: Plane and Axisymmetric Geometries, in "Advances in Turbulence 2", H.-H.Fernholz and H.E.Fiedler, eds., Springer-Verlag, Berlin, 1989, pp.114-121 (Procs. 2nd European Turbulence Conference, Berlin, Aug.30 - Sept.2, 1988).

Drain, L.E. and Martin, S. (1985) Two-Component Velocity Measurements of Turbulent Flow in a Ribbed-Wall Flow Channel, Procs. Int. Conf. on Laser Velocimetry - Advances and Applications, Manchester, U.K., Dec. 16-18, 1985, Paper No.3, pp.99-112.

Durst, F. and Rastogi, A.K. (1979) Theoretical and Experimental Investigations of Turbulent Flows with Separation, Procs. 1st Symposium on Turbulent Shear Flows, Pennsylvania State University, University Park, PA, USA, 18-20 April 1977 (Turbulent Shear Flows 1, F. Durst, B.E. Launder and F.W. Schmidt, eds., Springer-Verlag, Berlin-Heidelberg-New York, 1979, pp.208-219).

Durst, F. and Rastogi, A.K. (1980) Turbulent Flow Over Two-Dimensional Fences, Procs. 2nd Symposium on Turbulent Shear Flows, Imperial College, London, July 1979 (Turbulent Shear Flows 2, L.J.S. Bradbury et al., eds., Springer-Verlag, Berlin, 1980, pp.218-232).

Engleman, M.S. (1990) FIDAP Theoretical Manual, Version 5.0, Fluid Dynamics International, Evanstone, Ill., USA, 1990.

Feigenbaum, M.J. (1978) Quantitative Universality for a Class of Nonlinear Transformations, J. of Statistical Phys., Vol.19, pp.25-52, 1978.

Feigenbaum, M.J. (1980) The Transition to Aperiodic Behavior in Turbulent Systems, Commun. Math. Phys., Vol.77, pp.65-86, 1980.

Fergizer, J.H. (1977) Large Eddy Numerical Simulations of Turbulent Flows, AIAA Journal, Vol.15, No.9, pp.1261-1267, 1977.

Fergizer, J.H. (1981) Higher-Level Simulations of Turbulent Flows, Report No.TF-16, Thermosciences Division, Dept. of Mechanical Engineering, Stanford University, Stanford, CA, USA, March 1981.

Fergizer, J.H. and Leslie, D.C. (1979) Large Eddy Simulation - A Predictive Approach to Turbulent Flow Computation, Procs. AIAA Computational Fluid Dynamics Conference, AIAA paper 79-1441, 1979.

Fiedler, B. and Moeng, C.H. (1985) A Practical Integral Closure Model for Mean Vertical Transport of a Scalar in a Convective Boundary Layer, J. Atmos. Sci., Vol.42, pp.359-363, 1985.

Findikakis, A. (1981) Large Eddy Simulations of Stratified Flows, Dissertation, Dept. of Civil Engineering, Stanford University, Stanford, CA, USA, 1981.

Focke, W.W. and Knibbe, P.G. (1986) Flow Visualization in Parallel-Plate Ducts with Corrugated Walls, J. Fluid Mech., Vol.165, pp.73-77, 1986.

Focke, W.W., Zachariades, J. and Olivier, I. (1985) The Effect of the Corrugation Inclination Angle on the Thermohydraulic Performances of Plate Heat Exchangers, Int. J. of Heat and Mass Transfer, Vol.28, No.8, pp.1469-1479, 1985.

Fodemski, T.R. (1987) The Simulation of Flow and Heat Transfer in Channels with Ribbed Surfaces, Procs. 2nd Int. Symp. on Transport Phenomena in Turbulent Flows, Univ. of Tokyo, Tokyo, Japan, Oct. 25-29, 1987, pp.867-880.

Fodemski, T.R. (1989) The Performance Analysis of a Ribbed Channel Based on Computer Simulation of Flow and Heat Transfer, Procs. 7th Nat. Conf. of the UIT (Unione Italiana di Termofluidodinamica), Florence, Italy, 15-17 June 1989, pp.97-108.

Fodemski, T.R. (1990) Computer Simulation Study of Thermodynamic Performance of Corrugated Ducts, Procs. 9th Int. Heat Transfer Conf., Jerusalem, Israel, Aug. 19-24, 1990, Paper 7-M-21 - Heat Transfer 1990, G. Hetsroni, ed., Vol.3, pp.241-246, 1990.

Fodemski, T.R. and Collins, M.W. (1988) Flow and Heat Transfer Simulations for Two- and Three-Dimensional Smooth and Ribbed Channels, Procs. 2nd UK Nat. Heat Transfer Conf., Glasgow, UK, 14-16 Sept. 1988 - Mechanical Engineering Publications, London, 1988, pp.845-860.

Fodemski, T.R., Voke, P.R. and Collins, M.W. (1986) Numerical Grid Generation Applied to Spectral Turbulent Simulations, Procs. 1st Int. Conf. on Numerical Grid Generation in Computational Fluid Dynamics, Landshut, W. Germany, 14-17 July, 1986.

Fodemski, T.R., Voke, P.R. and Collins, M.W. (1987) Flow Simulation in Channels With Distorted Geometry Using a Spectral Code With Coordinate Transformation, Int. J. Num. Meth. in Fluids, Vol.7, No.3, pp.277-290, 1987.

Gaiser, G. and Kottke, V. (1989.a) Flow Phenomena and Local Heat and Mass Transfer in Corrugated Passages, Chem. Eng. Technol., Vol.12, pp.400-405, 1989.

Gaiser, G. and Kottke, V. (1989.b) Visualisation of Flow Phenomena and Local Heat and Mass Transfer in Corrugated Passages, Procs. 5th Symp. on Flow Visualization, Prague, Czechoslovakia, Aug. 21-25, 1989 - Flow Visualization V, R. Reznicek, ed., Hemisphere, 1989, pp.835-842.

Gaiser, G. and Kottke, V. (1990) Effects of Corrugation Parameters on Local and Integral Heat Transfer in Plate Heat Exchangers and Regenerators, Procs. 9th International Heat Transfer Conference, Jerusalem, Israel, Aug. 19-24, 1990 - Heat Transfer 1990, G. Hetsroni, ed., pp.85-90, 1990.

Gao, S., Leslie, D.C. and Voke, P.R. (1991) Large Eddy Simulation of Thermal Impinging Jets, Report ME-FD/91.02, Department of Mechanical Engineering, University of Surrey, Guildford, UK, Nov. 1991.

Gaskell, P.H. and Lau, A.K.C. (1987) Curvature Compensated Convective Transport: SMART, a new Boundedness Preserving Transport Algorithm, Int. J. for Numer. Meth. in Fluids, 1987.

Gavrilakis, S. (1987) Work on LES Using the FLOW3D Code from October '86 to March '87, Unpublished Report, 1987.

Gavrilakis, S., Tsai, H.M., Voke, P.R. and Leslie, D.C. (1986) Large Eddy Simulation of Low Reynolds Number Channel Flow By Spectral and Finite Difference Methods, in 'Direct and Large Eddy Simulation of Turbulence', Schumann, U. and Friedrich, R., eds. - Notes on Numerical Fluid Mechanics, Vol.15, pp.105-188, Braunschwieg, 1986.

Germano, M., Piomelli, U., Moin, P. and Cabot, H. (1991) A Dynamic Subgrid-Scale Eddy Viscosity Model, Phys. Fluids A, Vol.3, No.7, pp.1760-1765, July 1991.

Gleick, J. (1987) Chaos, Viking Penguin Inc., New York, 1987 [Italian edition: Caos, Rizzoli Libri S.p.A., Milano, 1989].

Gollub, J.P. and Benson, S.V. (1980) Many Routes to Turbulent Convection, J. Fluid Mech., Vol.100, pp.449-470, 1980.

Gosman, A.D., Khalil, F.E. and Whitelaw, J.H. (1979) The Calculation of Two-Dimensional Turbulent Recirculating Flows, Procs. 1st Symp. Turbulent Shear Flows, Pennsylvania State University, Pennsylvania, USA, 1977 -Turbulent Shear Flows 1, F.Durst et al., eds., Springer-Verlag, Berlin-Heidelberg-New York, 1979, pp.237-255

Gosman, A.D. and Pun, W.M. (1974) Lecture Notes for Course Entitled "Computation of Recirculating Flows", Heat Transfer Sec. Report HTS/74/2, Imperial College, London, 1974.

Grötzbach, G. (1982) Direct Numerical Simulation of Laminar and Turbulent Bénard Convection, J. Fluid Mech., Vol.119, pp.27-53, 1982.

Grötzbach, G. (1985) Application of the TURBIT-3 Subgrid Scale Model to Scales Between Large Eddy and Direct Simulations, Procs. EUROMECH 199, 'Direct and Large Eddy Simulation of Turbulent Flows', Technical University of Munich, FRG, Sept.30-Oct.2, 1985.

Grötzbach, G. (1986) Direct Numerical and Large Eddy Simulation of Turbulent Channel Flows, in Encyclopaedia of Fluid Mechanics, N.P. Cheremisinoff (ed.), Gulf. Publishing Co., Vol.6, 1986.

Grötzbach, G. (1988) Turbulent Heat Transfer in an Internally Heated Fluid Layer, Procs. 3rd Int. Symp. on Refined Flow Modelling and Turbulence Measurement, Tokyo, July 26-28, 1988.

Grötzbach, G. (1990) Simulation of Turbulent Flow and Heat Transfer for Selected Problems of Nuclear Thermal-Hydraulics, Procs. Int. Conf. on Supercomputing in Nuclear Applications, Mito, Japan, March 12-16, 1990.

Grötzbach, G. and Schumann, U. (1977) Direct Numerical Simulation of Turbulent Velocity, Pressure, and Temperature Fields in Channel Flows, Procs. 1st Symposium on Turbulent Shear Flows, Pennsylvania State University, University Park, PA, USA, 18-20 April 1977 (Turbulent Shear Flows 1, F. Durst, B.E. Launder and F.W. Schmidt, eds., Springer-Verlag, Berlin-Heidelberg-New York, 1979, pp.371-385).

Guezennec, Y.G. (1989) Stochastic Estimation of Coherent Structures in Turbulent Boundary Layers, Phys. Fluids A, Vol.1, No.6, pp.1054-1060, June 1989.

Guilbert, P.W. (1989) Comparison of Monte Carlo and Discrete Transfer Methods for Modelling Thermal Radiation, Harwell Report AERE-R 13423, HCCP/R22/1989, March 1989.

Hager, W.H. (1988) Applied Numerical Linear Algebra, Prentice-Hall Int. Ed., 1988.

Han, J.C. (1984) Heat Transfer and Friction in Channels with Two Opposite Rib-Roughened Walls, ASME J. of Heat Transfer, Vol.106, pp.774-781, Nov.1984.

Han, J.C., Glicksman, L.R. and Rohsenow, W.M. (1978) An Investigation of Heat Transfer and Friction for Rib-Roughened Surfaces, Int. J. Heat Mass Transfer, Vol.21, pp.1143-1156, 1978.

Hanjalic, K. and Launder, B.E. (1972) Fully Developed Asymmetric Flow in a Plane Channel, J. Fluid Mech., Vol.51, Part 2, p.301, 1972.

Hanjalic, K. and Stosic, N. (1983) Hysteresis of Turbulent Stresses in Wall Flows Subjected to Periodic Disturbances, Procs. 4th Symposium on Turbulent Shear Flows, Karlsruhe, W.Germany, Sept. 12-14, 1983 (Turbulent Shear Flows 2, F. Durst et al., eds., Springer-Verlag, Berlin-Heidelberg-New York, 1983, pp.287-300).

Hanson, P.J., Jones, I.P. and Kightley, J.R. (1989) Harwell-FLOW3D Command Language Frontend, Harwell Report AERE-R (draft), Sept. 1989.

Harlow, F.H. and Welch, J.E. (1965) Numerical Calculation of Time-Dependent Viscous Incompressible Flow of Fluid with Free Surface, Phys. Fluids, Vol.8, No.12, pp.2182-2189, 1965.

Hausen, H. (1976) Warmeubertragung im Gegenstrom, Gleichstrom und Kreutzstrom, Springer-Verlag, 2nd ed., 1976

Hatziavramidis, D.T. and Hanratty, T.J. (1979) The Representation of the Viscous Wall Region by a Regular Eddy Pattern, J. Fluid Mech., Vol.95, Part 4, pp.655-679, 1979.

Hawkins, I.R. and Kightley, J.R. (1989) Grid Adaption for Turbulent Flow Problems, Numerical Methods in Laminar and Turbulent Flow, Vol.6, part 2, C. Taylor et al., eds., Pineridge Press, Swansea, UK, 1989, pp.1651-1661 (Procs. 6th Int. Conf. held at Swansea, UK, July 1989).

Head, M.R. and Bandyopadhyay, R. (1981) New Aspects of Turbulence Structure, J. Fluid Mech., Vol.107, pp.297-338, 1981.

Henry, F.S. and Collins, M.W. (1989) Prediction of Swirling Flow in Annular Channels, Numerical Methods in Laminar and Turbulent Flow, Vol.6, part 2, C. Taylor et al., eds., Pineridge Press, Swansea, UK, 1989, pp.1857-1867 (Procs. 6th Int. Conf. held at Swansea, UK, July 1989).

Henry, F.S., Collins, M.W. and Ciofalo, M. (1991) Prediction of Swirling Flow in a Corrugated Channel, Procs. ASE '91 (2nd Int. Conf. on Application of Supercomputers in Engineering), Boston, Mass., USA, 13-15 Aug. 1991.

Herring, J.R. (1979) Subgrid Scale Modeling - An Introduction and Overview, Procs. 1st Symposium Turbulent Shear Flows, Pennsylvania State University, University Park, PA, USA, 18-20 April 1977 (Turbulent Shear Flows 1, F. Durst, B.E. Launder and F.W. Schmidt, eds., Springer-Verlag, Berlin-Heidelberg-New York, 1979, pp.347-352).

Herring, J.R., Orszag, S.A., Kraichnan, R.H. and Fox, D.G. (1974) Decay of Two-Dimensional Homogeneous Turbulence, J. Fluid Mech., Vol.66, Part 3, pp.417-444, 1974.

Hinze, J.O. (1975) Turbulence, 2nd ed., McGraw-Hill, 1975.

Horiuti, K. (1982) Study of Incompressible Turbulent Channel Flow by Large-Eddy Simulation, Theoretical and Applied Mechanics, Vol.31, pp.407-427, 1982.

Horiuti, K. (1985.a) Large Eddy Simulation of Turbulent Channel Flow by One-Equation Modeling, J. Phys. Soc. Japan, Vol.54, pp.2855-2865, 1985.

Horiuti, K. (1985.b) Large Eddy Simulation of Turbulent Channel Flows, Procs. EUROMECH 199, 'Direct and Large Eddy Simulation of Turbulent Flows', Technical University of Munich, FRG, Sept.30-Oct.2, 1985.

Horiuti, K. (1989) The Role of the Bardina Model in Large Eddy Simulation of Turbulent Channel Flow, Phys. Fluids A, Vol.1, No.2, pp.426-428, Feb.1989.

Humphrey, J.A.C. (1979) Turbulent Flow in an Asymmetrically Roughened Duct of Square Cross Section, in 'Laser Velocimetry and Particle Sizing', H.D.Thompson and W.H.Stevenson, eds., Hemisphere, 1979, p.220.

Humphrey, J.A.C. and Whitelaw, J.H. (1979) Turbulent Flow in a Duct with Roughness, Procs. 2nd Symposium on Turbulent Shear Flows, Imperial College, London, 1979 (Turbulent Shear Flows 2, L.J.S. Bradbury et al., eds., Springer-Verlag, Berlin-Heidelberg-New York, 1980, pp.174-188).

Hunter, J.C. and Collins, M.W. (1987) Holographic Interferometry and Digital Fringe Processing, J. of Physics D, Vol.20, pp.683-691, 1987.

Hunter, J.C. and Collins, M.W. (1990) The Processing of Data from Optical Whole-Field Measurement Methods and Large Eddy Simulation Predictions to Investigate Coherent Structures in Fluid Flow, Int. J. of Optoelectronics, Vol.5, No.5, pp.405-438, 1990.

Hunter, J.C., Tsai, H.M., Lockett, J.F., Voke, P.R., Collins, M.W. and Leslie, D.C. (1988) A Comparison of Large Eddy Simulation Predictions of a Thermal Layer with Holographic Interferometry, Procs. 5th Int. Conf. Num. Methods in Thermal Problems, Montreal, 1988.

Hussain, A.K.M.F. (1983) Coherent Structures - Reality and Myth, Phys. Fluids, Vol.26, p.2816, 1983.

Hussain, A.K.M.F. and Reynolds, W.C. (1975) Measurements in Fully Developed Turbulent Channel Flow, ASME J. Fluids Engng., Vol.97, pp.568-580, Dec. 1975.

Hussaini, M.Y. and Zang, T.A. (1987) Spectral Methods in Fluid Dynamics, Ann. Rev. Fluid Mech., Vol.19, pp.339-367, 1987.

Iannello, M. (1992) Simulazione numerica della dispersione atmosferica a scala locale, Graduation Thesis in Nuclear Engineering, University of Palermo, 1992 [in Italian].

Incropera, F.P. and DeWitt, P. (1985) Introduction to Heat Transfer, John Wiley & Sons, London, 1985.

Ingram, D.I., Bailey, D.J., Read, G.T. and Hawkins, I.R. (1989) Numerical Grid Generation Package - Part 1: User Guide; Part 2: Examples, Harwell Reports, Sept. 1989 (unpublished).

Issa, R.I. (1986) Solution of the Implicitly Discretized Fluid Flow Equations by Operator-Splitting, J. Comp. Phys., Vol.62, No.1, pp.40-65, 1986.

Issa, R.I., Gosman, A.D. and Watkins, A.P. (1986) The Computation of Compressible and Incompressible Recirculating Flows by a Non-Iterative Implicit Scheme, J. Comp. Phys., Vol.62, No.1, pp.66-82, 1986.

Jackson, C.P. and Winters, K.H. (1989) A Guide to Post-Processing Using the TGIN Language, Harwell Report AERE-R (draft), 2nd edition, March 1989.

Jayatilleke, C.L.V. (1969) The Influence of Prandtl Number and Surface Roughness on the Resistance of the Laminar Sublayer to Momentum and Heat Transfer, Progr. Heat Mass Transfer, Vol.1, pp.197-329, U. Grigull and F. Hahne, eds., 1969.

Jones, I.P. (1991) CFDS Software - Validation Report: Part 1, AEA-InTec Report, Harwell Laboratory, Nov. 1991.

Jones, I.P., and Hanson, P.J. (1989) Harwell-FLOW3D Command Language User Guide, Harwell Report AERE-R (Draft), March 1989.

Jones, I.P., Kightley, J.R., Thompson, C.P. and Wilkes, N.S. (1985) FLOW3D, a Computer Code for the Prediction of Laminar and Turbulent Flow, and Heat Transfer: Release 1, Harwell Report AERE-R 11825, 1985.

Jones, I.P., Kightley, J.R., Thompson, C.P. and Wilkes, N.S. (1986) FLOW3D Release 1: User Manual, Harwell Report AERE-R 11893, 1986.

Kacker, S.C. (1971) Estimation of Friction Factor of Rough Surfaces from the Pressure Distribution Around a Roughness Element, CEGB Report RD/B/N 1967, April 1971.

Karayiannis, T.G., Ciofalo, M. and Barbaro, G. (1991) Convective Heat Transfer in Partitioned Cavities, Procs. 11th Int. Symp. 'INTERKLIMA 91', Zagreb, Yugoslavia, 12-14 June 1991, pp.51-63.

Karayiannis, T.G., Ciofalo, M. and Barbaro, G. (1992) Natural Convection in a Single- and Two-Zone Rectangular Enclosure, Int. J. of Heat and Mass Transfer, Vol.35, No.7, pp.1645-1657, 1992.

Kasagi, N., Kuroda, A. and Hirata, M. (1989) Numerical Investigation of Near-Wall Turbulent Heat Transfer Taking Into Account the Unsteady Heat Conduction in the Solid Wall, ASME J. of Heat Transfer, Vol.111, pp.385-392, May 1989.

Kerr, R.M. (1990) Velocity, Scalar and Transfer Spectra in Numerical Turbulence, J. Fluid Mech., Vol.211, pp.309-332, 1990.

Kightley, J.R. (1985) The Conjugate Gradient Method Applied to Turbulent Flow Calculations, Harwell Report AREE CSS 184, 1985.

Kightley, J.R. and Jones, I.P. (1985) A Comparison of Conjugate Gradient Preconditioning for Three-Dimensional Problems on a CRAY-1, Comp. Phys. Commun., Vol.37, pp.205-214, 1985.

Kim, J. (1983) The Effect of Rotation on Turbulence Structure, Procs. 4th Symposium on Turbulent Shear Flows, Karlsruhe, FRG, Sept.12-14, 1983 (Preprints, pp.6.14-6.19).

Kim, J. and Moin, P. (1979) Large Eddy Simulation of Turbulent Channel Flow - ILLIAC IV Calculations, in 'Turbulent Boundary Layers -Experiments, Theory, and Modeling', The Hague, Netherlands, AGARD Conf. Procs. No.271, paper 14, 1979.

Kline, S.J., Reynolds, W.C., Schraub, F.A. and Rundstadler, P.W. (1967) The Structure of Turbulent Boundary Layers, J. Fluid Mech., Vol.30, pp.741-773, 1967.

Kobayashi, T., Kano, M., and Ishihara, T. (1984) Prediction of Turbulent Flow in Two-Dimensional Channel with Turbulence Promoters (1st Report, Numerical Predictions by Large Eddy Simulation), Bull. JSME, Vol.27, No.231, pp.1893-1898, Sept. 1984.

Kobayashi, T., Kano, M., Ishihara, T. and Saga, T. (1985.a) Prediction of Turbulent Flow in Two-Dimensional Channel with Turbulence Promoters (2nd Report, Numerical Prediction by k-ε Model and Comparison with Experimental Results), Bull. JSME, Vol.28, No.246, pp.2940-2947, Dec. 1985.

Kobayashi, T., Kano, M., and Ishihara, T. (1985.b) Prediction of Turbulent Flow in Two-Dimensional Channel with Turbulence Promoters (3rd Report, Improvement of Large Eddy Simulation and Formation of Streaklines), Bull. JSME, Vol.28, No.246, pp.2948-2953, Dec. 1985.

Komori, S., Murakami, Y. and Ueda, H. (1989) Detection of Coherent Structures Associated with Bursting Events in an Open-Channel Flow by a Two-Point Measuring Technique Using Two Laser-Doppler Velocimeters, Phys. Fluids A, Vol.1, No.2, pp.339-348, Feb.1989.

Kreplin, H.P. and Eckelmann, H. (1979) Behavior of the Three Fluctuating Velocity Components in the Wall Region of a Turbulent Channel Flow, Phys. Fluids, Vol.22, No.7, pp.1233-1239, July 1979.

Kwak, D., Reynolds, W.C. and Ferziger, J.H. (1975) Three-Dimensional Time-Dependent Computation of Turbulent Flows, Report No.TF-5, Department of Mechanical Engineering, Stanford University, Stanford, CA, USA, 1975.

Lam, C.K.G. and Bremhorst, K.A. (1981) Modified Form of the k-ε Model for Predicting Wall Turbulence, ASME J. of Fluids Engng., Vol.103, pp.456-460, 1981.

Landahl, M.T. (1990) On Sublayer Streaks, J. Fluid Mech., Vol.212, pp.593-614, 1990.

Landau, N. (1944) Acad. Sci. USSR, Vol.44, p.341, 1944.

Landau, N. and Lifschitz, N. (1959) Fluid Mechanics, Pergamon Press, Oxford, 1959 [French Edition: Physique Théorique. Tome VI: Mécanique des Fluides, Editions MIR, Moscou, 1971, pp.151-155].

Lanford, O.E. (1981) Strange Attractors and Turbulence, in 'Hydrodynamic Instabilities and Transition to Turbulence', H.L.Swinney and J.P. Gollub, eds., Springer-Verlag, Berlin-Heidelberg-New York, 1981, Chapter 2, pp.7-26.

Latimer, B.R. and Pollard, A. (1989) Comparison of Pressure-Velocity Coupling Solution Algorithms, Numer. Heat Transfer, Part B, Vol.8, pp.635-652, 1985.

Laufer, J. (1954) The Structure of Turbulence in Fully Developed Pipe Flow, NACA Report No.TR-1174, 1954; see also Laufer, NACA TN-1053, 1950.

Launder, B.E. (1978) Heat and Mass Transport - Chapter 6 in 'Turbulence', P. Bradshaw, ed., Springer-Verlag, Berlin, 2nd Edition, 1978.

Launder, B.E. (1988) On the Computation of Convective Heat Transfer in Complex Turbulent Flows, ASME J. of Heat Transfer, Vol.110, pp.1112-1128, 1988.

Launder, B.E., Priddin, C.H. and Sharma, B.I. (1977) The Calculation of Turbulent Boundary Layers on Spinning and Curved Surfaces, ASME J. of Fluids Engng., Vol.99, pp.231-239, 1977

Launder, B.E. and Spalding, D.B. (1974) The Numerical Computation of Turbulent Flows, Comp. Meth. in Appl. Mech. and Engng., Vol.3, pp.269-289, 1974.

Lawn, C.J. (1976) Flow Measurements to Establish the Mechanism of Heat Transfer from a Rib Roughened Surface, CEGB Report RD/B/N 3514, 1976.

Lee, M.J., Kim, J. and Moin, P. (1990) Structure of Turbulence at High Shear Rate, J. Fluid Mech., Vol.216, pp.561-583, 1990.

Leonard, A. (1974) Energy Cascade in Large Eddy Simulation of Turbulent Fluid Flows, Advances in Geophysics, Vol.18, Part A, pp.237-248, 1974.

Leonard, B.P. (1979) A Stable and Accurate Convective Modelling Procedure Based on Quadratic Upstream Interpolation, Comp. Meth. Appl. Mech. Engng., Vol.19, pp.59-98, 1979.

Lesieur, M. and Rogallo, R. (1989) Large Eddy Simulation of Turbulent Diffusion in Isotropic and Stably-Stratified Turbulence, ERCOFTAC Bulletin III, pp.5-6, June 1989.

Leslie, D.C. and Quarini, G.L. (1979) The Application of Turbulence Theory to the Formulation of Subgrid Modelling Procedures, J. Fluid Mech., Vol.91, Part 1, pp.65-91, 1979.

Li, T.Y. and Yorke, J.A. (1975) Period Three Implies Chaos, Amer. Math. Monthly, Vol.82, p.985, 1975.

Lilly, D.K. (1966) On the Application of the Eddy Viscosity Concept in the Inertial Subrange of Turbulence, Report NCAR-123, National Center for Atmospheric Research, Boulder, Colo., USA, 1966.

Lilly, D.K. (1967) The Representation of Small-Scale Turbulence in Numerical Simulation Experiments, Procs. IBM Scientific Computing Symposium on Environmental Sciences, Thomas J. Watson Res. Center, Yorktown Heights, 1967, IBM-Form No.320-1951, pp.195-210.

Liou, T.-M., Chang, Y. and Hwang, D.-W. (1990) Experimental and Computational Study of Turbulent Flows in a Channel With Two Pairs of Turbulence Promoters in Tandem, ASME J. of Fluids Engng., Vol.112, pp.302-310, Sept. 1990.

Liou, T.-M. and Kao, C.-F. (1988) Symmetric and Asymmetric Turbulent Flows in a Rectangular Duct with a Pair of Ribs, ASME J. of Fluids Engng., Vol.110, pp.373-379, Dec. 1988.

Lo, S.M. (1987) Numerical Prediction of Particle Acceleration Due to Interfacial Drag. An Application of the Two-Fluid Model IPSA Implemented in the FLOW3D Computer Code, Harwell Report AERE-R 12599, 1987.

Lo, S.M. and Hope, C.B. (1989) The Implementation of a Multi-Phase Flow Model into Release 2 of the Harwell-FLOW3D Computer Code. Part 1: Momentum Transfer, Harwell Report AERE-R 13652, Sept. 1989.

Lockett, J.F. (1987) Heat Transfer from Roughened Surface Using Laser Interferometry, Ph.D. Thesis, Dept. of Mech. Engng., The City University, London, 1987.

Lockett, J.F. and Collins, M.W. (1986) Problems in Using Holographic Interferometry to Resolve the Four-Dimensional Character of Turbulence. Part I: Theory and Experiment; Part II: Image and Data Processing, Int. J. Opt. Sensors, Vol.1, No.3, pp.211-234, 1986.

Lockett, J.F. and Collins, M.W. (1990) Holographic Interferometry Applied to Rib-Roughness Heat Transfer in Turbulent Flow, Int. J. of Heat and Mass Transfer, Vol.33, No.11, pp.2439-2449, 1990.

Lockett, J.F., Hunter, J.C., Voke, P.R. and Collins, M.W. (1985) Investigation of Convective Heat Transfer Enhancement Using Real-Time Holographic Interferometry, Procs. 6th Int. Conf. on Photon Correlation and Other Optical Techniques in Fluid Mechanics, Univ. of Cambridge, Cambridge, UK, July 1985.

Lomax, H. (1982) Some Prospects for the Future of Computational Fluid Dynamics, AIAA Journal, Vol.20, No.8, p.1033, 1982.

Lonsdale, R.D. (1989) ASTEC, Release 1.7 B: User Manual, AEA-Dounreay Report, Nov. 1989.

Lorenz, E.N. (1963) Deterministic Nonperiodic Flow, J. Atmos. Sci., Vol.20 pp.130-141, 1963.

Lorenz, E.N. (1979) Predictability: Does the Flap of a Butterfly's Wings in Brazil Set Off a Tornado in Texas?, Procs. Annual Meeting of the American Association for the Advancement of Science (Invited Lecture), Washington, DC, 29 Dec. 1979.

Love, M.D. and Leslie, D.C. (1977) Studies of Subgrid Modelling with Classical Closures and Burgers' Equation, Procs. 1st Symposium on Turbulent Shear Flows, Pennsylvania State University, University Park, PA, USA, 18-20 April 1977 (Turbulent Shear Flows 1, F. Durst, B.E. Launder and F.W. Schmidt, eds., Springer-Verlag, Berlin-Heidelberg-New York, 1979, pp.353-369).

Lumley, J.L. (1992) Some Comments on Turbulence, Phys. Fluids A, Vol.4, No.2, pp.203-211, Feb. 1992.

Lummer, M. and Baumann, W.W. (1989) Direct Numerical Simulation of an Incompressible Plane Mixing Layer, Numerical Methods in Laminar and Turbulent Flow, Vol.6, part 2, C. Taylor et al., eds., Pineridge Press, Swansea, U.K., 1989, pp.1603-1613 (Procs. 6th Int. Conf. held at Swansea, UK, July 1989).

McDonough, J.M. and Bywater, R.J. (1986) Large-Scale Effects on Local Small-Scale Chaotic Solutions to Burgers' Equation, AIAA Journal, Vol.24, No.12, pp.1924-1930, Dec. 1986.

McDonough, J.M., Bywater, R.J. and Buell, J.C. (1984.a) An Investigation of Strange Attractor Theory and Small-Scale Turbulence, AIAA Paper 84-1674, AIAA 17th Fluid Dynamics, Plasma Dynamics, and Laser Conference, Snowmass, Colo., USA, June 25-27, 1984.

McDonough, J.M., Buell, J.C. and Bywater, R.J. (1984.b) A Comparison of Routes to a Strange Attractor in One-Dimensional Local Models of Turbulent Free and Forced Convection, ASME Paper 84-WA/HT-16, Dec. 1984.

McMillan, O.J. and Ferziger, J.H. (1979) Direct Testing of Subgrid-Scale Models, AIAA Journal, Vol.17, No.12, pp.1340-1346, Dec. 1979.

McMillan, O.J., Ferziger, J.H. and Rogallo, R.S. (1980) Tests of New Subgrid Scale Models in Strained Turbulence, Procs. AIAA 13th Fluid & Plasma Dynamics Conference, AIAA paper No.80-1339, 1980.

Mandelbrot, B.B. (1977) Fractals: Form, Chance, and Dimension, W.H.Freeman & Co., San Francisco, 1977.

Mansour, N.N., Ferziger, J.H. and Reynolds, W.C. (1979) Large-Eddy Simulation of a Turbulent Mixing Layer, Report No.TF-11, Thermosciences Division, Dept. of Mechanical Engineering, Stanford University, Stanford, CA, USA, 1978.

Mansour, N.N., Moin, P., Reynolds, W.C. and Ferziger, J.H. (1979) Improved Methods for Large-Eddy Simulation of Turbulence, Procs. 1st Symposium on Turbulent Shear Flows, Pennsylvania State University, University Park, PA, USA, 18-20 April 1977 (Turbulent Shear Flows 1, F. Durst, B.E. Launder and

F.W. Schmidt, eds., Springer-Verlag, Berlin-Heidelberg-New York, 1979, pp.386-401).

Mantle, P.L. (1966) A New Type of Roughened Heat Transfer Surface Selected by Flow Visualisation Techniques, Procs. 3rd International Heat Transfer Conference, Chicago, USA, 1966, Vol.1, pp.45-55.

Mantle, P.L., Freeman, A.R. and Watts, J. (1971) Conductivity Effects of Ribbed Surface Heat Transfer, Int. J. of Heat and Mass Transfer, Vol.14, pp.1825-1834, 1971.

Martin, S. and Drain, L.E. (1986) Investigation of Turbulent Flow in a Ribbed Wall Flow Channel Using Two Component Laser Doppler Anemometry, Harwell Report AERE-R 12080, March 1986.

Mason, P.J. (1987) Large Eddy Simulation of a Convective Atmospheric Boundary Layer, Procs. 6th Symp. Turbulent Shear Flows, Toulouse, France, Sept. 7-9, 1987 (Preprints, pp.12.4.1-12.4.4).

Mason, P.J. (1991) Large Eddy Simulation of Turbulent Diffusion, Procs. Int. Conf. 'New Techniques in Mathematical and Computational Modelling of Turbulent Diffusion and Mixing in Industrial and Environmental Problems', Loughborough University, UK, March 26-28, 1991.

Mason, P.J. and Callen, N.S. (1986) On the Magnitude of the Subgrid-Scale Eddy Coefficient in Large-Eddy Simulations of Turbulent Channel Flow, J. Fluid Mech., Vol.162, pp.439-462, 1986.

Mason, P.J. and Thomson, D.J. (1987) Large-Eddy Simulations of the Neutral-Static-Stability Planetary Boundary Layer, Quarterly J. Roy. Meteor. Soc., Vol.113, pp.413-443, 1987.

Mètais, O. and Lèsieur, M. (1989) Large-Eddy Simulations of Isotropic and Stably-Stratified Turbulence, in "Advances in Turbulence 2", H.-H.Fernholz and H.E.Fiedler, eds., Springer-Verlag, Berlin, 1989, pp.371-376 (Procs. 2nd European Turbulence Conference, Berlin, Aug.30-Sept.2, 1988).

Militzer, J., Nicoll, W.B. and Alpay, S.A. (1977) Some Observations on the Numerical Calculation of the Recirculation Region of Twin Parallel Symmetric Jet Flows, Procs. 1st Symposium on Turbulent Shear Flows, Pennsylvania State University, University Park, PA, USA, 18-20 April 1977 (Preprints).

Miner, E.W., Swean, T.F.jr., Handler, R.A. and Leighton, R.I. (1989) Evaluation of Wall-Damping Models by Comparison with Direct Simulations of Turbulent Channel Flow, Numerical Methods in Laminar and Turbulent Flow, Vol.6, part 2, C. Taylor et al., eds., Pineridge Press, Swansea, U.K., 1989, pp.273-284 (Procs. 6th Int. Conf. held at Swansea, UK, July 1989).

Moeng, C.-H. (1984) A Large-Eddy Simulation Model for the Study of Planetary Boundary Layer Turbulence, J. Atmos. Sci., Vol.41, No.13, pp.2052-2062, July 1984.

Moeng, C.-H. (1986) Large-Eddy Simulation of a Stratus-Topped Boundary Layer. Part I: Structure and Budgets, J. Atmos. Sci., Vol.43, No.23, pp.2886-2900, Dec. 1986.

Moeng, C.-H. (1987) Large-Eddy Simulation of a Stratus-Topped Boundary Layer. Part II: Implications for Mixed-Layer Modeling, J. Atmos. Sci., Vol.44, No.12, pp.1605-1614, June 1987.

Moeng, C.-H. and Wyngaard, J.C. (1984) Statistics of Conservative Scalars in the Convective Boundary Layer, J. Atmos. Sci., Vol.41, pp.3161-3169, 1984.

Moeng, C.-H. and Wyngaard, J.C. (1986) An Analysis of Closures for Pressure-Scalar Covariances in the Convective Boundary Layer, J. Atmos. Sci., Vol.43, No.21, pp.2499-2513, Nov. 1986.

Moeng, C.-H. and Wyngaard, J.C. (1988) Spectral Analysis of Large-Eddy Simulations of the Convective Boundary Layer, J. Atmos. Sci., Vol.45, No.23, pp.3573-3587, Dec. 1988.

Moin, P. and Kim, J. (1980) On the Numerical Solution of Time-Dependent Viscous Incompressible Fluid Flows Involving Solid Boundaries, J. Comp. Phys., Vol.35, pp.381-392, 1980.

Moin, P. and Kim, J. (1982) Numerical Investigation of Turbulent Channel Flow, J. Fluid Mech., Vol.118, pp.341-377, 1982; also: NASA TM-81309, 1981.

Moin, P., Reynolds, W.C. and Ferziger, J.H. (1978) Large-Eddy Simulation of Incompressible Turbulent Channel Flow, Report No.TF-12, Thermoscience Division, Dept. of Mech. Engng., Stanford University, Stanford, CA, USA, 1978.

Moin, P., Rogers, M.M. and Moser, R.D. (1985) Structure of Turbulence in the Presence of Uniform Shear, Procs. 5th. Symposium on Turbulent Shear Flows, Cornell University, Ithaca, New York, Aug. 7-9, 1985 (Preprints, pp.17.21-17.26).

Moin, P., Shih, T.-H., Driver, D. and Mansour, N.N. (1990) Direct Numerical Simulation of a Three-Dimensional Turbulent Boundary Layer, Phys. Fluids A, Vol.2, No.10, pp.1846-1853, Oct.1990.

Morinishi, Y. and Kobayashi, T. (1990) Large Eddy Simulation of Backward Facing Step Flow, Proc. Int. Symp. on 'Engineering Turbulence Modeling and Experiments', Dubrovnik, Yugoslavia, W. Rodi and E.N. Ganic, eds., Elsevier, 1990.

Murakami, S., Mochida, A. and Hibi, K. (1987) Three-Dimensional Simulation of Air Flow Around a Cubic Model by Means of Large-Eddy Simulation, J. Wind Engineering and Industrial Aerodynamics, Vol.25, pp.291-305, 1987.

Nakayama, W. (1982) Enhancement of Heat Transfer, Procs. 7th International Heat Transfer Conference, Munich, FRG, 1982 - Heat Transfer 1982, Vol.1, pp.223-240.

Nallassamy, M. (1987) Turbulence Models and Their Applications to the Prediction of Internal Flows: A Review, Computers & Fluids, Vol.15, No.2, pp.151-194, 1987.

Nicolaides, C. and Hanratty, T.J. (1983) Computer Simulation of the Time Varying Velocity Field in the Viscous Wall Region, Procs. 4th Symposium on Turbulent Shear Flows, Karlsruhe, FRG, Sept. 12-14, 1983 (Preprints, pp.3.21-3.24).

Nicolis, G. and Prigogine, I. (1987) Exploring Complexity: An Introduction, R.Piper GmbH & Co., Munich, 1987 [italian edition, "La complessita' - Esplorazioni nei nuovi campi della scienza", G.Einaudi editore s.p.a., Torino, 1991].

Nieuwstadt, F.T.M. (1990) Direct and Large-Eddy Simulation of Free Covection, Procs. 9th International Heat Transfer Conference, Jerusalem, Israel, Aug. 19-24, 1990, Paper KN-3 - Heat Transfer 1990, G. Hetsrony et al., eds., Vol.1, pp.37-47, 1990.

Nieuwstadt, F.T.M. (1991) Large-Eddy Simulation of Line Source Dispersion in an Atmospheric Boundary Layer, Procs. Int. Conf. 'New Techniques in Mathematical and Computational Modelling of Turbulent Diffusion and Mixing in Industrial and Environmental Problems', Loughborough University, UK, March 26-28, 1991.

Nieuwstadt, F.T.M. and Brost, R.A. (1986) The Decay of Convective Turbulence, J. Atmos. Sci., Vol.43, No.6, pp.532-546, March 1986.

Nieuwstadt, F.T.M. and DeValk, J.P.J.M.M. (1987) A Large Eddy Simulation of Buoyant and Non-Buoyant Plume Dispersion in the Atmospheric Boundary Layer, Atmos. Envir., Vol.21, No.12, pp.2573-2587, 1987.

Nishikawa, S., Watanabe, Y., Fujitani, K., Himeno, R. and Takagi, M. (1991) Computational Study on Three-Dimensional Flow Around a Heavy-Duty Truck Body, Procs. EUROTECH-Direct '91, Thermofluids Engineering, Birmingham, UK, 2-4 July 1991.

Nishino, K. and Kasagi, N. (1989) Turbulence Statistics Measurements in a Two-Dimensional Channel Flow using a Three-Dimensional Particle Tracking Velocimeter, Procs. 7th Symp. Turbulent Shear Flows, Stanford University, CA, USA, Aug. 1989 - Vol.2, paper 22-1.

Noauthor (1990.a) Harwell-FLOW3D, Release 2.3: User Manual, Harwell Report, July 1990 (unpublished).

Noauthor (1990.b) Shark Skin Inspires New Surface Technology, Eureka on Campus, Spring 1990, pp.14-16.

Noauthor (1990.c) The PHOENICS Reference Manual, Report CHAM/TR/100, CHAM Ltd., London, 1990.

Noauthor (1990.d) STAR-CD Manual, Computational Dynamics, London, 1990.

Noauthor (1990.e) FLUENT Manual Version 3.3, CREARE.X Inc., Hanover, New Hampshire, USA, 1990.

Nusselt, V. (1927) Die Theorie des Winderhitzers, Z.Ver.Dt.Ing., Vol.71, pp.85-91, 1927.

Okada, K., Ono, M., Tomimara, T., Okuma, T., Konno, H. and Ohtani, S. (1972) Design and Heat Transfer Characteristics of New Plate Heat Exchanger, Heat Transfer - Japanese Research, Vol.1, pp.90-95, 1972.

Orszag, S.A. (1970) Analytical Theories of Turbulence, J. Fluid Mech., Vol.41, Part 2, pp.363-386, 1970 (Boeing Symposium on Turbulence).

Orszag, S.A. (1971) Numerical Simulation of Incompressible Flows Within Simple Boundaries: Accuracy, J. Fluid Mech., Vol.49, Part 1, pp.75-112, 1971.

Orszag, S.A. (1980) Spectral Methods for Problems in Complex Geometries, J. Comp. Phys., Vol.37, pp.70-92, 1980.

Orszag, S.A. and Kells, L.C. (1980) Transition to Turbulence in Plane Poiseuille and Plane Couette Flow, J. Fluid Mech., Vol.96, Part 1, pp.159-205, 1980.

Orszag, S.A. and Patterson, G.S. (1972) Numerical Simulation of Three-Dimensional Homogeneous Isotropic Turbulence, Phys. Rev. Letters, Vol.28, No.2, pp.76-79, 1972.

Panda, R., Sonnad, V., Clementi, E., Orszag, S.A. and Yakhot, V. (1989) Turbulence in a Randomly Stirred Fluid, Phys. Fluids A, Vol.1, No.6, pp.1045-1053, June 1989.

Patankar, S.V. (1980) Numerical Heat Transfer and Fluid Flow, McGraw-Hill, New York, 1980.

Patankar, S.V. (1988) Recent Developments in Computational Heat Transfer, ASME J. of Heat Transfer, Vol.110, pp.1037-1045, 1988.

Patankar, S.V. and Spalding, D.B. (1972) A Calculation Procedure for Heat, Mass and Momentum Transfer in Three-Dimensional Parabolic Flows, Int. J. of Heat and Mass Transfer, Vol.15, pp.1787-1806, 1972.

Perrone, G. (1991) Simulazione numerica del moto e dello scambio termico in rigeneratori rotanti, Graduation Thesis in Nuclear Engineering, University of Palermo, Palermo, Italy, 1991 [in Italian].

Perry, A.E. (1986) A Description of Eddying Motions and Turbulence, Procs. 9th. Australasian Fluid Mechanics Conference, Auckland, 8-12 December, 1986, pp.7-12.

Perry, A.E. and Chong, M.S. (1982) On the Mechanism of Wall Turbulence, J. Fluid Mech., Vol.119, pp.173-217, 1982.

Perry, A.E., Chong, M.S. and Henbest, S. (1986) A Theoretical and Experimental Study of Wall Turbulence, J. Fluid Mech., Vol.165, pp.163-199, 1986.

Piomelli, U., Moin, P. and Ferziger, J.H. (1988) Model Consistency in Large Eddy Simulation of Turbulent Channel Flows, Phys. Fluids, Vol.31, No.7, pp.1884-1891, July 1988.

Piomelli, U., Ferziger, J.H., Moin, P. and Kim, J. (1989) New Approximate Boundary Conditions for Large-Eddy Simulations of Wall-Bounded Flows, Phys. Fluids A, Vol.1, No.6, pp.1061-1068, June 1989

Piomelli, U., Zang, T.A., Speziale, G.C. and Hussaini, M.Y. (1990) On the Large Eddy Simulation of Transitional Wall-Bounded Flows, Phys. Fluids A, Vol.2, No.2, pp.257-265, Feb. 1990.

Piomelli, U., Cabot, H., Moin, P. and Lee, S. (1991) Subgrid-Scale Backscatter in Turbulent and Transitional Flows, Phys.Fluids A, Vol.3, No.7, pp.1766-1771, July 1991.

Pletcher, R.H. (1988) Progress in Turbulent Forced Convection, ASME J. of Heat Transfer, Vol.110, pp.1129-1144, Nov. 1988.

Pomeau, Y. and Manneville, P. (1980) Intermittent Transition to Turbulence in Dissipative Dynamical Systems, Commun. Math. Phys., Vol.74, pp.189-197, 1980.

Prandtl, L. (1925) Berichte uber Untersuchungen zur ausgebildete Turbulenz, Z.A.M.M., Vol.5, p.136, 1925.

Provenzale, A. (1991) Simulazione numerica della turbolenza e della dispersione di effluenti aeriformi nello strato limite atmosferico, Graduation Thesis in Nuclear Engineering, University of Palermo, Palermo, Italy, 1991 [in Italian].

Rapier, A.C. (1977) A Correlation of Flow and Heat Transfer Data for Surfaces Roughened with Transverse Square Ribs of Pitch-to-Height Ratio of 7.2, UKAEA Report ND/R/63(W), 1977.

Rashidi, M. and Banerjee, S. (1990) The Effect of Boundary Conditions and Shear Rate on Streak Formation and Breakdown in Turbulent Channel Flows, Phys. Fluids A, Vol.2, No.10, pp.1827-1838, Oct.1990.

Reynolds, O. (1883) An Experimental Investigation of the Circumstances Which Determine Whether the Motion of Water shall be Direct or Sinuous, and the Law of Resistance in Parallel Channels, Phil. Trans. Roy. Soc., Vol.174, p.935, 1883.

Reynolds, W.C. and Cebeci, T. (1978) Calculation of Turbulent Flows - Chapter 5 in 'Turbulence', P. Bradshaw, ed., Springer-Verlag, Berlin, 2nd Edition, 1978.

Rhie, C.M. (1981) A Numerical Study of the Flow Past an Isolated Airfoil with Separation, Ph.D. Thesis, Dept. of Mechanical and Industrial Engng., University of Illinois at Urbana-Champaign, USA, 1981.

Rhie, C.M. and Chow, W.L. (1983) Numerical Study of the Turbulent Flow Past an Airfoil with Trailing Edge Separation, AIAA Journal, Vol.21, pp.1527-1532, 1983.

Rizk, M.K. and Menon, S. (1988) Large Eddy Simulation of Axisymmetric Excitation Effects on a Row of Impinging Jets, Phys. Fluids, Vol.31, No.7, pp.1892-1903, July 1988.

Rizk, M.K. and Menon, S. (1989) Large Eddy Simulation of Excitation Effects on a VTOL Upwash Fountain, Phys. Fluids A, Vol.1, No.4, pp.732-740, April 1989.

Roache, P. (1972.a) On Artificial Viscosity, J. Comp. Phys., Vol.10, pp.169-184, 1972.

Roache, P. (1972.b) Computational Fluid Dynamics, Hermosa Publishers, Albuquerque, NM, USA, 1972.

Rogallo, R.S. (1977) An ILLIAC Program for the Numerical Simulation of Homogeneous Incompressible Turbulence, NASA TM-73203, 1977.

Rogallo, R.S. (1981) Numerical Experiments in Homogeneous Turbulence, NASA TM-81315, 1977.

Rogers, M.M., Moin, P. and Reynolds, W.C. (1986) The Structure and Modeling of the Hydrodynamic and Passive Scalar Fields in Homogeneous Turbulent Shear Flow, Report No.TF-25, Thermosciences Division, Dept. of Mechanical Engineering, Stanford University, Stanford, CA, USA, Aug. 1986.

Rogers, M.M. and Moser, R.D. (1985) Structure of Turbulence in the Presence of Uniform Shear, Procs. 5th Symposium on Turbulent Shear Flows, Cornell University, Ithaca, NY, USA, Aug. 7-9, 1985 (Preprints).

Rohsenow, W.M. et al., eds. (1986) Handbook of Heat Transfer Applications - Chapter 4 (Compact Heat Exchangers), McGraw-Hill, 2nd ed., 1986.

Rose, H.A. (1977) Eddy Diffusivity, Eddy Noise and Subgrid-Scale Modelling, J. Fluid Mech., Vol.81, Part 4, pp.719-734, 1977.

Rosenblad, G. and Kullendorff, A. (1975) Estimating Heat Transfer Rates from Mass Transfer Studies on Plate Heat Exchange Surfaces, Warme- u. Stoffubertr., Vol.8, pp.187-191, 1975.

Rubesin, M.W. (1979) Subgrid- or Reynolds-Stress Modeling for Three-Dimensional Turbulence Computation, Procs. AGARD Meeting on Turbulent Flows, The Hague, Netherlands, 1979.

Ruelle, D. (1978) Dynamical Systems with Turbulent Behaviour, in 'Mathematical Problems of Theoretical Physics', Lecture Notes in Physics, Vol.80, p.341, Springer-Verlag, Berlin-Heidelberg-New York, 1978.

Ruelle, D. and Takens, F. (1971) On the Nature of Turbulence, Commun. Math. Phys., Vol.20, pp.167-192, 1971.

Runchal, A.K. (1987) CONDIF: A Modified Central Difference Scheme for Convective Flows, Int. J. for Numer. Meth. in Engng., Vol.24, pp.1593-1608, 1987.

Schmidt, H. and Schumann, U. (1989) Coherent Structure of the Convective Boundary Layer Derived from Large-Eddy Simulations, J. Fluid Mech., Vol.200, pp.511-562, 1989

Schmitt, L. and Friedrich, R. (1987) Application of the Large-Eddy Simulation Technique to Turbulent Backward Facing Step Flow, Procs. 6th Symp. Turbulent Shear Flows, Toulouse, France, Sept. 7-9, 1987.

Schumann, U. (1975) Subgrid Scale Model for Finite Difference Simulations of Turbulent Flows in Plane Channels and Annuli, J. Comp. Phys., Vol.18, pp.376-404, 1975.

Schumann, U. (1989) Large-Eddy Simulation of Turbulent Diffusion with Chemical Reactions in the Convective Boundary Layer, Atmos. Envir., Vol.23, No.8, pp.1713-1727, 1989.

Schumann, U., Hauf, T., Höller, H., Schmidt, H. and Volkert, H. (1987) A Mesoscale Model for the Simulation of Turbulence, Clouds and Flow Over Mountains: Formulation and Validation Examples, Beitr. Phys. Atmosph., Vol.60, pp.413-446, 1987.

Schumann, U. and Herring, J.R. (1976) Axisymmetric Homogeneous Turbulence: a Comparison of Direct Spectral Simulations with the Direct-Interaction Approximation, J. Fluid Mech., Vol.76, Part 4, pp.755-782, 1976.

Schumann, U. and Patterson, G.S. (1978) Numerical Study of Pressure and Velocity Fluctuations in Nearly Isotropic Turbulence, J. Fluid Mech., Vol.88, Part 4, pp.685-709, 1978.

Shand, A.M. (1990) Particle Image Velocimetry in a Crossed Corrugated Acrylic Section, Harwell Report AEA-EE-0088, Dec.1990.

Silveira-Neto, A., Lesieur, M., Grand, D. and Metais, O. (1991) 3D Large-Eddy Simulations of Turbulence Behind a Backward-Facing Step, ERCOFTAC Bulletin No.9, pp.13-14, June 1991.

Smagorinsky, J. (1963) General Circulation Experiments with the Primitive Equations: Part.I. The Basic Experiment, Monthly Weather Review, Vol.91, pp. 99-164, 1963.

Smith, R.M. (1990) The Current Status of Turbulence Modelling in the Fluid Flow Code FEAT, January 1985, CEGB Report TPRD/B/0591/N85, 1985 (see also updated version, Jan. 1990).

Sommeria, G. (1976) Three-Dimensional Simulation of Turbulent Processes in an Undisturbed Tradewind Boundary Layer, J. Atmos. Sci., Vol.33, pp.216-241, 1976.

Sommeria, G. and Deardorff, J.W. (1977) Subgrid-Scale Condensation in Models of Nonprecipitating Clouds, J. Atmos. Sci., Vol.34, pp.344-355, 1977.

Spalding, D.B. (1972) A Novel Finite Difference Formulation for Differential Expressions Involving Both First and Second Derivatives, Int. J. for Numer. Meth. in Engng., Vol.4, pp.551-559, 1972.

Spalding, D.B. (1978) Discussion on "Turbulence Models for Heat Transfer", Procs. 8th International Heat Transfer Conference, Toronto, Canada, 1978 - Heat Transfer 1978, Vol.8: Discussions, p.8, Hemisphere, 1978.

Spalding, D.B. (1980) Mathematical Modelling of Fluid Mechanics, Heat Transfer and Mass Transfer Processes, Mech. Eng. Dept. Report No. HTS/80/1, Imperial College, London,1980.

Sparrow, E.M. and Tao, W.Q. (1983) Enhanced Heat Transfer in a Flat Rectangular Duct with Streamwise-Periodic Disturbances at One Principal Wall, ASME J. of Heat Transfer, Vol.105, pp.851-861, Nov.1983.

Speziale, C.G. (1985) Galilean Invariance of Subgrid-Scale Stress Models in the Large-Eddy Simulation of Turbulence, J. Fluid Mech., Vol.156, pp.55-62, 1985.

Stasiek, J. and Collins, M.W. (1991) Liquid Crystal Mapping of Local Heat Transfer in Crossed Corrugated Geometrical Elements for Air Heat Exchangers, Procs. EUROTECH-Direct '91, Thermofluid Engineering, Birmingham, UK, July 2-4, 1991.

Stone, H.L. (1968) Iterative Solution of Implicit Approximations of Multidimensional Partial Differential Equations, SIAM J. Numer. Anal., Vol.5, No.3, pp.530-558, Sept. 1968.

Swinney, H.L. and Gollub, J.P. (1978) The Transition to Turbulence, Physics Today, pp.41-49, Aug. 1978.

Swinney, H.L. and Gollub, J.P., eds. (1981.a) Hydrodynamic Instabilities and Transition to Turbulence, Springer-Verlag, Berlin-Heidelberg-New York, 1981.

Swinney, H.L. and Gollub, J.P. (1981.b) Introduction - Chapter 1 in 'Hydrodynamic Instabilities and Transition to Turbulence', H.L. Swinney and J.P. Gollub, eds., Springer-Verlag, Berlin-Heidelberg-New York, 1981, pp.1-6.

Taylor, G.I. (1970) Some Early Ideas About Turbulence, J. Fluid Mech., Vol.41, Part 1, pp.3-11, 1970.

Taylor, G.I. and Green, A.E. (1937) Mechanism of Production of Small Eddies from Larger Ones, Proc. Roy. Soc. London, Vol.A158, pp.499-521, 1937.

Teissèdre, C. and Dang, K. (1989) Spectral Transfer Analysis for Subgrid Scale Modelling, Numerical Methods in Laminar and Turbulent Flow, Vol.6, part 2, C. Taylor et al., eds, Pineridge Press, Swansea, U.K., 1989, pp.2069-2079 (Procs. 6th Int. Conf. held at Swansea, UK, July 1989).

Thompson, C.P. and Wilkes, N.S. (1982) Experiments with Higher-Order Finite Difference Formulae, Harwell Report AERE-R 10493, 1982.

Thompson, J.F., Warsi, Z.U. and Mastin, C.W. (1982) Boundary Fitted Coordinate Systems for Numerical Solution of Partial Differential Equations - A Review, J. Comp. Phys., Vol.47, pp.1-108, 1982.

Tsai, H.M. and Leslie, D.C. (1990) Large Eddy Simulation of a Developing Turbulent Boundary Layer at a Low Reynolds Number, Int. J. for Numer. Meth. in Fluids, Vol.10, pp.519-555, 1990.

Tsai, H.M., Leslie, D.C. and Voke, P.R. (1989.a) Report to CEGB on Large Eddy Simulation of Thermal Striping, Report QMC ER-1010, Queen Mary College, University of London, 1989.

Tsai, H.M., Leslie, D.C. and Voke, P.R. (1989.b) Prediction of Extremal Events by Numerical Simulation, Procs. 7th Symp. Turbulent Shear Flows, Stanford University, CA, USA, Aug. 1989, paper 4-4.

Tsai, H.M., Leslie, D.C. and Voke, P.R. (1991) Thermal Striping: Structures in Interacting Jets, in "Turbulence and Coherent Structures", O.Mètais and M.Lèsieur, eds., Kluwer Academic, 1991, pp.125-138 (selected papers from Turbulence '89).

Ushijima, K. (1991) Estimation of Sub-Grid and Grid Scales Turbulence for LES Simulation of the Impinging Jet Experiment, Nuclear Electric Memo. TD/STB/MEM/0195, Technology Division, Nuclear Electric, UK, 1991.

VanDriest, E.R. (1956) On Turbulent Flow Near a Wall, J. Aero. Sci., Vol.23, No.11, pp.1007-1011, 1956.

VanDoormal, J.P. and Raithby, G.D. (1984) Enhancement of the SIMPLE Method for Predicting Incompressible Fluid Flows, Numer. Heat Transfer, Vol.7, pp.147-163, 1984.

Voke, P.R. (1982) Fluid Dynamic Simulations in Curvilinear Coordinate Systems, Harwell Report AERE-R 10548, Oct. 1982.

Voke, P.R. (1989) Multiple Mesh Simulation of Low Reynolds Number Turbulent Channel Flow, Numerical Methods in Laminar and Turbulent Flow, Vol.6, part 2, C. Taylor et al., eds, Pineridge Press, Swansea, U.K., 1989, pp.1567-1579 (Procs. 6th Int. Conf. held at Swansea, UK, July 1989).

Voke, P.R. (1990) Multiple Mesh Simulation of Turbulent Flow, Report QMW EP-1082, Queen Mary College and Westfield College, University of London, UK, 1990.

Voke, P.R. and Collins, M.W. (1983.a) Large Eddy Simulation: Retrospect and Prospect, Physico-Chemical Hydrodynamics, Vol.4, No.2, pp.119-161, 1983.

Voke, P.R. and Collins, M.W. (1983.b) Fluid Dynamic Simulations in General Coordinates, Numerical Methods in Laminar and Turbulent Flow, Vol.3, C. Taylor, J.A. Johnson and W.R. Smith, eds., Pineridge Press, Swansea, U.K., 1983, pp.1204-1213 (Procs. 3rd Int. Conf. held at Swansea, UK, July 1983).

Voke, P.R. and Collins, M.W. (1984.a) Large Eddy Simulation of Turbulent Flow in Plane and Distorted Channels, Paper HTFS RS 551, HTFS Sponsors Conference, University of Conventry, Coventry, U.K., 1984, pp.349-358.

Voke, P.R. and Collins, M.W. (1984.b) Forms of the Generalised Navier-Stokes Equations, J. Engng. Math., Vol.18, pp.219-233, 1984.

Voke, P.R., Tsai, H.M. and Collins, M.W. (1985) The Use of Chebychev Polynomials in Spectral Fluid Dynamic Simulations, Procs. Conference on Computation in Fluid Dynamics, Univ. of Reading, UK, 1985.

Von Karman, Th. (1937) J. Aero. Sci., Vol.4, p.131, 1937.

Vreugdenhil, C.B. (1989) Computational Hydraulics, Springer-Verlag, Berlin, 1989.

VV.AA. (1989-1992) Local Heat Transfer and Fluid Flow Fields in Crossed Corrugated Elements for Rotary Heat Exchangers - Reports 1 to 10, Thermofluids Engineering Res. Centre, City University, London, October 1989 to May 1992.

Warburton, C. (1972) The Results of Heat Transfer and Pressure Drop Tests in the BNC Air Rig on Surfaces Roughened by Transverse Ribs, CEGB Report RD/B/M/1956, Central Electricity Generating Board, UK, 1972.

Watts, J. and Williams, F. (1981) A Technique for the Measurement of Local Heat Transfer Rates Using Copper Foil, CEGB Report RD/8/5023 N81, HTSG/N(81)18, April 1981.

Weinstein, L.M., Beeler, G.B. and Lindermann, A.M. (1985) High Speed Holocinematographic Velocimetry for Studying Turbulent Flow Control Physics, AIAA Paper 85-0526, AIAA Shear Flow Control Conference, Boulder, Colo., USA, March 11-14, 1985.

Werner, H. and Wengle, H. (1989) Large-Eddy Simulation of Turbulent Flow Over a Square Rib in a Channel, in "Advances in Turbulence 2", H.-H.Fernholz and H.E.Fiedler, eds., Springer-Verlag, Berlin, 1989, pp.418-423 (Procs. 2nd European Turbulence Conference, Berlin, Aug.30-Sept.2, 1988).

Wilkes, N.S. (1980) Prediction of the Turbulent Fluid Flow Through a Channel with Rib Roughened Surfaces, Harwell Report AERE-R 9874, 1980.

Wilkes, N.S. (1981) The Prediction of Heat Transfer from Surfaces Roughened by Transverse Ribs, Harwell Report AERE-R 10293, 1981.

Wilkes, N.S. (1991) A Comparison of Commercially Available Computer Programs for Predicting Fluid Flows, Harwell Report AEA-IT (Draft), April 1991.

Wilkes, N.S. and Clarke, D.S. (1989) Algebraic and Direct Stress Modelling Using a Body-Fitted Finite Difference Method with a Non Staggered Grid, Numerical Methods in Laminar and Turbulent Flow, Vol.6, part 2, C. Taylor et al., eds, Pineridge Press, Swansea, U.K., 1989, pp.1627-1637 (Procs. 6th Int. Conf. held at Swansea, UK, July 1989).

Wilkes, N.S. and Firth, R.J. (1981) Prediction of Fluid Flow Over a Transverse Ribbed Surface Using Finite Difference Methods with a k-ε Turbulence Model, UKAEA Report RD/B/5098 N81, HTSG/N(80)32, Sept. 1981.

Wilkes, N.S., Guilbert, P.W., Shepherd, C.M. and Simcox, S. (1989) The Application of Harwell-FLOW3D to Combustion Problems, Harwell Report AERE-R 13508, June 1989.

Wilkes, N.S., Thompson, C.P., Kightley, J.R., Jones, I.P. and Burns, A.D. (1985) On the Numerical Solution of 3-D Incompressible Flow Problems, Harwell Report AERE-CSS 179, 1985.

Wilkie, D. (1966) Forced Convection Heat Transfer from Surfaces Roughened by Transverse Ribs, Procs. 3rd International Heat Transfer Conference, Chicago, USA, 1966, Vol.1, pp.1-9.

Williams, F. and Watts, J. (1970) The Development of Rough Surfaces with Improved Heat Transfer Performance and a Study of the Mechanisms Involved, Procs.4th International Heat Transfer Conference, Paris-Versailles, 1970.

Wilmott, A.J. (1969) The Regenerative Heat Exchanger Computer Representation, Int. J. of Heat and Mass Transfer, Vol.12, pp.997-1014, 1969.

Winters, K.H. (1984) ENTWIFE Command Reference Manual (Release 1), Harwell Report AERE-R 11079, 1984.

Winters, K.H. and Jackson, C.P. (1984) A Note on the Keyword Input Facility, INPROC, Harwell Report AERE-M 3375, 1984.

Winters, K.H. and Jackson, C.P. (1989) TGIN Language Reference Manual: OUTPUT DATA Commands, Harwell Report AERE-R (Draft), 2nd edition, March 1989.

Wyngaard, J.C., ed. (1984) Large-Eddy Simulation - Guidelines for Its Application to Planetary Boundary Layer Research, DTIC, AD-A146381, 1984.

Yakhot, V. and Orszag, S.A. (1985) Renormalization Group Formulation of Large Eddy Simulation, in 'Nonlinear Dynamics of Transcritical Flows', H.L. Jordan, H. Oertel and K. Roberts, eds., Lecture Notes in Engineering 13, Springer - Verlag, Berlin, 1985, pp.155-174.

Yakhot, V., Orszag, S.A. and Yakhot, A. (1987) Heat Transfer in Turbulent Fluids - I. Pipe Flow, Int. J. of Heat and Mass Transfer, Vol.30, No.1, pp.15-22, 1987.

Yeh, T.T. and Van Atta, C.W. (1973) Spectral Transfer of Scalar and Velocity Fields in Heated-Grid Turbulence, J. Fluid Mech., Vol.58, Part 2, pp.233-261, 1973.

Yorke, J.A. and Yorke, E.D. (1981) Chaotic Behavior and Fluid Dynamics, in 'Hydrodynamic Instabilities and Transition to Turbulence', H.L.Swinney and J.P. Gollub, eds., Springer-Verlag, Berlin-Heidelberg-New York, 1981, Chapter 4, pp.77-95.

Yoshizawa, A. (1982) A Statistically-Derived Subgrid Model for the Large-Eddy Simulation of Turbulence, Phys. Fluids, Vol.25, pp.1532-1538, 1982.

Yoshizawa, A. (1983) A Statistical Theory of Thermally-Driven Turbulent Shear Flows, with the Derivation of a Subgrid Model, J. Phys. Soc. Japan, Vol.52, pp.1194-1205, 1983.

Yoshizawa, A. (1986) Statistical Theory for Compressible Turbulent Shear Flows, with the Application to Subgrid Modeling, Phys. Fluids, Vol.29, No.7, 1986.

Yoshizawa, A. (1987) Large-Eddy Simulation of Turbulent Flows, Chapter 32 in 'Encyclopedia of Fluid Mechanics', N.P. Cheremisinoff, ed., Vol.6, pp.1277-1297, Gulf Publ. Co., 1987.

Yoshizawa, A. (1989) Subgrid-Scale Modelling with a Variable Length Scale, Phys. Fluids A, Vol.1, No.7, pp.1293-1295, July 1989.

Yoshizawa, A. and Horiuti, K. (1985) Large-Eddy Simulation of Turbulent Channel Flow by One-Equation Modeling, J. Phys. Soc. Japan, Vol.54, pp. 2855-2865, 1985.

Zogg, M. (1972) Dissertation, Technische Hoeschule Zurich, 1972.

Appendix A - Definitions and main formulae of tensor calculus

A.1 Coordinate transformation

Let x^i be cartesian coordinates and ξ^i generalized coordinates. A computational domain of arbitrary shape in the "physical" space x^i can be mapped into a simple parallelepiped of the "computational" space ξ^i (see Figure 3.2). Let a non-singular coordinate transformation between the x^i's and the ξ^i's exist, so that both the functions $\xi^i = \xi^i(x^1,x^2,x^3)$ and their inverses $x^i = x^i(\xi^1,\xi^2,\xi^3)$ are single-valued. Any body-fitted grid in the "physical" space x^i can be generated by specifying the functions $x^i(\xi^j)$, either analytically or in discrete form, e.g. by specifying the coordinates x^i of all cell corners.

The geometrical properties of the coordinate transformation are described by the Jacobian matrix:

$$J_i^{\ k} = \partial x^k/\partial \xi^i \qquad \text{(A.1.a)}$$

or from the inverse Jacobian matrix:

$$J_i^{\ k} = \partial \xi^k/\partial x^i \qquad \text{(A.1.b)}$$

The determinant $J=\det(J_i^{\ k})$ is called the Jacobian of the transformation and is nonzero everywhere for non-singular transformations. The terms:

$$A_i^{\ k} = J\,\overline{J}_i^{\ k} \qquad \text{(A.1.c)}$$

form the adjugate Jacobian matrix.

The elements of the Jacobian matrices allow two systems of basis vectors to be defined in the curvilinear space ξ^i: a system of covariant vectors $\mathbf{e}_{(i)} = \partial \mathbf{x}/\partial \xi^i$ (tangential to the coordinate lines) and a system of contravariant vectors $\mathbf{e}^{(i)} = \partial \xi^i/\partial \mathbf{x}$ (normal to the coordinate surfaces ξ^i=constant). Their cartesian components (in the x^i-system) are given by:

$$[\mathbf{e}_{(i)}]_k = J_i^{\ k} \qquad \text{(A.2.a)}$$

$$[\mathbf{e}^{(i)}]_k = J_k^{\ i} \qquad \text{(A.2.b)}$$

The Jacobian J is the volume of the parallelepiped Ω spanned by the covariant basis vectors $\mathbf{e}_{(i)}$. The area vectors (normal to the faces of Ω and having moduli equal to the corresponding areas) are:

$$\mathbf{A}^{(1)} = \mathbf{e}_{(2)} \times \mathbf{e}_{(3)} \qquad \text{(A.3.a)}$$

and similar; they can also be expressed as:

$$\mathbf{A}^{(i)} = J\, \mathbf{e}^{(i)} \qquad \text{(A.3.b)}$$

so that, see Eqn.(A.2.b), their cartesian components are given by:

$$A^{(i)}{}_k = J\, \bar{J}_k^{\,i} = A_k{}^i \qquad \text{(A.4)}$$

i.e., the vectors $\mathbf{A}^{(i)}$ are the rows of the adjugate Jacobian matrix, Eqn.(A.1.c).

A.2 Scalars, vectors and tensors

a) Scalars - A scalar field Q is invariant, i.e. its values do not depend on the particular reference frame used.

b) Vectors - A vector $\mathbf{v}$ can be expressed as a linear combination of either the covariant basis vectors $\mathbf{e}_{(i)}$:

$$\mathbf{v} = v'^{i}\, \mathbf{e}_{(i)} \qquad \text{(A.5.a)}$$

or the contravariant basis vectors $\mathbf{e}^{(i)}$:

$$\mathbf{v} = v'_i\, \mathbf{e}^{(i)} \qquad \text{(A.5.b)}$$

(summation over repeated indices is not implied here). The coefficients v'_i and v'^{i} are respectively called covariant and contravariant components of $\mathbf{v}$. The apex will be omitted for the components of $\mathbf{v}$ in a cartesian frame x^i; in this case, covariant and contravariant components coincide ($v^i = v_i$).

In changing the reference frame from $\xi^{i(old)}$ to $\xi^{i(new)}$ the covariant components are transformed as:

$$v'_i{}^{(new)} = v'_j{}^{(old)} \partial \xi^{j(old)} / \partial \xi^{i(new)} \qquad (A.6.a)$$

i.e., like the partial derivatives of a scalar field, while the contravariant components are transformed as:

$$v'^{i(new)} = v'^{j(old)} \partial \xi^{i(new)} / \partial \xi^{j(old)} \qquad (A.6.b)$$

i.e., like the differentials of the independent variables.

The transformation rules (A.6) may also be used as the <u>definition</u> of covariant and contravariant (simple) scalar systems. Of course, they still hold if either of the old or new coordinate systems is cartesian.

c) <u>Tensors</u> - A tensor **T** can be defined as a double system of covariant (T_{ij}), contravariant (T^{ij}) or mixed ($T_i{}^j$) scalars, which follow the transformation rules:

$$T_{ij}^{(new)} = T_{lk}^{(old)} \left[\partial \xi^{l(old)} / \partial \xi^{i(new)}\right] \left[\partial \xi^{k(old)} / \partial \xi^{j(new)}\right] \qquad (A.7.a)$$

$$T^{ij(new)} = T^{lk(old)} \left[\partial \xi^{i(new)} / \partial \xi^{l(old)}\right] \left[\partial \xi^{j(new)} / \partial \xi^{k(old)}\right] \qquad (A.7.b)$$

$$T_i{}^{j(new)} = T_l{}^{k(old)} \left[\partial \xi^{l(old)} / \partial \xi^{i(new)}\right] \left[\partial \xi^{j(new)} / \partial \xi^{k(old)}\right] \qquad (A.7.c)$$

Of special relevance is the <u>metric tensor</u> **g**, expressed in covariant and contravariant components, respectively, by:

$$g_{ij} = J_i{}^k J_i{}^k = \left[\partial x^k / \partial \xi^i\right] \left[\partial x^k / \partial \xi^j\right] = \mathbf{e}_{(i)} \cdot \mathbf{e}_{(j)} \qquad (A.8.a)$$

$$g^{ij} = \bar{J}_k{}^i \bar{J}_k{}^j = \left[\partial \xi^i / \partial x^k\right] \left[\partial \xi^j / \partial x^k\right] = \mathbf{e}^{(i)} \cdot \mathbf{e}^{(j)} \qquad (A.8.b)$$

It is easily shown that the determinant g of **g** equals J^2, i.e., $J=\sqrt{g}$. The metric tensor can be used to "raise" and "lower" indices, i.e. to express the contravariant components of a vector or tensor in terms of the covariant ones, etc.; for example:

$$v^j = g^{ij} v_j \qquad (A.9.a)$$

$$T^{ij} = g^{li} g^{kj} T_{lk} \qquad (A.9.b)$$

Rather than working with the contravariant components v'^i of a vector field $\mathbf{v}$, it is more physical to work with the normal flux components, defined as:

$$v_\perp^i \equiv \sqrt{g}\, v'^i \tag{A.10}$$

i.e., proportional to the contravariant components v'^i. It is easily shown that:

$$v_\perp^i = \mathbf{v}\cdot\mathbf{A}^{(i)} \tag{A.11}$$

in which $\mathbf{A}^{(i)} = \sqrt{g}\,\mathbf{e}^{(i)}$ are the area vectors defined previously.

A.3 Covariant derivation

a) Scalars - The partial derivatives of a scalar field Q with respect to the (general) coordinates ξ^i form a simple covariant system; i.e., the derivatives $\partial Q/\partial\xi^i$ are the covariant components of the vector ∇Q. Its contravariant components can be obtained by using the metric tensor to raise indices, as discussed in Section A.2:

$$(\nabla Q)^i = g^{ij}\,(\nabla Q)_j = g^{ij}\,\partial Q/\partial\xi^j \tag{A.12}$$

b) Vectors - Consider a vector $\mathbf{v}$ having components v'_i or v'^i in the general coordinate system ξ^i, and components v^i $(\equiv v_i)$ in the cartesian system x^i. It is easy to verify that the partial derivatives of the components v'_i or v'^i with respect to the coordinates ξ^l do not constitute a tensor, i.e. are not transformed according to Eqns.(A.7) when the reference frame is changed. Thus, any differential equation, e.g. Eqn.(3.1), which is written in terms of partial derivatives, cannot be generalized as it stands to reference systems other than cartesian. Therefore, it is necessary to recast it into an invariant form; this is done by introducing the so called "covariant derivatives" of a vector $\mathbf{v}$.

As $v'_i = v^k\,\partial x^k/\partial\xi^i$, the generic partial derivative $\partial v'_i/\partial\xi^l$ can be written as:

$$\frac{\partial v'_i}{\partial \xi^l} = \frac{\partial}{\partial \xi^l}\left(v^k \frac{\partial x^k}{\partial \xi^i} \right) = \frac{\partial v^k}{\partial \xi^l}\frac{\partial x^k}{\partial \xi^i} + v^k \frac{\partial^2 x^k}{\partial \xi^l \partial \xi^i} \qquad \text{(A.13.a)}$$

or, observing that $v^k = v'^n \, \partial x^k/\partial \xi^n$ and $\partial v^k/\partial \xi^l = (\partial v^k/\partial x^j) * (\partial x^j/\partial \xi^l)$:

$$\frac{\partial v'_i}{\partial \xi^l} = \frac{\partial v^k}{\partial x^j}\frac{\partial x^j}{\partial \xi^l}\frac{\partial x^k}{\partial \xi^i} + v'^n \left[\frac{\partial x^k}{\partial \xi^n}\frac{\partial^2 x^k}{\partial \xi^l \partial \xi^i} \right] \qquad \text{(A.13.b)}$$

It is easily shown that, among the three terms of Eqn.(A.13.b), only the first term at the RHS possesses a tensor nature (i.e., is transformed according to Eqns.(A.7)). It constitutes the tensor $\nabla_l v'_i$ of the <u>covariant derivatives</u> of **v**. The term in brakets in Eqn.(A.13.b) is called <u>Christoffel symbol of the first kind</u>, and is synthetically denoted as [il,n]:

$$[il,n] \equiv \frac{\partial x^k}{\partial \xi^n}\frac{\partial^2 x^k}{\partial \xi^l \partial \xi^i} \qquad \text{(A.14)}$$

Eqn.(A.13.b) can now be written in a form involving the covariant derivatives:

$$\nabla_l v'_i = \frac{\partial v'_i}{\partial \xi^l} - [il,n]\, v'^n \qquad \text{(A.15)}$$

Eqn.(A.15) contains both covariant components v'_i and contravariant components v'^n; in order to express $\nabla_l v'_i$ in terms of covariant components only, the metric tensor g^{ij} can be used to raise the appropriate indices: $v'^n = g^{ij} v'_j$. Thus, Eqn.(A.15) can be written:

$$\nabla_l v'_i = \frac{\partial v'_i}{\partial \xi^l} - \{il,j\}\, v'_j \qquad \text{(A.16.a)}$$

in which the terms:

$$\{il,j\} \equiv g^{jn}[il,n] = g^{jn} \frac{\partial x^k}{\partial \xi^n} \frac{\partial^2 x^k}{\partial \xi^l \partial \xi^i} \qquad (A.17)$$

are called Christoffel symbols of the second kind, or connection coefficients.

Eqn.(A.16.a) expresses the covariant derivatives of **v** in terms of its covariant components v'_i. Similarly, it can be shown that:

$$\nabla_l v'^i = \frac{\partial v'^i}{\partial \xi^l} + \{jl,i\}\, v'^j \qquad (A.16.b)$$

which expresses the covariant derivatives of **v** in terms of its contravariant components v'^i.

Of particular interest is the covariant divergence of a vector field **v**. From Eqns.(A.8), (A.17) it follows that the connection coefficients can be written as:

$$\{ij,k\} = \frac{1}{2} g^{kl} \left\{ \frac{\partial g_{jl}}{\partial \xi^i} + \frac{\partial g_{il}}{\partial \xi^j} - \frac{\partial g_{ij}}{\partial \xi^l} \right\} \qquad (A.18.a)$$

and in particular, for j≡k:

$$\{ik,k\} = \frac{1}{2} g^{kl} \frac{\partial g_{kl}}{\partial \xi^i} \qquad (A.18.b)$$

From the derivation rules for determinants [Finzi and Pastori 1961] it follows that the last equation can be written:

$$\{ik,k\} = \frac{1}{2g} \frac{\partial g}{\partial \xi^i} = \frac{1}{2} \frac{\partial \ln g}{\partial \xi^i} \qquad (A.18.c)$$

Now, by definition the covariant divergence of **v** is (using for example contravariant components):

$$\nabla_l v'^i \equiv \frac{\partial v'^i}{\partial \xi^i} + \{ji,i\}\, v'^j \qquad \text{(A.19)}$$

in which summation over i and j is understood. By substistuting Eqn.(A.18.c), written for {ji,i}, into Eqn.(A.19), one has:

$$\nabla_i v'^i = \frac{\partial v'^i}{\partial \xi^i} + \frac{1}{2g}\frac{\partial g}{\partial \xi^j} v'^j \qquad \text{(A.20.a)}$$

and, after some algebraic manipulation and changes of indices:

$$\nabla_i v'^i = \frac{1}{\sqrt{g}}\frac{\partial}{\partial \xi^i}(\sqrt{g} v'^i) \qquad \text{(A.20.b)}$$

This is the covariant divergence of the vector field **v** expressed in terms of its contravariant components v'^i and of the Jacobian $J = \sqrt{g}$.